NASA TECHNICAL TRANSLATION

NASA TT F-356

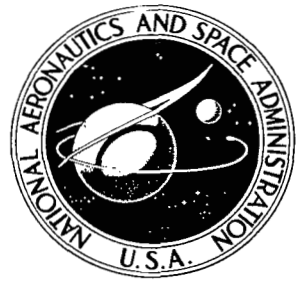

NASA TT F-356

RADIATION SAFETY DURING SPACE FLIGHTS

by V. G. Bobkov, et al.

Atomizdat, Moscow, 1964

NATIONAL AERONAUTICS AND SPACE ADMINISTRATION • WASHINGTON, D. C. • MAY 1966

RADIATION SAFETY DURING SPACE FLIGHTS

By V. G. Bobkov, V. P. Demin, I. B. Keirim-Markus,
Ye. Ye. Kovalev, A. V. Larichev, V. A. Sakovich,
L. N. Smirennyy, and M. A. Sychkov

Translation of "Radiatsionnaya Bezopasnost'
pri Kosmicheskikh Poletakh."
Atomizdat, Moscow, 1964.

NATIONAL AERONAUTICS AND SPACE ADMINISTRATION

For sale by the Clearinghouse for Federal Scientific and Technical Information
Springfield, Virginia 22151 – Price $7.00

TABLE OF CONTENTS

CHAPTER PAGE NO.

RADIATION SAFETY DURING SPACE FLIGHTS

V.G. Bolkov, V.P. Demin, I.B. Keirim-Markus, Ye.Ye. Kovalev', A.V. Larichev, V.A. Sakovich, L.N. Smirennyy, M.A. Sychkov

ABSTRACT

This is one of the first Soviet books which examines the problem of safety from radiation danger during space flight in detail. The book covers the following areas: cosmic radiation dosimetry, radiation conditions in space, interaction between radiation and matter, protection from space radiation.

Chapter 1 discusses the dosimetry of cosmic radiation. The experimental and mathematical dosimetry methods are reviewed. The effects of ionizing radiation on human beings and dosimetry methods are then examined.

Chapter 2 deals with primary galactic radiation in space (PCR), its interaction with the earth's magnetic field, its origin, and the tissue dose rate resulting from it. Radiation levels during several Soviet manned flights are presented.

Chapter 3, entitled "Solar Cosmic Radiation (SCR)," discusses the origin, frequency, mechanism, spectrum, resulting tissue dose rate, and methods of forecasting SCR.

Chapter 4 deals with the inner (i.e. close) radiation zone of the earth. The results derived from Soviet and American satellite experiments are described. The resulting dose is given.

Chapter 5 discusses the outer radiation zone of the earth, i.e., at altitudes of several hundred kilometers. The zone was mapped by Soviet and American satellites. The spectrum, structure, and resulting tissue dose are presented.

Chapter 6, entitled "Interaction of High-Energy Protons with Shielding Material," considers protons having energies of several tens and hundreds of Bev, which comprise the main part of corpuscular radiation from the SCR and from the inner radiation zone of the earth.

Chapter 7 discusses the shielding of manned spacecrafts from protons found in the inner radiation zone of the earth and those due to solar flares.

Chapter 8 treats shielding from electrons and electromagnetic radiation for flights near the earth.

Chapter 9 discusses nuclear engines and other nuclear power devices. Performance of chemical, nuclear, and electric (ion and plasma) jet engines is compared. The following nuclear engines are described: thermal-exchange type with homogeneous and heterogeneous reactors, electric-energy nuclear engine, turbogenerator nuclear engine, thermoemission type, and a type using nuclear explosions. Numerous American nuclear engine projects are reviewed.

Chapter 10 discusses shielding problems for space vehicles having a nuclear reactor. Nuclear spacecraft designs containing shielding are described.

INTRODUCTION

Two dates - October 4, 1957, and January 2, 1959 - marked the beginning of man's conquest of cosmic space. The launching of the first artificial earth satellite and the first cosmic rocket in the Soviet Union meant that the first and second cosmic velocities were finally surpassed. In addition, the gravitational barrier was overcome, which had blocked man's path to the cosmos for several ages. /3*

Flights in cosmic spacecrafts - which were carried out in the Soviet Union by Yu. A. Gagarin, G. S. Titov, A. G. Nikolayev, P. R. Popovich, V. F. Bykovskiy, by the first woman-cosmonaut V. V. Nikolayev-Tereshkova, and in the United States by John Glenn, M. Carpenter, by W. Shirra, and G. Cooper - showed that the remaining barriers on the path to the cosmos had been successfully overcome: unusual living conditions, weightlessness, acceleration at lift-off and at landing, and overheating during deceleration in the atmosphere. Moreover, intensive studies on cosmic space, which were stimulated by the successes in launching space vehicles, led to the discovery of new factors which were previously unknown. They showed that one very serious obstacle must still be encountered in the conquest of cosmic space - the radiation barrier.

Several years ago, it was assumed that cosmic radiation outside of the earth's atmosphere represents a very weak stream of particles having very great energy, which is stable in time. Calculations which were performed by separate authors (Tobias, Schaefer) showed that the danger from this radiation is not great, although it entails a certain amount of uncertainty, since the biological effect of this type of radiation has not been studied experimentally.

Radiation zones of the earth were discovered (Van Allen, Vernov, and Chudakov) with the aid of equipment which was placed on artificial earth satellites. On the basis of the first estimates, the dose rate in the radiation zones amounted to about 100 roentgens per hour, and thus the radiation zones of the earth were unexpectedly found to be a new source of radiation, which had to be taken into consideration. Some data pointed to the fact that similar radiation zones, which were possibly more powerful, existed around other planets (Jupiter, Venus), and these would be encountered during interplanetary flights. /4

The growing interest in cosmic radiation made it necessary to direct attention to the small sporadic variations in cosmic rays, which had been well known for a long period of time and which were

---

* Note: Numbers in the margin indicate pagination in the original foreign text.

compared with solar activity in 1942 (Forbush). Intensive studies, particularly studies on the phenomena occurring in February, 1956, showed that from time to time the sun is a source of powerful, corpusclar streams. According to some estimates, these streams create doses on the order of 10^4 rad in interplanetary space. The penetrating capacity of this radiation is such that some authors propose using protective screens having a thickness of 2-4 m, in order to lower the dose to permissible amounts. Thus,solar cosmic radiation is the second new factor comprising the radiation danger during cosmic flight. It is all the more serious because the radiation appears in an unexpected way, and the possibility of predicting it and taking protective measures against its stream is problematical to a considerable extent. These statements clearly illustrate the seriousness of the radiation barrier as an obstacle which is encountered on the path toward mastering the cosmos.

The problems of safety against radiation have been investigated intensely in recent years, in connection with the apparent significance of radiation danger during cosmic flights. A new branch of science - radiation safety during cosmic flights - has developed at an essentially very rapid tempo, along with its branches: dosimetry of cosmic radiation, protection from cosmic radiation, and others - each of which has specific characteristics.

Thus, for example, a new problem arises in the dosimetry of cosmic radiation - measurement of the tissue dose of radiation having very great energy and linear density of energy transfer. The problem arises anew as to the magnitude of the dose, which determines the result of radiation arising from a very irregular distribution of the doses in the organism, and under the effective radiation with relative biological effectiveness (RBE) which changes within extreme limits. The problems thus arise of developing new apparatus which would make it possible to measure this magnitude of the dose, taking the RBE into consideration, and to measure the distribution of the dose with respect to volume of the body and with respect to time. The necessity of predicting the radiation dose by means of different methods and equipment is thus apparent.

In order to provide protection from radiation, the distinct problems arise as to protection by means of partial absorbtion of charged particles, utilization of shadow protection, equipment and supplies which can be used as protection elements, and a radiation protection installation. The principal estimates show that atomic energy must be used for long cosmic flights. Thus, the necessity arises of combining protection from cosmic radiation with protection against radiation from the nuclear energy apparatus.

The characteristics of cosmic radiation dosimetry are discussed in this book, and the radiation conditions in cosmic space, the main interaction between cosmic radiation and matter, and protection from cosmic radiation are analyzed.

The authors have set themselves the problem of presenting a description, which is as complete as possible, of the problem of radiation safety during cosmic flights in chapters which deal with the sources of radiation, its levels, methods for measuring the doses, and the physical methods for providing protection against the radiation. In such an essential and rapidly-developing region, facts and concepts are constantly being reappraised, so that in time, when the book is published, there will doubtless be elements in it which are obsolete. Therefore, it must be regarded as a snapshot of data (and, possibly, information of the authors) in the given field. Since this is one of the first books which examines in detail the problems of radiation safety during cosmic flights, it will naturally have many defects, and the authors will appreciate any criticisms from the readers. /5

Chapters I and III in the book were written by I. B. Keirim-Markus, Chapter II and Chapter IV - by M. A. Sychkov, Chapter V and VIII by A. V. Larichev, Chapter VI by Ye. Ye. Kovalev, Chapter VII by Ye. Ye. Kovalev'and L. N. Smirenniy, Chapter IX by V. G. Bobkov, and Chapter X - V. P. Demin and V. A. Sakovich.

The authors are indebted to all their co-workers who assisted in compiling this book.

CHAPTER 1

DOSIMETRY OF COSMIC RADIATION

1.1 Absorbed Dose

Life on the earth has developed under the protection of an /7
air covering, whose mass over each square centimeter of the surface amounts to 1 kg. Intense radiation of a different nature is in operation outside of the atmosphere, which includes ionizing radiation which is called cosmic rays. This primarily includes streams of charged atomic particles having high energy - protons, α-particles, atomic nuclei of light and medium elements from Li to Fe. In addition, streams of rapid electrons occur in the cosmic rays; these electrons, interacting with the atmosphere or with the casing of cosmic devices, produce X-ray radiation. They are also emitted by the sun.

Under the influence of cosmic rays, secondary radiation is formed, which is composed of neutrons and mesons, and cascades and stars of elementary particles are produced. Thus, all types of ionizing radiation are encountered in cosmic space. The energy of the particles and quanta of cosmic radiation reaches a magnitude of 10^{11} - 10^{18} ev; it far exceeds the amount which man has been able to obtain on earth by artificial means. As is apparent from its name, ionizing radiation actively influences matter, causing ionization and excitation of atoms and molecules, which sometimes leads to appreciable macroscopic changes which are for the most part harmful. Strong irradiation has a destructive effect on living nature. This explains the necessity for controlling and measuring ionizing radiation in the study and conquest of cosmic space.

Since radiation, which is very familiar to laboratories on the earth, comprises cosmic radiation, the problem of measuring its effect is in many respects solved by the methods of dosimetry of ionizing radiation - a branch of technical physics which has extensively developed during recent decades in connection with the utilization of atomic energy (Ref. 1 - Ref. 7). In addition, particles having very great energy are encountered in cosmic rays; the interaction of these particles with matter has not been given adequate study, and the dosimetry of these particles has developed very slightly. /8

A basic measurement for the interaction of ionizing radiation with a substance has been the radiation energy which is transmitted to the substance per unit of mass. This quantity is called the absorbed radiation dose D, and it is measured in ergs per gram or in rads (1 rad = 100 erg/g). The unit of electronvolts per gram (ev/g) and the derivatives of it 1 Mev/g = 10^6 ev/g = $1.60.10^{-8}$ rad are also

used. The dimensionality is $[D] = [L^2T^{-2}]$, i.e., is the same as the dimensionality of the square of velocity.

Absorbed doses on the order of 10^4 rad up to millirads are of great interest with respect to the effect of cosmic radiation on man and living nature. Radiation effects on inert matter expands this region up to quantities on the order of 10^{10} rad.

The following general relationship exists between the absorbed dose and the radiation energy E, which passes through a unit of area in the direction r:

$$D = -\frac{1}{\varrho}\cdot\frac{dE}{dr} = -\frac{1}{\varrho}\sum_i\left(n_i\frac{d\mathcal{E}_i}{dr_i} + \mathcal{E}_i\frac{dn_i}{dr_i}\right). \qquad (1.1)$$

Here ρ is the density of the substance, and n_i and r_i represent the stream and propagation direction of elementary particles and quanta of radiation having the energy $\mathcal{E}_i$.

With a certain approximation, we can write $\frac{d\mathcal{E}}{dr} = 0$, and $-\frac{dn}{dr} \approx \mu n$ for the quanta of electromagnetic radiation, where μ is the coefficient of electron transformation. Consequently, we have

$$D = \frac{1}{\varrho}\sum_i \mu_i n_i \mathcal{E}_i. \qquad (1.2)$$

For charged particles, we have

$$D = \sum_i n_i (S_i + \nu_i \mathcal{E}_i). \qquad (1.3)$$

where $S_i = -\frac{d\mathcal{E}_i}{d\rho r_i}$ represents the ionization energy losses, or the stopping power. We shall call the quantity ν_i the coefficient of the nuclear transformation

$$\nu_i = \frac{\sigma_i}{\varrho}\cdot\frac{\sum_j \mathcal{E}_j + \sum_k \frac{\varrho R S_k}{2}}{\mathcal{E}_i}. \qquad (1.4)$$

Here, σ_i is the macroscopic cross section of nuclear interactions. In the summation process, consideration is given to all the secondary charged particles which are emitted as a result of the interaction, substituting either their total energy $\mathcal{E}_i$, or the stopping power S_k, depending on the magnitude of their mean free path as compared with the radius of the elementary volume ρR (see below). The second term in the parenthesis of formula (1.3) is usually small as compared with the first one, and for low particle energy it can be frequently disregarded. We then have

/9

$$D = \sum_i n_i S_i. \qquad (1.5)$$

For neutral particles, we have

$$D = \sum_i \nu_i n_i \mathcal{E}_i. \qquad (1.6)$$

The absorbed dose which is produced by a single stream of radiation, which is uniform with respect to its composition and the energy of the particles or the quanta, will be called the specific absorbed dose

$$\delta = \frac{D}{\Pi}, \qquad (1.7)$$

where Π is the total stream of particles (quanta). The dimensionality is $[\delta] = [L^4T^{-2}]$. If the radiation composition is known, we then have

$$D = \sum_i n_i \delta_i, \qquad (1.8)$$

where summation is made over all types and energies of particles and quanta.

The dose which is absorbed per unit of time is called the absorbed dose rate P, and is expressed in rads per second and in similar units. The dimensionality is $[P] = [L^2\ T^{-3}]$. Relationships which are similar to formulas (1.1) - (1.8) can be written for the absorbed dose rate, if the radiation intensity I is substituted instead of E, and the stream density φ_i is substituted, instead of n_i (particles/cm^2.sec, etc.).

The absorbed dose rate of cosmic rays at the boundaries of the earth's atmosphere amounts to 10^{-8} - 10^{-7} rad/sec. However, the radiation from solar flares can increase it up to a magnitude on the order of 1 rad/sec. In the radiation zones of the earth, the absorbed dose rate per unit of cosmic apparatus reaches $10^3/10^4$ rad/sec, and the possibility cannot be overlooked that even more powerful radiation may be encountered in interplanetary space (Ref. 1 - Ref. 7).

The interaction between ionizing radiation and substances of differing composition varies, and therefore a different absorbed dose can be transmitted to substances located in the same field of radiation. If this difference usually does not exceed tens of per cent for charged particles, then for electromagnetic radiation the absorbed dose in heavy substances is frequently much greater than in light substances. Thus, the magnitude of the absorbed dose cannot serve as a measurement for the amount of radiation, without being defined in more concrete terms. In order to characterize electromagnetic radiation unequivocally, its effect on a specially-selected substance is measured: dry air under normal /10

conditions (0° C, 760 mm Hg.). In order to avoid distortion due to transition effects close to the boundaries of the different media, the measurements are carried out under conditions of electron equilibrium, i.e., in free air space at a distance from other bodies which is greater than the mean free path of secondary electrons. The absorbed dose in air, which is measured under these conditions, is called the irradiation dose (or exposure dose).

The roentgen serves as the unit of irradiation dose. The roentgen (p) is the amount of electromagnetic radiation which forms, in 1.293 mg of air, secondary electrons which produce ion charges of each sign in it along one electrostatic unit (e.e.). The quantity 1.293 mg represents the mass of 1 cm^3 of air under normal conditions. Since 34.0 ev is required for the formation of one pair of ions in air, and the elementary charge (electron charge) equals $4.80 \cdot 10^{-10}$ e.e., it can be readily calculated that the dose absorbed in air

$$\frac{34}{4{,}8 \cdot 10^{-10} \cdot 1{,}293 \cdot 10^{-3}} = 5{,}48 \cdot 10^{13} \frac{ev}{g} = 5{,}48 \cdot 10^{13} \cdot 1{,}6 \cdot 10^{-12} =$$

$$= 87{,}8 \frac{erg}{g} = 0{,}878 \text{ rad}$$

corresponds to the irradiation dose in 1 p, by definition.

The primary problem in dosimetry of ionizing radiation is to determine the amount of X-ray radiation which influences the living tissue. One measurement method, which has been used most extensively, is the ionization method - i.e., the method based on measuring ionization of gas under the effective radiation. Air is the simplest element to use for this gas, especially since it is very similar to biological tissue in its interaction with X-rays. The irradiation dose is sometimes called the ionization dose, in connection with the measurement method. Up until the present, not only the amount of radiation, but also the effect of radiation on matter, have frequently characterized the irradiation dose, and it has been measured in roentgens.

As long as it is a question of electromagnetic radiation, the error is not too great, although such an estimate is ambiguous. Even for muscle tissue, the absorbed dose of the irradiation dose in one p can range between 0.919 and 0.972 rad, depending on the energy of radiation quanta. For tissue of the bones, it can range between 0.927 and 9 rad. At the same time, rapid neutrons, which ionize the air to an insignificant amount, create large absorption doses in the tissue due to large energy transfer to hydrogen atoms, which do not exist in air. Therefore, the effect of radiation on a substance must be characterized by the absorbed dose, and in particular by the tissue absorbed dose, if one is speaking of living beings.

The study of the dose field near the earth and in interplanetary space has only just begun, and there are only a few publications (Ref. 8 - Ref. 11). Information regarding cosmic radiation consists of data on the magnitude of particle streams, quanta streams, and the radiation

energy spectrum. The utilization of relationships (1.1) - (1.6) makes it possible to go from these quantities to the absorbed radiation dose. /11

For X-ray and γ-radiation, according to equation (1.2), it is necessary to know the mass coefficient of electron transformation μ/ρ, and it is then possible to determine the magnitude of the specific absorbed dose:

$$\delta = \mu \frac{\mathcal{E}}{\varrho}. \tag{1.9}$$

The dependence of the quantity $\chi = \delta/\delta_{tis}$ - where δ_{tis} is calculated for the muscle tissue - on energy is shown graphically for several substances in Figure 1.1.

The values of the quantity

$$N_1 = \frac{1}{\delta} = \frac{\varrho}{\mu\mathcal{E}} \frac{\text{quantum}}{\text{см}^2 \cdot \text{rad}} \tag{1.10}$$

for tissue are shown in Figure 1.2. N_1 represents the magnitude of a γ-quanta stream which forms an absorbed dose per 1 rad. These data are shown in Figure 1.2, together with δ_{tis}.

In accordance with definition and formula (1.2), in order to calculate the radiation dose in roentgens it is necessary to multiply the absorbed dose, which is given in rads, by the ratio between the coefficients for electron transformation of γ-radiation in air and in the medium μ_B/μ, and to then divide by 0.878 rad/roentgen.

It has already been indicated above that formula (1.2) is approximate. For large amounts of radiation quanta energy, it must be taken into consideration that only part of the energy of secondary electrons is absorbed by the medium close to the point where the quantum interacts with a substance. In addition, photonuclear reactions begin to play a certain role. Therefore, at quanta energies which are more than 3 Mev, a quantity which is similar to ν [formula (1.4)] must be used, instead of the trivial coefficient of electron transformation μ.

Formulas (1.5) and (1.8) must be used to calculate the absorbed electron dose. The specific absorbed dose is:

$$\delta = S = -\frac{1}{\varrho} \cdot \frac{dE}{dx}, \tag{1.11}$$

i.e., it equals the ionization loss of electron energy or the stopping power. The quantity S can be calculated for electrons according to the Bethe-Möller formula (Ref. 12):

$$S = \frac{4\pi e^4 NZ}{mc^2}\left[\ln\frac{mc^2}{I(Z)(1-\beta)^{3/4}} - 0{,}98\right] \approx$$
$$\approx \frac{4\pi e^4 NZ}{mv^2}\ln\frac{mv^2}{2I(Z)}\sqrt{\frac{e}{2}} \qquad (1.12)$$

/12

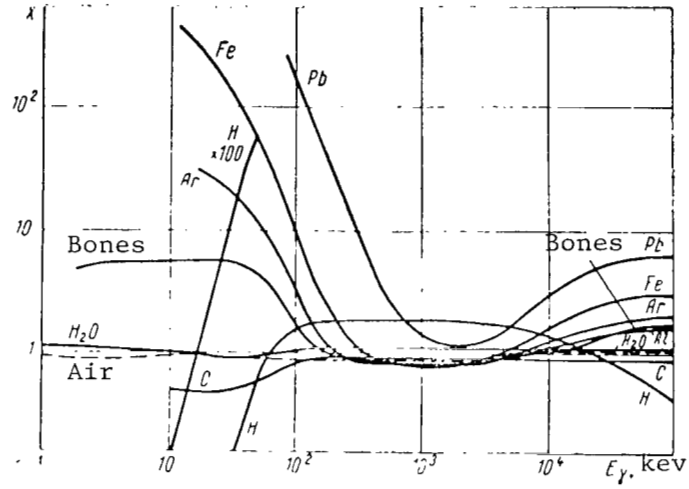

Figure 1.1

Dependence of $X = \delta/\delta_{tis}$ on Quanta Energy.

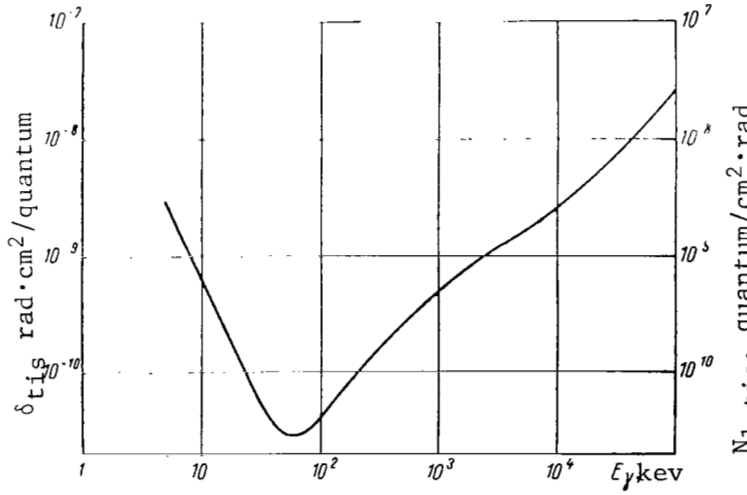

Figure 1.2

Specific Tissue Dose δ_{tis} and Quanta Stream N_{1tis} Which Forms the Tissue Dose per 1 rad.

The approximate equation (1.12) is valid for non-relativistic electron energies ($\leqslant 10^4$ ev). In the formula, $N = \frac{6.02 \cdot 10^{23}}{A}$ is the number of atoms per 1 g of substance: Z is the number of electrons per atom; e is the electron charge; m is its mass; v is the velocity; c is the speed of light; $\beta = \frac{v}{c}$, $I(Z) \approx 12.5Zev$ is the mean ionization of the substance. /13

For electron energy which is greater than 2 Mev, the Bethe-Möller formula is applicable only for rarefied gases, and is inaccurate for condensed media, which are polarized during the passage of an electron. As a result, the magnitude of the ionization losses in liquid and solid bodies decreases, as compared with the magnitude which is determined according to formula (1.12), and for very large energies it does not depend on the composition of the medium.

The values of $S_{tis} = \delta_{tis}$, $N_1 = \frac{1}{S_{tis}}$ and the relative stopping power $X_e = \frac{S}{S_{tis}}$ are given for certain substances in Figures 1.3 and 1.4.

The absorbed dose of mesons, protons, and heavier ions can be calculated with the aid of formulas (1.3) and (1.8). It is apparent that the specific absorbed dose is

$$\delta = S + v\mathcal{E} = S + \delta_{\text{n.u.}*} \tag{1.13}$$

The ionization energy losses can be calculated according to the relationship given by Bethe-Möller:

$$S = \frac{4\pi e^4 NZ}{mv^2} z^2 \left[\ln \frac{2mc^2}{I(Z)} - \ln(1-\beta^2) - \beta^2\right] \approx \approx \frac{4\pi e^4 NZ}{mv^2} z^2 \ln \frac{2mv^2}{I(Z)}, \tag{1.14}$$

where z is the particle charge. For mesons and protons, z = 1, and for α-particles, z = 2. The remaining nomenclature is the same as in formula (1.12). /14

When the charged particle velocities become comparable to electron velocities in atoms, the particles readily damp out and lose electrons, and their charge changes due to this. This process is not taken into consideration by formula (1.14), and leads to an error which amounts to approximately 20 per cent, when the energy of protons decreases down to 50 kev, and of α-particles - down to 800 kev, etc.

The dependences of the quantities S, X, and N_1 for protons having different energy, in different substances, are shown in Figures 1.5 and 1.6. For other particles, in accordance with formula (1.14) S can be calculated by multiplying the quantity S of protons - which have the same

---

* Note: n.u. designates nuclear unit.

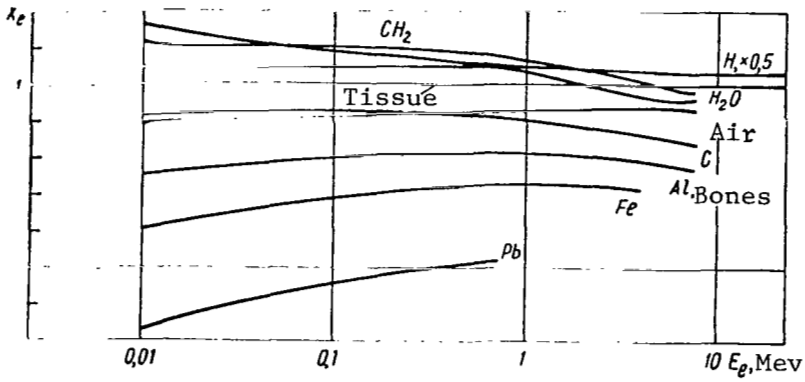

/13

Figure 1.3

Relative Stopping Power $X_e = S/S_{tis}$ for Electrons

velocity as the particles under consideration - by z^2. The proton energy will be greater than the particle energy in proportion to the ratio between the particle mass and the proton mass. The second term in equation (1.13) can frequently be disregarded, as, for example, for protons having an energy less than 100 Mev. In other cases, $\delta_{n.u.} = \nu E$ makes a considerable contribution to the specific absorbed dose. We shall now turn to determining ν in somewhat greater detail.

Let the unit stream which falls into the atmosphere equal 1 particle/cm^2 . We shall select a spherical volume in the atmosphere, having the radius R , which is located so that the course traversed by a particle intersects it along the diameter (Figure 1.7). The particle energy which is transmitted to the atmosphere within the limits of the sphere is: /16

$$E_1 = -\int_0^{2R} \frac{d\mathcal{E}}{dx}\, dx = \mathcal{E}_1(0) - \mathcal{E}_1(2R), \qquad (1.15)$$

where $\mathcal{E}_1(0)$ is the particle energy before crossing the sphere, and $\mathcal{E}_1(2R)$ is after the energy loss on the course 2R (we are still considering only ionization losses).

The absorbed dose, which is averaged over the spherical volume, is:

$$D_1 = \frac{3E_1}{4\pi R^3 \varrho}. \qquad (1.16)$$

If it is taken into consideration that the probability of a

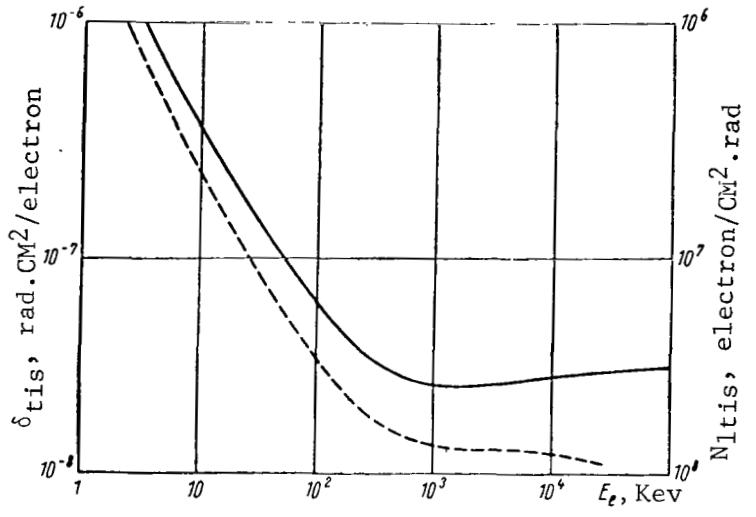

/14

Figure 1.4.

Specific Tissue Dose δ_{tis} of Electrons and the Electron Stream $N_{1\ tis}$ which Forms the Tissue Dose per 1 rad:

———————— is the Total Ionization;

---------- is the Primary Ionization.

particle passing through a given section of the atmosphere decreases /16 in proportion to πR^2, then - going to the limit - we obtain the specific absorbed dose

$$\delta_1 = [D_1 \pi R^2]_{R\to 0} = \left[\frac{3E_1\pi R^2}{4\pi R^3 \varrho}\right]_{R\to 0} = -\left[\frac{3}{4R} 2R \frac{\frac{d\mathcal{E}_1}{d\varrho x}(2R) + \frac{d\mathcal{E}_1}{d\varrho x}(0)}{2}\right]_{R\to 0} = -\frac{3}{2}\frac{d\mathcal{E}_1}{d\varrho x}(0). \quad (1.17)$$

The mean free path of a particle in the sphere does not equal $2R$ - as was obtained, since we assumed that the particle crosses the diameter - but rather $\frac{4}{3}R$. Taking this into consideration, we obtain $\delta = -\frac{d\mathcal{E}}{d\rho x}$, as would be expected if all the ionization losses are used in the calculation.

Since the position of the sphere was taken to be arbitrary, let us place the center of the sphere at the point where nuclear interaction of the particle takes place, as the result of which several secondary, charged particles are emitted. The energy of each secondary particle /17 which is transmitted to the atmosphere, within the limits of the sphere, is:

$$E_2 = -\int_0^R \frac{d\mathcal{E}_2}{dx}\,dx = \mathcal{E}_2(0) - \mathcal{E}_2(R). \qquad (1.18)$$

The absorbed dose of the secondary particle, which is averaged over the sphere, is:

$$D_2 = \frac{3}{4}\,\frac{E_2}{\pi\varrho R^3}. \qquad (1.19)$$

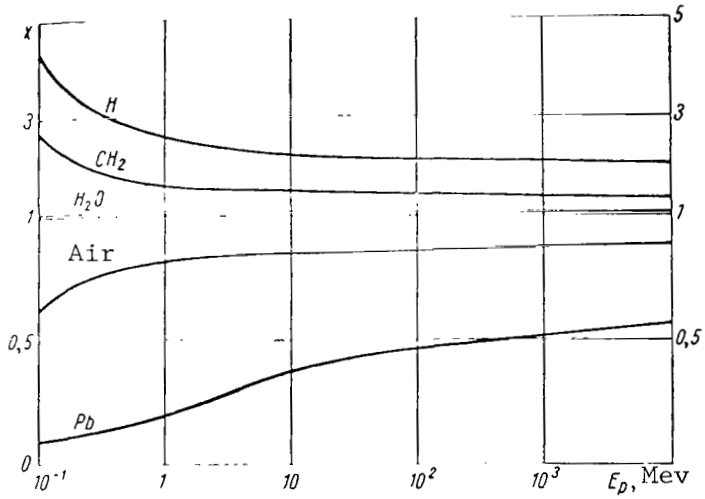

/15

Figure 1.5.

Relative Stopping Power $X = S/S_{tis}$ for Protons

/17

We should now like to point out that the probability for the emission of secondary particles is proportional to the volume of the sphere $\frac{4}{3}\pi R_3$, and to the macroscopic cross-section of nuclear interactions of a primary particle in the medium σ under consideration. The part of the specific absorbed dose which is caused by a secondary particle is:

$$\delta_2 \left[D_2\sigma\,\frac{4\pi R^3}{3}\right]_{R\to 0} = \left[\frac{3E_2\,\sigma}{4\pi R^3\varrho}\cdot\frac{4}{3}\pi R^3\right]_{R\to 0} = \left[\frac{\sigma E_2}{\varrho}\right]_{R\to 0} =$$

$$\left[-\frac{\sigma R}{2}\left\{\frac{d\mathcal{E}_2}{d\varrho x}(R) + \frac{d\mathcal{E}_2}{d\varrho x}(0)\right\}\right]_{R\to 0} = \left[\frac{1}{2}\,\sigma S_2 R\right]_{R\to 0} \qquad (1.20)$$

For all secondary, charged particles, we have

$$\delta_{\text{tot}} = \left[\frac{\sigma R}{2}\sum_i n_i S_i\right]_{R\to 0} \to 0, \qquad (1.21)$$

where n_i is the number of a given type of particles which are

emitted during the interaction.

Thus, extrapolation to zero leads to the conclusion that nuclear interactions do not make a contribution to a specific absorbed dose. Under this approach, a specific absorbed dose of neutrons and γ-quanta also becomes zero.

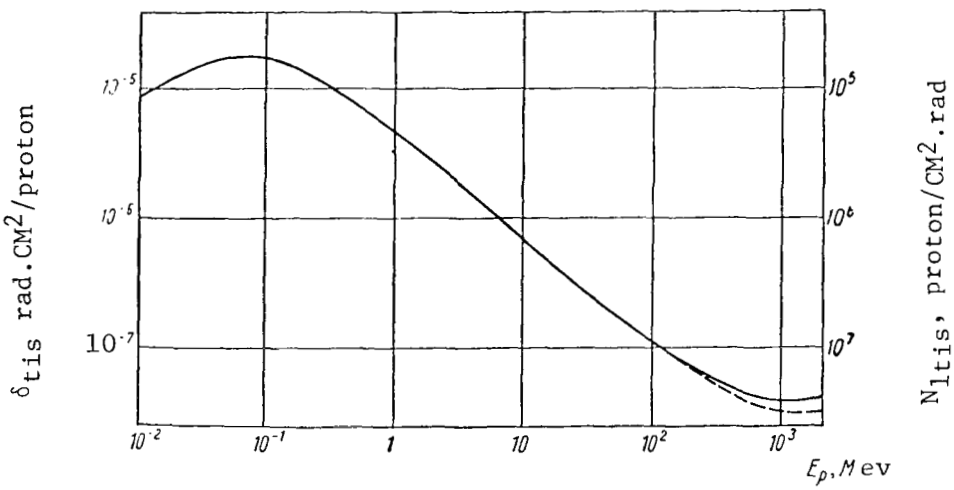

/15

Figure 1.6

Specific Tissue Dose δ_{tis} of Protons and the Proton Stream $N_{1\ tis}$, which Forms the Tissue Dose per 1 rad.

---------- Without Considering $\delta_{n.u.}$

/17

However, the mathematical extrapolation which was applied above does not, strictly speaking, have any physical meaning, since the process of ionization and excitation of atoms in the medium is discrete. The concept of the absorbed dose, as well as the concept of temperature, is applicable in averaging the energy (which is transmitted to the medium) over a certain volume which is not too small. Otherwise, it can happen that the absorbed dose is unusually large where the ionized atoms are located, and equals zero throughout the rest of the medium. Thus, it is necessary to select a certain finite quantity R, which is dependent on the formulation of the problem (dimensions of a chromosome section, nucleus of a cell, the entire cell, and the macroscopic dimensions, etc.). If the particle energy is such that

$$S = -\frac{dE}{d\varrho x},$$

then for such "long-range" particles, we have

$$\delta_{n\ell^*} = \sigma R \sum_i \frac{n_i S_i}{2} = \nu_\ell^* \mathcal{E}_1, \tag{1.22}$$

where

$$\nu_{\ell^*} = \frac{\sigma}{\varrho} \cdot \frac{\varrho R}{2} \cdot \frac{\sum_i n_i S_i}{\mathcal{E}_1}. \tag{1.23}$$

Thus, the contribution from the "long-range" particles to the specific absorbed dose is determined by the dimensions of the the "elementary volume" ρR . In later calculations, it is assumed that R = 1 cm.

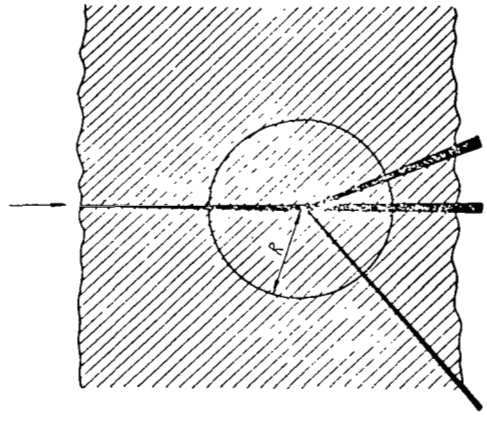

Figure 1.7

Determination of $\delta_{n.u.}$

If another extreme case is taken, when the total range of a particle is confined to the distance R , then integration in equation (1.18) leads to $\mathcal{E}_2(0)$. It can then be simply assumed that, at certain points along the course traversed by a primary particle, the entire energy of a secondary particle $\mathcal{E}_2$ is discharged. The number of such "short-range" particles per unit of course length amounts to $n\sigma/\rho$, and consequently we have:

$$\delta_{s^*} = \frac{n\sigma}{\varrho} \mathcal{E}_2. \tag{1.24}$$

For all secondary "short-range" particles, in contrast to the"long-range" particles considered above, we have

* Note: ℓ = long-range; s = short-range ; n.ℓ. = nuclear long-range.

$$\delta_{\text{n.s.}} = \frac{\sigma}{\varrho}\sum_j n_j \mathcal{E}_{2j} = \frac{\sigma \sum_j n_j \mathcal{E}_{2j}}{\varrho \mathcal{E}_1}\,\mathcal{E}_1 = \nu_S \mathcal{E}_1, \tag{1.25}$$

$$\nu_S = \frac{\sigma}{\varrho \mathcal{E}}\sum_j n_j \mathcal{E}_j, \tag{1.26}$$

and the total formula

$$\delta = \delta_1 + \delta_{\text{n.}\ell} + \delta_{\text{n.s.}} = \delta_1 + \delta_{\text{n.u.}} = S + \frac{\sigma}{\varrho \mathcal{E}_1}\left(\frac{\varrho R}{2}\sum_i n_i S_i + \sum_j n_j \mathcal{E}_{2j}\right)\mathcal{E}_1 \quad S + \nu \mathcal{E}_1. \tag{1.27}$$

The neutrons themselves do not ionize the medium. In their interaction with the medium, the neutrons - which have an energy of up to several tens of megaelectron volts - produce secondary charged particles, which can be regarded as "short-range" particles in many cases. Therefore, the specific absorbed dose of neutrons is

$$\delta = \delta_{\text{n.s.}} = \nu_S \mathcal{E} \tag{1.28}$$

[compare with formula (1.6)] . The specific dose for neutrons is usually one-two orders of magnitude smaller than for protons with the same energy. The only exception to this is interaction between slow neutrons and certain substances in which exothermic nuclear reactions are very likely to occur. Certain values of δ, X, and N_1 are shown in Figures 1.8 and 1.9.

The magnitude of the absorbed dose is usually not the same in /19
different sections of a body which is located in the radiation field. Therefore, it is not always sufficient, nor even always possible, to characterize the effect of radiation upon a body by the calculated or measured absorbed dose at one point. In certain cases, the effect of radiation can be described by the mean absorbed dose

$$\bar{D} = \frac{1}{M}\int_M D\,dm, \tag{1.29}$$

where M is the mass of the body.

Sometimes, for example, during irradiation of gases or liquids, the irradiation effect is also determined by the integral absorbed dose E - i.e., the total radiation energy which is transmitted to the body:

---

* Note: n.s. = nuclear short-range.

$$E = \bar{D}M = \int_M D\,dm. \qquad (1.30)$$

The integral absorbed dose is measured in ergs, megaelectron volts, gram-rads, and other similar units.

In the general case, it is not possible to characterize the effect of radiation upon a body by a single quantity, and it is necessary to know the distribution of the absorbed dose throughout the body - i.e., the distribution of penetrating doses. The composition of the radiation, the intensity, the streams - all of this changes within the body due to attenuation of the radiation falling upon the body, accumulation of secondary radiation, inverse dissipation, self-screening, and for other reasons. By way of an example, let us use an equilibrium radiation spectrum in an aqueous medium, which is constantly irradiated by certain radiation sources (Table 1.1).

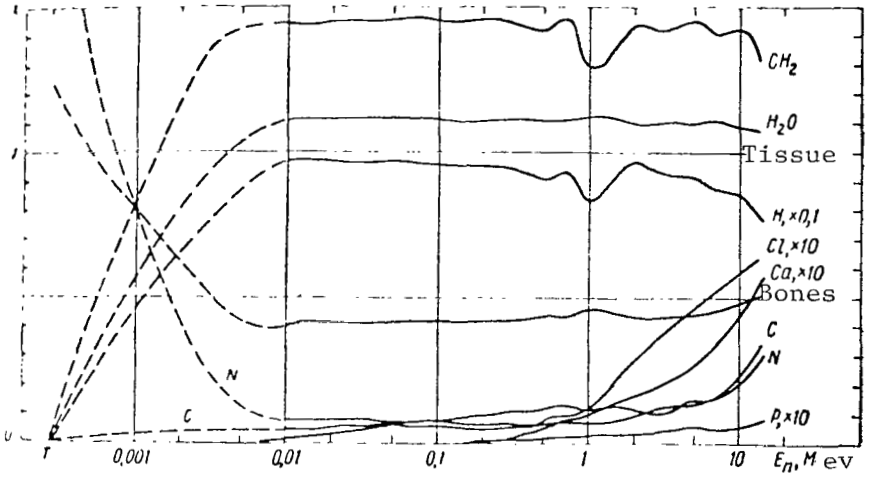

Figure 1.8

Dependence of δ/δ_{tis} on Neutron Energy.

Thus, the calculation of penetrating doses with the aid of the formulas given above is an unusually time-consuming problem. If the fact is taken into account that it is only possible to obtain comprehensive data about the spectrum and composition of radiation in rare cases, it then become apparent that an experimental method, and not a calculating method, is a basic method for dosimetry of ionizing radiation. The calculation of absorbed doses is usually used for predictions and orientations. /21

The effect of ionizing radiation upon man and other living creatures depends on many factors. Naturally, it is primarily

TABLE 1.1

DOSAGE COMPOSITION OF RADIATION FOR AN EQUILIBRIUM SPECTRUM IN WATER (REF. 10)

Interval of Kinetic Energies ΔE Kev	Linear Intensity of Local Energy Losses S, Kev/microns	Contribution to the Absorbed Dose ΔD, x 10^{10} ev/g·rad					
		Electromagnetic Radiation 25 Mev	γ-Rays Co^{60}	X-rays 220 kv	β-Radiation T^3	α-Particles Po^{210}	α-Particles 1 Mev
Electrons							
19 700-25 000	-	5	-	-	-	-	-
13 100-19 660	-	88	-	-	-	-	-
9 800-13 100	-	141	-	-	-	-	-
6 550-9 800	-	298	-	-	-	-	-
4 900-6 550	-	263	-	-	-	-	-
3 300-4 900	-	410	-	-	-	-	-
2 450-3 300	-	292	-	-	-	-	-
1 650-2 450	-	394	-	-	-	-	-
1 230-1 650	-	259	-	-	-	-	-
820-1 230	0.103	332	262	-	-	-	-
610-820	0.109	209	509	-	-	-	-
410-610	0.118	258	726	-	-	-	-
310-410	0.131	158	443	-	-	-	-
205-310	0.151	187	505	-	-	-	-
154-205	0.178	112	282	-	-	-	-
102-154	0.217	133	312	3	-	-	-
77-102	0.268	81	173	34	-	-	-
51-77	0.345	105	198	178	-	-	-
38-51	0.447	68	115	253	-	-	-
26-38	0.595	93	140	444	-	-	-
19-26	0.782	64	88	322	-	-	-
13-19	1.05	91	115	466	42	-	-
9.6-13	1.39	65	78	345	222	-	-
6.4-9.6	1.86	94	108	487	634	-	-
4.8-6.4	2.46	69	77	320	548	-	-
3.2-4.8	3.30	102	112	400	701	-	-
2.4-3.2	4.34	76	82	243	460	1	-
1.6-2.4	7.0	113	122	299	543	16	-
1.2-1.6	11.0	84	90	185	311	32	-
0.8-1.2	16.6	129	138	241	372	86	-
0.6-0.8	25.3	98	105	163	228	94	-
0.4-0.6	36.6	153	164	232	301	186	2
0.3-0.4	50.4	120	128	170	207	170	38
0.2-0.3	66.6	187	200	256	296	297	135
0.15-0.2	81.0	140	149	186	209	244	177
0.1-0.15	90.2	216	230	285	315	398	487
0-0.1	93.0	556	592	731	804	1062	1089
α-Particles							
5 000-6 000	47.4	-	-	-	-	195	-
4 000-5 000	51.5	-	-	-	-	651	-
3 000-4 000	63.4	-	-	-	-	656	-
2 000-3 000	83.7	-	-	-	-	663	-
1 000-2 000	111.1	-	-	-	-	679	-
600-1 000	141	-	-	-	-	283	1503
300-600	154	-	-	-	-	229	1215
100-300	153	-	-	-	-	183	971
0-100	133	-	-	-	-	118	626
Total	-	6243	6243	6243	6243	6243	6243

determined by the magnitude of the tissue dose. When irradiation continues in small doses over a long period of time, the appearance of harmful effects is controlled by a very weak section of the organism, or the so-called "critical organ". The fact is that different organs and systems of the human organism or of other organisms have a differing sensitivity to radiation. Thus, for example, the crystalline lens of the human eye, the sex glands, and the hemogenic organs are most susceptible to the effect of ionizing radiation. On the other hand, the bones and thyroid glands are distinguished by relative resistance. Therefore, according to the effective sanitary laws (Ref. 13), the maximum permissible level of occupational irradiation of these organs is six times greater than for organs of the first group.

/22

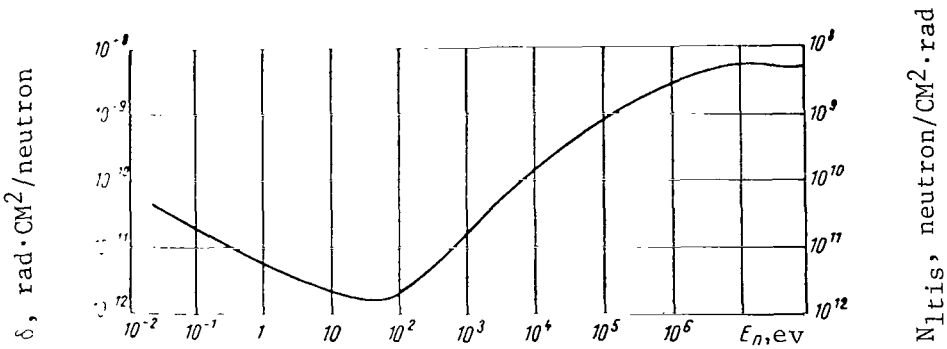

/21

Figure 1.9.

Specific Tissue Dose δ_{tis} of Neutrons and a Neutron Stream N_{1tis} which Produces a Tissue Dose (First Collision) per rad.

It is absolutely clear that, if these organs are subjected to the same irradiation, the crystalline lens, the sex organs, and hemogenic organs will be the critical organs. If, for example, radioactive iodine is found in a human organism, which is concentrated in the thyroid gland, and if the dose which is absorbed in it exceeds the tissue dose in other parts of the organism by more than six times, the thyroid gland will be the critical organ.

/22

The conception of a critical organ makes it possible to characterize the chronic effect of radiation on man by one quantity - the tissue dose in the critical organ. It is usually possible to determine which of the organs in the body is the critical organ in a simple way by a qualitative estimate of the radiation composition. In many cases of general irradiation of the organism, those sections of the body where the tissue dose is largest are the critical organs. Then the chronic irradiation of the organism can be characterized by one maximum tissue dose - D_M.

With general irradiation of the organism in large doses, the radiation damage rapidly encompasses the entire organism, and the effect of radiation will apparently be more correctly indicated by the mean tissue dose $\bar{D}$, rather than by the maximum dose. However, it must always be remembered that one quantity - whether it be the maximum dose, the mean tissue dose, or the integral absorption dose - cannot characterize in a comprehensive manner the radiation effect on a biological object.

By way of an example, for the distribution of the radiation field throughout the organism, tissue doses in a paraffin model of a dog are shown (Figure 1.10); these doses were obtained from irradiation by a flat stream of protons having an energy of 510Mev (Ref. 14). An analysis of the curves for the tissue dose and the proton stream, as well as the changes in the specific tissue dose within the model, point to the fact that secondary radiation is accumulated in the model, primarily protons with an energy in the region of 100-150 Mev. Its contribution to the absorbed dose at a depth of more than 10 cm amounts to 30-40%. The maximum tissue dose occurs at a depth of 11 cm, and amounts to 120% of the tissue dose, measured in the absence of the model ("in air") and apparently equals $\delta_{tis}\,\Pi$ [see formula (1.7)]. The tissue dose on the surface amountsto 100% from the side of the bundle, while from the opposite side it amounts to 85% of the tissue dose "in air", while the mean tissue dose almost coincides with it.

It can be seen from the statements given above that chronic irradiation in small doses and irradiation in large doses are characterized by different quantities. Consequently, the biological effect of radiation is determined not only by the tissue dose, but also depends on its distribution in time - i.e., it depends on the tissue dose rate. This dependence is apparent to a certain extent in the irradiation of inert objects. Thus, the effect of background radiation on the surface of the earth upon an x-ray film does not usually produce a latent photographic image. For a large absorbed dose rate, the changes in photoemulsion are greater than during radiation with a dose rate of 10^{-5} - 10 rad/min. /23

The effect of the tissue dose rate on the results derived from the irradiation of living creatures can be explained as the appearance of regenerating processes in the biological subjects. The phenomenological theory of Bler (Ref. 15) assumes that a certain part f of the immediate aftereffects of radiation is irreversible, and part $(1 - f)$ is balanced according to an exponential law with the coefficient β, so that the changes resulting from irradiation in the living organism decrease with time t, which has elapsed after the irradiation, as a certain effective tissue dose

$$D_{\text{eff}} = D[f + (1 - f)\,e^{-\beta t}]. \qquad (1.31)$$

The period of semi-regeneration is

$$T = \frac{0{,}693}{\beta}, \qquad (1.32)$$

i.e., the time - during which the reversible part of the radiation changes decreases by a factor of two, according to data given by Devidson (Ref. 15) - amounts to: for mice, 3 - 8 days; for a rat, 6 - 9 days; for a dog, 14 - 18 days; for an ass, 20 - 28 days; and for man, 25 - 45 days.

Figure 1.10

Tissue Doses of Protons having an Energy of 510 Mev in a Dog Model (Ref. 14):

1 - Tissue Dose, x 10, rad; 2 - The Same for Two-Way Irradiation; 3 - Stream of Protons, x 10^8, cm^{-2}; 4 - The Same for Primary Protons (calculated); 5 - Specific Tissue Dose, x 10^{-8}, rad. cm^2.

The quantity T = 28.75 days = 690 hours (β = 0.001 1/hours) for man was used in the calculations by Devidson. Using this quantity T, we can assume that the entire irradiation of man for (0.1 - 0.2) T = 2 - 4 days can be regarded as simple irradiation. For interactions which extend over a longer period of time, processes of regeneration appear. Thus, for example, if a man is subjected to irradiation in a dose of 100 rad, and to repeated irradiation for 28.75 days at a dose of 50 rad, then the immediate aftereffects of the second irradiation will be the same as after simple irradiation

/24

at a dose of $100e^{-0.001 \cdot 690} + 50 = 100$ rad, and not the same as after irradiation in a dose of 100 + 50 = 150 rad.

For purposes of simplicity, it was assumed in this example that $f = 0$. When man or other mammals is irradiated with γ-rays or other types of radiation with small linear density of ionization, the quantity is $f \approx 0.1$.

It should be noted that the theory of Blair has not been developed sufficiently nor does it have an adequate experimental basis. Apparently, the magnitude of f depends on the nature of the ionizing radiation, and for radiation with a high linear ionization density f is significantly greater than 0.1. In other words, the aftereffects of radiation in a different dosage, by two types of radiation which differ with respect to the quantity δ, will not be the same. Thus, different types of radiation have different biological effectiveness.

The relative biological effectiveness of radiation can be characterized by its coefficient Q (quality coefficient). For x-ray radiation having an energy of 80-200 kev, whose biological effect has been studied in the greatest detail, Q is assumed to equal to unity. For any other type of ionizing radiation, the RBE coefficient is numerically equal to the tissue doses of x-ray radiation and a given radiation, which cause a similar biological effect. The RBE coefficient represents the same conditional quantity, as, for example, the maximum tissue dose, as a characteristic of radiation effects. For different irradiation conditions by one and the same radiation and for different irradiation aftereffects, the RBE coefficients have different values, and do not coincide for different living organisms. Since certain types of radiation can cause a specific effect, which does not appear with x-ray irradiation, the RBE concept sometimes loses any meaning. This pertains to certain types of chromosome aberrations, to dimness of the crystalline lens under the influence of rapid neutrons, etc. However, the RBE coefficient has the same essential value, because it makes it possible to characterize the biological effect of irradiation unequivocally (Ref. 13) for several cases which are of practical importance.

The harmful aftereffects of chronic irradiation of the human organism in small doses from different types of radiation are characterized by the RBE coefficients, which are contained in compulsory sanitary laws (Table 1.2). A graph showing the dependence /25
of Q on the linear density of charged particle energy losses $\delta_{tis} = S_{tis}$, in accordance with the recommendations given by the International Commission on Radiological Units (Ref. 16), is shown in Figure 1.11.

TABLE 1.2

RBE COEFFICIENT Q FOR CHRONIC IRRADIATION (REF. 13)

Form of Radiation	$\bar{S}$, kev/micron of Tissue	RBE Coefficient
X-Ray and γ-Radiation	0.2 - 5	1
β- Particles and Electrons	0.2 - 5	1
Thermal Neutrons	5 - 20	3
Rapid Neutrons	20 - 60	10
Protons and α-Particles	20 - 200	10
Multi-charged Ions and Recoil Nucleus	150 - 5000	20

As can be seen from Table 1.2 and Figure 1.11, the RBE coefficient for radiation increases with an increase in S_{tis}. Radiation with a higher ionization density is biologically more harmful. Thus, late aftereffects from the total irradiation of a human organism by a tissue dose of rapid neutrons per 30 rad will be the same as from a tissue dose of x-rays per 300 rad. On the other hand, soft γ-radiation of radioactive Co^{60}, which forms less dense ionziation than x-ray radiation, has less biological effectiveness. For it, Q equals 0.7 - 0.8, and the same irradiation aftereffects appear after that as are accumulated around 400 rad. For a concentrated radiation action, /26 which leads to an intense form of radiation sickness, the difference in the biological effect of radiations with different S_{tis} is less clearly expressed. Thus, for rapid neutrons in this case Q has a value on the order of two.

When cosmonauts are on a long interplanetary flight, the tissue dose of primary cosmic radiation which acts upon them will be determined by the RBE coefficients, which are shown in Table 1.2. In the case of strong over-exposure during a brief solar flare, the immediate harmful aftereffects will be determined by smaller values of Q (the dashed line in Figure 1.11). In the case of radiation having a mixed composition, the magnitude of the absorbed dose in rads, due to the difference in the biological effectiveness, cannot serve as an unequivocal characteristic of the biological effect of irradiation. For example, 5 rad of x-ray radiation and 5 rad of multi-charged ions (a total of 10 rad) produce the same aftereffects as 100 rad of x-ray radiation and 0.25 rad of multi-charged ions (a total of 100.25 rad), since Q = 20 for multi-charged ions.

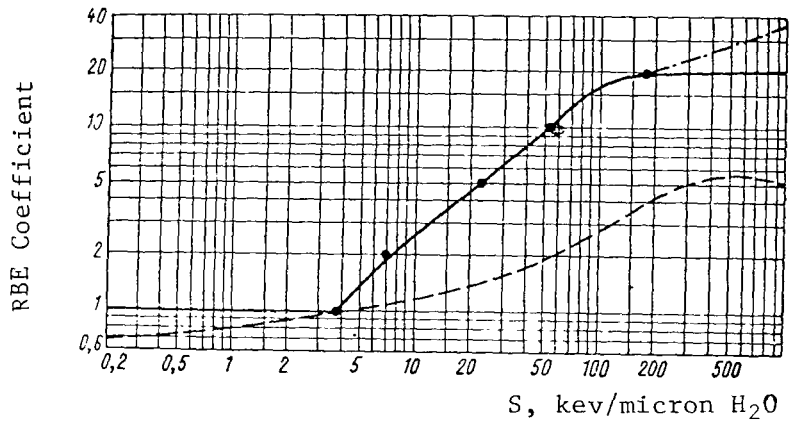

Figure 1.11

Dependence of the RBE Coefficient on the Density of Linear Energy Losses.

-.-.-.-. Represents the Extrapolation Variant in the Region of Large S; -•-•-•-•- Is based on Data (Ref. 16) for Chronic Occupational Irradiation; - - - - - Represents Provisional Dependence of the RBE Coefficient For Direct Aftereffects of Intense Irradiation of Man.

Therefore, in order to estimate the biological effect of radiation, the tissue should be measured in units of rem (biological equivalent of a rad). In terms of energy, 1 rem of a given type of radiation equals 1 rad, shared by the RBE coefficient

$$1 \text{ rem} = \frac{1 \text{ rad}}{Q} = \frac{100}{Q} \text{ erg/g}. \qquad (1.33)$$

Thus, 1 rem will be less than 1 rad, under the condition that $Q > 1$. The tissue dose, expressed in rem's (D, rem), equals the tissue dose expressed in rads, multiplied by the RBE coefficient:

$$D \text{ (rem)} = D \text{ (rad)} \; Q. \qquad (1.34)$$

Thus, for $Q > 1$, the tissue dose in rem units is numerically larger than the dose in rads, since the first is expressed in smaller units than is the second. The example given above will now be as follows: 5 rad of x-ray radiation equals 5 rem, and 5 rad of multi-charged ions equal 100 rem; the total is thus 105 rem. 100 rad = 100 rem of x-ray radiation and 0.25 rad = 5 rem of multi-charged ions also equal a total of 105 rem. The biological effect of irradiation in both cases is the same as from 105 rad (or rem) of x-ray radiation.

Not only the biological effect of ionizing radiation depends on the quantity S. The results produced by irradiation of inanimate

bodies are also frequently significantly different, sometimes qualitatively different, during irradiation by different types of radiation. Thus, rapid neutrons and protons in comparatively small doses of about 10^2 rad cause a significant change in the conductivity of several semi-conducting elements, while irradiation by soft x-ray radiation has no effect up to very large doses. The product yield of several radiochemical reactions depends essentially on the density of linear energy losses of radiation, which must be taken into account, for example, in utilizing chemical dosimeters. The readings of almost all other types of dosimeters also depend on the quantity S, especially for large values of it. /27

The statements given above point to the fact that the problem of making a quantitative estimate as to radiation action is reduced to determining the absorbed dose in rads, but even for a mixed radiation composition, additional information is sometimes required regarding its component composition. It is particularly complex to determine the degree of radiation effect on large animals and on man, when it is necessary to have certain information regarding the penetrating radiation doses and the dynamics of irradiation. In order to simplify the problem, contemporary radiation dosimetry utilizes the tissue dose in a critical organ, expressed in rem's or the mean tissue dose as an unequivocal measurement of irradiation. The selection of the critical organ and the RBE coefficients depend on the irradiation conditions and its aftereffects, which must be predicted or clarified.

1.2. Methods of Dosimetry

Let us now turn to the methods employed to measure the absorbed dose. All of the well-known methods can be used in principle for dosimetry of cosmic radiation. At the present time, the only limitation entailed in measurements on cosmic apparatus are the maximum weight decrease, an increase in safety, and an increase in the volume of information obtained.

The methods employed in dosimetry of ionizing radiation have been extensively developed and discussed in detail in several monographs (Ref. 1-7, Ref. 17-23). Therefore, we shall confine ourselves to systematizing the methods and to their dosimetric characteristics, as well as to individual examples. All of the methods, which have been used, or will be used for dosimetry of cosmic radiation, can be divided into ionization, luminescent, semi-conducting, photographic, and chemical methods, depending on the effect which is utilized in them.

Ionization methods of dosimetry (Ref. 1-2, Ref. 17-19) are based on measuring the ionization of a gas which is formed under the

effect of radiation. The ionization current in gas discharge counters - the number of ionization impulses produced by the passage of charged particles - is measured in ionization chambers. These methods make it possible to measure the absorbed dose rate. In combination with storage elements- electric condenser, scaler, and commutator - they also make it possible to measure the absorbed dose. Ionization recorders are readily connected to telemetry channels and to automatic devices.

The ionization current I in the chamber is determined by the relationship

$$I = \frac{Pm}{w}, \tag{1.35}$$

where P is the absorbed dose rate; m is the mass of irradiated gas in the chamber; w is the formation energy of a pair of ions - i.e., the mean absorbed radiation energy which is necessary for ionization of one of the atoms (one of the molecules) of gas. The quantity w lies within the limits 20-40 ev ($3 - 6 \cdot 10^{-11}$ erg). /28

The absorbed dose rate of cosmic radiation on the surface of the earth $10^{-8} - 10^{-7}$ rad/sec generates, consequently, a current of about $10^{4} - 10^{5}$ electron/sec or $10^{-16} - 10^{-15}$ amp in 1 g of gas. Since it is very complex to measure such small currents, it is necessary to have a chamber with a volume of several liters of gas at atmospheric pressure, or a chamber with gas at a pressure of several atmospheres. Thus, the measurement of the combined intensity of cosmic rays at stations on the earth is carried out by Compton ionization chambers (Ref. 20) with a volume of 20 l, filled with pure argon up to 50 at. In one of the first works on the absorbed dose distribution on satellites (Ref. 8), an aluminum ionization chamber was used with a volume of 43 ml, filled with argon at a pressure of 13.6 at. However, during the flight the hermetic sealing of the chamber was disturbed, and the pressure in it decreased, due to which the measurements were unreliable.

The upper limit for the measurement of the absorbed dose rate is practically unlimited, and it is only necessary to stipulate the condition of a saturation current, thus creating a sufficiently high electric field intensity in the chamber. This entails no difficulties when measuring the electromagnetic radiation of electrons or protons. However, heavy ions create such dense ionization in the tracks that a considerable portion of the ions is lost during the recombination process, and the corresponding absorbed dose is not recorded during the measurement of the ionization current.

Let us investigate what determines the "hard behavior" of the ionization chambers or the dependence of the ionization current on

the radiation energy per unit of tissue dose rate. For electromagnetic radiation, the "hard behavior" is practically equivalent to the dependence of the quantity X on energy (see Figure 1.1). If the dimensions of the chamber cavity are not great as compared with the mean free path of the secondary electrons, which are created at the chamber walls by the electromagnetic radiation, then the ionization of the gas is determined by these electrons, and the "hard behavior" in the example given above is determined by the quantity X for aluminum. If another extreme case is used, when the cavity dimensions are much greater than the mean free path of secondary electrons from the gas, then the "hard behavior" will be determined by the quantity X for argon.

In the intermediate cases, the relative role of the wall and gas effect is determined by the relationship (Ref. 1):

$$\frac{\text{Wall}}{\text{Gas}} = \frac{RX_1}{L} \qquad (1.36)$$

where R is the mean free path of secondary electrons, X_1 is the relationship of δ for the wall material and the gas, and L is the /29
cavity dimensions. It is apparent that this relationship depends on the energy of the radiation quanta. One of the explicit cases is shown in Table 1.3 (Ref. 1).

TABLE 1.3

RELATIVE CONTRIBUTION OF THE WALL AND THE GAS TO THE CURRENT OF THE IONIZATION CHAMBER (REF. 1)

Quanta Energy, kev	30	300	3000
$\frac{\text{Wall}}{\text{Gas}}$	0.5	80	1500

For a decrease in the "hard behavior" of the electromagnetic radiation, it is advantageous to utilize chambers with walls made of light materials - conductive plastics, and aluminum - and to fill them with air or with tissue - equivalent gas mixtures, for which X = const in the entire energy region which is of interest. The fact should be taken into consideration that absorption at the chamber walls, if they are not thin enough, can influence the "hard behavior" during measurements of electromagnetic radiation and other soft electromagnetic radiation.

For charged particles, the "hard behavior" is also primarily determined by the quantity X (see Figures 1.3 and 1.5). Since usually $S >> \delta_{n.u.}$ [formula (1.13)], the wall effect can almost always be disregarded, and the quantity for gas must be used as X Except for the possible instability of the quantity X , the fact must be taken into consideration that for a majority of gases w decreases somewhat with an increase in the linear energy losses of charged particles. Thus, in air for electrons having an energy of $10^3 - 10^6$ ev, w = 34 ev , and for α-particles having an energy of about 5 Mev, w = 35 ev. For more densely ionizing radiation, the change in the quantity w has been studied very little. However, it is known that in pure, inert gases w barely depends on S within wide limits.

Such behavior of inert gases can be explained by the fact that the probability of recombination in them is small. In dense tracks of strongly-ionizing particles, comparatively few ions can recombine with electrons, until the track is dissipated under the effect of the electric field of the ionizing chamber. Therefore, in chambers which are filled with purely inert gases, the conditions of an absorption current, under which the ionization current is proportional to the absorbed dose rate, can be more readily created. A mixture of inert gases, which is tissue-equivalent for charged particles, is comprised by weight of 5% Ar and 95% He (Ref. 24). In the range of proton energy from 10 to 1000 Mev, the quantity X equals 1.15 ± 0.05 for such a mixture.

A gas discharge counter reacts to each charged particle which /30
passes through it by impulses having the same amplitude, and therefore it is a counter of charged particles. With the aid of the counters, there is practically no restriction on the lower limit for the measurement of the absorbed dose rate. However, for a comparatively small radiation rate of about 10 microrad/sec, the counters stop functioning. Only weakly-effective counters which are in series, of the SI-1-BG and SI-3-BG types, in current modes make it possible to widen the measurement region up to several rads per minute. The comparatively low upper limit for measurements on gas discharge counters has not once led to their breakdown during measurements on artificial earth satellites (Ref. 25).

The "hard behavior" of a counter, as well as of a dosimeter, is determined by the behavior of the sensitivity ε to a stream of particles or quanta N_1 , which forms the tissue dose per 1 rad. The sensitivity of counters to electromagnetic radiation is determined by the probability with which secondary electrons are formed at the counter wall and with which they fall into the sensitive counter area. Typical curves are shown in Figure 1.12.

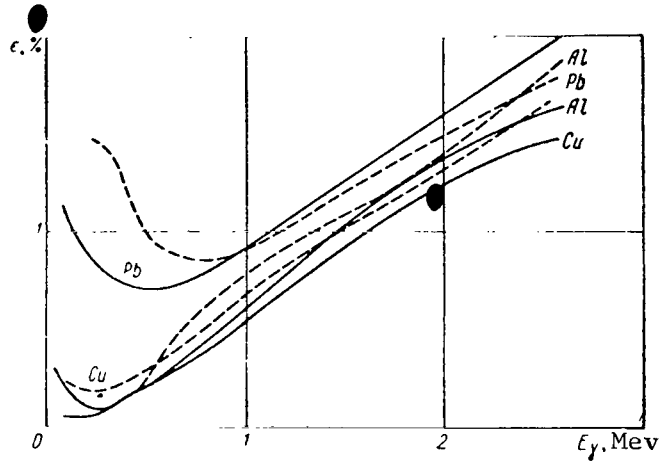

Figure 1.12

Sensitivity to γ-Radiation of Gas Discharge Counters with Different Cathodes:

— · · ——— see (Ref. 26);
---------- see (Ref. 2).

The "hard behavior" of a Viktorin 509 dosimeter with a gas discharge counter (Ref. 27) is shown in Figure 1.13. Counters with a steel wall - which are similar to STS-5 and STS-6 counters in series, and which are surrounded by a layer of 2mm Fe - also have a moderate "hard behavior" in the energy zone of γ-rays quanta from 50 to 1250 kev (Figure 1.14) (Ref. 28).

Charged particles are recorded with gas discharge counters with the sensitivity $\varepsilon \approx 1$, and therefore the "hard behavior" depends directly on the quantity N_l for biological tissue (see Figure 1.4 and 1.6). The smaller is the particle energy, the lower /31
is the counting rate which they produce for a given tissue dose rate. Many, or all of the slow particles, whose mean free path is comparable with the thickness of the counter wall, are absorbed at the walls, which leads to an additional decrease in the counting rate.

The quantity S_{tis} increases somewhat with an increase in the energy of the charged particles above the critical energy, while $N_{l\ tis}$ decreases, due to which the counting rate decreases for a given tissue dose rate. For electrons, the critical energy is about 1 Mev; for protons, it is about 3 Bev (3000 Mev). It is important to note that in a stream of protons having an energy of 40-60 Mev the counter readings will be 4-7 times smaller than from protons having an energy of 600-6000 Mev, which produce the same tissue dose. Therefore, additional information must be obtained about the

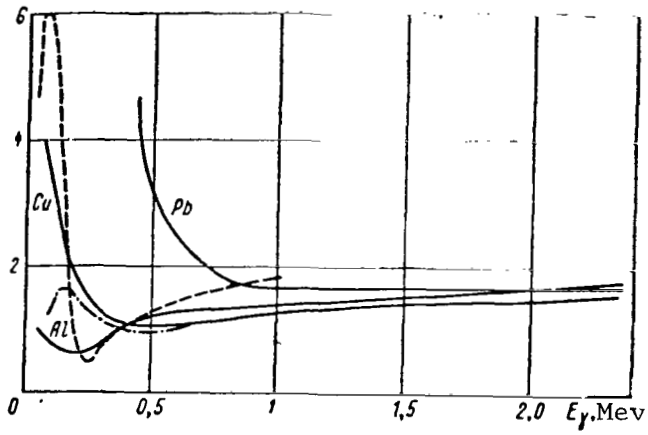

Figure 1.13

Typical "Hard Behavior" of γ-Radiation for Gas Discharge Counters:

———— see (Ref. 28); -.-.-.-.- Copper or Steel Counter with 2 mm Fe Filter (Ref. 28); ---------- see (Ref. 27). $\frac{N}{P}$, 10^7, pulse/cm^2·rad is Plotted Along the Ordinate Axis.

radiation composition when determining the tissue dose based on the counter recording.

Gas discharge counters represent the basic means of detecting radiation on space apparatus; they are extensively utilized in sounding balloons and in stations on the earth. It follows from the statements presented above that their readings must be interpreted in different ways, depending on whether they measure galactic radiation, electromagnetic radiation, or radiation from solar flares. /32

The tissue dose rate in the inner radiation zone of the earth (Ref. 29) has been calculated on the basis of gas discharge counter readings. Judging from the radiation in the inner zone, protons with the mean quantity S_{tis} = 10 - 20 Mev cm^2·g^{-1}, produce P = 50 - 100 rad·hours^{-1} (behind a protection of 1 g·cm^{-2}). If the counter impulses were produced by electromagnetic radiation, having quanta energy which approximately equals 500 kev, then the same readings would correspond to P $\approx$ 250 rad·hours^{-1}.

Gas discharge counters have been utilized to identify radiation composition in the exterior radiation zone of the earth (Ref. 25). One of two counters was covered with a filter of 4 g/cm^2 of Pb + 0.6 g/cm^2 Fe; the other was unprotected. Based on the filter transmission of about 0.1%, it was established that comparatively

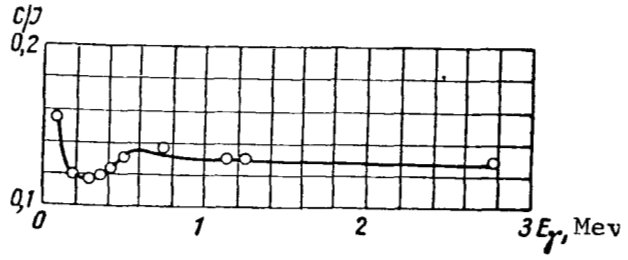

Figure 1.14

"Hard Behavior" of γ-Radiation of a Counter with a Filter (Ref. 28)

soft electromagnetic radiation influenced the counters, and it was thus possible to obtain information to be used in changing from the counting rate to the tissue dose rate.

Luminescent dosimetry methods (Ref. 1-3, Ref. 19, Ref. 21, 22) are based on inducing luminescence by ionizing radiation.

In scintillators, the passage of charged particles produces brief luminosity-scintillation impulses, which make it possible to compute the individual particles, or to measure the absorbed dose rate on the basis of the total luminosity. It is also thus possible to measure the absorbed dose based on the light sum. The measurement zone, with the aid of scintillating detectors, is limited by only the performance of the recording arrangement.

A scintillation counter, which represents the combination of a scintillator and a photoelectric multiplier (PEM), is a proportional counter - in other words, the scintillation amplitudes are proportional within specific limits to the energy of the charged particle transmitted to the scintillator. In order to avoid the PEM counting noise impulses, a discriminator unit is usually placed behind the scintillation counter; this discriminator passes impulses having an amplitude which is larger than a given amplitude - for example, larger than the amplitude of the noise impulses. Thus, part of the impulses from the scintillation is retained. Therefore, the sensitivity of the scintillation counter is a complex function of the particle energy and the discrimination level, and it is difficult to use the scintillation counter as a dosimeter.

Only in individual cases - for example, when a large scintillator measures protons having high energies - almost all of the scintillations produce impulses in the PEM which are much larger than the noise impulses. Then, the counting rate is proportional to the /33

proton stream, and the "hard behavior" is determined by the quantity $N_{1\ tis}$.

Frequently, the individual scintillation impulses are not measured, but rather the mean photocurrent of the PEM. After deduction of the dark PEM current, the magnitude of the photocurrent is proportional to the amount of luminescence light which is emitted per unit of time, and consequently it is proportional to the production of the integral or mean absorbed dose rate in the scintillator per energy luminescence yield η:

$$I_\phi \sim Pm\eta, \tag{1.37}$$

where P is the mean absorbed dose rate, and m is the scintillator mass.

Since the tissue dose rate is $P_{tis} = \frac{P}{X}$, we then have

$$P_{tis} \sim \frac{I_\phi}{m\eta X}, \tag{1.38}$$

and the "hard behavior" $X\eta$ of the scintillation counter in a current mode is determined by the quantity X , and by the dependence of η on energy. This verification of the formulas (1.37) and (1.38) is valid, if the dimensions of the scintillator are not so large that it significantly distorts the radiation field.

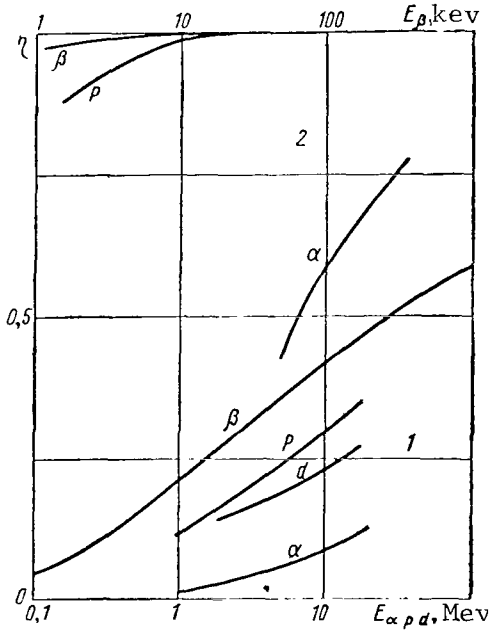

Figure 1.15

Dependence of η on the Energy of Charged Particles for Anthracene (1) and NaJ(Tl) (2).

For the majority of scintillators, η decreases with an increase in the density of the linear energy losses. Normally, the dependence of η on S is characterized by the so-called α/β-relationship, i.e., the relationship between the amplitude of the scintillation counter impulses and the α-particle and an electron, which leave the same energy in the scintillator. For scintillators made of organic crystals - anthracene, stilbene, scintillating plasmas and liquids - the α/β-relationship is on the order of 1/10. For ion crystals, of the NaJ(Tl), and the KJ(Tl) type, the α/β-relationship is on the order of 1/2. For certain zinc sulfide phosphors and for crystals of LiJ-Eu, the α/β-relationship is close to unity, or even larger than unity. More detailed information regarding η can be obtained from Figure 1.15.

The "hard behavior" of γ-radiation for non-organic scintillators is large, due to an increase in X in the region of small energy (Figure 1.16). Just as for gas discharge counters, it can be partially balanced with the aid of filters. Organic phosphors (Figure 1.17) have a comparatively small "hard behavior"; however, their sensitivity to soft γ-radiation is low. In order to eliminate the "hard behavior", the decision was made to utilize mixed scintillators with the addition of haloid derivatives (Ref. 30), or to introduce ZnS-Ag into organic phosphors (Ref. 31). /34

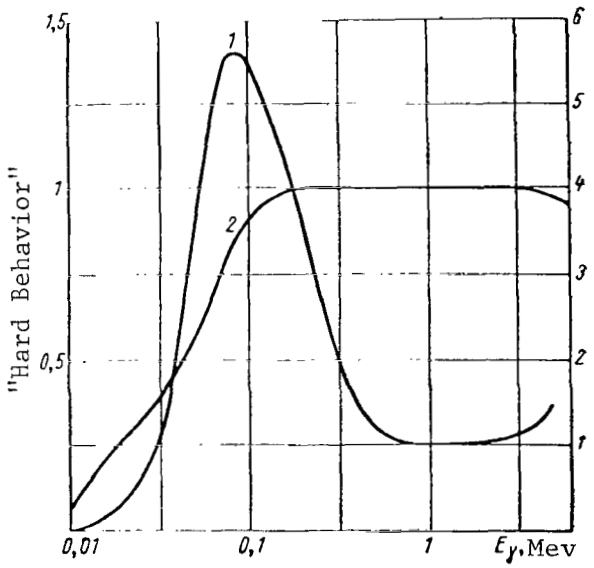

Figure 1.16

"Hard Behavior" of γ-Radiation of NaJ(Tl) Crystals (1) and Anthracene Crystals (2) with a Thickness of 25 mm (Ref. 2).

These additions do not, however, eliminate the "hard behavior" of organic phosphors during the measurement of charged particles, when it is determined by the change in η, which is particularly significant in the presence of heavy charged particles. Thus, the

contribution of α-particles, having energies of about 10 Mev, to the tissue dose will be lowered by 3-5 times, as compared with protons having high energies. Therefore, non-organic scintillators, having a smaller dependence of η - and a comparatively weak dependence of X - on the particle energy, are more suitable for dosimetry of charged particles.

The sensitivity of scintillation counters in a current regime is determined by the level of the PEM dark current, and depends on the choice of the PEM and on the scintillator dimensions. In each case, the scintillation counters make it possible to measure the absorbed dose rate of primary cosmic radiation. A comparison of the photocurrent and the counting rate of the scintillation counter (Ref. 32) makes it possible to determine the mean magnitude of S for primary cosmic radiation, which is equal to $7 \cdot 10^{-8}$ rad × cm^2/particle. A similar method was used to identify protons in the inner radiation zone of the earth over the South Atlantic, at an altitude of 300 Km (Ref. 11). Scintillation counters have been extensively used for measuring cosmic radiation, both in spacecraft , and in stations on the earth, where, for example, scintillation neutron detectors are utilized with a dimension of about 1 m^2 (Ref. 33). /35

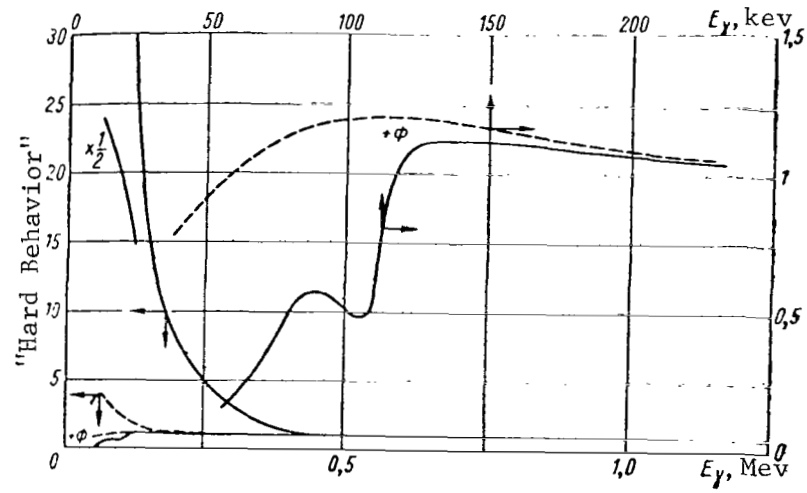

Figure 1.17

"Hard Behavior" of γ-Radiation of Luminescent Dosimeters:

———————— ILC Without a Filter and With 1.3 mm Pb + 0.5 mm Al(+ φ); ---------- IKS Without a Filter and With 0.6 mm Sn + 0.5 mm Al(+ φ).

The upper limit for the measurements made by scintillation counters in a current regime is determined by the performance of the recording arrangement. In an impulse regime, it depends on the

length of scintillation and on the scintillator dimensions. The counting rate is proportional to the scintillator dimensions, and cannot be larger than a quantity on the order of $\frac{1}{\tau}$, i.e., 10^8 imp/sec for organic scintillators, and 10^6 imp/sec for NaJ(Tl), CsJ(Tl) crystals, etc. When a scintillator, having a cross-section of 10 cm^2, is used to measure the tissue dose of protons having high energies, the counting rates also correspond to about 1 rad/sec and 10 m rad/sec.

Other luminescent dosimetry methods are based on accumulating the absorbed radiation energy in the phosphors, with further liberation of the accumulated light sum in the form of a luminescent glow. In flaring phosphors [the ILC* method (Ref. 34, Ref. 1], the light sum is luminesced in the form of a luminescent flare under the effect of infrared light on the excited phosphor. In thermal phosphors, /36 the accumulated light sum is emitted when the phosphor is heated (Ref. 35 - Ref. 37). These methods make it possible to measure the absorbed dose, but do not make it possible to follow the changes in its rate continuously. In return, the luminescent recorders are autonomous and small-dimensional, and do not require power sources or additional integrating devices.

An important characteristic of detectors which store the irradiation effect is the capacity to retain the information for a long period of time. ILC dosimeters at room temperature lose about 12% of the light sum in three days, and from that point on retain the readings for a month or longer. Thermal luminescent dosimeters, based on $CaSO_4$-Mn (Ref. 35) lose 25% of the light sum in 8 hours, and are not suitable for long measurements. Glass IKS* dosimeters retain the information for an indefinitely long period of time (Ref. 37).

The lower limit for the measurement zone is 1-2 m rad [$CaSO_4$-Mn thermal phosphor (Ref. 35), ILC (Ref. 34)] or 20 m rad [thermal, luminescent glass, IKS (Ref. 37)], while the largest quantities which can be determined equal 10^3 rad (ILC) or even 10^6 rad (IKS). The "hard behavior", just as for scintillators, is determined by the composition of $X\eta$. However, the dependence of η on S has not been studied. It is well known that for IKS dosimeters the α/β-ratio equals 0.17 for irradiation with α-particles, having an energy of 5 Mev, and 0.5 - for products of the nuclear reaction Li (n, α) (Ref. 37).

The magnitude of X can be calculated with the aid of the equations given above. Based on data given in the work (Ref. 14), in measurements on the tissue dose of protons with ILC dosimeters, $X = 0.69 \pm 0.03$ in the proton energy zone from 100 to 1000 Mev. In dosimetry of electromagnetic radiation, the attenuation of radiation in the phosphor must be taken into consideration, which

*Note: ILC designates Individual Luminescent Control. IKS dosimeters are radiation dosimeters based on thermoluminescence measurements in aluminum phosphate glass.

can be described by the multiplier:

$$\frac{1-e^{-\mu x}}{\mu_{tis}}, \tag{1.39}$$

where x represents the dimensions of the luminescent detector, and μ and μ_{tis} represent, respectively, the coefficients of electron transformation of γ-rays in the phosphor material and in tissue. Figure 1.17 shows the "hard behavior" of γ-rays for ILC and IKS dosimeters. The "hard behavior" of luminescent dosimeters can be balanced with filters made of heavy material. As can be seen from this Figure, it is possible to eliminate the "hard behavior" in the energy zone of γ-quanta from 40 kev (IKS) or from 120 kev (ILC), and above.

Luminescent dosimeters were used as individual dosimeters during space flights on the Soviet spacecraft-satellites and the spacecrafts such as "Vostok" (Ref. 9). During the space flight of Yu. A. Gagarin, the tissue dose, which was measured by an ILC dosimeter, equaled 2 ± 1 m rad. Along with compensating filters made of 1.3 mm lead, aluminum filters were used which were 3.2 mm /37
thick, which was equivalent to 1.3 mm Pb in terms of stopping power. Dosimeters without filters were also used. Based on the difference in dosimeter readings, it was established that electromagnetic radiation appeared in the cabin of the spacecraft , i.e., their orbit just bordered on the edge of the inner radiation field of the earth.

Semiconducting radiation detectors have begun to appear only in recent years (Ref. 23). The first attempts to use them as particle counters on artificial earth satellites are well-known (Ref. 38). Semiconducting detectors usually represent an electron semiconductor, whose resistance changes in an irregular manner during the passage of a charged particle. The electric impulse which is forthcoming is proportional, in terms of amplitude, to the energy of the particles which remain in the detector. Semiconducting detectors are distinguished by very small dimensions, and they do not require high voltage power supplies, as do ionization detectors or scintillation detectors. They have still not been used extensively, due to the difficulty entailed in manufacturing them.

In photographic detectors, semiconducting processes also occur under the effect of radiation. However, the final result is photochemical changes, which lead to the reduction of silver in photoemulsion grains (Ref. 2). The photo method is quite extensively utilized in studies on cosmic rays. In particularly small-grained, nuclear emulsions or in emulsion cups (emulsion chambers), traces of individual charged particles are obtained.

The characteristics of these charged particles are used to determine the energy, charge, and particle mass, as well as their interaction with the emulsion. An emulsion was successfully developed on board a satellite (Ref. 39).

The photoemulsion method provides basic information regarding the spectrum and composition of primary cosmic rays, in the inner radiation zone of the earth. These data make it possible to calculate the tissue dose rate. One drawback of this method is the large amount of time which is consumed, and the large amount of time - which is related to this - required to obtain any results. In addition, by furnishing comprehensive information regarding the radiation composition, nuclear emulsions make it possible to estimate the RBE radiation (Figure 1.11), and consequently the tissue dose which is expressed in rem .

Based on the general blackening of the film, ordinary photo- and roentgen films make it possible to measure the tissue dose in rads, but they have a certain "hard behavior". For charged particles, the "hard behavior" is determined by the production of X per K - the number of emulsion grains which are restored during the absorption of 1 Mev of energy in the emulsion. Both quantities decrease with an increase in S , so that the sensitivity of the photoemulsion decreases for particles having a large ionization density. There are very few data with respect to K . It is known that for the majority of films K decreases by a factor of two during the change from electrons, having an energy of 1 Mev, to electrons having an energy of 40 kev (a change in S from 3 to $13 \cdot 10^{-8}$ rad/cm^2·electron) (Ref. 40).

The "hard behavior" of γ-radiation is 50-fold for quanta energy /38
of about 50 kev, but - with the aid of lead filters which are 0.75mm thick or filters made of cadmium which are 1.12 mm thick - it is possible to balance it in the energy region from 60-100 kev, and above (Figure 1.18). A filter made of cadmium, in a current of thermal neutrons, emits γ-rays which produce a tissue dose rate which approximately equals the tissue dose rate of thermal neutrons. Therefore, based on the blackening of the photo film under the cadmium filter, it is possible to determine the mixed tissue dose of γ-rays and thermal neutrons.

The combination of a photo film with a scintillating screen, made of $ZnS-Ag_1B$, is more sensitive; this makes it possible to measure the dose in fractions of a millrem of thermal neutrons [the IPCN* method (Ref. 41)] . Photoemulsions in series retain the information for a long period of time.

One of the drawbacks of photodosimetry is the comparatively

* Note: IPCN designates Individual Photocontrol of Streams of γ-radiation and Thermal Neutrons.

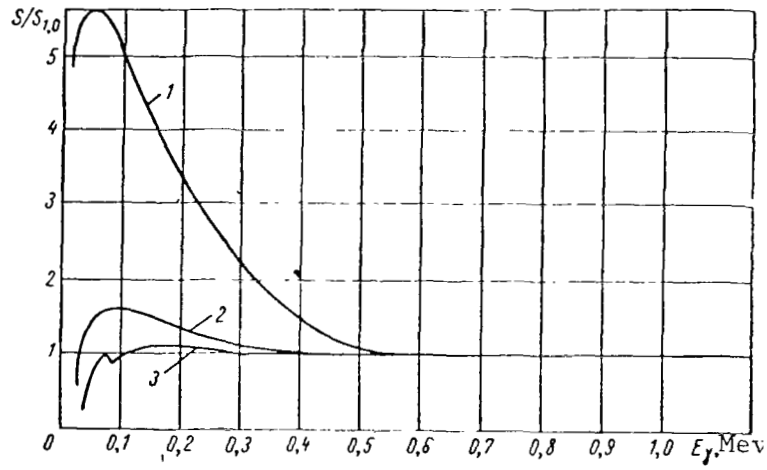

Figure 1.18

"Hard Behavior" of γ-Radiation of a Photofilm Without a Filter (1), and With Filters made of Cadmium having a Thickness of 1.12 mm + 0.5mm Al (2), and with Filters made of Lead having the Thickness 0.75mm + 0.5mm Al (3).

restricted measurement zone, whose width usually does not exceed 1:50. In order to eliminate this drawback,several different types of film can be used, which differ in terms of sensitivity. At the present time, a two-layer PM-5-4, roentgen film is being issued, whose external layer make it possible to measure doses from 20 m rad. This is the largest sensitivity for photo films. If the absorbed dose is large, and the film is black, then - after wiping off the upper emulsion layer with warm water - one can determine the absorbed doses up to 40 rad based on the blackening of the second layer. There are photo films for higher absorbed doses up to $5 \cdot 10^4$ rad.

Along with other methods, the photo method made it possible to measure the doses of cosmic radiation during the group flight of A. G. Nikolayev and P. R. Popovich (Ref. 9). In particular, with the aid of the IPCN it was possible to estimate the upper limit of the neutron tissue dose. /39

Chemical methods of dosimetry (Ref. 2, Ref. 7, Ref. 42, Ref. 43) are based on recording products from radiation-chemical reactions, which take place under the effect of ionizing radiation. Typical examples are the Frike dosimeter and chlorinated hydrocarbons. The Frike dosimeter represents a weak ($\sim 10^{-3}$ M) solution of $FeSO_4$ in 1N H_2SO_4 . Under the effect of radiation, part of the ions of two-valent iron change to a three-valent formula. The concentration of three-valent iron is measured by any method which represents the

measurement of the mean absorbed dose in solution. The dosimeter retains information for a long period of time, and makes it possible to measure from several hundredths of a rad up to 10^6 rad.

The Frike method is distinguished by good tissue equivalence; for almost all types of radiation, X = const in a wide energy zone. However, the yield of three-valent iron G - i.e., the number of ions formed during absorption of 100 ev of energy - decreases with an increase in S (Figure 1.19) which causes the "hard behavior" of the dosimeter.

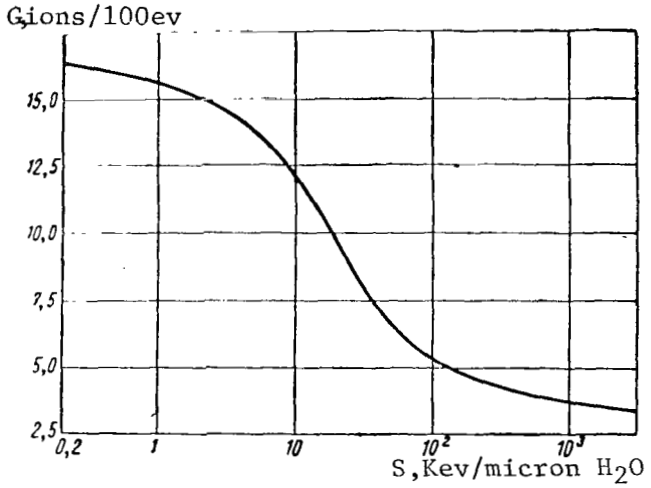

Figure 1.19.

Change in the Yield G of a Frike Dosimeter as a Function of the Quantity S.

In chlorinated hydrocarbons, under the effect of ionizing radiation, a chlorine is liberated, whose concentration can be measured by any method by determining the absorbed dose. Certain similar chemical systems make it possible to measure smaller absorbed doses than the Frike dosimeter, beginning with tens of rads. Along with that, dosimeters based on chlorinated hydrocarbons are distinguished by less stability and poorer tissue equivalents. /40

In this brief summary of the dosimetry methods, we have barely discussed the problem of dosimetry of neutrons, which is of less importance for cosmic radiation. By analogy with the examples which have been considered, one can readily determine independently the possibilities for measuring the tissue dose of neutrons, along with other similar problems.

All of the dosimetry methods enumerated above make it possible, at best, to determine the tissue dose of cosmic radiation, expressed

in rads. (Nuclear emulsions represent the only exception to this.) Along with that, it must be evident that, in order to make a correct estimate of the aftereffects resulting from irradiation by such a complex radiation as cosmic radiation, it is necessary to know the distribution of tissue doses in the human body (or in animals), to know the relative biological sensitivity of the sum of existing types of radiation, and the distribution of the absorbed dose in time.

The solution of these problems depends to a significant extent on the future development of dosimetry of cosmic radiation, on future experimental studies on penetrating doses, on the composition of radiation under typical conditions of cosmic flights, and also on the development of dosimetry methods and apparatus which takes into account RBE radiation and the time factor. The first steps in these directions have already been taken (Ref. 44)

REFERENCES

1. Aglintsev, K. K. Dosimetry of Ionizing Radiation (Dozimetriya ioniziruyushchikh izlucheniy). Gostekhizdat (State Technical and Theoretical Press), Moscow, 1957.

2. Cain, J., Brownell, G. Radiation Dosimetry (Radiatsonnaya Dozimetriya). Izd-vo Inostr. Lit (Foreign Literature Publishing House), Moscow, 1958.

3. Dosimetry of Ionizing Radiation (Dozimetriya ioniziruyushchikh izlucheniy). Gostekhizdat, Moscow, 1956. Reports of Foreign Scientists at the International Conference on the Peaceful Utilization of Atomic Energy, Geneva, 1955 (Dokl. inostr. uchenykh na Mezhdunarodn. Konf. po mirnomu ispol'z. atomnoy energii. Zheneva).

4. Collection: Studies in the Field of Dosimetry of Ionizing Radiation (Issledovaniya v oblasti dozimetrii ioniziruyushchikh izlucheniy). Izd-vo AN SSSR (USSR Academy of Sciences Publishing House), Moscow, 1957.

5. Collection of Radiochemical and Dosimetric Methodologies (Sbornik radiokhimicheskikh i dozimetricheskikh metodik). Medgiz (State Medical Press), Moscow, 1959.

6. Collection of Works on Certain Problems in Dosimetry and Radiometry of Ionizing Radiation (Sbornik rabot po nekotorym voprosam dozimetrii i radiometrii ioniziruyushchikh izlucheniy). Atomizdat (Atomic Energy Publishing House), Moscow, 1960, 1961.

8. Rosen, A., Sonett, Ch. P., Coleman, P. I. J. Geophys. Res., 64, 709, 1959.

9. Keirim-Markus, I. B., and others. Measurement of the Radiation Dosages on 2, 4, and 5 Spacecraft-Satellites (Izmereniye doz radiatsii na 2, 4, i 5 kosmicheskikh korablyakh-sputnikakh). In the Collection: "Artificial Earth Satellites" (Iskusstvennyye Sputniki Zemli), No. 12, Izd-vo AN SSSR, Moscow, 1962; Keirim-Markus, I. B., and others. Measurement of the Radiation Dosages Obtained by Yu. A. Gagarin, and G. S. Titov during the First Space Flights (Izmereniye doz izlucheniya, poluchennykh Yu. A. Gagarinym i G. S. Titovym vo vremya pervykh kosmicheskikh poletov). In the Collection:"Artificial Earth Satellites"(Iskusstvennyye Sputniki Zemli), No. 15, Izd-vo AN SSSR, Moscow, 1963; Keirim-Markus, I.B., et al. Kosmicheskiye Issledovaniya, 1, 1, 179, 1963.

10. Burch, P. R. J. Radiation Res., 6, 289, 1957.

11. Savenko, I. A. and others. Measurement of the Absorbed Dose on the Third Spacecraft-satellite (Izmereniye pogloshchennoy dozy na tret'yem kosmicheskom korable-sputnike). In the Collection: Artificial Earth Satellites", (Iskusstvennyye Sputniki Zemli), No. 13, Izd-vo AN SSSR, Moscow, 1962.

12. Basic Physics Formulas (Osnovnyye formuly fiziki). Edited by D. Menzel. Izd-vo Inostr. Lit., Moscow, 1957. /41

13. Sanitary Rules for Working with Radioactive Substances and Sources of Ionizing Radiation (Sanitarnyye pravila raboty s radioaktivnymi veshchestvami i istochnikami ioniziruyushchikh izlucheniy). Atomizdat, Moscow, 1960.

14. Problems of Radiation Safety during Cosmic Flights (Problemy radiatsionnoy bezopasnosti kosmicheskikh poletov). Atomizdat, Moscow, 1964.

15. Devidson, G. O. Biological Aftereffects of General Gamma-Irradiation of Man (Biologicheskiye posledstviya obshchego gamma-oblucheniya cheloveka). Atomizdat, Moscow, 1960.

16. Snyder, W. S., Neufeld, J. Radiation Res., 6, 67, 1957.

17. Veksler, V. I., Groshev, L. V., Isayev, B. M. Ionization Methods for Studying Radiation (Ionizatsionnyye metody issledovaniya izlucheniy). Gostekhizdat, Moscow, 1949.

18. Shtaub, G. Recording Methods (Metody registratsii) in the Collection: "Experimental Nuclear Physics" (Eksperimental'-

naya yadernaya fizika). Edited by E. Segrè. Part I, Chapter 1. Izd-vo Inostr. Lit., Moscow, 1955.

19. Price, B. J. Recording Nuclear Radiation (Registratsiya Yadernogo Izlucheniya). Izd-vo Inostr. Lit. Moscow, 1960.

20. Compton, A. H., Wollan, E. O., Bennet, R. D. Rev. Scient. Instrum., 5, 415, 1934.

21. Burks, J. Scintillation Counters (Stsintillyatsionnyye schetchiki). Izd-vo Inostr. Lit., Moscow, 1955.

22. Vyazemskiy, V. O., and others. The Scintillation Method in Radiometry (Stsintillyatsionnyy metod v radiometrii). Gosatomizdat, Moscow, 1961.

23. Semiconductor Detectors. Nucleonics, 18, 5, 98, 1960; Pisarevskiy, A. P. and others. Pribory i Tekhnika Eksperimenta, 6, 14, 1961.

24. Kuznetsov, V. G. Thesis (Diplomnaya rabota). MIFI (Moscow Engineering Physics Institute), Moscow, 1963.

25. Van Allen, J. A. Nature, 184, 4682, 219, 1959.

26. Bradt, H., Gugelot, P. C. et al, Helv. phys. acta, 19, 77, 1946

27. Day, F. H. Circ. 507, NBS USA, 1951.

28. Sinclair, W. K. Nucleonics, 7, 21, 1960; Sakharov, V. N. Atomnaya Energiya, 3, 7, 61, 1957.

29. Van Allen, J. A., Frank, L. A. Nature, 183, 430, 1959.

30. Breitling, G. Z. angew. Phys., 4, 401, 1952.

31. Belcher, E. H., Geilinger, J. E. Brit. J. Radiol., 19, 103, 1957.

32. Vernov, S. N., and others. Dokl. AN SSSR (Reports of the USSR Academy of Science), 125, 304, 1959.

33. Clarke, G. W. IRE Trans. Nucl. Sci., 7, 2-3, 164, 1960.

34. Antonov-Romanovskiy, V. V., and others. Meeting of the USSR Academy of Sciences on the Peaceful Utilization of Atomic Energy. (Sessiya AN SSSR po mirnomu ispol'zovaniyu atomnoy energii). OFMN (Division of Physics and Mathematics) Meeting. Izd-vo AN SSSR, Moscow, 1955; Belov, I. P., and others. Pribory i Tekhnika Eksperimenta, 4, 74, 1959.

35. Nosenko, B. M., and others. Zh. Tekhn. Fiz., 26, 9, 20, 46, 1956; Optika i Spektroskopiya, 3, 4, 345, 1957; Arkhangel'-skaya, V. A., and others. Optika i Spektroskopiya, 4, 5, 681, 1958.

36. Ginther, R. J., Kirk, R. D. J. Electrochem. Soc., 104, 365, 1957; Patterson, D. Friedman, H. J. Opt. Soc. America, 47, 12, 1136, 1957.

37. Keirim-Markus, I. B., and others. "Steklo" (Bulletin of the State Glass Institute), No. 2 (111), 77, 1961; Bochvar, I. A. and others. Ibid, No. 2, 1963; Atomnaya Energiya, 15, 1, 48, 1963.

38. Jones, A. R. Nucleonics, 18, 10, 86; 88; 90, 1960; McKenzie, F. M., Ewan, G. T. IRE Trans. Nucl. Sci., 8, 1, 50, 1961.

39. Second Soviet Spacecraft (Vtoroy sovetskiy kosmicheskiy korabl'). Izd-vo Pravda (Pravda Publishing House), Moscow, 1960. Veprik, Ya. M., Kurnosova, L. V., and others. Experiment on the Development of Photoemulsion Layers on the Second Spacecraft-Satellite (Opyt proyavleniya fotoemul'sionnykh sloev na bortu vtorogo kosmicheskogo korablya-sputnika). In the Collection: "Artificial Earth Satellites" (Iskusstvennyye Sputniki Zemli), No. 11, 35, Izd-vo AN SSSR, Moscow, 1961.

40. Dudley, R. A. Nuclenonics, 12, 5, 24, 1954.

41. Keirim-Markus, I. B., Pesotskaya, A. P. Individual Photocontrol of Streams of γ-Radiation and Thermal Neutrons (IPCN Method) (Individual'nyy fotokontrol' potokov γ-izlucheniya i teplovykh neytronov (IFKN metod). In the Collection: Radiochemical and Dosimetric Methodologies (Radiokhimicheskiye i dozimetricheskiye metodiki). Medgiz, Moscow, 1959.

42. Kabakchi, A. M., Gramolin, V. A. Usp. Khimii (Advances in Chemistry), 27, 4, 459, 1958.

43. Sokolova, I. K. Med. Radiologiya, No. 4, 78, 1959; No. 4, 68, 1960; No. 5, 69, 1962.

44. Rossi, H. H., Rosenzweig, W. Radiology, 64, 3, 404, 1955. Radiation Res., 2, 5 , 1955; Radiation Res., 10, 5, 522, 532, 1959.

CHAPTER 2

PRIMARY (GALACTIC) COSMIC RADIATION (PCR)

2.1 Zero Magnetic Effects

Cosmic radiation particles, which reach the earth from cosmic space, enter the magnetic field of the earth, which extends for several tens of kilometers from its surface. The magnetic field of the earth can be represented as a dipole field, which has the moment $8.1 \cdot 10^{25}$ gauss·cm^3. The dipole center is displaced with respect to the center of the earth by 342 km. The geomagnetic poles have the coordinates 78.5° North latitude, 69° West longitude, and 78.5° South latitude, 111° East longitude. Thus, the geomagnetic equator forms an angle, which equals 11.5°, with the geographic equator. /42

It is well-known that a charged particle is deflected by the magnetic field. If the particle energy is less than a certain amount, it generally cannot reach the surface of the earth's atmosphere. For particles with a given energy, which have the charge Z, at each point on the earth's surface the geomagnetic field isolates a region of allowed directions, which are contained in a cone with the apex at a given point (the so-called allowed or main cone). For particles with a large energy, the aperture of the main cone increases. Along with that, there is a region of excluded directions (Stormer cone), into which particles cannot enter which have a momentum which is smaller than a certain critical value, which is determined by the expression:

$$P_{cr} = 60|Z|\left(\frac{1-\sqrt{1 \pm \cos\gamma\cos^3\lambda}}{\cos\gamma\cos\lambda}\right)^2 \frac{\text{Bev}}{c}, \qquad (2.1)$$

where c is the speed of light; λ is the geomagnetic latitude; γ is the angle formed by the velocity vector with the latitudinal circle. $\gamma = 0$ for particles which move to the West, and $\gamma = \frac{\pi}{2}$ for particles which move in the meridian plane. The signs $\pm$ correspond to the sign of the particle charge. There is a penumbra region between the main cone and the Stormer cone; this region consists of alternate excluded and allowed directions.

Formula (2.1) shows that the magnitude of the critical momentum P_{cr} depends on the latitude. Thus, the momentum of protons falling in the vertical direction - which can reach the surface of the earth's atmosphere at the equator - must exceed 14.9 Bev/c. (For protons falling at an angle less than 90°, the value of /43

the critical momentum decreases).

The angle between the trajectories of the particles and the magnetic force lines becomes smaller as the poles are approached, and the magnitude of the momentum at which the particle can reach the earth decreases. In principle, at the pole all the particles with any momentum can reach the surface of the earth's atmosphere[1]. The dependence of the intensity of the cosmic radiation on latitude is called the latitudinal effect. The existence of a latitudinal effect was shown experimentally in 1927-1929 by Clay (Ref. 1).

The important conclusion that the cosmic radiation consists of particles which have an electric charge was based on the latitudinal effect. The magnitude of the critical momentum for particles having a given charge sign, which pass from the east to the west, is not the same - which is shown in formula (2.1). The interval of allowed impulses for positively-charged particles, coming from the west, is greater than for particles coming from the east (it is correspondingly smaller for negatively-charged particles). This phenomenon is called the east-west asymmetry. Consequently, the axis of the main cone for positively-charged particles is directed to the west, while for negatively-charged particles it is directed to the east.

Due to the fact that asymmetry was discovered in a number of particles coming from the west and east in several experiments, the conclusion was drawn that almost all particles of primary cosmic radiation have a positive charge. Thus, the effect of the magnetic field of the earth upon cosmic radiation leads to the fact that, during motion along the meridian from the magnetic pole to the equator, particles will first be dislodged which are coming in from the east from a group of positively-charged cosmic particles having the same energy; thus, the vertical direction is excluded. Finally, the particles can reach the surface of the earth's atmosphere only in directions which lie within the limits of the narrow cone which is open at the west. With further progress toward the equator, these directions can be excluded - i.e., particles having a given energy cannot generally reach the earth

---

[1] It is well-known that during a period of normal solar activity, ionization which is created by the PCR remains almost constant for values of the geomagnetic latitude which are larger than 58° - i.e., there are very few particles with an energy below 1 Bev/nucleon (the threshold of the geomagnetic truncation by the latitude is about 60°). The absence of low-energy particles at the high latitudes is called high-latitudinal truncation, which is caused by the presence of magnetic fields in the solar system; these fields are created by streams of an ionized gas which is given off by the sun.

at low latitudes.

2.2. Composition of Primary Cosmic Radiation

The determination of the PCR nucleus charge is based on measuring a specific ionization - for example, with the aid of photoemulsion or scintillation and proportional counters - but unfortunately this is accompanied by a rather large amount of error. In addition, in order to achievesufficient accuracy it is necessary to have a large selection of recorded events, but this is particularly difficult for nuclei which are rarely encountered. In order to increasethe statistical accuracy, nuclei having close numbers can be combined into a group, excluding protons and α-particles, which are considered separately. The nuclei of lithium, beryllium and boron represent a group of light nuclei (L) with Z = 3 - 5; the nuclei of carbon, oxygen, nitrogen, and fluorine represent a group of mean nuclei (M) with Z = 6 - 9. All nuclei with Z $\geqslant$ 10 are combined into the group of neavy nuclei (H). Finally, nuclei with Z $\geqslant$ 20 form a group of very heavy nuclei (vH). The percentile content of each element within the group is not known accurately; however, the mean atomic number $\bar{A}$ for each group (Ref. 4) can be estimated on the basis of certain data (Ref. 2, Ref. 3, Ref. 37). /44

The composition of cosmic radiation is shown in Table 2.1 (Ref. 5). The relative abundance of the elements throughout the world is also shown in this table.

TABLE 2.1

COMPOSITION OF PRIMARY RADIATION AND RELATIVE ABUNDANCE OF ELEMENTS THROUGHOUT THE WORLD

Nuclei Group	Z	$\bar{A}$	Content in Cosmic Rays, %	Abundance Throughout the World, %
p	1	1	100	100
α	2	4	15.5	7.7
L	3 ÷ 5	10	0.24	10^{-6}
M	6 ÷ 9	14	1.20	0.20
H	$\geqslant$ 10	31	0.4	0.03
vH	$\geqslant$ 20	51	0.1	0.003

As can be seen from the Table, cosmic rays are primarily composed of protons and α-particles. The nuclei content from other elements does not exceed 2%. The PCR composition approximately

corresponds to the abundance of the elements throughout the world. However, attention should be drawn to the following two facts:

1) In cosmic rays, there are quite a few nuclei of light elements, which barely exist throughout the world. It can be assumed that the nuclei of light elements, which are observed close to the earth, have a secondary origin, being the product of nuclear spallations of heavy and mean nuclei during their interaction with the interstellar medium.
2) In cosmic rays, there are considerably more nuclei of heavy and very heavy elements than there are throughout the world. This can be caused (Ref. 4) by the specific mechanism of acceleration, by which heavy particles are primarily speeded up. The data given in Table 2.1 regarding the PCR composition correspond to an energy region up to 10^{13} ev/nucleon.

The composition of cosmic radiation in the high-energy region in unknown. The presence of neutrons, γ-rays, electrons, and positrons in cosmic rays has still not been accurately established.

There are indications (Ref. 6) that γ-rays comprise 0.1% of the energy stream above the atmosphere. The amount of electrons (or positrons) amounts to about 1% in cosmic rays, according to different data (Ref. 7, Ref. 8). /45

2.3. Energy Spectrum

The differential spectrum for all nuclei of primary cosmic radiation having energies greater than 1 Bev/nucleon has the form

$$n(E)\,dE = c'E^{-\gamma}\,dE. \tag{2.2}$$

Here E is the total particle energy per 1 nucleon, i.e.:

$$E = E_к + M_p c^2 \approx E_K + 1,$$

where E_k is the kinetic particle energy, and $M_p c^2$ = 0.938 Bev is the rest mass of a proton. According to data given in the literature, the magnitude of the coefficient γ equals 2.0 - 2.5 (Ref. 4, Ref. 9-11).

The integral spectrum - i.e., the number of particles having energies larger than E - can be found from the relationship

$$N(>E) = \int_E^\infty n(E)\,dE = \frac{c}{\gamma - 1} E^{-(\gamma-1)} \tag{2.3}$$

The magnitude of the integral stream of primary cosmic radiation depends on the level of solar activity. For years which correspond to the maximum solar activity, the integral stream equals 2.3 - 2.5 particle/cm^2·sec (Ref. 5, Ref. 12 - 14). In years of minimum solar activity, the stream is higher, while the ionization created by it increases by 1.5 - 2 times (Ref. 13, Ref. 15, Ref. 16).

Within the limits of a time interval which is much less than the 11-year cycle for the change in solar activity, the intensity of cosmic radiation is almost constant. The negative gradient of intensity in the direction of the sun amounts to (15 ± 20)% per astronomical unit (1 a.u. = 149 500 000 km) (Ref. 17).

In the region below 1 Bev/nucleon, the integral spectrum due to high-latitudinal truncation tends toward "saturation", and the differential spectrum reaches a maximum for a certain energy below 1 Bev/nucleon (Ref. 4, Ref. 37). Thus, the maximum of the differential spectrum for protons lies in the region 0.8-1.2 Bev (Ref. 19).

The maximum of the differential spectrum for α-particles corresponds to E = 300 Mev/nucleon (Ref. 20 - 22). However, the magnitude of the energy equals 500-600 Mev/nucleon (Ref. 23). The spectrum for heavier nuclei, according to data given in the work (Ref. 23), is similar to the spectrum for α-particles. On the other hand, according to data given in the work (Ref. 22), it was found that there is a tendency for the spectrum maximum to be displaced in the region of high energies, with an increase in the particle charge: from 300 Mev/nucleon for α-particles to 500-600 Mev/nucleon for nuclei of the M group.

A study of the spectrum in the low-energy region is difficult due to variations in the PCR, and also due to the fact that the sun emits soft protons during solar flares. Therefore, in this region the spectrum of cosmic radiation has not been determined sufficiently well. It is assumed that, during the years of an extreme minimum in solar activity, there is no apparent high-latitudinal truncation (Ref. 4). However, data which have been obtained during the period of the minimum in 1954-1955 are contradictory. According to results obtained in 1954 (Ref. 24), high-latitudinal truncation was absent, and an increase in the proton stream was observed up to 100-150 Mev. /46

Measurements (Ref. 19), which were also carried out during the period of minimum solar activity, showed the presence of a maximum in the differential proton spectrum which was located in

the region of 0.8 - 1.2 Bev - just as for the case of maximum solar activity. It is possible that these data will be refined during the solar minimum in 1964-1965.

In the region of high energies (greater than 10^{13} ev/nucleon), there is also an element of uncertainty in the energy spectrum of the PCR, which is due to the difficulty entailed in measuring a particle stream of low intensity.

2.4. Isotropy of Cosmic Rays

As is well-known, the motion of a charged particle in a magnetic field occurs in a spiral-like manner along the magnetic force line. The trajectory radius of curvature for a proton, which has energies of 10^9 - 10^{10}ev - which are characteristic for cosmic rays - in a field with an intensity of 10^{-6} - 10^{-5}oe, (Ref. 25, Ref. 26) is negligible as compared, for example, with the distance to the closest stars, and, as compared with the dimensions of the galaxy. Thus, a charged particle performs many rotations along a spiral before it reaches the earth. During this time, it can be reflected several times from a magnetic cloud, going from one force line to another. In addition, the force lines themselves have a very complex nature. For these reasons, cosmic radiation is isotropic. The degree of anisotropy can usually be characterized by the following coefficient:

$$\frac{I_{max} - I_{min}}{I_{max} + I_{min}},$$

where I_{max} and I_{min} represent the maximum and minimum streams beyond the influence of the magnetic field in any direction. Within an accuracy of statistical error, anisotropy - if it exists - does not exceed 1% for an energy of about 10^{14} - 10^{16}ev, and 3% for energy which approximately equals 10^{17}ev (Ref. 27, Ref. 28). Thus, within the limits of the accuracy achieved, radiation anisotropy was not detected.

2.5. Time Variations in Cosmic Radiation Intensity

Systematic measurements of cosmic radiation intensity have been carried out for the last several decades. On the basis of these studies, the existence of time variations in cosmic radiation has been definitely established. Unfortunately, at the present time it is almost impossible to observe variations in primary cosmic radiation. Therefore, on the basis of secondary radiation variations which are observed on the earth, one must determine the variations, which correspond to them, in the primary component

/47

at the boundary of the atmosphere.

There are several well-known methods (Ref. 29 - 32) for determining this connection between changes in primary radiation and the corresponding changes in secondary radiation. However, one principal difficulty is encountered in changing from variations in secondary radiation to variations in primary cosmic radiation. This consists of the fact that the change in cosmic rays at sea level could either be a result of a change in the spectrum of primary cosmic radiation, having a large number of low-energy particles, or as a result of a smaller change in the particles having large energies.

Usually, a distinction is made between periodic and non-periodic variations. Daily, seasonal, 27-day, and 11-year variations belong to the first group. Temperature and barometric effects, which have an atmospheric origin, belong to the same group. The second group includes variations which are related to solar flares on the sun and magnetic storms (Forbush decrease). Since the amplitude of the variations does not exceed several percents, it can be assumed that the intensity of primary cosmic radiation is constant. These PCR variations are observed in space close to the earth. PCR variations in cosmic space have been studied very little. It is only known that a PCR variation exists in cosmic space which is correlated with the 11-year period of solar activity, while the ionization caused by the PCR during the years of minimum and maximum solar activity differs by a factor of 1.5 - 2.

2.6. Origin of Cosmic Rays

At the present time, the problem as to the origin of cosmic radiation has not been decisively solved. The problem of this origin includes two other problems: 1) the source of cosmic rays, and 2) the mechanism by which cosmic particles are accelerated up to energies which are observed. Even when cosmic rays were first studied, an attempt was made to determine their origin, by determining the predominant direction followed by these rays in reaching the earth. However, this attempt was unsuccessful, since cosmic radiation is found to be isotropic.

There are several hypotheses regarding the mechanism by which cosmic particles are accelerated: the theory of electrostatic acceleration in extended electric fields, and different theories for acceleration in electric fields which are induced by the rotation of magnetized celestial bodies (binary stars, stars with variable magnetic fields, etc.). All of these theories have

proved to be untenable, since they cannot explain the characteristic form of the cosmic ray spectrum, the presence of particles with ultra-high energies, and the absence of electrons. /48

At the present time, it is assumed that interstellar space in the galaxy is filled with a gas, primarily hydrogen, with a mean density of 10^{-25} g/cm^3, or 1 atom of hydrogen per 10 cm^3. The interstellar gas does not have a uniform distribution. There is information to the effect that bunching (clusters) exists, in which the density can amount to 10^{-23} - 10^{-22} g/cm^3. When a mass of interstellar gas having differing density moves, magnetic fields arise which move along with the gas in which they are formed. According to the statistical theory of Fermi (Ref. 33), a charged particle - which moves in a spiral-like manner among migratory magnetic fields - can collide with the magnetic cloud which is moving with a comparatively low velocity (on the order of 10 km/sec). The particle is reflected, and thus energy can be both lost and acquired. If the particle moves toward the cloud, then it acquires additional energy during the collision, and if the particle collides with a cloud moving in the same direction, energy is lost. The probability for one or the other type of collision is proportional to the relative velocities of the particle and the cloud. Therefore, collisions of the first type are somewhat more probable, since the relative velocity in this case is larger. Thus, as a result of statistical averaging, the particle energy increases.

However, except for this process, there is a constant loss of energy by ionization of interstellar matter. The increase in the particle energy will exceed the loss by ionization only if the particle has a certain initial energy. This energy amounts to about 10^9 ev for protons; for heavy nuclei, it is somewhat larger. The mechanism for initial acceleration of particles is not considered in the statistical theory of Fermi, which makes this theory incomplete. One type of energy loss is characteristic for electrons having high energies. This represents radiation losses which are caused by the acceleration of electrons in interstellar magnetic fields (for protons and heavy nuclei, the radiation losses are negligible). Consequently, the electrons are not accelerated, even if an electron has an energy on the order of 10^9 ev.

Thus, the Fermi theory provides a good description of the absence of electrons in primary cosmic radiation. It also provides an excellent explanation for the presence of cosmic radiation particles having very large energies. In addition, the energy spectrum for protons, which is calculated theoretically, coincides closely with the observed spectrum. However, this theory cannot explain the similar form for the spectrum of protons and heavy nuclei. In order that the cosmic radiation intensity be continuously

located at the existing level, injection of protons and heavy nuclei must occur, which would compensate for particles which are lost during the absorption process. The statistical theory of Fermi does not provide a satisfactory answer to this question. /49

According to existing observational data, cosmic rays are formed on the sun during eruptions of supernova stars.[1] The observed radio emission of supernova fragments points to the presence in them of electron clouds having high energies. Therefore, it is natural to assume that protons and heavy nuclei can also be accelerated in their shells.

Calculations, which were carried out by I. S. Shklovskiy (Ref. 34), showed that the intensity of primary cosmic radiation, which is observed at the present time, can be explained by the emission of high-energy particles during supernova flares. V. L. Ginzburg (Ref. 4, Ref. 35-37) carried out a similar examination of the possible mechanism for acceleration in supernova. The theory which he developed for the origin of cosmic rays is also based on the mechanism of statistical acceleration. However, it is assumed that the particle acquires additional energy in the magnetic fields which are formed in the shell of the supernova, due to the random motion of the matter ejected during the flare. Statistical acceleration in magnetic fields of supernova is more effective than in interstellar space.

During the flares of supernova stars, the maximum energy to which protons can be accelerated can reach 10^{17}ev, which corresponds to 10^{19}ev[2] for heavy nuclei - i.e., the acceleration of particles in supernova shells can in itself create particles having very large energies. The necessity of a large initial acceleration, which the Fermi theory requires, is eliminated here, since the acceleration process can be initiated with small energies.

Thus, based on current data, the origin of cosmic rays can be represented as follows. Primary cosmic radiation arises primarily within the limits of our galaxy as a result of eruptions of supernova

---

[1] Supernova stars, or simply supernova, are particular astronomical objects, whose optical luminosity suddenly increases by hundreds of millions of times. Then, the supernova shell begins to expand, and the brightness slowly decreases. Supernova flares are observed very rarely - on the average, there is one in 200 - 300 years.

[2] Therefore, it is very important to determine whether the observed particles with energies of 10^{19}ev are protons or heavy nuclei.

stars. During the eruption, a large amount of ionized gas is ejected, primarily hydrogen - of which the shell for the star is composed - and nuclei of heavy elements. Interacting with interstellar matter, the heavy nuclei disintegrate, forming a spectrum of charges. The acceleration of the nuclei takes place primarily by the magnetic fields which are created during the eruption of the supernova. Further acceleration of cosmic radiation particles can occur in the interstellar magnetic fields. /50 The electric spectra of accelerated particles thus have a similar form. As they wander for a long period of time (on the order of 10^8 years) among the interstellar magnetic fields, the particles change the direction of their motion several times, due to which almost total isotropy of cosmic rays close to the earth is produced. Electrons are also formed during the eruption of supernova. However, the acceleration of the electrons does not occur due to large radiation losses.

Low-energy cosmic rays are also generated on the sun during solar flares. However, the proportion of them in the total stream of cosmic radiation is small.

2.7. Doses

Initial Data

The absorbed dose, which is created by primary cosmic radiation, is calculated according to a method which will be described in Section 7.5. The initial data for the calculation are as follows:

1) The differential energy spectrum is of the type described in formula (2.2)

$$n(E)\,dE = cE^{-2.4}\,dE,$$

for all nuclei. The spectrum corresponds to the period of high solar activity (Figure 2.1);

2) The integral current stream of cosmic radiation equals 2.3 particles/$cm^2 \cdot sec$;

3) The composition of cosmic radiation is selected according to data given in Section 2.2.

Particles having energies above 10^{11} ev/nucleon were disregarded in the calculation. The estimate showed that the error thus arising does not exceed 1%.

The absorbed dose was calculated for each component of cosmic radiation.

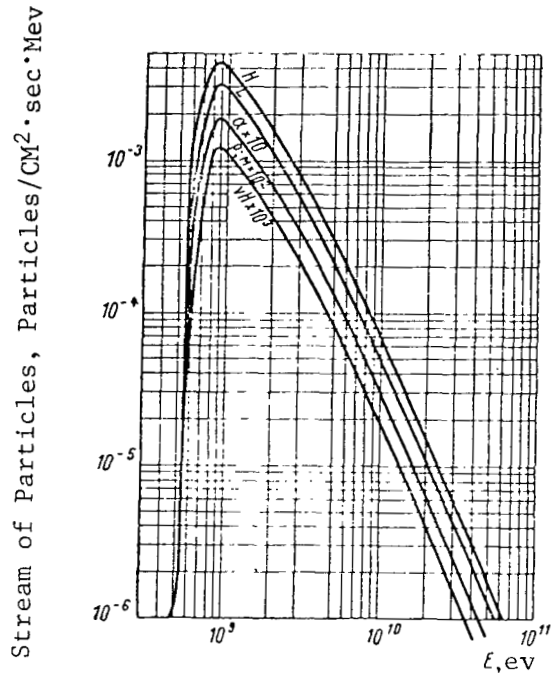

Figure 2.1

Differential Spectra of Different PCR Components

Calculation Results

Doses in Interplanetary Space. In the majority of works devoted to the problem of cosmic flights, conclusions are drawn as to the radiation danger caused by PCR which are based on the magnitude of the local dose. This conception, which is incorrect in principle, /51 can be valid when applied to PCR, whose composition includes particles having very large energies. Nevertheless, it is interesting to know the distribution of the absorbed dose in the body. It is known that there are heavy nuclei in the PCR, which have a very high ionization capacity. Therefore, it is not immediately apparent that a change in the dose absorbed in the body will be small, and consequently that the local dose conception can be utilized.

A calculation was made of the depth distribution of the dose absorbed in the body, and of the mean tissue dose created by the PCR, both in the absence of shielding and behind shielding made of light material of differing widths. The distribution by depth of the dose absorbed in the body is shown in Figure 2.2. Due to the great hardness of the PCR, the dose differential with respect to body depth is insignificant. When the shielding is up to 10 g/cm^2

thick, the dose absorbed in the body increases from the surface to the center, which is related to the retardation of high-energy particles in the body, and consequently to an increase in their ionization losses. If shielding thickness is increased further, the particles begin to be absorbed in the body. Thus, the dose in the direction toward the center first stops increasing, and then decreases with a certain shielding thickness.

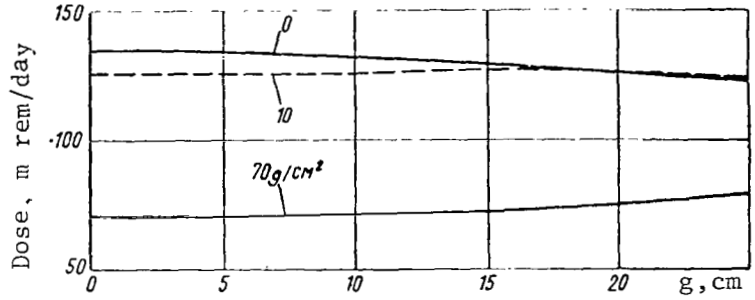

Figure 2.2

Distribution by Depth of the Absorbed Dose Created by the PCR in the Body, Behind a Shielding Made of a Light Material Having Differing Thickness.

During long space flights, the large PCR is a chronic irradiation factor. Therefore, the maximum dose absorbed in the body must be used as a criterion for radiation safety. However, as can be seen from Figure 2.2, the dose differential in the body does not exceed approximately 10% and consequently the radiation danger caused by the PCR can be estimated according to the mean tissue dose.

Table 2.2 lists the results derived from a calculation of the mean tissue doses created by different PCR components in the absence of shielding.

According to the preliminary calculations, the contribution made by nuclei of the L group to the dose amounts to several tenths of a percent, and is not indicated in Table 2.2. It can be seen from the table that heavy nuclei and very heavy nuclei form a significant part of the dose. In the presence of shielding, the contribution of heavy elements to the dose increases with an increase in the shielding thickness.

The total radiation effect of the PCR when there is no shielding /52 equals 22.4 mrad/days or 127.6 mrem/days. With an increase in the shielding thickness, the PCR dose barely changes up to a shielding thickness of 10 - 15 g/cm^2 (Figure 2.3). For very large shielding thickness (on the order of 70 - 100 g/cm^2), the dose

TABLE 2.2

MEAN TISSUE DOSE RATE FOR DIFFERENT PCR COMPONENTS (NO SHIELDING).

Dose Characteristics		Nucleus Group					PCR
		p	α	M	H	vH	
Absorbed Dose	mrad/days	6.2	3.7	3.4	5.0	4.1	22.4
	mrem/days	6.2	3.7	11.1	34.0	72.6	127.6
Contribution to the Dose %	physical	27.7	16.5	15.2	22.3	18.3	100
	biological	4.9	2.9	8.7	26.6	56.9	100
RBE		1	1	3.3	6.8	17.7	5.7

decreases by a factor of 1.5 - 2.

Table 2.3 presents a comparison of the PCR dose calculated in this work with different values which are given in other works.

As can be seen from the Table, the magnitudes of the dose which are calculated here do not contradict the data given in the literature.

Estimate of Secondary Radiation. Due to the absence of data regarding the interaction of high-energy multi-charged particles with matter, at the present time it is almost impossible to calculate the doses created by secondary radiation, which is formed in the shielding and in the body of the cosmonaut. A rough estimate of the increase in the absorbed dose due to the accumulation of secondary particles can be made by analyzing the dependence of the total ionization, which is created by primary cosmic radiation in the atmosphere, upon altitude.

When galactic radiation interacts with the atmosphere, secondary particles are formed: nucleons, electrons, mesons, photons. Therefore, beginning at 30 - 40 km, ionization increases as the surface of the earth is approached, and reaches a maximum at an altitude of 20 km from its surface. The thickness of the air layer, in which secondary radiation is accumulated, amounts to 55 - 60 g/cm^2 - i.e.,

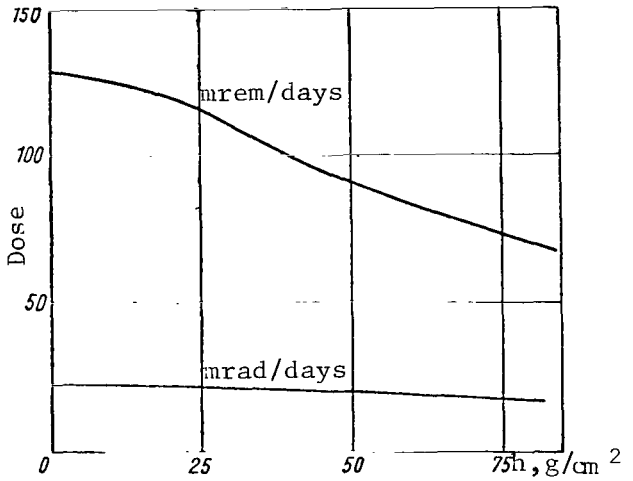

Figure 2.3

Dependence of the PCR Dose on the Thickness of Shielding made from a Light Material.

it is comparable to the maximum mean free path of particles in the body of the cosmonaut (2R = 50 g/cm^2), who is equipped with shielding (2 - 10 g/cm^2). Thus, taking the fact into account that the composition of the air and the composition of the tissue are approximately the same, one can identify the processes by which secondary reaction is formed in the body of the cosmonaut and in the layer of air. However, measurements of the altitude effect of ionization, which is caused by primary cosmic radiation (Ref. 38, Ref. 39), can be carried out with free-air ionization chambers or Geiger-Muller counters. Due to the fact that these counters do not have a tissue-equivalent nature, they cannot measure the absorbed dose in tissue.

TABLE 2.3

PCR DOSES NORMALIZED TOWARD A PARTICLE STREAM WHICH EQUALS 2.3 $\frac{1}{\text{cm}\cdot\text{sec}}$.

Data	Absorbed Dose	
	mrad / Days	mram / Days
Calculated	22.4	127.6
[38]	17.5	-
[15]	19-27	96-137
[47]*	27.4	192

* The physical dose is given, taking the RBE value of Q=7 into account, which is recommended by the authors (Ref. 47).

In addition, the transitional processes in dense substances and in the atmosphere are not identical. In a dense medium, the absorption of mesons is caused only by energy losses during their interaction with electron shells of atoms (ionization losses). In a gas-like medium, due their instability, part of the mesons decompose, and consequently a stream of mesons will be attenuated to a greater extent in air. It is true that a stream of μ-mesons, at the maximum ionization, amounts to 10% (Ref. 38) of the total number of particles, while the specific ionization of μ-mesons in light substances is almost constant and amounts to about 2 Mev/g·cm^2. In addition, if the fact is taken into consideration that the specific ionization of certain other components can be significantly greater, then the contribution of mesons to the total ionization can be expected to be unimportant. The contribution of secondary radiation to the absorbed dose, which is estimated within an accuracy of these approximations, amounts to 50 - 100%. /54

Thus, in interplanetary space, the dose which is formed by primary cosmic radiation, amounts to 34 - 45 mrad/days or 190 - 250 mrem/days.

Doses in Space Near the Earth. As the surface of the earth is approached, ionization decreases by approximately a factor of two, due to an increase in the screening action of the earth (the solid angle at which the earth is viewed increases), and by several factors (depending on the geomagnetic latitude) due to an increase in intensity of the geomagnetic field which deflects cosmic particles. In order to calculate the dose formed by the PCR in space near the earth, graphs were constructed (Ref. 15) showing the dependence of the dose magnitude on the geomagnetic latitude for different distances from the surface of the earth (Figure 2.4).

The mean dose, which is absorbed in the body of the cosmonaut during an orbit which lasts for a long period of time, can be calculated by the following formula:

$$D(i) = \frac{1}{\tau}\int_{t}^{t+\tau} P[\Lambda_i(t), h(t)]\, Q\, dt, \qquad (2.4)$$

where t is the flight time; τ is the period of one complete revolution of the satellite; h(t) is the distance from the surface of the earth as a function of time; i is the angle of inclination for the satellite orbit plane to the equatorial plane of the earth; $\Lambda_i(t)$ is the mean geomagnetic latitude for given i as a function of time; $P[\Lambda_i(t), h(t)]$ is the dose rate formed by cosmic radiation at a given latitude $\Lambda_i(t)$ and altitude h(t), mrad/days; Q is the coefficient of relative biological sensitivity. The quantity Q is also a function of $\Lambda_i(t)$ and h(t). The maximum value Q = 5.7 can be selected as the upper estimate. /55

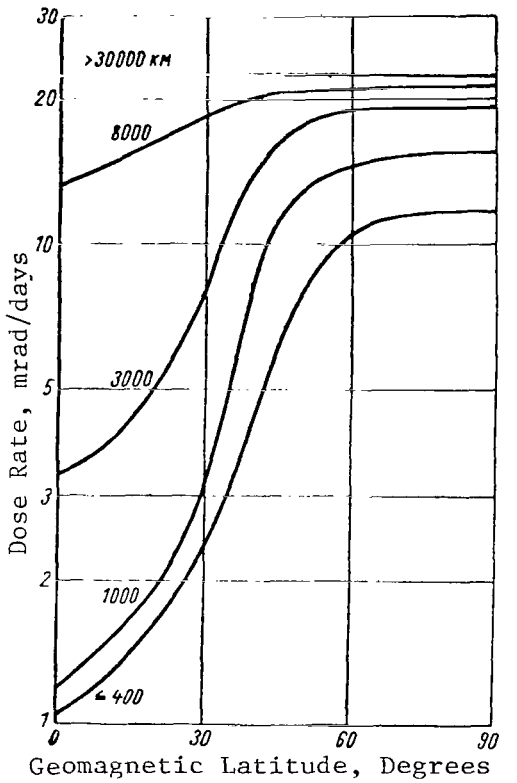

Figure 2.4

Dependence of the PCR Dose on the Geomagnetic Latitude for Different Altitudes Above the Surface of the Earth.

The quantities which are calculated for flights along various orbits are shown in Table 2.4.

As can be seen from the Table, the maximum absorbed dose for a trajectory having the parameters $i = 65°$, $h = 200 - 600$ km, amounts to 5.6 mrad/day or - if the secondary radiation is taken into consideration - 8 - 11 mrad/day. During the flight of the second spacecraft along a similar orbit on August 19 - 20, 1960, doses of primary cosmic radiation were measured directly, which amounted to 6 - 10 mrad/day. This provides good confirmation of the calculated data.

The estimates which are thus obtained for the dose, formed by primary cosmic radiation, showed that these doses exceed by several factors the maximum permissible values which are used at the present time for occupational irradiation. This means that,

during flights which last more than several years, the possibility of chronic forms of radiation defects will have to be taken into consideration, if protective measures against radiation are not taken.

TABLE 2.4

MEAN TISSUE DOSE VALUES OF PCR IN SPACE NEAR THE EARTH, WITH A SHIELDING THICKNESS OF 0 - 5gm/cm^2, mrem/days*

Angle of Inclination of Orbit Plane %	Altitude Above the Surface of the Earth km			
	200—600	1000—1500	2500—3500	7000—8000
0	5,0 (1,2)	5,5 (1,4)	15,2 (12,0)	59,6 (14,5)
45	12,7 (3,1)	20,8 (5,1)	38,5 (30,3)	73,7 (18,0)
65	22,8 (5,6)	33,3 (8,1)	51,0 (40,1)	77,9 (19,0)
90	27,3 (6,7)	37,4 (9,1)	54,1 (42,6)	78,7 (19,3)

* The dose in mrad/day is shown in the parentheses.

It should be kept in mind that the biological effect of multi-charged ions having high energies has not been studied as yet, and can have its own characteristics. Primary cosmic radiation does not create any danger during short cosmic flights (Ref. 40).

2.8. Measurement of the Radiation Dose During the First Cosmic Flights (Chapters 1, 9).

The orbits of the first, fourth and fifth spacecrafts were /56
located at a distance of 180-340km from the surface of the earth. This region is located below the radiation zones of the earth. Primary cosmic radiation and radiation from solar flares represent the sources of penetrating radiation here. Based on the well-known data regarding the possible composition of radiation and the doses during flights along cosmic orbits, sets of autonomous, dosimetric recorders (SDP) were used to measure the integral doses of radiation. These recorders included luminescent ILC dosimeters (Ref. 40, Ref. 41) with a range of $2 \cdot 10^{-3}$ -$1 \cdot 10^{3}$ rad, and film photodosimeters with a range of $2 \cdot 10^{-3}$ - $1 \cdot 10^{-1}$ rem for detecting slowed neutrons close to the experimental animals (Ref. 42).

The dosimeters were supplied with different filters in order to analyze the radiation composition. A filter made of 0.75 mm lead, which closed one half of the photodosimeters, served to compensate for their "hard behavior" for electromagnetic radiation in the energy range from 50 kev to 3 Mev. Filters made of 1.3 mm lead,

which were placed on certain ILC dosimeters, had the same purpose. Other ILC dosimeters did not have additional filters, because they were closed with a layer of 3.2 mm aluminum, which was equivalent - in stopping power - to a layer of 1.3 mm lead for protons having an energy of 5 - 300 Mev and electrons having an energy of 0.025 - 1 Mev.

Table 2.5 lists the results derived from measurements of the radiation dose using the ILC method. Data on photodosimeters are not given, since the integral radiation doses were in all cases lower than the sensitivity threshold of the method: 0.2 rad for photodosimeters and $2 \cdot 10^{-3}$ rem for the IPCN. As can be seen from the Table, reliable data were only obtained on the second spacecraft. Data from the first and fifth spacecrafts at least did not contradict data from the first. The values make it possible to conclude that, during the flights of the second, fourth, and fifth spacecrafts, radiation from solar flares had no effect on the radiation conditions within the cabin.

On the second spacecraft, readings given by dosimeters having filters made of aluminum were larger than from dosimeters having compensating lead filters. It can thus be concluded that electromagnetic radiation was included in the recorded radiation, apart from the PCR. This electromagnetic radiation was probably caused by the fact that this spacecraft passed through the outer radiation zone of the earth at high altitudes. The effective quanta energy of this radiation occurred in the region of 100 kev, which is indicated by the small difference between the reading given by dosimeters with filters made of aluminum, and without filters. This is also indicated by the conformity between the results derived from measurements of the calculated PCR doses, using dosimeters having compensating lead filters. If the electromagnetic radiation were harder, then the readings from dosimeters with filters made of aluminum and lead would be similar to each other, since the "hard behavior" of ILC dosimeters is small in the energy region above 300 - 400 kev. On the other hand, if the electromagnetic radiation were soft, then the difference between the readings of dosimeters without filters and with filters made of aluminum would be large. The doses of electromagnetic radiation did not lead, however, to a significant change in the radiation conditions. /57

Thus, the SDP sets, which were used on the spacecraft, made it possible to measure the radiation doses directly, which were accumulated during flights along orbits at an altitude of 180 - 340 km above the surface of the earth. The measured radiation doses of 6 - 10 mrad/day coincide with the results derived from calculating the PCR dose, and point to the fact that the radiation

conditions were safe, and were not complicated by radiation from solar flares during the flights of these spacecrafts.

TABLE 2.5

RADIATION DOSES WITHIN THE SPACECRAFT, mrad

Experiment	ILC Dosimeter Readings		
	Without Filter	with 3,2 мм Al	with 1,3 мм Pb
Second Spacecraft, Flight Duration of 25 Hours	13	12	6
	12	11	7,5
	14	10 *	10 **
Mean	13	11	~8,0
Fourth Spacecraft, Flight Duration of 1.5 Hours	7,4	4,3	—1,5
	5,5	0,4	7,9
	—2,1	—5,5	0,9
	—2,2	—0,9	—3,3
	—4,6	—	—2,6
Mean	0,8	~—0,4	~0,3
Fifth Spacecraft, Flight Duration of 1.5 Hours	0,6	—0,6	3,2
	1,9	3,9	2,5
	—1,1	3,9	—0,5
	0,6	1,9	—1,8
	—0,7	—	—0,1
	—1,0	1,3	—2,2
Mean	0,05	~2,1	~0,2

* Thickness of 3mm filter
** Thickness of 1mm filter

During the flights along the orbits of the spacecrafts "Vostok" and "Vostok-2", the radiation dose was also primarily formed by primary cosmic radiation. During the flights, the first cosmonauts were equipped with a set of individual dosimeters having a wide measurement range. Apart from the ILC dosimeters and the film dosimeters, during the flight of G. S. Titov, thermoluminescent glass was used, which made it possible to record the dose of γ-rays and protons having high energies in the region from 0.1 to 10^6 rad, and to retain information for a long period of time without any restrictions (Ref. 43). /58

Table 2.6 lists the data obtained from readings of the ILC dosimeters. Thermoluminescent and photodosimeters had readings which did not differ from zero.

The results, which were obtained in the flight of G. S. Titov,

practically coincided with the data which have been described for the flight of the second spacecraft. The difference between the readings given by dosimeters with different filters points to the presence of electromagnetic radiation, having energies of 10^5 ev. It can be assumed that this radiation was caused by the spacecraft passing though the outer radiation zone, in the region of the south-Atlantic anomaly and at high altitudes (Ref. 44, Ref. 45). The energy of the electrons which produced the electromagnetic radiation in the covering of the spacecraft was not less than 0.5 - 1 Mev (Ref. 18)

TABLE 2.6

DOSES OF COSMIC RADIATION (ILC DOSIMETER READINGS)

Cosmonaut	Doses of Cosmic Radiation, mrad						
	Without a Filter	3.2 mm Aℓ			1.3 mm Pb		
Yu. A. Gargarin	1.6	2.9	2.4	1.3	0.8	2.2	3.0
G. S. Titov	12.0	12.0	12.4	15.0	8.0	10.0	8.0

The recurrence of the results in the two experiments makes it possible to assume that radiation from solar flares did not make any significant contribution to the absorbed dose, and that it was caused primarily by primary cosmic radiation.

REFERENCES

1. Clay, I. Proc. Acad. Amst., 33, 711, 1930; Physica, 1, 363, 1934.

2. Waddington, C. J. Progr. Nucl. Phys., 8, 1, 1960.

3. Ayzu, Kh., et al. In the Book: Transactions of the International Conference on Cosmic Rays (Trudy mezhdunarodnoy konferentsii po kosmicheskim lucham). Vol. III, Izd-vo AN SSSR (USSR Academy of Sciences Publishing House) Moscow, 1960.

4. Ginzburg, V. L. Uspekhi Fiz. Nauki (Progress in the Physical Sciences), 74, 3, 522, 1961.

5. Madey, R. Preprint Amer. Astronaut. Soc. No. 15, 1962.

6. Perlow, G. J., Kissinger, C. N. Phys. Rev., 81, 522, 1951; 84, 572, 1951.

7. Critchfield, C., Ney, E., Oleksa, S. Phys. Rev., 85, 461, 1952.

8. Earl, J. A. Phys. Rev. Letters, 6, 125, 1961.

9. Syrovatskiy, S. I. Zh. Eksperim. i Teor. Fiz., 40, 6, 1788, 1961.

10. McDonald, F. B. Phys. Rev. 109, 1367, 1958.

11. Waddington, C. J., Fowler, P. H. Phyl. Mag., 1, 637, 1956.

12. Vernov, S. N., Chudakov, A. Ye. Doklady AN SSSR, 125, 2, 304, 1959.

13. Foelsche, T. Estimates of Radiation Doses in Space on the Basis of Current Data. International Committee on Space Research. Washington D. C., April 30 - May 11, 1962.

14. Vernov, S. N., Chudakov, A. Ye. Uspekhi Fiz. Nauki, 70, 585, 1960. /59

15. Reitz, D. Aerospace Engng., 20, 4, 28, 1960.

16. Shaefer, H. I. Aerospace Med., 31, 10, 807, 1960.

17. Fan, C. Y. et al. Phys. Rev. Letters, 5, 6, 272, 1960.

18. Peterson, L. E., Winckler, I. R. J Geophys. Res., 64, 7, 697, 1959.

19. McDonald, F. B., Webber, W. R. PICCR, AII, 428, 1962.

20. Fowler, P. N., Waddington, C. J. et al. Phyl. Mag., 2, 157, 1957.

21. Dyuk, P. Dzh. In the Book: Transactions of the International Conference on Cosmic Rays (Trudy Mezhdunarodnoy konferentsii po kosmicheskim lucham). Vol. III, Izd-vo AN SSSR, Moscow, 1960.

22. Tamai, E. Phys. Rev., 117, 1345, 1960.

23. Aizu, H., Fujimoto Y. et al. Phys. Rev., 116, 436, 1959; 121, 1206, 1961.

24. Neher, H. V. Phys. Rev., 103, 228, 1956; 107, 588, 1957; Winckler, I. R., Anderson, K. A. Phys. Rev., 108, 148, 1957.

25. Alfvén, H. Cosmical Electrodynamics (Kosmicheskaya elektrodinamika). Izd-vo Inostr. Lit. (Foreign Literature Publishing House), Moscow, 1952.

26. Fermi, E. Primary Cosmic Radiation (Pervichnoye kosmicheskoye izlucheniye). Izd-vo Inostr. Lit., Moscow, 1956.

27. Rossi, B. In the Book: Transactions of the International Conference on Cosmic Rays (Trudy Mezhdunarodnoy konferentsii po kosmicheskim lucham). Vol. I, Izd-vo AN SSSR, Moscow, 1959.

28. Delvayl, Dzh. et al. In the Book: Transactions of the International Conference on Cosmic Rays (Trudy Mezhdunarodnoy konferentsii po kosmicheskim lucham). Vol. III, Izd-vo AN SSSR, Moscow, 1960.

29. Dorman, L. I. Variations in Cosmic Rays (Variatsii kosmicheskikh luchey) Gostekhizdat (State Technical Publishing House), Moscow, 1957.

30. Simpson, J. A. et al Phys. Rev., 90, 934, 1953.

31. Fonger, W. H. Phys. Rev., 91, 351, 1953.

32. Nagashima, K. J. Geomag. Geoelectr., 5, 141, 1953.

33. Fermi, E. Phys. Rev., 75, 1169, 1949.

34. Shklovskiy, I. S. Cosmic Radio Emission (Kosmicheskoye radioizlucheniye). Gostekhizdat, Moscow, 1956; Shklovskiy, I. S. Astron. Zhurnal, 37, 256, 1960.

35. Ginzburg, V. L. et al. Uspekhi Fiz. Nauk, 62, 2, 37, 1957.

36. Ginzburg, V. L. Uspekhi Fiz. Nauk, 71, 3, 411, 1960.

37. Ginzburg, V. L., Syrovatskiy, S. I. The Origin of Cosmic Rays (Proiskhozhdeniye kosmicheskikh luchey). Izd-vo AN SSSR, Moscow, 1963.

38. Schaefer, H. J. Advances in Space Science. V. I. New York, London, 1959.

39. Singer, S. Physics of Elementary Particles and Cosmic Radiation (Fizika elementarnykh chastits i kosmicheskikh izlucheniy). Izd-vo Inostr. Lit., Moscow, 1960.

40. Antonov-Romanovskiy, V. V., Keirim-Markus, I. B. et al. Meeting of the USSR Academy of Sciences on the Peaceful Utilization of Atomic Energy. Division of Physics and Mathematics Session (Sessiya AN SSSR po mirnomu ispol'zovaniyu atomnoy energii. Zasedaniye OFMN). pg. 342, Izd-vo AN SSSR, Moscow, 1955.

41. Belov, I. P., Kalugin, K. S., Keirim-Markus, I. B. et al. Pribory i Tekhnika Eksperimenta, 4, 74, 1959.

42. Keirim-Markus, I. B., Pesotskaya, A. P. Collection of Radiometric

and Dosimetric Methodologies (Sbornik radiometricheskikh i dozimetricheskikh metodik). Medgiz (State Medical Publishing House), Moscow, 1959.

43. Bochvar, I. A. et al. Steklo (Bulletin of the State Glass Institute) ("Steklo", Byull. Gosudarstvennogo instituta stekla), 14, No. 2 (III), 77-89, 1961.

44. Kurnosova, L. V., Kolobyanina, T. N. et al. Discovery of a Radiation Anomaly over the Southern Part of the Atlantic Ocean at Altitudes of 310-340 km (Obnaruzheniye anomaliy radiatsii nad yuzhnoy chast'yu Atlanticheskogo okeana na vysotakh 310-340 km). In the Collection: Artificial Earth Satellites (Iskusstvennyye sputniki zemli), No. 8, Izd-vo AN SSSR, Moscow, 1961.

45. Ginzburg, V. L. et al. A Study of the Intensity of Charged Particles during the Flights of the Second and Third Spacecraft-Satellites (Izzledovaniye intensivnosti zaryazhennykh chastits vo vremya poletov 2-go i 3-go korabley-sputnikov). In the Collection: Artificial Earth Satellites (Iskusstvennyye sputniki zemli), No. 10, Izd-vo AN SSSR, Moscow, 1961.

46. Matusevich, Ye. S., Tsypin, S. G. Atomnaya Energiya, 15, 6, 499, 1963.

CHAPTER 3

SOLAR COSMIC RADIATION (SCR)

3.1. Origin of Corpuscular Solar Radiation

Sudden changes, which amount to 5 - 6 % on the surface of the earth, are sometimes observed along with periodic changes in the intensity of cosmic radiation, which was discussed in the preceding chapter. Between 1936 - 1956, such bursts of cosmic radiation, which could be observed throughout the earth, appeared four times in all, and therefore this is regarded as a very rare phenomenon. /60

Forbush (Ref. 1) and Ehmert (Ref. 2) first established on February 28, 1942, that this phenomenon was directly related to chromosphere flares on the sun. With the development of neutron monitors of cosmic radiation (Ref. 3) in 1950, which made it possible to increase the sensitivity of the measurements carried out on the earth, intense streams of radiation having a solar origin were repeatedly observed, and sounding balloons, ionosphere observations, and other methods were used more and more extensively to study them.

Intense SCR was observed after chromosphere flares on March 7, 1942; July 25, 1946; November 19, 1949; February 23, 1956; July 7, 1958; May 11 - 15, and July 10 - 17, 1959; May 4, and November 12 - 20, 1960 and at other times. Large corpuscular streams were observed one - four times for 4 - 5 years during the period of an increase or (more frequently) a decrease in solar activity (Ref. 4). Eight very powerful streams (Ref. 5) were observed from 1936 to 1960. The weakest streams - which could not reach the lower layers of the atmosphere, but which could be measured very well with sounding balloons, high-altitude rockets, and satellites - appeared much more frequently, 5 - 13 times per year (Ref. 4, Ref. 6, Ref. 7), or approximately once a month during the periods of an active sun - sometimes in groups one behind the other (Ref. 8).

Before discussing the origin of the ionizing radiation from solar flares, it is relevant for us to recall certain information about the sun (Ref. 9, Ref. 10). It represents an incandescent sphere made of plasma, with a surface temperature of about 5800° K and a mean density of 1.41 $g \cdot cm^{-3}$. It is assumed that toward the center of the sun the temperature increases up to 15 - 20 million degrees, the density reaches 130 $g \cdot cm^{-3}$, and the pressure reaches 150 - 200 million tech. atm. Under these conditions, thermonuclear reactions take place within the sun, which represent the source of

solar energy.

Above the surface of the sun - its photosphere - there is a very rarefied atmosphere; its inner portion - which extends for 12 - 14 thousand km above the photosphere - is called the chromosphere. The gas pressure (plasma) in the chromosphere amounts to about 80 mm Hg at the surface of the photosphere; the temperature amounts to from 6 - 7 to 20 thousand degrees. The slightly-luminescent solar corona, which is even more rarefied, extends behind the chromosphere. The temperature of the solar corona reaches 1 million degrees, and the density in the inner part reaches 10^{-15} g·cm^{-3} . Brighter, straight and curved coronal rays - which are sometimes closed by arcs on the surface of the sun, and which sometimes extend clear down to the earth orbit - are visible in the solar corona, which has an irregular, "frayed" form. /61

According to the radiation spectrum, almost all the known elements have been discovered in the solar composition. These elements include technetium, which points directly to nuclear processes occurring in the depths of the sun, because it has a comparatively small lifetime and must be constantly created anew in nuclear reactions. Hydrogen comprises 62.3% of the solar atmosphere mass; helium - 36%; and oxygen - 1%. The remaining elements must comprise less than 1% of the mass.

According to the atomic composition, the following constitute the solar atmosphere: hydrogen - 81.76%; helium - 18.17%; oxygen - 0.03%; magnesium - 0.02%; nitrogen - 0.01%; silicon - 0.006%; carbon and sulfur - 0.003%; iron - 0.0008%; etc. Lines of calcium, hydrogen, helium, and magnesium appear in the chromosphere radiation spectrum. They impart a red color to the chromosphere.

The surface of the sun does not seem to be uniform, and seems to consist of light kernels - granules. These are regions having a dimension of 200 - 1000 km, which are extremely unstable. The granules constantly shift along the surface of the sun at a velocity of 2 - 4 km/sec, appearing and disappearing in several minutes. It is assumed that the granules are the effect of convection currents of solar matter, which carry hot streams from the depths of the sun to the outside, and the colder streams - from the surface deep down to the interior. In addition, these currents maintain the temperature of the photosphere.

Much larger, bright filaments - faculae - which arise above the level of the photosphere - are also observed on the surface of the sun. The faculae usually form entire active regions - facular fields or facular plages. The brighter facular plages

are smaller than the plages which are less bright. At the edges of the solar disc, it can be seen that luminescent reeds, in the form of blades of grass, rise above the granules in the active regions. These reeds have a thickness on the order of 10^2km and a height of about 10^4km; they constitute the chromosphere. These are the so-called spicules. In the course of several minutes, the spicules rise from the photosphere, and then seem to melt, transmitting their matter to the solar atmosphere. Above the facular fields in the chromosphere, bright regions are observed, in the radiation of which the lines of ionized calcium are particularly intense. These regions are called calcium floccula.

/62

Figure 3.1

Photograph of the Sun on April 7, 1947 (Ref. 9)

The most noteworthy elements on the solar surface, which are frequently visible to the naked eye, are the sun spots - i.e., comparatively dark regions having an irregular form are located among the facular fields (Figure 3.1). The temperature of the photosphere within the limits of the spots is significantly lower, and amounts to 3700 - 4800° K. A lighter, fibrous penumbra, which has sharp edges of an irregular form and which surrounds the central nucleus, is particularly noticeable in the larger spots - which sometimes amount to more than 1% of the visible area of the solar disc. Sometimes the spots intersect the light filaments (Figure 3.2).

The assumption has been made that the spots are located below the level of the photosphere, and the penumbra represents the sides;

the filaments represent convection streams of solar matter of a type of granule, which can be seen in a cross-section view and in a side view, to a certain extent. Actually, the movement of solar matter from the shade to the exterior parts of semi-shade, and vice versa, has been recorded.

Due to the rotation of the sun, the spots move along the visible solar disc from the east to the west over a period of 27-35 days; they move more rapidly at the equator, and more slowly at the high latitudes. In addition, the spots are displaced somewhat through the photosphere. Gradually developing from barely-noticeable pores, having a diameter on the order of 10^2km, the spots exist from a period of several days up to several months, sometimes passing two /63
or three times along the visible solar disc. Pairs and groups of spots are frequently formed. As groups of spots develop, enormous spots appear with a penumbra, and the entire active region - the facular field - expands. After a certain period of time, the spots begin to decrease and disappear, and the facular field is reduced. However, the solar spots frequently last for a long period of time, and they can be reformed again and again. Sometimes grey regions appear in the facular field: penumbras without a dark nucleus.

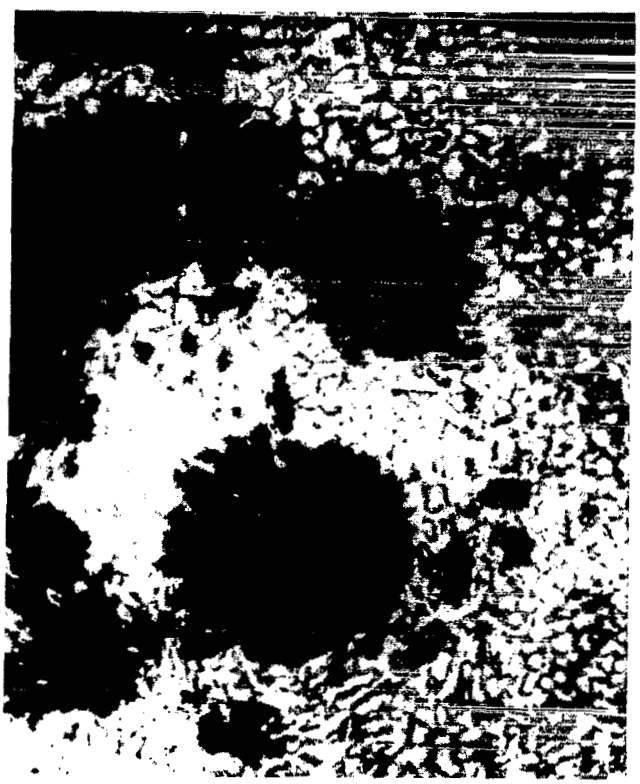

Figure 3.2

Photograph of a Group of Solar Spots (Ref. 11)

The frequency of appearance, the number of the spots, and the area of the solar disc which is occupied by the active regions characterize the solar activity. It undergoes period fluctuations, reaching a maximum of 50 - 200 spots per year after 7.3 - 17 years - on the average of each 11.13 years (Figure 3.3). The periods of maximum solar activity after 6.0 years, on the average, are replaced by periods of a quiet sun, when the number of spots decreases, so that sometimes not one spot is visible on its surface over a period of several weeks.

The last maximum activity, which was the largest for 200 years, /64
was observed in 1957 - 1958. The First International Geophysical Year was coordinated with it. The next activity minimum occurs in 1964 - 1966. In addition to 11-year periodicity of solar activity, a secular cycle is noted, with a period of about 80 years. The maximum of the secular cycle also occurs in our epoch.

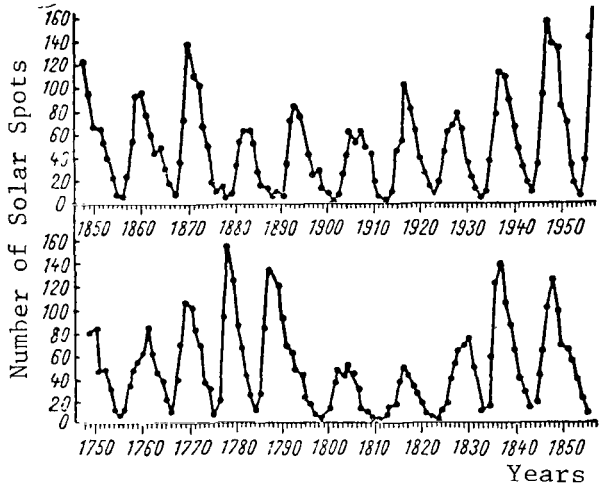

Figure 3.3

Number of Solar Spots (Ref. 9)

Local magnetic fields are related to the solar spots. The intensity of these fields is directed vertically to the surface of the sun, and amounts to 3000 oe. At the boundary of the spots, the force lines of the magnetic field bend, and return to the surface of the sun. Outside of the active regions, the magnetic field is small. At high latitudes and at the solar poles, the magnetic field is approximately the same as on the surface of the earth, and amounts to less than 1 oe.

It should be noted that the spots frequently appear as pairs with a different magnetism law. If spots with a northern magnetism are located in front in the northern hemisphere of the sun, then spots

with a southern magnetism move in front in the southern hemisphere. The tendency for spots having opposite magnetism to be repulsed can be observed. The fine structure of granules and faculae between such spots is sometimes remarkably similar to the distribution of iron filings between poles of a magnet.

During the initial period of solar activity, the spots appear primarily at the higher latitudes - about 35°. They then appear close to the equator, while during the period of the minimum they disappear at about 6° of solar latitude. The magnetism of the solar hemisphere changes its sign with a new cycle of solar activity. At times, both solar poles have the same magnetism. When the spots /65
appear anew, they are again observed at first at large latitudes, but this time spots with a southern magnetism are located in front in the northern hemisphere, and spots with a northern magnetism are located in front in the southern hemisphere.

In order to explain these phenomena, Babcock (Ref. 80) assumed that the force lines of the weak magnetic field of the sun pass only slightly under its surface. Due to the fact that the equatorial regions rotate more rapidly than the polar regions, the plasma substance of the sun absorbs the magnetic tubes of force in the equatorial zone, stretching them out in the form of loops along the equator, which they can encircle several times. Ultimately, these loops are broken apart, and their ends reach the solar surface in the form of pairs of opposite regions of increased magnetism. During this period, the entire magnetic field of the sun undergoes great disturbances, and then is again restored - but with the opposite field direction.

On the basis of these ideas, the solar spots can be regarded as those locations on the solar surface where local magnetic fields are so large that they freeze the motion of convection streams and thus cause cooling of the corresponding section of the photosphere. The weaker magnetic field in the region of the penumbra leads to the reverse effect, changing the turbulent, vortex motion of the convection streams into laminar, ordered motion. It thus intensifies and accelerates convection, and leads to the appearance of brighter facular fields around the spots, and to the intensification of solar activity in these regions.

Clearly-visible, emitted clouds of luminescent plasma - protuberances which lies above the chromosphere - are located at the edge of the solar disc, over the active regions. The protuberances are projected on the solar disc in the form of dark filaments, which reach gigantic dimensions at times. Single protuberances exist for several months, and others rapidly disappear. Sometimes the protuberances decrease

inversely with the filaments, which are similar (in terms of structure) to the lines of the magnetic field; sometimes they are broken off from the sun, which is most frequently observed at the locations of the solar spots. Since the second cosmic velocity on the surface of the sun equals 619 km/sec, the velocities of such eruptive protuberances reach hundreds and thousands of kilometers per 1 sec. The appearance frequency and the strength of the protuberances is also related to the periods of solar activity.

The surge of eruptive protuberances frequently follows chromosphere flares (Ref. 10, Ref. 12) - i.e., a sudden, local increase in the brightness of the chromosphere, which is particularly strong in the Hα-emission line of hydrogen. The chromosphere flares are observed over the region of solar spots which are usually large, with an extended penumbra, frequently appearing between spots with opposite magnetism. Sometimes the flare passes - as if it were pulsating - along the facular filament.

The chromosphere flares differ in terms of strength or in terms of class. A flare of class 1 encompasses 1.10^{-4} of the visible surface of the solar disc (1 + - greater than 1.10^{-4}, but less than 2.10^{-4}, etc.). The most powerful flares belong to class 3; 3 + , or 4 +. Apart from a brightness increase in the visible light, during a chromosphere flare the intensity of the ultraviolet and the soft x-ray radiation increases, and corpuscular radiation is produced. Bursts appear in the radial emission of the solar atmosphere. Sometimes, brief impulses of electromagnetic radiation are observed. /66

The brightness of the flare increases for several minutes - not more than ten - and then slowly fades away, sometimes remaining above the general level of the chromosphere luminescence for tens of hours. The photosphere temperature during the flare increases to 6.5 thousand degrees (Ref. 13). The appearance of an emission line for helium, which is sometimes observed during a flare, points to the fact that the chromosphere temperature can reach 25 thousand degrees.

Chromosphere flares on the sun and the processes accompanying them frequently produce geophysical disturbances - radio noises, ionosphere disturbances which lead to disruptions in radio communications, magnetic disturbances and storms, aurora polaris, and finally an increase in cosmic radiation - more precisely, the appearance of powerful corpuscular streams coming from the sun, which are of the greatest interest for this book.

Thus, the sun is a constant source of corpuscles, of solar "wind" (Ref. 14) originating from flocculi (Ref. 15), protuberances, and chromosphere flares. It is assumed that 10^{14} - 10^{15}g/sec of protons move from the sun to the earth with velocities of 300-4000km/sec

(energies of 1 - 100 kev), so that the stream of protons at the earth amounts to about $5 \cdot 10^9$ $cm^{-2} \cdot sec^{-1}$ (Ref. 2, Ref. 16 - 18). The hypothesis has even been formulated (Ref. 16) that the oceans on the earth were formed as a result of solar protons being captured, with the subsequent oxidization of hydrogen. The diffusive luminescence of the night sky is explained by the constant introduction of neutralized hydrogen atoms into the earth's atmosphere (Ref. 19).

On the other hand, on the basis of measurements carried out with ion traps which were placed on the soviet cosmic rockets, K. I. Gringauz assumes that there is no constant solar "wind", and that only streams of positively-charged particles on the order of $10^8 - 10^9$ $cm^{-2} \cdot sec^{-1}$ are emitted at times (Ref. 11, Ref. 20). Thus, although there is still no generally-accepted idea regarding the solar "wind", slow protons and ions of helium coming from the sun constantly arrive in the vicinity of the earth.

There are also different hypotheses regarding the origin of streams of hard corpuscular radiation from the sun. Some individuals assume that, due to the non-stationary magnetodynamic processes in the region of solar spots, the magnetic field compels the plasma to be compressed. As the result of this, the plasma rapidly warms up, and the plasma substance is ejected from this region (Ref. 21). The plasma ions are accelerated up to large energies in the local magnetic fields of the active solar regions. /67

V. P. Shabanskiy (Ref. 22) assumes that the plasma warms up to $4 \cdot 10^7$ °K, under the influence of shock waves which are propagated throughout the colder plasma which flows out to the region of solar spots. A thermonuclear reaction develops, during which protons - having an energy of 3 - 14 Mev - and α-particles - having an energy of 4 Mev - are formed. From the earth, the region in which the thermonuclear reaction develops is observed as a chromosphere flare.

Plasma streams are emitted from the region of the thermonuclear reaction at a velocity on the order of 1000 km/sec. The rapid particles which are formed during the reaction are captured by the magnetic traps in the upper layers of the chromosphere, and are gradually stored up there. During enormous flares, the trap overflows, and the corpuscles which are thus freed receive an additional acceleration. It is assumed that this process can explain the appearance of protons, having an energy on the order of 10^4 Mev, in the SCR spectrum. Apparently, the appearance of protons having large energies is always accompanied by surges of matter with a velocity on the order of 1000 km/sec to an altitude of 0.5 million km (Ref. 12).

Helium ions are also present with protons in solar corpuscular streams. There are fewer helium ions than there are protons, just as in the solar composition (Ref. 17, Ref. 23, Ref. 24). Multi-charged

ions (Ref. 23, Ref. 25) have also been detected, and tritium nuclei have been observed (Ref. 26). When the magnitude of their streams was compared with proton streams, it was found that the SCR composition is similar to the composition of the solar atmosphere. There are fewer heavy nuclei by one order of magnitude than there are in the PCR. Thus, the composition of radiation which is emitted during a flare indicates that it originates in the sun. Solar flares are the source of electrons. When these electrons interact with the magnetic fields of the sun, radio emission arises, and x-ray radiation arises as a result of braking in the solar atmosphere (Ref. 11, Ref. 27).

By way of a summation, it can be stated that processes are always occurring on the sun, as a result of which protons are emitted which have energies of tens of kiloelectron volts; the density of their stream in the vicinity of the earth amounts to $10^8 - 10^9$ $cm^{-2} \cdot sec^{-1}$. During chromosphere flares, the conditions are formed for the generation of powerful streams of hard protons and heavier ions of solar matter. The flares are accompanied by an increase in the ultraviolet and x-ray radiation, electromagnetic radiation of electrons, and radio emission.

During the periods of solar activity, the SCR streams are observed more frequently, appearing about once a month. The much greater SCR intensity, which is observed at sea level, appears much less frequently - not more than 1 - 2 times per year during an active sun.

3.2. Propagation of Solar Corpuscular Radiation in Interplanetary Space /68

The nature of the magnetic field in the solar system is of great importance in understanding the laws underlying the propagation of corpuscular solar radiation. According to the Zeeman effect, it has been established from observations of radio emission that the mean intensity of the magnetic field in the galaxy is less than, or equal to, $2 \cdot 10^{-5}$ oe ($\leqslant 2\gamma$) (Ref. 28). If it is assumed that isotropy of galactic cosmic radiation, having energies on the order of 10^{10}ev/nucleon, is established within the solar system under the effect of the magnetic field, the same amount can be obtained.

Measurements which were carried out on the cosmic rocket "Pioneer V" showed that the mean value of the magnetic field projection in the region of the earth's orbit amounts to 2.7γ (Ref. 29). Individual charged particles, having a small energy, cannot reach the earth from the sun, due to the curvature of their trajectory by the magnetic field. In addition, the weak magnetic fields must be readily destroyed even by very rarefied clouds of plasma substance which surround the sun.

There is no doubt that the magnetic field within the limit of the earth's orbit is created by solar action, if only to a partial extent. The changes in the intensity of galactic cosmic radiation, which are related to the periods of solar activity, also point to this. Simpson (Ref. 30 - 32) assumes that the force lines of the inner planetary field radiate out from the sun in radial directions, and acquire a random nature behind the orbit of the earth. This is confirmed in the works of Vitkevich, which are devoted to a study of non-uniformities of the supercorona of the sun using radio-astronomical methods. This characteristic of the magnetic field must be caused by the solar "wind", i.e., by radial motion of the plasma. The strength of the magnetic field must decrease by the square of the distance from the sun.

The magnetic force lines in the ecliptic plane are slightly curved toward the direction of motion of the earth (Ref. 33). The data shown in Figure 3.4 can serve to substantiate this. As can be seen from the figure, the clouds of magnetized plasma from the western half of the solar disc reach the earth much sooner - frequently after 1 - 2 hours -, while from the eastern half they appear after 4 - 6 hours, and frequently after 20 -40 hours (18 hours, on the average) (Ref. 34). The different frequency with which the SCR appears also points to this: of all the flares on the western half of the solar disc, ten cases of large SCR intensity were observed over 20 years; this intensity rapidly increased and, in individual cases, appeared in the absence of a visible chromosphere flare (corpuscular radiation from the edge of the sun). Corpuscular radiation comes from the center and eastern part of the sun very rarely, and increases slowly (Ref. 8, Ref. 34).

In the opinion of Gold (Ref. 35, Ref. 36), powerful magnetic fields, which occur above the active solar region, have the form of elongated loops, which leave this region and sometimes extend behind /69
the orbit of the earth. It is evident that this point of view does not contradict the opinion set forth by Simpson. Charged particles having a large energy - for example, protons with an energy of 10 Bev (Ref. 35) - move in such fields toward the earth, rolling in a spiral-like manner on the magnetic force lines. Particles, which are emitted at small angles to the force lines, reach the earth after 10 - 40 minutes, after they are emitted by the sun. In the region of the disordered magnetic field behind the orbit of the earth and in the magnetized plasma clouds, diffusion of the charged particles which escape slowly must occur.

When the particles move along the lines of the interplanetary magnetic field, they can enter the region of the earth only from points on the sun which are connected with them by the magnetic force lines. Several observations confirm this viewpoint. Thus, during a flare on February 23, 1956, a partial stream of corpuscular radiation

was detected on the earth by neutron monitors 10 - 30 minutes after the chromosphere flare (Ref. 32, Ref. 37). The flare began at 03.31 world time, it reached a maximum at 03.42, and ended at 04.15.

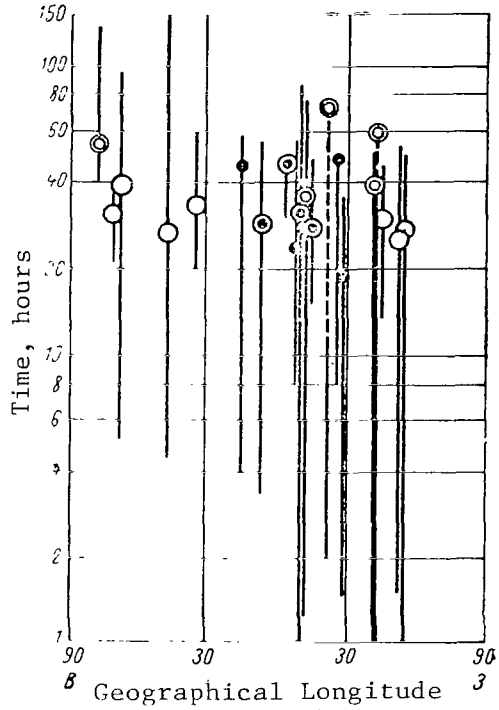

Figure 3.4

Time Required to Reach the Earth by Emitted Plasma Clouds of Solar Flares, as a Function of Geographical Longitude of the Flare (Ref. 34).

Vertical lines indicate the time during which geomagnetic disturbances were observed; the marks on the lines indicate the magnitude of the disturbances in units of γ: ⊙ - 400 γ; ● - (400 - 200) γ, O - (200 - 100) γ, ⊙ - 100 γ.

A sharp increase in the intensity of neutrons above different points on the earth's surface began at 03.41 - 03.51, the intensity reached a maximum at about 03.54 - 04.30, and then slowly decreased during the course of 20 hours. During the first minutes, the corpuscular streams proceeded in the direction of the sun, and very rapid protons first appeared, with energies on the order of 10 Bev; after 10 - 15 minutes, slower protons appeared. The directions at which the particles arrived gradually included the entire sky, because the motion of the particles acquired a diffusive nature, and from 03.58 on they were observed throughout the entire terrestrial sphere, including the nocturnal side. /70

According to the ideas presented above, the SCR scattering occurs in regions of disordered magnetic fields behind the orbit of the earth. Thus, the radiation gradually diffuses toward the earth, becoming weaker due to the loss of particles in the galaxy. Actually, the energy spectrum of the SCR on February 23, 1956, changed slowly, and the dependence of the stream density on time closely coincided with the solution for a diffusion-type of equation (Ref. 32)

$$N(t) = \frac{B\, e^{-R^2/4D\,(t-t_0)}}{8\,[\pi D\,(t-t_0)]^{3/2}}, \qquad (3.1)$$

where D is the diffusion coefficient, R is the distance from the source of the particles, and t_0 is the initial moment of time. The dimensions for the region of diffusion distribution of corpuscular streams were estimated as 750 million km from a comparison of the calculated data with the experimental observations.

The phenomena, which were observed after the chromosphere flare on February 23, 1956, were characteristic for solar cosmic radiation of relativistic energies, which reaches the earth after 10 - 30 minutes following the appearance of a flare on the sun. The radiation is propagated by a wide cone, and encompasses a large part of the solar system, being diffused within it after several days. The intensity of the radiation in interplanetary space is very large sometimes. According to data given by Winckler (Ref. 38), on February 23, 1956, the density of the proton streams reached 10^5 $cm^{-2} \cdot sec^{-1}$. It is important to point out that for relativistic streams directional, angular distribution from the side of the sun is a first characteristic. The diffusion streams are distributed in an isotropic manner with respect to angles.

The phenomena, such as were observed on February 23, 1956, Winckler calls relativistic phenomena (Ref. 38), and Waddington (Ref. 5) relates them to Class B. Solar cosmic radiation of this class was observed on February 28, 1942, March 7, 1942, July 25, 1946, November 19, 1949, August, 1950 (weak), July 16, 1959, May 4, 1960, and November 12, 15, and 20, 1960 (the latter, which was from flares, was weak) (Ref. 25). Due to the large energy, which exceeds 1 Bev, which the protons attain for such flares, it is possible to record them by secondary neutrons at sea level, sometimes throughout the entire earth (proton energies greater than 15 Bev). The latter cases are isolated. In addition to the statements given above, it can be noted that all cases of relativistic SCR, except one, are produced by flares which are observed in the western part of the solar disc (Ref. 25), and even behind its western edge, as was the case on November 20, 1960 (Ref. 8, Ref. 39, Ref. 40).

In the majority of cases, corpuscular radiation - which is undoubtedly related to solar flares - appears in the region of the

earth after several hours, and even days after the flare (Ref. 34, Ref. 41, Ref. 42) (see Figure 3.4). This delay does not coincide with the velocity of protons for an energy of 10 - 10^3 Mev. At the present time, it is assumed that during chromosphere flares the /71
sun emits clouds of plasma with a magnetic field which is frozen in them. This magnetic field creates a magnetic trap for charged particles. Actually, during the flight of the cosmic rocket "Pioneer V" it was possible to observe such a cloud by an increase in the interplanetary magnetic field up to 5 - 60 γ , simultaneously with a magnetic storm on the earth (Ref. 29).

Bunches of magnetized plasma are propagated with a velocity on the order of 1000 km/sec in a cone with an aperture angle of 60 - 90° (Ref. 33). Charged particles gradually diffuse from the plasma cloud in accordance with equation (3.1) as can be seen from Figure 3.5 (Ref. 43). The thickness of the plasma bunch reaches 10^8 km, and it passes around the earth sometimes for 1 - 2 days (Ref. 33). After this, the corpuscular radiation can reach the earth, diffusing from the region of the disordered, interplanetary magnetic field over a period of several days.

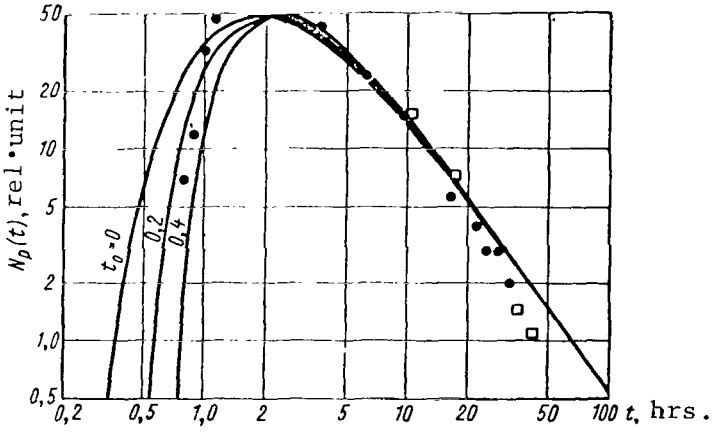

Figure 3.5.

Dependence of Proton Stream Density of SCR on Time (Ref. 42).

The Solid Lines Indicate Solution of the Diffusion Equation (3.1).

The features described above are characteristic for SCR, which Winckler (Ref. 38) calls non-relativistic, and which Waddington refers to SCR of Class A (Ref. 5). Non-relativistic corpuscular streams appear rather frequently after flares of Class 2 - 3 +, sometimes one behind the other - as, for example, in July, 1959. The particle streams are sometimes very large, and their density

reaches 10^7 $cm^{-2} \cdot sec^{-1}$ (Ref. 38).

The interesting case of several chromosphere flares, following one behind the other and accompanied by SCR, was observed in September, 1960 (Ref. 42). On September 2, 1960, at 07.06, a chromosphere flare of Class 3 occurred on the sun, which was the source of a plasma cloud having a magnetic field which was frozen in it. Only 8 hours after this, the neutron monitors on the earth noted /72
a slight increase in the stream of cosmic rays, which reached a maximum at 19 hours. At 22.34, a new flare of Class 3 led to the eruption of a non-magnetic gas cluster and on September 3, 1960, at 00.40, a third flare of Class 3 was formed, which served as the source of corpuscular radiation. It was accompanied by solar radio noises, which pointed to the introduction of electron streams into the solar atmosphere simultaneously with the emission of protons beyonds its boundaries. A new Class 3 flare, at 01.12, was accompanied by a brief burst of x-ray radiation, which was observed at the upper atmospheric layers on the diurnal side of the earth and which was caused by the braking of electrons, which were emitted during the flare, in the solar atmosphere. The readings of the neutron monitors began to increase, and somewhat later an increase was also noted in the intensity of cosmic rays in the upper atmospheric layers. The readings of the neutron monitors, which characterized the density of proton streams having an energy greater than 500 Mev, reached a maximum after 9 hours; at the upper atmospheric layers, the density of the proton streams, having energies of about 250 Mev, reached a maximum after 10 - 11 hours, and the density of proton streams with energies of about 100 Mev - after 14 hours on September 3, 1960.

Measurements which were made on high-altitude rockets, which operated at mean latitudes, showed that the composition of proton streams going toward the earth included particles having energies on the order of 10 Mev, which traversed a trajectory from the sun for several hours. Solar cosmic radiation continued up to September 6, 1960.

The front of the magnetic plasma from the first flare, moving /73
with a velocity of about 1000 km/sec, reached the region of the earth after 43 hours - at 02.30 world time on September 4, 1960, causing a magnetic storm. After that, a Forbush decrease began in the PCR, which was recorded by neutron monitors. Since the Forbush decrease pointed to a change in the magnetic field in the vicinity of the earth, the conclusion was drawn that the first plasma bunch brought magnetic fields with it.

The plasma bunch from the second chromosphere flare did not

cause a Forbush decrease, and apparently did not carry a noticeable magnetic field with it. However, it caused magnetic disturbances on the earth at 18.30, 16 hours after the first disturbance - i.e., after the same amount of time as the interval between the first two flares.

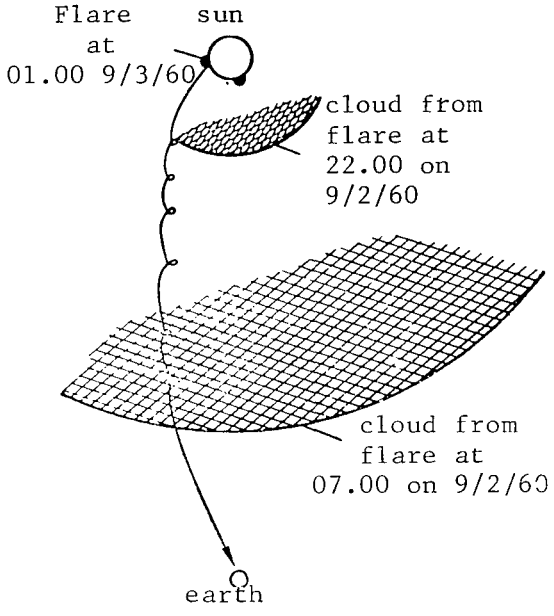

Figure 3.6

Propagation of Solar Corpuscular Streams on September 2 and 3, 1960 (Ref. 42).

A schematic picture of the SCR sequence is shown in Figure 3.6 (Ref. 42). The fact that the SCR propagation required several hours can be explained by the diffusion of corpuscular radiation in the plasma clouds, and the appearance of protons, having energies on the order of 10 Mev, at the boundary of the atmosphere at mean latitudes can be explained by a disturbance of the magnetic field of the earth, caused by plasma bunches. However, this phenomenon will be examined in the following section.

Another case of successive flares on April 27 - 30, 1960, is shown in Figure 3.7 (Ref. 25, Ref. 34). The solar flare on the eastern edge of the solar disc formed a magnetic plasma bunch with protons, having a low energy less than 10 kev (1). This bunch caused a magnetic storm upon reaching the earth (2). On the next day, a new flare of Class 3 in the same active solar region was accompanied by the emission of rapid corpuscles 3, which were injected

into the region of space occupied by the plasma cloud from the first flare. Therefore, after 1.5 hours - i.e., which was unusually rapid for flares on the eastern half of the sun - the SCR reached the earth 4. After reaching the maximum corpuscular radiation on the earth, its intensity decreased, due to the departure of corpuscles /74
from the plasma cloud as the result of diffusion 5. At this time, the sun emitted one plasma cloud, and a new Class 3 flare was formed on the west side of the solar disc, which was accompanied by SKI 6. The interaction of this corpuscular stream with the foregoing cloud caused its partial dispersal, diffusion, and a slow increase of the SCR on the earth, as compared with the normal pattern of radiation from flares on the western half of the solar disc (dashed line). When the plasma clouds from flares on April 28 and 29 reached the earth, magnetic disturbances 7 and 8 were observed.

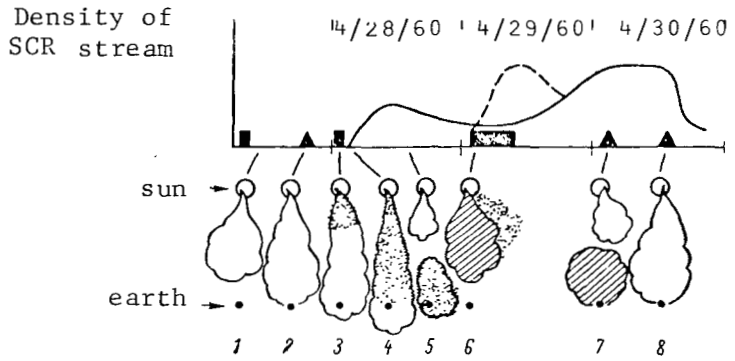

Figure 3.7

Multiple SCR on April 27 - 30, 1960 (Ref. 25, Ref. 34).

The Rectangles on the Time Axis are Chromosphere Flares; the Triangles Represent the Beginning of Geomagnetic Disturbances.

It follows from the sequence of these events that both rapid corpuscular streams and plasma bunches which have been emitted with slow particles can be formed during a chromosphere flare. The rapid corpuscles are not captured by the cloud of magnetized plasma which is emitted during the flare, because it has still not been formed (Ref. 25).

Thus, the SCR is propagated from the sun to the earth along a trajectory which is slightly curved toward the motion of the earth along its orbit, so that radiation from flares on the western half of the sun is observed more frequently than is radiation on the eastern half. Relativistic SCR (Class B), for which proton energies

up to 15 - 50 Bev are characteristic, reaches the earth with a velocity which is close to the speed of light, and appears 10 - 40 minutes after the chromosphere flare. A directional, angular distribution is characteristic for this radiation.

Non-relativistic SCR (Class A), which is frequently observed after relativistic SCR, is characterized by proton energies of 10 - 500 Mev. It can appear in the vicinity of the earth, together with a cloud of magnetized plasma which has captured it, or it can be scattered in the clouds which move toward the earth at velocities on the order of 1000 km/sec. There is an interval of several hours up to several tens of hours between a flare on the sun and the detection of SCR on the earth; at first, the harder particles appear, and then the softer particles.

Due to diffusion in the magnetic plasma bunches and in the interplanetary field, the SCR can continue for a long period of time - several days, i.e., much longer than the flare giving rise to it. In accordance with the laws of diffusion, the damping of the SCR occurs approximately proportionally to $t^{-3}/_{2}$. This radiation has an isotropic, angular distribution (Ref. 25).

3.3. Interaction of the SCR with the Geomagnetic Field

The magnetic field of the earth screens the charged particles coming from the sun, in the same manner as the galactic cosmic radiation; it does not permit particles to reach the earth which have a hardness which is less than a maximum hardness for a given geomagnetic lattitude. Therefore, for example, it is frequently impossible to detect non-relativistic SCR at latitudes below 60° /75
(Ref. 38), for which the maximum proton energy is greater than 300 Mev. The closer the point of observation is to the poles, the softer is the SCR spectrum, and the SCR must reach the geomagnetic latitudes above 70° more frequently and be more intense.

However, it can be seen in the examples given above that in many cases the earth encounters a cloud of magnetic plasma, which can temporarily distort and compress the earth's magnetic field, or can partially neutralize it beyond the limits of the atmosphere (Ref. 43). The distortion of the magnetic field causes magnetic disturbances and storms, and disturbs the configuration of the earth's radiation zones, contributing to their introduction into the atmosphere and to the formation of aurora polaris (Ref. 19).

With a strong disturbance of the geomagnetic field, soft corpuscles of the SCR penetrate to the atmosphere of the earth;

these corpuscles are usually deflected by the magnetic field (Ref. 44). Protons having small energies are observed at every latitude, just as during the case examined above in September, 1960. Protons having energies less than 40Mev (or electrons which are softer than 3 Mev) were observed with the aid of sounding balloons at a latitude of about 60° (Ref. 41, Ref. 45). Soft radiation was observed at every latitude and at late stages of the SCR after a flare on February 23, 1956 (Ref. 32).

Since a plasma cloud encompasses a large part of inner planetary space, a Forbush decrease in the PCR begins simultaneously with magnetic storms. It is significant that during the Forbush decrease the soft part of its spectrum is attenuated to a greater extent. In addition, the spectrum for protons coming from the sun becomes softer (Ref. 41, Ref. 45), since they can more readily penetrate to the mean latitudes, at which observations are usually carried out.

Relativistic SCR precedes magnetic disturbances; in the case of non-relativistic SCR, the beginning of a magnetic storm can sometimes serve as a signal for an increase in the corpuscular stream.

Apart from magnetic disturbances, ionosphere disturbances are observed when plasma bunches penetrate to altitudes from 100 to 300 km; these ionosphere disturbances are apparent, in particular, in the absorption of cosmic radio noises at frequencies in the 28 and 50 Megacycle bands. The most powerful plasma streams, which accompany the SCR, attenuate the radio emission at a frequency of 28 Megacycles by a factor of 30 or more (Ref. 9, Ref. 46).

3.4. Energy Spectrum and Composition of Corpuscular Radiation of Solar Flares

Corpuscular radiation from solar flares penetrates the atmosphere to a depth of 300 g/cm^2 (Ref. 41). Therefore, along with the utilization of the earth's magnetic field as a spectrometer, it is possible to determine the energy spectrum of the SCR by its attenuation in the atmosphere, by comparing data obtained at different latitudes (Ref. 41, Ref. 47, Ref. 48).

During the SCR, after a flare on May 10, 1959, the atomic composition and radiation spectrum were determined directly with the aid of stacks of nuclear emulsions placed on sounding balloons (Ref. 49). An analogous experiment was repeated on rockets which were launched after solar flares at 14.08 on September 3 (Ref. 50, /76

Ref. 51) and at 16.04 on November 13, 1960 (Ref. 23).

It has been established that corpuscular radiation from solar flares consists primarily of protons. However, it has been observed that its composition includes from 3 to 15% helium ions, and also heavier ions with a charge from +6 to +18(Ref. 17, 23, 24, 48 - 50, 52, 53). Ions with charges of $3 \leqslant Z \leqslant 5$ have not been detected.

A stream of ions with the charge $6 \leqslant Z \leqslant 8$ comprises about 0.1 - 0.2% of the total corpuscular stream (Ref. 23, 49, 50), and in the $10 \leqslant Z \leqslant 18$ region it is on the order of 0.05% (Ref. 50). Thus, the SCR composition includes one order of magnitude fewer heavy ions than does the PCR composition; in addition, it is similar to the composition of the solar atmosphere, which points to the solar origin of the SCR.

It is difficult to determine whether the atomic composition of corpuscular radiation remains unchanged during different flares and during one flare, since very little experimental data have been obtained up to the present. There are isolated indications that the radiation composition varies. Thus, at 16.04, on November 13, 1960, 60 protons, 75 α-particles, and one ion with a charge of 7 were recorded in the SCR with the aid of geophysical rockets (Ref. 23). Thus, in this case the α-particles comprised more than half of the particle stream. Tritium nuclei were discovered in the casing of the earth satellite "Discoverer XVII"; these nuclei were 100 times greater than could be explained as the result of nuclear reactions under the influence of the PCR (Ref. 26).

Electrons are undoubtedly present in the SCR composition, along with positive ions. This is confirmed by the fact that during flares, electromagnetic radiation and radio emission are generated in the solar atmosphere, the radiation zones of the earth change considerably after large flares (Ref. 54, Ref. 55), and the plasma clouds as a whole are electroneutral. However, very little is known about the stream and energy spectrum of electrons. There are apparently no mesons in cosmic rays from the sun (Ref. 8).

Since the SCR consists primarily of protons, and since there are very few data about the remaining components, it is advantageous to examine the energy radiation spectrum for protons. The spectra of heavier ions are probably similar. We should note that in individual cases, when electromagnetic radiation was observed (Ref. 27, 56, 57), its spectrum lay within the 20 - 80 kev region (Ref. 27) and the 200 - 500 kev region (Ref. 56). The dose rate at the boundary of the atmosphere is on the order of 10^{-9} and 10^{-6} roentgen$\cdot$sec^{-1}, respectively - i.e., it was too small to represent any radiation danger.

Foelsche (Ref. 4) collected detailed information about the proton spectrum in SCR occurrences which have been studied more extensively. On the basis of several primary sources, he attempted to reconstruct proton spectra from flares on November 12, 1960, at different stages of the SCR. The differential proton spectra, which were constructed on the basis of data given by Foelsche, are shown in Figure 3.8, together with data given by A. N. Charakhch'yan (Ref. 45), which are characteristic for weak SCR streams. It can be seen from this figure that the proton spectra differ during different flares, and cannot be expressed by one power function. An approximation of the curves in Figure 3.8 leads to the expressions for the differential energy spectra of the protons, which are compiled in Table 3.1

/77

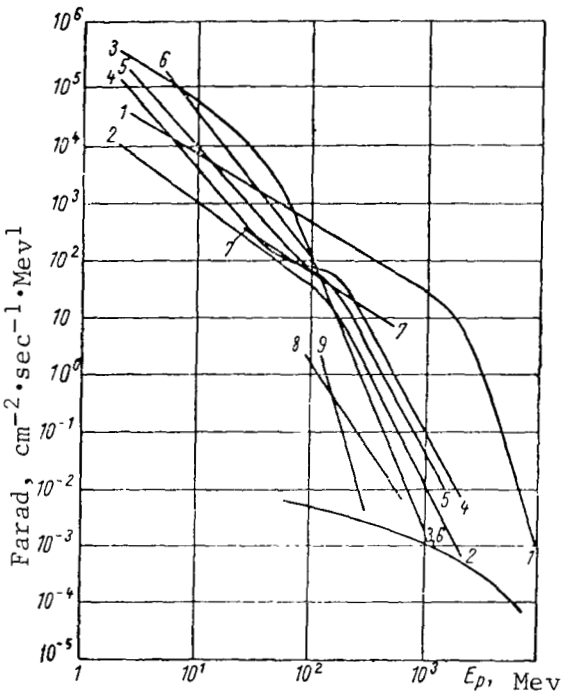

Figure 3.8

Differential Proton Spectra of SCR (Ref. 4, Ref. 45). The Numbers on the Curves Correspond to the Numbers of the Spectra in Table 3.1. The Lower Curve Represents the PCR.

It follows from Figure 3.8 and Table 3.1 that for large energies, the proton spectra sharply decrease with the exponent from 3 to 7. The lower limit of this spectra region lies within the 50 - 150 Mev region, and during the flare on February 23, 1956, it comprised 1.5 - 2 Bev. According to data given by Charakhch'yan and others,

the large values of the exponent 6 - 7.5 are characteristic for cases when the magnetic field around the earth is disturbed: magnetic storms and a Forbush decrease are observed. Thus, as was indicated above, the protons can be observed at every latitude. It is possible that the spectra outside of the limits of the earth's magnetic field have a similar form.

Smaller values for the exponent from 3 to 5 are observed when the geomagnetic field is not disturbed - when it influences the protons like a spectrometer, deflecting the protons from the equatorial regions to a greater extent, the smaller they are, and when the non-relativistic SCR reaches the atmosphere only at high geomagnetic latitudes, on the order of 60° or more. /78

In the lower energy region, which Foelsche extrapolates up to several megaelectronvolts, the exponent has a value from 1.2 to 2.5. This spectral region extends to the side of large energies up to 30 - 100 Mev, and during the SCR after a flare on February 23, 1956, the flat part of the spectrum amounted to 2 Bev. As can be seen from the data obtained on February 23, 1956, and November 12, 1960 (see Figure 3.8), the spectral slope changes very little with time, but the spectra become somewhat softer as the intensity decreases.

The proton spectrum from a flare on November 12, 1960, has a complex form. The stream density of protons having a large energy decreases with time, and the intensity in the soft part of the spectrum continues to increase constantly up until the observation was terminated - i.e., for 32 hours. It is not impossible that the experimental spectrum of the protons is the result of SCR overlapping /79 from two flares, which follow one behind the other and which produce two maxima in the readings of the neutron monitors - 3 and 7 hours after the flare of Class 3+, at 13.22 world time, on November 12, 1960 (Ref. 58, Ref. 59). It is also possible that Foelsche could not accurately coordinate the experimental data obtained by several authors at different locations and by different methods (Ref. 50, 52, 58 - 60), and the spectra which he obtained differed from the actual ones.

The unusual feature of spectra for relativistic SCR on February 23, 1956, and November 12, 1960, consists of the fact that the flat part of the proton spectrum extends far into the region of large energy, up to 1.5 - 2 Bev. Therefore, such radiation is distinguished by a great penetrating power, and it is difficult to provide a protection from it.

The radiation spectrum from the flare on May 10, 1959, is characteristic for non-relativistic SCR. This is the largest

TABLE 3.1

DIFFERENTIAL ENERGY PROTON SPECTRA OF SOLAR COSMIC RADIATION /78
[APPROXIMATION FROM DATA (REF. 4, REF. 45)]

	Date	Time from Beginning of SCR, Hrs.	Differential proton Spectrum Φ $cm^{-2} \cdot sec^{-1} \cdot Mev$
1	2/23/1956	0	$1.3 \cdot 10^5 E^{-1.2}$ (3 Mev - 1 Bev); $1.7 \cdot 10^{22} E^{-6.5}$ (2 - 20 Bev)
2	2/23/1956	19	$3.5 \cdot 10^4 E^{-1.5}$ (3-150 Mev) $8 \cdot 10^9 E^{-4}$ (150 Mev - 2 Bev)
3	5/10/1959	33	$1 \cdot 10^6 E^{-1.5}$ (3 - 30 Mev) $7.2 \cdot 10^{11} E^{-4.9}$ (50-500 Mev)
4	11/12/1960	0 - 10	$1 \cdot 10^6 E^{-2.4}$ (3-40 Mev) $5 \cdot 10^{10} E^{-3.7}$ (150 Mev - 2 Bev)
5	11/12/1960	10 - 14	$2 \cdot 10^6 E^{-2.4}$ (3-70 Mev) $4 \cdot 10^9 E^{-3.7}$ (100 Mev - 1.5 Bev)
6	11/12/1960	14 - 32	$1.5 \cdot 10^8 E^{-2.6}$ (5-100 Mev) $9 \cdot 10^{11} E^{-4.9}$ (100-500 Mev)
7	Averaged Data (Ref. 45)	-	$1.9 \cdot 10^6 E^{-3}$ (70 - 600 Mev)
8	Averaged Data During the Forbush Decrease (Ref. 45)	-	$1 \cdot 10^{15} E^{-7}$ (100-250 Mev)

Note. The energy intervals for protons, in which the given analytical expressions for the form of the spectrum are valid, are shown in the parentheses.

of the proton streams having mean energy (in tens of megaelectronvolts) which have been encountered to the present time, and - along with the SCR on February 23, 1956 and November 12, 1960 - it can provide an idea of the most dangerous cases of corpuscular solar radiation.

As can be seen from Figure 3.8, the differential density of the proton stream, having energies of about 10 Mev, amounted to $10^3 - 5 \cdot 10^4$ $cm^{-2} \cdot sec^{-1} \cdot Mev^{-1}$ in these cases (Ref. 38), and possibly 10^8 $cm^{-2} \cdot sec^{-1} \cdot Mev^{-1}$, if the contribution of the softer protons is taken into account (Ref. 47, Ref. 53). As was already noted, such /80
corpuscular streams are observed only after very powerful chromosphere flares of Class 3 - 4, which occur not more frequently than

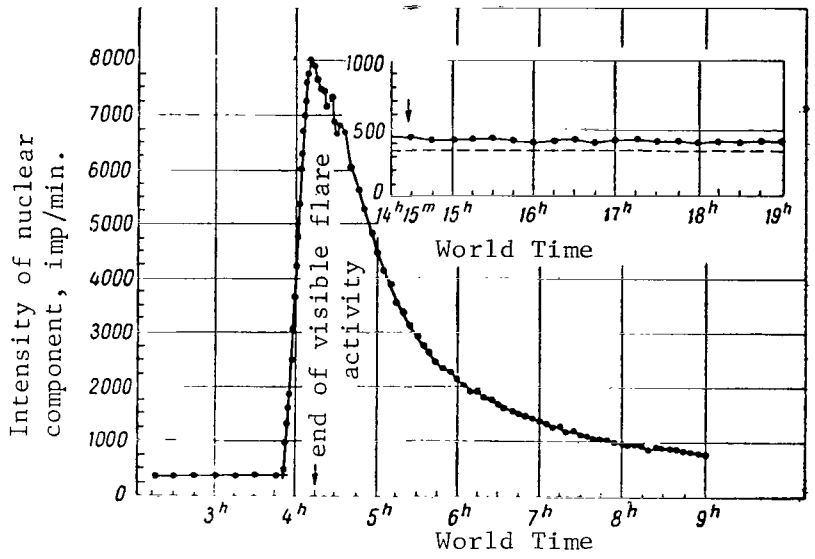

Figure 3.9

Increase and Damping of Solar Corpuscular Streams After the Flare on February 23, 1956. Data Obtained by Neutron Monitors (Ref. 32).

1 - 2 times per year during the period of solar activity, and do not occur during the years of low solar activity.

The weak SCR, which appear comparatively frequently, are characterized by spectra 7 and 8 (Table 3.1), by the differential density of a proton stream having an energy of about 10 Mev, which amounts to 10 $cm^{-2} \cdot sec^{-1} \cdot Mev^{-1}$, and by a total density stream $10 - 10^2 cm^{-2} \cdot sec^{-1}$ (Ref. 45, Ref. 61). This is usually non-relativistic radiation, which increases comparatively slowly - as can be seen from Figure 3.5 and 3.7 - sometimes over a period of tens of hours, and which is then damped according to the law $\sim t^n$ with an exponent n on the order of 1.5 - 3 (Ref. 38, Ref. 45, Ref. 62).

The density change with time of a stream of relativistic protons can be seen in the example of radiation from a flare on February 23, 1956 . It is possible to trace the arrival on the earth of protons having such energies by readings on neutron monitors (Figure 3.9) (Ref. 32). In contrast to non-relativistic radiation, the stream density increases in a very short time,

20 - 40 minutes, and then decreases according to the law t^{-n} with n on the order of 1 - 2 (Ref. 32, 38, 63). It follows from the statements made in the preceding section that - apart from the original conditions at the time of the flare - both the spectrum and the time dependence of the SCR depend to a significant degree upon the interaction of corpuscular streams with clouds of plasma which is emitted by the sun. Therefore, they cannot be represented by single laws, nor can they be predicted for an explicit case.

3.5. Tissue Doses of Corpuscular Radiation from Solar Flares

The material presented above makes it possible to formulate quantitative estimates of the tissue dose from SCR. However, we must first clarify what dose must be determined. Cosmic radiation from solar flares continues from several hours up to several days. It can be regarded as a short-term process from the point of view of influencing the human organism, because the processes for development of radiation damage during the action of the SCR cannot develop to a sufficient extent. As was pointed out in Chapter 1, the immediate aftereffects of this type of irradiation can be characterized by the mean tissue dose. Consequently, it is necessary to approximate the mean tissue dose from the SCR in the human organism as the criterion for the damaging effect of the SCR.

Small RBE coefficients, which are similar to those expressed by the dashed curve in Figure 1.11, are characteristic for the immediate aftereffects produced by short-term irradiation. When the mean tissue doses are calculated in rems, it is necessary to use the values of this curve or similar data regarding the RBE coefficients.

In many cases, the spectrum for the SCR protons is steep at the side of large energies. For such radiation, a sharp drop in the tissue dose from the surface of the body to the interior is characteristic. Therefore, it can be shown that the mean tissue dose is not dangerous, and the magnitude of the surface dose on the skin or on the crystalline lens of the eye can cause burns or more serious aftereffects. In these cases, it is necessary to determine the magnitude of the surface dose and the tissue dose on the crystalline lens of the eye, because for soft radiation the critical organs of the human body are the skin, the hypodermic muscle tissue, and the crystalline lens of the eye (Ref. 64). It must thus be taken into consideration that a tissue dose of greater than 600 - 1000 rem for a brief period of time causes skin burns, /81

and a tissue dose of more than 6000 rem causes their necrosis.

Schaefer (Ref. 65 - 67) calls attention to the irregularity in the distribution of tissue doses from the SCR when calculating their distribution in a human model, in the form of a tissue equivalent sphere having a diameter of 52 cm and a mass of 75 kg. As he noted, if the cosmonaut shuts his eyes tightly during the SCR, then the tissue dose in the crystalline lens decreases by 30%. Schaefer proposed characterizing the irradiation by tissue doses at a depth of 1mm, 1 and 10 cm, but his proposal cannot be regarded as having a serious basis.

At the present time, the fact cannot be overlooked that during a long interplanetary flight individuals will be repeatedly subjected to the influence of SCR in small doses. For such chronic irradiation, it is important to approximate the probability with which individual aftereffects will appear, which are determined not by the mean tissue dose (Chapter 1), but by the tissue dose in the critical organs, and the RBE coefficients for such influence will be large (the solid curve in Figure 1.11).

In order to provide a sufficiently comprehensive estimate of the radiation danger of SCR, it is thus necessary to determine the mean tissue dose and the surface dose (or the dose on the crystalline lens) with the RBE coefficients, which are characteristic for acute irradiations, and the tissue dose in the critical organ (maximum tissue dose) with RBE coefficients which are characteristic for chronic irradiation. Further analysis and the accumulation of experience will probably make it possible to contract the necessary amount of information about the tissue doses of the SCR at a later time.

According to the data given by Schaefer, the tissue dose rate from the SCR from a non-relativistic flare on May 10, 1959, behind a shielding of 2 g/cm^2 amounted to 20 rad/hour on the surface of a spherical human model; 15 rad/hour - at a depth of 0.3 g/cm; and about 0.1 rad/hour- in the center of the sphere. The mean tissue dose rate equaled approximately 4 rad/hour (Schaefer carried out calculations for the tissue dose, and the absorbed dose in an air-equivalent medium, but in similar provisional calculations such an inaccuracy is admissible).

If it is conditionally assumed that the total tissue dose from the SCR of the non-relativistic flare on May 10, 1959, was 15 times greater than the calculated amounts of the dose rate, then the mean tissue dose after the flare would amount to 60 rad or, with a RBE coefficient on the order of 2, it would amount to about /82

120 rem - i.e., it would be a larger amount, but an endurable one. At the same time, the skin dose would amount to 300 rad, or about 600 rem, and the tissue dose on the crystalline lens - 225 rad or about 450 rem. Such doses could lead to a loss in the human capacity for work, although the mean tissue dose would not be excessively large. It must be pointed out that this example refers to comparatively soft radiation from nonrelativistic flares. Relativistic SCR causes more uniform irradiation of the organism.

Other authors, in calculating the tissue doses of SCR, did not take into account the radiation distribution in the human body and the effect of self-screening during irradiation from all sides, which is typical for cosmic flight conditions. Usually, the magnitude of the tissue dose in the center of the cavity within a spherical casing having a given thickness is given, because this dose can be calculated comparatively simply. It is always greater than the surface dose and the mean tissue dose, and therefore provides an exaggerated concept of the radiation danger from SCR .

The absorbed dose in air behind a shielding of about 1 g/cm^2 has been calculated for several cases of SCR (Ref. 25). These data are compiled in Table 3.2 - 3.3, along with data given by other authors. It can be seen from these data primarily that the estimates of the tissue doses from the SCR, which were made by various authors, basically concur with each other in order of magnitude, although they differ by several factors, as a rule. Such a /84
disagreement is understandable, if one takes into account the inaccuracy of the initial data regarding the spectrum, the proton stream, its dependence on time, and also the diverse approach in calculating the tissue dose. The contribution, which is not taken into account in all the calculations, to the tissue dose from the secondary radiation from the cosmic apparatus casing (primarily neutrons) can increase the tissue dose by 10 - 50% in rads for a soft spectrum of SCR protons - i.e., the fact that it is disregarded does not essentially change the given estimates of the dose (Ref. 4, Ref. 68).

It can be seen from Table 3.3 that the tissue doses from SCR in many cases far exceed the quantities created by the PCR or by the radiation zones of the earth when they are crossed, even behind protective layers on the order of 25 - 400 g/cm^2. Thus, according to these estimates the SCR represents the primary radiation danger during cosmic flights.

TABLE 3.2

ABSORBED DOSES FROM SCR

Date	Flare Class	Proton Energy Region Mev	Absorbed Dose, rad	Comments
Feb. 23,1956	3+	$100 \leqslant E \leqslant 20\ 000$ $\bar{E} = 370$ (Ref. 25)	40 (in air)	Behind 1 g/cm^2. In the first 19 hrs., no data on the OE>1 Bev (Ref. 25)
			80-400(in Tissue)	Behind 2 cm water (Ref. 4
			25-50 (in Tissue)	Behind 25cm water Ref.68)
			25 rem	Behind 260 cm carbon (Ref. 5)
			Maximum < 50 - 60 rad/hour	Behind 2-5 g/cm^2 far from the earth (Ref. 38, 69)
Aug. 22,1958	2	$\bar{E} = 100$	4	Behind several centimeters of water (Ref. 5)
May 10,1959	3+	$100 \leqslant E \leqslant 500$	14 (rem) maximum 20 rad/hr	Behind 22 cm carbon (Ref. 70) /83
			Mean tissue 4 rad/hr	Behind 2 g/cm^2 (Ref. 65)
			15 000(in tissue)	Behind 2 cm water (Ref. 4
			25 (in tissue)	Behind 25cm water Ref.68)
May 12,1959	3+	$\bar{E} = 38$(Ref. 25)	700 (in air)	Behind 1 g/cm^2 (Ref. 25)
			2500 (in tissue)	Behind 2 cm water (Ref. 4
			6 (in tissue)	Behind 25cm water Ref.68)
July 14,1959	3+	$\bar{E} = 46$(Ref. 25)	30000(in air)	Behind 1 g/cm^2 from 3 SCR for 6 consecutive days (Ref. 25)
			15000(in tissue)	Behind 2 cm water (Ref. 4
			25(in tissue)	Behind 25cm water Ref.68)
			Maximum 10000 rad/hour	Behind 2-5 g/cm^2 (Ref. 38)

TABLE 3.2 /83
(continued)

Date	Flare Class	Proton Energy Region Mev	Absorbed Dose rad	Comments
July 15,1959			Maximum 9 rad/hour	Behind 2-5 g/cm^2 (Ref. 38)
Apr. 1, 1960	3+	$\overline{E}$ = 40 (Ref. 25)	$7 \cdot 10^{-3}$(in air) Maximum 26 mrad/hour	Behind 1 g/cm^2 (Ref. 25) Behind 2-5g/cm^2 (Ref. 38)
October 12-20, 1960	3+	$10 \leqslant E \leqslant 8000$, $\overline{E}$ = 50 (Ref. 25)	2000 (in air) 600-800(in tissue) 6 - 9 (in tissue)	Behind 1 g/cm^2 (Ref. 25) Behind 2 cm water (Ref. Behind 25cm(4, water (Ref. (68)
July 18,1961	3+	$\overline{E}$ = 50 (Ref. 25)	80 (in air)	Behind 1 g/cm^2 (Ref. 25)

The obtained values for the tissue dose must be compared with the scale of radiation damage set forth in Chapter 1. It must thus be kept in mind that for soft radiation, similar to the SCR after the flare on May 10, 1959, the mean tissue dose is 5 times less than /85 the surface dose, and 10 times less than the tissue dose in the center of the cavity within the cosmic apparatus casing (Ref. 65). For harder radiation, the difference is less.

The comparison shows that in cosmic apparatuses having casings of a normal thickness of 2 - 5 g/cm^2, in many cases the contact with powerful SCR would lead to serious aftereffects for the crew. In order to reduce the magnitude of the tissue dose to an endurable one, a strong shielding on the order of 25 g/cm^2 is necessary according to some estimates, and 250 - 400 g/cm^2 according to other estimates. Detailed calculations of the shielding are set forth below in Chapter 7. Using the data on the proton stream as a basis, we shall calculate the tissue dose here.

If the differential energy spectrum for protons in the form

$$\frac{dN}{dE} = \Pi_0 E^{-n}, \tag{3.2}$$

is known, then the differential tissue dose is

TABLE 3.3

Type of cosmic radiation	Proton Energy Mev	Absorbed Dose, rad	Comment
Powerful non-relativistic SCR	>40	150 - 750 (in tissue)	Behind 2 g/cm^2
		12 - 30 (in tissue)	Behind 5 g/cm^2 (Ref. 71)
		2 - 5 (in tissue)	Behind 10g/cm^2 $Q \leqslant 2$
Powerful SCR, Class A	>100	3000	For a stream of 10^8cm^{-2}
		100	For a stream of 10 cm^{-2} behind 5 g/cm^2 carbon or 8 g/cm^2 mallorium (Ref. 5)
Powerful SCR, Class B	>500	45000	For a stream of $3.6 \cdot 10^{11}$cm^{-2}
		100	For a stream of $3.6 \cdot 10^{11}$cm^{-2} behind 400 g/cm^2 carbon or 700 g/cm^2 mallorium (Ref.5)
PCR	$\bar{E}$ = 4000 (Ref. 25)	5 (in air)	During 1 year (Ref. 25)
Radiation zones of the earth	$\bar{E}$ = 144 (Ref. 25)	6 (in air)	1 hour after intersection, for a shielding thickness of 1 g/cm^2 (Ref. 25)

$$D'(E)\,dE = \Pi_0 \delta(E)\, E^{-n} dE, \qquad (3.3)$$

where $\delta(E)$ is the specific tissue dose for protons having energies from E to E + dE (see Chapter 1). The total tissue dose in a small volume of tissue, placed in a proton stream with a given spectrum, or the surface tissue dose in the case of a stream falling in a normal direction is determined by the integral

$$D = \Pi_0 \int_{E_{\min}}^{E_{\max}} \delta(E) E^{-n} dE = 4 \cdot 10^{-2} \Pi e^4 NZ \Pi_0 m_e^{-1} \int \frac{1}{v^2} \ln \frac{2m_e v^2}{I(Z)} E^{-n} dE =$$

$$= 1{,}25 \cdot 10^4 \Pi e^4 NZ \Pi_0 M m_e^{-1} \int E^{-n-1} \ln \frac{4m_e E}{IM} dE =$$

$$= 1{,}3 \cdot 10^{-6} \frac{\Pi_0}{n} \left[\frac{1}{E_{\min}^n} \left(3{,}1 + \frac{1}{n} + \ln E_{\min}\right) - \right.$$

$$\left. - \frac{1}{E_{\max}^n} \left(3{,}1 + \frac{1}{n} + \ln E_{\max}\right) \right] \text{rad}, \qquad (3.4)$$

(see equation 1.14). Here M is the mass of a proton at rest, which equals 1836 m_e, and E is the kinetic energy of the proton, Mev. For a muscle tissue $NZ = 3.36 \cdot 10^{23}$ g^{-1}, I(Z) = 100ev = 10^{-4}Mev (Ref. 72).

The final formula is valid in the energy regions from approximately 0.1 to 1000 Mev. The tissue dose, created by protons having energies outside of these limits, for SCR can be disregarded outside of the shielding, and behind a shielding of moderate thickness - judging from the known spectrum. The terms 3.1 + ln E as a function of the proton energy assume the values which are shown in Table 3.4.

TABLE 3.4 /86

Proton Energy E, Mev	0,1	1	3	5	10	30	50	70	100	250	600	1000	2000	20 000
$3{,}1 + \ln E$	0,8	3,1	4,2	4,7	5,4	6,5	7,0	7,4	7,7	8,2	9,5	10	11	13

The results derived from measuring the SCR are frequently represented in the form of integral spectra

$$\Pi(>E) = \Pi_1 \left(E^{-m} - E_{\max}^{-m}\right). \qquad (3.5)$$

Since the integral and differential forms of the expression for the energy spectrum are connected by the relationship

$$\Pi_0 = \Pi_1 m, \; n = m + 1 \qquad (3.6)$$

for the integral spectrum, the tissue dose can be written in the form

$$D = 1{,}3 \cdot 10^{-6} \frac{\Pi_1 m}{m+1} \left[\frac{1}{E_{\min}^{m+1}} \left(3{,}1 + \frac{1}{m+1} + \ln E_{\min}\right) - \right.$$

$$\left. - \frac{1}{E_{\max}^{m+1}} \left(3{,}1 + \frac{1}{m+1} + \ln E_{\max}\right) \right] \text{rad}. \qquad (3.7)$$

It is apparent that the formulas are valid for the tissue dose rate P, similarly to the dependences (3.4) and (3.7), in which D is replaced by P, and Π_0 and Π_1 - by Φ_0 and Φ_1 (if the density of the proton stream is represented in the form $d\Phi/dE = \Phi_0 E^{-n}$ or $\Phi(>E) = \Phi_1 E^{-m}$. The results derived from the calculations for the spectra shown in Table 3.1 are given in Table 3.5. When the calculations were performed, the spectral sections were disregarded which were not contained in the approximating power functions of Table 3.1. However, as can be seen from Table 3.5, this does not introduce any significant error in the calculated values. In addition, only the first term is essential in equations (3.4) and (3.7). Therefore, the simple expressions

$$D \approx \frac{10^{-5}\Pi_0}{nE_{\min}^n} = \frac{10^{-5}\Pi_1 m}{(m+1)E_{\min}^{m+1}} \text{ rad}. \qquad (3.8)$$

can be used to calculate the tissue dose.

It is apparent that the surface tissue dose rate is less than the values calculated above, due to the self-screening by the body, but it is not more than two times smaller, if the stream of SCR is isotropically distributed by angles. The values obtained from the calculation for the tissue dose rate are much greater than the estimated values given by other authors (Table 3.2), since the calculation was made for protons having energies which started at approximately 3 Mev - i.e., almost under conditions of no protection. It can be seen from Table 3.5 that the tissue doses thus assume very large values, which reach approximately /87
10^4 rad after the flare.

The tissue dose is calculated without taking the screening effect of the human body into account. As was noted above, one of the criteria for the radiation danger of SCR must be the mean tissue dose. In calculating this mean tissue dose, it is necessary to determine the doses in terms of depth and to average them over the body volume; it must thus be taken into consideration that the passage of protons through the tissue layer changes their spectrum. In order to calculate the magnitude of the tissue dose at the depth x, the approximate empirical dependence between the proton energy E and their range x can be used (Ref. 71)

$$E = E_0 x^h, \qquad (3.9)$$

from which it follows that

$$dE = kE_0 x^{h-1} dx, \qquad (3.10)$$

$$dE/dx = \delta(x) = kE_0 x^{h-1} \qquad (3.11)$$

TABLE 3.5

CALCULATION OF THE TISSUE DOSE RATE OF SCR ACCORDING TO FORMULA (3.4)

Date	Time from start, hours	Tissue Dose Rate	
		rad/sec	rad/hrs.
2.23.1956	0	$0{,}14\,(1{,}3-0{,}003)+3{,}4\cdot10^{15}\,(3{,}6\cdot10^{-21}-1{,}6\cdot10^{-27})=0{,}18$	650
2.23.1956	19	$0{,}03\,(0{,}94-0{,}005)+2{,}6\cdot10^{3}\,(1{,}6\cdot10^{-8}-7\cdot10^{-13})=0{,}028$	100
5.10.1959	33	$0{,}87\,(0{,}92-0{,}04)+1{,}9\cdot10^{5}\,(3{,}5\cdot10^{-8}-2\cdot10^{-14})=0{,}77$	2800
11.12.1960	0—10	$0{,}54\,(0{,}33-0{,}001)+1{,}8\cdot10^{4}\,(7{,}1\cdot10^{-8}-8\cdot10^{-12})=0{,}18$	650
11.12.1960	10—14	$1{,}1\,(0{,}33-3\cdot10^{-4})+1{,}4\cdot10^{3}\,(3{,}2\cdot10^{-7}-8\cdot10^{-11})=0{,}36$	1300
11.12.1960	14—32	$7{,}5\,(0{,}078-5\cdot10^{-5})+2{,}4\cdot10^{5}\,(1{,}3\cdot10^{-9}-2\cdot10^{-14})=0{,}58$	2100
Averaged Data (Ref. 45)	—	$0{,}82\,(2{,}8\cdot10^{-5}-5\cdot10^{-8})=23\cdot10^{-6}$	0,08
Averaged Data during Forbush decrease (Ref. 45)	—	$1{,}9\cdot10^{8}\,(8\cdot10^{-14}-1\cdot10^{-16})=15\cdot10^{-6}$	0,05

From Formula (3.2), we thus have

$$\frac{d\Pi}{dx}=k\Pi_0E_0^{1-n}x^{k-kn-1} \tag{3.12}$$

Behind the tissue layer having the thickness R, which is measured in the direction of motion of a flat proton stream, we have /88

$$\left.\begin{aligned}\frac{d\Pi}{dx}&=k\Pi_0E_0^{1-n}(x-R)^{k-kn-1}\quad\text{for}\quad x>R\\ \frac{d\Pi}{dx}&=0\quad\text{for}\quad x\leqslant R\end{aligned}\right\} \tag{3.13}$$

It is now possible to write the expression for the magnitude of the tissue dose at the depth R

$$D=\int\frac{d\Pi}{dx}\,\delta(x)\,dx=k^2\Pi_0E_0^{2-n}\int_{x_{min}}^{x_{max}}(x-R)^{k-kn-1}x^{k-1}dx. \tag{3.14}$$

Here $x_{min}=(E_{min}/E_0)^{1/k}$ and $x_{max}=(E_{max}/E_0)^{1/k}$ is the range of protons having the energies E_{min} and E_{max}. If $x_{min}\leqslant R$, integration is carried out from zero. If $x_{max}<R$, the integral becomes zero.

Waddington (Ref. 5) introduces the multiplier $e^{-\frac{\lambda}{R}}$, in expressions (3.13) - (3.14), taking into account the attenuation of the proton stream due to their absorption in the nuclear interactions. Since the mean absorption path of protons λ has a magnitude on the order of 100 g/cm^2 carbon, the similar term in the thickness region under consideration barely differs from unity, and it can be omitted.

For tissue, E_0 = 32 Mev (for a range of 1 g/cm^2) k = 0.56. [For aluminum, E_0 = 28 Mev, k = 0.57, for carbon - according to data given by Waddington (Ref. 5) - E_0 = 29.7 Mev, k = 0.58]. Substituting these quantities in formula (3.14), we obtain:

$$D \approx 320\Pi_0 32^{-n} \int_{x_1}^{x_2} (x - R)^{-0,55n-0,44} x^{-0,44} dx, \qquad (3.15)$$

where $x_1 = (E_{min}/32)^{1.785}$ or zero, $x_2 = (E_{max}/32)^{1.785}$ or zero. Analogous expressions are valid for calculating the tissue dose behind a shielding made of tissue-like materials: water, organic liquids, and plastics.

The tissue dose at any point of the body can be obtained by integration of expression (3.15) with respect to all directions, taking into account the layer thickness from the point up to the surface and the proton stream in the given direction. In the general form, such a problem is fairly complex, and therefore the problem is restricted to simplifications (Ref. 65 - 67). Detailed calculations are given in Chapter 7.

For rough estimates below the magnitude of the tissue dose, behind a layer of matter having the thickness R, it is possible to utilize expression (3.8), substituting the quantity $E_{min} + E_0 R^k$, instead of E_{min}. For tissue, we have

$$D(R) \geqslant \frac{10^{-5}\Pi_0}{n(E_{min} + 32R^{0,56})^n} \text{ rad}. \qquad (3.16)$$

The smaller are R and n, the more correct is the formula.

With the aid of this formula, let us approximate the tissue dose from SCR protons in the center of a spherical volume. In this simple case, integration over angles is unnecessary. Let us carry out the calculation for R, which equal 10 and 25 cm tissue, which approximately corresponds to the dimensions of the head and torso of the human being. The energy of protons with such range equal 116 and 244 Mev, respectively. For the SCR spectra which are shown Table 3.1, values are obtained which are given in Table 3.6. The quantity for R = 0 corresponds to the tissue dose in the absence of self-attenuation in the

/89

body, and half of it (column 3) approximately equals the surface tissue dose.

TABLE 3.6

TISSUE DOSE RATE P_R rad/sec IN THE CENTER OF A SPHERE WITH THE RADIUS R, cm.

Spectrum No. from Table 3.1	P_0 Table 3.4	1/2 P_0	P_{10}	$\frac{2P_{10}}{P_0}$, %	P_{25}	$2P_{25}/P_0$, %
1	$1{,}8\cdot10^{-1}$	$9\cdot10^{-2}$	$3{,}4\cdot10^{-3}$	4	$1{,}5\cdot10^{-3}$	2
2	$2{,}8\cdot10^{-2}$	$1{,}4\cdot10^{-2}$	$1{,}8\cdot10^{-4}$	1	$5{,}3\cdot10^{-6}$	0,04
3	$7{,}7\cdot10^{-1}$	$3{,}9\cdot10^{-1}$	$1\cdot10^{-4}$	0,03	$2{,}7\cdot10^{-6}$	$7\cdot10^{-4}$
4	$1{,}8\cdot10^{-1}$	$9\cdot10^{-2}$	$2{,}6\cdot10^{-3}$	3	$1{,}8\cdot10^{-4}$	0,2
5	$3{,}6\cdot10^{-1}$	$1{,}8\cdot10^{-1}$	$2{,}2\cdot10^{-4}$	1	$1{,}5\cdot10^{-5}$	0,08
6	$5{,}8\cdot10^{-1}$	$2{,}9\cdot10^{-1}$	$1{,}1\cdot10^{-4}$	0,04	$3{,}2\cdot10^{-6}$	$1\cdot10^{-3}$
7	$2{,}3\cdot10^{-5}$	$1{,}2\cdot10^{-5}$	$3{,}7\cdot10^{-6}$	30	$4{,}10^{-7}$	3
8	$1{,}5\cdot10^{-5}$	$8\cdot10^{-6}$	$4\cdot10^{-6}$	50	0	0

It can be seen from the Table that irradiation of the body is primarily surface irradiation, and the tissue dose in the center of the volume amounts to percents and portions of a percent of the surface dose, but - during the passage of hard SCR - it amounts to tens and, in inidvidual cases, hundreds of rads. As will be seen in Chapter 7, the non-uniform manner in which the body is irradiated by hard radiation from SCR decreases behind a shielding. This is indicated by the distribution of the tissue dose for SCR spectra (Nos. 7 and 8, Table 3.6), which were determined by beginning with a proton energy of 70 - 100 Mev - i.e., behind a layer of matter of 5 - 10 g/cm^2.

A correct estimate of the radiation danger from the obtained values for the tissue dose can be made only by taking into account the coefficients of relative biological effectiveness Q(δ). These coefficients must be taken from the curves in Figure 1.11 and must be included under the integral sign in equations (3.4), (3.14), and (3.15):

$$D = \Pi_0 \int_{E_{\min}}^{E_{\max}} Q[\delta(E)]\,\delta(E)\,E^{-n}dE \quad \text{rem} \tag{3.17}$$

or

$$D = 320\Pi_0 \cdot 32^{-n} \int_{x_{\min}}^{x_{\max}} Q[\delta(x)]\,(x-R)^{-0,56n-0,44}x^{-0,44}dx \tag{3.18}$$

It is also possible to approximate the RBE coefficient for the effective radiation spectrum at a given point, calculating the /90

mean value $\bar{\delta}$ and finding the value Q which corresponds to it from Figure 1.11. Multiplying the calculated magnitude of the tissue dose, given in rads, by Q, we obtain the tissue dose expressed in rems. Because the dependence $Q(\delta)$ is not linear, and is slower, such an approximation provides a somewhat exaggerated value of the RBE coefficient and the dose in rems.

The following formulas may be used to calculate $\bar{\delta}$:

$$\bar{\delta}(0) = \frac{D(0)}{\Pi(0)} = \frac{\Pi_0 \int \delta(E) E^{-n} dE}{\Pi_0 \int E^{-n} dE} =$$

$$= 1{,}3 \cdot 10^{-6} \frac{n-1}{n} \left[\frac{1}{E_{\min}^n} \left(3{,}1 + \frac{1}{n} + \ln E_{\min}\right) - \frac{1}{E_{\max}^n} (3{,}1 + \right.$$

$$\left. + \frac{1}{n} + \ln E_{\max}) \right] \left[\frac{1}{E_{\min}^{n-1}} - \frac{1}{E_{\max}^{n-1}} \right]^{-1} \approx$$

$$\approx 10^{-5} \frac{n-1}{n} E_{\min}^{-1} \text{rad} \cdot \text{см}^2 = 600 \frac{n-1}{n} E_{\min}^{-1} \text{Mev} \cdot \text{см}^2/\text{g} \qquad (3.19)$$

or

$$\bar{\delta}(R) = \frac{D(R)}{\Pi(R)} = \frac{\int \frac{d\Pi}{dx} \delta(x)\, dx}{\int \frac{d\Pi}{dx} dx} =$$

$$= \frac{k^2 E_0}{n-1} \cdot \frac{\int_{x\,\min}^{x\,\max} (x-R)^{k-kn-1} x^{k-1} dx}{(x_{\max} - R)^{k(1-n)} - (x_{\min} - R)^{k(1-n)}}. \qquad (3.20)$$

Utilizing the approximate expression (3.16), we can also write

$$\bar{\delta}(R) > 10^{-5} \frac{n-1}{n} (E_{\min} + 32R^{0,56})^{-1} \text{rad} \cdot \text{см}^2 =$$

$$= 600 \frac{n-1}{n} (E_{\min} + 32R^{0,56})^{-1} \text{ Mev} \cdot \text{см}^2/\text{g} \qquad (3.21)$$

As would be expected, the magnitude of $\bar{\delta}$ does not depend on the stream density Π_0, and is determined by the spectral slope and its position in the energy scale. The more steeply the spectrum drops (larger than n) and the softer it is (less than $E_{\min}$), the larger is $\bar{\delta}$ - and, consequently, the RBE coefficient.

According to our preliminary estimates (Ref. 71), behind a layer of matter which is greater than 2 g/cm^2 the $\bar{\delta}$ lies within the limits of 15 - 37 Mev·cm^2/g, even for non-relativistic flares with a soft spectrum - i.e., the RBE coefficients do not exceed 2. If the soft part of the proton spectrum is taken into account, $\bar{\delta}$ /91

is larger for the surface dose (Table 3.7). More accurate values are calculated in Chapter 7.

TABLE 3.7

MEAN VALUE $\overline{\delta}$ ON THE BODY SURFACE AND IN THE CENTER OF A TISSUE-EQUIVALENT SPHERE HAVING RADIUS R [ESTIMATES ACCORDING TO FORMULAS (3.19) AND (3.21)]

Spectrum No. from Table 3.1	Mean Value $\overline{\delta}$, Mev·cm^2/g for R, cm			Spectrum No. from Table 3.1	Mean Value $\overline{\delta}$, Mev·cm^2/g for R, cm		
	0	10	25		0	10	25
1	30	∿ 1	∿ 1	5	120	4	2
2	70	2	2	6	70	4	2
3	70	4	2	7	6	4	2
4	120	4	2	8	5	5	2

It follows from the Table that on the body surface $\overline{\delta}$ assumes values, for which the RBE coefficient is larger than unity both for chronic, and for short-term, concentrated irradiation. Thus, it must not be forgotten that the RBE coefficient of SCR protons can be greater than unity, and the dose - expressed in rems - can be two or more times greater than the tissue dose determined in rads.

The values of $\overline{\delta}$ in the interior of the body are greatly decreased because of the rough assumptions which were used to obtain formula (3.21). The small values of $\overline{\delta}$ for radiation from weak flares, with spectra No. 7 and No. 8, are caused by the fact that these spectra are only determined in the region of relatively large proton energies.

All of the calculations presented above make it possible to obtain the tissue dose, formed by protons due to their interaction with electrons in the medium (ionization losses), but they do not take into account the contribution made by nuclear interreactions to the dose. However, for protons having spectra which are similar to the SCR spectrum (see Table 3.1), not more than several percents of the tissue dose in rads belong to the share of nuclear interactions with the tissue, which is useless to include in the calculation, for the

accuracy with which the initial data were obtained (Ref. 71). The accumulation of secondary particles in the cosmic apparatus casing and in the human body can considerably increase the amount of tissue dose (Ref. 72), which can be seen from Figure 1.10. Some estimates of the contribution made by secondary particles are presented in Chapter 7.

It was pointed out above that α-particles comprise a significant part of the SCR. The tissue dose of α-particles can be calculated similarly to the calculations for protons, if the fact is taken into account that the charge of an α-particle is two times larger than the proton charge, and the mass is four times larger. Formulas (3.4) and (3.8) assume the following form for α-particles: /92

$$D = 4\cdot 4\cdot 1{,}3\cdot 10^{-6}\frac{\Pi_{0\alpha}}{n}\left[\frac{1}{E^n_{\min}}\left(3{,}1-\ln 4+\frac{1}{n}+\ln E_{\min}\right)-\right.$$
$$\left.-\frac{1}{E^n_{\max}}\left(3{,}1-\ln 4+\frac{1}{n}+\ln E_{\max}\right)\right]=2{,}1\cdot 10^{-5}\frac{\Pi_{0\alpha}}{n}\times$$
$$\times\left[\frac{1}{E^n_{\min}}\left(1{,}7+\frac{1}{n}+\ln E_{\min}\right)-\right.$$
$$\left.-\frac{1}{E^n_{\max}}\left(1{,}7+\frac{1}{n}+\ln E_{\max}\right)\right]\approx\frac{10^{-4}\Pi_{0\alpha}}{nE^n_{\min}}. \qquad (3.22)$$

Thus, the surface tissue dose of α-particles is one order of magnitude larger than that for a proton stream having the same energy spectrum. If it is true that a stream of α-particles comprises about 10% of the proton stream, then they increase the surface tissue dose by a factor of two, as compared with the dose created by single protons.

Since $E = 4E_0R^k$ for α-particles, where E_0 is the same as for protons in accordance with formula (3.9), equation (3.16) assumes the form

$$D(R)>\frac{10^{-5}\Pi_{0\alpha}}{n\,(E_{\min}+130K^{0{,}56})^n}. \qquad (3.23)$$

Thus, for tissue layers at a depth which is larger than the range of α-particles having energies $E_{\min}$, the tissue dose of α-particles decreases more rapidly than the tissue dose for protons, and consequently its contribution is less.

The specific absorbed dose of α-particles is larger than for protons, and this means the RBE coefficient is larger. For the mean value $\bar{\delta}$ of α-particles, the following approximate formulas

are valid:

$$\bar{\delta}_\alpha(0) \approx 8000\frac{n-1}{n}E_{min}^{-1} \text{ Mev}\cdot\text{cm}^2/\text{g} \tag{3.24}$$

$$\bar{\delta}_\alpha(0) \approx 13\delta_p(0), \tag{3.25}$$

$$\bar{\delta}_\alpha(R) > 800\frac{n-1}{n}(E_{min} + 130R^{0,56})^{-1} \text{Mev}\cdot\text{см}^2/\text{g} \tag{3.26}$$

Thus, the contribution made by α-particles to the tissue dose, expressed in rems, is even more significant than for calculations made in rads, and in several cases it apparently prevails. Therefore, it is extermely important to compile data on streams of α-particles in the SCR.

3.6 Forecasting Cosmic Radiation from Solar Flares

It can be seen from the material presented in this chapter /93
that our information regarding the formation mechanism of solar corpuscular streams, their intensity, composition, and propagation in space is still rather approximative and has many gaps. It is therefore natural that the prediction of the probability for encountering SCR as well as the possible doses of radiation is still in an elementary state. In addition, it is impossible to plan for the worst case, because this presents insurmountable difficulties for the accomplishment of space flights, in many cases. Consequently, a certain small probability for encountering SCR must be used as a criterion.

A distinction must be made between a long-term forecast for several years ahead, a strategic prognosis so to speak, an operative prognosis - for several days - weeks -, and a tactical prognosis - for tens of minutes - hours. A long-term prognosis is necessary for planning interplanetary expeditions, conquest of the moon and other cosmic bodies having no atmosphere, and other similar problems. The cyclic nature of solar activity must lie at the basis of such prognosis. It can be seen particularly clearly in Figure 3.10 that during periods of a quiet sun the probability for the occurrence of powerful SCR is small (Ref. 4).

If the probability for the occurrence of SCR is based on the number of sun spots, it can then be concluded from Figures 3.3 and 3.10 that during two - six years of minimum solar activity (4 years, on the average), this probability decreases by not less than a factor of 4, as compared with the years of a maximum solar activity. As compared with the maximum, the number of solar spots decreases by a factor of 9 - 10, on the average, and the probability

for the ejection of SCR decreases, probably to an even greater extent, and amounts to about 0 - 3 cases per year. In a year of maximum solar activity, and in 1 - 2 subsequent years, 10 - 15 cases of SCR having significant intensity are observed per year, out of which 1 - 2 are very powerful (Ref. 25).

The years of a quiet sun are observed 3 - 8 years after a maximum year (after 6 years, on the average). Therefore, it can be assumed that 1964 - 66 will be more favorable for cosmic flights, with respect to the danger of encountering SCR, and 1967 (Ref. 7) or 1969 - 1970 (Ref. 5) will again be unfavorable. As was indicated above, our epoch occurs at the maximum secular cycle of solar activity. In a period of about 2000 years, the frequency with which the SCR occurs will apparently be at the lowest point.

An operative prognosis is necessary for flights close to the earth, flights around the moon, placing cosmic apparatus into orbit, and other similar operations. At the present time, such a prognosis is most necessary, but it is still far from reliable. Since corpuscular radiation from chromosphere flares is almost always observed during great solar activity, it is /95
important to establish the main signs which indicate the probability of SCR formation. Such signs include (Ref. 7): 1) large groups of solar spots with a complex, multipolar magnetic field and frequent weak flares; 2) unusually clear facular fields; 3) the frequent appearance of solar radio noises and a high level of solar radio emission; 4) hot regions in the solar corona, which are characterized by the appearance of yellow lines of Ca^{XV}.

If there are no such signs, it is a period of relative radiation safety, if the possibility of the sudden appearance of SCR from the western edge of the sun is not taken into consideration.

The periods, in which the signs indicated above are absent, can last for a rather long period of time during the years of minimum solar activity. However, this criterion is too rigid for maximum solar activity, when its application can impose restrictions for long periods of time. Therefore, attempts must be made to discover more accurate signs for the occurrence of SCR.

In the works by Anderson (Ref. 73, Ref. 74), an attempt is made to connect the observation of SCR with the penumbral section of solar spots. As was indicated at the beginning of the Chapter, the penumbra are regions of greatest activity, over which chromosphere flares occur most frequently. Consequently, the criterion selected by Anderson is not accidental. In addition, it is known

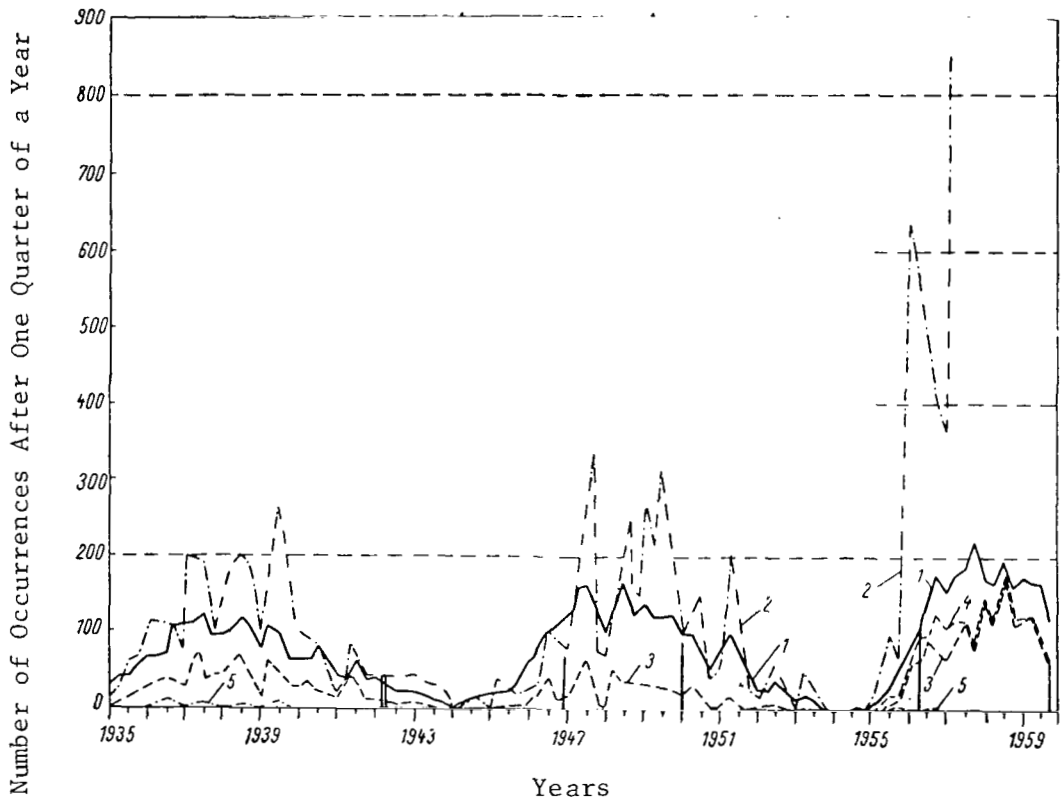

/94

Figure 3.10

Connection Between Number of Solar Spots, Chromosphere Flares on the Sun, and SCR (Ref. 4):

1 - Solar Spots; 2 - Class 1 Flares; 3 - Class 2 Flares; 4 - Class 2 Flares; 5 - Class 3 Flares; Vertical Lines Indicate most Powerful SCR.

that the penumbra is formed in very large sun spots and groups of spots, which are characteristic for very active regions on the solar surface, and the criterion given by Anderson can characterize solar activity very simply.

In 1957 - 1959, out of 55 cases, a correlation between the SCR and the penumbral area was observed in 53 cases. Corpuscular radiation appeared no earlier than two days after the formation of the penumbra. Thus, there is an additional possibility of being warned several days in advance of the SCR occurrence. In the opinion of Anderson (Ref. 73), in making forecasts on the basis of this criterion, after 7 days it is possible to make an error in 6% of the

cases. In another work (Ref. 7), the data obtained during 1949 - 1961 were analyzed in detail on the basis of Anderson's criterion. A period of time two days after there had not been one spot with an extended penumbra on the solar surface - whose dimensions at any time during the existence of the spot exceeded $1 \cdot 10^{-3}$ of the surface dimensions of the solar hemisphere - were chosen as the period safe for space flights.

The results derived from the analysis are shown in Table 3.8, where the number of cases in which SCR is observed, the number of four-day flights during the year which would be allowed according to Anderson's criterion, the number of flights which would, in fact, coincide with the appearance of SCR, and the number of days during the year which would be allowed for flights according to Anderson's criterion are indicated. The same data are then given for flights lasting 7 days. The data, for which /96
the smallest diameters of the penumbra of $5 \cdot 10^{-4}$ and $3 \cdot 10^{-4}$, respectively, are used as a criterion, are shown in the parentheses and in the brackets. It can be seen from the Table that the latter criterion is adequate in the overwhelming majority of cases (68 out of 70, i.e., 97%). In addition, its application leads to the fact that from 1/2 to 4/5 of the year are prohibited for space flights, whereas the SCR is observed for a comparatively smaller period of time - so that this criterion is too rigorous.

The data concerning prognosis results for the most powerful SCR, which leads to large tissue doses of radiation, are set forth in Table 3.9. It is apparent that in these cases the initial criterion of Anderson ($1 \cdot 10^{-3}$) fails in one case out of ten - i.e., in 11% of the cases - and, consequently, it is necessary to apply more rigid criteria.

On the whole, the proposed method for forecasting favorable periods entails greater error, the longer the period of time it covers, because the active regions on the sun are unstable and develop rather rapidly at new locations. In addition, in individual cases the chromosphere flares and the SCR appear in the absence of penumbra, and even in the absence of solar spots - for example, September 30, 1961 (Ref. 73). Cases have already /97
been mentioned, in which SCR was recorded, which had been ejected from the region of the flare behind the edge of the solar disc (Ref. 8, Ref. 12, Ref. 40). Therefore, Anderson's criterion must be used as a statistical one.

Assuming that up to four large flares may be observed during a year of an active sun, during which the doses from the SCR approximate a dangerous level, Anderson (Ref. 73) calculated the probability for entering the field of corpuscular radiation during

TABLE 3.8

APPLICATION OF ANDERSON'S CRITERION FOR DETERMINING THE POSSIBILITY OF SPACE FLIGHTS LASTING 4 AND 7 DAYS (REF. 7) /96

Year	4 Days				7 Days		
	Number of appearances of radiation	Number of allowed flights	Comparison of them with radiation	Number of allowed days per year	Number of allowed flights	Their comparison with radiation	Number of allowed days per year
1949	6	55 1/2	3	222; 61%	33 5/7	3	236; 65%
		(18)	(0)	(72; 20%)	(13)	(1)	(91; 25%)
1950	4	70 1/2	2	282; 77%	40 2/7	2	282; 77%
		(28 1/4)	(0)	(113; 31%)	(18 2/7)	(0)	(128; 35%)
1951	4	63 1/4	3	253; 69%	40 1/7	3	278; 76%
		(33 3/4)	(2)	(135; 37%)	(23 5/7)	(2)	(166; 45%)
		[25]	[2]	[100; 27%]	[17]	[2]	[119; 33%]
1956	5	35	1	140; 38%	25	1	175; 48%
1957	14	21	1	84; 23%	16	1	112; 31%
1958	12	19	0	76; 21%	14	0	98; 27%
1959	6	19	0	76; 21%	12	0	84; 23%
1960	13	34	1	136; 37%	23	1	161; 44%
1961	6	71 1/2	2	286; 86%	42 1/7	3	295; 88%
(1.11)		(56 3/4)	(2)	(227; 68%)	(25 4/7)	(3)	(179; 54%
		[31 3/4]	[0]	[127; 38%]	[18 4/7]	[0]	[130; 39%]

a ten-day flight as being less than $4 \cdot 10/365 \sim 10\%$. The probability that the flight time might coincide with two large streams of SCR amounted to a small quantity on the order of 0.6%. However, since the flares frequently follow in groups, the probability for such coincidence is doubled (Ref. 4, Ref. 75). Typical examples of a series of SCR are shown in Figure 3.11 (Ref. 25).

Short-term prognosis is necessary, in order that the spacecraft crew can take safety measures - to land on the earth, to employ additional methods of protection, to switch on protective force fields, and to take prophylactic, medicinal measures. There is no doubt that one of the main methods of short-term prognosis is the observation of solar spots and chromosphere flares. The appearance of a Class 2+ flare or more, particularly in the center and at the western part of

TABLE 3.9

PROGNOSIS OF TIME ALLOWED FOR SPACE FLIGHTS, AND THE MOST POWERFUL SCR (REF. 7)

Year	Number of SCR occurrences	Comparison of them with allowed time	
		for 4 days	for 7 days
1942	2	0	0
1946	1	0	0
1949	1	0	0
1956	1	0	0
1959	1	0	0
1960	2	0	0
1961	1	0	1
19 years	9	0	1

the solar disc, is a signal that the radiation level must be traced - especially if the flare is accompanied by radiation or radio bursts. After the active region has passed beyond the edge of the sun, in the course of 1 - 2 days the flare becomes dangerous.

Electromagnetic radiation from the solar atmosphere arises, as was indicated above, during the passage of electrons which were formed simultaneously with the SCR at the time of the chromosphere flare. Therefore, it is a signal that rapid corpuscles have been ejected. The electromagnetic radiation is propagated in a rectilinear manner, and the trajectories followed by the corpuscular streams from the sun to the earth are curved. Therefore, not every case in which electromagnetic radiation is recorded will coincide with the appearance of SCR. On the other hand, corpuscular radiation from the edge of the sun will not be indicated in advance by the electromagnetic radiation. In certain cases of electromagnetic radiation, it was soft (Ref. 11, Ref. 27, Ref. 56), due to which fact it must be observed from sounding balloons or from on board spacecrafts. /98

Radio bursts in solar radiation occur during interaction of electrons, which are emitted during the chromosphere flare, with the magnetic fields of the facular solar fields at an altitude of

40 - 100 thousand km. This radio emission is observed in the 30 - 60 cm wave region, and in the meter region. In individual cases, the radio emission increases by a million times, as compared with the background, after several seconds. There are precise methods for determining the location of radio emission sources on the solar surface. It is assumed that radio noises from the sun, of type III, are related to the emission of corpuscles; these radio noises last several seconds, and are characterized by a gradually-increasing wavelength in the meter region. The radio noises which last for a longer period of time have a closer relationship to the SCR (Ref. 7, 8, 12, 39, 40, 46). The same statements which were made regarding the course

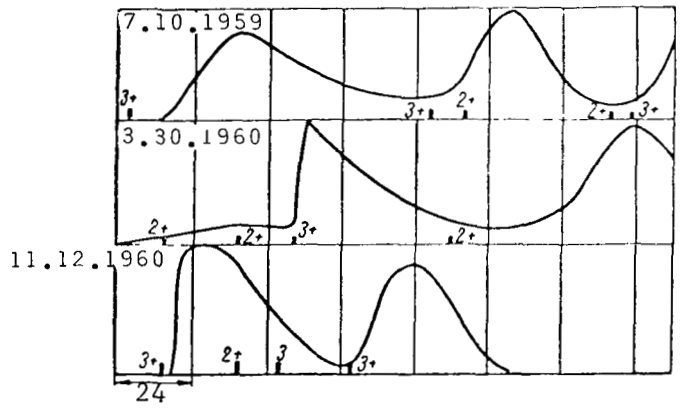

Figure 3.11

Cases of Successive Appearance of Certain SCR. The Increase and Damping of Radiation has a Different Form (Ref. 25)

The squares designate chromosphere flares.

followed by electromagnetic radiation propagation can be naturally applied to radio bursts. It is important that radio bursts and electromagnetic radiation carry, at the speed of light, advance warning about the emission of rapid corpuscles from the sun - i.e., that a chromosphere flare has produced SCR - and whether corpuscles will be actually observed behind it depends on the propagation trajectory. /99

Dodson (Ref. 76 - 78) examined a criterion, according to which it is possible to distinguish between a chromosphere flare which is accompanied by SCR. His criterion set forth large dimensions (flare class) brightness, and the velocity at which it increases as non-specific signs. Flares, which appear in the

central part of the solar disc in the region of large spots having strong magnetic fields, are correlated with the appearance of SCR to a greater or lesser degree. For a flare which produces SCR, it is characteristic that its brightness in the radio emission reaches a maximum after the visible radiation passes through a maximum. The region of the flare overlaps, either completely or to a significant extent, the penumbral region of the main spot in a group of spots, and radio noises of IV-type are observed during the overlapping. The appearance of a protuberance system in the form of loops, during the damping stage, is also characteristic for such flares.

The flares producing the SCR appear at the location of dark filaments, which disappear several hours or minutes before the flare, and appear again after it is terminated. Such flares occur most frequently in very active regions on the solar surface. Thus, during the International Geophysical Year, in 2/3 of all the cases, the corpuscular emission occurred in facular fields, in which 60 or more spots were counted along the solar disc during its passage. All the flares which produced proton radiation during 1959 were observed in two active regions in all.

The dangerous flares are more frequently observed in the facular plages, which pass along the solar disc two or more times, although this does not mean that this active region is not dangerous during the first passage (Ref. 76 - 78).

The latter possibility of short-term prognosis is based on the fact that an increase in the SCR intensity lasts tens of minutes - in the case of relativistic SCR from flares on the western half of the solar disc - and for hours and tens of hours - if the radiation is formed on the eastern half. Special dosimetric equipment - which responds to the first and second time derivative of the tissue dose magnitude - can produce a signal in the initial phase of the flare which announces the danger, and can provide an estimate of the possible irradiation level. In this way, it will be possible to provide a protection from the largest part of the SCR dose.

At the present stage of knowledge, it can be assumed that cosmic radiation from solar flares represents the primary radiation danger during cosmic flights, particularly since it is still impossible to predict it and to guard against it to a sufficiently reliable extent. A study of the nature of chromosphere flares and SCR as well as the laws underlying SCR propagation, and the development of prognosis /100 methods over various periods of time represent one of the main tasks in the problem of mastering interplanetary space and space near the earth.

The role of solar cosmic radiation in the general problem of radiation safety during space flights will become clearer after the discussion in the following pages on the levels of tissue doses in the radiation zones of the earth.

REFERENCES

1. Forbush, S. E. Phys. Rev., 70,771, 1946.

2. Ehmert, A. Z. Naturforsch., a3, 264, 1948.

3. Adams, N. Philos. Mag., 41, 503, 1950.

4. Foelsche, T. COSPAR Meeting, 4/30-5/11, 1962. Internat. Comm. on Space Res., 1962.

5. Waddington, C. J. J. Brit. Interplan. Soc., 277, 1962.

6. Reid, G. C., Leinbach, H. J. Geophys. Res., 64, 1801, 1959.

7. Malitson, H. H. IAS 30th Annual Meeting, New York, 1/22-24, 1962, Paper No. 62-8.

8. Carmichael, H. et al. Phys. Rev. Letters, 6, 49, 1961.

9. Menzel, D. G. Our Sun (Nashe solntse). Fizmatgiz, Moscow, 1963.

10. Kulikovskiy, P. G. Handbook for the Astronomer Lover (Spravochnik lyubitelya astronomii). Fizmatgiz, Moscow, 1961.

11. Gringauz, K. I. Some Results of Experiments Performed in Interplanetary Space with the Aid of Traps of Charged Particles on Soviet Cosmic Rockets (Nekotoryye rezul'taty opytov, provedennykh v mezhplanetnom prostranstve s pomoshch'yu lovushek zaryazhennykh chastits na sovetskikh kosmicheskikh raketakh). In the Collection: Iskusstvennyye Sputniki Zemli, No. 12, Izd-vo AN SSSR, Moscow, 1962.

12. Hansen, R. T. Phys. Rev. Letters, 6, 260, 1961.

13. Yefremov, A. I., et al. Study of Short-Wave Solar Radiation (Issledovaniye korotkovolnovoy radiatsii solntsa). In the Collection: Iskusstvennyye Sputniki Zemli, No. 10, Izd-vo AN SSSR, Moscow, 1961.

14. Biermann, L. Z. Astrophys., 29, 274, 1951; Z. Naturforsch., a7, 127, 1952; Observatory, 77, 109, 1957.

15. Mustel', E. R. Astron. Zh., 38, 385, 1961.

16. de Turville, C. M. Nature, 190, 4771, 156, 1961.

17. Shklovsky, I. S. Ann. Geophys., 14, 414, 1958.

18. Sonett, C. P. Phys. Rev. Letters, 5, 46, 1960.

19. Krasovskiy, V. I. Uspekhi Fiz. Nauk, 75, 501, 1961.

20. Gringauz, K. I. Newspaper Izvestiya of February 21, 1962.

21. Parker, E. N. Astrophys. J., 7, 1958.

22. Shabanskiy, V. P. Astron. Zh., 38, 844, 1961.

23. Biswas, S., Fichtel, C. E., Guss, D. E. Amer. Geophys. Union Western National Meeting, 12/27, 1961. (Cited in [Ref. 25].)

24. Freier, P. S., Biswas, S., Stein, W. J. Geophys, Res., 66, 8, 1961.

25. Masley, A. J., Goedeke, A. D. Institute of the Aerospace Sciences, Paper No. 10/62, 1962.

26. Fireman, E. L., et al. Phys. Rev., 123, 1935, 1961.

27. Vette, J. I., Casal, F. G. Phys. Rev. Letters, 6, 334, 1961.

28. Scient. Amer., 203, 5, 1961.

29. Coleman, P. J., Jr., et al. Phys. Rev. Letters, 5, 43, 1960.

30. Meyer, P., Parker, E. N., Simpson, J. A. Phys. Rev., 104, 768, 1956.

31. Simpson, J. Nuovo cimento, Suppl. X, 8, 133, 1958.

32. Simpson, J. H. Variations in Primary Cosmic Radiation of Solar Origin. (Variatsii pervichnogo kosmicheskogo izlucheniya solnechnogo proiskhozhdeniya). In the Collection: Solar Activity and Cosmic Rays (Solnechnaya aktivnost' i kosmicheskiye luchi). Izd-vo Inostr. Lit., Moscow, 1962.

33. Dvoryashin, A. S. and others. Astron. Zh., 38, 419, 1961. /101

34. Obayashi, T., Hakura, J. J. Geophys. Res., 65, 3143, 1960.

35. Gold, T. Streams of Particles with High Energies in the Solar System and Close to the Earth (Potoki chastits s vysokoy energiyey v solnechnoy sisteme i vblizi zemli). In the Collection: Solar Activity and Cosmic Rays (Solnechnaya aktivnost' i kosmicheskiye luchi). Izd-vo Inostr. Lit., Moscow, 1962.

36. Cocconi, G., et al. Nuovo cimento, Suppl. X, 8, 161, 1958.

37. Rose, D. C., Katzmann, J. Canad. J. Res., 34, 884, 1956.

38. Winckler, J. R. Radiat. Res., 14, 521, 1961.

39. Coates, R., et al. Astron. J., 64, 326, 1959.

40. Covington, A. E., Harwey, G. A. Phys. Rev. Letters, 6, 51, 1961.

41. Charakhch'yan, A. N., Tulinov, V. F., Charakhch'yan, T. N. Zh. Eksperim. i Teor. Fiz., 39, 249, 1960.

42. Winckler, J. R., et al. Phys. Rev. Letters, 6, 488, 1961.

43. Solar Corpuscular Streams and their Interaction with the Magnetic Field of the Earth (Solnechnyye korpuskulyarnyye potoki i ikh vzaimodeystviye s magnitnym polem zemli). Izd-vo Inostr. Lit., Moscow, 1962.

44. Gorchakov, Ye.V., Bazilevskaya, S. A. Measurement of Intensity of Charged Particles after a Chromosphere Flare on July 7, 1958 (Izmereniye intensivnosti zaryazhennykh chastits posle chromosfernoy vspyshki 7 iyulya 1958). In the Collection: Iskusstvennyye Sputniki Zemli, No. 8, Izd-vo AN SSSR, Moscow, 1961.

45. Charakhch'yan, A. N., et al. Zh. Eksperim. i Teor. Fiz., 40, 1961.

46. Smith, A.G. Radioastronomy (Radioastronomiya), Izd-vo Inostr. Lit., Moscow, 1962.

47. Van Allen, J. A., Winckler, J. R. Phys. Rev., 106, 5, 1072, 1957.

48. Charakhch'yan, A. N., et al. Zh. Eksperim. i Teor. Fiz., 38, 1031, 1960.

49. Yagoda, H., Filz, R., Fukui, K. Phys. Rev. Letters, 6, 626, 1961.

50. Fichtel, C. E., Guss, D. E. Phys. Rev. Letters, 6, 495, 1961.

51. Davis, L. R., et al. Phys. Rev. Letters, 6, 492, 1961.

52. Ney, E. P., Stein, W. J. Geophys. Res., 66, 2550A, 1961.

53. Anderson, K. A., et al. J. Geophys. Res., 64, 1133, 1959.

54. The Collection "Radiation Zones of the Earth" (Radiatsionnyye poyasa zemli). Izd-vo Inostr. Lit., Moscow, 1962.

55. Vernov, S. N., Chudakov, A.Ye. Uspekhi Fiz. Nauk, 70, 4, 585, 1960.

56. Peterson, L. E., Winckler, J. R. J. Geophys. Res., 64, 697, 1959.

57. Chubb, T. A., Friedman, H., Kreplin, R. W. J. Geophys. Res., 65, 1831, 1960.

58. Steljes, J. F., Carmichael, H., McCracken, K. G. J. Geophys. Res., 66, 5, 1363, 1961.

59. Ogilvie, K. W., Bryant, D. A., Davis, L. R. J. Geophys. Res., 67, 3, 929, 1962.

60. Winckler, J. R. 32nd Meeting AMA, 4/25, 1961.

61. Van Allen, J. A. Radiat. Res., 14, 5, 540, 1961.

62. Anderson, K. A., Enemark, D. C. J. Geophys. Res., 65, 2657, 1960.

63. Dorman, A. I. Variations in Cosmic Rays (Variatsii kosmicheskikh luchey). Gostekhizdat, Moscow, 1957.

64. Sanitary Rules for Working with Radioactive Substances and Radiation (Sanitarnyye pravila raboty s radioaktivnymi veshchestvami i izlucheniyami). Gosatomizdat, Moscow, 1960.

65. Schaefer, H. J. Aerospace Med., 31, 10, 807, 1960.

66. Schaefer, H. J. Advances in Space Sciences. V. I. Academic Press. Inc., New York, 1959.

67. Schaefer, H. J. Further Evaluations of Tissue Depth Doses in Proton Radiation Fields in Space. U.S. Naval School of Aviat. Medicine. Report No. 17, 5/24, 1960.

68. Keller, J. W., Schaeffer, N. M. Shielding of Manned Vehicles from Space Radiation. 31st Annual Meeting of Aerospace Medical Assoc., Miami Beach, May, 1960.

69. Mayer, P., Parker, N., Simpson, J. A. Phys. Rev., 104, 768, 1956.

70. Barbieri, L. J., Lampert, S. Radiation Shielding and Manned Satellite Design Considerations. National IAS + ARS Joint Meeting, 61-163-1857, Los Angeles, 6/13-16, 1961.

71. Ivanov, V. I., et al. Doses of Cosmic Radiation (Dozy kosmicheskoy radiatsii). In the Collection: Iskusstvennyye Sputniki Zemli, No. 12, Izd-vo AN SSSR, Moscow, 1962.

72. Yeger, R. Dosimetry and Protection from Radiation (Dozimetriya i zashchita ot izlucheniy). Gosatomizdat, Moscow, 1961.

73. Anderson, K. A. Preliminary Study of Prediction Aspects of Solar Cosmic Ray Events, NASA TN D-700, 1961.

74. Anderson, K. A., Fichtel, C. E., NASA TN D-671, 1961. /102

75. Adamson, D., Davidson, R. E. Statistics of Solar Cosmic Rays as Inferred from Correlation with Intense Geomagnetic Storms, NASA TN D-1010, 1962.

76. Dodson, H. W., Hedeman, E. R. Astron. J., 65, 51, 1960.

77. Dodson, H. W., Hedeman, E. R. Arkiv Geofys., 3, 469, 1961.

78. Dodson, H. W. Proc. Nat. Acad. Sci. USA, 47, 901, 1961.

79. Ney, E. P., Winckler, J. R., Freier, P. S. Phys. Rev. Letters, 3, 183, 1959.

80. Babcock, H. D., Babcock, H. W. Science, 117, 465, 1953; Babcock, H. W. Astrophys. J., 133, 572, 1961.

CHAPTER 4

INNER RADIATION ZONE OF THE EARTH

4.1. Location of the Zone

As the result of experiments carried out by Soviet and American physicists on artificial earth satellites and cosmic rockets, the presence of a zone of corpuscular radiation near the earth has been recently discovered, which has subsequently been called the inner radiation zone. /103

The first data about the high-intensity zone at an altitude of about 1000 km were obtained by the American artificial earth satellites "Explorer I" and "Explorer III". The boundaries of the inner radiation zone were first established in studies made on the third Soviet satellite, whose trajectory lay in the latitudinal region from + 65° to - 65°. The inner zone of the earth's corpuscular radiation was localized within a region, bounded by the magnetic force lines which intersect the earth's surface at the geomagnetic latitude of 45° (Ref. 1). It begins at an altitude of 500 - 600 km in the Western Hemisphere, and at an altitude of about 1500 km in the Eastern Hemisphere. It extends up to altitudes of 5000 - 10 000 km. The non-symmetrical nature of the zone is caused by the displacement of the magnetic dipole with respect to the geographic center of the earth. The presence of powerful magnetic anomalies on the surface of the earth also deform the radiation zone. A drop in the inner radiation zone, in the southern part of the Atlantic Ocean, to an altitude of 320 km was discovered in an experiment carried out on the second spacecraft (Ref. 2). This drop is caused by the South-Atlantic magnetic anomaly. The maximum radiation intensity is observed at an altitude of about 3400 - 3600 km (Ref. 1, 3 - 6).

During the flight of "Explorer VI", the spatial distribution of proton intensity at altitudes of 1000-2000 km was measured - i.e., at the lower boundary of the zone. The measurement results are given in the works (Ref. 7, Ref. 8). A theoretical calculation of the spatial distribution of the equal intensity lines for protons, having the energy $E_p > 75$ Mev, which was based on the hypothesis of neutron albedo, was made in another work (Ref. 9). This study also determined a change in the proton stream with the distance from the

center of the earth, in the plane of the geomagnetic equator for protons having energies of $E_p > 30$ Mev and $E_p > 75$ Mev (Figure 4.1). However, the upper boundary of the high-intensity zone (on the order of 10^4 protons/cm^2·sec) is located at very great distances from the earth, according to the calculations (up to 7000 km), which contradicts the experimental data. The

/104

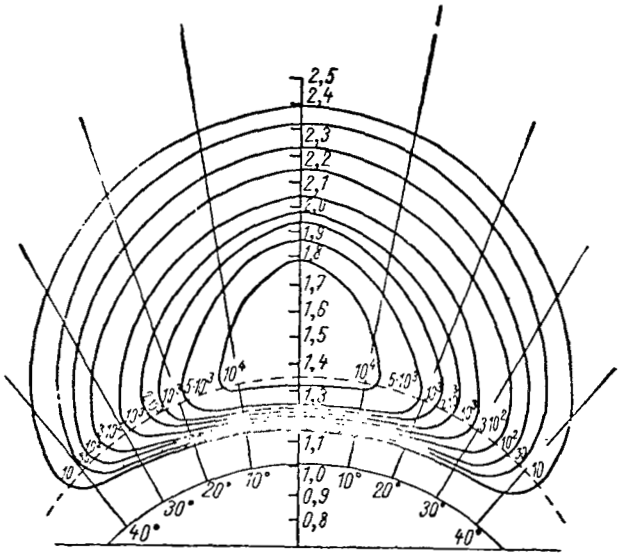

Figure 4.1

Omnidirectional Stream of Protons $\left[\frac{\text{proton}}{\text{cm}^2\cdot\text{sec}}\right]$ Having the Energy $E_p > 30$ Mev as a Function of the Geomagnetic Latitude and Distance from the Center of the Earth.

Data before the dashed line are taken from work (Ref. 9); data above the dashed line - extrapolation.

spatial distribution was formulated on the basis of the following premises: 1) the distribution of a stream, having the energy $E_p > 30$ Mev , close to the lower zone boundary was selected in accordance with the experimental data (Ref. 7, Ref. 8); 2) the spatial distribution in the far-removed regions of the zone was determined by extrapolation of the experimental data, taking the data derived from a theoretical calculation into account (Ref. 9). However, attention was paid to the fact that the high-intensity zone terminates at a distance of about 4500 km (Ref. 7). The upper boundary of the inner zone is located at a distance of 8000 - 9000 km from the surface of the earth, according to experimental

and theoretical data; 3) the non-symmetrical nature of the zone, caused by the displacement of the magnetic dipole with respect to the center of the earth and the magnetic anomalies, was not taken into account. An approximate picture was thus formed for the spatial distribution of the inner radiation zone of the earth, which is shown in Figures 4.1 and 4.2.

It is obvious that the picture for the spatial distribution of the inner zone must be corrected as new experimental data are obtained. Thus, measurements on the interplanetary station "Mars-I" showed that the high-intensity zone was farther removed from the surface of the earth than had been previously assumed (Ref. 10). It is probable that the spatial distribution of the inner radiation zone can be defined more accurately, after the experimental data which were obtained on "Mars-I" have been processed. /105

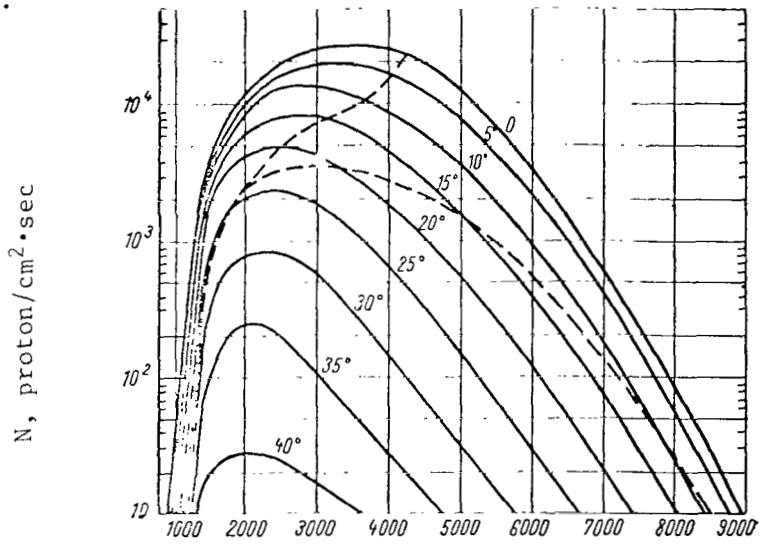

Figure 4.2

Omnidirectional Integral Stream of Protons (E_p > 30 Mev) of the Inner Radiation Zone as a Function of the Distance from the Earth's Surface and the Geomagnetic Latitude.

Dashed lines - zones of umbra and penumbra.

4.2. Origin

The existence of an inner radiation zone is related to the magnetic field of the earth. A charged particle moves in this field along a helical trajectory, which spirals around the magnetic

force line. Upon encountering the high latitudes in the region with increased magnetic field (the so-called magnetic mirrors), the particle is reflected and begins to move to the other side. Thus, the magnetic field of the earth forms a certain "magnetic trap", in which the charged particles can be accumulated. There are differing hypotheses with respect to the origin of the charged particles which enter the inner radiation zone.

It was initially assumed that the formation of trapped radiation is related to the injection of solar plasma inside the geomagnetic field, with subsequent geomagnetic acceleration of the particles up to observable energies (Ref. 11, Ref. 12). However, there must be a symmetrical relationship between the capture and loss of particles - i.e., if a particle cannot leave the trap, then one cannot enter it. This hypothesis has not been corroborated experimentally (Ref. 13). /106

In the works of other authors (Ref. 5, 14 - 18), the hypothesis is formulated that the inner zone is formed due to the decay of albedo neutrons, which are formed as a result of nuclear spallations, caused by primary cosmic radiation in the atmosphere. These neutrons can penetrate the geomagnetic field without any hinderance, so long as they are not subjected to radioactive decay

$$n \xrightarrow[\tau_{1/2}=11{,}7\ \text{min}]{} p + e^- + \nu.$$

During the decay of neutrons which have energies of 10^6 - 10^9 ev, a proton practically retains the direction of motion (and, consequently, the energy) of the neutron producing it. The electrons scatter in an isotropic manner, and have the well-known spectrum of β-decay. The observed composition and radiation spectrum in the inner zone satisfactorily coincides with the quantities calculated on the basis of this hypothesis.

The real lifetime of a proton in the magnetic trap (about 10^7 sec) also closely coincides with the calculated value.

4.3 Composition

The nature of the particles comprising the inner radiation zone has still not been decisively established. However, the experimental data which have been obtained can be explained very well, if it is assumed that protons with a high energy (tens and hundreds of megaelectronvolts) make up the composition of the zone. In addition, there are direct arguments in favor of the proton component - for example, the directed, radioactive nature

of a NaJ crystal, which was observed on the third artificial earth satellite (Ref. 1). In addition to high-energy protons, the inner zone composition also includes low-energy particles (not exceeding 1 Mev), which are apparently electrons.

The relative radiation composition in the inner zone depends on the location of the observation point. Thus, for example, the radiation in the upper part of the zone contains fewer energy particles than does the radiation in the lower part.

In the center of the inner zone (at an altitude of about 3500 km at the magnetic equator), the experimental values for the streams are as follows (Ref. 11):

Protons: omnidirectional intensity /107

$$I_0(>40 \text{ Mev}) = 2 \cdot 10^4 \frac{\text{proton}}{\text{cm}^2 \cdot \text{sec}}$$

(within an accuracy of the multiplier 2).

Electrons: maximum of omonidirectional intensity

$$N(>20 \text{ kev}) = 2 \cdot 10^9 \frac{\text{electron}}{\text{cm}^2 \cdot \text{sec} \cdot \text{sterad}}$$

(within an accuracy of the multiplier 10)

$$N(>600 \text{ kev}) \approx 1 \cdot 10^7 \frac{\text{electron}}{\text{cm}^2 \cdot \text{sec} \cdot \text{sterad}}$$

(within an accuracy of the multiplier 2).

4.4. Particle Spectra and Intensity

Experimental Spectra. One of the first measurements of the proton spectrum in the inner radiation zone of the earth was carried out with the aid of stacks of nuclear emulsions during the flight on April 7, 1959 (Ref. 19). The flight was made at latitudes of 3°N - 20°N at a maximum altitude of 1200 km. The layer of material over the emulsions was 6 g/cm^2, which made it possible to identify protons having energies of $E_p > 75$ Mev. The differential spectrum which was obtained in the energy interval from 75 to 700 Mev can be written in the form:

$$N(E)\,dE = N_0 E^{-n} dE,$$

where $n = 1.84 \pm 0.08$; $N_0 = (2.1 \pm {}^{1.0}_{0.7}) \cdot 10^3 \frac{\text{proton}}{\text{cm}^2 \cdot \text{sec} \cdot \text{Mev}^{-n+1} \cdot \text{sterad}}$

In the measured energy interval, the differential proton spectrum

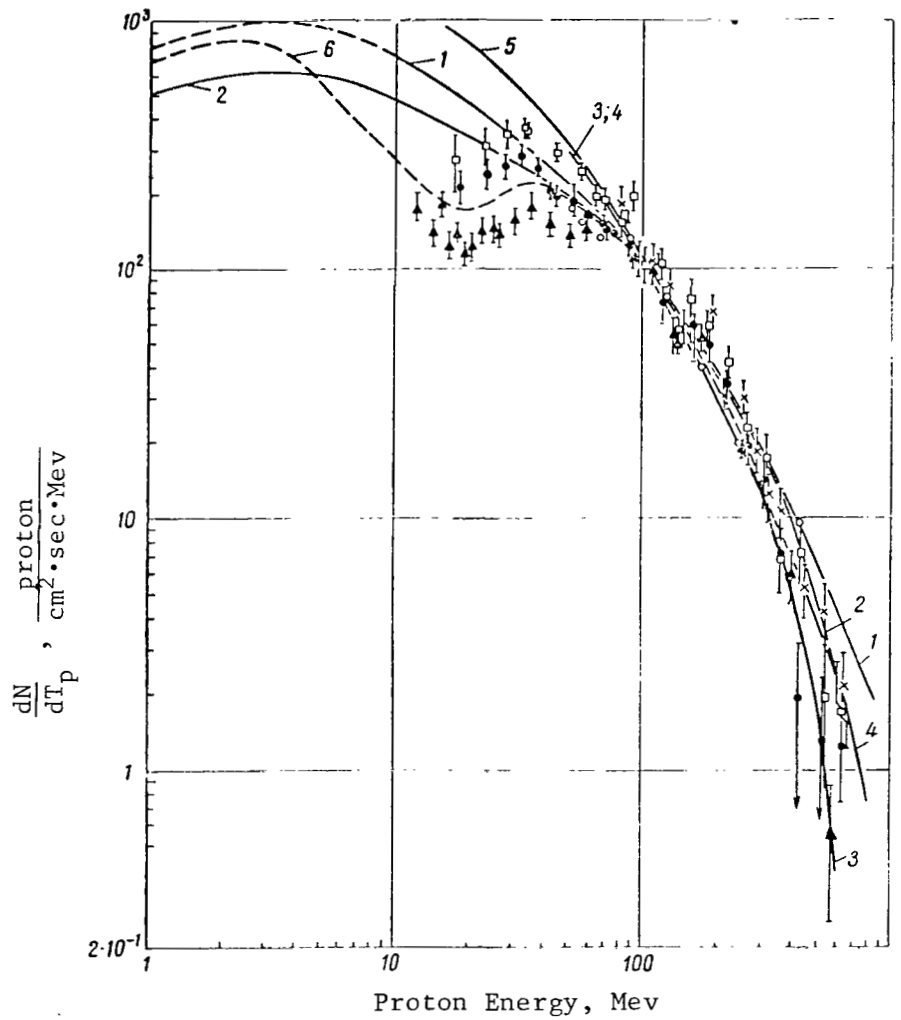

/108

Figure 4.3

Differential Proton Spectra of the Inner Radiation Zone (Normalized for Energy of 100 Mev).

The Experimental Points Correspond to Data: x - (Ref. 10); □ - (Ref. 24); ▲ - (Ref. 27); o - (Ref. 17); • - (Ref. 28); 1 - Calculated Spectrum (Ref. 13); 2 - Alternative Spectrum (Ref. 21, Ref. 22); 3 - Calculated Spectrum (Energy Limits of the Spectrum E = 650 Mev) (Ref. 9); 4 - Calculated Spectrum (Energy Limit of the Spectrum E = 1000 Mev) (Ref. 9); 5 - Alternative Spectrum (Ref. 7); 6 - Averaged Spectrum Utilized in Our Calculations.

can also be written in exponential form

$$N(E)\,dE = N_0 e^{-E/E_0}\,dE,$$

where $E_0 = 120 \pm 5$ Mev; $N_0 = 0.84 \pm 0.7$ $\frac{\text{proton}}{\text{cm}^2 \cdot \text{sec} \cdot \text{Mev} \cdot \text{sterad}}$.

The omnidirectional, integral stream of protons, obtained by integration of formula (4.1) with respect to energy, within the limits $75 \leqslant E \leqslant \infty$ at an altitude of 1000 - 1230 km and a mean latitude of about 10° N, amounts to 800 ± 200 $\frac{\text{proton}}{\text{cm}^2 \cdot \text{sec}}$.

In subsequent experiments on October 13, 1959 (Ref. 13), the proton spectrum was determined in a wider energy interval up to 18 Mev. The results derived from both experiments are shown in Figure 4.3. The theoretical curve, which was calculated on the basis of the hypothesis for albedo neutron decay, is shown here (Ref. 13). The theoretical curve is normalized to the experimental data for protons, having energies of 100 Mev.

The proton spectrum in the energy interval from 42 to 570 Mev /109
was studied in another work (Ref. 22). The proton spectrum which was obtained closely coincides with the hypothesis for albedo neutron decay for protons having an energy of $E_p > 100$ Mev and with the experimental data (Ref. 13). In the low-energy part of the spectrum, a maximum was determined at 80 Mev and a minimum at 60 Mev. Since these measurements were made after a large solar flare (July 10 - 16, 1959), this type of spectrum can be caused by solar protons.

During the flight of the American artificial satellite "Explorer VI" (August 7 - October 2, 1959), the differential spectrum of protons was measured in the latitudinal interval from - 25.3° to - 31.8° (a mean altitude of 2225 km) (Ref. 23). For protons having energies of $E > 30$ Mev, the spectrum has the form $E^{-1.65}$ throughout the entire latitudinal interval (6.5°) which made it possible for the authors to extend this spectrum to -21°. The spectrum obtained closely coincides with the theoretical spectrum and with other experimental data for protons having energies above 100 Mev. The slight difference can be explained by the fact that the exponent n decreases with a decrease in the proton energy. Thus, for example, for the theoretical spectrum it decreases to 0.72 in an energy region which is less than 30 Mev. Since the spectra, which were obtained in the experiment (Ref. 13, Ref. 22), pertain to higher energies, their exponent must be greater, which was observed in actuality.

Thus, the proton spectrum at the intensity maximum of the

inner zone, at a latitude of -29.2°, has the form:

$$N(E)\,dE = 1{,}14E^{-1{,}66}dE \ \frac{\text{proton}}{\text{cm}^2\cdot\text{sec}\cdot\text{Mev}^{0.66}}$$

The proton spectra, which were measured with the aid of counters at an altitude of 940 - 1100 km (Ref. 24), also have the form of the power function with the exponent $n = 1.42 (E_p > 17.5$ Mev) and $n = 1.68$ ($E_p > 23$ Mev).

During the flight of the rocket "Atlas" on October 13, 1960, the proton spectrum was determined with the aid of nuclear emulsions (Ref. 25). The flight trajectory was similar to the trajectory which the same authors studied on July 21, 1959. For a proton spectrum in the energy region $80 < E < 660$ Mev , the power law was obtained with the exponent $n \geqslant 1.7$, which coincides with previous measurements. This also shows that there is no change in the spectrum with time.

During the flight of "Atlas" on October 13, 1960, other authors obtained proton spectra with energies of $E_p > 17$ Mev (Ref. 26). The energy distribution of the protons which was determined closely coincides with the data obtained by them previously. No maximum was observed at an energy of about 75 Mev, which was noted in the work (Ref. 22). Just as in the other work (Ref. 25), the maximum was obtained at 35 Mev and the minimum at 20 Mev, and the value of the total proton stream with energies of $E_p > 45$ Mev closely coincided with them.

Some data derived from an experimental study of the proton spectra for the inner radiation zone are set forth in Table 4.1. /110

Theoretical Proton Spectra. A calculation of the spectra is based on the hypothesis of albedo neutron decay. If the stream and spectrum of the neutrons leaving the atmosphere are known, it is possible to calculate the equilibrium proton spectrum in a magnetic trap. The spectrum for protons having the energy $E_p \geqslant 1$ Mev was calculated (Ref. 20) on the basis of the experimental spectra for neutrons formed by cosmic rays in the earth's atmosphere.

It was assumed that the protons lose their energy only by ionization of the medium.

The proton spectrum was calculated (Ref. 13) on the basis of the albedo neutron stream, which was determined in another work (Ref. 20). It was assumed in these calculations that the protons lose energy not only due to ionization, but also due to nuclear interactions. This is particularly important for protons having

TABLE 4.1

ENERGY PROTON SPECTRUM OF THE INNER RADIATION ZONE

Altitude, km	Magnetic latitude, degree	n	Energy region, Mev	Recording Method	Author
1230 max. 1200 mean	25	1.84	75 - 700	Emulsion	(Ref.19)
1170 max. 1080 mean	22	1.80	80 - 600	" "	(Ref.22)
1600	27.5	1.70	40 - 100	" "	(Ref. 7)
940	26	1.42	> 17.5	Geiger-	(Ref.24)
1100	19	1.68	> 23	Mueller Counters	
2225 mean	- 28.2 mean	1.65	> 23.6	The same	(Ref.23)

energies above 80 Mev. The spectrum was determined in the energy interval $10 < E < 700$ Mev under the following assumptions:

1) The neutron injection coefficient within the radiation zone does not depend on neutron energy - i.e., it is assumed that the probability for neutrons being captured by atoms of the atmosphere on their way to the magnetic trap is the same for the entire neutron spectrum;

2) The protons leave the magnetic trap due to ionization and nuclear interactions.

In a more detailed calculation of the spectra (Ref. 9), it was assumed that 1) the albedo neutrons do not have an isotropic distribution (for $E_n > 50$ Mev). This effect decreased the injection coefficient with an increase in the neutron energy; 2) the protons in the zone continuously lose energy due to ionization; 3) they disappear during nuclear interactions, and 4) protons, having an energy above a certain critical value, leave the zone due to the loss of adiabatic invariance.

The consideration of these factors leads to the fact that the proton spectrum in the region $E_p > 300$ Mev becomes steeper and corresponds to the experimental data. The theoretical spectra /111
(Ref. 9, 13, 20) are shown in Figure 4.3. The spectra are normalized to a proton energy of 100 Mev.

Analysis of the Theoretical and Experimental Spectra. The theoretical spectra (Ref. 9, 13, 20) closely coincide with the experimental spectra in the energy interval 80 < E < 300 Mev. In the region E > 300 Mev , the experimental spectra are steeper than the theoretical spectra (Ref. 13, Ref. 20). This is caused by the following reasons:

a) There is an additional mechanism for the loss of high-energy protons (non-adiabatic and hydromagnetic effects);

b) The probability for the capture of neutrons by the atmosphere decreases with an increase in the neutron energy;

c) The energy distribution for albedo neutrons is steeper than was assumed in the works (Ref. 13, Ref. 20).

The spectrum which is derived on the basis of these factors (Ref. 9) coincides with the experimental data. In the region E_p < 80 Mev, the experimental spectra differ from the theoretical spectra: instead of a monotonic decrease of the spectrum with an increase in energy, a maximum is observed at a proton energy of 35 Mev, and a minimum at an energy of 20 Mev. The spectrum decrease at a proton energy of 20 Mev is, apparently, due to the presence of a maximum in the cross-section of non-elastic interaction of neutrons with nitrogen and oxygen nuclei, at this energy. There is a minimum in the energy distribution of neutrons at an energy of 20 Mev, which was not taken into consideration in the calculations. If this explanation is valid, then the experimental spectrum must approximate the theoretical spectrum in the region E_p < 10 Mev. It should be noted that the calculational data for energies below 50 Mev are less reliable, due to the indeterminate form of the neutron spectrum.

The form of the spectrum in the low-energy region (E_p < 30 Mev) depends greatly on the latitude. Measurements which were carried out on September 19, 1960 - six days after a solar flare (Ref. 7) - showed that the proton spectrum in the low-energy region becomes steeper ($\sim E^{-4.5}$) at high latitudes, while the intensity also increases. These changes in the spectrum are due to solar protons. It is assumed that the protons, moving in a spiral-like manner in the polar region, generate neutrons as they enter the atmosphere. Decomposing in the zone, the neutrons form protons, which are captured by the magnetic trap. This process lasts for a very short period of time - about 1 day - which is comparable with the lifetime of the protons which are thus formed. Thus, impulse injection of the protons exists within the zone in the polar region; this injection decreases with time. Since ten - twelve flares occur during a year, an anomalous component is constantly present in the zone, which depends upon a certain proton spectrum of cosmic origin.

An anomalous proton spectrum is localized within a definite region of the zone. The presence of low-energy protons on the full-defined force lines has a theoretical basis (Ref. 27). The /112
protons of solar origin, which are formed at high latitudes, move along the magnetic force lines toward the low latitudes, where they are excluded due to hard truncation (Ref. 9).

The spatial distribution of low-energy protons of solar origin (Ref. 27) is shown in Figure 4.4.

A study was made of the anomalous proton spectrum (Ref. 28) in the low-energy region up to 1 Mev. These results closely coincide with the data derived in another work (Ref. 7).

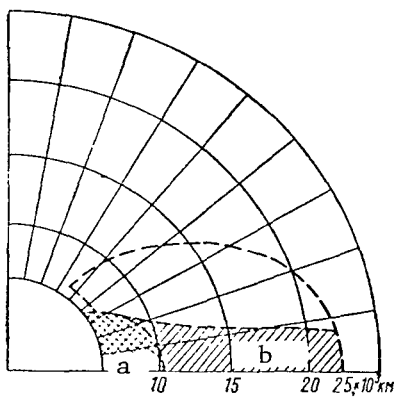

Figure 4.4

Spatial Distribution of Low-Energy Protons of Solar Origin:

The shade is the region where protons of solar origin are excluded; the semi-shade - the region in which there may be low-energy protons, but they cannot have stable orbits.

a- Shade; b- Semi-Shade

4.5. Time Variations

Data which were obtained previously point to the fact that the intensity and composition of particles within the zone are relatively constant. Intensity fluctuations, which were noted in the work (Ref. 1), do not exceed 15%.

In experiments conducted on the American satellite "Explorer VII", particle fluctuation was discovered in the inner radiation zone. These data must be verified. However, time variations in the inner zone can

exist, if it is assumed that the captured particles are formed as the result of albedo neutron decay. Actually, a stream of primary cosmic rays - and, consequently, the intensity of the neutrons formed by them - depends on the degree of solar activity. It is known that during the period of minimum solar activity the intensity of the generated neutrons increases by approximately a factor of 2 (Ref. 29, Ref. 30).

The discovery of a time variation in the radiation intensity in the inner zone, during minimum solar activity, can prove the validity of the assumption regarding the neutron origin of the inner radiation zone.

4.6. Doses

The absorbed dose, formed by protons of the inner radiation zone, was calculated according to a method described in Section 7.5. The spectrum obtained by an analysis of the experimental and theoretical data served as the basis for the calculations.

1. In the region where the anomalous component does not exist, the experimental proton spectra, which are normalized to 100 Mev, have almost identical form. The spectrum for the calculations was selected on the basis of results derived from recent measurements (Ref. 26, Ref. 31). Both spectra which were obtained coincide in the region $E_p > 100$ Mev. They have an identical form in the region less than 100 Mev, but differ somewhat in terms of intensity. Therefore, the reference spectrum was found by averaging these two spectra. /113

In the region $E < 10$ Mev, as was noted above, the experimental and theoretical spectra must coincide. Consequently, the reference spectrum in the region $1 \leqslant E_p \leqslant 10$ Mev is obtained by extrapolation. It should be noted that the data on the spectrum in the low-energy region (< 20 Mev) are less reliable, due to the difficulty entailed in calculating additional factors (residual atmosphere, walls of the rocket and counters, etc.). However, this is not important from the point of view of estimating the dose formed in the body of the cosmonaut, since protons having such energies are absorbed by relatively small protection thicknesses.

2. In the region of the anomaly, the spectrum is found in the following way: in the region $E \geqslant 100$ Mev, just as in Section 1; in the region $10 \leqslant E \leqslant 50$ Mev, according to data given in the work (Ref. 7). The region $50 \leqslant E \leqslant 100$ Mev is constructed by interpolation. Extrapolation in the region $1 \leqslant E \leqslant 10$ Mev was

carried out on the basis of data given in the work (Ref. 32).

The spectrum constructed for protons in the inner radiation zone of the earth is shown in Table 4.2 and in Figures 4.3 and 4.5.

TABLE 4.2

PROTON SPECTRUM OF THE INNER RADIATION ZONE, USED IN THE CALCULATIONS.

E_p, Mev	$\frac{dN}{dE}$, $\frac{\text{proton}}{\text{cm}^2 \cdot \text{sec} \cdot \text{Mev}}$	E_p, Mev	$\frac{dN}{dE}$, $\frac{\text{proton}}{\text{cm}^2 \cdot \text{sec} \cdot \text{Mev}}$	E_p, Mev	$\frac{dN}{dE}$, $\frac{\text{proton}}{\text{cm}^2 \cdot \text{sec} \cdot \text{Mev}}$	E_p, Mev	$\frac{dN}{dE}$, $\frac{\text{proton}}{\text{cm}^2 \cdot \text{sec} \cdot \text{Mev}}$
1	680	12	220	70	147	250	21
2	830	14	195	80	130	275	16,5
3	800	16	180	90	115	300	13,7
4	670	20	172	100	104	350	8,6
5	540	25	185	120	80	400	5,36
6	450	30	210	140	62	450	3,3
7	380	35	220	160	50	500	2,0
8	330	40	214	180	40	550	0,95
9	290	50	190	200	33	600	0,4
10	265	60	168	225	26	650	0,2

It was assumed in the calculations that the spectral form of protons having cosmic origin is constant for any point in space. In actuality, as was indicated above, the proton spectrum softens in the upper part of the radiation zone. However, it is impossible to take this effect into consideration due to the lack of experimental data. /115

Calculation Results. The values for the local and mean tissue dose, produced by protons of a normal spectrum when no shielding is present, are shown in Table 4.3.

TABLE 4.3

DOSES FORMED BY PROTONS OF A NORMAL SPECTRUM IN THE INNER RADIATION ZONE OF THE EARTH

Absorbed Dose	rad/hour	rem/hour
Mean Tissue	35	46
Local	60	193

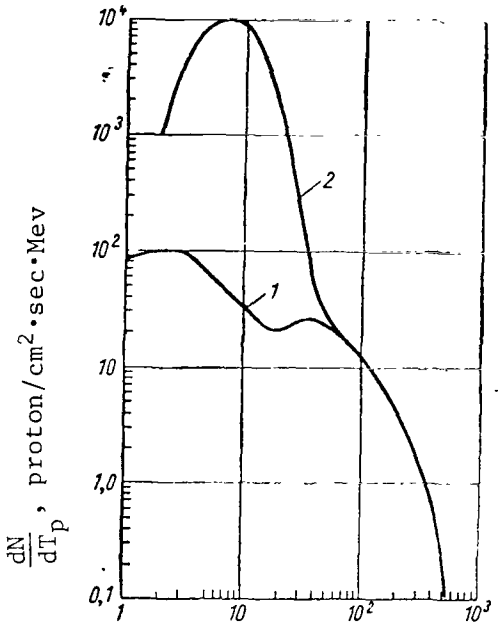

Figure 4.5

Normal (1) and Anomalous (2) Spectra of Protons in the Inner Radiation Zone, Used in the Calculations.

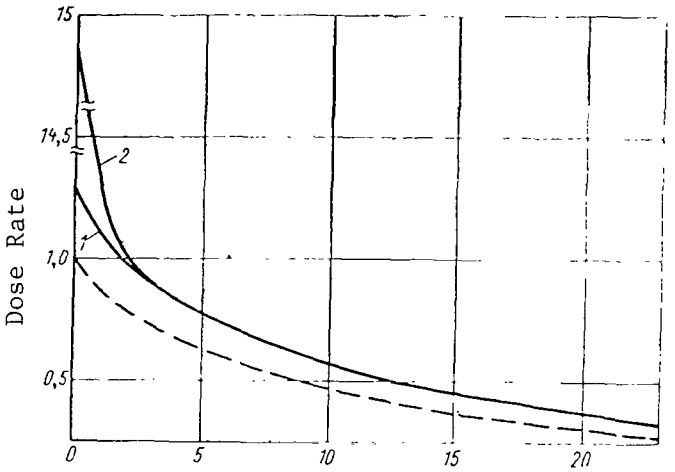

Figure 4.6

Distribution by Depth of the Dose Absorbed in the Body, Formed by Protons of the Inner Radiation Zone of the Earth:

1 - Normal part of the Spectrum;
2 - Anomalous; ———— mrem/sec;
--------- mrad/sec.

The course followed by the depth distribution of the absorbed dose greatly depends on the presence of an anomalous part of the spectrum at the given point in the zone. The distribution by depth of the absorbed dose, behind a shielding having a thickness of 1 g/cm^2, after which the anomalous part of the spectrum barely influences the course of the depth distribution, is shown in Figure 4.6. The calculated values for the physical local dose closely coincide with the data given in the work (Ref. 21). However, the biological dose is greatly overestimated. This can be explained by the fact that unjustifiably large RBE values were used in the calculations: in the energy region $E_p \leq 10$ Mev $Q = 10$; $10 < E_p < 100$ Mev $Q = 10 - 1$; $E_p \geq 100$ Mev $Q = 1$.

/115

The utilization of exaggerated RBE values (Ref. 21) leads to

the fact that the distribution by depth of the absorbed dose greatly decreases from the surface of the body to the center. On the other hand, the depth distributions (Ref. 33) have a form which is too flat, since the calculation was made for a very hard initial spectrum.

REFERENCES

1. Vernov, S. N., Chudakov, A. Ye. Uspekhi Fiz Nauk, 70, 585, 1960.

2. Vernov, S. N., et al. Dokl. AN SSSR, 140, 1041, 1961.

3. Van Allen, J. A., McIlwain, C. E. J. Geophys. Res., 64, 271, 1959.

4. Van Allen, J. A. and Frank, L. A. Nature, 183, 430, 1959.

5. Vernov, S. N. In the Book: Transactions of the International Conference on Cosmic Rays (Trudy mezhdunarodnoy konferentsii po kosmicheskim lucham). Vol. III, Izd-vo AN SSSR, Moscow, 1960.

6. Vernov, S. N., Chudakov, A. Ye., et al. Dokl. AN SSSR, 125, 304, 1959.

7. Naugle, J. E. and Kniffen, D. A. Phys. Rev. Letters, 7, 3, 1961.

8. McIlwain, C. E. J. Geophys. Res., 66, 3681, 1961.

9. Lenchek, A. M. and Singer, S. F. J. Geophys. Res., 67, 4, 1263, 1962.

10. TASS Report, Newspaper Pravda on May 17, 1963.

11. Van Allen, J. A. J. Geoph. Res., 64, 1683, 1959.

12. Van Allen, J. A. Paper Presented at Joint Meeting of National Academy of Sciences and American Physical Society on May 1, 1958. /116

13. Freden, S. C. and White, R. S. J. Geophys. Res., 65, 1377, 1960.

14. Vernov, S. N., Grigorov, N. L. et al. Dokl. AN SSSR, 124, 1022, 1959.

15. Singer, S. F. Phys. Rev. Letters, 1, 171, 181, 1958.

16. Kellog, P. J. Nuovo Cimento, 11, 48, 1959.

17. Hess, W. N. J. Geophys. Res., 65, 3107, 1960.

18. Hess, W. N. et al. J. Geophys. Res., 66, 665, 1961.

19. Freden, S. C. and White, R. S. Phys. Rev. Letters, 3, 9, 1959.

20. Hess, W. N. Phys. Rev. Letters, 3, 11, 1959.

21. Dye, D. L. and Noyes, J. C. J. Astron. Sci., VII, 3, 1960.

22. Armstrong, A. H. et al. J. Geophys. Res., 66, 351, 1961.

23. Hoffman, R. A., Arnoldy, R. L. and Winckler, J. R. J. Geophys. Res., 67, 1, 1962.

24. Holly, F. E. et al. J. Geophys. Res., 66, 1377, 1627, 1961.

25. Heckman, H. H. and Armstrong, A. H. J. Geophys. Res., 67, 4, 1255, 1962.

26. Freden, S. C. and White, R. S. (Citation given in [Ref. 9]).

27. Lenchek, A. M. J. Geophys. Res., 67, 6, 2145, 1962.

28. Bame, Conner, Hill, Holly.(Citation given in [Ref. 9]).

29. Madey, R. Preprint Amer. Astronaut. Soc., No. 15, 1962.

30. Reitz, D. Aerospace Engng., 20, 4, 28, 1961.

31. Freden, S. C. and White, R. S. J. Geophys. Res., 67, 1, 25, 1962.

32. Holmes, J. " Nerv " Data Alters Thinking and Shielding. Missiles and Rockets, 3, 8, 1961.

33. Keller, J. W. and Schaeffer, N. M. Electr. Eng., 79, 12, 1049, 1960.

CHAPTER 5

OUTER RADIATION ZONE OF THE EARTH

5.1. Experimental Data

As a result of measurements, which were carried out in the /117
USSR and USA with the aid of artificial satellites and cosmic rockets, it was discovered that close to the earth there is an outer (electron) radiation zone, which is captured by the magnetic field of the earth. This zone is the most extensive (in terms of space which can be occupied around the earth) and the most favorable for flights from the earth and for orbiting spacecrafts with living beings around the earth. It occupies a large part of the space around the earth, leaving only two large cones, with an aperture half-angle of about 20°, free of radiation.

In order to estimate the degree of radiation danger during flights in the electron zone, it is necessary to have data about the spatial location of the zone, the streams of electrons in different regions of the zone, and about the electron spectrum. These data wereobtained in a study of the radiation zones with the aid of Soviet and American artificial earth satellites and cosmic rockets.

Corpuscular and electromagnetic radiation in space is usually determined by gas-discharge counters, having different screens, and scintillation counters having different energy discrimination thresholds; these counters are placed on satellites and rockets (Ref. 1, 2, 3). It is possible to obtain information about the quantitative and qualitative composition of radiation by comparing the simultaneous results derived from radiation measurements by different detectors. Information about the spectral composition of radiation in the outer radiation zone was determined this way at different latitudes. Measurements with the aid of ion traps also play an important role in studying corpuscular radiation. The outer radiation zone of the earth was first discovered as a result of measurements carried out on the second (1957) and third (1958) Soviet artificial earth satellites.

The zone boundaries were established on the basis of the points at which the counting speed of the counter increased by a factor of two, as compared with the counting speed outside of the zone (Ref. 1). Figure 5.1 shows samples of recordings made by a scintillation counter during the flights of the third artificial satellite at northern latitude regions. The latitude λ and the longitude φ /118

are plotted along the abcissa axis. The altitude intervals for the flight of the satellite above the earth are also shown in the figure. It can be seen from the figure that the boundaries of the second zone can be quite clearly defined on the basis of a sharp increase in the counting speed of the counter. The results derived from the third satellite repeatedly entering the zone and leaving the zone in the Northern Hemisphere are shown in Figure 5.2. Let us present the following data in order to clarify the results which are obtained: in the Eastern Hemisphere, the mean entrance point into the electron zone corresponds to the geographical latitude $\lambda = 60.5°$ and the altitude H = 270 km. The mean exit point from the zone corresponds to the lower latitude $\lambda = 55.5°$ and the higher altitude H = 600 km.

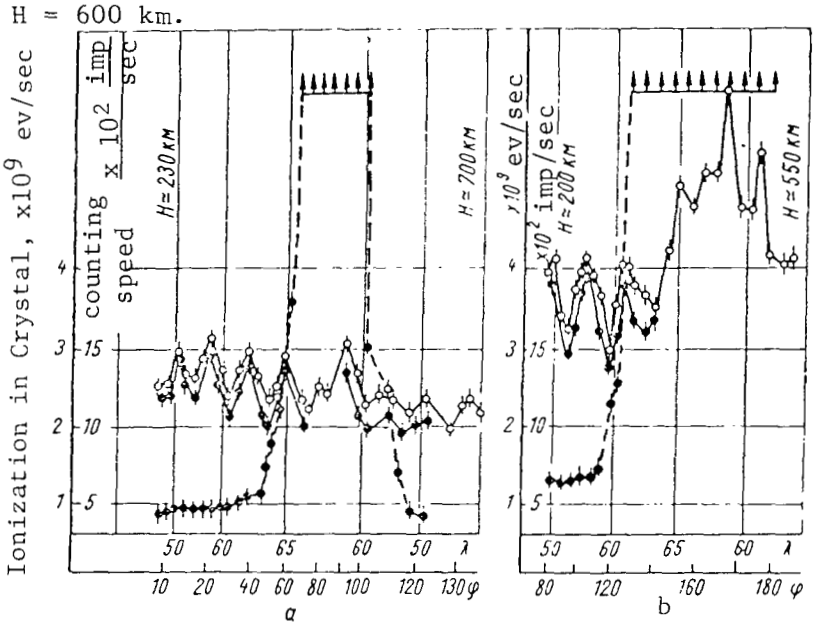

Figure 5.1

Sample Recordings made by the Scintillation Counter During Flights of a Satellite at High Latitudes in the Northern Hemisphere:

----- counting speed; o-o-o-o ionization in a crystal according to measurements of the dynode current; -●-●-●-● ionization in a crystal according to measurements of the anode current (Ref. 1).

It is interesting to trace the intensity changes in radiation of the electron zone along the force lines of the magnetic dipole of the earth. The force line, which is drawn through the mean exit point from the zone ($\lambda = 55.5°$ and H = 600 km), passes through the point $\lambda = 57°$ at an altitude of H = 270 km; at this point there is practically no radiation in the zone. On the other hand, the

force line, which is drawn through the point $\lambda = 60.5°$ and H = 270 km (entrance point into the zone), passes through the point $\lambda = 59°$ at an altitude of H = 600 km, where the radiation intensity is several times greater than the intensity at the entrance point. It can be seen from these examples that the radiation intensity along the magnetic force line sharply increases as one leaves the surface of the earth. An analogous pattern was observed during the flights of the thrid artificial satellite in the Southern Hemisphere, but at higher altitudes. For example, the satellite passed the Antarctic region at an altitude of about 1800 km; therefore, a significant increase was observed in the counting rate here (for example, 40 times greater, as compared with the Northern Hemisphere). /119

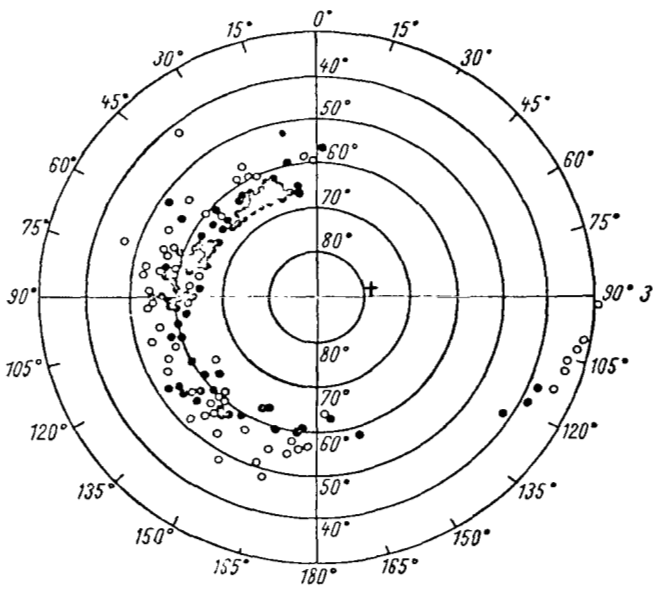

Figure 5.2

Location of the Coordinates for the Entrance (Points) and Exit (Circles) of the Satellite from the Electron Zone in the Northern Hemisphere at Low Latitudes.

The cross designates the position of the geomagnetic pole (Ref. 1).

The results derived from determining the outer boundary of the electron zone, on the basis of measurements carried out on the third artificial satellite, are shown in Figure 5.3, for the Northern and Southern Hemispheres respectively. These boundaries are conveniently characterized by the geomagnetic latitudes - i.e., by the geographic

latitudes at which the terrestrial surface is intersected by the given magnetic force lines. It was found that the outer boundary of the electron zone is determined by the geomagnetic latitude 69° ± 2° for the Northern Hemisphere, and by 65° ± 2° for the Southern Hemisphere (Ref. 4).

The location of the Northern and Southern regions of the electron zone was formulated very comprehensively on the basis of radiation measurements on the second and third Soviet spacecraft-satellites (1960). A map of the measurements carried out on the spacecraft-satellites is shown in Figure 5.4 (Ref. 5). It can be seen from the Figure that the zones of increased radiation in the Northern and Southern Hemispheres have a rather symmetrical distribution with respect to the equator, and there is a well-defined relationship between them. The region in the Southern Atlantic comprises one exception to this. /122

The boundaries of the electron zone at high altitudes, in the region of the geomagnetic equator, were determined during flights of the first and second Soviet cosmic rockets, and also during flights of the American rockets "Pioneer III" and "Pioneer IV". The trajectory of the first (January 2, 1959) and of the second (September 12, 1959) cosmic rockets, the change in the radiation intensity[1] along the rocket trajectory, the relative position of the first and second radiation zones in space near the earth, and the force lines of the magnetic dipole of the earth (the geomagnetic latitude is indicated on each line) are shown in Figure 5.5. The distance from the center of the earth along the geomagnetic equator is plotted along the abscissa axis. Figure 5.6 illustrates the position of lines of equal radiation intensity in the first and second radiation zones in the plane of the geomagnetic meridian, and also the ascending and descending branches of the rocket "Pioneer III" (Ref. 6).

It can be seen from these data that the contour of the electron zone is fairly symmetrical with respect to the geomagnetic coordinates, and practically repeats the path followed by the force lines of the magnetic dipole of the earth.[2] In addition, the radiation intensity along the force lines of the magnetic field sharply decreases as the surface of the earth is left behind. This fact led in its time to the conclusion that the radiation zones are radiation regions which are /123

[1] Ionization in a crystal of the scintillation counter was used here to measure the radiation intensity.

[2] Strictly speaking, the magnetic field of the earth is deflected from the dipole field - for example, in the regions of Brazil, the South Atlantic, and Siberia. However, in these regions extensions of the electron zone were observed, which repeated the path followed by the magnetic field.

captured in a magnetic trap. The fact that changes in the position of the maximum radiation intensity of the outer zone are correlated with magnetic storms and aurorae polaris serve to confirm the validity of this conclusion (Ref. 7). There are also two regions in which the aurorae polaris reoccurs with the maximum frequency: the region of the geomagnetic latitudes around 80°, and the region which extends from 60 to 70° in the geomagnetic latitudinal region. The nature of the aurorae in the latter region can be explained - even if only partially - by the intrusion of electrons from the outer radiation zone into this region.

/120

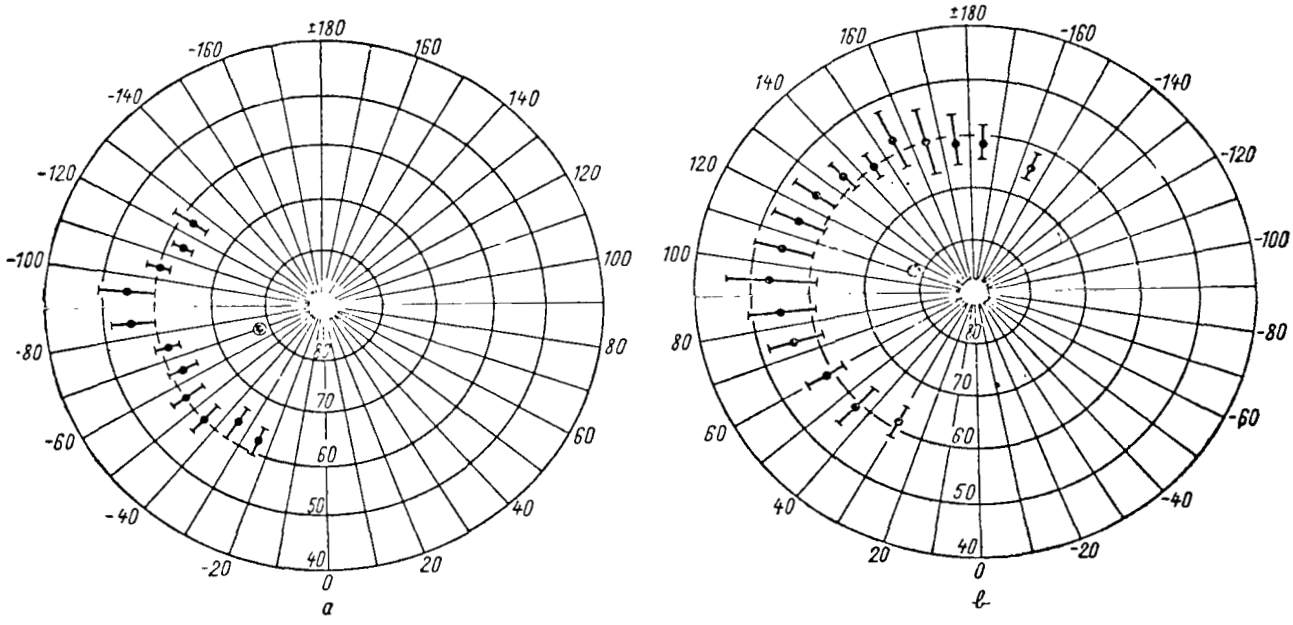

Figure 5.3

Location of the Outer Boundary for the Electron Zone in the North (a) and in the South (b) Hemispheres.

Small circle with a dot designates geomagnetic pole (Ref. 4)

The correlation between the position of maximum radiation intensity of the electron zone with magnetic storms can be illustrated by the following data. In January, 1959, the maximum (first Soviet cosmic rocket) was observed at a distance of about 27 000 km from the center of the earth; in December, 1958, (the rocket "Pioneer III") - at a distance of about 23 000 km; in March, 1959 (the rocket "Pioneer IV") - at a distance of about 20 000 km; and in September, 1959 (second Soviet cosmic rocket) - at a distance of about 18 000 km. Since the flights in March and September, 1959,

were made a short time after strong magnetic storms, the conclusion can be drawn that the magnetic storms shift the maximum radiation intensity close to the surface of the earth.

/121

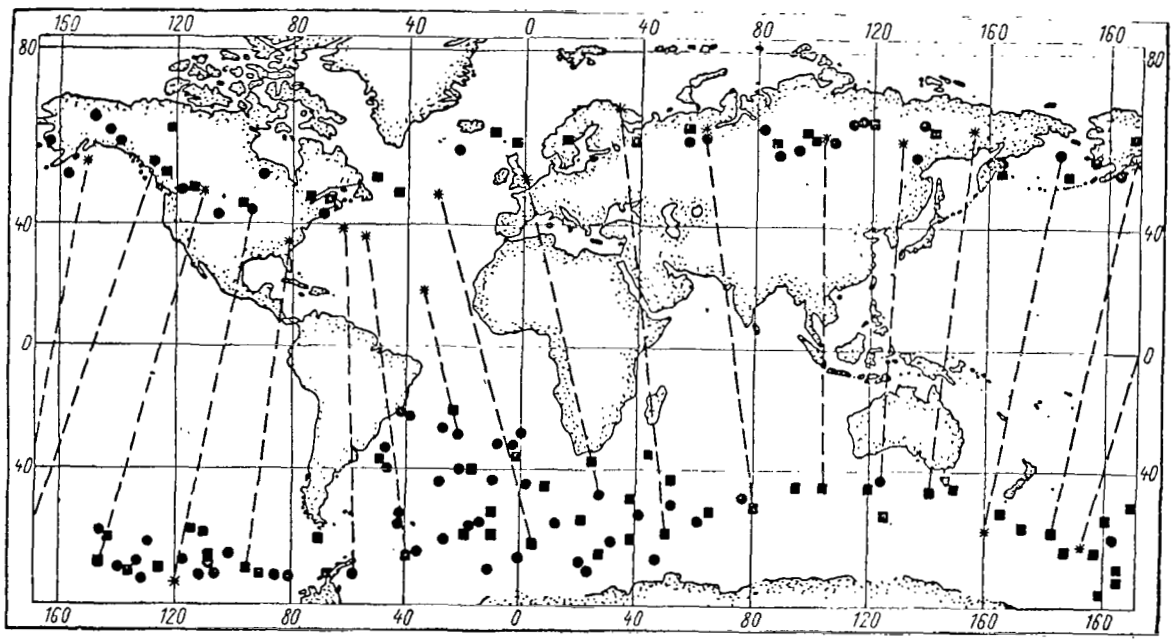

Figure 5.4

Distribution of Radiation Intensity in Zones of Increased Radiation in the North and Southern Hemispheres:

Small circles - based on data from the second spacecraft-satellite; squares - based on data from the third spacecraft satellite; dashed lines connect the main points with the conjugate points, which are indicated by asterisks (Ref. 5).

The so-called "Argus" (USA) experiment served to provide experimental corroboration for the possibility of electrons being captured by the magnetic field of the earth (Ref. 8). /123 /124 In August - September, 1958, at an altitude of 480 km from the surface of the earth, three successive nuclear explosions with a strength of 1 - 2 km were set off (the coordinates of the explosions were 8 - 12° west longitude, and 38 - 50° south latitude). It was found that each time the electrons from the explosion were propagated along the magnetic force lines, in the space between the proton and electron zones in the form of a cloud having a thickness of 90 - 150 km. The angular

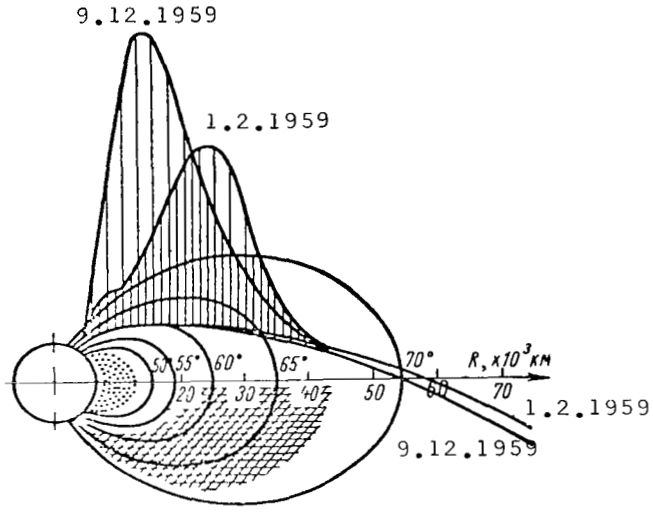

/122

Figure 5.5

Trajectories of the First and Second Cosmic Rockets at the Geomagnetic Coordinates and Change in Radiation Intensity Along the Trajectories.

The separate force lines of the magnetic field and the location of the proton (black dots) and electron (cruciform shading) zones are shown (Ref. 1).

/124

distribution for the intensity of the captured electrons was at a maximum in the direction perpendicular to the magnetic force lines, with the upper limit of the distribution half-angle of 15°. The rate at which the intensity decreased with time was approximately inversely proportional to time. The lifetime of electrons with a threshold energy of 1 Mev amounted to several days, and the lifetime of electrons with a threshold energy of 170 kev - about 20 days - i.e., electrons with lower energies had longer lifetimes. Measurements of the electron spectrum showed that there was a shortage of high-energy particles as compared with the β-spectrum for fission products (maximum energy of about 7 Mev). It is apparent that when electrons having energies which range from 0 - 7 Mev enter the region of the electron zone, they can also be captured in the magnetic trap, and their basic characteristics must follow the pattern noted above. Let us now examine the experimental data on the electron spectrum in the outer radiation zone. On the basis

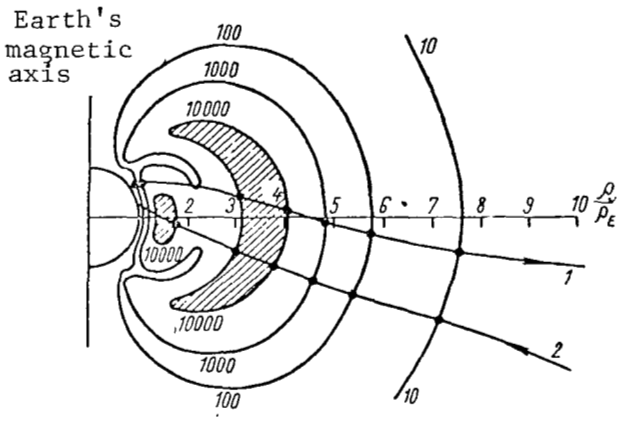

/123

Figure 5.6

Structure of the Radiation Zones and the Position of Equal Intensity Lines of the Captured Radiation in the Plane of the Geomagnetic Meridian:

Ascending (1); Descending (2) Trajectory Branches of the Rocket "Pioneer III" (Ref. 6).

of experimental results, certain determinations of the electron spectrum have been made in several works (Ref. 1, 6, 9 - 11), but the authors started with erroneous concepts about the total electron stream, which could effect a determination of the electron spectrum. /124

Based on measurements carried out on the second Soviet cosmic rocket with the aid of ion traps (Ref. 12), estimates of the total electron stream give a value which approximately equals $4 \cdot 10^7$ $cm^{-2} \cdot sec^{-1}$ for electrons having energies greater than 0.2 kev. Generalization of the experimental data obtained on September 5, 1961, provides a value for the total non-directional electron stream of $1 \cdot 10^8$ $cm^{-2} \cdot sec^{-1}$, for electrons having energies greater than 40 kev (Ref. 13). The latter value for the total stream will be used to estimate the radiation danger in the outer radiation zone. The results derived from a study of the electron spectrum are shown in Figure 5.7. It can be seen that the electron spectrum decreases rather sharply with an increase in the electron energy, and practically terminates in the energy region of about 5 Mev. /125

Let us represent the integral electron spectrum (i.e., the

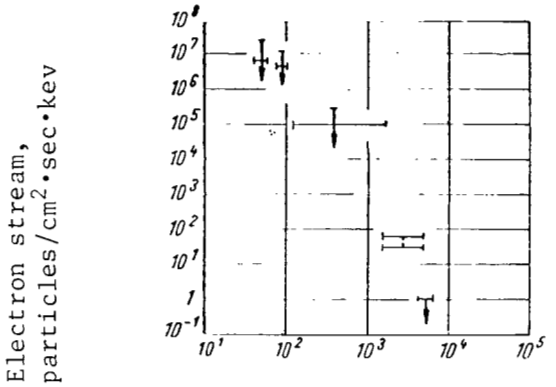

/124

Figure 5.7

Experimental Picture of the Electron Spectrum in the Outer Zone (Ref. 13)

spectrum for a number of electrons having energies greater than a given energy), as was already done by S. N. Vernov and others (Ref. 9), in the form:

$$N\,(<E_0) \sim E_0^{-\gamma}. \tag{5.1}$$

We then have the differential spectrum

$$N\,(E_0)\,dE_0 = AE_0^{-(\gamma+1)}\,dE_0, \tag{5.2}$$

where A is the normalization factor. For $E_0 \geq 0.1$ Mev, a satisfactory approximation of the law (5.2) is obtained for data on the spectrum (Ref. 13) for $\gamma \approx 2$, and the normalization constant is determined from the condition

$$\int_{0.1}^{5} N\,(E_0)\,dE_0 = 1 \cdot 10^8. \tag{5.3}$$

After the first approximation is corrected, the following law is obtained for the differential electron spectrum

$$N\,(E_0) \cdot dE_0 = 1{,}8 \cdot 10^6 E_0^{-3}\,dE_0, \tag{5.4}$$

where the energy E_0 is to be substituted in megaelectronvolts.

The results derived from utilizing formula (5.4) to calculate the number of electrons having the energies ($E_0 \pm 0.005$) Mev, which intersect a surface at 1 cm^2 in all directions after 1 second, are

shown in Table 5.1, for a total non-directional electron current 10^8 $cm^{-2} \cdot sec^{-1}$.

TABLE 5.1

THE DIFFERENTIAL ELECTRON SPECTRUM CALCULATED ACCORDING TO FORMULA (5.4)

E_0, Mev	$N(E_0)\Delta E_0$	E_0, Mev	$N(E_0)\Delta E_0$
0,05	$6 \cdot 10^7$	1,20	$1,04 \cdot 10^4$
0,08	$2,7 \cdot 10^7$	1,50	$0,54 \cdot 10^4$
0,10	$1,8 \cdot 10^7$	2,00	$0,225 \cdot 10^4$
0,20	$2,25 \cdot 10^6$	2,50	$0,115 \cdot 10^4$
0,30	$0,67 \cdot 10^6$	3,00	$0,67 \cdot 10^3$
0,40	$2,8 \cdot 10^5$	3,50	$0,42 \cdot 10^3$
0,50	$1,44 \cdot 10^5$	4,00	$0,28 \cdot 10^3$
0,60	$0,83 \cdot 10^5$	4,50	$0,198 \cdot 10^3$
0,80	$3,5 \cdot 10^4$	5,00	$1,44 \cdot 10^2$
1,00	$1,8 \cdot 10^4$		

For the first two energies (0.05 and 0.08 Mev), the differential streams were obtained from data given in the work (Ref. 13), based on a slower spectrum decrease with an increase in energy. For all the other energy values, the calculation was based on formula (5.4). The results derived from integrating the separate sections of the spectrum, given by formula (5.4), satisfactorily coincide with the corresponding values given in the work (Ref. 13). The differential energy spectrum which is obtained for the electrons can serve for an estimate of the radiation danger in the outer zone. /126

We should note that this spectrum can be a rather rough approximation of the electron spectrum at the intensity maximum of the second zone, which can be detected at any moment of time at a given point in space near the earth. Apparently, this spectrum can be used as a mean, characterizing the composition of radiation in the zone, and it is always possible to normalize the change in total radiation intensity with the distance from the earth, on the basis of the existing experimental data obtained on the Soviet and American satellites and rockets. The data shown in Figure 5.8, for example, can be used to determine the nature of the change in the radiation intensity of the outer zone with the distance from the earth. This figure shows the experimental results obtained during flights through the electron zone of Soviet and American cosmic rockets. The ordinate axis is used to plot the ionization in a crystal and the counting speed of the counters, which recorded the

electromagnetic radiation of electrons - which was formed as the electrons passed through the casing - and partly recorded the electrons which were able to pass through the casing. If the conditional assumption is made that the electron spectrum is constant throughout the entire outer zone, then the pattern followed by /127
the curve of the counter recordings will characterize the change in the electron dose and the electromagnetic radiation with the distance from the earth.

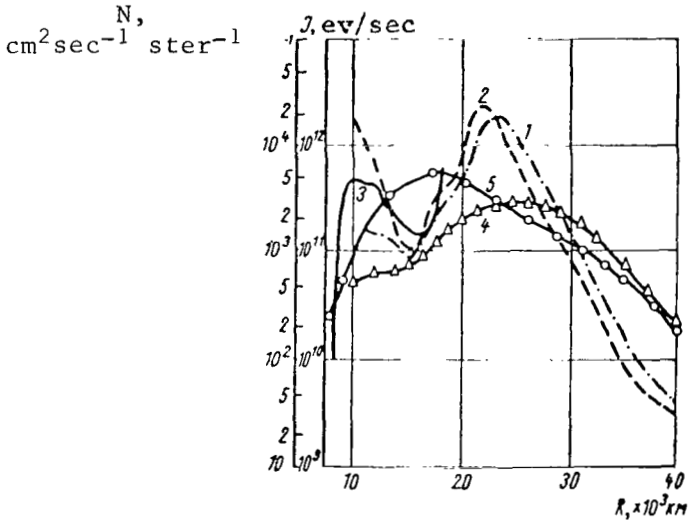

Figure 5.8

Dependence of Radiation Intensity in the Electron Zone on the Distance from the Center of the Earth:

1 and 2 - Based on Measurements on the Rocket "Pioneer III" (Ascending and Descending Branches); 3 - According to Measurements on the Rocket "Pioneer IV"; 4 and 5 - Based on Measurements of the Total Ionization on the First and Second Cosmic Rockets, Respectively (Ref. 7).

Thus, it can be seen from the experimental results that it is possible for electrons having energies up to 5 Mev to be captured by the magnetic field of the earth. The capturing region, which forms the electron zone, is practically symmetrical with respect to the geomagnetic coordinates, and is contained between the force lines which are characterized by the geomagnetic latitude from 55° to 67°. At high latitudes, the boundaries of the electron zone are located at an altitude of 300 - 600 km, and in the region of the

equator - at a distance up to 50 thousand km from the surface of the earth.

It should be noted that, as a result of radiation studies with the aid of ion traps, Soviet scientists discovered one electron zone, called the farthermost radiation zone, at distances from 50 to 70 thousand km from the earth (Ref. 12, 14, 15), which consists primarily of low-energy electrons.

5.2. Origin of the Electron Zone

Measurements of the magnetic field of the earth, at many points and in space close to the earth, have shown that at large distances this field can be represented in the form of a dipole field, which is inclined (with respect to the earth's axis) toward Canada by approximately 11.5°. At small distances, there are significant deviations from the dipole field at many points. In space near the earth, the strength of the earth's magnetic field is rather large, so that charged particles, having energies exceeding 10^{10} ev, can enter it without a significant trajectory distortion. Particles having sufficiently small energies will move in the magnetic field along trajectories, whose radius of curvature is much less than the distance from a given point to the dipole center. In this case, the particle will move along the force line of the field, rolling along it in a spiral-like manner. When the particle enters a region where there is an increase in the magnetic field, a field component can appear which is perpendicular to the spiral axis. If the magnetic field is sufficiently large at a given point, the particle is reflected. Thus, the particle will perform a complex, fluctuating motion between the two reflection points. During the motion of the particle, its magnetic moment remains almost constant (Ref. 1):

$$\mu = \frac{mv^2}{2H} = \text{const}, \tag{5.5}$$

where m and v_1 represent the mass and velocity component of the particle which is perpendicular to the force line, respectively; H represents the strength of the magnetic field.

If the particle moves at the equator at an angle of θ_0 to the force line, then reflection occurs at the latitude λ_{max} which is determined from the equation: /128

$$\sin^2 \theta_0 = \cos^6 \lambda_{max} \sqrt{4 - 3\cos^2 \lambda_{max}} \tag{5.6}$$

Since the magnetic field changes at the given force line, during the spiral motion of the particle the radius of curvature for its trajectory ρ is changed, increasing as the dipole center is left

behind. Due to this, a rotational motion of the spiral axis around the magnetic field occurs, i.e., drift appears, whose velocity is determined from the relationship:

$$v_{dr} = \frac{\varrho [\operatorname{grad} H \cdot \bar{H}]}{2H^2} v_{\perp}. \tag{5.7}$$

The period for the longitudinal drift of the particle can be determined from the following relationship (Ref. 4, Ref. 16):

$$\tau_{dr} = \frac{30}{E_0} \text{ min}, \tag{5.8}$$

where E_0 is the electron energy, Mev. The lifetime of the electron in the zone is

$$\tau_{el} = \frac{2 \cdot 10^6 \cdot E_0^2}{N} \text{ days} \tag{5.9}$$

where N is the air density, atom/cm^3.

It can be seen from relationship (5.9) that the air density influences the lifetime of the electron; this density increases sharply with a decrease in altitude. For example, at an altitude of 1200 km, the air density is $8 \cdot 10^5$, while at an altitude of 300 km, it is $3.5 \cdot 10^9$ atom/cm^{-3}. Therefore, during its lifetime an electron with an energy of 0.1 Mev, at an altitude of 300 km, is shifted longitudinally by an angle of 0.01°.

The reflection points are moved as a result of the atmosphere influencing the particle motion. With a decrease in the elevation of the reflection points, the lifetime of the particle sharply decreases. Thus, the particle is ejected (escapes) from the magnetic trap. However, if the injection of particles into the trap precedes their escape from the trap, this can lead to the appearance of large streams of captured particles in the zone. One of the possible mechanisms for the injection of electrons into the magnetic trap is the direct introduction of solar corpuscular streams into the electron zone. This process is particularly probable during the periods of magnetic storms, when large deformations of the zone are observed. Large streams of charged particles, which accompany the magnetic storms, can partially impair the magnetic trap and press the zone close to the surface of the earth. The restoration of the zone to its normal state can occur under the influence of the non-uniform magnetic field of the earth in the region of the smaller magnetic field gradients - i.e., in the region of large latitudes. The process by which solar corpuscular streams are directly

introduced into the magnetic trap seems the most probable one for extremely large particle clusters, whose energy exceeds the energy of the earth's magnetic field ($H^2/8\pi$). /129

Another probable process for the injection of particles into the electron zone is the introduction into the capturing region of particles which are formed as a result of albedo neutron decay of cosmic rays. These neutrons are formed during the interaction between the proton component of cosmic rays and atoms of atmospheric air; they can penetrate to rather large altitudes in the region of dense atmospheric layers.

Since the lifetime of a neutron is finite, after a certain time interval they decay into protons and electrons. The fact that the radiation zones contain protons and electrons points to the validity of this injection mechanism. In contrast to protons, electrons - which are formed during the process by which albedo neutrons decay - have an almost isotropic distribution; therefore, a specific portion of them will be captured in the magnetic trap. It is natural that part of the neutrons decays at comparatively low altitudes, where the atmospheric density is rather large - i.e., part of the electrons can be lost before capture by the magnetic field of the earth or they can lose part of their energy. The spectrum of captured electrons will differ from the electron spectrum of neutron β-decay. Figure 5.9 shows the results derived from calculating the equilibrium[1] spectrum of captured electrons (Ref. 17), taking into account the possible, main losses. It is assumed that slow albedo neutrons are responsible for the formation of electrons. It can be seen from the figure that the electrons which are thus produced can form only a definite part of the electron spectrum in the capturing region of the outer zone, and that other processes participate in the formation of the existing spectrum - for example, electron acceleration in the magnetic field of the earth. The presence of high-energy electron components in the electron zone can also be explained by the decay of rapid albedo neutrons of cosmic rays. Calculations have shown (Ref. 18) that electrons, which are formed during the β-decay of rapid albedo neutrons, can also be captured by the magnetic field of the earth. Figure 5.10 shows the results derived from calculating the possible minimum and maximum course followed by the curve

[1] Equilibrium is used here in the sense that entrance of the electrons into the trap and ejection of them from it does not occur at once (in time). Therefore, an equilibrium spectrum, which is more or less constant in terms of composition, occurs only after a certain period of time.

for the high-energy electron spectrum, taking into account the energy losses. A comparison of the results obtained with the experimental electron spectrum (Ref. 12) shows that they coincide fairly well in qualitative terms in the high-energy region. Quantitative divergences can be explained both by errors in the calculation, and by other effects connected with the electrons entering the magnetic trap. The effect produced by the direct introduction of solar corpuscular streams in the magnetic field of the earth can be included among the latter. Nevertheless, it is also fairly plausible that neutron β-decay has a significant influence on the formation of the electron zone. /131

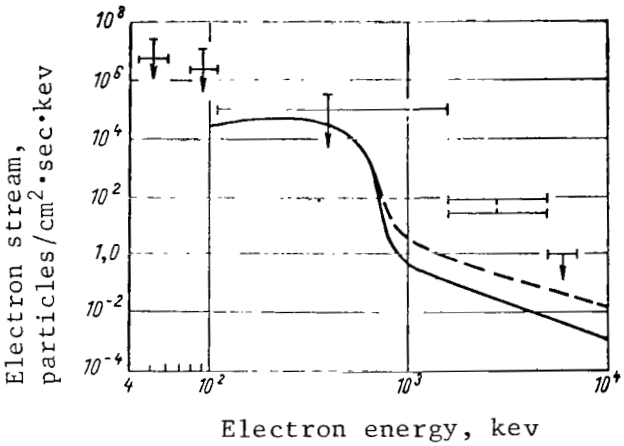

/130

Figure 5.9

A Comparison of the Calculated Electron Spectrum of the Outer Zone (Solid Line) and the Experimental (Dashed Line) Spectrum (Ref. 17).

Due to the presence of two possible significant sources of electrons in the outer zone, bifurcation of the zone into two regions can be expected (Ref. 19): one caused by the electrons of albedo neutron β-decay with a strength E_2, and one caused by the introduction of solar particles into the earth's magnetic field with a strength of E_3. In view of the relative stability of the first electron source, the region E_2 must be distinguished by sufficient stability. On the other hand, the region E_3 is subject to significant changes both in radiation intensity and in the location of maximum intensity, due to the sporadic nature of the second source of particles. For example, during the regeneration phase of a magnetic storm, an increase by several factors is observed in the radiation intensity of region E_3, along with a subsequent shift in /131

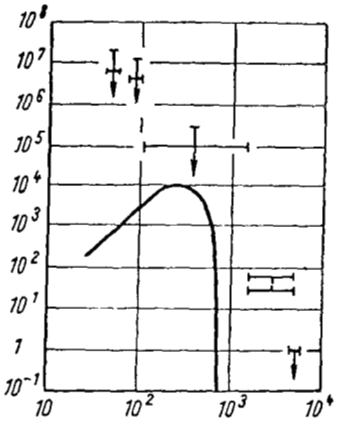

/130

Figure 5.10

Comparison of the Experimental Electron Spectrum in the Outer Zone with the Calculated Electron Spectrum of Neutron β-Decay (Ref. 18). The Stream of Electrons, particles/cm^2·sec·kev , is Plotted along the Ordinate Axis.

the intensity maximum to low altitudes by approximately 10%, so that /131
region E_3 merges, partially or completely, with region E_2 in the region of high latitudes. This is why two regions are not always observed. The bifurcation of the electron zone was noted in other studies (Ref. 20 - 24). An idealized picture of the location of regions E_2 and E_3 in the electron zone is shown in Figure 5.11.

We would like to point out in conclusion that, due to the difference in the mechanisms by which the regions E_2 and E_3 are formed, a difference must also be expected between the electron spectra in these regions.

5.3 Electron Tissue Dose

When radiation is propagated in a medium, the tissue dose as a function of the nature of the radiation will have its own specific depth distribution. For example, in the case of charged particles and γ-radiation of small energy, the tissue dose decreases with the penetration depth, so that the maximum dose occurs at the surface of the irradiated medium. In the case of hard γ-radiation, the tissue dose maximum is shifted to a certain characteristic depth.

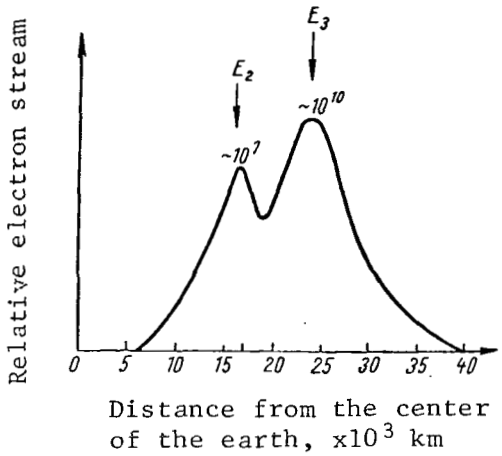

/130

Figure 5.11

Idealized Picture of the Division of the Electron Zone into Regions E_2 and E_3 (Ref. 19).

It is apparent that electrons in the outer zone will primarily /131
have a decreasing depth distribution of the tissue dose. Since the electron energies in the zone are comparatively small, in biological tissue they will be completely stopped at rather small distances (an electron with an energy of 1 Mev has a range of about 0.48 cm).

Let us now estimate the radiation danger in the electron zone. The tissue dose rate, created by electrons of the zone in a biological subject, will serve as the danger criterion. In the first approxi- /132
mation, the tissue dose rate can be estimated according to the electron ranges in biological tissue, assuming that the mean electron energy in the zone is about 0.1 Mev and a stream of electrons, impacting per unit of surface, is $\frac{N_0}{2} = 0.5 \cdot 10^8$ cm^{-2}·sec^{-1}.

$$P(E_0) = \frac{N_0}{2} \cdot \frac{1.6 \cdot 10^{-6}}{100} \cdot \frac{E_0}{R(E_0)} = 4 \left(\frac{\text{rad}}{\text{sec}}\right), \qquad (5.10)$$

where $R(E_0)$ is the electron range (g/cm^2) with an energy of E_0; the coefficient $1.6 \cdot 10^{-6}$ is inserted for the conversion of megaelectronvolt units into ergs; and the coefficient 100 - for the conversion of erg/g units into rads.

It can be seen from formula (5.10) that the absorbed dose rate from electrons in the zone is rather large, so that a lethal dose can be formed in a few minutes. However, an estimation based

on formula (5.10) does not take into account the distribution by depth of the absorbed energy, and essentially yields a value which is averaged over the entire range of electrons in biological tissue. For small electron energies, such an estimate leads to a significant underestimate of the tissue dose - as compared with the initial section of the range - and to an overestimate as compared with the final section of the electron range. For example, the depth dose from a source of βradiation p^{32} (maximum energy of 1.7 Mev) at a distance of 0.3 mm from the skin surface amounts to 75%; at a distance of 2 mm - 15%; at a depth of 3 mm (muscle tissue) - 6%.

But the complications involved in estimating radiation danger consist not only of considering the distribution by depth of the tissue dose, but also of considering the increased sensitivity to radiation of individual layers of biological tissue. Thus, the horny layer of skin having a thickness of 7 mg/cm^2 is practically insensitive to radiation; muscle tissue is also only slightly sensitive. The so-called living skin layers have a greater sensitivity, as compared with muscle tissue; the effective thickness of these layers is assumed to equal 0.1 cm, in accordance with the recommendations made by the International Commission on Protection from Radiation.

Thus, in order to correctly estimate radiation danger, it is necessary to determine the absorbed dose in the living layer at a thickness of 0.1 cm, which is located behind the horny skin layer. The dose rate, absorbed in the living skin layer, from the electron spectrum of the outer zone is estimated as follows:

$$P_{\ell *} = k \int_{E_{0\,\min}}^{E_{0\,\max}} \frac{N_0(E_0)}{2}\, dE_0 \left(-\frac{dE_0}{dx}\right) \Delta x_\ell = 14 \left(\frac{\text{rad}}{\text{sec}}\right), \qquad (5.11)$$

where $E_{0_{min}}$ and $E_{0_{max}}$ represent the minimum and maximum electron energy, respectively; $\left(-\frac{dE_0}{dx}\right)$ - the energy losses of electrons having energy E_0 per unit of path in biological tissue; Δx_ℓ - thickness of the living tissue layer; k - the constant dependent on the choice of units. /133

The quantities $(-dE_0/dx)\,\Delta x_\ell$ for electron energies in the region 0.1 - 2.0 Mev [1] were used to calculate the absorbed dose

---

* Note: ℓ designates 'living'.

[1] In the energy region 0.1 - 0.4 Mev, a correction was introduced in the quantity $\left(-\frac{dE_0}{dx}\right)\Delta x_\ell$ for energy losses in the horny skin layer (Ref. 24).

rate in a living layer P_{ℓ} . The values (dE_0/dx), which were given in another work (Ref. 25), were used for larger energies.

It can be seen that a more accurate calculation according to formula (5.11) yields a value for the absorbed dose which is 3.5 times greater, as compared with that derived by formula (5.10). Therefore, the latter formula can be used only for simplified, approximate calculations in those cases when sufficiently correct values for the initial quantities (for example, stream of electrons, their spectrum) are not known.

The above estimates of radiation danger in the electron zone are purely illustrative in nature, since they hold for a hypothetical case when the biological subject is located in the zone without any shielding. Under real cosmic flights, the biological subjects are usually protected by a large amount of substance of 1 - 10 g/cm^2. Therefore, the danger must be estimated by taking into account a real shielding, which can significantly lower the electron dose. However, during the damping process in a substance, electrons emit electromagnetic x-ray radiation with a fairly large penetrating capacity. When the shielding thickness is large, the dose caused by electromagnetic radiation predominates behind the shielding.

Estimates of the radiation danger in the outer zone give a value of about 10 roentgen/min for the maximum dose rate with a shielding of 0.5 g/cm^2 , and about 6 roentgen/min for a shielding of 5 g/cm^2 (Ref. 26). These estimates (Ref. 27) show that the dose rate can reach 200 roentgen/hour for a shielding thickness of 5 g/cm^2 (made of graphite). If about 3 g/cm^2 lead are added to this shielding, the dose rate decreases to 1 roentgen/hour. It can be seen from the given estimates that a flight through the electron zone maximum is almost impossible, if the shielding thickness is ≤ 5 g/cm^2 . However, exaggerated initial data were used (Ref. 28) in estimating the radiation danger (Ref. 26, Ref. 27). Estimates which take into account the experimental data on the electron spectrum (Ref. 13) provide a value for the dose rate of about 0.05 roentgen/hour, for a shielding thickness of 5 g/cm^2 (see Chapter 8 for more details), which indicates that it is safe enough for flights to pass through the electron zone maximum.

REFERENCES

1. Vernov, S. N., Chudakov, A. Ye. Uspekhi Fiz. Nauk, 70, 4, 585, 1960.

2. Van Allen, J. A., Frank, L. A. Nature, 183, 4659, 430, 1959.

3. Van Allen, J. A., Frank, L. A. Nature, 184, 4682, 219, 1959.

4. Gorchakov, Ye. V. Outer Radiation Zone and Aurora Polaris (Vneshniy radiatsionnyy poyas i polyarnyye siyaniya). In the Collection: Iskusstvennyye Sputniki Zemli, No. 9, Izd-vo AN SSSR, Moscow, 1961.

5. Vernov, S. N. et al. Radiation Zones of the Earth at Altitudes of 180-250 km (Radiatsionnyye poyasa zemli na vysotakh 180-250 km). /134 In the Collection: Iskusstvennyye Sputniki Zemli, No. 13, Izd-vo AN SSSR, Moscow, 1962.

6. Van Allen, D. A. Uspekhi Fiz. Nauk, 70, 4, 715, 1960.

7. Dolginov, S. Sh., et al. Magnetic Measurements on the Second Cosmic Rocket (Magnitnyye izmereniya na vtoroy kosmicheskoy rakete). In the Collection: Iskusstvennyye Sputniki Zemli, No. 5, Izd-vo AN SSSR, Moscow, 1961.

8. "Argus" Operation. Material from the Syposium on Effects of Artificial Radiation at High Altitudes (Operatsiya "Argus". Materialy simposiuma po effektam iskusstvennoy radiatsii na bol'shikh vysotakh). Atomizdat, Moscow, 1960.

9. Vernov, S. N., et al Dokl. AN SSSR, 124, 5, 1022, 1959.

10. Vernov, S. N. et al. Radiation Measurement during the Flight of the Second Cosmic Rocket (Izmereniye radiatsii pri polete vtoroy kosmicheskoy rakety). In the Collection: Iskusstvennyye Sputniki Zemli, No. 5, Izd-vo AN SSSR, Moscow, 1961.

11. Logachev, Yu. I. Determination of the Electron Spectrum in the Outer Radiation Zone during the Flight of the Second Cosmic Rocket (September 12, 1959)(Opredeleniye spektra elektronov vneshnego radiatsionnogo poyasa pri polete vtoroy kosmicheskoy rakety (12 sentyabrya 1959)). In the Collection: Geomagnetizm i Aeronomiya, No. 1, Izd-vo AN SSSR, Moscow, 1961.

12. Gringauz, K. I., et al. Study of Interplanetary Ionized Gas, Energy Electrons, and Corpuscular Solar Radiation with the Aid of Tri-electrode Traps of Charged Particles on the Second Soviet Cosmic Rocket (Izucheniye mezhplanetnogo ionizovannogo gaza, energichnykh elektronov i korpuskulyarnogo izlucheniya solntsa pri pomoshchi trekhelektrodnykh lovushek zaryazhennykh chastits na vtoroy sovetskoy kosmicheskoy rakete). In the Collection: Iskusstvennyye Sputniki Zemli, No. 6, Izd-vo AN SSSR, Moscow, 1961.

13. O'Brien, B. J. et al. J. Geophys. Res., 67, 1, 397, 1962.

14. Gringauz, K. I. et al. Ionized Gas and Rapid Electrons in the Vicinity of the Earth and in Interplanetary Space (Ionizovannyy gaz i bystryye elektrony v okrestnosti zemli i v mezhplanetnom prostranstve). In the Collection: Iskusstvennyye Sputniki Zemli, No. 6, Izd-vo AN SSSR, Moscow, 1961.

15. Gringauz, K. I. et al. Dokl. AN SSSR, 132, 1062, 1960.

16. Welch, J. A., Witaker, W. A. J. Geophys. Res., 64, 909, 1959.

17. Hess, W. N. J. Geophys. Res., 67, 5, 1699, 1962.

18. Nakada, M. P. J. Geophys. Res., 68, 1, 47, 1963.

19. Stolov, H. L. J. Geophys. Res. 67, 1, 404, 1962.

20. Fan, C. Y., Meejer, P., Simpson, J. A. Proc. Internat. Space Sci. Sympos., 1960.

21. Rosen, A., Sonett, C. P., Coleman, P. J. Geophys. Res., 64, 709, 1959.

22. Arnoldy, R. L., Hoffman, R. A., Winckler, J. R. J. Geophys. Res., 65, 1361, 1960.

23. Rothwell, P., McIlwain, C. E. Bull. Amer. Phys. Soc., 5, 261, 1960.

24. Kozlov, V. F., Solenkov, V. F. Individual Photocontrol of Beta-Irradiation."Collection of Works on Certain Problems of Dosimetry and Radiometry of Ionizing Radiation" (Individual'nyy fotokontrol' beta-oblucheniya. "Sbornik rabot po nekotorym voprosam dozimetrii i radiometrii ioniziruyushchikh izlucheniy"). Edited by Yu. V. Sivintsev. No. 1, Atomizdat, Moscow, 1960.

25. Radiation Dosimetry (Radiatsonnaya dozimetriya). Edited by Cain, J., and Brownell,G. Izd-vo Inostr. Lit., Moscow, 1958.

26. MacDonald, D., Burry, R., Eirman, W. S. Amer. Astronaut. Soc., Preprint 61-101, 1961.

27. Keller, Y. W., Schaeffer, N. M. Electr. Eng. , 97, 12, 1049, 1960.

28. Van Allen, D. A. Transactions of the International Conference on Cosmic Rays (Trudy mezhdunarodnoy konferentsii po kosmicheskim lucham). Vol. III, Izd-vo AN SSSR, Moscow, 1960.

CHAPTER 6

INTERACTION OF HIGH-ENERGY PROTONS WITH THE SHIELDING MATERIAL

6.1. Introduction

High-energy protons (tens and hundreds of megaelectronvolts) /135
comprise the main part of corpuscular radiation from solar flares and the inner radiation zone of the earth. Calculated values for the doses of proton radiation point to a serious radiation danger, which is related to intense streams of high energy protons in cosmic space. Due to this fact, it is necessary to provide for radiation safety of cosmonauts.

There are several possible methods which make it possible to decrease to a certain extent the radiation danger during space-flights, which is caused by intense streams of high-energy protons. These include, first of all, the judicious selection of the flight trajectory for the spacecrafts, so that the spacecrafts do not intersect the zone of increased radiation. They also include the organization of a reliable system for predicting solar flares, which would notify the cosmonaut at the proper time regarding increased radiation danger. On the other hand, there are possible methods for preventing intense particle streams from entering the inhabited cabin of the spacecraft. For this purpose, some authors consider it advantageous to utilize electrostatic or electromagnetic screening of the craft, by creating protective fields of the corresponding configuration. Other authors propose so-called material shielding, which is based on utilizing special shielding materials, combinations of them, construction elements for the craft, fuel supplies, etc. They assume that this type of shielding is the only really feasible shielding at the present time, and it apparently retains its value over a long period of time. In this respect, an examination is made of the main problems which arise in the utilization of shielding materials for decreasing radiation danger caused by high-energy protons.

The problem of providing shielding from radiation during space flights is very complex. In principle, it is comparatively easy /136
to lower the radiation dose to the established permissible level. The difficulties are encountered in the necessity of solving this problem for minimum weight or dimensions of the shielding. It need hardly be pointed out that very rigid requirements are imposed on the weight of the shielding for spacecrafts. It is sufficient to point out that, when spacecrafts are launched having different

destinations, the ratio of the payload - including the "non-useful" weight of the crew's shielding against radiation - and the initial rocket weight for chemical fuel can amount to 1:60 - 500 (Ref. 1).

The significant limitation on the weight of the shielding for spacecrafts, which is imposed by the resources of modern rocket technology, determines the requirements of the accuracy with which the shielding is calculated, the selection of shielding materials, and the constructive formulation of the shielding. Thus, the possibility of utilizing fuel tanks and certain supplies which are stored for a long period of time as shielding elements in the spacecraft construction acquires great importance.

It is well-known that ordinarily, in calculating the shielding, it is necessary to set aside a definite reserve "in ignorance", due to a certain element of uncertainty in the initial data which are utilized in these calculations. In the final analysis, this reserve appears in the form of additional shielding weight. It is apparent that this reserve "in ignorance" must be kept to a minimum in the shielding of spacecrafts from protons. In order to have a valid calculation of the spacecraft shielding, which provides sufficient radiation safety for the crew at minimum additional weight, it is necessary to have reliable initial data with respect to the radiation levels and the radiation composition for the given conditions of the cosmic flight, with respect to the permissible radiation action under these conditions, and the patterns of the radiation dose attenuation in the shielding materials.

Existing data about the composition of radiation and doses of radiation under spaceflight conditions are not fully comprehensive or reliable. In recent years, this type of data has been repeatedly reexamined and changed. These considerations have forced the individuals who are planning the shielding to examine different extreme cases, which in the last analysis inevitably lead to an increase in the shielding weight of the spacecraft. In this respect, the significant increase in studies on the radiation fields in cosmic space must be noted. It is to be hoped that the completion of the extensive program of satellite launchings - of the "Kosmos" series in the Soviet Union and the "Explorer" and "Discoverer" series in the USA - will greatly extend the existing information about radiation in cosmic space, and will make it possible to obtain reliable initial data for calculating shielding.

Similar remarks can be made with respect to the permissible radiation levels under conditions of spaceflight, as regards reliability and validity of these quantities. In addition, /137

it should be pointed out that radiation is not the only factor which influences man under conditions of spaceflight. Under these conditions, there is the combined action of radiation, linear and vibration overloads, the changed gaseous composition of the air medium in the inhabited cabin, and other factors which are characteristic for hermetically-sealed locations (Ref. 2). The action of these factors can have a definite influence on the magnitude of the permissible level. In its turn, the latter can lower the endurance limits with respect to these factors. At the present time, extensive model studies are being carried out on high-energy proton accelerators, which are aimed at determining the valid quantities for radiation action with respect to spaceflight conditions (Ref. 3).

Let us further examine the questions which are related to the problem of attenuating the dose of proton radiation in the shielding. This problem is complex for several reasons. In the case of γ-radiation it is fully sufficient to determine the dose at a shielded point, which is located beyond the shielding. This is related to the nature of depth distributions of γ-radiation which very slightly depend on the shielding thickness, and cannot be taken into account in the calculations. Mean- and high-energy protons, which comprise the main portion of proton radiation in cosmic space, have ranges which are comparable to the shielding thicknesses and the effective dimensions of the human body. Due to this fact, depth distributions of the protons depend significantly on the shielding thickness. For this reason, it is necessary to take into account the nature of the depth distributions of the proton dose in the body, when determining its effectiveness.

There are also important features in the geometry of shielding from protons in cosmic space. Under terrestrial conditions, the radiation source is surrounded by shielding (particle accelerator, nuclear reactor, etc.), while under spaceflight conditions the shielding insulates the cosmonaut from external radiation.

However, the main difficulties which are encountered in the problem of shielding from protons are caused by the fact that the relative biological effectiveness of the main radiation components beyond the shielding must be taken into account. From this point of view, the problem of shielding from γ-radiation is simpler. The biological effectiveness of γ-radiation and of all secondary radiation produced in the shielding (scattered radiation, secondary electrons) is assumed to be the same. The bundle energy decreases as the protons pass through the shielding, due to loss by ionization and excitation of the atoms comprising the shielding material. Correspondingly, the ionization energy losses increase. At the present time, the clear dependence of the relative biological effectiveness on the ionization energy losses - or, as is assumed

in radiological literature, on the linear density of energy losses (Ref. 4) - is the generally-accepted point of view. Thus, the /138
effective value of the RBE increases as a monoenergetic bundle of protons passes through the shielding. The largest RBE value is observed for small proton energies - i.e., close to the end of its range - and approximately equals 13 (Ref. 5). This means that the biological effect is the same for irradiation by protons with such energies, with a dose which is 13 times less than that for γ-radiation. When protons from solar flares or the inner zone of the earth pass through the shielding, whose spectral distribution decreases rather sharply in the high-energy region, a significant portion of the protons after the shielding will have ranges which are smaller, as compared with the effective dimensions of the human body. This fact must not be overlooked in shielding calculations.

In addition, as the result of nuclear interactions of protons with the shielding material and biological tissue, a different type of secondary particles are formed (protons, neutrons, α-particles deuterons, tritons, mesons, and heavy nuclei) which have linear energy loss values which significantly differ from the initial values for a proton bundle impacting on the shielding. Thus, the calculations for shielding from protons must also include the additional contribution to the biological dose which is made by secondary particles, formed as a result of the interaction of protons with the shielding substance and biological tissue. For this purpose, it is necessary to know the composition of the radiation which is influencing the biological tissue, as well as the spectral distribution of separate components. In principle, it would be sufficient to know the spectrum of linear energy losses at different depths in the biological tissue, after different shielding layers. If the spectrum of linear energy losses is used, an attempt can be made to determine the depth distribution of the biological dose, and on the basis of these data to estimate the effectiveness of the shielding layer. The following facts should be noted. Linear energy losses are not the only factor which determines the biological effect of radiation and, correspondingly, the RBE coefficient. The biological effectiveness of radiation depends in a complex manner on the nature of the radiation action (acute or chronic action), the form of the biological subject, magnitude of the dose, etc.

In addition to the indicated difficulties which are encountered in examining the problem of shielding from protons, difficulties are also entailed which are caused by insufficient data concerning the attenuation of the physical dose of proton radiation in the shielding. The existing data concerning the passage of protons through matter are incomplete, from this point of view. It is sufficient to make

a detailed study of the problems of ionization losses and ranges of protons, although in the region of very low-energy protons - where electrons are captured by a proton - such data must be refined to an additional extent (Ref. 6). There are also data on the inelastic interaction of protons; however, quantitative data on the outflow of /139 secondary particles are essentially insufficient for determining the contribution made by these particles to the biological dose beyond the shielding. All of these problems will be examined in detail below.

6.2. Main Forms of Proton Interaction with the Shielding Material and Biological Tissue

Two cases can be distinguished in an examination of proton interaction with the shielding material and biological tissue. In the first case, the interaction process is caused by the presence of an electric charge in the proton (electromagnetic interaction). The protons can undergo electromagnetic interaction both with electrons, and with the atomic nuclei of the substance. The probability for undergoing a certain type of electromagnetic interaction depends on the so-called collision parameter - i.e., on the distance between the trajectories of the impacting particle and the atom before the collision. Three basic types of interaction can be distinguished as a function of the impact parameter (Ref. 7).

1. The impact parameter is much larger than the atom dimensions. The impacting proton interacts with the atom as a whole, causing its excitation or ionization.

2. The impact parameter is comparable to the atom dimensions. The impacting proton interacts with one of the atom electrons. If the electron receives energy in this way which is sufficiently large, as compared with its binding energy, this process can be regarded as the collision between a proton and a free electron.

3. The impact parameter is smaller than the atom dimensions. The main result of the interaction is the deviation of the proton, in the Coulomb field of the nucleus, from the direction of initial motion (elastic scattering).

Thus, as a result of electromagnetic interaction a proton can either lose part of its energy - by excitation and ionization of atoms and by the formation of δ-electrons (secondary electrons which can, in their turn, cause ionization of atoms) - or can undergo elastic scattering in the field of the nucleus. Collisions with

electrons (so-called ionization losses) play a basic role in energy losses by the protons when passing through the substance. Thus, elastic collisions between protons and atomic nuclei play an insignificant role, with the exception of the region of very low-energy protons (Ref. 6). As the result of many subsequent electromagnetic interactions, the initial proton energy changes into smaller and smaller portions, and in the last analysis changes into excitation and ionization energy of atoms in the medium.

As a result of the interaction with nuclei (multiple Coulomb scattering), successive scattering of the protons at comparatively small angles occurs, when protons pass through the shielding material - apart from energy losses during collisions with atomic electrons. Multiple Coulomb scattering leads to a certain /140
"diffusion" of the initial proton bundle, while collisions between protons and electrons cannot make any significant contribution in this case.

In the second of the cases mentioned above, protons interact with nuclei, with the participation of nuclear forces. Nuclear interactions lead, on the one hand, to attenuation of the bundle impacting on the shielding due to absorption of protons by the atomic nuclei of the substance, and - on the other hand - to the formation of new particles (secondary particles). The amount of secondary particles formed in one nuclear interaction, as well as their energy and angular distribution, depend primarily on the energy of the incident proton and on the nature of the nuclei in the medium.

The result produced by the nuclear interaction of a proton with the shielding material or biological tissue can be as follows, depending on the energy of the protons impacting on the shielding (Ref. 8). For proton energies which are less than 100 Mev, the output of secondary particles is small (one or two protons, neutrons, deuterons, α-particles, and γ-quanta), and the energies of these particles are small. We should note that the output of secondary, low-energy particles from the shielding, due to small ranges, can be small. However, their formation directly in biological tissue can make a significant contribution to the absorbed dose, due to the large values of linear energy losses and, correspondingly, the high R_{BE} values.

For proton energies which are greater than 100 Mev, the output of secondary particles becomes greater, and their energy also increases. For proton energies which are greater than 500 Mev, the process by which mesons having high energies are formed begins to play an important role. Secondary particles, which are formed by

protons in this energy region, can be roughly divided into two groups. The first group includes low-energy particles, whose energy is less than 100 Mev. This group of particles consists primarily of protons, neutrons, deuterons, tritons, and heavier nuclei. The second group of high-energy particles, whose energies occur in the region from 100 Mev up to the energy of a primary proton, primarily consist of protons, neutrons and π-mesons.

For a low-energy group of particles, which are formed by a proton with an energy of more than 500 Mev, the statements with respect to their small output from the shielding remain valid, and it is possible that they make a significant contribution to the biological dose. High-energy secondary particles can undergo a nuclear interaction in the shielding material or in tissue, and this pertains not only to protons, but also to neutrons and to charged π-mesons. Neutral π-mesons comprise an exception to this, because the probability that they may disintegrate into two quanta is extremely great.

As a result of successive nuclear interactions of the secondary particles in the shielding substance or in tissue, a cascade process can occur, which will develop until the secondary particles have the capacity to cause nuclear interactions. The development /141
of showers and their penetration into the substance determine high-energy secondary particles, whose direction of motion is primarily similar to the direction of a primary proton. For this reason, the shower also develops close to this direction, gradually becoming diffused as the substance is penetrated.

The relative role of electromagnetic and nuclear proton interactions in the shielding substance and in biological tissue is of great importance with respect to shielding from protons, for the proton energy region in which we are interested.

Let us examine a monoenergetic proton bundle $N_p(0)$ proton/cm^2·sec, which impacts on the shielding made of substance having the mass number A (Ref. 8, Ref. 9). It is well-known that in the first approximation the cross-section of inelastic (nuclear) interaction σ_a is close to the geometric cross-section for all energies of protons which exceed by several factors the magnitude of the Coulomb barrier. Thus, it can be approximately assumed that $\sigma_a \approx \pi(1.3\cdot10^{-13}\cdot A^{1/3})^2$ cm^2. The corresponding range with respect to inelastic interaction equals

$$\lambda = \left(\frac{\sigma_a N_0}{A}\right)^{-1} \text{ g/cm}^2$$

where N_0 is the Avogadro number. The portion of the proton bundle

undergoing nuclear interaction will be on the average, for the depth x (g/cm^2):

$$\alpha = \frac{N_p(0) - N_p(x)}{N_p(0)} = 1 - e^{-x/\lambda}, \qquad (6.1)$$

where $N_p(x)$ is the bundle intensity at the depth x.

Let us examine, for example, protons having energies of 500 Mev, which impact on a shielding made of carbon. For carbon, $\lambda \approx 70$ g/cm^2. The range of protons with energies of 500 Mev in carbon is 130 g/cm^2, taking into account only electromagnetic interactions (Ref. 10). However, equation (6.1) shows that in this case $\alpha = 0.83$. This means that for a carbon thickness of 130 g/cm^2, about 83% of the protons which impact on the shielding undergo nuclear interaction, forming secondary particles. Only about 17% of the protons will lose their energy completely, due to electromagnetic interactions on the path through 130 g/cm^2 carbon. It can also be seen from this example that the conception of the range, determined on the basis of electromagnetic interactions, has a limited value from the point of view of shielding from protons having energies of 500 - 1000 Mev, since nuclear interactions cannot be disregarded in this energy region.

In addition, it can be shown (Ref. 9) that at low proton energies, nuclear interactions cannot be disregarded for shielding thickness which are close to the proton range. As a rough estimate, we can assume that nuclear interactions can be disregarded, and /142
in shielding calculations it is possible to use the range - energy relationships, if not more than 20% of the protons impacting on the shileding undergo nuclear interaction in the shielding - whose thickness is close to the proton range. In the case of a carbon shielding, equation (6.1) for $\alpha = 0.2$ yields the proton range $x \approx 16$ g/cm^2, which corresponds to an energy of 150 Mev. Thus, if we assume a 20% criterion", then for a proton energy less than 150 Mev nuclear interactions can be disregarded in a shielding whose thickness equals the range. Analogous calculations for a lead shielding yield a value for this limiting energy, which corresponds to $\alpha \leqslant 0.2$, of about 180 Mev.

Thus, even for moderate proton energies, the nuclear proton interaction cannot be disregarded for a shielding thickness which is close to the proton range. We should also note that the considerations presented above cannot be directly applied to biological tissue. In this case, it is first necessary to define the limiting value α more accurately, and this must be done by taking into account the relative biological effectiveness of secondary

particles. Corresponding approximate calculations show that the nuclear contribution to the absorbed tissue dose, taking the RBE into account, is very significant even for small proton energies, and that, correspondingly, nuclear proton interactions cannot be disregarded.

Let us further examine the relative role of nuclear and electromagnetic interactions of protons, as a function of the shielding thickness. Table 6.1 presents the probabilities for protons - which penetrate different thicknesses of a shielding made of carbon and lead - to undergo nuclear interaction.

It can thus be seen that the relative role of nuclear interactions essentially depends on the shielding thickness and, for a given thickness, slightly depends on the proton energy. The latter fact can be explained by the rather weak dependence of the inelastic interaction cross-section on the proton energy, in the energy region of 100 - 1000 Mev in each case. In a more detailed examination, the dependence of the secondary particle output, as well as their energy and angular distribution, on the energy of the incident proton must be taken into consideration.

Consequently, for small shielding thicknesses (less than 10 g/cm^2), the attenuation of protons having the energies 100 - 1000 Mev is determined almost completely by electromagnetic interaction of protons in the shielding material. The nuclear interaction in this shielding thickness region can be disregarded, and only nuclear interactions in biological tissue must be taken into account when calculating the dose of protons beyond the shielding.

For large shielding thicknesses (more than 50 g/cm^2 and up to a thickness corresponding to the range) the conclusions given above remain valid. In this case, nuclear interactions must /143
be taken into consideration both in the biological tissue, and in the shielding itself. The problem of calculating the shielding is primarily complicated by the fact that there are no significant data. The separate examination, which was carried out above, of small and large thicknesses for a shielding from protons is of great practical importance. The corresponding calculations [for example, (Ref. 10)] show that for Class A flares (fast proton spectrum; the flare is not detected with an intensity increase at sea level) the shielding thickness must be about 5 g/cm^2 carbon, or 8 g/cm^2 tungsten alloy. Such a shielding thickness will be adequate for a brief passage through the inner radiation zone of the earth (Ref. 11). The problem of a shielding from Class B flares is considerably more

TABLE 6.1

PROBABILITY OF PROTON NUCLEAR INTERACTIONS AS A FUNCTION OF SHIELDING THICKNESS.

Proton Energy, Mev	Shielding Thickness g/cm^2	Portion of Protons not Undergoing Nuclear Interactions in the Shielding	
		Carbon	Lead
100	5	0,95 — — —	0,98 — — —
150	5 10	0,95 0,90 — —	0,98 0,95 — —
300	5 10 50 —	0,95 0,91 0,61 —	0,98 0,96 0,80 —
600	5 10 50 100 150	0,95 0,90 0,58 0,33 0,19	0,97 0,95 0,77 0,59 0,46
1000	5 10 50 100 150 200	0,95 0,90 0,60 0,34 0,20 0,12	0,98 0,95 0,79 0,62 0,49 0,38

complex (hard proton spectrum; the flare is detected with an intensity /144 increase at sea level). The required shielding thickness for Class B flares (Ref. 10) is 400 g/cm^2 carbon, or 700 g/cm^2 tungsten alloy. If it assumed that the radius of the inhabited compartment is 150 cm, then the total shielding weight is (in tons):

	Class A Flare	Class B Flare
Carbon	1.42	115
Tungsten Alloy	2.26	200

Consequently, if a Class B Flare is taken into account when calculating the thickness of the protective casing for the inhabited compartment, then the total shielding weight is far beyond the limits of the reasonable weight. The solution to this problem must apparently be sought in a combined shielding, which is composed of a shielding casing for the inhabited compartment (5 - 10 g/cm^2 of light substance) and an unique radiation shelter (Ref. 10) with a restricted inner volume (100 - 1000 g/cm^2, preferably of heavy substance), which is designed for sheltering the cosmonaut for a short period of time during intense Class B flares and other occurrences of a similar type. If it is assumed that the inner radius of a spherical shelter is 50 cm, then the total shelter weight for Class B flares is, in the case of carbon (400 g/cm^2), 106 tons, and for tungsten alloy (700 g/cm^2) - 45 tons (Ref. 10).

Thus, in the practical aspect the problem of shielding from protons is sharply divided into two parts. In planning the overall shielding of the inhabited compartment, one must be concerned with small shielding thicknesses, which are calculated on the basis of data regarding electromagnetic proton interactions in the shielding, taking into account nuclear interactions in biological tissue. In planning the radiation shelter, one must consider large shielding thicknesses, which are calculated by taking into account both electromagnetic and nuclear interactions in the shielding and in biological tissue.

6.3 Electromagnetic Proton Interaction with Matter

Proton Collisions with Electrons of Atoms in Matter

Let us first examine "close" proton collisions with atom electrons - i.e., collisions with a collision parameter which is comparable to the dimensions of the atom. For close collisions, the energy which is transmitted to the electron is large as compared with its binding energy, so that the electron can be assumed to be free before the collision. This simplifies an examination of the interaction process. Utilizing the laws for conservation of energy and impulse, we can obtain the following expression for the energy of a recoil electron (T_e) as a function of the angle of escape θ : /145

$$T_e(\theta) = 2m_e c^2 \frac{p^2 c^2 \cos^2\theta}{\left[m_e c^2 \left(p^2 c^2 + m_p^2 c^4\right)^{1/2}\right] - p^2 c^2 \cos^2\theta}, \qquad (6.2)$$

where m_p and p represent the mass and impulse of the proton before a collision; m_e - the electron mass; c - the velocity of light. With a decrease in the escape angle θ, which is

formed by the direction of motion for the particle before the collision and the trajectory of the recoil electron, the energy T_e - which is transmitted to the electron - increases and reaches a maximum value for $\theta = 0$ ("head-on" collision):

$$T_{e\,\max} = T(\theta = 0) = 2m_e c^2 \frac{p^2c^2}{m_e^2c^4 + m_p^2c^4 + 2m_e c^2 \left(p^2c^2 + m_p^2c^4\right)^{1/2}}. \qquad (6.3)$$

Since $m_p >> m_e$, the term $m_e^2c^4$ can be disregarded in the denominator (6.3):

$$T_{e_{\max}} = 2m_e^2 \frac{p^2c^2}{m_p^2c^4 + 2m_e c^2\left(p^2c^2 + m_p^2c^4\right)^{1/2}}. \qquad (6.4)$$

If the energy of the impacting proton is $T_p << \frac{m_p^2c^2}{m_e} = 2 \cdot 10^6$ Mev, which is completely fulfilled in our case, then expression (6.4) will have the form:

$$T_{e_{\max}} = 2m_e c^2 \left(\frac{p}{mc}\right)^2 = \frac{2m_e c^2 \beta^2}{1-\beta^2} = 2\left(\frac{m_e}{m_p}\right) T_p, \qquad (6.5)$$

where $\beta = v/c$ is the relative proton velocity. Thus, the maximum transfer of energy to the electron depends only on the velocity of the incident proton. The maximum velocity of the recoil electron equals the doubled proton velocity. Recoil electrons, whose energy exceeds the ionization energy of the atom, can, in their turn, dislodge electrons from the atom, causing its ionization (δ-electrons). A proton having the energy of 100 Mev can produce a δ-electron with an energy of 218 kev in a head-on collision. However, the probability that such a recoil electron will be formed is extremely small. Collisions, with the recoil electrons escaping at large angles and, correspondingly, with small energies, are more probable:

$$T_e(\theta) \approx T_{e_{\max}} \cos^2\theta = 2\left(\frac{m_e}{m_p}\right) T_p \cos^2\theta. \qquad (6.6)$$

The maximum angle is $\theta = 90°$, which corresponds to recoil electrons with zero energy.

Let us further examine the probability for the collision between a proton and a free electron. Let us designate the differential probability for the collision of a proton with an electron by $\Phi(T_p, T_e)$. Then, for the penetration of a layer $dx(g/cm^2)$ by a proton, the probability for the formation of a recoil electron with energies from T_e to $T_e + dT_e$ will be: /146

$$\Phi(T_p, T_e)\, dT_e dx.$$

In the general case, the probability for the collision $\Phi(T_p, T_e)$ depends on the spin of the impacting particle. For protons with energies $T_p << 2 \cdot 10^6$ Mev, the spin interaction can be disregarded. A quantum mechanical examination in this case leads to the following expression:

$$\Phi(T_p, T_e)\, dT_e = 2\pi N_0 \frac{Z}{A} r_0^2 \frac{m_e c^2 dT_e}{\beta^2 (T_e)^2} \left(1 - \beta^2 \frac{T_e}{T_{e\ \max}}\right), \qquad (6.7)$$

where N_0 is the Avogadro number; Z and A - the atomic number and mass number of atoms in the medium; r_0 - the classical electron radius. For small energies of T_e, as compared with $T_{e\ \max}$, expression (6.7) can be reduced to classical Rutherford formula.

We should note that, in accordance with expression (6.7), the probability for the interaction of a proton with an electron is proportional to the density of the electrons, and inversely proportional to the energy T_e which is acquired by the recoil electron. The latter fact means that collisions with large impact parameters are more probable than collisions with small parameters. In other words, small energy losses are more probable than large energy losses, during interaction of protons with free electrons.

If we know the energy P_e and the probability for collisions with such energy transfer, $\Phi(T_p, T_e)dT_e$, we can readily obtain the magnitude of the energy which is lost on a course of 1 g/cm^2, as a result of the interaction between a proton and free electrons. For this purpose, it is necessary to take the sum of all values for the energy which is lost by the proton, beginning with a certain value $T_{e\eta}$, at which the electron can be assumed to be free before the collision, and ending with the value $T_{e\ \max}$. Thus, we obtain the following expression:

$$-\frac{dE}{dx}(T_e \geqslant T_{e\eta}) = \int_{T_{e,\eta}}^{T_{e\ \max}} T_e \Phi(T_p, T_e)\, dT_e. \qquad (6.8)$$

The quantity $T_{e,\eta}$ serves as the energy limit dividing two regions of far ($T_e \leqslant T_{e,\eta}$) and close ($T_e \geqslant T_{e,\eta}$) collisions. This quantity can be selected from the following considerations (Ref. 7). On the one hand, the quantity $T_{e,\eta}$ must be large enough that all electrons can be assumed to be free, for all close collisions. On the other hand, this quantity must be so small that the incident particle can be regarded as a point charge for all far collisions. Both conditions are practically satisfied, if $T_{e,\eta}$ lies in the 10^4 - 10^5 ev region.

Performing integration in expression (6.8) and assuming that /147
$T_{e\ max} > T_{e,\eta}$, we obtain

$$-\frac{dE}{dx}(T_e \geqslant T_{e,\eta}) = 2C\frac{m_e c^2}{\beta^2}\left(\ln\frac{T_{e\ max}}{T_{e,\eta}} - \beta^2\right) = \\ = 2C\frac{m_e c^2}{\beta^2}\left(\ln\frac{2m_e c^2\beta^2}{(1-\beta^2)T_{e,\eta}} - \beta^2\right), \qquad (6.9)$$

where C = 0.1536 Z/A, cm^2/g.

In order to obtain the total energy loss for a proton, it is also necessary to determine the losses for far collisions, which lead to a small energy transfer. In the case of the latter, the energy which is acquired by a recoil electron is comparable to its binding energy, so that before the collision, the electron cannot be regarded as being free. Far collisions must be regarded as the interaction of a proton with an atom as a whole, and the different processes which lead to excitation and ionization of the atom must be taken into consideration when calculating the energy transfer. The main level is thus assumed to be the initial state of the atom, and the final state - one of the excited levels, which can pertain to a discrete (excitation) or to a continuous (ionization) spectrum.

Bohr developed a theory of energy loss for far collisions, on the basis of a quantomechanical description of the incident proton - atom system. The expression for energy loss, for far collisions, assumes the form

$$-\frac{dE}{dx}(T_e \leqslant T_{e,\eta}) = 2C\frac{m_e c^2}{\beta^2}\left[\ln\frac{2m_e c^2\beta^2 T_{e,\eta}}{(1-\beta^2)I^2(Z)} - \beta^2\right]. \qquad (6.10)$$

Here I(Z) represents the mean ionization potential of an atom with the atomic number Z. Formula (6.10) is valid for the following conditions: the velocity of the incident proton is much greater than the electron velocities in the atom, and the energy limit $T_{e,\eta}$ is large, as compared with the binding energy, and small as compared with the maximum energy which is transmitted to the electron $T_{e,\ max}$.

Ionization Energy Losses of Protons

The total energy, which is lost by a proton in penetrating 1 g/cm^2 of matter, as the result of far and close collisions with atom electrons, is

$$-\left(\frac{dE}{dx}\right)_{ion} = -\left[\frac{dE}{dx}(T_e \geqslant T_{e,\eta}) + \frac{dE}{dx}(T_e \leqslant T_{e,\eta})\right] \qquad (6.11)$$

and this is called the ionization energy losses of protons. Taking the sum of expressions (6.9) and (6.10), we obtain

$$-\left(\frac{dE}{dx}\right)_{\text{ion}} = 2C\frac{m_e c^2}{\beta^2}\left\{\ln\left[\frac{2m_e c^2\beta^2}{(1-\beta^2)I(Z)}\right]^2 - 2\beta^2\right\} = \\ = 2C\frac{m_e c^2}{\beta^2}\left\{\ln\left[\frac{2m_e v^2}{I(Z)}\right]^2 - 2\ln(1-\beta^2) - 2\beta^2\right\}. \quad (6.12)$$

As would be expected, the expression for total energy losses, for far and close collisions, does not depend on an arbitrarily-chosen value for the energy limit $T_{e,\eta}$. /148

In accordance with formula (6.12), the ionization energy losses for non-relativistic energies rapidly decrease with an increase in energy. This is related to the fact that, for a given collision parameter, the interaction between a proton and atoms of the medium becomes less effective with a decrease in the flight time for the proton close to the atom - i.e., with an increase in its velocity β. For very large velocities, β is close to 1 - i.e., the multiplier $1/\beta^2$ becomes constant. In this velocity region, the change in the multiplier $1/(1-\beta^2)$ in the argument of the logarithm in expression (6.12) is significant; it leads to an increase in the ionization losses with a further energy increase in the relativistic region. Thus, the curve for ionization losses has a minimum which is located at about 1.5 - 3 Bev, depending on the atomic number of the substance. With an increase in the atomic number, the minimum is shifted to low energies.

It should be noted that for ionization losses formula (6.12) cannot be assumed to hold in a wide energy region. In particular, when it was derived, it was assumed that the velocity of the incident proton is much greater than the velocities of the atomic electrons. This condition imposes a serious limitation on the applicability of formula (6.12) in the region of low energies; it can be applied for light and medium substances for a proton energy which is greater than 1 - 2 Mev. This formula can be used in the low-energy region, if a correction is introduced into it which takes into account the total effect of the atom shells (Ref. 12, Ref. 13).

In addition, in the region of very low energies, where the proton velocity becomes so small that the capture of electrons is possible, the decrease in the effective proton charge must be taken into account in addition. This effect is significant in the region of proton energies which are less than 100 kev (Ref. 14). Finally, in the energy region less than 5 - 10 kev an additional mechanism comes into play for the energy loss of protons in matter - elastic collisions of protons with nuclei. The relative role of

energy losses due to elastic collisions with nuclei increases with a decrease in the proton energy, and for an energy of 1.5 kev the energy losses due to electron and nuclear collisions are identical (Ref. 5). A correction for proton collisions with nuclei is not important, from the point of view of energy losses of protons in the shielding. However, the contribution made by collisions between low-energy protons and nuclei of the biological tissue can be significant, if the fact is taken into consideration that the relative biological effectiveness of such collisions can be regarded as more significant than the corresponding value for electron collisions (Ref. 6). In an examination of energy losses of a proton by ionization and excitation, it is assumed that atoms of a substance are insulated. For dense substances, it can be assumed that the atoms are insulated only in the case of close collisions. In principle, screening /149
of the impacting proton field is possible for far collisions, due to dielectric polarization of the medium - due to which the interaction with electrons is attenuated and, correspondingly, the ionization proton losses are decreased. This phenomenon is called the density effect. Density effect has been studied by several authors (Ref. 15 - 19). Qualitative data, which are set forth in the work (Ref. 17), have been regarded as being the most reliable until recently (Ref. 7, Ref. 20). However, it should be noted that in the formula for ionization losses (6.12) the correction for the density effect depends on the magnitude of the mean ionization potential for atoms. In earlier works (Ref. 17, Ref. 18) estimates of the density effect were based on the values for the ionization potentials, which cannot be regarded as completely reliable in the light of new data (Ref. 21, Ref. 22). In this connection, preference must be given to the calculation results (Ref. 19), which are based on the ionization potential values (Ref. 21) and which are close to the data obtained during systematic measurements of ionization potentials for different substances in a wide energy region (Ref. 22).

Thus, several corrections must be introduced in formula (6.12), which thus make it possible to expand the applicability of this formula both in the region of very low proton energies, and in the region of very high proton energies. If these corrections are taken into consideration, formula (6.12) assumes the form

$$-\left(\frac{dE}{dx}\right)_{\text{ion}} = 2CZ^2_{\text{eff}}(v)\frac{m_e c^2}{\beta^2}\left\{\ln\left[\frac{2m_e v^2}{I(Z)}\right] - 2\ln(1-\beta^2) - 2\beta^2 - u - \delta\right\}, \qquad (6.13)$$

where $Z_{eff}(v)$ is the effective proton charge; u is the correction for the effect of the atom shell, and β is the correction for the density effect. The criterion of the Born approximation (Ref. 19) serves as the condition under which the effective proton charge $Z_{eff}(v) = 1$:

$$v \gg v_0 = \frac{e^2}{\hbar}, \tag{6.14}$$

where v_0 is the atomic unit of velocity (the electron velocity in the first Born orbit of a hydrogen atom), which equals 2.183·10cm/sec.

If relationship (6.14) is not fulfilled, then the capture and loss of electrons by the proton begins, and Z_{eff} becomes less than unity. A theoretical examination of the energy losses thus is very difficult, and this problem has not been solved up to the present time. However, there are fairly reliable experimental data in this area. Therefore, the effect of electron capture and losses by ionization losses in a region of small energies is determined on the basis of existing empirical data.

The introduction of a correction for the capture and loss of electrons by a proton, in the form of the co-factor Z_{eff}^2 is based on the assumption that ionization losses for particles with an arbitrary charge Z_{eff} are Z_{eff}^2 times larger than the losses /150
of singly-charged particles.

Utilizing the calculations given in other works (Ref. 23-25), Neufeld and Snyder (Ref. 6) formulated a curve for the dependence of Z_{eff} on the proton velocity v , expressed in atomic units - v_0 ($v_0 = 2.183 \cdot 10^8$ cm/sec). This curve shows the "averaged" behavior of protons, and is based on measurements of proton charges in different media (hydrogen, helium, nitrogen, oxygen, argon, neon). The values of Z_{eff} for several values of the proton energy (Ref. 6) are given in Table 6.2.

It can be seen from the Table that electron capture is an important process when slow protons penetrate matter. Thus, for a proton energy on the order of several kiloelectronvolts, a large part of the time a proton exists as a neutral hydrogen atom.

If the effect of different atom shells in taken into account, the correction u can be determined in the form (Ref. 26):

$$u = \frac{2}{Z}(C_K + C_L + \cdots), \tag{6.15}$$

where C_K and C_L are the corrections for the K- and L-shells. The

TABLE 6.2.

EFFECTIVE CHARGE Z_{eff} OF A PROTON

v/v_0	T_p, Kev	Z_{eff}	v/v_0	T_p Kev	Z_{eff}
0,4	4,0	0,10	1,6	64,8	0,60
0,6	9,1	0,10	2,0	101	0,82
0,8	16,2	0,15	2,4	146	0,93
1,0	25,3	0,23	2,8	198	0,98
1,2	36,4	0,33	3,2	259	1,00
1,4	51,0	0,47			

values of C_K and C_L were calculated in another work (Ref. 13).

The effect of the bond for the K-shell will be considerable, if the proton energy is less than $T_p \leq 0.025Z^2$ Mev (Ref. 14) - i.e., less than 22 Mev for copper, 4 Mev for aluminum, and 0.4 Mev for beryllium. However, the contribution which the K-shells make to the ionization losses is small, at least for mean and heavy elements. For the remaining shells, the effect of the bond becomes significant for small energies, and the contribution made by these shells is essential. It should be pointed out that - in spite of the presence of a great many experimental data - comprehensive calculations have not been carried out up to the present in the region of small energies, taking the electron bond in the atom into account (Ref. 14).

The correction δ, which takes into account the density effect (Ref. 18, Ref. 19), can be determined from the formula

$$\delta = 4{,}606x + b + a(x_1 - x)^m \qquad x_0 < x < x_1, \tag{6.16}$$

where $x = \lg\left(\frac{p}{m_p c}\right) = \lg\left(\frac{\beta}{\sqrt{1-\beta^2}}\right)$; the constants c, a, x_1, x_0 and /151

m depend on the type of substance. The values for these constants are given in Table 6.3 for several substances. For sufficiently large proton energies, for which $x > x_1$, we can confine ourselves to the first two terms in formula (6.16). The values of x_0, which are given in the last column of Table 6.3, correspond to the proton energy for which the correction for the density effect δ is very small (δ = 0.02 - 0.06) (Ref. 19). Table 6.4 lists the values for the proton energy which correspond to different values of x_0.

TABLE 6.3

CALCULATION OF CORRECTION FOR DENSITY EFFECT (REF. 19)

Substance	$-b$	a	m	x_1	x_0
Li	3,07	0,374	3,05	2	—0,05
Be	2,83	0,413	2,82	2	—0,10
Graphite	3,22	0,531	2,63	2	—0,05
Mg	4,54	0,0938	3,56	3	0,10
Al	4,21	0,0906	3,51	3	0,05
Fe	4,62	0,127	3,29	3	0,10
Cu	4,74	0,119	3,38	3	0,20
Ag	5,75	0,251	2,88	3	0,20
Sn	6,28	0,0404	2,52	3	0,20
W	6,03	0,0283	3,91	4	0,30
Au	6,31	0,0436	3,62	4	0,30
Pb	6,93	0,0652	3,41	4	0,40
U	6,69	0,0652	3,37	4	0,30
H_2O	3,47	0,519	2,69	2	0,23
H_2	9,50	0,505	4,72	3	1,85
He	11,18	2,13	3,22	3	2,21
N_2	10,68	0,125	3,72	4	1,86
O_2	10,80	0,130	3,72	4	1,90
Ne	11,72	0,258	3,18	4	2,14
Ar	12,27	0,0255	4,36	5	2,02
Kr	13,12	0,0771	3,57	5	2,12
Xe	13,57	0,150	3,07	5	1,90
CH_4	9,56	0,0552	4,22	4	1,55
$(CH_2)_2$	9,52	0,0700	3,94	4	1,54
$(CH)_2$	9,95	0,0841	3,91	4	1,61
CO_2	10,32	0,0865	4,03	4	1,72

Thus, the correction for the density effect is very small /152
(relative decrease of ionization losses is not less than 0.5%), if the proton energy does not exceed approximately 300 Mev in the case of very light elements (lithium, beryllium, carbon); 400 - 800 Mev in the case of light and average elements (magnesium, aluminum, iron, copper, tin); and approximately 1500 Mev in the case of heavy elements (tungsten, gold, lead, uranium). For gas-like substances, the density effect is insignificant up to very high proton energies (20 Bev).

Quantitative Data Regarding Ionization Losses of Protons

Several authors have calculated the ionization energy losses of protons (Ref. 12, Ref. 26 - 30). However, with the exception of the work by Sternheimer (Ref. 26), data which were not reliable enough were utilized for the values of the ionization potentials. The qualitative data regarding ionization losses of proton are given

TABLE 6.4

PROTON ENERGY CORRESPONDING TO DIFFERENT VALUES OF x_0

x_0	−0.10	−0.05	0.10	0.20	0.40	0.80	1.0	1.5	2.0
T_p, Mev	260	315	580	810	1580	4900	8500	19 900	65 400

/151

below; these are based on the data given by Sternheimer (Ref. 26), since they are the most reliable and comprehensive at the present time. These data encompass an energy region from 2 Mev to 100 Bev, and are obtained by taking the density effect into account, which greatly lowers the ionization losses for an energy of more than 2 Bev. The calculations of Sternheimer are carried out on the basis of the following expression, which is similar to formula (6.13): /152

$$-\left(\frac{dE}{dx}\right)_{\text{ion}} = \frac{C}{\beta^2}\left[B + 0{,}69 + 2\ln\frac{p}{m_p c} + \ln T_{e\max} - 2\beta^2 - u - \delta\right] \text{Mev/g}\cdot\text{см}^{-2}, \qquad (6.17)$$

where $C = 0.1536\,\frac{Z}{A}$; $B = \ln(mc^2/I^2)$; p is the proton moment, and $T_{e\ max}$ is the maximum electron energy, Mev .

Sternheimer (Ref. 26) calculated the ionization losses for six substances: beryllium, carbon, air, aluminum, copper, and lead. The main constants utilized in these calculations are given in Table 6.5.

TABLE 6.5

VALUES OF I , C, AND B FOR CALCULATING IONIZATION LOSSES (REF. 26)

Substance	I, ev	G, Mev/g·cm^2	B
Be	64	0,0681	18,64
C	78	0,0768	18,25
Air	94	0,0768	17,89
Al	166	0,0740	16,73
Cu	371	0,0701	15,13
Pb	1070	0,0608	13,01

Table 6.6 lists the values for ionization energy losses of protons for the indicated substances. Due to the large values of I , which are utilized in Sternheimer's calculations, the data presented in this Table are somewhat lower than the corresponding /154

TABLE 6.6

IONIZATION ENERGY LOSSES $\left(\frac{dE}{dx}\right)_{ion}$ OF PROTONS IN Be, C, Al, Cu, Pb AND AIR

/153

T_p, Mev	Ionization Energy Losses of Protons, Mev/g·cm^{-2}					
	Be	C	Air	Al	Cu	Pb
2	131,9	140,6	134,0	110,8	78,93	41,14
3	97,45	104,4	99,86	83,16	61,83	34,62
4	78,06	83,97	80,53	67,44	51,27	29,85
5	65,59	70,74	68,00	57,19	44,08	26,36
6	56,69	61,29	58,99	49,84	38,73	23,65
7	50,15	54,28	52,32	44,38	34,71	21,54
8	45,03	48,81	47,11	40,09	31,50	19,81
9	40,99	44,47	42,96	36,67	28,94	18,40
10	37,63	40,87	39,51	33,80	26,77	17,18
12	32,44	35,29	34,15	29,35	23,38	15,23
14	28,62	31,17	30,20	26,04	20,83	13,73
16	25,65	27,96	27,10	23,45	18,82	12,52
18	23,30	25,42	24,66	21,39	17,22	11,54
20	21,38	23,34	22,66	19,70	15,91	10,73
22,5	19,41	21,21	20,61	17,95	14,54	9,874
25	17,80	19,46	18,93	16,52	13,42	9,163
27,5	16,47	18,01	17,53	15,32	12,48	8,564
30	15,34	16,79	16,35	14,31	11,68	8,050
35	13,53	14,82	14,44	12,67	10,38	7,203
40	12,15	13,32	12,98	11,41	9,383	6,548
45	11,05	12,12	11,82	10,41	8,584	6,020
50	10,15	11,14	10,87	9,584	7,925	5,581
55	9,412	10,33	10,09	8,902	7,378	5,213
60	8,788	9,645	9,420	8,325	6,914	4,900
65	8,254	9,062	8,852	7,831	6,514	4,629
70	7,791	8,556	8,360	7,402	6,167	4,391
75	7,38	8,112	7,928	7,026	5,861	4,181
80	7,026	7,719	7,546	6,693	5,590	3,996
90	6,424	7,061	6,904	6,132	5,133	3,682
100	6,933	6,526	6,382	5,674	4,760	3,424
110	5,527	6,079	5,950	5,292	4,449	3,209
120	5,187	5,706	5,587	4,973	4,187	3,027
130	4,896	5,388	5,276	4,700	3,961	2,870
140	4,644	5,112	5,007	4,464	3,767	2,734
150	4,424	4,872	4,773	4,258	3,594	2,616
160	4,232	4,659	4,567	4,077	3,445	2,511
180	3,908	4,304	4,221	3,768	3,192	2,333
200	3,647	4,016	3,942	3,522	2,989	2,189
225	3,384	3,728	3,660	3,272	2,783	2,042
250	3,173	3,497	3,434	3,072	2,616	1,924
275	3,000	3,307	3,248	2,908	2,480	1,828
300	2,853	3,148	3,093	2,771	2,366	1,747
325	2,730	3,013	2,961	2,655	2,268	1,678
350	2,625	2,896	2,848	2,555	2,185	1,619
375	2,534	2,797	2,751	2,469	2,112	1,568
400	2,453	2,709	2,666	2,392	2,049	1,523
450	2,321	2,563	2,524	2,268	1,945	1,448
500	2,215	2,448	2,413	2,169	1,863	1,390

(continued on next page)

Continuation of Table 6.6 /154

T_p, Mev	Ionization Energy Losses of Protons, Mev/g·cm^{-2}					
	Be	C	Air	Al	Cu	Pb
550	2,129	2,355	2,323	2,090	1,795	1,343
600	2,059	2,278	2,249	2,022	1,741	1,305
700	1,950	2,159	2,136	1,921	1,658	1,246
800	1,871	2,074	2,055	1,849	1,598	1,205
900	1,812	2,009	1,995	1,795	1,555	1,175
1 000	1,767	1,960	1,950	1,754	1,522	1,153
1 250	1,692	1,879	1,877	1,687	1,471	1,120
1 500	1,649	1,833	1,838	1,649	1,443	1,104
1 750	1,623	1,806	1,819	1,629	1,429	1,099
2 000	1,608	1,791	1,809	1,618	1,422	1,099
2 250	1,599	1,782	1,806	1,613	1,420	1,102
2 500	1,595	1,778	1,808	1,611	1,422	1,108
2 750	1,593	1,777	1,812	1,613	1,425	1,114
3 000	1,593	1,778	1,818	1,615	1,429	1,121
3 500	1,597	1,784	1,834	1,624	1,440	1,135
4 000	1,604	1,793	1,851	1,635	1,452	1,150
4 500	1,612	1,802	1,870	1,647	1,465	1,164
5 000	1,621	1,813	1,889	1,659	1,478	1,178
6 000	1,638	1,834	1,924	1,682	1,502	1,204
7 000	1,655	1,854	1,958	1,704	1,524	1,227
8 000	1,670	1,873	1,989	1,724	1,544	1,248
9 000	1,685	1,890	2,017	1,743	1,562	1,267
10 000	1,699	1,905	2,044	1,759	1,579	1,284

values obtained previously (Ref. 28).

The calculations performed by Sternheimer encompass the proton energy region, beginning with 2 Mev. For smaller energies, formula (6.17) can produce an unreliable result, even if corrections are taken into account for K- and L-shells, because for these energies the capture of electrons by an incident proton is possible. On the other hand, no special requirement is apparent in the values of $\left(\frac{dE}{dx}\right)_{ion}$ for different substances in this energy region. Biological tissue comprise an exception to this, for which the ionization losses in the energy region less than 2 Mev are of particular interest. Calculations of ionization losses for biological tissue, in the low-energy region, were carried out by Snyder and Neufeld (Ref. 5, Ref. 6).

Utilizing the available experimental data regarding ionization losses for protons having small energies, and also introducing corrections for the effective proton charge (Table 6.2), Snyder and Neufeld determined the curve for the dependence of ionization losses,

beginning with a proton energy on the order of 1 kev. In their calculations, they utilized the composition of the biological tissue, which is given in Table 6.7. This dependence is shown in Figure 6.1 (curves 1 and 2), as well as the contribution to the energy losses which is made by collisions between protons and nuclei of atoms in the tissue (curve 3). These data can be utilized to determine the biological dose of protons, taking into account the end points of the range, which are very important since a significant part of the protons penetrating the shielding will have ranges which are confined within the limits of the human body. In the general case, the contribution made by the collisions between protons and nuclei cannot be disregarded, because one can expect larger values for the relative biological effectiveness for collisions between protons and nuclei, than for collisions between protons and electrons (Ref. 6). Biological injuries of the tissue during collisions between protons and nuclei are directly related to the change in the molecular structure which is thus produced. On the other hand, during collisions between protons and electrons, an indirect effect occurs in the form of excitation or ionization of atoms of the tissue molecules, which can then lead to a disturbance of the molecules.

/155

/156

TABLE 6.7

COMPOSITION OF BIOLOGICAL TISSUE (REF. 5) /155

Substance	Composition of Biological Tissue		Substance	Composition of Biological Tissue	
	% in Weight	atom/cm^3		% in Weight	atom/cm^3
H	10.1	$6.02 \cdot 10^{22}$	N	4.0	$0.171 \cdot 10^{22}$
C	12.1	$0.603 \cdot 10^{22}$	O	73.6	$2.74 \cdot 10^{22}$

The maximum value for ionization energy losses of protons in the biological tissue is 1000 Mev/g$\cdot$cm^{-2}, for proton energies of about 70 kev. Analogous values for certain substances (Ref. 19) are set forth in Table 6.8. /156

Range-Energy Ratio for Protons

The mean path traversed by a particle having a given energy before stopping - i.e., before total energy loss - is called the range of a charged particle in matter. For protons

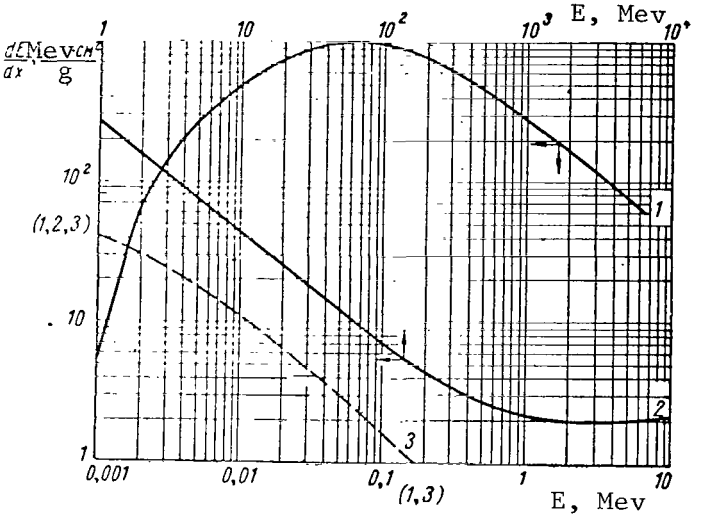

Figure 6.1

Dependence of Ionization Losses on Proton Energy (1, 2). Energy Losses Caused by Collisions Between Protons and Nuclei of Atoms in the Tissue (3).

TABLE 6.8

MAXIMUM VALUES FOR IONIZATION LOSSES OF PROTONS FOR SEVERAL SUBSTANCES (REF. 14).

Substance	$-\left(\frac{dE}{dx}\right)_{max}$, Mev/g·cm^{-2}	Energies T_p, Corresponding to $-\left(\frac{dE}{dx}\right)_{max}$, kev
H	3400	30
Air	620	100
Al	440	72
Au	100	160

having energies less than 1000 Mev, ionization losses represent the main form of energy loss; therefore, the range of a proton can be determined as follows:

$$R(T_p) = \int_0^{T_p} \frac{dR}{dE} dE = -\int_0^{T_p} \frac{dE}{\left(\frac{dE}{dx}\right)_{\text{ion}}}. \qquad (6.18)$$

It is difficult to calculate the range for protons according to this formula, due to the fact that the theory of ionization losses is essentially unsuitable in the region of small energies. For this reason, integration from zero cannot be carried out in expression (6.18). Ordinarily, this difficulty is overcome by an empirical selection of the integration constant, so as to obtain the best agreement with the most reliable experimental data. Thus, the following relationship can be used, instead of expression (6.18):

$$R(T_p) = R(T_{p,1}) + \int_{T_{p,1}}^{T_p} \frac{dE}{-\left(\frac{dE}{dx}\right)_{\text{ion}}}. \qquad (6.19)$$

If it is assumed that T_p, 1 = 2 Mev, as was done in another work (Ref. 26), then the following values for the ranges R(2 Mev) can be used: beryllium - 0.0091 g/cm^2 (Ref. 31); carbon - 0.0084 g/cm^2 (Ref. 26); Air - 0.0087 g/cm^2 (Ref. 12); aluminum - 0.0115 g/cm^2 (Ref. 31); copper - 0.0190 g/cm^2 (Ref. 31); lead - 0.0410 g/cm^2 (Ref. 26). The value for the range in carbon was obtained by interpolation of the data for beryllium, air, and aluminum (Ref. 12, Ref. 31), and in lead - by extrapolation of the data for gold (Ref. 31).

By performing integration in expression (6.19), utilizing formula (6.17) and the value of R (2 Mev), Sternheimer (Ref. 26) obtained the values for the ranges of protons having energies up to 100 Bev. These values are given for six substances in Table 6.9. A comparison of the values for the ranges which are given in this Table and the results derived from earlier calculations for air and aluminum (Ref. 27), and for beryllium, carbon, copper and lead (Ref. 28), shows that the difference is approximately from 1% to 9% for proton energies of 10 Bev. The greatest difference is observed for carbon (6.4%) and beryllium (9.2%) (Ref. 26). The main reasons for the divergence between the results obtained by Sternheimer and earlier calculations are related to the utilization of higher values for the ionization potentials, which led to a certain decrease in the ionization proton losses. They are also related to the introduction of a correction for the density effect, which decreased the ionization losses somewhat in the energy region 2 - 10 Bev.

TABLE 6.9

RANGES OF PROTONS IN Be, C, Al, Cu, Pb AND AIR
R, g/cm^2

T_p, Mev	Ranges of Protons					
	Be	C	Air	Al	Cu	Pb
2	0,0091	0,0084	0,0087	0,0115	0,0190	0,0410
3	0,0180	0,0168	0,0175	0,0221	0,035	0,0676
4	0,0296	0,0275	0,0287	0,0355	0,0513	0,0988
5	0,0436	0,0406	0,0423	0,0517	0,0724	0,1345
6	0,0601	0,0558	0,0581	0,0704	0,0967	0,1746
7	0,0789	0,0732	0,0761	0,0917	0,1240	0,2190
8	0,0999	0,0926	0,0963	0,1155	0,1542	0,2674
9	0,1232	0,1141	0,1185	0,1416	0,1874	0,3198
10	0,1487	0,1376	0,1428	0,1700	0,2234	0,3761
12	0,2061	0,1904	0,1974	0,2337	0,3035	0,5000
14	0,2719	0,2508	0,2598	0,3062	0,3943	0,6385
16	0,3459	0,3187	0,3299	0,3872	0,4954	0,7912
18	0,4278	0,3937	0,4073	0,4766	0,6066	0,9576
20	0,5175	0,4759	0,4920	0,5742	0,7276	1,138
22,5	0,6404	0,5884	0,6078	0,7073	0,8922	1,381
25	0,7750	0,7116	0,7346	0,8526	1,071	1,644
27,5	0,9212	0,8452	0,8720	1,010	1,265	1,926
30	1,079	0,9891	1,020	1,179	1,472	2,229
35	1,426	1,307	1,346	1,551	1,927	2,885
40	1,817	1,663	1,712	1,967	2,434	3,614
45	2,249	2,057	2,116	2,427	2,992	4,411
50	2,722	2,488	2,557	2,928	3,599	5,275
55	3,234	2,954	3,035	3,469	4,253	6,202
60	3,784	3,456	3,549	4,051	4,954	7,192
65	4,371	3,991	4,097	4,670	5,699	8,243
70	4,995	4,559	4,678	5,327	6,488	9,352
75	5,655	5,160	5,293	6,021	7,321	10,52
80	6,349	5,792	5,940	6,750	8,195	11,74
90	7,840	7,148	7,327	8,313	10,06	14,35
100	9,461	8,623	8,835	10,01	12,09	17,17
110	11,21	10,21	10,46	11,84	14,27	20,19
120	13,08	11,91	12,20	13,79	16,58	23,40
130	15,06	13,72	14,04	15,86	19,04	26,80
140	17,16	15,62	15,99	18,04	21,63	30,37
150	19,37	17,63	18,03	20,34	24,35	34,11
160	21,68	19,73	20,17	22,74	27,19	38,02
180	26,61	24,20	24,73	27,85	33,23	46,29
200	31,91	29,02	29,64	33,34	39,71	55,14
225	39,03	35,49	36,23	40,72	48,39	66,98
250	46,67	42,42	43,29	48,61	57,66	79,61
275	54,78	49,77	50,79	56,98	67,49	92,95
300	63,33	57,53	58,68	65,79	77,82	107,0
325	72,30	65,65	66,95	75,02	88,61	121,6
350	81,64	74,12	75,56	84,62	99,85	136,7
375	91,34	82,91	84,50	94,58	111,5	152,4
400	101,4	91,99	93,73	104,9	123,5	168,6
450	122,3	111,0	113,0	126,4	148,6	202,3
500	144,4	131,0	133,3	148,9	174,9	237,6
550	167,5	151,8	154,4	172,4	202,2	274,2

(Continued on Next Page)

(Continuation of Table 6.9)

T_p, Mev	Ranges of Protons					
	Be	C	Air	Al	Cu	Pb
600	191,3	173,4	176,3	196,7	230,5	312,0
700	241,3	218,6	222,0	247,6	289,5	390,5
800	293,7	265,9	269,8	300,7	350,9	472,2
900	348,1	314,9	319,2	355,6	414,4	556,3
1 000	404,0	365,3	370,0	412,0	479,4	642,2
1 250	548,9	495,8	500,9	557,7	646,8	862,7
1 500	698,8	630,7	635,7	707,7	818,7	1088
1 750	851,7	768,2	772,5	860,4	992,9	1315
2 000	1007	907,3	910,3	1014	1168	1543
2 250	1165	1047	1049	1169	1344	1770
2 500	1319	1188	1187	1324	1520	1996
2 750	1476	1328	1325	1479	1696	2221
3 000	1633	1469	1463	1634	1871	2445
3 500	1946	1750	1737	1943	2220	2888
4 000	2259	2029	2008	2250	2566	3326
4 500	2570	2308	2277	2555	2908	3758
5 000	2879	2584	2543	2857	3248	4185
6 000	3493	3133	3067	3456	3919	5024
7 000	4100	3675	3583	4046	4580	5847
8 000	4702	4212	4089	4629	5232	6655
9 000	5298	4743	4589	5206	5876	7450
10 000	5889	5270	5081	5777	6512	8234

Range Straggling of Protons

Protons having identical energies traverse a somewhat different /159
course in matter up until total damping. This effect is called range straggling and is caused by statistical fluctuations of ionization energy losses for protons. The effect of range straggling of protons in different substances must be estimated, from the point of view of calculating shielding from protons.

Range straggling of protons in nuclear emulsion was studied by Barkas and others (Ref. 32). Results have also been derived from calculating the range straggling of protons with energies of up to 1 Bev for copper (Ref. 33), and up to 10 Bev for iron (Ref. 34). However, the most detailed data were obtained by Sternheimer (Ref. 35), who examined the range straggling of protons having energies from 2 Mev up to 100 Bev for beryllium, carbon, aluminum, copper, lead, and air. The calculations of Sternheimer were based on a slightly modified expression, which was obtained by Lindhard and Scharff (Ref. 36) for the mean-square range straggling σ^2 in the relativistic region. This expression has the following form:

$$\sigma^2 = 4\pi e^4 n \int_0^{T_p} \frac{\left(1 - \frac{1}{2}\beta^2\right)}{(1-\beta^2)\left[1 + 2\left(\frac{m_e}{m_p}\right)(1-\beta^2)\right]^{-1/2}} \times \times \left(-\frac{dE}{dx}\right)_{\text{ion}}^{-3} K dT, \tag{6.20}$$

where n is the number of electrons per 1 cm^3 of substance; $\beta = v/C$, T_p - the kinetic proton energy, for which the range straggling is determined. The multiplier K takes into account the effect of the electron bond in an atom for small proton energies. This multiplier was obtained by Bethe (Ref. 12).

In contrast to Lindhard and Scharff (Ref. 36), Sternheimer studied the more general expression for the maximum energy transfer by a proton to a free electron, which is valid up to very high energies (Ref. 35). In the interesting energy region, both expressions practically coincide. Let us determine the relative range straggling in the following way:

$$\varepsilon = \left(\frac{\sigma}{R}\right) 100. \tag{6.21}$$

The expression for σ^2 can be rewritten

$$\sigma^2 = 1{,}0022C \int_0^{T_p} \frac{\left(1 - \frac{1}{2}\beta^2\right)}{(1-\beta^2)\left[1 + 2\left(\frac{m_e}{m_p}\right)(1-\beta^2)\right]^{-1/2}} \times \times \left(-\frac{dE}{dx}\right)_{\text{ion}}^{-3} K dT, \tag{6.22}$$

where $C = 0.153\ Z/A$, $Mev/g \cdot cm^{-2}$ (values of C for several substances are given in Table 6.5); $\left(-\frac{d\Xi}{dx}\right)_{\text{ion}}$ - mass ionization losses, $Mev/g \cdot cm^{-2}$ and σ, g/cm^2. The values for the multiplier K were calculated by Sternheimer according to the formula given by Bethe (Ref. 12). These values are given in Table 6.10 for beryllium, aluminum, and lead. /160

TABLE 6.10

VALUE OF THE MULTIPLIER K, TAKING INTO ACCOUNT THE EFFECT OF THE ELECTRON BOND IN THE ATOM.

Substance	Proton Energy, Mev						
	1	2	5	10	50	100	200
Be	1,37	1,24	1,12	1,07	1,02	—	—
Al	—	1,33	1,27	1,19	1,06	1,04	—
Pb	—	—	1,31	1,22	1,19	1,16	1,11

TABLE 6.11

RELATIVE RANGE STRAGGLING OF PROTONS $\varepsilon = \sigma/R \cdot 100$

T_p, Mev	Relative Straggling, %					
	Be	C	Air	Al	Cu	Pb
2	1,704	1,867	1,981	1,968	2,293	2,659
4	1,550	1,631	1,679	1,814	2,030	2,331
6	1,469	1,526	1,564	1,720	1,875	2,187
8	1,419	1,466	1,498	1,649	1,779	2,079
10	1,382	1,424	1,452	1,597	1,749	1,994
15	1,322	1,357	1,376	1,507	1,667	1,865
20	1,286	1,315	1,335	1,450	1,609	1,828
25	1,259	1,285	1,304	1,408	1,562	1,783
30	1,238	1,263	1,280	1,377	1,526	1,742
40	1,206	1,230	1,244	1,330	1,468	1,674
50	1,183	1,203	1,218	1,297	1,425	1,619
60	1,165	1,183	1,197	1,271	1,390	1,574
70	1,149	1,166	1,180	1,249	1,363	1,536
80	1,135	1,152	1,165	1,231	1,339	1,505
100	1,112	1,128	1,141	1,201	1,300	1,464
120	1,094	1,109	1,121	1,178	1,271	1,431
140	1,078	1,093	1,104	1,157	1,245	1,401
160	1,065	1,078	1,087	1,140	1,225	1,376
200	1,041	1,054	1,060	1,112	1,190	1,333
250	1,017	1,029	1,036	1,084	1,155	1,289
300	0,997	1,009	1,016	1,060	1,127	1,254
350	0,980	0,991	0,999	1,040	1,104	1,225
400	0,966	0,976	0,984	1,023	1,085	1,200
500	0,942	0,952	0,959	0,996	1,052	1,160
600	0,924	0,932	0,939	0,974	1,028	1,127
800	0,897	0,904	0,909	0,943	0,991	1,081
1000	0,879	0,886	0,889	0,921	0,966	1,049
1500	0,856	0,862	0,860	0,891	0,928	1,002
2000	0,850	0,855	0,850	0,882	0,915	0,981

Table 6.11 presents the results derived from calculations of the relative range straggling, which were carried out by Sternheimer for beryllium, carbon, aluminum, copper, lead, and air (Ref. 35). As can be seen from this Table, the relative range straggling depends slightly on the type of substance. In addition, the relative range straggling for proton energies which are greater than 2 Mev is fairly small, not more than 2 - 3%. In this connection, the effect of the range straggling of protons can be practically disregarded in calculations for shielding. The distribution of the range straggling close to the mean value of R (see Table 6.9) is determined by the relationship /161

$$P(R')\,dR' = \frac{1}{2\sigma\sqrt{\pi/2}} \exp\left[-\frac{1}{2\sigma^2}(R'-R)^2\right] dR, \qquad (6.23)$$

where P(R')dR' is the probability that the actual (measured) range straggling will occur between R' and R' + dR'. Equation (6.23) shows that the small difference between the values

for the mean and the most probable ranges can be disregarded. This difference causes the very slight deviation of the range distribution from a symmetrical Gauss distribution (Ref. 37).

Method for Determining Proton Ranges in Substances With a Known Ionization Potential

Detailed data about proton ranges in a wide energy region exist only for a limited number of materials. In addition, it would be desirable to have the range-energy relationship for such construction materials as aluminum alloys, stainless steel, titanium alloys, plastics, etc.

In order to determine the ionization proton losses in compound substances, it is possible to use the summation rule of Bragg, which is approximate. However, in the general case only small deviations can be expected, which are caused by the effect of chemical bonds upon the mean ionization potential. In the majority of cases, the deviations from this rule do not exceed 2% - i.e., they do not exceed the experimental limits of error (Ref. 5, Ref. 14).

In this connection, Sternheimer's method is of interest, which determines the range - energy relationship for all substances with a known mean ionization potential (Ref. 38). The method is based upon the dependence of ionization losses on the mean ionization potential I. However, the preliminary determination of ionization losses is not required when it is used to determine the range in an arbitrary substance.

Interpolating the range - energy relationship for beryllium, aluminum, copper, and lead, Sternheimer obtained a generalized expression for the range as a function of energy and the mean ionization potential. The approximate accuracy in determining the range by this method was no worse than 1% for mean ionization potential values in the range from 64 ev (Be) to 1070 ev (Pb). /162

In order to obtain the generalized expression for the range $R(T_p)$, formula (6.13) can be written in the form

$$-\left(\frac{dE}{dx}\right)_{\text{ion}} = \frac{Z}{A} M(\beta)\left[\ln\frac{N(\beta)}{I^2} - 2\beta^2 - \delta - u\right], \qquad (6.24)$$

where Z and A are the atomic number and mass number of the substance; $M(\beta)$ and $N(\beta)$ - are functions of only the velocity

$v = \beta c$. If the ionization losses are expressed in units of $Mev/g \cdot cm^{-2}$, we then have

$$M(\beta) = \frac{0.1536}{\beta^2}, \tag{6.25}$$

$$N(\beta) = \frac{2m_e v^2 T_{e\,max}}{1 - \beta^2} \tag{6.26}$$

If it is further assumed that the contribution made by the corrections δ and u depends only on the mean ionization potential I, then the integral in expression (6.19) for the proton range can be written in the form:

$$\int_{2\ Mev}^{T_p} \frac{dE}{\left(\frac{Z}{A}\right) P(\beta, \ln I)}, \tag{6.27}$$

where P is the function of only the proton velocity and the mean ionization potential. The assumption that the correction for the density effect δ depends only on the ionization potential I cannot lead to any significant error for the following reasons: In the first place, this correction becomes significant only in the region of very high energies (more than 2 Bev); in the second place, there are indications (Ref. 18) that with an increase in I - i.e., with an increase in Z - the correction δ decreases monotonically. The correction δ depends also on the electron density, but since the latter depends only on Z, it can be assumed that the correction δ is determined almost entirely by the value of I, which is approximately proportional to Z. In this connection, the anticipated error will not be more than 1% (Ref. 38).

The correction for the shell effect, which is determined by formula (6.15), becomes significant for comparatively small proton energies. In general, for $T_p \geqslant 2$ Mev this correction is not very large (about 1%), and, in addition, it changes monotonically as a function of Z and, correspondingly, of I. The error, which is related to the assumption regarding the magnitude of this correction, will be correspondingly negligible.

Let us introduce the function $\Phi(T_p)$, determining it in the following way: /163

$$\Phi(T_p) = \frac{2Z}{A}[R(T_p) - R(2\ \text{Mev})]. \tag{6.28}$$

If the assumption regarding the corrections δ and u is taken into account, this function depends only on the proton energy T_p

and ln I . It is convenient to further introduce the function $G(T_p)$:

$$G(T_p) = \frac{\Phi(T_p, I)}{\Phi_{Al}(T_p)}, \tag{6.29}$$

where $\Phi(T_p, I)$ pertains to an arbitrary substance with the ionization potential I , and $\Phi_{Al}(T_p)$ pertains to aluminum. The values of the function $\Phi_{Al}(T_p)$, determined with the aid of Table 6.9, are shown in Table 6.12.

TABLE 6.12

VALUES OF THE FUNCTION $\Phi_{Al}(T_p)$

T_p, Mev	Φ_{Al}, g/cm²	T_p, Mev	Φ_{Al}, g/cm²	T_p, Mev	Φ_{Al}, g/cm²	T_p, Mev	Φ_{Al}, g/cm²
3	0,01016	100	9,639	25	0,8108	350	81,56
4	0,02313	110	11,400	27,5	0,9625	375	91,16
5	0,03871	120	13,280	30	1,1253	400	101,09
6	0,05681	130	15,276	35	1,4839	450	121,80
7	0,07734	140	17,381	40	1,8855	500	143,54
8	0,1002	150	19,593	45	2,328	550	166,19
9	0,1254	160	21,91	50	2,811	600	189,65
10	0,1528	180	26,83	55	3,333	700	238,6
12	0,2142	200	32,13	60	3,894	800	289,8
14	0,2841	225	39,24	65	4,491	900	342,8
16	0,3622	250	46,85	70	5,124	1000	397,2
18	0,4484	275	54,92	75	5,793	1250	537,6
20	0,5424	300	63,41	80	6,496	1500	682,2
22,5	0,6708	325	72,30	90	8,003	1750	829,4

If the dependence of the function $\Phi(T_p)$ on I only is taken into account, the function $G(T_p)$ can be written in the form $G(x)$, where

$$x = \lg\left(\frac{I}{I_{Al}}\right) = \lg\left(\frac{I}{166}\right), \tag{6.30}$$

and it is then possible to perform series expansion in powers of x :

$$G(x) = 1 + G_1 x + G_2 x^2 + G_3 x^3 + \ldots, \tag{6.31}$$

where the expansion coefficients G_1, G_2, and G_3 depend only on the proton energy T_p. For x = 0, apparently G = 1(I = I_{Al} = 166 ev). Sternheimer (Ref. 38) found that in expansion of (6.31) it is possible to confine oneself to the sum of the first four terms, /164

with a sufficient degree of accuracy. Thus, the accuracy was estimated by comparing the values for the function G , in the form of the sum of the first four terms of equation (6.31), with the values found from the known range - energy relationships for several substances. This comparison was made for carbon (I = 78 ev, x = 0.3280), air, (I = 94 ev, x = - 0.2470), nuclear emulsions (I = 331 ev, x = 0.2997), and silver (I = 586 ev, x = 0.5478). In all cases, the divergence between these values did not exceed 1% in a wide energy region (from 10 Mev to 1 - 10 Bev).

The values for the coefficients G_1, G_2, and G_3 were determined by comparing the values for the function $\Phi(T_p)$ for beryllium, copper, and lead - which were calculated by the method described - with the results derived from the calculation of $\Phi(T_p)$ for these elements, with the aid of Table 6.9. The values for these coefficients which were thus obtained are shown in Table 6.13. It should be noted that the values for the coefficients G_1, G_2, and G_3 change rather monotonically as a function of the proton energy T_p.

TABLE 6.13

VALUES OF THE COEFFICIENTS G_1, G_2, AND G_3

T_p, Mev	$G_1(T_p)$	$G_2(T_p)$	$G_3(T_p)$	T_p, Mev	$G_1(T_p)$	$G_2(T_p)$	$G_3(T_p)$
3	0,634	0,450	0,495	100	0,356	0,127	0,068
4	0,595	0,379	0,468	110	0,350	0,123	0,066
5	0,570	0,336	0,436	120	0,345	0,120	0,065
6	0,551	0,307	0,404	130	0,341	0,117	0,064
7	0,537	0,285	0,378	140	0,338	0,114	0,063
8	0,525	0,269	0,353	150	0,334	0,112	0,061
9	0,515	0,257	0,330	160	0,331	0,110	0,060
10	0,507	0,247	0,309	180	0,326	0,106	0,058
12	0,493	0,229	0,278	200	0,321	0,102	0,057
14	0,481	0,218	0,250	225	0,316	0,098	0,057
16	0,472	0,211	0,225	250	0,311	0,095	0,057
18	0,464	0,204	0,205	275	0,307	0,092	0,057
20	0,457	0,198	0,189	300	0,303	0,090	0,057
22,5	0,449	0,193	0,172	325	0,300	0,088	0,056
25	0,442	0,188	0,158	350	0,297	0,086	0,055
27,5	0,436	0,183	0,146	375	0,295	0,085	0,055
30	0,430	0,180	0,136	400	0,293	0,083	0,054
35	0,420	0,173	0,120	450	0,288	0,081	0,053
40	0,412	0,166	0,109	500	0,285	0,080	0,051
45	0,404	0,161	0,100	550	0,282	0,079	0,049
50	0,397	0,157	0,093	600	0,279	0,078	0,047
55	0,391	0,152	0,088	700	0,273	0,077	0,045
60	0,385	0,148	0,084	800	0,268	0,075	0,044
65	0,380	0,144	0,081	900	0,264	0,074	0,042
70	0,376	0,141	0,078	1000	0,259	0,073	0,041
75	0,372	0,138	0,076	1250	0,251	0,071	0,040
80	0,368	0,136	0,074	1500	0,243	0,068	0,039
90	0,361	0,131	0,071	1750	0,236	0,066	0,038

Utilizing expressions (6.28), (6.29) and (6.31), we obtain the following equation for the range of a proton $R(T_p, I)$ with the energy T_p in a substance with the ionization potential I: /165

$$R(T_p, I) = R(2\ \text{Mev}, I) + \left(\frac{A}{2Z}\right)\Phi_{Al}(T_p)(1 + G_1x + G_2x^2 + G_3x^3). \tag{6.32}$$

The quantity R(2 Mev), as was indicated above, must be obtained from the experimental data. This quantity changes from approximately 0.01 g/cm^2 for light elements (Be, C, Al) up to 0.04 g/cm^2 for heavy elements (Pb). The experimental values of R(2 Mev) can be found in another work (Ref. 31).

Expression (6.32) was confirmed by comparing the calculated values of $R(T_pI)$ with the tabular values for air (Table 6.9), and with the results derived from the calculations of Barkas for nuclear emulsions (Ref. 34). For air, the divergence between these values does not exceed 1% in the proton energy region from 10 Mev to 1 Bev. For proton energies greater than 1 Bev, the density effect begins to come into play for such materials as Be, Al, Cu, Pb. Therefore, formula (6.32), which was derived for the density of substances, is unsuitable for gases in this energy region. For emulsions, the proton energy region, in which the divergence does not exceed 1%, ranges from 10 Mev to 10 Bev.

Since tabular values of the ranges (Table 6.9) for Be, Cu and Pb were used in determining the expansion coefficients G_1, G_2, and G_3, it is of interest to estimate the determinational accuracy of proton ranges for elements between Cu and Pb, where the greatest divergences can be expected. Such calculations were made for values of the ionization potential I = 659 ev($x = 0.5988$) (Ref. 38). This value of I lies approximately in the middle of the interval from $x_{Cu} = 0.3493$ to $x_{Pb} = 0.8093$. It was found that in this case the divergence does not exceed 0.9%, for all values of the proton energies.

Thus, utilizing expression (6.32) and the tabular values of Φ_{Al}, G_1, G_2 and G_3(see Table 6.12 and 6.13), we can determine the range for a proton having a given energy in any substance, for which the mean ionization potential of an atom is known. Thus, the determinational accuracy of the range depends only on the accuracy of the values of R(2 Mev), and also the values of the ionization potential I .

Let us now present an example for calculating a range by this method. We shall determine the range of a proton having the energy

50 Mev in silver, utilizing the value I = 586 ev (Ref. 38). The corresponding value is $x_{Ag} = 0.5478$. In order to determine R(2 Mev), we shall utilize the results derived from measurements (Ref. 31), which give R(2 Mev) = 0.0263 g/cm^2. According to Table 6.13, for T_p = 50 Mev we find $G_1 = 0.397$, $G_2 = 0.157$, $G_3 = 0.093$, and according to formula (6.31), we obtain G = 1.2799. According to Table 6.12, we find Φ_{Al}(50 Mev) = 2.811 g/cm^2. For silver, 2Z/A = 0.8713. Thus, the second term in formula (6.32) equals 4.129 g/cm^2, and the final result is R(50 Mev) = 0.0263 + 4.129 = 4.155 g/cm^2. By a similar method, we find G = 1.2443 and R(100 Mev) = 13.79 g/cm^2, for T_p = 100 Mev. /166

Ionization Potentials of Atoms

The ionization potential of an atom cannot be calculated sufficiently accurately on the basis of the existing atom theory. In this connection, experimental methods for determining ionization potentials of an atom are of great importance. One of these methods consists of measuring the ionization losses in a thin layer of a known substance. Another possible method consists of the simultaneous measurement of the range and energy of particles. The first method makes it possible to clarify the dependence of the ionization potential on the particle energy, which has already been reported upon (Ref. 22, Ref. 39). A disadvantage of the second method is the averaging of the ionization potential I over a wide energy interval.

The experimental determination of an accurate value for the ionization potential is complicated by the exponential nature of the dependence of I on the magnitude of the ionization losses being measured. Due to this fact, the relative error in this determination is 3 - 10 times larger than the error entailed in the measurements - $(dE/dx)_{ion}$ or the range R. This can be readily shown by determining the derivative of dR/dI and utilizing expression (6.32):

$$\frac{dR}{dI} = \left(\frac{A}{2Z}\right)\Phi_{Al}(T_p)\frac{1}{2{,}303I}\frac{dG}{dx} =$$

$$= \left(\frac{A}{2Z}\right)\Phi_{Al}(T_p)\frac{(G_1 + 2G_2x + 3G_3x^2)}{2{,}303I} \qquad (6.33)$$

When this relationship was derived, the fact was taken into account that $\frac{dx}{dI} = \frac{1}{2.303I}$, and also the term $\frac{dR(2\ Mev)}{dI}$ - which is small in terms of magnitude - was discarded, which is admissible for $T_p \geqslant 10$ Mev. Let us introduce the quantity

$$q = \frac{I}{R}\frac{dR}{dI} = \frac{\frac{dR}{R}}{\frac{dI}{I}} ,$$

which connects the relative values of dR/R and dI/I. The values of q, which were calculated by Sternheimer (Ref. 38), are given in Table 6.14. The magnitude of q decreases with an increase in energy, and increases with an increase in Z. Thus, when the range of a proton having an energy of, for example, 100 Mev is measured, the error - which equals 1% - leads to an error in the determination of the ionization potential of an atom I, which amounts to $\frac{1}{q}$ 100% = 6.8% for graphite, and $\frac{1}{q}$ 100% = 4.7% for lead.

TABLE 6.14 /167

THE VALUES OF $q = \frac{dR}{R} / \frac{dI}{I}$ FOR DIFFERENT SUBSTANCES (REF. 40)

T_p, Mev	Values of q For				
	Be	C	Al	Cu	Pb
10	0,232	0,214	0,217	0,258	0,337
20	0,200	0,192	0,205	0,236	0,300
50	0,159	0,159	0,181	0,201	0,244
100	0,143	0,143	0,163	0,178	0,214
200	0,131	0,131	0,147	0,159	0,191
500	0,119	0,118	0,131	0,140	0,171
1000	0,106	0,106	0,119	0,128	0,155

On the other hand, it is apparent that the certain amount of indeterminancy in the values for the ionization potential I is not significant in determining a proton range, since $\frac{dR}{R} = q\frac{dI}{I}$, and q is always less than unity. This fact is of great importance in utilizing the method of Sternheimer, since the ionization potentials are only slightly reliable for many substances for which the range - energy relationship is desired.

The dependence of the ionization potential on the energy of an incident proton is of great importance. The existing theory for ionization losses provides a negative answer to this problem. However, experimental data, especially the results derived from the systematic studies of Vasilevskiy and Prokoshkin (Ref. 22) in a wide energy region of incident particles, clearly point to the

TABLE 6.15

IONIZATION ATOM POTENTIALS (ev) FOR DIFFERENT CHARGED PARTICLE ENERGIES (REF. 22)

Particle	Energy*, Mev	H**	C	Al	Cu	Sn***	Pb***	References
p	6—18	—	—	166±1	376±20	622±43	1076±104	[31, 41]
p	18	—	—	163±3	377±8	708±59	1179±104	[39]
p	19,8	—	—	166±1	366±5	621±7	1070±24	[42]
α	691 (173,9)	18±6	86±6	157±13	325±8		778±43	[22]
d	376,8 (188,5)	17,0±2,4	81,2±3,1	158±5	323±8	473±20	795±23	[22]
p	267	—	88±7	—	316±8	—	918±131	[22]
p	300	18±7	87±8	170±13	314±8	514±38	789±49	[40]
p	615	11,7±2,1	89±4	145±7	302±11		786±30	[22]
p	635	14±7	84±9	—	301±12	488±38	—	[43]
p	651	—	79±5	136±8	300±12	463±23	753±37	[22]

* The equivalent proton energy is shown in parentheses.

** Determined according to the difference "CH_2 - C".

*** The first three values were obtained from data for adjacent elements (for Sn with respect to Cd, for Pb with respect to Au), under the assumption that I = KZ and that the coefficient K is the same for adjacent elements.

TABLE 6.16

VALUES OF IONIZATION POTENTIALS FOR DETERMINING RANGES ACCORDING TO STERNHEIMER'S METHOD IN SIMPLE SUBSTANCES.

Substance	Z	I, ev	References	Substance	Z	I, ev	References
Hydrogen	1	15.6	(40)	Potassium	19	228	(44)
Helium	2	44	(28)	Manganese	25	315	(42)
Lithium	3	39	(44)	Iron	26	329	(42)
Beryllium	4	64	(31, 42)	Nickel	28	363	(21)
Boron	5	58	(45)	Copper	29	371	(26)
Carbon	6	78	(26)	Silver	47	587	(31, 42)
Nitrogen	7	80	(45)	Tin	50	708	(21)
Oxygen	8	92	(45)	Tantalum	73	962	(21)
Sodium	11	143	(44)	Tungsten	74	920	(43)
Magnesium	12	156	(44)	Gold	79	997	(42)
Aluminum	13	166	(31, 41, 42)	Lead	82	1070	(42)
Silicon	14	175	(44)	Uranium	92	917	(46)

existence of such a dependence. Table 6.15 presents the ionization potentials of certain substances for different energies of the charged particles.

The results which are given in this Table show the nature of the dependence of the ionization potential on the particle energy, and for heavy substances this dependence is quite significant. For light substances, the dependence of I on energy is not too great, in general, which makes it possible to calculate it with a certain degree of accuracy. Thus, throughout the entire energy region it is possible to utilize the value I = 166 ev for aluminum. Thus, the error entailed in determining the range of a proton having an energy of, for example, 651 Mev does not exceed 2.5%. For heavy substances, this error can amount to 5%.

The considerations presented above, with respect to the requirements for accuracy in the values of the ionization potential of an atom and its dependence on proton energy, were utilized in compiling /169
Table 6.16. The values of I which are given in this Table make it possible to determine the proton ranges, utilizing Sternheimer's method, with an accuracy which fully satisfies the effective calculations for shielding from protons.

In many cases, it may be necessary to determine the proton ranges according to Sternheimer's method for chemical compounds, mixtures, alloys, etc. For certain substances of this type, there are calculated or measured effective values of the ionization potentials (Table 6.17).

TABLE 6.17

VALUES OF IONIZATION POTENTIALS FOR DETERMINING RANGES ACCORDING TO STERNHEIMER'S METHOD IN COMPOUND SUBSTANCES (REF. 44)

Substance	I, ev	Substance	I, ev
LiH	39	C_6H_6	63.8
$C_6H_5CH_3$	62.3	CH_3OH	64.8
C_7H_{16}	52	C_5H_9Cl	86.2
H_2O	74	Air (Ref.26)	94

The following method may be used to determine the effective values of ionization potentials in compound substances. Let us posit a compound substance (chemical compound, alloy, mixture, etc.),

which consists of the elements Z_1, Z_2, Z_3 ... with the relative content n_1, n_2, n_3 ...(according to weight); in accordance with formula (6.17), we then have /170

$$-\left(\frac{dE}{dx}\right)^{i}_{\text{ion}} = \frac{C_i}{\beta^2}[B_i + C(\beta)], \tag{6.34}$$

where

$$C_i = 0{,}1536\frac{Z_i}{A_i}, \quad B_i = \ln\left(\frac{m_e^2}{I_i^2}\right)$$

and

$$C(\beta) = 0{,}69 + 2\ln\frac{p}{m_p c} + \ln T_{e\,\max} - 2\beta^2.$$

The proton energy was chosen so that $U = \delta = 0$; this can be satisfied with sufficient accuracy in the region 100 - 500 Mev. The effective value of ionization losses for a compound substance (Mev/g·cm^{-2}) is

$$-\left(\frac{dE}{dx}\right)^{\text{eff}}_{\text{ion}} = -\sum n_i\left(\frac{dE}{dx}\right)^{i}_{\text{ion}} = \sum_{i=1}^{n}\frac{n_i C_i}{\beta^2}[B_i + C(\beta)]. \tag{6.35}$$

On the other hand, we have

$$-\left(\frac{dE}{dx}\right)^{\text{eff}}_{\text{ion}} = \frac{C_{\text{eff}}}{\beta^2}[B_{\text{eff}} + C(\beta)], \tag{6.36}$$

and for determining C_{eff} it is possible to use the relationship

$$C_{\text{eff}} = 0{,}1536\sum_{i=1}^{n}\frac{n_i Z_i}{A_i}. \tag{6.37}$$

In addition, on the basis of expressions (6.35), (6.36) and (6.37) let us determine the value of $B_{\text{eff}} = \ln\left(\frac{m_e^2}{I_{\text{eff}}^2}\right)$, and correspondingly the value of I_{eff} for which we are seeking, for a compound substance.

Coulomb Scattering of Protons

When a proton penetrates matter, it undergoes Coulomb scattering,

which can be regarded as elastic electromagnetic interaction, since the particle energy does not change to a significant extent. In general, a proton also undergoes scattering both in the field of the nucleus, and in the field of the atom electrons. However, the probabilities for these two processes are significantly different.

Let us determine the differential probability for Coulomb proton scattering $\Phi(\theta)$ in the field of the nucleus. The quantity $\Phi(\theta)$ dwdx represents the probability that a proton, penetrating a layer of matter dx g/cm^2, undergoes Coulomb scattering at an angle θ within a solid angle dw (Ref. 7). If the finite dimensions of the nucleus and the screening of its field by electrons are disregarded, and also if the Born approximation is used, then the following expression could be obtained for the probability of scattering in the nucleus field: /170

$$\Phi(\theta)\,dw = \frac{N_0}{4}\cdot\frac{Z^2}{A}\,r_e^2\left(\frac{m_e c}{\beta p}\right)^2\left(1-\beta^2\sin^2\frac{\theta}{2}\right)\frac{d\omega}{\sin^4\frac{\theta}{2}}, \tag{6.38}$$

where $r_e = \dfrac{e^2}{m_e c^2}$ is the classical electron radius, and N_0 is the Avogadro number. If the examination is restricted to scattering only at small angles, for which the term $\beta^2\sin^2\frac{\theta}{2}$ can be disregarded as compared with unity, and $\sin\frac{\theta}{2}$ can be replaced by $\frac{\theta}{2}$, then expression (6.38) assumes the form

$$\Phi(\theta)\,dw = 4N_0\frac{Z^2}{A}\,r_e^2\left(\frac{m_e c}{\beta p}\right)^2\frac{d\omega}{\theta^4}. \tag{6.39}$$

Expression (6.39) is known under the name of the Rutherford scattering law.

The probability for Coulomb scattering of a proton $\Phi'\theta d\omega$ in the field of electrons has the following form:

$$\Phi'(\theta)\,dw = 4N_0\frac{Z}{A}\,r_e^2\left(\frac{m_e c}{\beta p}\right)^2\frac{d\omega}{\theta^4}, \tag{6.40}$$

i.e., it is Z times smaller than the probability for scattering in the nucleus field. For this reason, the contribution which is made by collisions with electrons is comparatively small. The investigation from this point on will be restricted to only scattering in the nucleus field. Expressions (6.38) and (6.39) were obtained under the assumption that the finite dimensions of the nucleus and the screening of its field by electrons can be disregarded. These assumptions impose definite restrictions in the angle interval θ, in which they are valid. For small angles, there is significant screening of the

nucleus field by electrons, which leads to a reduction in the quantity $\Phi(\theta)d\omega$. With an increase in the angle θ, the role of the screening effect gradually decreases. It is possible to determine a value for the angle θ_1, so that - when the condition $\theta >> \theta_1$ is fulfilled - the screening effect is insignificant, and the probability for scattering corresponds to the expression (6.38) or (6.39). The value for the angle θ_1 can be determined from the relationship

$$\theta_1 = \frac{Z^{1/3}}{137} \cdot \frac{m_e c}{p}. \qquad (6.41)$$

In the small angle interval, expression (6.39) must be replaced by the expression which takes into account the effect of screening on the scattering probability. Such an expression, which is valid for small scattering angles θ, has been obtained (Ref. 47): /172

$$\Phi(0)\,d\omega = 4N_0 \frac{Z^2}{A} r_e^2 \left(\frac{m_e c}{\beta p}\right)^2 \frac{d\omega}{(\theta^2 + \theta_1^2)^2}. \qquad (6.42)$$

For $\theta >> \theta_1$, expressions (6.39) and (6.42) almost coincide. However, for $\theta \approx \theta_1$, there is a significant divergence, and for $\theta \approx 0$ expression (6.39) loses any meaning.

For relatively large scattering angles, the finiteness of the nucleus dimensions is significant. Williams (Ref. 48) made a theoretical estimate of the effect of finite nucleus dimensions, under the assumption that the electric charge of the nucleus is distributed along a sphere having a definite radius. The interval of scattering angles θ, in which expression (6.39) is valid, is restricted in the region of large angles with the value θ_2, and we have

$$\theta_2 \cdot 200 A^{-1/3} \frac{m_e c}{p}. \qquad (6.43)$$

With an increase in the proton impulse p and with an increase in the mass number A, angle θ_2 decreases, and correspondingly the region, where expression (6.39) is valid, is reduced. For light elements and comparatively low proton energies, such that $p < 280A^{-1}/_3\, m_e c$, the finite nucleus dimensions do not have a significant influence on the probability for proton Coulomb scattering in the field of the nucleus, and formula (6.39) remains valid up to very large angles ($\theta \approx \pi$).

It is of interest to determine the mean square of the proton scattering angle after penetrating a certain thickness of the shielding x. For a thin shielding (Ref. 7), in which the proton energy losses can be disregarded, the mean square of the deflection angle $\langle\theta^2\rangle$ is determined by the relationship

$$\langle\theta^2\rangle = \theta_s^2 x, \qquad (6.44)$$

where

$$\theta_s^2 = \int \theta^2 \Phi(0)\, d\omega = \int \theta^2 \Phi(0)\, 2\pi\theta\, d\theta \qquad (6.45)$$

(for small angles of deviation, it can be assumed that $d\omega = 2\pi\theta d\theta$). If we utilize the expression for $\Phi(\theta)$ in the form of (6.39) for $\theta_1 < \theta < \theta_2$, and if we assume that $\Phi(\theta < \theta_1) = \Phi(\theta > \theta_2) = 0$ - and also if we use relationships (6.41) and (6.43) for the angles θ_1 and θ_2 - then we obtain (Ref. 7):

$$\theta_s^2 = \left(\frac{E_s}{\beta_{mean}}\right)^2 \frac{1}{x_0}, \qquad (6.46)$$

where x_0 is the radiation unit of length, E_s = 21 Mev. The values /173
of x_0 for several substances (Ref. 49) are given in Table 6.18. Thus, the mean square of the angle of deviation for a thin shielding is

$$\langle\theta^2\rangle = \left(\frac{E_s}{\beta_{mean}}\right)^2 \frac{x}{x_0}. \qquad (6.47)$$

It should be noted that this relationship is sufficiently accurate, since it is based on an approximate consideration of the finite nucleus dimensions and the screening of its field by electrons.

TABLE 6.18

RADIATION UNIT OF LENGTH x_0 FOR DIFFERENT SUBSTANCES

Substance	Z	A	x_0 g/cm^2	Substance	Z	A	x_0 g/cm^2
C	6	12.00	40.0	Pb	82.00	207.20	5.24
Al	13	27.00	22.7	Air	7.37	14.78	34.20
Fe	26	55.84	12.5				
Cu	29	63.57	11.5	Water	7.23	14.30	33.90

In addition, let us examine the manner in which multiple Coulomb scattering influences the distribution of a proton bundle beyond the shielding. In order to do this, it is possible to utilize the results derived in work (Ref. 50). Let a uniform bundle of protons, having the cross-section radius ρ_0, fall in a normal direction on a planar shielding unit having the thickness x. It is necessary to determine the distribution of the bundle in the plane which is parallel

to the shielding and which is located at a distance l from it (Figure 6.2, a). As a result of multiple scattering, a proton - which penetrates the shielding at the distance ρ from the axis of the bundle A - can be deflected from the initial direction B and can intersect this plane at the point C (Figure 6.2, b).

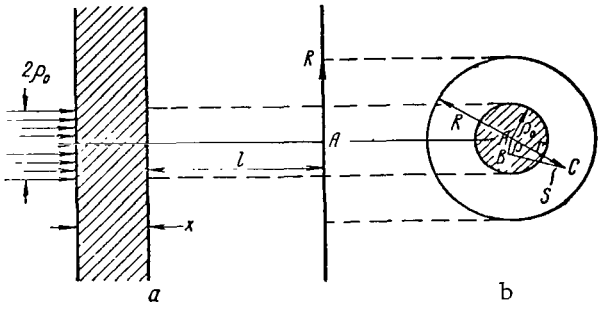

Figure 6.2

Calculation of Multiple Proton Scattering in a Shielding:

a - form along the bundle; b form of the bundle cross-section.

The probability for this, as pertains to a unit of surface, is determined by the relationship (Ref. 50): /174

$$P = \frac{1}{\pi r_0^2} e^{-s^2/r_0^2}, \tag{6.48}$$

where

$$r_0^2 = Q_s^2 \left[x\left(l^2 + lx + x^2/3\right)\right]. \tag{6.49}$$

For a thin shielding ($x \ll l$), the expression for r_0 can be reduced to the form

$$r_0^2 = Q_s^2 x l^2.$$

Utilizing the polar coordinates (r, θ), with the beginning at the center of the bundle A and assuming that $\theta = 0$ for the point B, we can write:

$$S^2 = r^2 + \rho^2 - 2r\rho\cos\theta. \tag{6.50}$$

The probability that a particle, after the shielding, enters a circle having the radius R with the center at the point A, which is located in the plane under consideration, will be

$$f = \int_0^{2\pi}\int_0^R P r\, d\theta\, dr = \frac{1}{\pi r_0^2}\int_0^{2\pi}\int_0^R r\, d\theta\, dr\, e^{-\frac{r^2+\rho^2-2r\rho\cos\theta}{r_0^2}} \tag{6.51}$$

Let us now turn to the relative quantities

$$r' = r/R,\ \varrho' = \varrho/R \text{ and } r_0' = r_0/R$$

$$f = \frac{1}{\pi (r_0')^2} \int_0^{2\pi} \int_0^1 e^{-\frac{(r')^2+(\varrho')^2-2r'\varrho'\cos\theta}{(r_0')^2}} r'\, d\theta\, dr'. \tag{6.52}$$

Thus, the function f depends only on two variables r_0' and ρ'. Carrying out integration with respect to θ,

$$\int_0^{2\pi} e^{\frac{2r'\varrho'\cos\theta}{(r_0')^2}} d\theta = 2\pi J_0\left(\frac{2r'\varrho'}{[r_0']^2}\right),$$

where J_0 is the Bessel function with an imaginary argument, we obtain

$$f = \frac{2}{(r_0')^2} e^{-\frac{(\varrho')^2}{(r_0')^2}} \int_0^1 J_0\left(\frac{2r'\varrho'}{[r_0']^2}\right) e^{-\frac{(r')^2}{(r_0')^2}} r'\, dr'. \tag{6.53}$$

Equation (6.53) has been integrated numerically (Ref. 50) for values $0 < r_0' < 0.75$ and $0 \leqslant \rho' \leqslant 1$, and the results derived from the calculations are shown in Figure 6.3, a. In order to determine the portion F of a stream of protons, which intersect a circle having the radius ρ_0 in the plane under consideration, it is necessary to integrate f with respect to the bundle cross-section. If the bundle has a uniform distribution with respect to a circle having the radius ρ_0 (Figure 6.2, b), we then have /176

$$F = \frac{2}{(\varrho_0')^2} \int_0^{\varrho_0'} f(r_0', \varrho')\, \varrho'\, d\varrho', \tag{6.54}$$

where $\rho_0' = \rho_0/R$.

The values of F have been obtained by numerical integration (Ref. 50) utilizing the diagrams of f (Figure 6.3, a). The results derived from calculating F are shown in Figure 6.3, b.

If the particle distribution in the bundle cross-section is not uniform, we then have

$$F = \frac{\int_0^{\varrho_0'} n(\varrho')\, f\varrho'\, d\varrho'}{\int_0^{\varrho_0'} n(\varrho')\, \varrho'\, d\varrho'},$$

where the function $n(\rho')$ determines the nature of the particle

distribution in the cross-section for a bundle impacting on the shielding.

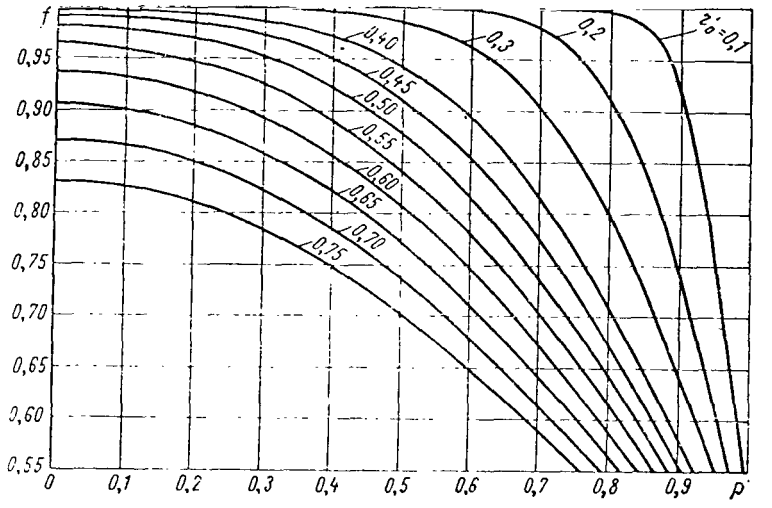

a

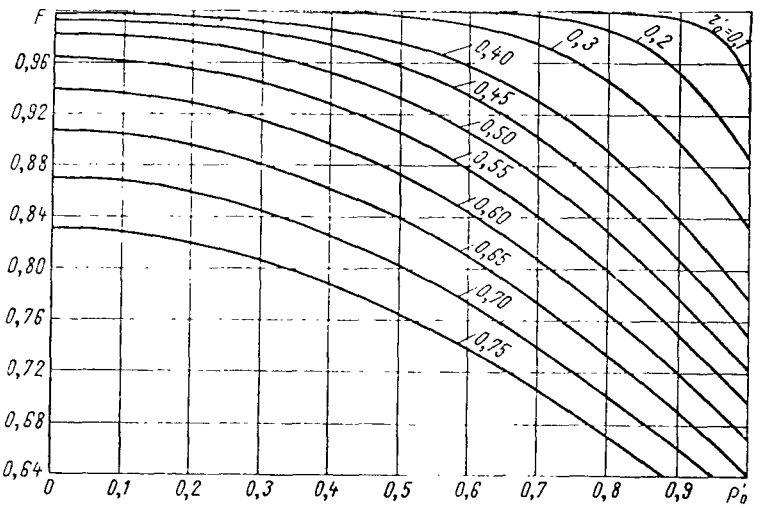

b

Figure 6.3

Probability for Multiple Scattering of "Narrow" (a) and "Wide" (b) Proton Bundles in a Shielding

/175

If the particle distribution in the bundle cross-section is such that a significant portion of it is concentrated close to the axis, then the distribution can be replaced by several uniform distributions with different values of ρ_0', i.e.,

/176

$$F(\rho_0') = \alpha_1 F(r_0', \rho_{0,1}) + \alpha_2 F(r_0', \rho_{0,2}) + \ldots,$$

where $\rho_{0,1}', \rho_{0,2}'$ ... and α_1, α_2 ... characterize different uniform distributions ($\Sigma\alpha_i = 1$). The values of $F(r_0', \rho_0', i)$ can be determined with the aid of Figure 6.3, b.

The results presented above can be utilized not only for the case when the radius of the bundle cross-section is $\rho_0 < R$, but also when the bundle cross-section exceeds the dimensions of the region R under consideration. On the basis of expressions (6.51) and (6.54), we can obtain

$$F = \frac{2}{\pi r_0'^2 a} \int_0^{\rho_0} \rho\, d\rho \int_0^{2\pi} d\theta \int_0^{R} r\, dr\, e^{-\frac{r^2+\rho^2-2r\rho\cos\theta}{r_0'^2}} \tag{6.55}$$

Since the final result does not depend on the order of integration, expression (6.55) can be applied to both cases ($\rho_0 < R$ and $\rho_0 > R$), if the smallest of the values for ρ_0 and R is chosen as the coefficient of α. Figure 6.3,b, can be utilized in a similar way, if the smallest of the ratios r_0/ρ_0 and r_0/R is chosen as r_0', and the smallest of the ratios ρ_0/R and R/ρ_0 is chosen as ρ_0'.

Thus, utilizing the given information with respect to the function $F(r_0, \rho_0, R)$, we can obtain a picture for the proton bundle distribution beyond the shielding, which is determined by multiple Coulomb scattering of protons in the shielding, for arbitrary values of the bundle radius, shielding thickness, proton energy, etc. /177

6.4 Nuclear Interaction of Protons with Matter

Classification of Nuclear Interaction

Collisions between incident protons and the nuclei of a substance can lead to entirely different results. The relative magnitude of the energy which is transmitted by the incident particle to the target nuclei can serve as the basis of classifying nuclear interactions. A distinction can be assumed between elastic processes, during which the incident particle loses a small portion of its energy (elastic scattering), and inelastic processes during which the particle loses a significant amount of energy (inelastic interaction).

Elastic scattering can be caused by Coulomb forces which act between the nucleus and the incident proton, by specific nuclear forces, or by optical properties of the nuclei. Coulomb proton

interaction was discussed in the preceding Section. Elastic nuclear scattering can be resonance, potential, and diffraction scattering. Resonance scattering of a proton takes place with the participation of nuclear forces, and is connected with the formation of a compound nucleus. With an increase in the proton energy, the role played by this process decreases, and for sufficiently large energies its contribution can be disregarded. Potential and diffraction scattering are caused by the optical properties of the nuclei; the relationship of these processes depends on the degree of "transparency" of the nucleus with respect to the incident particle. These two types of interaction do not differ experimentally (Ref. 51).

Inelastic proton collisions are related to intra-nuclear interactions of protons with the nucleus nucleons. In their turn, these interactions can be both elastic, and inelastic. In the first case, nucleons having a large energy can escape from the nucleus, including the incident proton, as well as α-particles and fragments. In the second case, proton collisions with the nucleus nucleons are inelastic - i.e., part of the proton energy is consumed in the formation of π-mesons and other particles; in this connection, this process has a definite energy threshold.

In the general case, a residual nucleus appears in a strongly-excited state, because part of the primary proton energy is consumed in the formation of particles, which cannot pass beyond it for various reasons and thereby increase the energy of the intra-nuclear motion. Thus, inelastic collisions of protons having large energies lead, in the general case, to the escape of one or more particles and to the excitation of the residual nucleus. /178 If the escaping particle is a proton, then the composition of the nucleus does not change, and such a process (p, p') is called inelastic scattering. In all other cases, when a particle escapes which is not an incident proton, or when particles escape in a large amount, this interaction is called a nuclear reaction. Interactions of the type (p, n), (p, d), (p, α) and others can serve as examples of "simple" nuclear reactions. Such reactions are also called single-particle reactions. A reaction of the type (p, n) is similar to an exchange process, and is called a proton charge exchange.

Nuclear reactions, which take place with the emission of a relatively large number of particles and nucleon bunching of the type H^2, H^3, He^3, He^4, are called spallation reactions (Ref. 51). Spallation reactions include the "simpler" nuclear reactions, which take place with the escape of a small number of particles - for example, reactions of the type (p, pn), (p, 2n), (p, p2n) etc.. If comparatively heavy nuclear fragments ($Z \geqslant 3$) are formed as a

result of a nuclear reaction, this reaction is called fragmentation. For nuclei at the end of the periodic element system, the fission process - under the influence of high-energy protons - plays a significant role.

Total Cross-Section of Nuclear Interaction

The total cross-section for processes of elastic and inelastic nuclear interaction of protons is called total cross-section of nuclear interaction, or simply total cross-section. If we designate the cross-section of elastic interaction by σ_s, and the cross-section of inelastic interaction by σ_a, for the total cross-section we can thus write

$$\sigma_t = \sigma_s + \sigma_a.$$

The experimental determination of the total cross-sections of a nuclear proton interaction is difficult due to the presence of multiple Coulomb scattering. Therefore, in contrast to neutrons, the attenuation of a proton bundle under conditions of so-called "good geometry" cannot be measured satisfactorily, especially for heavy elements. For this reason, either data which are obtained for neutrons are used, or measurements are made of the integral - angular distributions, and then the corresponding corrections are introduced (Ref. 52). The results derived from measuring the total cross-sections of a nuclear interaction are given in several works (Ref. 53-55).

It should be noted that the total cross-sections are not utilized in calculations for shielding from protons, because these quantities characterize the dislodgement of protons from the bundle for an ideal geometry, i.e., they pertain to an idealized case. The cross-section of inelastic interaction, which characterizes the dislodgement of protons from an incident bundle due to absorption by nuclei, and also the differential cross-section of elastic scattering, which characterizes the "diffusion" of a proton bundle due to scattering, are of practical use in shielding calculations.

Elastic Nuclear Interaction of Protons /179

An optical nucleus model, which was proposed by Fernbach and others (Ref. 56), has been used successfully to describe elastic nuclear scattering. The ideas for an optical nucleus model are based on the "transparency" of the nuclei with respect to high-energy particles. This model has been extensively used for analyzing the interaction processes of different particles and, in particular, of protons with the nuclei of the substance. The

optical nucleus model makes it possible to clarify many features of the interactions between high-energy protons and nuclei. However, it is difficult to obtain a universal system of parameters for this model, and the parameters themselves are not sufficiently accurate.

In an optical model for a transparent nucleus, the latter is regarded as a sphere having the radius R with the complex refractive index of the wave corresponding to the incident particle in the nuclear substance:

$$n = \frac{K_0 + K_1 + \frac{1}{2}iK}{K_0},$$

where K_0 is the wave number of the incident particle outside the nucleus ($K_0 = 1/\hbar\sqrt{2m_pT_p}$), K_1 is the change in the wave number for the particle when the nucleus is penetrated ($K_1 = K_0\sqrt{1 + V/T_p} - 1$, and V is the potential energy of the particle in the nucleus). The imaginary portion of this expression corresponds to the absorption of the incident wave, and the real portion corresponds to refraction. The absorption of the incident wave in the given case represents the optical analogy of the inelastic interaction of a proton and a nucleus; the refraction represents an analogy with elastic nuclear scattering.

In order to calculate the cross-section of elastic scattering on the basis of the optical nucleus model, it is necessary to know the spatial distribution of nucleons in the nucleus. If it is assumed, as was done in earlier works, that the nucleons have a uniform distribution in the nucleus, then we obtain the following for the cross-section of elastic scattering (Ref. 51):

$$\sigma_s = \pi R^2 \left\{ \left[1 + \frac{1 - e^{-KR}(1 + 2KR)}{2K^2R^2} \right] - \right.$$

$$- 4e^{-KR} \sin 2K_1R \left[\frac{2K_1R}{K^2R^2 + 4K_1^2R^2} + \frac{4K_1KR^3}{(K^2R^2 + 4K_1^2R^2)^2} \right] +$$

$$+ 4e^{-KR} \cos 2K_1R \left[\frac{2K_1R}{K^2R^2 + 4K_1^2R^2} + \frac{K^2R^2 - 4K_1^2R^2}{(K^2R^2 + 4K_1^2R^2)^2} \right] -$$

$$\left. - 4e^{-KR} \frac{K^2R^2 - 4K_1^2R^2}{(K^2R^2 + 4K_1^2R^2)^2} \right\}. \qquad (6.56)$$ /180

The coefficient of absorption K is determined by the nucleus parameters A and R, and by the mean nucleon-nucleon cross-section within the nucleus $\bar{\sigma}$:

$$K = \frac{3}{4} \frac{A}{\pi} \cdot \frac{\bar{\sigma}}{R^3},$$

where

$$\bar{\sigma} = Z/A\sigma_{pp} + (1 - Z/A)\sigma_{pn}$$

In the limiting case, $KR \to \infty$ (perfectly absorbing nucleus), the cross-section of elastic scattering σ_s equals the geometric cross-section of the nucleus, while $\sigma = \sigma_a = \pi R^2$. For a real nucleus, $\sigma_a < \pi R^2$; however, σ_s can reach a maximum value which equals $3.2\pi R^2$.

Investigating elastic nuclear scattering on the basis of an optical nucleus model, we can distinguish two extreme cases. The first of them corresponds to refraction of the incident wave in the nucleus without absorption, and is called potential elastic scattering. The cross-section of the potential scattering can be obtained from expression (6.56), setting $K = 0$. The second case corresponds to the penetration of an incident wave through the absorbing nucleus without refraction, and is called diffraction scattering. The diffraction effect is caused by the fact that the wave, penetrating the absorbing nucleus, differs in terms of amplitude from the undisturbed plane wave. The "shadow" region beyond the opaque screen-nucleus is diffused, due to diffraction. The angular distribution of protons which are scattered elastically assumes a form which is characteristic for optical diffraction.

In the general case, an analytical expression is not obtained for a differential cross-section of elastic scattering. For an opaque nucleus, the differential cross-section can be approximated by the Fresnel formula

$$\frac{d\sigma_s(\theta)}{d\Omega} = \left(\frac{\sigma_s}{\pi}\right)\left[\frac{J_1(K_n R \sin\theta)}{\sin\theta}\right]^2, \qquad (6.57)$$

where J_1 is the Bessel function of first order, and σ_s is determined by formula (6.56). The angular distribution of protons which are scattered elastically, in accordance with formula (6.57), consists of several maxima and minima, whose location in the final analysis depends on the proton energy. The main maximum corresponds to the angle $\theta_{max} = 0$; the first minimum is observed at the angle $\theta_{min} \approx \arcsin \lambda/R$. With an increase in the proton energy, this minimum is displaced toward the region of small angles θ.

Inelastic Nuclear Interaction of Protons

The initial feature of an inelastic interaction between protons and nuclei of a substance is its cross-section, the magnitude of which determines the initial stage of the process - absorption of a proton by a nucleus. In this connection, the cross-section of inelastic interaction plays a double role in the problem of shielding from

high-energy protons. On the one hand, it characterizes the dislodgement of protons from the bundle, as the shielding is penetrated, due to absorption; on the other hand, it represents the total cross-section of all processes which lead to escape of secondary particles from the nucleus - i.e., it characterizes the outflow of secondary radiation from the shielding to a definite extent. /181

The cross-section of inelastic interaction is determined most accurately by measuring the attenuation of a particle bundle with the aid of counters - telescopes (Ref. 51). There are several methods for determining σ_a experimentally. The first method can be reduced to measuring the attenuation of a collimated proton bundle in a fine absorber, under conditions of "poor geometry" (Ref. 51, 53, 57). The basic difficulties which are encountered in the utilization of this method consist of the fact that it is necessary to introduce corrections for the effect of secondary particles which are formed in the absorber, and also for Coulomb and diffraction scattering.

A second method consists of measuring the absorption of a proton stream in a thick absorber (Ref. 51, 58). The secondary particles which are formed in the absorber, as well as the protons which are scattered elastically to a certain extent, influence the measurement results. The definite limitation of this method is due to the dependence of the inelastic cross-section on the proton energy, which changes with an increase in the absorber thickness.

A third method consists of measuring the formation cross-section of each of the possible products resulting from inelastic interactions of a proton with a nucleus, and of totalling all of these cross-sections (Ref. 51). This method is based on radiochemical methods of studying nuclear reactions. Not all of the products resulting from the inelastic interactions of protons with nuclei can be determined experimentally by these methods. Therefore, the latter method is not sufficiently reliable by itself, since it can frequently produce results which are somewhat too low. Additional data can significantly improve the reliability of this method (Ref. 51). Finally, in order to determine the inelastic cross-section, it is possible to measure the range of the nuclear interaction with the aid of nuclear emulsions.

Table 6.19 presents the cross-sections - obtained by different experimental methods - of the inelastic interaction between protons and nuclei of different substances. The measurement errors comprise 5 - 10%. The cross-section of inelastic interaction is significantly different for different substances, and depends very slightly on the proton energy. Thus, in a wide energy region, the inelastic cross-section for carbon amounts to about 200 mb on the average, which corresponds to the range with respect to the nuclear interaction $R_{nuc} \approx 100$ g/cm^2 of carbon.

Utilizing Table 6.9, which presents the values for proton

TABLE 6.19

CROSS-SECTIONS OF INELASTIC PROTON INTERACTION, barn

Element	Proton Energy, Mev										
	34 [59]	61 [60]	134 [61]	185 [58]	240 [58]	290 [58]	305 [58]	657 [53]	860 [52]	870 [58]	895 [63]
Be	—	—	—	$\pm^{0,172}_{0,017}$	$\pm^{0,169}_{0,017}$	—	$\pm^{0,151}_{0,015}$	$\pm^{0,191}_{0,008}$	$\pm^{0,169}_{0,015}$	$\pm^{0,171}_{0,017}$	—
C	$\pm^{0,445}_{0,020}$	$\pm^{0,200}_{0,013}$	$\pm^{0,22}_{0,024}$	$\pm^{0,204}_{0,02}$	$\pm^{0,202}_{0,02}$	$\pm^{0,199}_{0,02}$	$\pm^{0,187}_{0,018}$	$\pm^{0,227}_{0,12}$	$\pm^{0,209}_{0,02}$	$\pm^{0,222}_{0,02}$	$\pm^{0,23}_{0,02}$
Al	$\pm^{0,600}_{0,042}$	$\pm^{0,392}_{0,025}$	$\pm^{0,373}_{0,037}$	$\pm^{0,408}_{0,04}$	$\pm^{0,383}_{0,04}$	$\pm^{0,416}_{0,04}$	$\pm^{0,334}_{0,3}$	$\pm^{0,418}_{0,022}$	$\pm^{0,394}_{0,01}$	$\pm^{0,394}_{0,04}$	$\pm^{0,37}_{0,03}$
Cu	—	—	$\pm^{0,752}_{0,068}$	$\pm^{0,746}_{0,07}$	$\pm^{0,667}_{0,07}$	$\pm^{0,717}_{0,07}$	$\pm^{0,608}_{0,06}$	$\pm^{0,850}_{0,05}$	$\pm^{0,728}_{0,017}$	$\pm^{0,708}_{0,07}$	$\pm^{0,74}_{0,05}$
Sn	$\pm^{1,930}_{0,100}$	$\pm^{0,995}_{0,070}$	$\pm^{1,286\ *}_{0,1}$	—	—	—	—	$\pm^{1,285}_{0,07}$	$\pm^{1,11}_{0,03}$	—	$\pm^{1,15\ **}_{0,02}$
Pb	$\pm^{1,775}_{0,120}$	$\pm^{1,490}_{0,077}$	$\pm^{1,78}_{0,14}$	$\pm^{1,55}_{0,15}$	$\pm^{1,57}_{0,16}$	—	$\pm^{1,48}_{0,1}$	$\pm^{1,930}_{0,11}$	$\pm^{1,68}_{0,04}$	$\pm^{1,62}_{0,16}$	$\pm^{1,66}_{0,05}$
U	—	—	—	$\pm^{1,90}_{0,19}$	$\pm^{1,77}_{0,18}$	$\pm^{1,85}_{0,18}$	$\pm^{1,60}_{0,16}$	$\pm^{2,215}_{0,1}$	—	—	—

* Data for Cd.

** Data for Sb.

ranges in different substances, one can readily find that a proton energy of about 435 Mev corresponds to the ionization range $R_{ion} = 100$ g/cm^2 in carbon. In a similar way it is possible to determine the value $R_{nuc} \approx 220$ g/cm^2 for lead and the proton energy, corresponding to $R_{ion} = R_{nuc} = 220$ g/cm^2, which approximately equals 475 Mev. /183

Thus, the values for proton ranges with respect to ionization losses R_{ion} and nuclear interactions R_{nuc} are equal for a proton energy in the 400 - 500 Mev region for different substances.

Theoretical calculations can be used, in addition to experimental methods, to determine the cross-section of inelastic proton interaction. The most fruitful method in this respect is that of random tests which was utilized in another work (Ref. 63). In particular, this work presents the results derived from calculating the "transparency" of nuclei as a function of proton energy, and the"transparency" is determined as $1 - \sigma_a/\sigma_0$, where σ_0 is the geometric nucleus cross-section. The geometric cross-section is $\sigma_0 = \pi r_0^2 A^2/3$. The value of r_0 was assumed to equal $r_0 = 1.3 \cdot 10^{-13}$ cm (Ref. 63), which yields values of σ_0 for the nuclei of Al, Cu, Bi, and U, equaling 478, 850, 1870 and 2039 mb, respectively. The calculated "transparencies" and cross-sections of inelastic interaction (Ref. 63) are shown in Table 6.20. These results show that the transparency changes from 28% for Al, to 3% for U. The existence of considerable nucleus transparency, with respect to high-energy protons, was historically one of the first - and one of the primary - indications that the cascade model was applicable for nuclear interactions. /184

TABLE 6.20

TRANSPARENCY OF CERTAIN NUCLEI AND THE CROSS-SECTIONS OF INELASTIC INTERACTION. /183

Al, $\sigma_0 = 478$ mb

E_p, Mev	$1 - \sigma_a/\sigma_0$	σ_a/σ_0	σ_a, mb
82	0,263±0,015	0,737	352
235	0.275±0,018	0,725	347
460	0,257±0,017	0,743	354
1840	0,134±0,012	0,866	413

(see next page for continuation)

(continuation of Table 6.20)

Cu, σ_0 = 850 mb

E_p, Mev	$1-\sigma_a/\sigma_0$	σ_a/σ_0	σ_a, mb
82	0,176±0,010	0,824	702
155	0,183±0,009	0,817	694
235	0,206±0,015	0,794	676
286	0,202±0,015	0,798	678
364	0,198±0,015	0,802	682
460	0,162±0,013	0,838	711
690	0,112±0,013	0,888	755
940	0,093±0,012	0,907	770
1840	0,090±0,011	0,910	772

U , σ_0 = 2039 mb

/184

E_p, Mev	$1-\sigma_a/\sigma_0$	σ_a/σ_0	σ_a, mb
82	0,058±0,007	0,942	1922
155	0,074±0,007	0,926	1890
235	0,084±0,009	0,916	1870
460	0,070±0,009	0,930	1895
940	0,032±0,007	0,968	1971
1840	0,037±0,007	0,963	1970

In the energy region of 82 - 460 Mev, the transparency and, consequently, the cross-section of inelastic interaction depends rather slightly on the proton energy. This can be explained by two factors. On the one hand, the influence of the Pauli principle, which excludes certain collisions in the nucleus, decreases with an increase in the proton energy, which leads to a decrease in the range of the proton between collisions in the nucleus. On the other hand, with an increase in energy, the total cross-sections of nucleon-nucleon collisions are reduced; this is manifested in the corresponding increase of the range between collisions.

A comparison between the measured (Ref. 52, 53, 58, 61, 62) cross-sections and calculated cross-sections of inelastic interaction for Al, Cu and U shows that the results derived from calculations using the method of random tests and the experimental data fully coincide to a satisfactory extent. However, there are systematic increases in the experimental values of σ_a for Al in the energy region up to 200 Mev (Ref. 51). The lack of reliable data on the cross-sections of inelastic interaction in the region of low-energy

protons should be pointed out.

Formation of Cascade Particles During Nuclear Interaction Between Protons and Matter

The processes of nuclear interaction for protons at high energies differ significantly from processes occurring at low and medium energies. The primary difference consists of the fact that the collision time between an incident particle and one of the nucleus nucleons is less than the time between nucleon collisions in the nucleus. This means that the first stage of the interaction between a proton and the nucleus can be regarded as successive collisions between an incident proton and individual nucleons of the nucleus. In their turn, these nucleons can have a rather high energy, and therefore their collisions with the remaining nucleus nucleons will have the /185
same nature. Secondary recoil nucleons under corresponding conditions can also participate in this process, which is similar to an avalanche or a cascade; as a consequence of this, the name cascade stage, or intranuclear cascade, has arisen. Recoil nucleons, which have an energy which is sufficient for leaving the nucleus, are called cascade particles. They have spherical, angular, and energy distributions. The flight direction of the cascade particles coincides primarily with the direction of the primary proton. The energy spectrum of cascade particles is characterized by a relatively large amount of high-energy particles.

It should be noted that intranuclear collisions of an incident particle with nucleus nucleons cannot be regarded as collisions between free nucleons outside of the nucleus. Although intranuclear collisions between an incident proton and nucleus nucleons can be regarded as collisions of two insulated bodies, the presence of the remaining nucleons is, nevertheless, apparent in the influence of the Pauli principle. In this case, the Pauli principle can be reduced to the exclusion of intranuclear collisions with an energy transfer which is less than a certain amount, which is characteristic for the given nucleus. The influence of the Pauli principle is most significant for relatively small energies of the incident proton.

After the intranuclear cascade is completed, in the general case the nucleus remains in an excited state, because part of the incident proton energy was transmitted to the recoil nucleons, which could not leave the nucleus for various reasons. The conversion of the nucleus from an excited state is basically accomplished by volatilization of nucleons and heavier particles. The formation of such particles during a nuclear proton interaction will be examined in the following Section.

The outflow of cascade particles during an inelastic collision of protons and nuclei, and the ratio between cascade neutrons and protons,

depend on the energy of the incident proton and the type of target nucleus. With an increase in the proton energy, the outflow of cascade particles significantly increases, and it is particularly noticeable for heavier nuclei (Figure 6.4). The dependence of the outflow of cascade particles on the mass number of the target nucleus is significant only for comparatively small energies of the incident proton. The mean number of cascade particles, per one inelastic interaction, changes for uranium from 0.57 for a proton energy of 82 Mev, to 8.7 for an energy of 1840 Mev (Ref. 63).

The general tendency for the outflow of cascade particles to depend on the mass number of the target nucleus is determined by the energy region of the incident proton. In a proton energy region of less than 800 Mev, the outflow of cascade particles decreases with an increase in the mass number. In a proton energy region of more than 800 Mev, the nature of this dependence gradually changes: at first (in the 700 - 1000 Mev region) the outflow of cascade /186
particles depends slightly on the mass number, and then (for energies greater than 1000 Mev) an increase in the outflow of cascade particles is observed with an increase in the mass number of the target nucleus. This can be explained by the fact that - although the intranuclear cascade in heavy nuclei includes a large number of nucleons - the energy, per one portion of cascade particles, is smaller than that for light nuclei. Therefore, it is possible for a comparatively small number of cascade nucleons to leave the nucleus. With an increase in the energy of the incident proton, the mean energy per one cascade nucleon in the nucleus increases, and in this way the outflow of a large number of cascade particles from the nucleus is facilitated. For rather large energies of the incident proton, the total number of nucleons participating in the development of the intranuclear cascade plays a basic role. In connection with this, the outflow of cascade particles at such energies increases with an increase in the mass number. Table 6.21 presents quantitative data on the outflow of cascade particles for different nuclei, as a function of the incident proton energy (Ref. 63).

TABLE 6.21

THE OUTFLOW OF CASCADE PARTICLES N + P (MEAN NUMBER OF CASCADE PARTICLES PER ONE INELASTIC INTERACTION OF A PROTON WITH A NUCLEUS)

T_p, Mev	Target Nucleus			T_p, Mev	Target Nucleus		
	Al	Cu	U		Al	Cu	U
82	1,47	1,23	0,57	460	3,4	3,3	2,94
155	1,97	1,7	1,23	690	4,2	4,3	4,1
235	2,4	2,22	1,7	940	5,0	5,31	5,3
286	2,65	2,54	2,0	1840	6,72	8,0	8,73

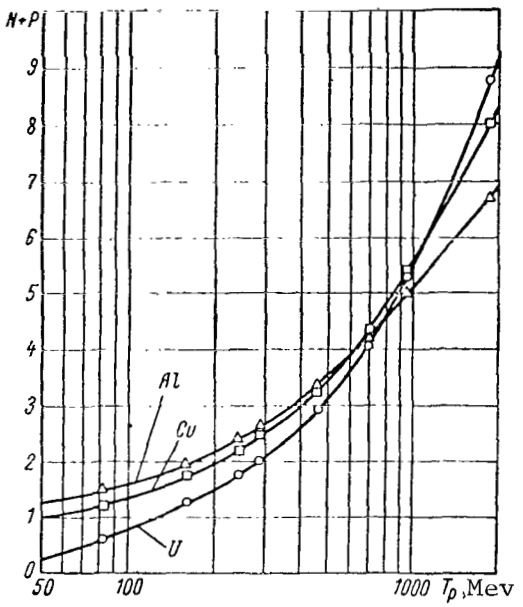

Figure 6.4

Outflow of Cascade Particles as a Function of the Incident Proton Energies.

The ratio between the number of cascade neutrons N and the number of protons P depends both on the mass number of the target nucleus, and on the energy of the incident proton. The relative number of cascade neutrons N/P sharply increases with an increase in the mass number of the target nucleus. For example, for a proton energy of 82 Mev, the ratio N/P amounts to 0.84 for the nuclei of Al, and 2.1 for U . This can be explained by the fact that the cross-sections of interaction (p, n) and (n, p) are greater than the cross-sections (p, p) and (n, n). Due to this fact, in heavy nuclei with a significant preponderance of neutrons, the range of neutrons is greater than for protons, which facilitates the outflow of cascade neutrons from the nucleus. In addition, in heavy nuclei with a large ratio between the number of neutrons and the number of protons, a relatively large number of cascade neutrons participate in the development of the intranuclear cascade; in contrast to protons, the Coulomb barrier does not impede the outflow of these cascade neutrons. /187

The dependence of the ratio N/P on the proton energy is rather slight for light and for heavy elements, and in the energy

region of 200 - 400 Mev a wide minimum is observed.

Table 6.22 presents quantitative data on the relative outflow of cascade neutrons and protons for different nuclei, as a function of the incident proton energy (Ref. 63).

TABLE 6.22

RELATIVE OUTFLOW OF CASCADE NEUTRONS AND PROTONS, N/P

T_p, Mev	Target Nucleus				
	Al	Cu	Ru	Bi	U
82	0,84	1,04	1,20	1,67	2,08
158	—	0,96	1,15	—	1,98
239	0,74	0,93	1,10	—	1,61
290	—	1,00	1,12	1,64	—
365	—	1,00	—	—	—
460	0,79	1,02	1,16	1,59	1,89
690	—	1,02	—	—	—
940	—	1,16	1,22	1,89	2,00
1840	0,92	1,18	1,25	1,75	2,08

Table 6.23 lists data on the outflow of cascade protons P and neutrons N , as a function of the proton energy for Al, Cu and U.

The outflows of cascade particles (see Table 6.21) represent quantities which characterize the mean amount of cascade nucleons, which arise as the result of inelastic interaction between a proton and a nucleus. For a given proton energy, cascade processes can occur with a different outflow of cascade particles. The relative probability for these processes depends on the proton energy, and competition exists between the various processes, /188
which is characteristic for the high-energy region. The relative role of various cascade processes, which correspond to different outflows of cascade nucleons, is shown for copper (Ref. 63) in Figure 6.5. The curve $\Delta A = 0$ corresponds to the capture of a proton with the formation of a compound nucleus; the probability for the formation of this nucleus is small for inelastic interaction between protons and nuclei of copper in the high-energy region. Thus, for an energy of 50 Mev, the probability for the formation of a compound nucleus is less than 40%, out of all the cases of inelastic interaction between a proton and the nucleus of copper - 64. For an energy of 100 Mev, this probability is about 6%, and finally - for a proton energy of more than 150 Mev - the formation of a compound nucleus can be completely disregarded. With an increase in the mass number of the target nucleus, the relative role of /189
the process by which a compound nucleus is formed increases. For

TABLE 6.23

VALUES FOR OUTFLOWS OF CASCADE PROTONS $\overline{P}$ AND NEUTRONS $\overline{N}$ FOR CERTAIN NUCLEI

T_p, Mev	Al		Cu		U	
	$\overline{P}$	$\overline{N}$	$\overline{P}$	$\overline{N}$	$\overline{P}$	$\overline{N}$
82	0,80	0,67	0,6	0,63	0,18	0,39
158	—	—	0,87	0,83	0,41	0,82
239	1,37	1,03	1,15	1,07	0,65	1,05
290	—	—	1,27	1,27	—	—
460	1,9	1,5	1,63	1,67	1,00	1,94
690	—	—	2,13	2,17	—	—
940	—	—	2,46	2,83	1,76	3,54
1840	3,5	3,22	3,77	4,23	2,83	5,90

/188

an energy of 100 Mev, about 30% of all the cases of inelastic interaction between a proton and a nucleus for uranium -238 take place with the formation of a compound nucleus. In the proton energy region which is less than 60 - 70 Mev, a "single-particle" cascade (curve $\Delta A = 1$ in Figure 6.5) - i.e., a cascade process which is accomplished by the escape of one particle (proton or neutron) - represents a basic process which competes with the process by which a compound nucleus is formed. The relative probability for this process reaches a maximum (about 59%) for a proton energy of approximately 70 Mev, and it then decreases, reaching a value of less than 10% for an energy of more than 350 Mev.

/189

A "two-particle" cascade is a basic competitive process in this case; the relative probability for this process reaches a maximum (about 45%) close to 130 Mev.

In the energy region up to 400 Mev, cascade processes are observed with the escape of up to six particles. However, the relative probability for these processes in this energy region is extremely small (less than 2%). The mean number of cascade particles for a given proton energy can be obtained in the following way, utilizing the graph in Figure 6.5:

$$\overline{(N+P)} = \sum_{i=1}^{A+1} i\varepsilon_i(T_p),$$

where $\varepsilon_i(T_p)$ is the relative probability for the cascade process, occurring with the escape of i particles. In the energy region up to 400 Mev, the mean number of cascade particles for

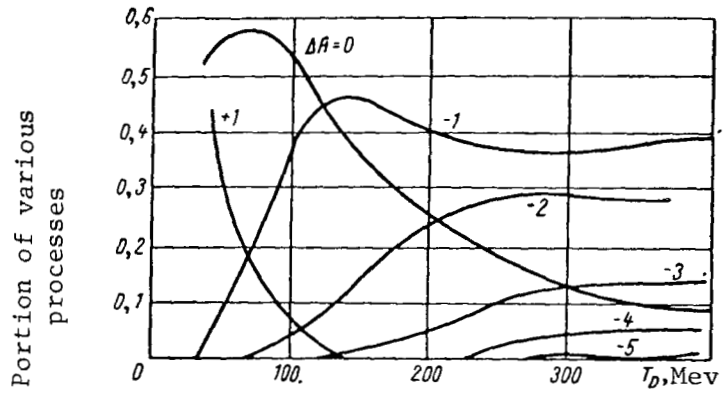

/188

Figure 6.5

Relative Role of Cascade Processes Corresponding to Different Outflows of Cascade Nucleons, for Copper.

copper does not exceed 3. With an increase in the incident proton energy, cascade processes with the escape of a large number of nucleons become possible in terms of energy; in this connection, for copper the mean number of cascade particles increases up to eight for T_p = 1840 Mev (Table 6.21). /189

It is of interest to examine the energy distribution of cascade nucleons. It is apparent that the energy spectrum of cascade nucleons will be very wide: from a certain minimum energy up to an initial energy of the incident proton. The minimum energy for the spectra of cascade protons and neutrons is different. For protons, it is caused by the Coulomb barrier which is taken into account in the calculations by the introduction of a "cut-off" energy of the cascade. Thus, the minimum energy of cascade protons for Al was assumed to equal 4.6 Mev in the calculations (Ref. 63).

In general, the energy distribution of cascade neutrons is similar to the spectrum for cascade protons, with the difference that the neutron spectrum must be displaced toward the low-energy region due to the absence of the Coulomb barrier effect for neutrons. The energy spectra of cascade protons escaping from Al and U nuclei are shown in Figure 6.6, for incident proton energies of 460 Mev and 1840 Mev. In both cases, the spectrum of the cascade protons escaping from the U nuclei is somewhat softer than for Al. This can be primarily explained by the /190

fact that a larger number of nucleons participate in the development of the cascade in heavy nuclei - and therefore a smaller amount of energy, on the average, falls to the share of each of them. The retention of the spectrum form in a wide energy region of incident protons, and also a comparatively small number of cascade protons for energies greater than 500 Mev, in the case of high-energy, incident protons, characterize the spectra of cascade protons. We should note that in the case of light nuclei a certain deviation from the monotonic nature of the spectrum - which is particularly noticeable for small initial energies - is observed in the spectrum of cascade protons close to the initial energy of the incident proton.

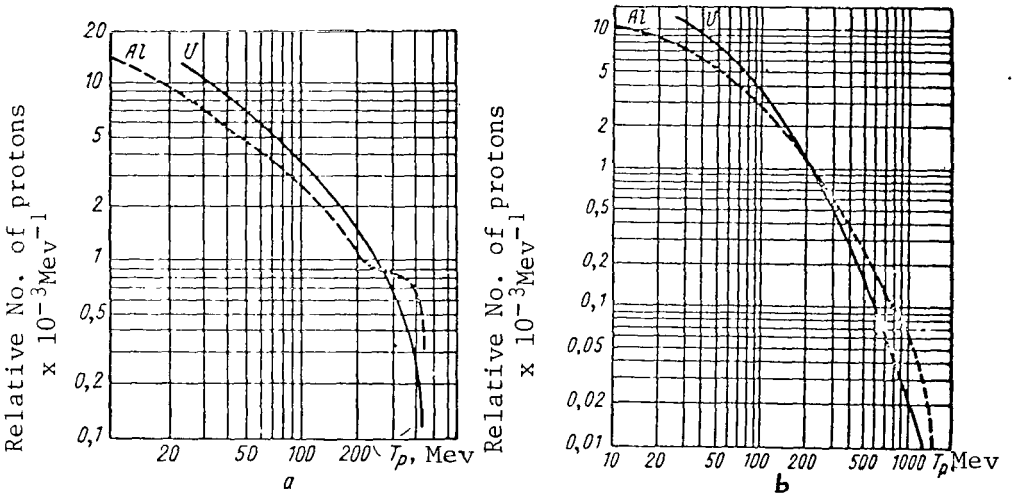

Figure 6.6

Energy Spectra of Cascade Particles for Al and U for Incident Proton Energies of 460 Mev (a) and 1840 Mev (b).

Attention should also be called to the following fact. The region of low energies must be designated as the most important part of the cascade proton spectrum, from the point of view of shielding problems. In the first place, small-energy protons comprise a significant part of the cascade proton spectrum. In the second place, the absorbed dose per one proton increases significantly with a decrease in the proton energy, and - finally - in the region of low proton energies the RBE reaches maximum values. Together with this, the greatest uncertainties exist in the low-energy region of the calculated spectra for cascade protons. The "cut-off" energy,which is introduced in the calculations in order to take the Coulomb barrier into account, represents a very indefinite quantity. In addition, there is the penetration of the Coulomb barrier, which

is ordinarily not taken into account in the calculations. Due to the escape of part of the nucleons, during the process by which the cascade develops, the mass and charge of the nucleus change, which somewhat decreases the height of the Coulomb barrier, and facilitates /191 the escape of protons in the final stage of the cascade (Ref. 51). The latter effect is particularly important in the regions of high-energy protons, where the mean number of cascade nucleons escaping from the nucleus is large.

It is also necessary to know the angular distribution of cascade particles, along with the energy distribution. It has been noted (Ref. 63) that the angular distribution of cascade protons and neutrons are essentially indistinguishable. One characteristic for the angular distribution of cascade particles is the forward direction with respect to the direction of motion of the incident proton. With an increase in the energy of the cascade particles, the anisotropy of angular distribution is intensified. For small cascade particle energies, the angular distribution is almost isotropic.

In addition to protons and neutrons, neutral π°-mesons and charged $\pi^{\pm}$-mesons can be formed during the development of the intranuclear cascade. Emission of cascade π-mesons is significant when the energy of the incident proton is more than 300 Mev, and sharply increases with a further increase in the proton energy. The dependence of the outflow of cascade mesons on the mass number of the target nucleus is fairly weak, and the outflow of mesons decreases somewhat with an increase in the mass of the nucleus. This can apparently be explained by the fact that the probability for the escape of mesons from the nucleus decreases with an increase in the nucleus dimensions to a greater extent than the probability for their formation increases during the development of a cascade in the nucleus. Table 6.24 presents the outflows of π-mesons for several energy values of an incident proton and several nuclei (Ref. 63).

As can be seen from this Table, the total outflow of cascade mesons, for a proton energy of 0.46 Bev, ranges from 0.10 to 0.15, and for proton energies of 1.84 Bev - from 1.02 to 1.19 - it is almost one order of magnitude larger, on the average. For comparatively small energies of the incident protons, the π^{+}-mesons occupy a primary place among the cascade π-mesons escaping from light and medium nuclei; the outflow of π°-mesons is approximately 1.6 times smaller (and the outflow of π^{-}-mesons is approximately 3 times smaller) than for π^{+}-mesons. For high energies of incident protons, the outflow ratio changes in favor of π°-mesons.

Only rough estimates are available for the spectrum of cascade

mesons. Table 6.25 presents the qualitative characteristics for the spectrum of cascade mesons. The spectrum can be divided into four energy intervals (Ref. 63). The effect of a target nucleus on the spectrum of cascade mesons is not significant. At the same time, the dependence of the spectrum form on the incident proton energy is quite clearly apparent.

Data on the angular distribution of cascade π-mesons are considerably less reliable than for cascade nucleons. This is caused by the greater uncertainty of the initial data. It can only be noted that the form of the meson angular distribution is greatly dependent on the incident proton energy. For high proton energies, a more clearly-expressed directional effect for the angular distributions can be observed close to the direction of the incident proton, which is apparent to a greater extent for light elements (Ref. 63). /193

Formation of Evaporative Particles During the Nuclear Interaction Between Protons and Matter.

For various reasons, a certain amount of nucleons participating in the development of an intranuclear cascade cannot leave the nucleus. As a result of several collisions, the energy of these nucleons is distributed between the nucleons of the nucleus, changing it into an excited state. The excitation energy of the nucleus depends on the type of preceding intranuclear cascade. For example, if the intranuclear cascade is not accomplished by the escape of cascade particles from the nucleus, then the nucleus excitation energy will equal the energy of the incident proton plus its binding energy in the nucleus. In the general case, the excitation energy is

$$E^* = T_p - \sum_{i=0}^{m} T_i - (m-1)B,$$

where T_p is the energy of the incident proton; T_i is the energy of the cascade particles escaping from the nucleus; m is the total number of escaping cascade particles; B is the mean binding energy for m cascade particles.

The results derived from calculating the mean excitation energy (Ref. 63) for inelastic proton interaction show that E*, in the region up to 500 Mev, slightly depends on the initial proton energy. With an increase in the proton energy by a factor of five, the mean excitation energy for all elements increases less than two times. With an increase in the mass number, the mean excitation energy of the nucleus increases; however, even for heavy nuclei, the excitation energy is only about 30% of the incident proton energy (for $T_p \approx 500$ Mev). For light nuclei, the excitation /194

TABLE 6.24

OUTFLOW OF CASCADE π-MESONS

Target Nucleus	Meson Type	Proton Energy, Bev			
		0,46	0,69	0,94	1,84
Al^{27}	π^0	0,049	—	—	0,516
	π^+	0,076	—	—	0,401
	π^-	0,019	—	—	0,253
	$\Sigma\pi$	0,144	—	—	1,170
Cu^{64}	π^0	0,035	0,113	0,196	0,483
	π^+	0,054	0,148	0,232	0,310
	π^-	0,021	0,047	0,112	0,263
	$\Sigma\pi$	0,110	0,308	0,540	1,056
Ru^{100}	π^0	0,036	—	0,184	0,501
	π^+	0,063	—	0,202	0,329
	π^-	0,019	—	0,103	0,355
	$\Sigma\pi$	0,118	—	0,489	1,186
Ce^{140}	π^0	0,031	—	—	0,461
	π^+	0,067	—	—	0,289
	π^-	0,022	—	—	0,272
	$\Sigma\pi$	0,120	—	—	1,022
Bi^{209}	π^0	0,034	—	0,187	0,447
	π^+	0,042	—	0,176	0,270
	π^-	0,023	—	0,161	0,315
	$\Sigma\pi$	0,099	—	0,524	1,030
U^{238}	π^0	0,044	—	0,164	0,427
	π^+	0,040	—	0,151	0,276
	π^-	0,025	—	0,114	0,314
	$\Sigma\pi$	0,108	—	0,430	1,017

/192

energy in this region does not exceed 10% of the incident proton energy. /194

With an increase in the incident proton energy from 500 Mev

TABLE 6.25

SPECTRUM OF CASCADE π-MESONS FOR DIFFERENT ENERGIES OF PROTONS IMPACTING ON THE NUCLEUS OF Cu AND U /193

Proton Energy, Mev	Characteristics of the Cascade Meson Spectrum for Energy Intervals of π-Mesons (Mev)			
	0 - 45	45 - 90	90-200	>200
For Cu Nucleus				
460	0.48	0.44	0.06	0.02
940	0.27	0.25	0.13	0.35
1840	0.23	0.19	0.09	0.49
For U Nucleus				
460	0.47	0.42	0.11	0.002
940	0.37	0.25	0.09	0.029
1840	0.26	0.19	0.14	0.44

to 2000 Mev, the heavier the nucleus, the more vigorously the excitation energy increases. However, the portion of excitation energy from the primary proton energy decreases to approximately 22% for uranium, and approximately 5% for aluminum (for $T_p \approx 2000$ Mev).

The excitation energy, which remains in the nucleus after the intranuclear cascade stage is completed, is distributed between several nucleons of the nucleus. Due to the fluctuation in the magnitude of the energy per one particle, it is possible for one of the nucleons to acquire energy which is sufficient for it to escape from the nucleus. Thus, the nucleus loses a significant part of its excitation energy. For high-energy protons, the excitation energy of the nucleus, in absolute magnitude, is quite significant; in this connection, systematic emission of several nucleons by the nucleus takes place. By analogy with the evaporation process of heated drops of liquid, this de-excitation process of the nucleus by emission of nucleons is called the evaporative stage of inelastic nuclear interaction of a proton, and the emitted nucleons are called evaporative particles.

An accurate determination of the evaporation process of nucleons from a nucleus is very complex, because it is necessary to take into account the decrease in the excitation energy ("cooling of the nucleus"), the change in the composition of the nucleus during successive evaporation, fluctuations in the number of evaporated particles, etc. In this connection, different simplifications are usually assumed in the calculations. The most reliable results have been obtained, apparently, in the calculations carried out by Dostrovsky and others (Ref. 64),

utilizing the Monte-Carlo method. The outflow of evaporative particles - i.e., the mean number of particles evaporated from the nucleus - depends on the type of nucleus and the initial excitation energy.

This outflow can be determined for a given excitation energy, if the mean energy, which is removed from the nucleus by one nucleon during the evaporation, is known. It is possible to represent the magnitude of the mean excitation energy, per one evaporative nucleon, (which is practically independent of the mass number A) in the form of the approximate relationship $\overline{E} = 8.9 + 0.97\,\varkappa$(Mev), where $\varkappa$ is the nuclear temperature ($\varkappa \approx \sqrt{10U/A}$). Then the mean number of evaporative particles equals the ratio of the mean excitation energy U and the mean energy $E_{nucleon}$:

$$\overline{N}_{evap.} = \frac{U}{\overline{E}} = \frac{U}{8{,}9 + 0{,}97\varkappa} = \frac{U}{8{,}9 + 3{,}1\sqrt{\frac{U}{A}}}.$$

This formula can be used for approximate estimates of the outflow of evaporative particles from various nuclei at different incident proton energies. It was indicated above that the mean excitation U slightly depends on the incident proton energy in the region $T_p < 500$ Mev - in particular, for this region $U_{Al} \approx 46$ Mev. This yields $\overline{N}_{evap} \approx 3.5$. In the case of uranium, for $T_p = 200$ Mev the mean excitation energy U = 100 Mev and $N_{evap} \approx 9$. Neutrons and protons predominate among the evaporative particles which escape from the nucleus. The dependence of the outflow of evaporative particles on the mass number is different for neutrons and protons, and in general the outflow of neutrons is greater than that for protons. Thus, at the nuclear temperature $\varkappa$ = 4 Mev, the outflow of evaporative neutrons from the nucleus, with the initial mass number A = 60 , is about four, and the outflow of protons - not more than one and a half. With an increase in the mass number, this difference increases significantly: for A = 240, the outflow of neutrons is about 22, and for protons - not more than three. The nuclear temperature $\varkappa$ = 4 Mev corresponds to the excitation energy of the nucleus $U \approx 1.6\,A$, which equals approximately 100 Mev for A = 60, and about 400 Mev for A = 240. In its turn, this corresponds to an incident proton energy of about 1.5 Bev. /195

With an increase in the excitation energy, the outflow of evaporative neutrons and protons increases in the following way. At the nuclear temperature $\varkappa$ = 6 Mev (excitation energy U = 216 Mev for A = 60 and U ≈ 864 Mev for A = 240; the incident proton energy is 2500 - 3000 Mev), the outflow of neutrons amounts to five-six for A = 60 and 32 - 34 for A = 240, whereas the outflow of protons is about three for A = 60, and about seven for A = 240. However, it should be noted that the dependence of the outflow of evaporative

particles on the mass number A is not a monotonic function, and the nonmonotonic nature is clearly expressed for protons to a large degree. The nonmomotonic nature of this dependence is caused by the so-called shell effect and the competition between the processes for the escape of neutrons and protons.

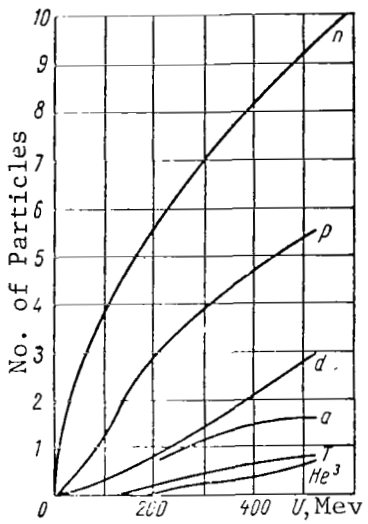

Figure 6.7

Outflow of Evaporative Particles as a Function of Excitation Energy of Copper-64.

In addition to neutrons and protons, there are deuterons, tritons, helium-3, and helium-4 among the evaporative particles. Let us examine the relative outflow of different evaporative particles, using the example of a copper-64 nucleus. The outflow of different evaporative particles from the nucleus of copper-64 is shown in Figure 6.7, as a function of the excitation energy. Neutrons and protons make up the main portion of evaporative particles.

The outflow of heavier particles is significant only for very large excitation energies. For the excitation energy U = 200 Mev, which corresponds to an incident proton energy of about 1850 Mev, there are about 55 neutrons, 28 protons, 8 deuterons, 7 α-particles, 3 tritons, and less than one helium-3 nucleus, on the average, among the evaporative particles per ten nuclei - i.e., about 10 particles per nucleus in all. Thus, neutrons comprise more than half of all the evaporative particles; protons comprise only half of the mean number of neutrons, and the remaining charged particles as a whole are not more than 1/5 of the total outflow. /196

Let us examine the energy spectrum of evaporative particles.

We shall do this, by using the example of Ni, Ag, and Au nuclei which are bombarded by protons having energies of 190 Mev, because for this case there are both calculational results (Ref. 65) and experimental data (Ref. 66). The spectra of evaporative particles were calculated by the Monte-Carlo method, while results which were obtained by Metropolis and others (Ref. 63), were used to describe the cascade stage which precedes the evaporation process. The spectra of evaporation neutrons (Ref. 65) have a maximum of about 1 Mev, and extend up to 10 - 15 Mev. A comparison with the experimental spectra shows a rather good agreement between the spectrum sections for $E_n > 2$ Mev, and a great divergence for smaller neutron energies. The calculated values are essentially too low, with respect to the experimental values. It was assumed that the utilization of a nucleus model having a diffusive boundary can improve this part of the calculated spectra.

The spectra of charged particles which are emitted during evaporation differ from the neutron spectra by the fact that the maximum is shifted to the region of high energies (5 - 10 Mev) for protons and deuterons, and to the region of 10-15 Mev for α-particles. This is caused by the influence of the Coulomb barrier of the nucleus. The divergence with experimental data can be primarily explained by not making an accurate allowance for corrections for the Coulomb barrier of the nucleus.

It should be noted that the spectrum form for charged particles of evaporation is slightly dependent on the excitation energy of the nucleus and, consequently, on the incident proton energy. In conclusion, let us examine the cumulative data on the outflow of cascade and evaporative particles during the interaction of protons, having energies of 190 Mev, with Ni, Ag, and Au nuclei (Ref. 65). These data are given in Table 6.26, along with the experimental results (Ref. 66).

In the first place, it should be noted that there is completely satisfactory agreement between the experimental and theoretical cross-sections for the formation of cascade and evaporative particles. In addition, if it is assumed that evaporative particles have an isotropic angular distribution, and the angular distribution of cascade particles is entirely confined to the leading hemisphere, the difference between the experimental cross-section values for leading and trailing hemispheres must be the cross-section for the formation of cascade particles. These values closely coincide with the calculated quantities for the formation cross-section of cascade particles. /197

On the basis of the data presented in Table 6.26, certain conclusions can be drawn with respect to the relationships between outflows of cascade and evaporative particles, outflows of a different type of particles, and others. Unfortunately, there are very few data of this type. Data on cascade particles are confined only to neutrons

TABLE 6.26

FORMATION CROSS-SECTIONS OF SECONDARY PARTICLES (mb/sterad) DURING THE BOMBARDMENT OF SEVERAL NUCLEI BY PROTONS HAVING ENERGIES OF 190 Mev

Nucleus	Secondary Particles and Experimental Conditions	n		p		d	t	He^3	He^4
Ni	Cascade	52	88	55	137	--	-	-	--
	Evaporative	36		82		13	2	4	26
	Experiment "Forward"	110		120	189	9	13	2	3	17	27
	Experiment "Backwards"			69		4		1		10	
Ag	Cascade	75	331	67	120	--	-	-	--
	Evaporative	256		53		22	7	3	58
	Experiment "Forward"	412		128	194	14	20	4	6	1.8	2.4	23	37
	Experiment "Backwards"			66		6		2		0.6		14	
Au	Cascade	131	1111	80	92	--	-	-	--
	Evaporative	980		12		--	-	-	2.4
	Experiment "Forward"	1085		136	170	--	-	-	15
	Experiment "Backwards"			34		--	-	-	10

Comments: 1. Experimental formation cross-sections of neutrons do not take into account cascade neutrons (Ref. 66).

2. Experimental formation cross-sections of charged particles are given for leading and trailing hemispheres (with respect to the direction of a proton bundle).

and protons. This type of data is necessary (Table 6.26) for light and mean nuclei (elements included in the composition of shielding and tissue), since the relationship between cascade and evaporative neutrons depends significantly on the type of nucleus. When a change is made from Au nuclei to Ni, this relationship changes by more than one order of magnitude. In addition, the spectral and angular distributions of cascade and evaporative particles are completely different. It is also important to have detailed data for a wide proton energy region. Some additional information can be obtained on the basis of experimental data, which are also not comprehensive enough. In this connection, it can be noted that only provisional calculations for the tissue doses of protons beyond the shielding can be made on the basis of existing information on nuclear proton interactions. These provisional calculations must be refined in the future, as new theoretical and experimental data are obtained. /198

REFERENCES

1. Klahr, C. N. Nucleonics, 19, 4, 92, 1961.

2. Lebedinskiy, A. V., Nefedov, Yu. G. In the Collection: "Problems of Space Biology" (Voprosy kosmicheskoy biologii). Edited by Sisakyan, N. M., and Yazdovskiy, V. I. Vol.II, pg. 11, Izd-vo AN SSSR, Moscow, 1962.

3. Problems of Radiation Safety During Space Flights (Problemy radiatsionnoy bezopasnosti kosmicheskikh poletov). Edited by Nefdov, Yu. G. Atomizdat, Moscow, 1964.

4. Recommendations of the Nat. Committee of Rad. Protection, NBS Handbook, 1959.

5. Snyder, W. S., Neufeld, J. Radiation Res., 6, 67, 1957.

6. Neufeld, J., Synder, W. Determination of Energy Scattering by Heavy Charged Particles in Tissue. "Collection of Materials from the Symposium on Individual Problems of Dosimetry" (Opredeleniye rasseyaniya energii tyazhelymi zaryazhennymi chastitsami v tkani. "Sbornik materialov simposiuma po otdel'nym voprosam dozimetrii"). pp. 33-44, Gosatomizdat, Moscow, 1962.

7. Rossi, B. High-Energy Particles (Chastitsy bol'shikh energiy) Gostekhteorizdat (State Technical and Theoretical Press), Moscow, 1952

8. Shen, S. P. Aerospace Med., 32, 901, 1961.

9. Shen, S. P. Astronaut acta, 8, 4, 228, 1962

10. Waddington, C. J. J. Brit. Interplanet. Soc., 18, 7, 277, 1962.

11. Ivanov, V. I. et al. Doses of Cosmic Radiation (Dozy kosmicheskoy radiatsii). In the Collection: Iskusstvennyye Sputniki Zemli, No. 12, Izd-vo AN SSSR, Moscow, 1962.

12. Livingston, M. S., Bethe, H. A. Revs. Mod. Phys., 9, 261, 1937.

13. Walske, M. C. Phys. Rev., 88, 1283, 1952; Phys. Rev., 101, 940, 1956.

14. Segrè, E. Experimental Nuclear Physics (Eksperimental'naya yadernaya fizika). Vol. 1, pg. 143. Izd-vo Inostr. Lit., Moscow, 1955.

15. Swann, W. F. G. J. Franklin Inst., 226, 598, 1938.

16. Fermi, E. Phys. Rev., 56, 1242, 1939; 57, 485, 1940.

17. Wick, G. C. Nuovo cimento, 1, 302, 1943.

18. Sternheimer, R. M. Phys. Rev., 88, 851, 1952; 91, 256, 1953.

19. Sternheimer, R. N. Phys. Rev., 103, 3, 511, 1956.

20. Kunin, P. Ionization Losses of Rapid Particles (Ionizatsionnyye poteri bystrykh chastits). In the Collection: "Meson" (Mezon). Edited by Tamm, I. Ye., Gostekhizdat, Moscow, 1947.

21. Caldwell, D. O. Phys. Rev., 100, 291, 1955.

22. Vasilevskiy, I. M., Prokoshkin, Yu. D. Ionization Potentials of Atoms (Ionizatsionnyye potentsialy atomov). Dubna, OIYaI (Joint Institute for Nuclear Research). 1961.

23. Stier, P. M. et al. Phys. Rev., 96, 973, 1954.

24. Stier, P. M., Barnett, C. F. Phys. Rev., 103, 896, 1956

25. Barnett, C. F., Reynolds, H. K. Phys. Rev., 109, 355, 1958.

26. Sternheimer, R. M. Phys. Rev., 115, 137, 1959.

27. Smith, J. H. Phys. Rev., 71, 32, 1947.

28. Aron, W. A. et al. Lawrence Radiation Laboratory, Report UCRL-121, Berkeley, 1951.

29. Rich, M., Madey, R. Lawrence Radiation Laboratory, Report UCRL-2301, Berkeley, 1954.

30. Barkas, W. H. Nuovo cimento, 8, 201, 1958.

31. Bichsel, Mozley, Aron, Phys. Rev., 105, 1788, 1957.

32. Barkas, W. H. et al. Phys. Rev., 98, 605, 1955.

33. Millburn, G. P., Schecter, L. Lawrence Radiation Laboratory, Report UCRL-2234, Berkeley, 1953.

34. Symon, K. R. Harvard University thesis, 1948.

35. Sternheimer, R. M. Phys. Rev., 118, 4, 1045, 1960.

36. Lindhard, J., Scharff M. Kgl. danske vid. selskab., Mat.-fys. medd., 27, 15, 1953.

37. Lewis, H. Phys. Rev., 85, 20, 1952.

38. Sternheimer, R. M. Phys. Rev., 118, 4, 1045, 1960.

39. Sachs, D. C., Richardson, J. R. Phys. Rev., 89, 1163, 1953. /199

40. Bakker, C. J., Segre, E. Phys. Rev., 81, 489, 1951.

41. Bichsel, H., Mozley, B. F. Phys. Rev., 94, 764, 1954.

42. Burkig, V. C., Mackenzie, K. R. Phys. Rev., 106, 848, 1957.

43. Zrelov, V. P., Stoletov, G. D. Zh. Eksperim. i Tekhn. Fiz., 36, 658, 1959.

44. Westermark, T. Arkiv kemi, 17, 10, 101, 1961.

45. Siri E., Isotropic Tracers and Nuclear Radiations. London, 1951.

46. Barkas, W. H., von Friesen, S. Nuovo cimento, 19, 1, 41, 1961.

47. Coudsmit, S. A., Saunder, J. L. Phys. Rev., 58, 36, 1940; 79, 219, 1950.

48. Williams, E. J. Proc. Roy. Soc., A169, 531, 1939.

49. Belen'kiy, S. Z. Cascade Processes in Cosmic Rays (Labinnyye protsessy v kosmicheskikh luchakh). Gostekhizdat, Moscow, 1948.

50. Sternheimer, R. M. Rev. Scint. Instrum., 25, 11, 1070, 1954.

51. Perfilov, N. A. et al. Nuclear Reactions under the Influence of High-Energy Particles (Yadernyye reaktsii pod deystviyem chastits vysokikh energiy). Gostekhizdat, Moscow-Leningrad, 1962.

52. Chen, F. F., Leavitt, C. P., Shapiro, A. M. Phys. Rev., 99, 3, 857, 1955.

53. Moskalev, V. I., Gavrilovskiy, B. V. Dokl. AN SSSR, 110, 972, 1956.

54. de Carvalho, H. G. Phys. Rev., 96, 398, 1954.

55. Marshall, J. et al. Phys. Rev., 91, 767, 1953.

56. Fernbach, S. et al. Phys. Rev., 75, 1352, 1949.

57. Dzhelepov, V. P., Moskalev, V. I. Dokl. AN SSSR, 110, 539, 1956.

58. Millburn, G. P. et al. Phys. Rev., 95, 1268, 1954.

59. Gooding, T. J. Nucl. Phys., 12, 241, 1959.

60. Meyer, V. et al. Phys. Rev., 117, 5, 1334, 1960.

61. Cassels, J. M. Lawson, J. D. Proc. Phys. Soc., A67, 410, 125, 1954.

62. Booth, N. et al. Proc. Phys. Soc., A70, 447, 209, 1957.

63. Metropolis, N. et al. Phys. Rev., 110, 185, 204, 1958.

64. Dostrovsky, I. et al. Phys. Rev., 111, 1659, 1958.

65. Dostrovsky, I. et al. Phys. Rev., 118, 781, 1960.

66. Bailey, L. E. Lawrence Radiation Laboratory, Report UCRL-3334, Berkeley, 1956; Gross, E. Lawrence Radiation Laboratory, Report UCRL-3330, Berkeley, 1956. (Data presented in the Work (Ref. 64)).

CHAPTER 7

SHIELDING FROM PROTONS IN THE INNER RADIATION ZONE OF THE EARTH AND SOLAR FLARES

7.1. Introduction

The preceding chapter presented fundamental information on the interaction of high-energy protons in shielding and in biological tissue. Let us carry this investigation further, and determine the manner in which these data can be applied to specific designs for shielding from protons in the inner radiation zone of the earth and from solar flares. In a general form, the problem of calculating shielding for a habitable cabin on a spacecraft can be formulated in the following way. For given initial conditions (trajectory, duration, and other spaceflight conditions), it is necessary to determine the basic requirements for a shielding (type and thickness of material, shielding arrangement, etc.) which would provide that the cosmonaut does not receive more than a given total radiation dose. The solution of this problem can be represented in the following stages. /200

First of all, the intensity and spectral composition of charged particle streams is determined, and the dose of irradiation from corpuscular radiation in the zones of the earth is calculated, on the basis of data regarding the spatial location of the radiation zones and data on the trajectory of the spacecraft. Then, for a given flight duration, an estimate is made of the dose provided by proton radiation from solar flares. Data on the frequency of solar flares, and the spectral distribution and intensity of the proton streams are thus taken into account.

In order to obtain the total dose obtained during a flight, the dose caused by primary cosmic radiation must be added to the dose from irradiation from terrestrial zones and solar flares. The total dose which is thus determined is compared with the permissible dose, which has been established on the basis of the spaceflight conditions. 50 rem is recommended as the admissible dose for spaceflights of short duration, and 25-30 rem per year when the flight lasts several years (Ref. 1). Thus, on the one hand, the limits of the admissible radiation action are taken into account, as well as the unusual features of future flights to be taken by man in space, on the other hand. The quantities which are presented must be regarded as provisional, requiring future /201

refinement as experimental data are accumulated on the biological effect of high-energy radiation, the combined effect of spaceflight factors, etc.

The necessary multiplicity factor for dose attenuation in the shielding is determined by comparing the total dose obtained during the flight with the admissible irradiation dose for the cosmonaut. Let us use K_0 to designate the multiplicity factor for attenuation of the total radiation dose in the shielding. We can then write:

$$\frac{1}{K_0} = \sum_{i=1}^{n} \frac{\varepsilon_i}{K_i},$$

where ε_i is the relative dose during the flight, and K_i is the multiplicity factor of the dose attenuation, corresponding to the $\underline{i\text{th}}$ component. The summation is made for all radiation components which influence the cosmonaut during the flight. On the basis of this relationship, for given flight conditions it is possible to determine the component or components of radiation which primarily determine the thickness and arrangement of the shielding. Thus, for example, for a spacecraft which is to orbit the moon for 14 days, having a shielding thickness of 13.86 g/cm^2 on the average (Ref. 2), the individual radiation components make the following contributions to the total dose of 102 rem during the flight: protons from solar flares 98 rem; primary cosmic radiation 2.8 rem; protons from the inner zone of the earth 0.6 rem; and electrons from the outer zone of the earth (including electromagnetic radiation which is produced by electrons in the shielding) 0.2 rem. In this case, the shielding thickness is completely determined by protons from solar flares. It is apparent that the relationship between the dosage contributions of different components depends on the specific flight conditions; however, in all cases, the dosage contribution made by protons from solar flares will most probably be significant.

In addition, the materials are chosen for the shielding which will reduce the total irradiation dose by the required amount during the flight. Different variants in the arrangement of the shielding materials are examined, and also the possibility of using the spacecraft construction, equipment, fuel supplies, etc. as shielding elements is determined. It should be noted that the selection of materials which will provide the required shielding with a minimum additional weight is a very complex problem. Its solution entails taking into account both the interaction of protons with the shielding material and the formation of secondary radiation in it, as well as the interaction of protons and secondary particles with the biological tissue. These problems have still not been solved completely and therefore approximations must be used in the calculations. In addition, the selection of

materials will depend on the shielding arrangement, which in its turn is determined by the general construction of the spacecraft, by the possibility of utilizing equipment and supplies for the shielding, etc. When the outer layers of shielding material are selected, it is necessary to also take into account the relative radiation resistance of different materials, as well as certain other specific requirements. /202

In conclusion, it is necessary to check the irradiation dose for the cosmonaut for the specific shielding arrangement and spacecraft construction, and to determine the presence of leakage, weak spots, etc. In the present chapter, the basic problems connected with calculating the shielding from protons coming from solar flares in the inner zone of the earth are discussed. First, the method will be discussed for designing a shielding from high-energy protons, which is based on utilizing the range-energy relationships which were presented in the preceding chapter. This method can provide only approximate estimates for a shielding from high-energy protons, and - as will be shown below - requires significant refinements.

7.2. Method for Designing a Shielding on the Basis of Range-Energy Relationships

The range-energy relationships are usually used (Ref. 2 - 10, and others) in designing a protection from protons coming from solar flares in the inner zone of the earth. Let us examine this method in greater detail, since it facilitates a clarification of certain general rules for a shielding from protons, and makes it possible to obtain approximate estimates of radiation danger during spaceflights.

If the values for the proton ranges in different substances are used, which were presented in Table 6.9, it can be seen that the minimum range among these substances (g/cm^2) corresponds to carbon. A shielding made of carbon, however, does not always provide a minimum weight. Using the example of a spherical cabin, let us examine the dependence of shielding weight on proton energy for different cabin radii. Figure 7.1 presents these dependences for an inner cabin radius of $R = 50$ cm and 150 cm. The shielding thickness for each material (carbon, polyethylene, aluminum, and lead) is assumed to equal the proton range for a given energy; the magnitude of the range can be found from Table 6.9. For relatively small proton energies (less than 250 - 400 Mev for a radius $R = 50$ cm and less than 450 - 650 Mev for a radius $R = 150$ cm), the lowest shielding weight is provided by light materials. A material containing hydrogen - polyethylene - has a weight advantage

of up to 2-2.5 times, as compared with lead. The reverse is true for high-energy protons: heavy materials are more suitable, especially for small inner dimensions of the shielded region. Thus, for T_p = 1000 Mev, a lead shielding for R = 150 cm is 1.6 times lighter than a polyethylene shielding, and for R = 50 cm it is four times lighter.

If the fact is taken into account that the weight relationship of shielding made from different materials depends on the proton energy, it is necessary to examine the dependence of shielding weight /203 on the type of shielding material for real proton spectra in cosmic space. The weight dependences of spherical shielding shells made of different materials upon the proton dose rate at the center of a cavity having the diameters 1.83 and 3.66 m, respectively, for the proton spectrum from a solar flare on May 12, 1959 (33 hours after the flare began) (Ref. 5) are shown in Figure 7.2. For relatively small shielding thicknesses (a dose rate of more than 0.5 rad/hour for a sphere diameter of 1.83 m, and more than 0.1 rad/hour for 3.66 m), light substances - especially hydrogen - have a significant /204 advantage in the shielding weight. For large shielding thicknesses, heavy substances are more advantageous.

The weight dependence for a shielding made of different materials upon the nature of the original proton spectrum can be illustrated with the following example (Ref. 7). For solar flares with a relatively soft proton spectrum (Class A flares), the shielding thickness comprises 5 g/cm^2 of carbon and 8 g/cm^2 of tungsten alloy, which corresponds to a weight of 166 kg of carbon and 250 kg of tungsten alloy for a shielding in the form of a sphere, having an inner radius of 50 cm. Flares of the hard type (Class B) require a shielding thickness which equals 400 g/cm^2 carbon and 700 g/cm^2 tungsten alloy, which gives a total weight for the spherical shielding shell (R = 50 cm) of 106 tons carbon and 45 tons tungsten alloy.

This corroborates the conclusion which was made previously that it is more advantageous to use heavier materials for a spherical shielding from high-energy protons, from the point of view of the range-energy relationships. With a decrease in the inner radius of the shielded area, the weight advantage is more significant. It should be noted that this conclusion is not final. As was shown in the preceding chapter, the crux of the matter is that the outflow of secondary particles in elementary inelastic interaction between protons and nuclei is considerably greater for heavy elements than for a majority of light elements. Thus, the outflow of secondary particles increases significantly with an energy increase. The selection of shielding materials must thus be based not only on the range - energy relationships, but also the outflow of secondary particles from different shielding materials must be taken into account. This problem will be discussed separately below.

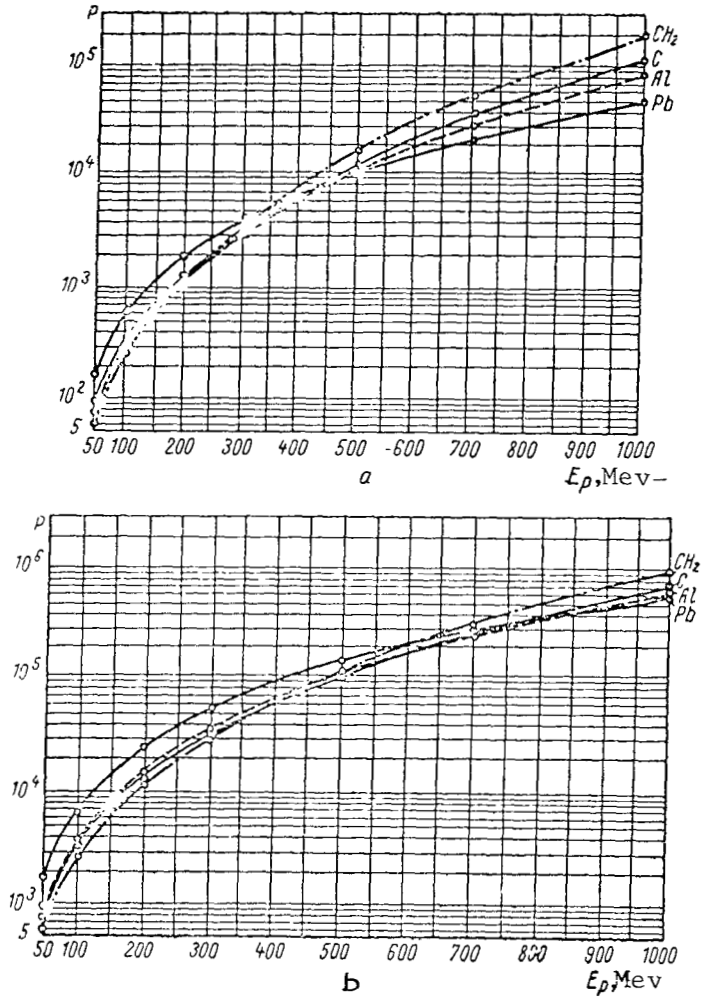

Figure 7.1

Weight of Spherical Shielding as a Function of Proton Energy for the Radius 50 cm (a) and 150 cm (b).

It is of interest to examine the manner in which the spectrum for protons, impacting on the shielding, changes as a function of its thickness. If we use δ to designate the shielding thickness and /205
$R(T_p)$ to designate the range of a proton having the initial energy T_p in the substance, we can then write

$$R(T_{p,\delta}) = R(T_{p,0}) - \delta, \qquad (7.1)$$

where $R(T_{p,\delta})$ is the so-called residual proton range - i.e., the range which corresponds to the proton energy $T_{p,\delta}$ after penetrating

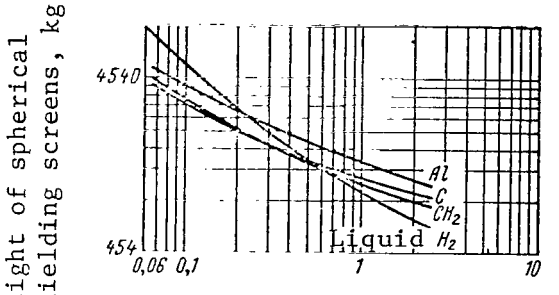

a

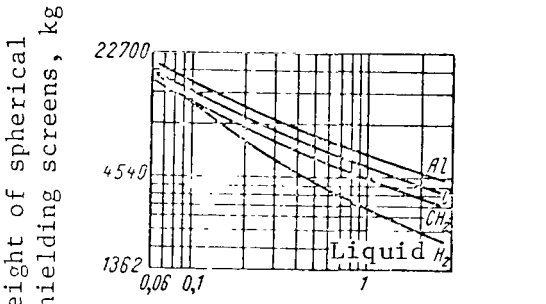

b

Figure 7.2

Weight of Spherical Shielding as the Function of Proton Dose Rate from Solar Flare on May 12, 1959, for a Sphere Diameter of 1.83 m (a) and 3.66 m (b).

the layer δ .

The dependence of range on proton energy can be approximated by a power function having the form

$$R(T_p) = KT_p^n, \tag{7.2}$$

where K and n depend on energy and on the atomic number Z of the shielding substance. Let us substitute the expression for $R(T_p)$ in formula (7.1)

$$K_\delta T_{p\delta}^{n\delta} = K_0 T_{p_{10}}^{n_0} - \delta. \tag{7.3}$$

Differentiating relationship (7.3), we obtain

$$dT_{p,\delta} = \frac{K_0 n_0 T_{p,0}^{n_0-1}}{K_\delta n_\delta T_{p,\delta}^{n\delta-1}} dE_0. \tag{7.4}$$

If a proton stream falls on the shielding with a spectrum having the form $N(T_{p,0})dT_{p,0}$, then the spectrum beyond the shielding δ - under the condition that the range for protons having the energy $T_{p,0}$ exceeds δ and that the scatter of the ranges can be disregarded - will have the form

$$N(T_{p,\delta})\,dT_{p,\delta} = N(T_{p,0})\,dT_{p,0} = N(T_{p,0})\,\frac{K_\delta n_\delta T_{p,\delta}}{K_0 n_0 T_{p,0}^{n_0-1}}\,dT_{p,\delta}. \quad (7.5)$$

In the energy region 40 - 1000 Mev, and for a shielding which is not too thick, the coefficients K and n are practically constant, so that we can assume

$$K_\delta n_\delta / K_0 n_0 \approx 1,$$

and the expression for the proton spectrum beyond the shielding will be

$$N(T_{p,\delta})\,dT_{p,\delta} \approx N(T_{p,0})\,\frac{T_{p,\delta}^{n-1}}{T_{p,0}^{n-1}}\,dT_{p,\delta}. \quad (7.6)$$

If the initial energy $T_{p,0}$ is such that $R(T_{p,0}) > \delta$, then the connection between $T_{p,\delta}$ and $T_{p,0}$ will have the form

$$T_{p,\delta} = T_{p,0} - \int_0^\delta \left(\frac{dE}{dx}\right)_{\text{ion}} dx. \quad (7.7)$$

Tabular values for the ranges $R(T_p)$ can also be used (see Table 6.9). In this case, the range $R(T_{p,0})$ is determined for a given value of $T_{p,0}$, and then the shielding thickness δ is subtracted from this quantity. The corresponding residual energy $T_{p,\delta}$ is determined for this remainder $R(T_\delta) = R(T_{p,0}) - \delta$ utilizing the tabular range values.

In formula (7.6), which connects the proton spectrum after the shielding with the original spectrum, the value for the coefficient n can be set equal to 1.81 for polyethylene, 1.77 for steel (Ref. 4), 1.70 for aluminum, and 1.72 for water (Ref. 2). The coefficient n decreases somewhat with an increase in the proton energy. However, the utilization of a constant value for this coefficient leads to a small error in the proton spectrum beyond the shielding and to a small exaggeration (on the order of several percent) in the radiation dose. /206

Figures 7.3 and 7.4 illustrate the spectra for protons beyond a shielding made of aluminum and water having a different

thickness (0.1 - 10 g/cm^2) for a spherical shielding shell (Ref. 2). Three types of original spectra are examined, the spectra for protons from solar flares on May 10, 1959 and February 23, 1956, and the proton spectrum of the inner zone of the earth (at a maximum). The solid curves correspond to exact numerical calculations, utilizing tabular range values; the dashed curves correspond to calculations based on an approximation of the range-energy relationship with a power function of the form (7.2). A comparison of these curves shows that this type of approximation yields results which are sufficiently close to the results derived from accurate calculations, and therefore is fully permissible.

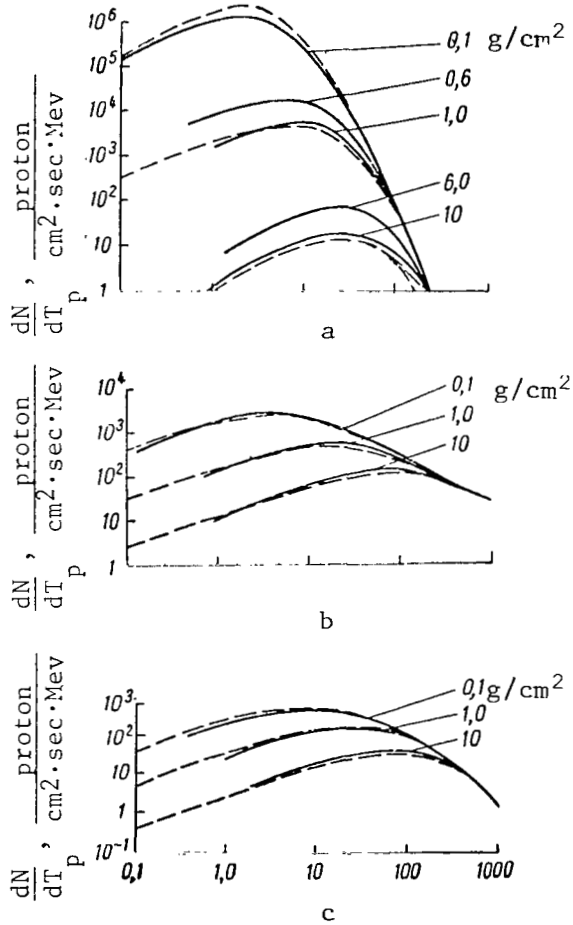

Figure 7.3

Spectrum for Protons from Solar Flares and the Inner Zone of the Earth Beyond Different Thicknesses of a Shielding made of Aluminum:

------- Calculation based on an approximate formula; ———— Accurate calculation; a - Solar flare on May 10, 1959; b - Solar flare on February 23, 1956; c - Maximum of the inner zone of the earth.

The form of the spectrum changes with an increase in the shielding thickness, with its soft part undergoing the greatest deformation. /207 As a result of this, the proton spectrum becomes harder as the shielding thickness increases, and the maximum is displaced toward the region of large energies. For a light shielding having a thickness of 10 g/cm^2 , the maximum was close to tens of mega-electronvolts for the solar flare on May 10, 1959, and about 100 Mev for the solar flare on February 23, 1956 and for the inner zone of the earth. If the proton spectrum change as a function of the shielding thickness is known, it is possible to determine the degree to which the radiation dose is attenuated in the shielding shell.

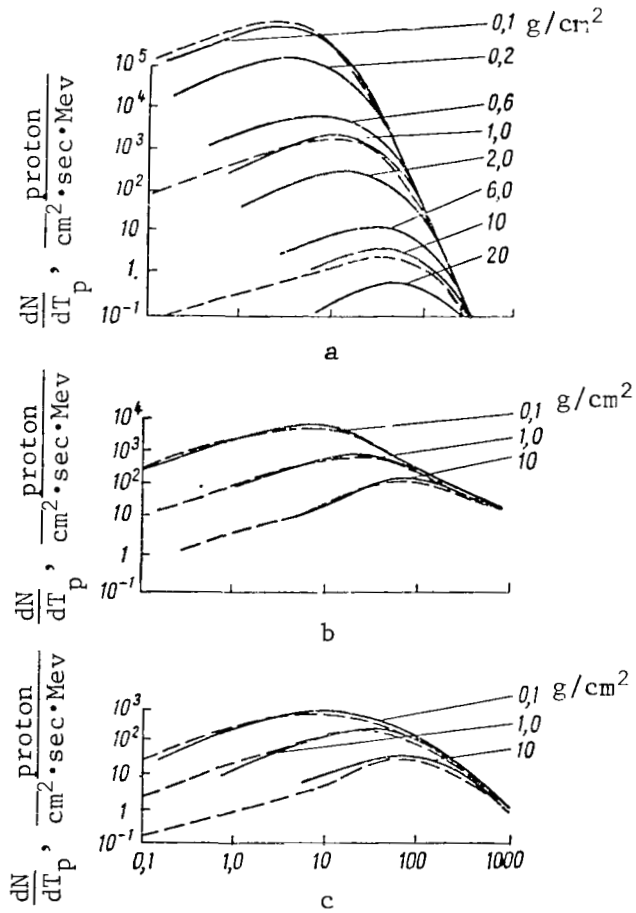

Figure 7.4

Spectrum for Protons from Solar Flares and the Inner Zone of the Earth Behind Different Thicknesses of Shielding Made of Water:

------ Calculation based on approximate formula; ———— Accurate calculations; a - Solar flare on May 10, 1959; b - Solar flare on February 23, 1956; c - Maximum of inner zone of the earth.

Let us examine (Ref. 2) the procedure to be followed in calculating the dose of protons from solar flares in the inner zone of the earth beyond a shielding made of aluminum and water. Let the surface of the shielding shell for the inhabited compartment of the spacecraft be given by the equation /208

$$r = G(\theta, \varphi), \tag{7.8}$$

where r, θ and φ represent the spherical coordinates with the origin joined to the center of the compartment. The number of protons dN (proton/cm^2·sec), having energies between T_p and $T_p + dT_p$, which move within the limits of the solid angle $d\Omega$ and which intersect a surface element of the shielding shell dA having the thickness $\delta(\theta, \varphi)$ - which is localized at the point r - is determined by the expression

$$dN = K(t)\, F(T_{p,\delta}, \delta)\, dT_{p,\delta}\, d\Omega, \tag{7.9}$$

where K(t) is the function which describes the change in the particle stream with time, and $F(T_{p,\delta}, \delta)$ represents the spectra proton distribution beyond a shielding having the thickness δ.

The differential dose rate, created by protons having energies from $T_{p,\delta}$ to $T_{p,\delta} + dT_{p,\delta}$, which penetrate a surface element of the shielding dA having the thickness $\delta(\theta,\varphi)$, is determined by the expression

$$dD = K(t)\, Q_p(T_{p,\delta})\, F(T_{p,\delta}, \delta)\, dT_\delta d\Omega, \tag{7.10}$$

where $Q_p(T_{p,\delta}) = 1.6\cdot10^{-8}\left(\frac{dE}{dx}\right)_{tis}$, rad·cm^2/proton represents the absorbed dose in tissue (rad), which corresponds to 1 proton/cm^2. Integrating expression (7.10) with respect to the shielding surface and with respect to the entire proton spectrum, for the dose rate within the inhabited compartment we obtain

$$D = 1{,}6\cdot10^{-8}K(t)\int_0^{T_{p,\delta}\max}\int_0^{\pi}\int_0^{2\pi} F(T_{p,\delta}, \delta)\cdot\left(\frac{dE}{dx}\right)^{\delta}_{tis}\sin\theta \times$$

$$\times \cos\theta\, dT_{p,\delta}\, d\theta\, d\varphi, \frac{\text{rad}}{\text{sec}}. \tag{7.11}$$

In order to determine the biological dose, it is necessary to take into account the relative biological effectiveness of protons behind the shielding, which - according to present opinions - depends on the magnitude of the linear energy losses $\left(\frac{dE}{dx}\right)$ in the tissue and the nature of the depth distribution of the absorbed dose in the body.

In this connection, the following relative biological effectiveness should be introduced in the integrand (7.11):

$$\eta = \eta\left[\left(\frac{dE}{dx}\right)^{\delta}\right] = \eta(T_{p,\delta}).$$

The final expression for the biological dose rate is /209

$$B = 1{,}6\cdot 10^{-8} K(t) \int_0^{T_{p,\delta\max}} \int_0^{\pi} \int_0^{2\pi} F(T_{p,\delta}, \delta)\left(\frac{dE}{dx}\right)^{\delta}_{\text{tis}} \times \eta(T_{p,\delta}) \sin\theta\cos\theta\, dT_{p,\delta}\, d\theta\, d\varphi, \cdot \frac{\text{rem}}{\text{sec}}. \quad (7.12)$$

The dose rates in the center of an aluminum spherical shell for different proton spectra:

$$dN = 0{,}256K(t)E^{-1{,}30}\, dE d\Omega$$
$$20 < E < 130\,\text{Mev}$$
$$dN = 0{,}786K(t)E^{-1{,}45}\, dE d\Omega$$
$$130 < E < 550\,\text{Mev}$$

which are calculated according to equation (7.12) (Ref. 2), are shown in Figure 7.5.

It should be noted that the dose rate, which is determined by equation (7.12), corresponds to the energy absorbed per unit of time in 1 g of tissue which is surrounded by air ("local" dose rate). This quantity can serve only for approximate estimates of the radiation action of protons beyond a shielding.

For small shielding thicknesses, the dose rate reached hundreds of thousands rem per 1 hour for the flare on May 10, 1959; for the flare on February 29, 1956 - almost a thousand rem per 1 hour; and for the proton zone - tens of rem per 1 hour. With an increase in the shielding thickness, the proton dose rate from the solar flare on May 10, 1959 dropped very rapidly: with a change from an aluminum thickness of $\delta = 0.1$ g/cm^2 to a thickness of $\delta = 1$ g/cm^2, the dose rate decreased by more than 1000 times. For an aluminum shielding thickness of $\delta = 10$ g/cm^2, the dose rate was about 1 rem/hour. Protons from the flare on February 23, 1956, and the inner zone were reduced in the shielding to a lesser extent, which was related to the harder proton spectrum. With a change from $\delta = 0.1$ g/cm^2 of aluminum to $\delta = 10$ g/cm^2, the dose rate decreased in all by only a few factors. For an aluminum thickness of $\delta = 10$ g/cm^2, the proton dose rate from the flare on February 23, 1956 was about 32 rem/hour, and from the inner zone - about 6 rem/hour. Even for a shielding thickness of $\delta = 100$ g/cm^2, the dose rate amounted to /210
12 rem/hour and 1 rem/hour for protons from the solar flare on February 23, 1956, and the inner zone of the earth, respectively.

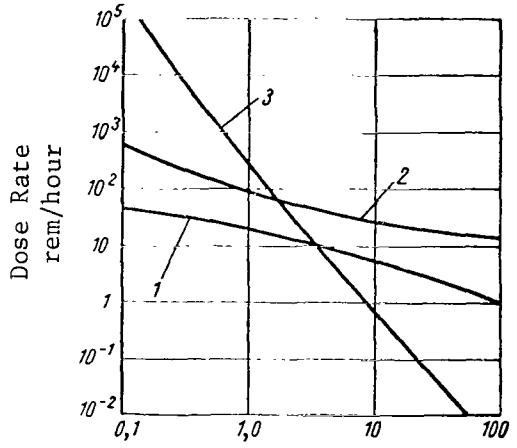

Figure 7.5

Radiation Dose Rate in the Center of a Spherical Shell made of Aluminum:

1 - Maximum of inner zone of the earth; 2 - Solar flare on February 23, 1956; 3 - Solar flare on May 10, 1959.

Integrating expression (7.12) with respect to the flight time of a spacecraft along a definite trajectory, one can obtain the total radiation dose. The total radiation doses during the flight (Ref. 2) are calculated as a function of the thickness of an aluminum shell, and the following assumptions are made in the calculations:

1) The proton stream during the solar flare on May 10, 1959, was kept at the level of maximum intensity for 30 hours;

2) The proton stream during the solar flare on February 23, 1956, decreased according to the law t^{-2} ;

3) The proton stream in the inner zone of the earth influences the spacecraft for 1 hour at a level of maximum intensity.

The local radiation dose in the center of a spherical shell does thus not exceed 10 rem for the inner zone (Figure 7.6). Because it takes the spacecraft about 5 - 15 minutes to cross this zone of the earth, and since only a small portion of this time will occur in the region with maximum intensity, the radiation dose will be small. However, if spacecrafts and artificial earth satellites remain for a /211 long period of time on orbits close to the intensity maximum of the

inner zone, substantial shielding thicknesses will be required (Ref. 2). Thus, in order to make sure that the total radiation dose is not greater than 1 rem for a 1-hour flight along these orbits, a shielding of about 100 g/cm^2 of aluminum is required (Ref. 2).

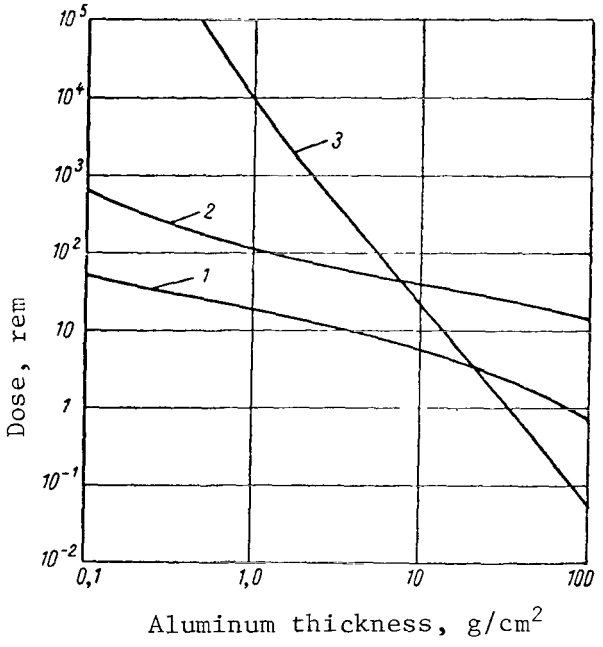

Figure 7.6

Radiation Dose in the Center of a Spherical Shell made of Aluminum:

1 - Maximum of the Inner Zone of the Earth; 2 - Solar Flare on February 23, 1956; 3 - Solar Flare on May 10, 1959.

Radiation doses which are produced by solar flares are rather large, especially for small shielding thicknesses (see Figure 7.6). For a shielding thickness of about 2 - 3 g/cm^2 , the proton dose for solar flares on May 10, 1959, and February 23, 1956, was about 100 - 1000 rem (Ref.2).

Thus, an estimate of the radiation danger on the basis of local doses leads to the conclusion that a shielding on the order of tens, and even hundreds, of grams per 1 cm^2 is required to shield the cosmonaut from protons coming from solar flares and the inner zone of the earth.

Let us further examine the basic drawbacks of this method for

designing a shielding from protons. The original premise of this method consists of the assumption that the dose beyond the thickness of the shielding, which equals the range of incident protons, equals zero. The meaning of proton range should be pointed out here. The proton range, which is determined by the equation

$$R = -\int_0^{T_p} \left(\frac{dE}{dx}\right)^{-1} dT_p,$$

is the mean range due to fluctuations in ionization losses - i.e., half of the protons traverse a path in the substance which is larger than R, and half - less than R. Thus, the assertion that the dose beyond a thickness which equals the range is equal to zero cannot be regarded as correct.

We shall try to estimate the dose of proton radiation beyond a shielding thickness which equals the mean range. In the general case, the fact must be taken into account that - due to multiple scattering - the mean range of a proton in the shielding does not coincide with the distance R* between the plane at which the bundle enters the shielding and the plane through which half of the initial proton stream passes. It is clear that R* is less than the mean range R . Let us determine this effect approximately (Ref. 11). Let us divide the range R into a large number of small lengths l_i, which make up the angle θ_i with the direction of the incident bundle. We then have

$$R = \sum_{i=1}^{n} l_i \text{ and } R^* = \sum_{i=1}^{n} l_i \cos\theta_i.$$

If θ are sufficiently small, then

$$R - R^* \approx \frac{1}{2}\sum_{i=1}^{n} l_i\theta_i^2 \approx \frac{zm_e}{2m_p}\int_0^R \lg \frac{T_{p,0}}{T_p(x)}\, dx.$$

If we utilize the approximate relationship /212

$$R \approx T_p^{1,75},$$

we then obtain

$$(R-R^*)/R \approx \frac{Z}{6{\cdot}400}.$$

It can be seen that multiple scattering does not lead to a significant difference between R* and R . Consequently, if the shielding thickness equals the mean proton range, then practically half of the initial proton bundle - which impacts on the shielding in a normal direction - enters the shielded region. In order to estimate the dose caused by these protons, let us utilize the results which are given in work

(Ref. 11), which pertain to a proton energy of 340 Mev. It follows from the results derived in this work that the dose of protons beyond a shielding thickness which equals R* amounts to 82% of the dose at the Bragg maximum, which, in its turn, can considerably exceed (up to 1.5 - 2 times) the initial proton dose.

Thus, the utilization of the range-energy relationship in designing shielding from protons can lead to a definite underestimation of the dose beyond the shielding. In this connection, in shielding designs it is necessary to utilize more comprehensive data on the penetration of protons through the shielding substance. Such data, obtained experimentally, are given in the following chapter, where a quantitative estimate of the error involved in utilizing the range-energy relationship for shielding designs is presented.

The fact that these results pertain to the local absorbed dose in tissue, or in a tissue-equivalent material, represents a subsequent disadvantage, which significantly reduces the value of the results obtained in shielding designs based on the range-energy relationships (Ref. 2 - Ref. 10). A calculation of the mean tissue doses and the depth distribution of the absorbed dose in the human body is more correct. These two approaches provide essentially different results, which can be illustrated with calculations (Ref. 4) whose results are given in Table 7.1.

The dose rate on the surface of the body was calculated under the assumption that the body completely screens half of the non-directional proton stream. The dose rate in the center of the body was calculated by taking into account the attenuation of the proton stream in tissue. Although these results do not give a comprehensive idea of the depth distribution of the absorbed dose in the body, they can still be utilized for qualitative estimates as to the role of the depth distribution, whose nature is essentially dependent on the shielding thickness. For small shielding thicknesses, the depth distribution has a clearly-expressed drop from the surface to the center of the body. For large thicknesses, the absorbed dose within the limits of the body changes very slightly (Ref. 12). This is connected with the ruggedization of the proton spectrum with /213
an increase in the shielding thickness. The conclusion, which can be drawn on the basis of data presented in Table 7.1, consists of the fact that the local absorbed dose cannot serve as a criterion for designing a shielding.

7.3. Experimental Data on the Penetration of Protons Through a Shielding

The preceding chapter discussed a method for designing shielding from protons coming from the inner zone of the earth and from solar

TABLE 7.1

DOSE RATE BEHIND DIFFERENT SHIELDING LAYERS FOR PROTONS FROM THE INNER ZONE OF THE EARTH ($2 \cdot 10^4$ proton/cm^2·sec)

Shielding Thickness, cm		Dose Rate rem/hr.			Shielding Thickness cm		Dose Rate rem/hr		
Steel	Polyethylene	Local	On the body surface	In the center of the body	Steel	Local Polyethylene	Local Polyethylene	On the body surface	In the center of the body
0.0	0.0	440.0	220.0	7.0	0.10	1.25	45.0	22.5	6.1
0.0	2.5	60.0	30.0	6.7	0.10	2.5	30.0	15.0	5.7
0.0	5.0	34.0	17.0	5.8	0.10	5.0	20.0	10.0	4.8
0.0	10.0	16.6	8.3	4.5	0.10	10.0	10.4	5.2	3.6
0.0	20.0	7.6	3.8	3.5	0.10	16.0	4.8	2.4	2.2
0.10	0.0	170.0	85.0	6.6	0.25	0.0	50.0	25.0	6.7

flares; this method was based on the range-energy relationship, and the necessity of including experimental data on the penetration of protons through the shielding was indicated. For this purpose, model experiments were carried out on a synchrocyclotron belonging to the Joint Institute for Nuclear Research (JINR). The characteristics of the proton bundle developed by the JINR cyclotron made it possible to form a model of the most important part of the energy spectrum for protons from the inner zone of the earth and solar flares. The accelerator emitted a narrow proton bundle having a diameter of 8 cm at a distance of 7 m from the output aperture, having a dispersion of about 40'. The total proton stream in the bundle amounted to $(1 - 4) \cdot 10^{11}$ proton/sec. The proton energy spectrum was distinguished by a high energy homogeneity: ±3 Mev for a mean proton energy of about 660 Mev (Ref. 13). The frequency of the acceleration cycles in the synchrocyclotron was 100 cycles. The duration of the proton momentum was about 500 microseconds. Due to the fact that protons having different angular and energy distributions will be encountered in cosmic space, model studies must make it possible to investigate a shielding from a wide parallel bundle of monoenergetic protons for different bundle energies and angles of incidence on the shielding.

The basic methodological problems involved in utilizing a /214
proton bundle from a synchrocyclotron can be reduced to simulating a

wide proton bundle with a narrow bundle, to determining the role of inclined bundle incidence on the shielding, to estimating the contribution made by secondary radiation found in the shielding, and to obtaining monoenergetic proton bundles having differing energy in the 50 - 700 Mev region (Ref. 14).

The reasoning developed for the problem of γ-ray penetration through matter (Ref. 15) can be used to simulate a wide monodirectional bundle of protons. As can be seen from Figure 7.7, protons from a narrow bundle, which arrive at the detectors located at points A_0, A_1, D_2 ... etc., correspond unequivocally to each proton in the narrow bundle which enters the detector A . The angles of deflection and the paths traversed in the shielding before and after the interaction are identical for these protons. It can also be seen that the conditions under which the shielding is penetrated by protons, which are not scattered, are identical in both cases.

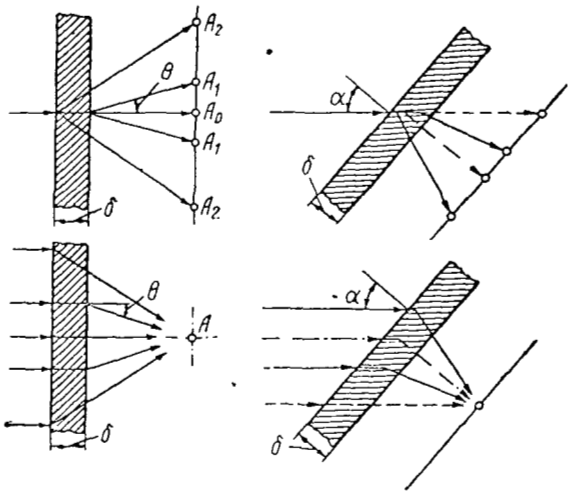

Figure 7.7

Diagram for the Conversion from a Narrow Bundle to a Wide Bundle.

Thus, if a narrow bundle is used to measure the absorbed radiation dose not only at the point A_0, but at a sufficient number of other points which are located in a plane parallel to the shielding itself, then on the basis of these data it is possible to obtain complete information regarding the attenuation of a wide parallel proton bundle in the shielding.

As was indicated in the preceding chapter, when protons penetrate the shielding, they lose their energy in collisions with atom electrons

(ionization losses), and they experience elastic (Coulomb and diffraction) scattering and inelastic interaction with nuclei of the substance. As the result, there is a gradual decrease in the proton energy, a deviation from the direction of initial motion, partial absorption of the proton bundle by nuclei of the substance, and the formation of secondary particles in the shielding. If this is taken into account, the integral absorbed dose rate Q(g·rad/sec) in a thin layer having the thickness d_0(g/cm^2), which is parallel to the shielding plane on which the narrow proton bundle falls in a normal direction, can be determined by the expression

$$Q = 2\pi K \Pi N d_0 \int_0^{\delta} dy \int_0^{\pi/2} e^{-\sigma_a y} \frac{d\sigma(\theta, y, T_p)}{a\Omega} S(\theta, y, T_p) \times \times \left(-\frac{\overline{dE}}{dx}\right)_{\theta, y} \operatorname{tg}\theta \, d\theta, \qquad (7.13)$$

where Π is the total proton stream in the bundle, proton/sec; K - the conversion factor; N - the number of atoms per 1 g of shielding substance; y - the distance in the shielding which is measured from the location of the bundle output; δ - shielding thickness, g/cm^2; σ - cross-section of inelastic interaction between protons and the shielding substance; $\frac{d\sigma(\theta, y, T_p)}{d\Omega}$ - effective differential cross-section which takes into account all processes involved in the elastic scattering of protons and the shielding substance; $S(\theta, y, T_p)$ - the dosage contribution of secondary particles formed in the shielding during nuclear proton interactions; $\left(-\frac{dE}{dx}\right)_{\theta, y}$ - the mass energy losses of protons, averaged for protons which are scattered at the angle θ, Mev·cm^2/g.

In addition, let us examine the case when a wide proton bundle, having the stream density Φ(proton/cm^2·sec) falls on the shielding in a normal direction. In this case, the absorbed dose rate D (rad/sec) beyond the shielding is

$$D = 2\pi K \Phi N \int_0^{\sigma} dy \int_0^{\pi/2} e^{-\sigma_a y} \frac{d\sigma(\theta, y, T_p)}{a\Omega} S(\theta, y, T_p) \times \times \left(-\frac{\overline{dE}}{dx}\right)_{\theta, y} \operatorname{tg}\theta \, d\theta. \qquad (7.14)$$

In a determination of the integral absorbed dose rate Q for a narrow bundle and the absorbed dose rate D for a wide bundle, the basic difficulties which are encountered are related to determining the

functions

$$\frac{d\sigma(\theta, u, T_p)}{d\Omega} \text{ and } S(\theta, y, T_p).$$

However, from the point of view of the procedure entailed in an experimental study of the shielding properties of the materials for a proton bundle from the synchrocyclotron, it is sufficient that these functions are identical in both of the cases under consideration. Thus, we obtain the following from expressions (7.13) and (7.14):

$$\frac{D}{\Phi} = \frac{Q}{\Pi d_0} = q, \tag{7.15}$$

i.e., the absorbed dose rate per one proton stream in a wide bundle equals the integral absorbed dose rate per one proton stream in a narrow bundle, which is transmitted by a layer of substance having the thickness of 1 g/cm^2. From this point on, we shall use the quantity q to designate the specific absorbed dose. It follows from relationship (7.15) that $D = q\Phi$. On the other hand, the absorbed dose rate D from a wide proton bundle having the stream density Φ, which is formed beyond a shielding layer having the thickness δ, can be written in the form

$$D = q_0 f(\delta, E_0)\Phi, \tag{7.16}$$

where $f(\delta, E_0)$ is the dosage factor of attenuation and buildup; the index "0" refers to a proton bundle before the shielding. It is apparent that

$$q = q_0 f(\delta, E_0). \tag{7.17}$$

In measurements with a narrow bundle, we have

$$f = \frac{Q(\delta)}{Q(0)},$$

where $Q(0)$ and $Q(\delta)$ are the integral absorbed dose rate in the absence of shielding, and beyond shielding having a thickness δ, respectively.

A study of a shielding from a wide proton bundle can be reduced to an experimental determination of q or Q. As follows from formula (7.13), in order to determine Q it is necessary to perform integration with respect to the detector volume, which is parallel to the shielding layer. Integration can also be performed experimentally by spacing out a sufficient number of recorders - dosimeters, and by totalling their readings. This method is advantageous due to the fact that the errors arising from the finite dimensions of the surface on which the detectors are located can be determined by the ratio of the readings given by the outermost detectors to the readings given by

detectors located in the center of the dosage field. The distribution of the absorbed dose behind the shielding, in a plane which is perpendicular to the bundle, is determined experimentally up to large distances from the bundle axis. The error which is estimated in this way, during measurements with detectors which are located at selected distances from the axis, does not exceed 5%.

Another method for determining Q is based on utilizing dosimeters with a rather large surface - for example, flat cells with a solution of Mohr's salt. The advantage of these dosimeters lies in the measurement simplicity. In addition, a chemical dosimeter differs very little from water in terms of composition. Therefore, the absorption of different types of radiation and energy occurs by means of interaction processes which are similar to the processes occurring in tissue or in liquids of the organism. In this connection, this type of dosimeter has a slight "hard behavior".

When an investigation is made of the inclined incidence of a wide proton bundle behind the shielding, it is also possible to utilize the dosage factor of attenuation and buildup, which - by analogy with the case of normal incidence - can be written in the form /217

$$f_\alpha(\delta_0 E_0) = \frac{Q_\alpha(\delta)}{Q_\alpha(0)}.$$

$Q_\alpha(0)$ and $Q_\alpha(\delta)$ represent the integral absorbed dose rate from a narrow bundle without a shielding, and behind a shielding having the thickness δ, which is located at the angle α toward the direction of the proton bundle (Figure 7.7). $Q_\alpha(\delta)$ is measured in the plane which is parallel to the shielding.

Let us deal with the problem of obtaining proton bundles having lower energies. Protons from a synchrocyclotron penetrate an absorber made of polyethylene, in which they lose part of their energy. The absorber thickness was selected in accordance with the data given in the work (Ref. 13). In order to improve the energy homogeneity of the bundle and to purify it from secondary radiation emanating from the absorber, the bundle was deflected by a magnet and passed through a collimator behind a shielding wall of three meters. The magnitude of the neutron stream was determined by comparing the readings from detectors which had essentially different sensitivity to neutrons and protons. For this purpose, detectors were utilized which measured the absorbed energy - such as chemical dosimeters, the luminescent dosimeter (ILC), and the thermoluminescent dosimeter made of glass (IKS) - and also indicators made of carbon and aluminum, which recorded the neutrons and protons with the aid of the reactions:

$$C\,(p, pn)C^{11};\quad Al\,(p, 3pn)Na^{24},$$
$$C\,(n, 2n)C^{11};\quad Al\,(n, \alpha)Na^{24}$$

As the experimental test showed, the sensitivity of the ILC and the IKS dosimeters to neutrons was more than one order of magnitude less than the sensitivity to protons. By comparing the reading from dosage detectors (chemical, ILC , and IKS) and from stream indicators (C and Al), it was found that the admixture of a neutron stream in the bundle coming from the collimator did not exceed 5 - 6% in the proton energy region of 100 -600 Mev. Consequently, the utilization of the method by which the proton energy was discarded made it possible to obtain a fairly pure proton radiation.

The proton energy behind the absorber was determined by magnetic analysis and with the aid of the range-energy relationship in lead and aluminum. The divergence between these two methods in the determination of energy did not exceed 6%.

The shielding properties of several materials (polyethylene, polycarbonate, polyvinylchloride, glass textolite, aluminum, lead, and others) were investigated in model studies on a proton bundle. The basic characteristics of these materials are presented in Table 7.2. Out of these materials, polyethylene has the largest hydrogen content and, consequently, the largest ionization losses. On the basis of its shielding properties, polyethylene is quite similar to water, and also liquid rocket fuel. This fact is very important, /218 because the water and fuel reserves can be used as shielding elements. Plastics and aluminum represent light materials which have good construction qualities.

Figure 7.8 presents the conditions for the described experiments. The proton bundle passed through the collimator having a diameter of 2 cm; then through the ionization chamber-monitor 6, and fell on the absorber layer 7 in a normal direction. The detector 8 was located close to the material being studied, whose thickness was increased from the end of the collimator. Luminescent and chemical dosimeters, as well as ionization chambers, were used as the detector for measuring the integral absorbed dose behind the shielding. The readings from the luminescent and chemical /219 dosimeters gave an averaged absorbed dose. Therefore, in order to obtain $Q(\delta)$, they were multiplied by the effective surface of the dosimeter cross-section. For measurements of $Q(\delta)$ with the aid of luminescent dosimeters, the latter were located close to each other on a surface of 40 x 30 cm^2.

A sectional chamber with a narrow output aperture (about 3.8 mg/cm^2, which corresponds to the proton range with energies of approximately 1.4 Mev) was utilized as the ionization chamber. The chamber was filled with a mixture of gases (35% argon and 65% helium, by weight), which made it possible to obtain the dependence of the chamber sensitivity on the proton energy, which was analogous to the dependence

TABLE 7.2

BASIC CHARACTERISTICS OF SHIELDING MATERIALS STUDIED /218

Material	Chemical Formula	Density g/cm^2	Composition of Material, % (by Weight)
Polyethylene	(CH_2)	0.94	C 85.6 H 14.4
Polycarbonate	$(C_{16}O_3H_{14})$	1.2	C 75.53 O 18.96 H 5.51
Polyvinylchloride	(C_2H_3Cl)	1.4	C 38.4 H 4.8 Cl 56.8
Glass Textolite on an EDF-6 resin base	-	1.8	O 37.5 Si 17.0 Al 1.78 Ba 15.9 Zn 2.72 B 3.22 C 20.1 H 1.78
Fibrous wire glass material (FWGM)		2.0	O 39.8 Si 19.62 Al 2.03 Ba 17.3 Zn 2.95 B 3.5 C 13.6 H 1.2
A-3 Aluminum	Al	2.7	not less than 98.0 Al
S-2 Lead	Pb	11.37	not less than 99.95 Pb

of ionization losses in tissue on the proton energy. With the aid of /219 this chamber, the dependence of the absorbed tissue dose on the shielding thickness was measured. The results derived from the experiments are shown in Figure 7.9, where the dependence of the factor of attenuation and buildup of the dose, in a wide proton bundle $f(\delta)$, on the shielding thickness δ is given.

The curves for the attenuation and buildup of the proton dose in different materials, in the energy region of 130 and 280 Mev, are similar to the classical curve given by Bragg. The gradual rise of the curve with an increase in the shielding layer thickness can be explained by an increase of the ionization losses as the protons are damped; the sharp drop beyond the maximum can be explained by the protons being stopped with a total loss of kinetic energy. For high-energy protons, the buildup of secondary radiation in the shielding - which is produced during inelastic nuclear interactions - is characteristic. As a result of the buildup of secondary radiation, a flat maximum is formed on the dependence curve $f = f(\delta)$

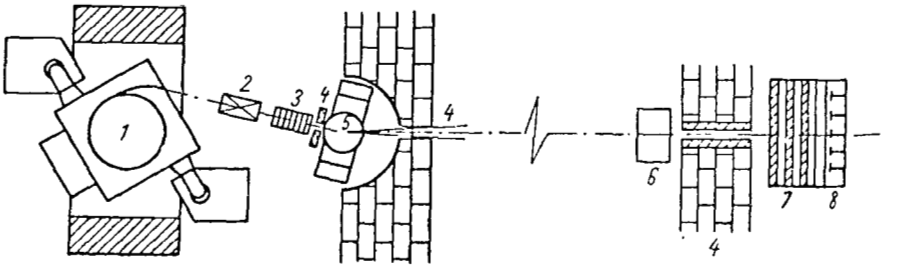

/218

Figure 7.8

Diagram of Model Experiments on a Shielding:

1 - Synchrocyclotron; 2 - Focusing Lens; 3 - Polyethylene Absorber; 4 - Collimator; 5 - Deflecting Magnet; 6- Ionization Chamber-Monitor; 7 - Material being Studied; 8 - Detector.

for a shielding thickness of about 10 - 20 g/cm^2; this maximum /219
indicates that there is equilibrium between the secondary radiation and the primary protons. It should be noted that the buildup of secondary radiation due to inelastic nuclear interactions becomes more significant with an increase in proton energy, and the Bragg maximum at the end of the range is more diffuse.

The form of the curve $f(\delta)$ for a wide proton bundle depends slightly on the shielding material. However, due to the difference in ionization losses, the shielding properties of the materials are not identical. Thus, for protons having an energy of 130 Mev, the absorbed dose behind a shielding made of polyethylene decreases almost to zero behind a layer of $\delta = 16.5$ g/cm^2, while in the case of lead the thickness of this layer is $\delta = 36$ g/cm^2.

Thus, in the given case the weight of a flat lead shielding is significantly greater than that of polyethylene. At the same time, for shielding thicknesses which are less than the mean range for protons having a given energy, the polyethylene shielding can be more effective than lead. Thus, for a shielding thickness of 8 g/cm^2, the dose behind a polyethylene shielding will be 1.3 times greater than behind lead. This must be taken into account when designing a shielding from proton radiation. For higher proton energies, the difference in the shielding properties of the materials is related to the buildup of secondary particles, which /221
are formed during nuclear interactions of primary protons with the shielding substance.

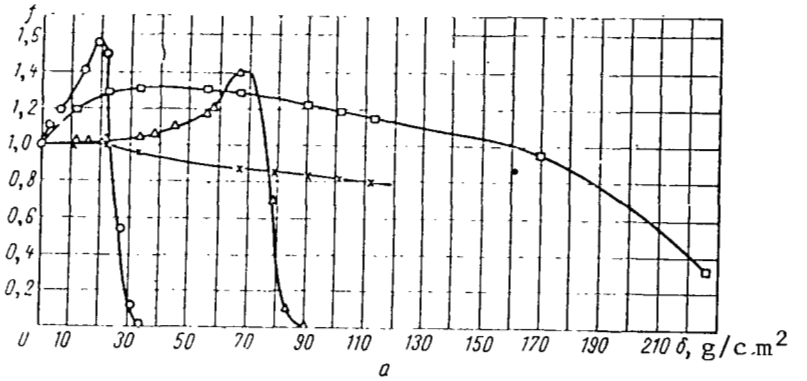

a

/220

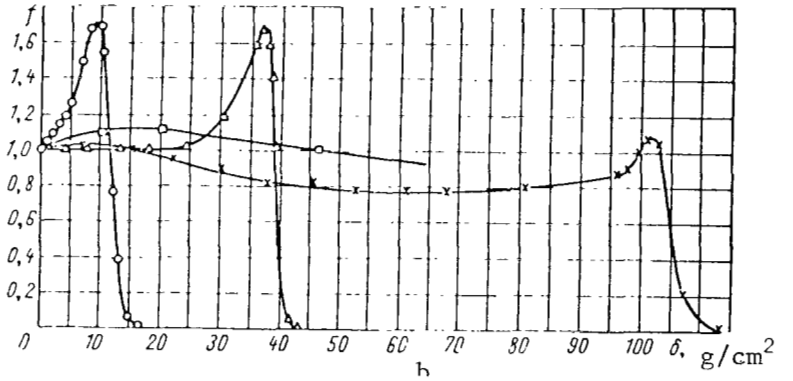

b

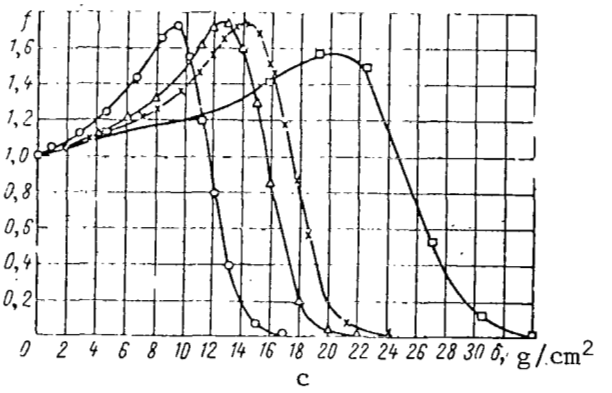

c

Figure 7.9

Attenuation of Tissue Proton Dose in the Shielding:

a - Lead(o - 130 Mev; Δ - 280 Mev; × - 405 Mev; □ - 660 Mev);
b - CH_2 (see a); c - For Incident Proton Energy of 130 Mev; (o - Polyethylene; Δ - Carbon; × - Aluminum; □ - Lead).

In conclusion, let us compare the values for the mean ranges R /221 with the experimental data on the shielding thickness, which

correspond to different ratios for the dose behind a shielding and without a shielding (Table 7.3).

TABLE 7.3

SHIELDING THICKNESSES WHICH CORRESPOND TO DIFFERENT VALUES OF THE FACTOR FOR ATTENUATION AND BUILDUP OF DOSE f(δ)

Shielding Material	Energy T_p min, Mev	R, g/cm^2	Shielding Thickness, corresponding to a Dose of 82% of the Maximum, g/cm^2	Shielding Thickness, Corresponding to a given Value of f, g/cm^2		
				0.5	0.1	0.01
Polyethylene	130	11.3	11	12.5	15	18
	250	36.0	32	39.0	41	43
	405	93.0	103	105.0	110	115
Aluminum	130	15.9	16	18.8	21	24
	250	48.6	--	--	--	--
	400	105.0	--	--	--	--
Lead	130	26.8	24	27.0	31	34
	250	79.6	70	79.0	85	90
	405	94.0	--	--	--	--

On the basis of the data presented in the Table, the conclusion can be drawn that the method for designing a proton shielding using the range-energy relationship needs to have significant refinements with respect to the experimental data.

7.4. Experimental Data on the Outflow of Neutrons from a Shielding

Neutrons predominate among the secondary particles which are formed as a result of nuclear interactions between protons and the shielding substance (Ref. 2). The formation of neutrons in elementary inelastic interaction between protons and nuclei of the substance was examined in the preceding Chapter. However, this information cannot be used directly in designing shieldings, due to the fact that it is necessary to know the spectral-angular distributions of the particles formed in calculating the outflow of neutrons from a shielding. Very few data of this type are available. Theoretical data on the formation of neutrons in elementary inelastic interactions do not encompass a sufficiently wide range of materials and proton energies. Therefore,

it is interesting to include experimental data on the outflow of neutrons from thick targets. The results derived from measuring neutron outflows from thick targets, which were bombarded by protons, are given in several works (Ref. 16 - 23).

In the region of comparatively small proton energies (up to 32 Mev), the outflow of neutrons from thick targets has been studied for a large number of elements (Ref. 22). The total neutron stream, emerging from a target, was determined by measuring the activation of a $MnSO_4$ solution, which occupied a tank of 1 x 1 x 1 m and which surrounded a cavity in which the target was placed.

The outflow of neutrons was determined for three cases: the total braking of protons having an energy of 32 Mev; the braking of protons having energies from 32 Mev to 18 Mev; and the total braking of protons having an energy of 18 Mev. Table 7.4 presents the results derived from the measurements. We should note that the outflow values presented in this Table provide the total number of neutrons escaping from the target on all sides.

The neutron outflow depends essentially on the type of target nucleus, and this dependence is not monotonic. When materials for a proton shielding are being chosen, it should be noted that the outflow of secondary neutrons is at a minimum for several materials. These include carbon, silicon, sulfur, and calcium. Thus, for carbon the neutron outflow amounts to $0.567 \cdot 10^{10}$ neutron/millimicron - i.e., approximately one neutron per 1000 protons falling on the target with an energy of 32 Mev. For calcium, this quantity is of the same order of magnitude, while for silicon and sulfur it is approximately twice as large. We should also note that for all primary elements, which constitute biological tissue, the outflow of secondary neutrons is comparatively small: about 1 - 4 neutrons per 1000 incident protons. At the same time, for several light elements which are suitable (from the point of view of the range-energy ratio) for use as shielding materials, the outflow of secondary neutrons is fairly large. These elements include, for example, beryllium, for which the outflow of secondary neutrons is about 30 per 1000 incident protons - i.e., 30 times greater than for carbon. For a majority of medium-weight and heavy elements, the outflow of secondary neutrons ranges from 10 to 20 neutrons per 1000 protons.

It is apparent that the experimental data which have been presented on the outflow of secondary neutrons must be taken into account when choosing proton shielding materials and when designing shieldings. It should also be noted that the outflow of secondary protons decreases considerably with an increase in the incident proton energy. Thus, for incident protons having an energy of 18 Mev, the outflow of secondary neutrons decreases for beryllium by a factor of 2.5; for aluminum, by a factor of 7; for silicon, by a factor of 10, etc. Secondary

neutrons are not present in carbon, for impacting proton energies which are less than 18 Mev. This fact is very important, because a significant part of the spectrum for protons from the inner radiation zone of the earth and from solar flares falls in the energy region which is less than 18 - 20 Mev. Since the proton ranges at such energies are small, for a shielding thickness of more than 1.0 - 2.0 g/cm^2, the radiation dose behind the shielding will be entirely caused by secondary particles which are formed in the shielding.

It should be noted that, since the proton spectrum of the /224
inner radiation zone of the earth extends up to several hundreds of megaelectronvolts - and in the case of solar flares, up to several thousands of megaelectronvolts - it is extremely important to have experimental information on the outflow of secondary particles also for protons, having energies on the order of hundreds of megaelectronvolts and higher. Unfortunately, experimental data on the outflow of secondary neutrons from targets, which are bombarded with protons having energies of about 100 Mev and higher, are restricted both with respect to the proton energy region, and with respect to the selection of target materials - particularly light elements. Detailed information on the outflow of secondary neutrons from targets which are bombarded with protons, having energies of 250 - 900 Mev, is given in another work (Ref. 23), although the outflow of neutrons from only heavy elements was studied in it (tin, tungsten, lead, and uranium). This type of data can be useful for planning shielding from protons. The crux of the matter is that in several cases (for example, radiation shelter having a small inner volume) the heavy materials are preferable to the light ones. Therefore, it is necessary to know the neutron outflow for such materials (Ref. 7).

With the aid of a selector, in the form of a telescope of Geiger, scintillation, and Cherenkov counters, groups of protons were selected from primary cosmic radiation which had mean energies of 300, 415, 560, 690, and 820 Mev (Ref. 23). In order to record neutrons coming from the target (22 - 44 g/cm^2), boron counters were used, which were located in a paraffin moderator, in the form of a vat with a side of about 120cm. The mean number of neutrons which were formed in a target of unit thickness (1 g/cm^2) was determined per one incident proton (Table 7.5) (Ref. 23).

Comparing the results derived from measurements for different target thicknesses (Pb or U), which pertain to 1 g/cm^2, we can see that the values for different thicknesses are close to each other. The existing difference can be caused by dissimilar absorption of an incident proton bundle (it leads to a decrease in the neutron outflow from thicker targets), and also by nuclear interactions of /225

TABLE 7.4

NEUTRON OUTFLOW FROM THICK TARGETS, BOMBARDED BY PROTONS (IN UNITS OF 10^{10} neutron/microcoulomb) /223

Target[1]	Proton Energy Interval[2], Mev		
	0—32	0—18	18—32
D(D_2O)	17,8± 1,2	4,78± 0,99	—
Li	9,69	3,16± 0,20	—
Be	17,70	6,95	,46
B	4,21	1,14± 0,10	—
C (also CH_2)	0,567± 0,037	0	0,567± 0,037
N (BN)	1,98± 0,33	0± 0,07	—
O (H_2O)	1,30± 0,08	0,08± 0,06	—
F (NaF)	4,15± 0,5	0,96± 0,17	—
Na	3,81	0,51± 0,07	—
Mg	1,98	0,25± 0,08	1,74± 0,10
Al	3,16	0,46± 0,06	2,64
Si	0,98	0,10± 0,06	—
P	2,44	0,35± 0,06	—
S	1,07± 0,10	0,008± 0,05	—
Cl (CCl_4)	3,74± 0,19	0,52± 0,10	—
K (K_2SO_4 & KCl)	1,46± 0,15	0± 0,26	—
Ca (CaO)	0,51± 0,08	0± 0,13	—
Sc_2O_3	6,34± 0,49	1,09± 0,17	—
Ti (also TiO_2)	7,61	1,76± 0,13	7,10
V	9,24	2,30± 0,15	—
Cr	6,69± 0,44	1,26± 0,16	—
Mn	7,16	1,27± 0,11	—
Fe	6,00	1,00± 0,09	4,78
Co (Co_2O_3)	8,20± 0,50	1,62± 0,18	—
Ni	3,06	0,32± 0,06	2,68
Cu	8,30	1,71± 0,12	6,45
Zn	7,16	1,32± 0,11	5,85
Zr	11,0	1,67± 0,13	8,67
Nb	11,5	—	—
Mo	11,5	2,02± 0,13	9,80
Ag	12,2	2,10± 0,15	9,65
Cd	12,8	2,14± 0,15	10,5
Sn	12,1	1,94± 0,19	10,0
Ta	12,6	1,40± 0,23	10,4
W	12,5	1,30± 0,19	10,2
Pt	11,4	1,11± 0,10	9,26
Au	10,8	1,05± 0,09	9,48
Hg (HgO)	10,1	0,86± 0,09	—
Pb	10,0	0,85± 0,09	9,15
U	23,3	2,28± 0,15	18,0

[1] In those cases where the neutron outflow was determined for a given element on the basis of measurements for a compound, the corresponding compound is indicated in the parentheses.

[2] In those cases when the measurement error is not indicated, it amounts to 4.5%.

TABLE 7.5

MEAN NUMBER OF NEUTRONS FORMED IN A TARGET PER ONE INCIDENT PROTON (RELATIVE TO 1 g/cm^2) /224

Target (thickness - g/cm^2)	Mean Proton Energy, Mev					
	300	415	510	560	690	820
Sn (33)	0,028	0,030	0,035	0,041	0,041	0,059
W (34)	0,027	0,056	0,050	0,037	0,069	0,083
Pb (22)	0,010	0,059	0,010	0,033	0,057	0,071
Pb (44)	0,035	0,051	0,055	0,070	0,061	0,096
U (22)	0,051	0,060	0,062	0,077	0,054	0,085
U (44)	0,047	0,074	0,073	0,069	0,091	0,112

secondary particles (it leads to an increase in the neutron outflow from thicker targets). /225

The introduction of corrections for the absorption of an incident proton bundle in the target somewhat decreases the difference in the outflows of secondary neutrons from targets having different thickness. The relationship between the outflows of neutrons, which are corrected for absorption of incident protons in targets having a thickness of 44 and 22 g/cm^2, is close to unity. However, during the change to large energies, this relationship increases, which points to the significant contribution made by secondary nuclear processes, which increase the neutron outflow from the target. It can be seen that this effect exists for thinner targets.

It is important to take the following fact into account in designing shielding from protons. The theoretical data which exist at the present time on the neutron outflow primarily pertain to elementary interaction of protons, and the experimental data for thick targets - as was indicated above - are very sparse. The significant role of "extranuclear" cascade processes, which was pointed out in the work (Ref. 23), significantly complicates a design for shielding from high-energy protons, especially for large shielding thicknesses. An attempt was made in this same study to determine the contribution made by secondary processes in targets having a thickness of 22 and 44 g/cm^2, which was based on the results derived from calculations by Metropolis and others (Ref. 24). The following basic assumptions were thus made: a) the energy and angular distribution of cascade neutrons are just the same as for cascade protons; b) the outflow of low-energy neutrons, formed by cascade protons, is just the same as for incident protons of corresponding energy; c) the interactions of higher order can be

disregarded (cascade particles of the second generation have a probability of about 50%, on the average, for nuclear interaction before the outflow from a target of 44 g/cm^2); d) the cross-section of inelastic interaction is constant in the 50 - 500 Mev region, and the corresponding effective mean free paths amount to 180 g/cm^2 for tin; 187 g/cm^2 for tungsten; 195 g/cm^2 for lead; and 206 g/cm^2 for uranium.

Table 7.6 presents the results derived from calculating the outflow of neutrons formed during secondary processes in a target (N_{sec}), and also the total outflow of neutrons from a target (N_{tot}), as well as the outflow of nuetrons formed in the elementary inelastic interaction of a proton (N_{first}).

It can be seen that neutrons, which are formed as the result of secondary interaction processes in the target, make up a considerable part of the total neutron outflow. With an increase in the target thickness, the contribution made by secondary neutrons increases significantly. This effect, apparently, must be taken into account when calculating the dose from protons behind a shielding having a thickness of about 100 g/cm^2.

In conclusion, let us compare the data on the neutron outflow for the proton energy region of 18 - 32 Mev, which pertain to the total neutron outflow in all directions (Ref. 22), and 300 - 820 Mev, /226 which provide the neutron outflow only in the leading hemisphere, with respect to the direction of the proton bundle (Ref. 23).

TABLE 7.6

OUTFLOW OF PRIMARY AND SECONDARY CASCADE NEUTRONS FROM TARGETS BOMBARDED BY HIGH-ENERGY PROTONS

Target (thickness g/cm^2)	Proton Energy, Mev								
	300			415			510		
	N_{first}	N_{sec}	N_{tot}	N_{first}	N_{sec}	N_{tot}	N_{first}	N_{sec}	N_{tot}
Sn(33)	4.8	1.0	5.8	4.7	1.4	6.1	5.6	1.5	7.1
W(34)	4.6	1.6	6.2	10.4	2.1	12.5	8.8	2.3	11.1
Pb(22)	8.0	1.2	9.2	11.8	1.6	13.4	7.1	1.8	8.9
Pb(44)	6.5	2.1	8.6	9.4	2.8	12.2	9.7	3.2	12.9
U(22)	10.7	1.7	12.4	11.9	2.3	14.2	11.8	2.6	14.4
U(44)	9.0	3.0	12.0	14.5	4.0	18.5	13.4	4.6	18.0
	560			690			820		
Sn(33)	6.4	1.7	8.1	6.1	1.9	8.0	9.3	2.2	11.5
W(34)	5.3	2.6	7.9	11.9	3.0	14.9	14.3	3.3	17.6
Pb(22)	5.4	2.0	7.4	10.1	2.3	12.4	12.5	2.8	15.3
Pb(44)	12.7	3.5	16.2	9.9	4.1	14.4	17.4	4.8	22.0
U(22)	15.0	2.9	17.9	9.0	3.4	12.4	15.3	4.0	19.3
U(44)	11.5	5.1	16.6	15.9	6.0	21.9	19.7	7.0	26.7

In view of the fact that evaporative neutrons have an angular distribution which is close to an isotropic distribution, one must make a reduction by two in comparing the results set forth in Table 7.4. In addition, it is necessary to compare the neutron outflows for identical target thicknesses. Thicknesses of tin, tungsten, lead, and uranium - 1.22; 1.45; 1.53 and 1.62 g/cm^2, respectively - correspond to damping of protons from 32 to 18 Mev. This comparison shows that, with a change to high energies for protons which are incident to the target, the neutron outflows increase by a factor of 5 - 10.

7.5 Method for Designing a Shielding from Protons in the Inner Zone of the Earth and from Solar Flares

After analyzing the works which have been published (Ref. 2 - 10), one can reach the conclusion that the design procedure utilized in these works has several significant drawbacks, and therefore cannot provide a reliable determination of shielding for space vehicles. Consequently, a procedure which eliminates these basic drawbacks must be developed for designing shielding from protons in the inner radiation zone of the earth and from solar flares. The development of such a procedure is far from complete, due to the lack of information on many problems, which are related to the penetration of protons through the shielding substance and biological tissue, and also due to the lack of information on protons in cosmic space. In this connection, only the basic premises and specific examples of a proton shielding design for cosmic space will be presented here.

The proposed procedure for designing a proton shielding consists of the following basic premises:

1. Information about flight conditions are utilized as the initial data for designing the shielding (trajectory and flight duration, construction of the spacecraft, and arrangement of its compartments, etc.). This information also includes proton streams /227
in cosmic space (spatial location of the increased radiation zone, intensity, spectral composition, and angular particle distributions, frequency and duration of solar flares, etc.). The permissible dose for the given flight conditions is determined on the basis of radio biological data, taking the indicated initial data into account.

2. The radiation danger is estimated by comparing the mean tissue absorbed dose in the cosmonaut's body with the permissible dose which is established for the given flight conditions. The

mean tissue absorbed dose designates the total energy which is transmitted by radiation to the body (integral dose), divided by the mass of the body. The fact is thus taken into account that the permissible dose is, in essence, the mean tissue dose created in the body during general irradiation. As is known, the local tissue dose - i.e., the dose absorbed in the mass of 1 g of tissue which is surrounded by air - cannot serve as the reference criterion in shielding designs.

3. Along with the mean tissue dose, the depth distribution of the absorbed dose in the cosmonaut's body is determined. The magnitude of the mean tissue dose characterizes the effect averaged over the entire body. The utilization of this quantity in determining the degree of radiation danger, strictly speaking, is valid only when the depth drop of the dose does not exceed a certain limiting value. Based on the relationship of the maximum permissible levels of irradiation under terrestrial conditions (0.1 rem/week for the entire body, and 0.6 rem/week for the skin), and taking the fact into account that the surface dose - as a rule - is maximum for cosmic space radiation, one can conclude that the admissible drop from the maximum to the mean tissue dose must be no greater than 6. If this drop exceeds the admissible value, the concept of the mean tissue dose must be utilized very carefully in estimating the radiation danger - including information on the depth distributions and on the biological effect of irradiation of organs located at a different depth in the body.

Since the depth distribution of the absorbed dose is determined /228
by the penetrating ability of primary radiation and of secondary radiation formed in the shielding and in the body, the nature of this distribution will depend on the form of the initial spectrum for protons, the thickness and material of the shielding. For this reason, the depth distribution of the absorbed dose in the body cannot be obtained from general considerations, and appropriate calculations are required.

4. The mean tissue dose and the absorbed depth dose must be expressed in rem units, i.e., the relative biological effectiveness of primary radiation and all secondary radiation formed in the shielding and in the body of the cosmonaut. Attention must thus be given to the fact that the magnitude of the RBE coefficient depends on the nature of the radiation action (acute or chronic). As applied to spaceflight conditions, this means that the RBE coefficient will differ for cases when the spacecraft remains for a long period of time in the inner zone, when the inner zone is crossed for a short period of time, or when the zone of intense proton streams of solar origin is crossed.

An alternative method for determining the radiation danger would be to compare the calculated mean tissue absorbed doses with the experimental values for the admissible dose, obtained in

biological experiments under similar conditions (the proton spectrum falling on the biological subjects, the depth distribution of the dose, the time characteristics of the radiation action, etc.). The unusual nature of the original conditions and the apparent difficulty entailed in this type of biological experiments significantly limit the possibilities of this method.

5. The dosage contribution made by each component of the initial proton spectrum to the depth dose beyond the shielding is determined with the aid of the attenuation and buildup functions of the tissue dose. The buildup of the tissue dose, caused by an increase in the ionization losses as the protons are damped in the shielding, must be kept in mind here. The attenuation and buildup functions of the tissue dose can be either calculated, by taking into account multiple scattering and statistical scatter of the ranges, or can be determined experimentally with the aid of tissue-equivalent ionization chambers. If the attenuation and buildup function of the tissue dose is known, it is possible to determine the addition to the value for the proton mean free path Δ_n, which corresponds to attenuation of the proton radiation dose in the shielding by n times. Thus, instead of the range - energy relationship $R = f(E_p)$, the dependence $\delta_n = R + \Delta_n = f(E_p)$ must be used in shielding designs. If the energy of the protons which are incident to the shielding is such that the shielding thickness is $\delta_n << R$, the consumption of proton energy by ionization losses in the shielding is taken into account when calculating the depth dose.

6. Along with the ionization losses of proton energy in the general case, it is necessary to take into account the bundle attenuation due to proton absorption in the shielding and in the body during inelastic nuclear interactions. This effect is /229
significant for a shielding thickness on the order of several tens of grams per $1\ cm^2$, and can be calculated both on the basis of experimental data, and by computational procedures.

7. The formation of secondary particles during nuclear interaction in the shielding substance and in biological tissue must be taken into account when calculating the mean tissue and depth doses behind the shielding. Since the relative biological effectiveness must thus be taken into account, it is necessary to include additional information on the spectral-angular distribution of secondary particles leaving the shielding, the spectral composition of secondary particles at different depths in the body, etc.

8. The inclined penetration of radiation through the shielding is taken into account when calculating the mean tissue

and depth doses, and attention is given to the angular distributions of the protons impacting on the shielding, and the arrangement of the inhabited compartment of the spacecraft. An idealized shielding model is selected for each variant in the arrangement of the inhabited compartment. In many cases, it is advantageous to utilize the model of a spherical shielding shell, which consists of sections having different thickness and made of different materials. The radius of the equivalent sphere is selected so that the total mass of the shielding substance is retained.

The dimensions of the sections and the shielding thickness corresponding to them are determined on the basis of information on the compartment arrangement, and on the basis of data regarding the angular distribution of protons which impact upon the shielding. The depth distribution of the dose in the body is determined for each section of the sphere, and the resulting depth distribution and mean tissue dose are obtained by superposition of the distributions. If the dependence of the mean tissue dose on the thickness of each sphere section, and the relative contribution of the shielding sections, are known, it is possible to determine the optimum shielding arrangement, which would guarantee no more than the admissible irradiation dose for a minimum total weight of the shielding. The shielding design must be checked for the selected arrangement.

Let us examine in greater detail the manner in which the mean tissue dose and the depth distribution are calculated. For purposes of simplicity, let us utilize a model of the body in the form of a shere, having the radius $R = 25$ cm, with a density of the tissue equivalent substance $\rho = 1$ g/cm^3, located in an isotropic proton stream. Let us set

$$\Phi dT_p = \frac{1}{4\pi}\frac{dN_n}{dT_p}dT_p —$$

for a stream of particles having energies ranging from T_p to $T_p + dT_p$.

The dose rate dP, formed in the sphere by protons penetrating the surface dS at the angle θ, will equal

$$dP = \frac{K}{4\pi}\frac{dN}{dT_p}dT_p\,d\Omega\,dS\cos\theta W\bar{\eta}(T_p), \qquad (7.18)$$

where W is the energy transmitted to the body by particles which have the initial energy $T_{p,0}$. If the path traversed by the particles in the tissue substance does not exceed $2R\cos\theta$, then $W = T_{p,0}$. /230

In the general case, we have

$$W = \int_0^{2R\cos\theta}\frac{dE}{dx}dx = T_{p,0} - T_{p,1}$$

The particle energy at the end of the path in the body $T_{p,1}$ can be found from the range-energy relationship.

The coefficient of relative biological effectiveness is $\bar{\eta}(T_p)$, averaged over the path traversed by the particle in the body - i.e.,

$$\bar{\eta}(T_p) = \frac{\int_{E_1}^{E_0} \eta(Tp)\, dT_p}{T_{p,0} - T_{p,1}}.$$

Integrating expression (7.18) with respect to a solid angle, the surface of the sphere, and the energy spectrum of the incident particles, we obtain

$$P_{int} = \frac{K}{4\pi} \int_{\Omega} \int_{S} \int_{T_p} \frac{dN}{dT_p} W \bar{\eta}(T_p) \cos\theta\, dT_p\, dS\, d\Omega =$$
$$= 4\pi R^2 K' \int_0^{\pi/2} \sin 2\theta\, d\theta \int_{T_{p,\min}}^{T_{p,\max}} \frac{dN}{dT_p} W \bar{\eta}(T_p)\, dT_p, \qquad (7.19)$$

where $T_{p,\min}$ and $T_{p,\max}$ are the energy limits for the spectrum of incident protons.

The mean tissue dose rate $P_{m.tis}$ equals

$$P_{m.tis} = 0{,}48 \cdot 10^{-9} \int_0^{\pi/2} \sin 2\theta\, d\theta \int_{T_{p,\min}}^{T_{p,\max}} \frac{dN}{dT_p} W \bar{\eta}(T_p)\, dT_p. \qquad (7.20)$$

If the energy T_p is expressed in Mev, then $P_{m.tis}$ is in rem/sec.

Since there are both particles which penetrate the body, and particles whose range falls within the body limits, in the spectrum of incident protons, the expression for the mean tissue dose rate can be conveniently written in the form

$$P_{m.tis} = 0{,}48 \cdot 10^{-9} \int_0^{\pi/2} \sin 2\theta\, d\theta \left\{ \int_{T_{p,\min}}^{T_p(2R\cos\theta)} \frac{dN}{dT_p} T_p \bar{\eta}(T_p)\, dT_p + \right.$$
$$\left. + \int_{T_p(2R\cos\theta)}^{T_{p,\max}} \frac{dN}{dT_p} (T_p - E_1) \bar{\eta}(T_p)\, dT_p \right\}, \text{ rem/sec} \qquad (7.21)$$

where $T_p(2R\cos\theta)$ is the proton energy with a range which equals $2R\cos\theta$ in the tissue.

Figure 7.10 shows the values for the mean tissue dose rate, /231

calculated in this way, as a function of the energy for protons which are incident to the body. The dependence of the local dose on the proton energy is given, for purposes of comparison. The maximum mean tissue dose corresponds to the proton energy region of 200 - 250 Mev. If the dependence of the mean tissue dose on the proton energy is utilized and if the proton spectrum behind the shielding is known, it is possible to determine the mean tissue dose behind the shielding for different initial spectra.

The depth distribution of the absorbed dose in the body can be obtained in the following way. Let us examine a volume element which is located at a distance h from the center of the sphere, and let us determine the absorbed dose in this volume. The absorbed dose rate will equal

$$\begin{aligned} dD &= \frac{K}{4\pi} \cdot \frac{dN}{dT_p} \times \\ &\times dT_{p,h} \sin\theta d\theta d\varphi \cos\theta \times \\ &\times \frac{dT_{p,h}}{dx} \frac{1}{\cos\theta} \eta(T_{p,h}) = \\ &= \frac{1}{4\pi} \frac{dN}{dT_{p,h}} \frac{dT_{p,h}}{dx} \eta(T_{p,h}) \times \\ &\times dT_{p,h} \sin\theta d\theta d\varphi. \end{aligned} \tag{7.22}$$

Performing integration with respect to the proton spectrum behind the shielding and the angles θ and φ, we obtain

$$\begin{aligned} D(r) = 0{,}18 \cdot 10^{-8} \int_0^{\pi} \cos\theta \, d\theta \int_{T_{p,h,\min}}^{T_{p,h,\max}} \frac{dN}{dT_{p,h,\min}} \times \\ \times \frac{dT_{p,h}}{dx} \eta(T_{p,h}) \, dT_{p,h}, \text{ rem/sec}. \end{aligned} \tag{7.23}$$

Expression (7.23) describes the depth distribution of the absorbed dose rate in the body. Utilizing this expression, we can also calculate the mean tissue dose

$$P_{\text{m.tis}} = \frac{1}{UQ} \int_0^R 4\pi r^2 D(r) \, dr = 1{,}92 \cdot 10^{-4} \int_0^{25} r^2 D(r) \, dr, \text{rem/sec}$$

The mean tissue dose values, calculated by the given independent methods, coincide within the limits of computational accuracy. /232

When the dose which is formed by protons beyond a spherical shell is calculated, in the general case it is necessary to take the fact into account that the effective path followed by the particles in the shielding can differ from the thickness of the spherical layer. An exact calculation of this effect requires a knowledge of the angular distribution for protons which are

/231

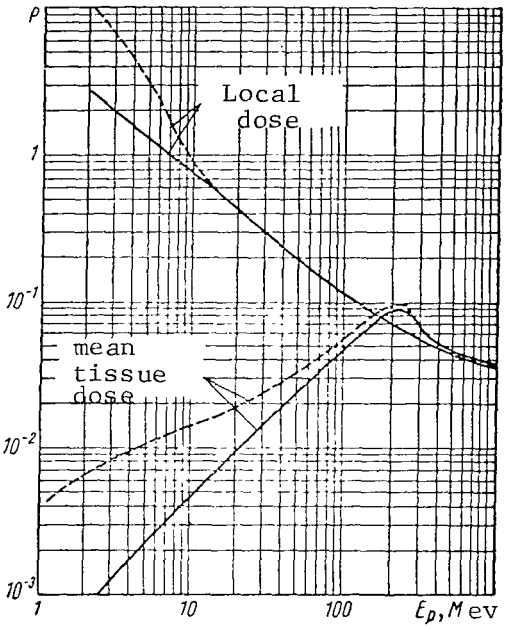

Figure 7.10

Mean Tissue Dose Rate as a Function of Proton Energy:

———————— Rate, $\frac{\text{microrad}\cdot\text{cm}^2}{\text{Mev}\cdot\text{proton}}$

- - - - - - - - - - - - - - - - Rate, $\frac{\text{microrem}\cdot\text{cm}^2}{\text{Mev}\cdot\text{proton}}$

/232

incident to the shielding. However, it is possible to make an approximate determination of the error entailed when the inclined penetration of protons through the shielding is disregarded. Let us determine the quantity $\Delta = \frac{\delta_{max} - \delta}{\delta}$, where δ is the thickness of the spherical shielding, and δ_{max} is the maximum distance traversed by protons in the shielding, which can be determined from the conditions under which the proton enters the body - whose equivalent radius is assumed to be $r = 25$ cm. Figure 7.11 shows the dependence on the shielding thickness for different radii of the spherical shell R. It can be seen that the effect produced by an inclined penetration of protons through the shielding is rather significant for small spherical shielding radii. If this effect is disregarded in designing a shielding adjacent to the body of the cosmonaut (radiation shelter of relatively small internal volume [Ref. 7], space suit, etc.), it can lead to serious errors. It can be assumed that this effect is insignificant when designing a shielding for the inhabited compartment which has rather large

dimensions. Thus, for a sphere radius of about 200 cm and a shielding thickness not less than 20 g/cm^2, its effective thickness exceeds the shell thickness by not more than 2%.

In addition, let us examine the results derived from calculations of the dose of proton radiation in the inner zone of the earth and from solar flares, for a spherical shell made of aluminum. The basic premises of the given procedure are taken into account in these calculations.

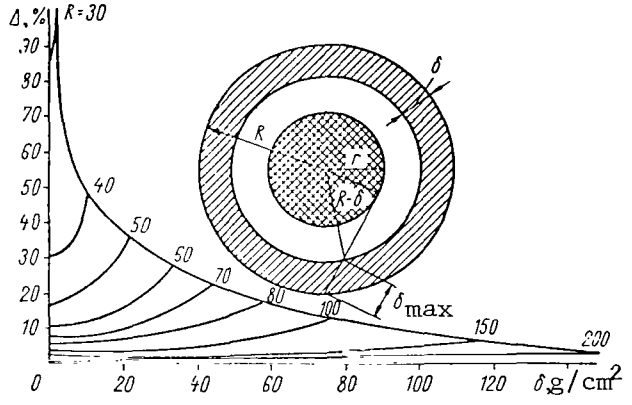

Figure 7.11

The Effect of Inclined Proton Penetration of the Shielding

The proton spectrum given in Chapter IV was utilized in calculating the proton doses of the inner zone of the earth. The calculation showed that the effect of the anomalous component of the proton spectrum in the inner zone is apparent only for small shielding thicknesses (less than 2 g/cm^2 aluminum). Table 7.7 presents some results derived from calculating the dose rate formed by protons at the intensity maximum of the inner zone, behind a shielding made of aluminum. /233

On the basis of these data, it can be concluded that the estimate of the dose, based on the energy transmitted to 1 g of tissue (local dose), is quite exaggerated: for small shielding thicknesses, the mean tissue dose is approximately 3 - 5 times less that the local dose. Thus, the nature of depth distributions of proton doses in the body is such (Figure 7.12) that it is fully justified to use the mean tissue dose as a criterion for radiation danger.

Table 7.8 presents the results derived from calculations of the mean tissue proton doses for different circular orbits, for a shielding thickness of 7.5 g/cm^2 aluminum.

TABLE 7.7

ABSORBED DOSE RATE AT THE INTENSITY MAXIMUM OF THE INNER ZONE OF THE EARTH

Dose	δ = 1.0 g/cm^2		7.5 g/cm^2		20 g/cm^2	
	mrad/sec	mrem/sec	mrad/sec	mrem/sec	mrad/sec	mrem/sec
Local	4.4	5.6	1.7	2.1	0.72	0.84
Surface	2.8	3.3	1.1	1.3	0.50	0.57
Mean Tissue	0.88	1.1	0.56	0.68	0.31	0.38

Flights along circular orbits, which are located at an altitude of up to 1000 km and more than 7500 km above the surface of the earth, lasting up to 10 days lead to an irradiation dose of not more than approximately 1 rem for the cosmonaut. At the same time, flights which are close to the intensity maximum of the inner zone, for a shielding /234 thickness of about 7.5 g/cm^2 lead to irradiation doses for the cosmonauts of 7.5 - 50 rem/day as a function of the angle of incination for the orbit plane. It can thus be assumed that it is fairly safe if the inner zone is crossed for a short period of time.

The data presented above must be supplemented by estimating the contribution which secondary radiation formed in the shielding makes to the dose. These estimates were made by utilizing results which have been given previously, and also data from another work (Ref. 2). The absorbed dose from secondary particles which are formed in a shielding, made of aluminum with a thickness of up to 20 g/cm^2, amounts to about 5 - 10% of the total dose. In the case of heavy shielding, this contribution can reach 30 - 40%. The relative

TABLE 7.8

MEAN TISSUE DOSE OF PROTONS PER DAY FOR A FLIGHT ALONG DIFFERENT CIRCULAR ORBITS (mrem/day)

h, км	Angle of Inclination for the Orbit Plane			
	0°	45°	65°	90°
250	<0,3	<0,3	<0,3	<0,3
500	~0,7	~0,7	~0,7	~0,7
1000	92	32	25	23
2500--3500	50 000	12 000	9000	7500
7500	115	23	18	17

contribution made by secondary particles increases with an increase in the shielding thickness. The contribution made by secondary particles, which were formed by protons in the body of the cosmonaut, was estimated on the basis of experimental data obtained for a proton bundle from a JINR* synchrocyclotron. It showed that this contribution does not amount to more than 20%. Consequently, due to the secondary particles formed in the shielding and in the body of the cosmonaut, the absorbed dose must increase by approximately 30%. /235

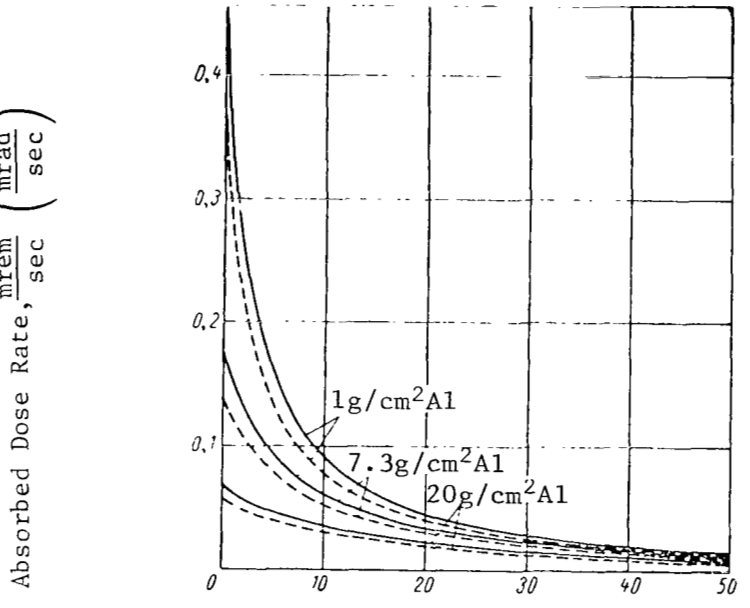

/234

Figure 7.12

Depth Distribution of the Absorbed Dose for Protons in the Inner Zone of the Earth:

———— mrem/sec; - - - - - - - - mrad/sec; the Substance Thickness is Plotted Along the Abcissa Axis, g/cm^2.

This estimate is also valid for protons from solar flares, especially for flares with a hard proton spectrum. /235

The proton spectra for two flares on November 12, 1960 and February 23, 1956 were used in calculating the doses of protons from solar flares behind a shielding. The possibility that the cosmonaut might be irradiated by protons from several solar flares - which can occur during a flight - was not taken into account in the designs which have been published for a shielding from protons coming from solar flares (Ref. 2 - 7, Ref. 9, Ref. 10). This fact cannot be disregarded for long spaceflights (Ref. 8, Ref. 26).

The dose, which was obtained by the cosmonaut due to protons

*Note: JINR designates Joint Institute of Nuclear Research.

from a single solar flare - of the type on February 23, 1956, or November 12, 1960 - , was calculated as a function of the shielding thickness. The results of these calculations are given in Table 7.9, where the magnitude of the local doses are given, for purposes of comparison, along with the mean tissue doses.

TABLE 7.9

ABSORBED DOSE FOR SOLAR FLARES ON 11/12/1960 AND 2/23/1956 FOR DIFFERENT SHIELDING THICKNESSES.

Shielding Thickness, g/cm^2 Al	11/12/1960			2/23/1956		
	Local	Mean Tissue		Local	Mean Tissue	
	rad	rad	rem	rad	rad	rem
0,1	40 000	230	520	2300	100	142
0,2	16 500	172	350	1500	100	135
0,3	9 700	145	273	1200	98	127
0,4	6 700	130	232	1000	94	120
0,5	5 000	118	203	880	91	116
0,6	4 000	110	182	780	88	110
0,7	3 300	102	167	720	85	107
0,8	2 700	98	154	660	84	102
0,9	2 350	93	144	610	82	100
1,0	2 050	88	135	570	80	98
1,5	1 200	73	107	420	74	89
2,0	810	63	89	340	70	83
2,5	600	56	75	290	65	79
3,0	470	50	65	250	62	73
4,0	320	40	51	198	56	65
5,0	230	34	42	165	50	58
6,0	175	30	36	137	45	53
7,0	140	26	32	120	41	48
8,0	115	24	28	104	38	44
9,0	95	21,5	25,5	93	36	41
10,0	80	19,9	23	83	34	39
20,0	28	10,7	12,2	40	20	24,5
50,0	7	3,3	3,7	13,8	11,6	12,7

Two important facts should be noted. /236

First, the local doses are significantly larger than the mean tissue doses, particularly for small thicknesses, where their ratio amounts to 20 - 200. With an increase in the shielding thickness up to tens of grams per 1 cm^2, the proton spectrum behind the shielding is so hard that the difference between the local dose and

the mean tissue dose disappears.

Secondly, in spite of the utilization of the RBE coefficients in calculating the depth distributions in the body, for conditions of chronic irradiation, the effective RBE values for the mean tissue doses barely differ from one. For the solar flare on November 12, 1960, it was not more than 2.5, for a thickness of 0.1 g/cm^2; and for the flare on February 23, 1956, it was not more than 1.5, respectively. For a shielding thickness on the order of 5 - 10 g/cm^2, the RBE value for the entire body is very close to one. In this connection, the estimates of the doses in units of rads and rems practically coincide - which, in general, corresponds to the nature of the radiation effect of protons from solar flares ("acute effect"). However, it must be kept in mind that there are not enough data on the biological effect of secondary particles formed in the shielding and the body of the cosmonaut, and also about the so-called late aftereffects of radiation from solar flares. The radiation doses for the two most intense proton flares which have occurred up to the present time (February 23, 1956, and November 12, 1960) should not exceed 50 and 35 rem, respectively, for a shielding thickness on the order of 7.5 g/cm^2 Al - which is 2 - 3 times less than previous estimates based on local doses.

Let us also examine the probability that the cosmonaut might be radiated by protons from several solar flares. Since information on the mechanism of solar flares is quite limited at the present time, it can be assumed that solar flares represent statistically independent events. The probability that during the flight of the spacecraft not any flares, only one flare, only two flares, etc. will take place is a finite quantity, which can be determined by the Poussin distribution

$$P_K = \frac{(nt)^K}{K!} e^{-nt},$$

where P_K is the probability for the occurrence of K flares during the flight time t ; n is the frequency of solar flares. The probability that not one flare (K = 0) will occur during the flight time equals

$$P_0 = e^{-nt}.$$

It can be assumed that the frequency of flares, such as that on November 12, 1960, equals

$$n = 0.03 \text{ 1/day}.$$

Table 7.10 presents the results derived from estimating the probability for the concurrence of several solar flares during the flight time as a function of the flight duration. /237

TABLE 7.10

PROBABILITY FOR SOLAR FLARES, OF THE TYPE ON NOVEMBER 12, 1960, FOR DIFFERENT SPACEFLIGHT DURATIONS.

Number of Flares, K	Flight Duration, Days							
	1	5	10	15	20	50	100	200
0	99,70	86,10	74,10	0,638	54,90	22,30	5,00	0,20
1	2,99	12,90	22,20	28,700	32,90	33,40	14,90	1,49
2	0,45	0,97	3,33	6,450	9,88	25,10	22,40	4,46
3	—	>0,10	0,40	0,968	1,98	12,50	22,30	8,92
4	—	—	—	—	0,30	4,70	16,80	13,40
5	—	—	—	—	—	1,41	10,10	16,10
6	—	—	—	—	—	0,35	5,04	16,10
7	—	—	—	—	—	—	2,16	11,80
8	—	—	—	—	—	—	—	10,30
9	—	—	—	—	—	—	—	6,90

The frequency of flares, such as that on February 23, 1956, can be assumed to equal

$$n = 0.0011 \quad 1/\text{day}.$$

This value was used in calculations, whose results are shown in Table 7.11.

Thus, the danger that the cosmonaut may be influenced by proton streams from several solar flares, such as that on November 12, 1960, must be taken into account during spaceflights which last more than 10 days. For a flight duration of about 20 days, the probability that such a flare does not occur is only about 51% in all. At the same time, the probability that only one flare will occur is 34%; two flares - 11%; three flares - 2.5%. It is apparent that at least two solar flares, such as that on November 12, 1960 must be taken into account when designing shieldings from protons, for flights lasting this period of time. If the admissible radiation dose during the flight is thus assumed to equal 50 rem, then the necessary shielding thickness made of aluminum amounts to about 10 g/cm^2 in accordance with Table 7.9, instead of 4 g/cm^2, for one flare of the same type. /238

For spaceflights lasting on the order of several months and more, there is a good probability that the cosmonaut will be radiated by protons from not only two flares, but also three, four, etc. Thus, for a flight of about 100 days the probability that there will be not one solar flare decreases to 5%, and the probability for the occurrence of one flare - to 15%. At the same time, the probability for two

TABLE 7.11

PROBABILITY (%) OF SOLAR FLARES, SUCH AS THE TYPE ON 2/23/1956 FOR DIFFERENT SPACEFLIGHT DURATIONS

Number of Flares, K	Flight Duration, Days						
	1	10	50	100	200	365	730
0	99,9	98,9	94,60	89,60	80,20	66,90	44,80
1	0,1	1,1	5,20	9,80	17,70	26,90	36,00
2	—	—	0,14	0,54	1,90	5,39	14,40
3	—	—	—	0,02	0,14	0,72	3,86
4	—	—	—	—	—	0,07	0,78

flares increases to 22%; three flares - 22%; four flares - 17%; five flares - 10% and six flares - 5%. The shielding thickness of the inhabited compartment must thus be increased. In addition, it should be pointed out that the probability for solar flares, such as that on February 23, 1956, becomes great for flights which last a long period of time. If the probability of several flares (about 2 - 3), such as that on November 12, 1960, are taken into account in designing the shielding - i.e., a shielding thickness on the order of 10 15 g/cm^2 is selected - then the radiation dose from protons, coming from a flare such as that on February 23, 1956, decreases to a significant extent.

The so-called limited risk criterion can be used as another possible method for estimating the radiation danger from protons coming from several solar flares. Such a criterion can be the 5%-probability that the cosmonaut will be radiated by a dose of more than 50 rem, with a probability restriction of 0.5% that the radiation dose will be more than 200 rem. Utilizing this criterion and the data presented in Tables 7.9, 7.10, and 7.11, one can draw the following conclusions:

1) If 50 rem (Ref. 1) are used as the permissible dose during the flight, then a shielding thickness on the order of 7 g/cm^2 provides for a flight duration of 10 days;

2) If 25 rem (Ref. 27) are used as the permissible dose, the shielding thickness must be increased up to 10 g/cm^2 for a flight duration of 10 days;

3) If the flight duration increases up to 20 days, the shielding thickness must be about 10 g/cm^2, if the permissible dose is assumed to equal 50 rem - and about 20 g/cm^2, if the permissible dose is assumed to equal 25 rem;

4) If the flight duration increases up to 100 days, the shielding

thickness must be about 20 g/cm^2, if the permissible dose is assumed to equal 50 rem, and about 40 g/cm^2 for 25 rem. These data pertain to a period of maximum solar activity. For the forthcoming period 1964 - 1966, these data can be regarded as upper limits.

In conclusion, it should be noted that the existing data on the frequency and duration of different types of solar flares, as well as the intensity and spectral-angular proton distributions, /239 are completely inadequate for an accurate determination of radiation danger and, correspondingly, the necessary shielding thicknesses for the inhabited compartments of the spacecrafts which will be undertaking long flights. Future studies in this area are necessary, as well as the development of reliable methods for long-range forecasts of solar flares, radiation warning, and dosimetry.

REFERENCES

1. Problems of Radiation Safety During Space Flights (Problemy radiatsionnoy bezopasnosti kosmicheskikh poletov). Edited by Yu. G. Nefedov. Atomizdat, Moscow, 1964.

2. Beck, A. J., Divita, E. L. Amer. Rocket Soc. Paper, 11, 1668, 1962.

3. Keller, J. W., Schaeffer, N. M. Electr. Engng, 79, 12, 1049, 1960.

4. Dye, D. L., Noyes, J. C. J. Astron. Sci., VII, 3, 64, 1960.

5. Robey, D. H. Astronaut. acta, 6, 4, 206, 1960.

6. Barnes, T. G. et al. Astron. Sci. Rev., 3, 1, 11, 1961.

7. Waddington, C. J. J. Brit. Interplanet. Soc., 18, 7, 277, 1962.

8. Foelsche, T. COSPAR Meeting. International Committee on Space Research, Washington, Apr. 30 - May 11, 1962.

9. Madey, R. American Astronautical Society 8th Annual National Meeting, January 16 - 18, Washington. Preprint 62-15, 1962.

10. Ivanov, V. I. et al. Doses of Cosmic Radiation (Dozy kosmicheskoy radiatsii). In the Collection: Iskusstvennyye Sputniki Zemli. No. 12, Izd-vo AN SSSR, Moscow, 1962.

11. Mather, Segre, E. Phys. Rev., 81, 1951.

12. Schaefer, H. J. Astronautics, 6, 2, 39, 1961.

13. Vasilevskiy, I. M., Prokoshkin, Yu. D. Atomnaya Energiya, 7, 3, 1959.

14. Afanas'yev, V. P. et al. Atomnaya Energiya, 16, 5, 1964.

15. Kirn, F. S. et al. Radiology, 63, 1, 94, 1954.

16. Ortel, W. C. G. Phys. Rev., 93, 561, 1954.

17. Cocconi, G. et al. Phys. Rev., 79, 768, 1950.

18. Montgomery, C. G., Tobey, A. R. Phys. Rev., 76, 1478, 1949.

19. Skyrme, D. M., Williams, W. S. C. Philos. Mag., 42, 1187, 1951.

20. Cohen, B. L. Phys. Rev., 98, 49, 1955.

21. Crandall, W. E. et al. J. Appl. Phys., 28, 273, 1957.

22. Juin-Kwei Tai. et al. Phys. Rev., 109, 6, 2086, 1958.

23. Bercovitch, M. et al. Phys. Rev., 119, 1, 412, 1960.

24. Metropolis, N. et al. Phys. Rev., 110, 185, 204, 1958.

25. Abel, J. American Astronautical Society 8th Annual National Meeting, January 16 - 18. Washington. Preprint 62-37, 1962.

26. Winckler, J. R. Aerospace Med., 32, 10, 893, 1961.

27. Kaprielyan S. Aerospace Manag., 5, 6, 14, 1962.

CHAPTER 8

SHIELDING FROM ELECTRONS AND ELECTROMAGNETIC RADIATION OF THE INNER RADIATION ZONE OF THE EARTH

8.1. Electromagnetic Radiation of Electrons

As was shown in Chapter 5, the main radiation danger in the /240
outer zone of the earth is represented by electrons, whose spectrum rapidly decreases with energy, and is practically terminated in the region of about 5 Mev. The electron stream at the intensity maximum of the zone is so great that a lethal dose can be formed in the human organism within several minutes, if there is no shielding. Realistic shielding thicknesses on spacecrafts (3 - 5 g/cm^2) are large enough to decrease to a significant extent the stream of electrons reaching the biological tissue, and thus to remove any immediate radiation danger from electrons. However, when electrons are absorbed in matter, electromagnetic x-ray radiation is formed, whose penetrating ability considerably exceeds the penetrating ability of electrons. Under specific conditions, this radiation can comprise a primary radiation danger during flights in the outer zone of the earth.

It is known that an electron can penetrate the Coulomb field of the nucleus when penetrating matter, as a result of which the trajectory is distorted - i.e., the electron is accelerated to a certain extent. The motion of a charged particle having acceleration is accompanied by electromagnetic radiation (Ref. 1), the so-called bremsstrahlung or x-ray radiation, whose spectrum - as is known - is continuous with quanta energies in the interval $0 - E_0$, where E_0 is the initial energy of the braked electron.

Rapid electrons emit a bundle of electromagnetic radiation at a cone, whose half-angle aperture θ is inversely proportional in order of magnitude to the electron energy

$$\theta \sim \frac{m_0 c^2}{E_0}, \qquad (8.1)$$

where m_0c^2 is the energy corresponding to the mass of an electron "at rest".

It can be seen from the cone angle determination that the angular distribution of electromagnetic radiation is "expanded" with a decrease in the electron energy E_0 , and in the first ap- /241
proximation tends toward an isotropic distribution for very low energies, i.e., for

$$E_0 \ll m_0 c^2 \qquad (8.2)$$

The spectral distribution of electromagnetic radiation is a rather complex function of the electron energy E_0 and the braking quantum $h\nu$. The intensity spectrum of electromagnetic radiation can be calculated approximately from the following relationship (Ref. 2):

$$J(h\nu)\,d(h\nu) = \text{const}\left[4\left(1 - \frac{h\nu}{E_0}\right) - 3\frac{h\nu}{E_0}\ln\left(\frac{E_0}{h\nu}\right)\right]. \qquad (8.3)$$

For numerical calculations, a Table showing the relative contribution $\varkappa$ of different spectral components to the intensity of electromagnetic radiation is also suitable (Ref. 3) (Table 8.1)[1].

TABLE 8.1

RELATIVE CONTRIBUTIONS OF DIFFERENT SPECTRAL COMPONENTS TO INTENSITY OF ELECTROMAGNETIC RADIATION OF MONOENERGETIC ELECTRONS

$h\nu/E_0$	$\varkappa$ (%)	$h\nu/E_0$	$\varkappa$ (%)
0—0,1	26,9	0,5—0,6	6,5
0,1—0,2	20,5	0,6—0,7	4,5
0,2—0,3	15,8	0,7—0,8	2,8
0,3—0,4	12,1	0,8—0,9	1,5
0,4—0,5	9,0	0,0—1,0	0,4

The percentile intensity for a given energy interval out of the total electromagnetic radiation intensity is given in Table 8.1.

The following expression is given for calculating the total intensity of electromagnetic radiation of monoenergetic electrons when they are totally damped out:

$$C(E_0 Z) = 5{,}77 \cdot 10^{-4} Z E_0^2 \frac{\text{Mev}}{\text{electron}}, \qquad (8.4)$$

where Z is the atomic number of the braking substance. When the braking substance has a complex composition, the effective atomic

[1] Table 8.1 is given for monoenergetic electrons (conversion electrons, accelerated low-energy electrons in accelerators, etc.).

number is calculated:

$$Z_{\text{eff}} = \frac{\sum_i \alpha_i Z_i^2}{\sum \alpha_i Z_i}. \tag{8.5}$$

Here α_i is the portion of atoms in the element with the atomic number Z_i.

It can be seen from an examination of formula (8.4) that the intensity of electromagnetic radiation is proportional to the atomic number of the braking medium and to the square of the electron energy. This fact must be kept in mind when constructing and designing shielding from electrons. /242

8.2. Calculating the Dose of Electromagnetic Radiation Within a Spacecraft Located in the Outer Zone

In order to solve this problem, we must define the initial conditions and several simplifying assumptions. Let the cabin, having a spherical form with the wall thickness $d(g/cm^2)$ made from a material having the atomic number Z, be at rest in the outer zone. We must calculate the electromagnetic radiation dose which the cosmonaut will obtain during the time interval t. It is apparent that this radiation dose can be expressed as follows, in a general form:

$$D(d) = P(d)\, t, \tag{8.6}$$

where $P(d)$ is the dose rate of electromagnetic radiation, which can be used as the criterion for radiation danger.

Since the cabin has a spherical form, the electromagnetic radiation which is formed in the cabin wall will affect the cosmonaut from all sides.

If the electron stream in the outer semi-space and the electromagnetic radiation which is formed are isotropic, then we obtain an isotropic source of electromagnetic radiation in the inner (with respect to the cabin wall) semi-space. For purposes of simplicity, we shall assume that all of the electromagnetic radiation arises in the upper layer of the cabin wall.

Based on such simplifying assumptions, we arrive at the conclusion that we have isotropic radiation sources which are distributed uniformly on a spherical surface. The dose rate in the center of the spherical source having isotropic monoenergetic sources of radiation, which are distributed uniformly, is determined

from the condition

$$P = K \int_s \frac{N_1 E ds}{4\pi r^2} = K N_1 E, \tag{8.7}$$

where r and ds represent the radius and surface element of the sphere; N_1 is the number of monoenergetic quanta having the energies E which are emitted per unit of time from units of sphere surface; K is the proportionality factor between the intensity and the dose rate.

It can be seen from equation (8.7) that in the given case the dose rate - within an accuracy of the constant factor - equals the total energy which is emitted by a unit of the spherical source surface, and does not depend on the sphere radius. An analogous equation for a spherical source with a continuous radiation spectrum has the form /243

$$P = \int_E K(E) N_1(E) E \, dE, \tag{8.8}$$

where $N_1(E)\,dE$ is the number of quanta, having energies in the E - EdE region, which is emitted by the source per unit of time from unit of surface.

Instead of $N_1(E)E$, we must substitute[1]

$$\frac{N(E_0)}{4} \varkappa(E) C(E_0, Z),$$

for the electromagnetic radiation source of electrons having the energy E_0, where $N(E_0)$ is the total nondirectional stream of electrons having the energy E_0. The dose rate from a continuous electron spectrum is

$$P_T = \frac{1}{4} \int_{E_0 \min}^{E_0 \max} N(E_0) C(E_0, Z) \, dE_0 \int_0^{E_0} \varkappa(E) K(E) \, dE. \tag{8.9}$$

If the cabin wall has the thickness d, then - taking the absorption of electromagnetic radiation and accumulation of scattered radiation in the shielding - the dose rate in the center of the cabin is

---

[1] In this expression, the total nondirectional stream of electrons is divided by 4, since it is assumed that electrons in the zone have an isotropic distribution. Therefore, only ¼ of the total nondirectional stream falls on a unit area of the shielding surface, taking the solid angle into account.

$$P_T(d) = \frac{1}{4}\int_{E_0\,\min}^{E_0\,\max} N(E_0)\,C(E_0, Z)\,dE_0 \times$$

$$\times \int_0^{E_0} \varkappa(E)\,B(E, d, Z)\,e^{-\mu(E)\,d}\,K(E)\,dE, \qquad (8.10)$$

where B(E, d, Z) is the accumulation factor of scattered energy, $\mu(E)$ - is the attenuation coefficient of γ-rays having the energy E in the wall material. Substituting $K(E) - 1.6 \cdot 10^{-8}\gamma(E)$ (to express the dose rate in rad/sec) in expression (8.10), we obtain

$$P_T(d) = 0{,}4 \cdot 10^{-8} \int_{E_0\,\min}^{E_0\,\max} N(E_0)\,C(E_0, Z)\,dE_0 \times$$

$$\times \int_0^{E_0} \varkappa(E)\,B(E, d, Z)\,e^{-\mu(E)\,d}\,\gamma(E)\,dE, \qquad (8.11)$$

where $\gamma(E)$ is the electron conversion factor in biological tissue, cm^2/g. For purposes of computational simplicity, the depth distribution of the dose in biological tissue is not taken into account here.

Equation (8.11) is integrated numerically, in view of the fact that such functions as $\mu(E)$ and $\gamma(E)$ do not have an acceptable analytical expression. In addition, for certain shielding materials and energies of γ-rays, not only are analytical expressions lacking for accumulation factors B(E, d, Z), but also their numerical values - for example, data are lacking on the accumulation factors for small energies. /244

A procedure for solving this problem, which was similar to that described above, was utilized in another work (Ref. 4). The primary difference consists of the fact that in this work the following expression is used to calculate the total electromagnetic radiation intensity, instead of $C(E_0, Z)$:

$$W(E_0, Z) = \omega E_0 = \frac{1{,}98 \cdot 10^{-4}\,(1{,}96E_0 + 2)}{1 + 0{,}35 \lg \frac{82}{Z}}\,ZE_0. \qquad (8.12)$$

Formula (8.12) was obtained (Ref. 5) by integration of the Bethe-Heitler cross-section (Ref. 6) for electromagnetic radiation throughout the entire energy region of the emitted quanta. The following expression for ionization losses was used to calculate the energy loss by electrons during collisions:

$$\left(-\frac{dE}{dx}\right)_{\text{initial}} = \text{const}\,Z\left[1 + 0{,}35 \lg\left(\frac{82}{Z}\right)\right], \qquad (8.13)$$

i.e., it was assumed that the ionization losses do not depend on the electron energy. This is correct in a rather narrow energy interval (Ref. 7) for the energy $E_0 \sim m_0c^2$. In the region of low electron energies ($E_0 < m_0c^2$), formula (8.12) yields an exaggerated result as compared with formula (8.4). In order to verify the correctness of either result in the low-energy region, a formula, which has been verified in practice (Ref. 8), can be used:

$$W' = \frac{4\pi}{18\sqrt{3}} \cdot \frac{e^2h}{c^3m} Z\nu_0^2 = 9{,}1 \cdot 10^{-4} ZE_0^2. \qquad (8.14)$$

Table 8.2 presents the results derived from calculating the outflow of electromagnetic radiation, according to formulas (8.4), (8.12), and (8.14) for certain values of the initial electron energy E_0.

It can be seen from Table 8.2 that in the energy region of 0.3 - 1 Mev the results derived according to Formulas (8.4) and (8.12) are similar to each other and, apparently, correctly reflect the true picture. In the energy region $E_0 \sim 0.2$ Mev, the results derived on the basis of formula (8.12) are 3 - 10 times larger than the corresponding results derived with formula (8.4). It can be seen from a comparison of the obtained values with the results derived by formula (8.14) that the results derived with formula (8.4) are closest to them. Thus, formula (8.4) is most suitable for calculating the outflow of electromagnetic radiation in the outer zone. The distribution of the electromagnetic radiation intensity with respect to energy can be calculated with the aid of data given in Table 8.1.

Turning now to formula (8.11), let us calculate the dose rate /245
of electromagnetic radiation in the following steps: 1) for each energy E_0 with a constant stream $N(E_0)$, let us calculate the intensity of electromagnetic radiation in tenths of energy intervals corresponding to the ratios $h\nu/E_0$ in tenths (see Table 8.1); 2) for the intensity in each energy interval, let us introduce an exponential law for radiation attenuation for several thicknesses of the shielding wall; 3) let us convert the data which are obtained to the absorbed dose rate in units of rad/sec; 4) let us introduce a correction for the buildup of scattered radiation in the shielding, utilizing the dosage buildup factor B(d, E, Z), and let us sum up the results over all the quanta energies from the first to the tenth interval; 5) let us convert the results obtained to the known electron spectrum in the outer zone[1] (Chapters 5 and 6), and let us

[1] Sections 1 and 5 are listed separately, in view of the fact that future studies on the outer zone can provide more accurate information regarding the electron spectrum. When the radiation danger is then determined, it will be sufficient to recalculate all of the results, beginning with Section 5, retaining the results from the other intervening calculations.

TABLE 8.2

RESULTS DERIVED FROM CALCULATING OUTFLOW OF ELECTROMAGNETIC RADIATION ACCORDING TO FORMULAS (8.4), (8.12), AND (8.14)

Energy E_0, Mev	Shielding Material	Z	Intensity $\times 10^{-4}$, $\frac{\text{Mev}}{\text{electron}}$ Calculated according to formula		
			(4)	(12)	(14)
1	Lead	82	475	650	750
	Aluminum	13	75	81.2	118
	Graphite	6	34.6	34.4	54.6
0.3	Aluminum	13	6.75	15.8	10.6
	Graphite	6	3.1	6.7	4.9
0.2	Aluminum	13	3	9.7	4.75
	Graphite	6	1.4	4.1	2.2
0.1	Aluminum	13	0.75	4.5	1.2
	Graphite	6	0.35	1.9	0.54
0.05	Aluminum	13	0.187	2.28	0.296
	Graphite	6	0.086	0.93	0.136

perform a graphic integration of the obtained dose rates with respect to the entire electron energy region from $E_{0_{min}}$ to $E_{0_{max}}$.

For purposes of computational simplification, integration is replaced by summation in Part 4. It is thus assumed that all of the braking quanta in each energy interval have an energy which equals the mean energy in the given interval.

The results derived from calculating the intensity of electromagnetic radiation of electrons according to Part 1 are shown in Figure 8.1. The calculations were carried out for an electron stream $1 \cdot 10^7$ $cm^{-2} \cdot sec^{-1}$ for a material having the effective atomic number $Z_{eff} = 6$ (graphite). In order to change to materials having other atomic numbers Z_{eff}, it is sufficient to multiply the results obtained by the ratio $Z_{eff}/6$. It can be seen from Figure 8.1 that the intensity of electromagnetic radiation greatly increases with an increase in the electron energy E_0 for identical electron streams. It is apparent that a quadratic increase with the energy E_0 must be observed for the total electromagnetic radiation intensity, in accordance with formula (8.4). /246

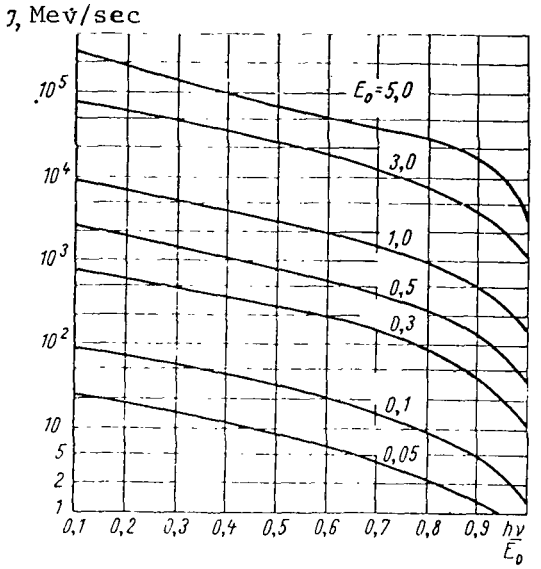

Figure 8.1

Outflow of Electromagnetic Radiation of Monoenergetic Electrons having Different Energies E_0, as a Function of the Relative Energy of Braking Quanta $h\nu/E_0$. The Total Electron Stream is $1 \cdot 10^7$ $cm^{-2} \cdot sec^{-1}$.

Let us now calculate the intensity of electromagnetic radiation after attenuation of the shielding shell, whose thickness is $d(g/cm^2)$. The calculations are carried out according to formula

$$J(d) = J e^{-\mu(\overline{h\nu})d}, \qquad (8.15)$$

where $\mu(\overline{h\nu})$ is the mass attenuation coefficient in a material with the atomic number $Z_{eff} = 6$ (graphite) for γ-rays, having the energy $\overline{h\nu}$. The values of μ were obtained by graphic interpolation of the data obtained in the work (Ref. 8). The following thicknesses of the shielding shell were selected, in order to encompass the majority of real cases: 0.1; 0.2; 0.5; 1.0; 3.0; 5.0; and 10.0 g/cm^2. The /247
small thicknesses correspond to the actual thicknesses of the normal wearing apparel for cosmonauts. Figure 8.2 shows the results derived from calculating electromagnetic radiation intensity behind a shielding thickness of 0.1; 1.0 and 10 g/cm^2 for electron energies of 0.1; 1.0 and 5.0 Mev. It can be seen that electromagnetic radiation intensity behind a shielding, from each energy interval of braking quanta for small energies of E_0, has a maximum which is caused by the fact that the low-energy components of electromagnetic radiation are more

intensely absorbed in the shielding shell having a given thickness. It is also caused by the fact that the braking spectrum has a decaying nature (with an increase in energy), and thus the electromagnetic radiation is filtered. It can also be seen that its intensity maximum for a given energy of E_0 is shifted to the region of larger energies of γ-radiation as the shielding thickness increases - i.e., the filtration is increased. However, for large energies of E_0, there is no maximum, since all the components of the braking spectrum have comparable penetrating capacity, and the filtration is weaker.

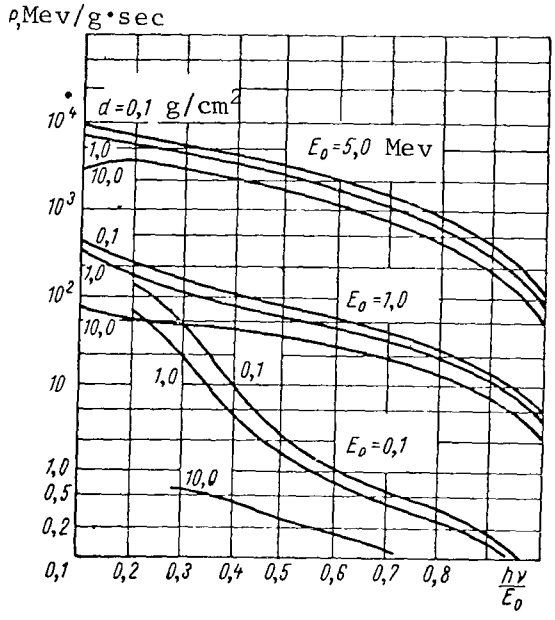

Figure 8.2

Intensity of Electromagnetic Radiation for Electrons having the Energies 0.1; 1.0 and 5.0 Mev for Different Shielding Thickness. The Total Electron Stream is $1 \cdot 10^7$ $cm^{-2} \cdot sec^{-1}$.

In order to convert the obtained values for electromagnetic radiation intensity into the absorbed dose rate, let us utilize a graph showing the dependence of the mass coefficient of energy absorption in biological tissue on the energy of γ-rays (Ref. 9). /248
Figure 8.3 shows the results derived from multiplying the data, which are given in Figure 8.2, by the absorption coefficient $\gamma(E)$, for the total electron stream $1 \cdot 10^7$ $cm^{-2} \cdot sec^{-1}$. It can be seen from the Figure that the relative contribution to the dose rate is somewhat increased in the region of low γ-ray energies (as compared with the relative contribution to the electromagnetic radiation intensity). This is true because the energy

absorption coefficient has a larger value in the region of low γ-ray energies, as compared with the region of high energy. There is no relative change in the contributions in the region of high energies, because the magnitude of the energy absorption coefficient for γ-rays, having the energy $E > 0.08$ Mev, changes very slightly with energy in biological tissue.

Let us now consider the buildup of scattered γ-rays in the shielding of a spacecraft. The buildup of scattered radiation is usually considered by introducing a buildup factor[1].

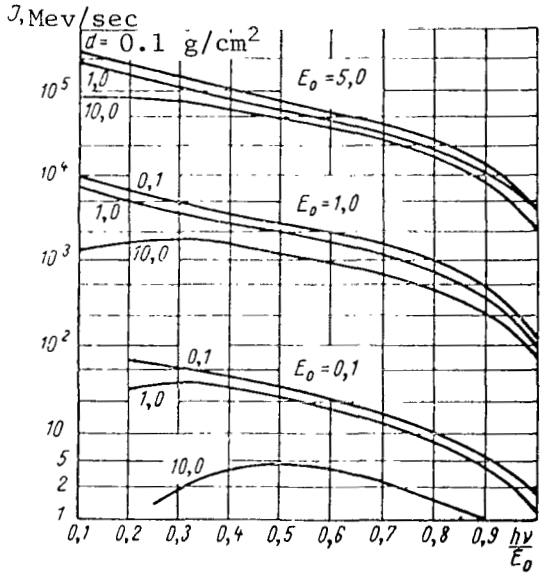

Figure 8.3

Dose Rate of Electromagnetic Radiation for Electrons having the Energy 0.1; 1.0 and 5.0 Mev for a Shielding Thickness 0.1; 1.0 and 10.0 g/cm².

The extensive data which exist on the buildup factor of γ-rays in different shielding materials (Ref. 10) encompass the energy region $E \geqslant 0.5$ Mev. For our purposes, data are also necessary on the buildup factor for the energy $E < 0.5$ Mev. The absorption coefficients of γ-rays in graphite ($Z = 6$) and the shielding thickness (in mean free paths) for these energies /249

[1] In the given case, it is necessary to introduce a dosage buildup factor.

- which correspond to the shielding thicknesses 10 g/cm^2, 5 g/cm^2 and 3 g/cm^2 which we have used - are given in Table 8.3.

TABLE 8.3

DEPENDENCE OF ABSORPTION COEFFICIENTS AND SHIELDING THICKNESS IN MEAN FREE PATHS ON THE ENERGY OF γ-RAYS

E, Mev	Absorption Coefficients, μ, cm^2/g	Shielding Thickness in Mean Free Paths		
		10 g/cm^2	5 g/cm^2	3 g/cm^2
0,02	0,3820	3,820	1,91	1,15
0,05	0,1780	1,780	0,89	0,53
0,10	0,1490	1,490	0,75	0,45
0,30	0,1050	1,050	0,52	0,32
0,50	0,0870	0,870	0,44	—
1,00	0,0636	0,636	0,32	—
2,00	0,0443	0,443	—	—
3,00	0,0354	0,354	—	—
4,00	0,0303	0,303	—	—
5,00	0,0269	0,269	—	—

It can be seen from Table 8.3 that for E > 0.5 Mev the maximum shielding thickness is less than one mean free path. It is well-known that in light elements the build-up decreases with an energy increase (other conditions being equal). Therefore, the most significant build-up will occur for energies of E < 0.5 Mev. where the shielding thickness is larger than one mean free path.

The experimental data on the dose buildup factors for γ-rays with the energies E < 0.5 Mev (Ref. 11) were utilized to determine the buildup of scattered radiation in the shielding. These data were obtained by measuring the dose rate behind a barrier shielding made of aluminum, having a thickness in 1, 2, 3, and 4 mean free paths. Ce^{141}(0.145 Mev), Hg^{203}(o.280 Mev), and Cs^{137}(0.661 Mev) served as the sources of radiation. A scintillation γ-dosimeter with a compensated "hard behavior" served as the radiation detector in the energy region E from 50 to 200kev (Ref. 12). The results derived from this study are given in Figure 8.4. The buildup factors for smaller energies of γ-rays were obtained by extrapolation of the experimental data in Figure 8.4. When corrections are introduced for the buildup of scattered γ-rays in graphite (Z = 6), the use of buildup factors for aluminum does not have to lead to a significant error. This is confirmed, for example, by the results derived from measuring the buildup factors for low-energy γ-rays in plastic. Figure 8.5 presents a comparison of the data obtained

on the dose buildup factors in plastic, aluminum, and iron. Even for a γ-ray energy of 0.145 Mev, there is only a small difference between the buildup factors in plastic and aluminum. /250

When corrections are introduced for the buildup factor, it is possible to restrict oneself to the following maximum energies of γ-rays: 0.5 Mev for a shielding thickness of 10 g/cm^2; 0.1 Mev for a shielding thickness of 5 g/cm^2; and 0.05 Mev for a thickness of 3 g/cm^2, which can be seen from Tables 8.3 and 8.4. For larger

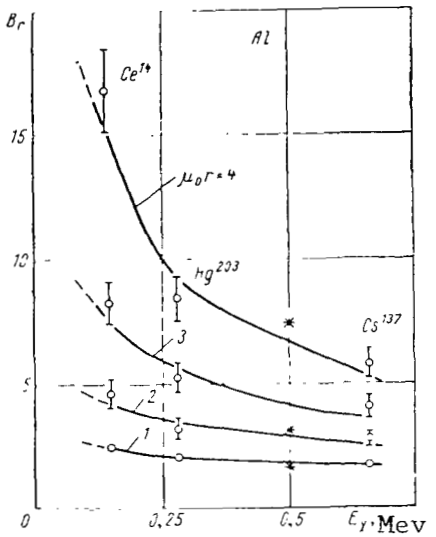

Figure 8.4

The Energy Dependence of the Dose Buildup Factor of γ-Rays in Barriers made of Aluminum having a Differing Thickness: * ——— Calculated by the Moment Method.

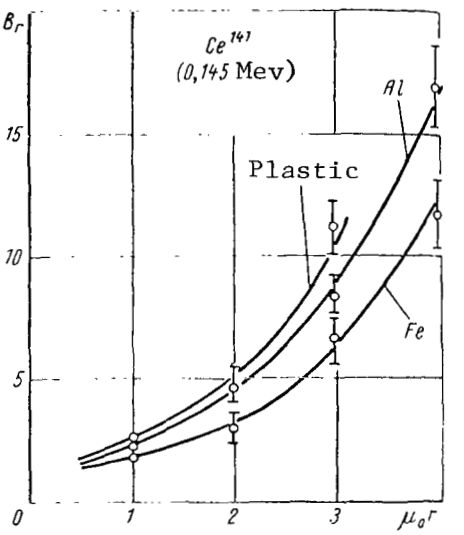

Figure 8.5

Comparison of Dosage Buildup Factors of γ-Rays of Ce^{141} (0.145 Mev) in Plastic, Aluminum, and Iron.

energies and smaller shielding thicknesses, the correction for the buildup factor will not be significant. Table 8.4 presents the results derived from determining the correction for the buildup factor with respect to the total dose rate of electromagnetic radiation for electrons having a given energy E_0. The magnitude of the correction for buildup is given in percents here, with respect to the total dose rate of electromagnetic radiation taken without correction. /251

It can be seen from the Table that the correction is quite significant for electron energies of $E_0 < 0.3$ Mev. After the

TABLE 8.4

DEPENDENCE OF CORRECTION FOR BUILDUP FACTOR OF SCATTERED γ-RAYS ON ELECTRON ENERGY

E_0, Mev	Correction Magnitude, %	E_0, Mev	Correction Magnitude, %
0.05	2400	1.00	100
0.10	650	5.00	15
0.30	200		

/250

correction was introduced for the buildup factor, the dose rate values were totalled over all the energy intervals of electromagnetic radiation energy, for each electron energy E_0. The results derived from this totalizing procedure are given in Table 8.5. /251

TABLE 8.5

DOSE RATE VALUES FOR THE TOTAL ELECTRON STREAM WITH A GIVEN ENERGY $1 \cdot 10^7$ $cm^{-2} \cdot sec^{-1}$, mrad/hour

E0 Mev	d, g/cm^2						
	0,1	0,2	0,5	1,0	3,0	5,0	10,0
0,05	2,58	1,84	1,09	0,60	0,33	0,327	0,146
0,10	4,46	4,18	3,50	3,81	2,83	1,34	0,375
0,30	31,8	27,20	15,10	6,85	2,18	1,87	1,520
1,00	35;5	34,60	32,80	30,70	25,30	21,80	19,40
2,00	118,0	117,00	113,00	108,00	88,00	76,90	67,60
3,00	266,0	235,00	227,00	218,00	210,00	209,00	144,00
4,00	456,0	452,00	447,00	428,00	368,00	319,00	240,00
5,00	697,0	691,00	675,00	656,00	570,00	495,00	476,00

The data given in Table 8.5 were reduced to the electron spectrum in the outer zone by multiplying the dose rate by the magnitude of the electron stream having a given energy, which was given in Table 5.1. The results derived from these calculations are given in Table 8.6. As can be seen from this Table, electrons having energies of 0.05, 0.10, and 0.3 Mev make the greatest contributions to the dose rate of electromagnetic radiation for electrons in the outer zone. A sharp decrease in the dose rate was observed in the energy region 0.10 - 1.0 Mev, and then there was a slow decrease to the maximum energy of electrons in the outer zone. /252

Graphic integration of the data given in Table 8.6, in the energy region of 0.05 - 5.5 Mev, was carried out in order to obtain the total dose rate of electromagnetic radiation from all electrons in the outer zone.

TABLE 8.6

DOSE RATE OF ELECTROMAGNETIC RADIATION FOR ELECTRONS IN THE OUTER ZONE (SEE TABLE 5.1), mrad/hour

E_0 Mev	d, g/cm^2						
	0,1	0,2	0,5	1,0	3,0	5,0	10,0
0,05	15,500	11,050	6,540	3,600	1,980	1,970	0,870
0,10	8,020	7,550	6,300	5,440	5,110	2,420	0,680
0,30	2,130	1,820	1,010	0,460	0,146	0,125	0,102
1,00	0,064	0,062	0,059	0,055	0,046	0,039	0,035
2,00	0,027	0,026	0,025	0,024	0,020	0,017	0,015
3,00	0,018	0,016	0,015	0,015	0,014	0,014	0,010
4,00	0,013	0,013	0,012	0,012	0,010	0,009	0,007
5,00	0,010	0,010	0,010	0,009	0,008	0,007	0,006

Table 8.7 (first column) presents the results derived from performing integration for all shielding thicknesses. The results derived from analogous calculations are given in the second column, but for an electron spectrum which was determined from data in the work (Ref. 13), for a total electron stream having the energy $E_0 > 0.03$ Mev, equaling 10^{11} cm$^{-2}\cdot$sec^{-1}.

The ratios of the last quantities to the corresponding first quantities fluctuate within the limits $0.5\cdot10^2$ (for large thicknesses) up to $2\cdot10^2$ (for small thicknesses). This indicates that there was a greater amount of error, particularly in the soft part of the spectrum, in earlier estimates of the spectrum for electrons in the outer zone. Calculations of the dose rate for electromagnetic radiation (Ref. 4) yielded results which exceeded our estimate (second column) - which was based on earlier information regarding the electron spectrum - by approximately 25 times.

In conclusion, it should be noted that the data obtained can be readily extended to other shielding elements (for example, aluminum, Dural, etc.) by multiplying the values obtained by the ratio $Z_{eff}/6$. This should not cause a large error, since the mass absorption coefficients for γ-rays and the buildup factors, included in formula (8.11), differ very little from each other for substances having similar atomic numbers. All of the other values in Formula (8.11) either do not depend on Z_{eff} or are proportional to it.

8.3. Determination of Radiation Danger from Penetrating Electrons in the Outer Zone

It was shown in Chapter 5 that the electron spectrum in the outer zone lies between 0.05 - 5 Mev. The determination given above for radiation danger arising from electromagnetic radiation can not be regarded as exhaustive, since electrons with this spectrum can frequently penetrate the shielding shell having a small thickness.

TABLE 8.7

CHANGE IN THE TOTAL DOSE RATE OF ELECTROMAGNETIC RADIATION WITH THE SHIELDING THICKNESS FOR TWO DETERMINATIONS OF THE SPECTRUM FOR ELECTRONS IN THE OUTER ZONE

d, g/cm^2	0,1	0,2	0,5	1,0	3,0	5,0	10,0
P_T, $\frac{\text{mrad}}{\text{hour}}$	228	200	140	107	82	49	18
P'_T, $\frac{\text{mrad}}{\text{hour}}$	51 000	38 200	21 000	9000	4060	2700	1200

The absorbed dose rate from electrons having the energy E_0, which penetrate a shielding shell having the thickness d, can be calculated according to the formula

$$P_{e1}(d) = \frac{1}{4}\int_{E_{0\min}}^{E_{0\max}} N(E_0)\,1{,}6\cdot 10^{-8}\left(-\frac{dE_0}{dx}\right)\Delta x_{\ell} e^{-\mu(E_0)\,d} dE_0, \qquad (8.16)^*$$

where $N(E_0)$ is the total nondirectional stream of electrons having the energy E_0 per unit energy interval; $\left(\frac{-dE_0}{dx}\right)\Delta x_{\ell}$ is the energy losses of electrons having the energy E_0 in a living layer of biological tissue; $\mu(E_0) = \frac{0.693}{\Delta(E_0)}$ is the attenuation coefficient for electrons having the energy E_0; $\Delta(E_0)$ is the layer of half-attenuation in the shielding material.

Results given in the work (Ref. 14) were used to calculate the magnitudes of the half-attenuation layers. The values of the half-attenuation layers were taken for aluminum, which could not produce a large error, since the magnitudes of the half-attenuation layers and the electron ranges in light elements, expressed in g/cm^2, are quite close to each other [see (Ref. 15)for example].

Table 8.8 presents the results derived from calculating the contributions to the dose rate from individual electron components for the spectrum of the outer zone (see Chapter 5).

The dose rates from the total electron spectrum for the outer zone were calculated by graphic integration of data given in Table 8.8, for different shielding thicknesses. The results of the graphic /254

* The electron energy change during attenuation in the shielding is not taken into account in formula (8.15).

TABLE 8.8

DOSE RATE OF ELECTRONS, mrad/hour

E_0 Mev	Shielding Thickness g/cm^2				
	0,1	0,2	0,5	1,0	3,0
0,6	3,2	—	—	—	—
0,6	32,4	17,7	—	—	—
1,0	288	82,5	1,08	—	—
1,5	148	73	6,5	0,25	—
2,0	72	41	9,6	0,90	—
3,0	23,8	17,2	6,5	1,22	$1,4\ 10^{-3}$
3,5	16,2	11,6	5,1	1,13	$3,9\ 10^{-3}$
4,0	10,8	8,25	3,8	1,08	$6\ 10^{-3}$
5,0	5,7	4,7	2,5	0,9	$1,5\ 10^{-3}$

integration are given in Table 8.9.

TABLE 8.9

TOTAL ELECTRON DOSE RATE FOR THE OUTER ZONE FOR DIFFERENT SHIELDING THICKNESSES

d, g/cm^2	0.1	0.2	0.5	1.0	3.0
P_{el} $\frac{mrad}{hour}$	29 200	13 600	2343	394	0.08

It can be seen from Table 8.8 that the dependence of the electron dose rate on their energy passes though a maximum for all thicknesses. The location of the maximum is displaced toward the region of high energies as the shielding thickness increases, which points to filtration of low-energy electrons by the shielding.

Finally, we would like to point out the rather sharp decrease in the electron dose rate as compared with the electromagnetic radiation , when the shielding thickness increases.

8.4. Total Radiation Dose in the Outer Zone

After a calculation of the dose rate from electromagnetic radiation and from penetrating electrons in the outer zone, the total radiation danger can be determined. The data from Tables 8.7 and 8.9 are combined in Table 8.10, and the total dose rate is given.

It can be seen that for shielding thicknesses $\leqslant 1.10\ g/cm^2$, electrons penetrating the shielding make an overwhelming contribution

TABLE 8.10

QUANTITIES P_T, P_{el}, AND THE TOTAL DOSE RATE P FOR DIFFERENT SHIELDING THICKNESSES

d, g/cm^2	0,1	0,2	0,5	1,0	3,0	5,0	10,0
P_T, mrad/hour	228	200	140	107	82,3	48,6	17,9
P_{el}, mrad/hour	29 200	13 600	2340	394	0,08	0	0
P, mrad/hour	29 430	13 800	2480	501	82,4	48,6	17,9

to the dose rate. Electromagnetic radiation plays a dominating role only for thicknesses which are larger than 1.0 g/cm^2.

Figure 8.6 graphically illustrates the dependence of the total dose rate on the shielding thickness. With the aid of this graph, /255
it is possible to estimate the total radiation dose, which the cosmonaut can receive while flying in the outer zone of the earth. We should remember that the data given in Figure 8.6 pertain to the radiation intensity maximum of the outer zone. Therefore, it is possible to estimate the maximum possible dose in the outer zone on the basis of these data - i.e., the dose during a flight in the outer zone, estimated according to the intensity maximum

$$D\max(d) = P(d)\, t. \qquad (8.17)$$

In order to obtain the maximum dose, on the basis of a known shielding thickness d,it is sufficient to find the dose rate P on the graph, and then the maximum dose will be determined by relationship (8.16).

In order to determine the dose which is actually possible during a flight in the outer zone, it is necessary to know the dose rate distribution along the flight trajectory P(H) and the time at which the object is located at a given latitude $\frac{dH}{v(H)}$. Then the dose will be determined from the relationship

$$D(d) = \int_{H\,\min}^{H\,\max} P(d, H)\frac{dH}{v(H)}, \qquad (8.18)$$

/256

where H is the point coordinate; v(H) is the velocity of the spacecraft at a given point. The quantity P(d, H) can be found from Figure 8.6 by normalization at the relative magnitude of radiation intensity in the outer zone, during a flight along a given trajectory. The results

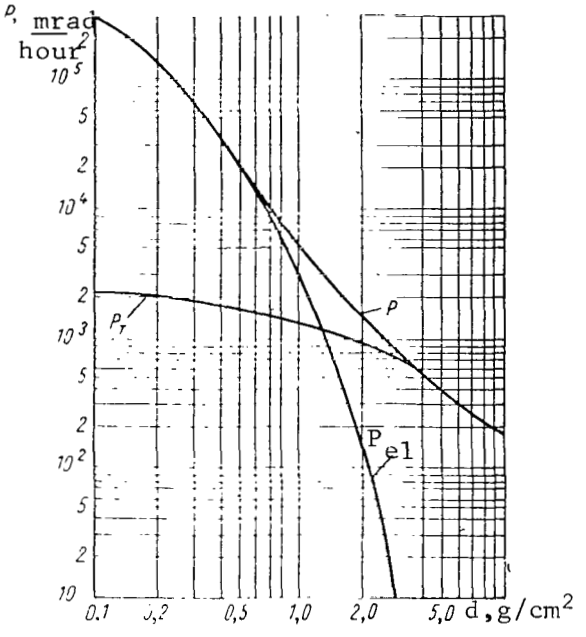

Figure 8.6

Dependence of the Electron Dose Rate P_{el}, Electromagnetic Radiation P_T, and the Total Dose Rate P on the Shielding Thickness, at the Intensity Maximum of the Electron Zone.

given in the works (Ref. 4, 16, 17) can be utilized for this purpose. With respect to the time at which an object is located at a given point, it can be determined from the flight conditions - i.e., from the velocity of the spacecraft and the program to be accomplished. If the time at which an object is located at all the latitudes is the same (i.e., the velocity at which a given latitude is crossed is constant), then the total dose throughout the entire flight can be determined as

$$D(d) = tK \int_{H\,\min}^{H\,\max} P(d, H)\, dH, \tag{8.19}$$

where t is the total time which an object remains in the outer zone; K is the constant, which is dependent on the selection of units. If the admissible radiation dose during flights in cosmic space D_0 is known, it is possible to vary either the time at which the cosmonaut is located at a given trajectory, or the necessary shielding shell thickness. The calculation must be made according to equation (8.19), assuming that $D(d) = D_0$.

8.5. Practical Considerations on Shielding from Radiation in the Outer Zone

The radiation danger at the intensity maximum of the outer zone was determined above. It was shown that for small thicknesses of the shielding shell (< 1.0 g/cm^2), heavy electrons which can penetrate the shielding make the primary contribution to the radiation dose. For the thicknesses $d > 1.0$ g/cm^2, electromagnetic radiation makes the primary contribution to the dose. There are thus two main requirements for shielding from radiation in the outer zone: 1) the shielding must be made of a material having a small atomic number, in order to decrease the generation of electromagnetic radiation, and 2) the shielding must be prepared from a material having a high atomic number, in order to increase the absorption of electromagnetic radiation.

These two conditions are satisfied by a combined shielding, which consists, for example, of a layer of material having a low Z (external layer) and a layer of material having a high Z (internal layer). If the fact is taken into consideration that electrons having energies of 0.1 and 0.2 Mev make a significant contribution to the dose of electromagnetic radiation (they cannot cause electromagnetic radiation with a high energy), the addition of a layer of lead, having a thickness of 0.25 g/cm^2, to the inner side of the shielding decreases the dose of electromagnetic radiation by a factor of approximately 3 - 4. A similar estimate was made, for example, in the work (Ref. 4). In addition to this, we must point out that a combined shielding, whose layers are arranged as indicated above, considerably decreases the buildup of scattered radiation (Ref. 10, Ref. 18), reducing it to approximately /257
the buildup in a material having a high atomic number. This effect is intensified with an energy decrease. A comparison of the buildup factors for γ-rays having an energy of 0.145 Mev and aluminum and iron (see Figure 8.2) shows that a difference of 1.5 - 2 times can be attained. The use of a lead layer, instead of iron, in a combined shielding must increase the difference in the buildup effect to an even greater extent.

However, the considerations expressed above on the construction of a radiation shielding must be applied within certain limits. For a thickness of the external layer which is less than 1.0 g/cm^2, the small addition of a material having a high atomic number can lead to considerable electromagnetic radiation. Let us now turn to formula (8.17) and estimate the permissible time that a cosmonaut may remain in the outer zone. For this estimate, it is necessary to define the permissible radiation dose for flights in space. Let us define 25 rad as the permissible dose and let us set the shielding thickness at $d = 5$ g/cm^2; we then have

$$t_{perm} = \frac{D_0}{P(s)} = \frac{25}{0.0486} \approx 500 \text{ r} \approx 20 \text{ days}$$

Thus, a shielding thickness which is permissible in practice can be selected for flights within the limits of the outer zone. However, let us take into account only radiation of the outer zone, and not radiation from solar flares - whose shielding requires a special examination. In addition, a permissible dose of 25 rad was assumed in the estimates which is not completely valid, since during a spaceflight several other harmful factors influence man - whose combined influence on a living organism requires a special study.

REFERENCES

1. Heitler, W. Quantum Theory of Radiation (Kvantovaya teoriya izlucheniy). Izd-vo Inostr. Lit., Moscow, 1956.

2. Wyard, S. J. Proc. Phys. Soc., A65, 389, 377, 1952.

3. Wyard, S. J. Nucleonics, 13, 7, 44, 1955.

4. Keller, Y. W., Schaeffer, N. M. Electr. Engng., 79, 1049, 1960.

5. Wu, C. S. Phys. Rev., 59, 6, 481, 1941.

6. Nelipa, N. F. Introduction to the Theory of Multiple Particle Scattering (Vvedeniye v teoriyu mnogokratnogo rasseyaniya chastits). Atomizdat, Moscow, 1960.

7. Blokhin, M. A. Physics of X-Rays (Fizika rentgenovskikh luchey). Gostekhnizdat, Moscow, 1953.

8. White, Grodstein, Gladis, NBS Circ., 583, 1957.

9. Leypunskiy, O. I. et al. Propagation of γ-Quanta in Matter (Rasprostraneniye γ-kvantov v veshchestve). Fizmatgiz, Moscow, 1960.

10. Gol'dshteyn, G. Bases of Reactor Shieldings (Osnovy zashchity reaktorov). Gosatomizdat, Moscow, 1961.

11. Larichev, A. V., Mitin, V. I. Dose Build-up Factors of γ-Rays with Small Energy (Faktory nakopleniya dozy γ-luchey maloy energii). In the Collection: Problems of Shielding from Radiation and Dosimetry(Voprosy zashchity ot izlucheniy i dozimetrii). No. 1, Gosatomizdat, Moscow, 1962.

12. Larichev, A. V., Levchenko, V. P. Scintillation γ-Dosimeter

with Compensation for "Hard Behavior" (Stsintillyatsionnyy γ-dozimetr s kompensatsiyey "khoda s zhestkost'yu"). In the Collection: Problems of Shielding from Radiation and Dosimetry (Voprosy zashchity ot izlucheniy i dozimetrii). No. 1, Gosatomizdat, Moscow, 1962.

13. Logachev, Yu. I. Geomagnetizm i Aeronomiya. No. 1, Izd-vo AN SSSR, Moscow, 1961. /258

14. Gusev, N. G. Handbook on Radioactive Radiation and Shielding (Spravochnik po radioaktivnym izlucheniyam i zashchite). Medgiz, Moscow, 1956.

15. Aglintsev, K. K. Dosimetry of Ionizing Radiation (Dozimetriya ioniziruyushchikh izlucheniy). Gostekhizdat, Moscow, 1957.

16. Vernov, S. N., et al Measurement of Radiation on the Flight of the Second Cosmic Rocket (Izmereniye radiatsii pri polete vtoroy kosmicheskoy rakety). In the Collection: Iskusstvennyye Sputniki Zemli, No. 5, Izd-vo AN SSSR, Moscow, 1961.

17. MacDonald, D. Burry, R., Eierman, W. S. American Astronaut. Soc., Preprint No. 61-101, 1961.

18. Larichev, A. V., Klimanova, L. F. Angular and Energy Distributions of γ-Rays of Co^{60} Scattered in a Heterogeneous Medium of Al + Pb.(Uglovyye i energeticheskiye raspredeleniya γ-luchey Co^{60} rasseyannykh v geterogennoy srede Al + Pb). In the Collection: Instruments and Methods of Analyzing Radiation (Pribory i metody analiza izlucheniy). No. III, Gosatomizdat, Moscow, 1962.

CHAPTER 9

NUCLEAR ENERGY SOURCES ON SPACE VEHICLES

9.1. Necessity of and Prospects for Application of Nuclear Energy During Spaceflights

One of the basic problems, which is also the most complex, /259
in rocket technology is the problem of developing a highly-effective engine. The following types of rocket engines can be used for interplanetary flight: engines which utilize chemical energy of liquid or solid fuels; engines which utilize the recombination energy of free radicals; engines which utilize solar energy; nuclear engines with a reactor of solid or liquid nuclear fuel; nuclear engines with a reactor of a gas-like nuclear fuel; electric jet (ion and plasma) engines; engines utilizing a series of nuclear explosions; thermonuclear and photon engines.

The main, characteristic parameters of engines are the specific impulse, the ratio of the thrust to the initial weight, and the specific weight of the power unit (Ref. 1). By way of an example, let us examine the operation of a rocket engine (RE), the layout for which is shown in Figure 9.1 (Ref. 1 - 3).

Under pressure, the working medium is supplied to the engine reactor, where - as a result of heating - the liquid working medium is evaporated. The gas-like working medium, which is heated up to a high temperature, expands into the nozzle canal from the pressure at the output of the active zone to the pressure at the nozzle output, and flows into the surrounding medium at a large velocity. Due to this, the reactive force (thrust force) of the engine is formed.

Examining all of the forces which act upon the solid walls of the engine, we can readily determine the force resulting from these forces - i.e., the thrust force. It can be readily shown that the following expression can be obtained as a result for the thrust force:

$$F = \frac{G}{g} v + f(P - P_{н}), \text{ kil. force}, \qquad (9.1)$$

where G is the fuel consumption, kg/sec; g is the acceleration of gravity, m/sec^2; v is the velocity at which the gas escapes from the nozzle, m/sec; f is the area of the nozzle outflow cross-section, /260
cm^2; p is the pressure at the nozzle output, atm; p_H is the outside pressure, atm.

For a pressure at the nozzle output which equals the pressure of the surrounding medium, the thrust force equals

$$F = \frac{G}{g} v. \tag{9.2}$$

However, this absolute magnitude of the developed thrust does not characterize the performance of the RE. A qualitative index for RE operation is the specific thrust (or specific impulse), i.e., the thrust per unit of fuel consumed

$$J_s = \frac{F}{G}. \tag{9.3}$$

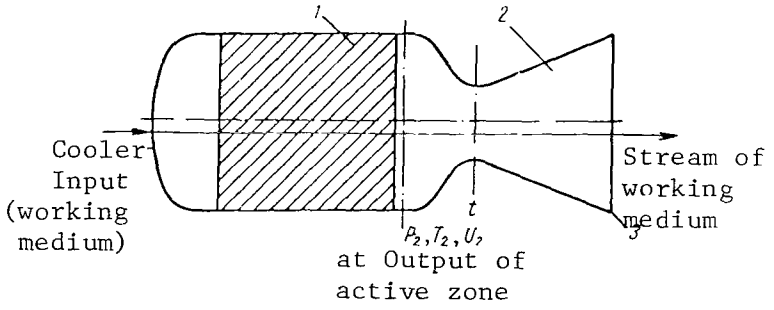

Figure 9.1

Layout of a Rocket Engine:

1- Source of Thermal Energy, Reactor; 2- Nozzle; 3- Nozzle Output.

It follows from the latter equation that the greater the specific thrust, the less the consumption of fuel which is necessary to obtain a given thrust. Therefore, attempts should be made to obtain the largest possible specific thrust. In a vacuum, the thrust and specific thrust are quantities which are not dependent on the pressure of the surrounding medium - i.e., quantities which characterize only the engine - and are frequently used to appraise a rocket engine.

A rocket engine is a type of fuel engine and, consequently, its operation is connected with a change in pressure, temperature, and velocity of motion for gases. By examining the thermodynamic cycle of the engine, one can obtain the following relationship between the cycle operation and the specific thrust (for a calculated regime of engine operation in a vacuum, i.e., when $p_H = 0$) (Ref. 4):

$$J_s = \left[\frac{2}{g}\frac{k}{k-1}\frac{RT_2}{M}\left(1-\frac{p}{p_2}\right)^{\frac{k-1}{k}}+\left(\frac{v_2}{g}\right)^2\right]^{1/2}+$$
$$+\left(\frac{p}{p_2}\right)^{\frac{k-1}{k}}\left[\frac{k-1}{2k}\frac{R}{Mg}\frac{T_2}{\left(1-\frac{p}{p_2}\right)^{\frac{k-1}{k}}}\right]^{1/2}, \qquad (9.4)$$

where $K = \frac{C_p}{C_v}$ is the adiabatic index; C_p is the specific heat, /261

which is the mean integral heat with respect to temperature, at a constant pressure in the temperature interval from T_2 to T; C_v is the specific heat at a constant volume; T_2 is the maximum gas temperature at the output of the active zone; p_2 is the pressure before the nozzle input; p is the pressure at the nozzle output; R is the gas constant; v_2 is the velocity of the working medium at the output of the active zone; M is the molecular weight of the working medium.

It thus follows from formula (9.4) that the working medium with a low molecular weight will provide a large specific thrust for a given maximum temperature. This method of utilizing the energy from nuclear reactions opens up very great possibilities in the selection of the energy carrier in the engine. A substance with the smallest possible molecular weight can be selected as the working medium which receives the energy from the nuclear reactions and applies it in the form of heat. Data on the specific thrust, which can be obtained when atomic energy is utilized, show that the thrust - which is larger than for normal fuels - can be achieved only at a high temperature in the chamber, or by utilizing hydrogen as the working medium for the engine.

Apart from the basic characteristic parameters of the RE which were discussed above, there are several qualitative and quantitative characteristics which determine the performance of the engine, but very few of them can be analyzed with the necessary degree of reliability at the present time. Such characteristics include the resource (operational time of the engine without repair); the vulnerability with respect to different influences in a surrounding cosmic space - for example, meteorites; the efficiency of the elements comprising the engine, or the extent to which the given principle for creating thrust can be actually realized at the present level of our scientific and technical knowledge.

Table 9.1 presents several parameters of different types of rocket engines. The comparative characteristics of the engines are also given in Figure 9.2 (Ref. 5, Ref. 6).

TABLE 9.1

PARAMETERS OF DIFFERENT ROCKET ENGINES

Engine	Specific Impulse (Specific Thrust)	Ratio of Thrust to Weight	Lifetime
Operating on chemical fuel	200 - 430	0.01 - 200	Several minutes.
Nuclear	500 - 1100	0.01 - 10	From several minutes to several hours.
Electric Jet (ion and plasma)	1000 - 30000	10^{-2} - 10^{-6}	Several weeks.

When the development of rocket technology was in its initial /262
stages, the problem of creating a highly-effective engine tended to be solved by utilizing chemical fuel energy. It is possible to leave the gravitational field of the earth, which is necessary for spaceflight, only by utilizing chemical rocket engines with multi-stage rockets due to the inadequate specific impulse.

In spite of the tremendous successes which have been achieved recently in the development of chemical engines (both liquid rocket engines, and solid fuel rocket engines), they have several disadvantages which restrict their application for interplanetary flight. A basic disadvantage is the limited specific impulse, which - although it increases from year to year - does not exceed a limiting value of approximately 450 kg·sec/kg (liquid hydrogen with liquid fluorine, etc.). With respect to the limited specific impulse, if even a small effective load is placed on a rocket for an interplanetary flight, it leads to an enormous initial weight and colossal rocket dimensions. Besides technical difficulties, this entails an enormous cost for building such a rocket.

The specific thrust of chemical engines can be increased in two ways: by increasing the pressure in the combustion chamber and by investigating new, high-energy fuels. The pressure increase in the combustion chamber entails additional difficulties in the fuel supply system and also causes various other construction difficulties.

Solid fuel rocket engines have several advantages over liquid fuels, in terms of simplicity, greater reliability, and small specific weight.

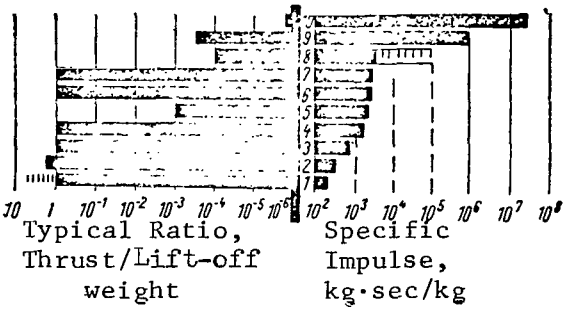

Figure 9.2

Approximate Comparative Characteristics of Engines for Interplanetary Flight:

1- Modern liquid and powder rocket engines; 2- Best Possible Chemical Engine; 3- Customary Nuclear Rocket Engine; 4- Combination of Nuclear and Chemical Engine; 5- Solar Power Device; 6- Engine of Free Radicals; 7- Nuclear Engine with Gaseous Fuel Unit; 8- Ion Engine; 9- Thermonuclear; 10- Photon.

However, in view of the limited specific impulse, both solid /263
fuel rocket engines and liquid rocket engines barely meet the demands imposed on an engine which can make an interplanetary flight. Therefore, they can be regarded only as temporary replacements for such an engine during the first stages of interplanetary flight, or as starting engines for the first rocket stages for the lift-off of an interplanetary rocket and exit from the gravitational field of the earth.

In order to overcome the barrier of the specific impulse, which is imposed by a chemical rocket engine, it is necessary to use primarily new types of engines. Thus, the utilization of energy which is liberated during the recombination of metastable free radicals makes a significant contribution to the specific impulse. For example, an engine which utilizes energy liberated during the recombination of atomic hydrogen provides a specific impulse up to 1500 kg·sec/kg. The problem which is encountered here consists of obtaining and storing on board the rocket "frozen" active metastable radicals.

However, the limitation of chemical energy sources must be clearly pointed out, which makes rockets based on chemical fuel unsuitable for long spaceflights. Actually, the energy capacity of accumulators equals 1.3 sq.m.·hour per 1 kg. The energy capacity of normal electrochemical batteries (for example, silver oxide - zinc) equals 0.22 sq.m.·hour per 1 kg. When the chemical oxidation reaction is used, the energy capacity of 1 kg fuel is 2.6 sq.m.·hour. It is possible to obtain approximately

$4 \cdot 10^5$ sq.m.·hour from the disintegration of 1 kg radioactive isotope. $2 \cdot 10^7$ sq.m.·hour of thermal energy is liberated from the fission of 1 kg uranium. The greatest advances in the development of a rocket engine for interplanetary flight can be expected from the use of nuclear energy in the engine.

Nuclear energy sources can be conditionally divided into three types, with respect to their methods of application:

1) Nuclear rocket engines (NRE) with the working medium being directly heated in the active zone, which are based on the thermal-exchange principle. In such engines, a nuclear reactor is directly employed for heating the gases flowing out of the rocket engine nozzles (Ref. 6, Ref. 7);

2) Nuclear-electric rocket engines (NERE). In such engines, the energy from fission, fusion, or disintegration of the nuclei is converted by a certain method into electric energy, which is utilized for ionization, heating, and acceleration of the working medium;

3) Nuclear engines which utilize a series of nuclear explosions for creating thrust.

The fact that such a classification is conditional is apparent in the fact that there may be engine systems which combine the different types of engines given above. In engines with reactors, operating on solid and gaseous nuclear fuel, nuclear energy is used for heating the /264
working medium which is stored on the rocket. The working medium then expands into the normal rocket nozzle, and flows into space. If the fact is taken into account that the specific impulse is proportional to the square root of the ratio of the temperature in the chamber to the molecular weight of the emitted gases [see formula (9.4)], it is possible to obtain a doubled specific impulse in a nuclear rocket engine - if hydrogen is used as the working medium (since the molecular weight of hydrogen is 2, and the lowest molecular weight of the gases emitted from the chemical engine is about 9). The reactor operates with solid nuclear fuel at a temperature of the working medium, which is equivalent to the temperature in the chamber of the liquid chemical engine.

Methods for Increasing Specific Impulse

When a liquid or gaseous nuclear fuel is used, it is possible to utilize the energy from nuclear reactions more completely, by bringing the temperature in the chamber up to 25 000 - 30 000° C. If hydrogen is used as the working medium, which breaks down completely at these temperatures, it is possible to obtain a specific impulse on the order of 3000 kg·sec/kg. However, the difficulties which are encountered with a reactor operating with a gaseous nuclear fuel - with cooling of the chamber, nozzle, etc. - are so great that they cannot be

overcome at the present time.

One method for significantly increasing the specific impulse could be a temperature increase of the gas stream leaving the reactor, before it expands into the nozzle, with the aid of an electric arc supplied by a current which is generated by utilizing the reactor thermal energy. But nuclear engines offer the most comprehensive utilization of energy from nuclear reactions for jet motion. In these engines, a stream of products resulting from nuclear reactions (which are either nuclear fission fragments or products of thermonuclear fusion) occurring in the nuclear reactor comprise the gas jet stream; this stream of nuclear reaction products can be directed, for example, by utilizing magnetic fields.

The extremely high temperature which develops during nuclear reactions, which amounts to about a billion degrees particularly for thermonuclear reactions, makes it possible to obtain a specific impulse of 1,000,000 kg·sec/kg in such an engine. The existence of such an engine in the near future is not possible, if only due to the unsolved problem of the directionality of particles - products resulting from nuclear reactions, not mentioning other problems.

Very high velocities for a directional stream of particles, and consequently very high specific impulses, can be achieved in a relatively more simple manner in an ion engine, where the ions and electrons - which are obtained as the result of ionization of the working medium in the reactor - are accelerated by the electro- /265
magnetic field up to enormous velocities and escape into space.

For a practicable ion engine with a high specific impulse on the order of 100,000 kg·sec/kg, the total thrust which is developed by the engine is quite small - on the order of several kilograms. The ratio of thrust to rocket weight is considerably less than unity, and therefore the ascent and escape of the interplanetary rocket from the gravitational field of the earth must be performed by auxiliary engines, which create the necessary thrust. However, outside of the gravitational field, and in the absence of resistance, the thrust created by the ion engine is sufficient for the acceleration of the interplanetary rocket up to the required velocity.

Thus, an ion engine can be regarded as one of the most probable engines for interplanetary flight in the near future. There are also possibilities for plasma engines.

Finally, the photon engine will represent the limits of progress in jet motion. If it were possible to direct a photon stream

having ultrahigh energy in one direction, a limiting specific impulse on the order of 10^8 kg·sec/kg would be obtained. The ratio of thrust to rocket weight will thus be extremely low. The creation of a photon engine belongs in the distant future.

9.2. Nuclear Rocket Engines Based on the Thermal Exchange Principle (Ref. 6 - 22)

Introduction

Since a controlled fission reaction was first carried out, many projects have been planned (Ref. 8, 9 and others) for utilizing nuclear energy to obtain jet thrust. Rocket engines with a thermal-exchange type of nuclear reactor have been examined in other works in sufficient detail (Ref. 6, 10). In these works, the problems of such engines were discussed, including an analysis of the construction, aspects of heat transfer, gas - and hydrodynamic, thermodynamic, ballistic flight, physics of reactors and shielding from radiation, and the results derived from careful mathematical analysis were presented, along with a justification for the physical bases of these results.

In principle, three arrangements of nuclear reactors will be examined, in which the fissionable material can be in a solid, liquid or gas state (Ref. 11). The simplest nuclear reactor has a solid fissionable material. The geometry for thermal-exchange, rocket nuclear reactors can be different. Nevertheless, all reactors can be divided into two basic categories, on the basis of the structure of the active zone: homogeneous and heterogeneous.

Homogeneous Reactors

The active zone of a thermal-exchange type of homogeneous reactors is not strictly homogeneous, but it can be assumed to be if the dimensions of the structural connections are small as compared with the neutron scattering length in the active zone. In constructions of thermal-exchange rocket reactors having a complex structure, this condition is usually satisfied. /266

For the most optimum characteristics (for minimum volume) of heat exchangers, in the operation of which temperature is a limiting factor, it is necessary that the heat release per unit of time be maximum at a certain point close to the input section of the coolant stream, and that it decrease monotonically along it from the given point.

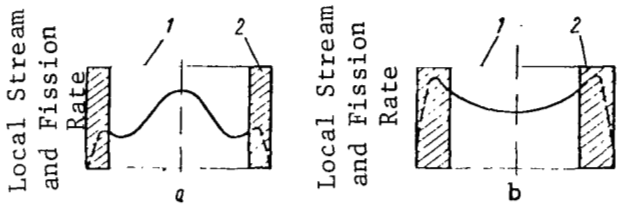

Figure 9.3

Radial Distribution of a Neutron Stream in the Homogeneous Active Zone in the Presence of a Thin (a) and Thick (b) Reflector:

1- Active Zone; 2- Reflector.

The fission rate distribution can approximate the distribution corresponding to maximum efficiency of the apparatus, by varying the local fuel concentration, or by selecting the appropriate reactor geometry. In terms of provisional technology for producing fuel elements, it is desirable to have uniform loading of the reactor by a nuclear fuel, and to form the fission intensity distribution by varying the neutron stream distribution. In each homogeneous active zone without a reflector, or with a fine reflector layer, the neutron stream drops down toward the periphery; therefore, in such reactors it is best to direct the coolant along the radius toward the periphery. Unfortunately, such a direction for the coolant is not always the most desirable for several reasons.

In a reactor without a coolant, in which the active zone has good decelerating power, the neutron stream and the fission rate decrease toward its periphery; in a reactor with a thick reflector and an active zone with poor decelerating power, the fission rate is maximum at the periphery of the active zone. By supplying the homogeneous active zone with an outer reflector made of a suitable material having the appropriate form and thickness, one can approximately obtain a uniform, radial distribution of the neutron stream, which represents an average distribution between the distributions in the two extreme cases given above (Figure 9.3). Usually, the required reflector weight is too large to produce good engine performance with a nuclear reactor. Therefore, a compromise must be made between varying the fuel loading and the use of reflectors. /267

Heterogeneous Reactors

In reactors with a heterogeneous active zone, attention must be paid to the nonuniform distribution of the neutron stream within the limits of each individual section and throughout the active zone of the reactor as a whole.

The ideas presented on the homogeneous active zone are valid for the neutron stream distribution in the active zone as a whole, namely: it is possible to smooth out the distribution curve for the total fission rate solely by using the appropriate outer reflector or by varying the fuel loading from one section to another, or by combining both methods to a certain extent. The fission rate distribution within the limits of each individual fuel unit in the moderator is determined by the same physical considerations. Each fuel unit is in a certain sense a system (reduced scale) with a self-sustaining fission reaction in the endless reflector-moderator located in a uniform neutron stream. The deceleration of the neutrons is caused almost entirely here by the properties of the moderating material in the active zone. The stream and fission rate always have a maximum at the outer boundary of the fuel unit, and it is particularly efficient to use a radial coolant stream in such a reactor, toward the center of each fuel unit. In order to provide the appropriate thermal exchange efficiency with an axial coolant stream (along the fuel unit) it is necessary that the concentration of the fuel change along the radius within the limits of the unit. The fission rate distribution curves in the active zone of a heterogeneous reactor are shown in Figure 9.4 for two extreme cases. It is much more complex to calculate the stationary neutron distribution for reactors having a heterogeneous active zone, than it is for homogeneous reactors. Nevertheless, reactors with a heterogeneous active zone are of great practical interest. In these reactors, the critical mass is less apparent in the fuel than it is in homogeneous ones, for rather thin shells made of slightly absorbent material. In addition, heterogeneous reactors can operate almost exclusively on thermal neutrons, with those small dimensions for which homogeneous reactors with a non-hydrogenous moderator (for example, with a beryllium or graphite moderator) must operate on rapid neutrons. Figure 9.5 schematically presents two reactors of the active zone type (Ref. 10, Ref. 12).

In a homogeneous reactor (Figure 9.5, a), uranium is uniformly distributed in a graphite moderator which is perforated by canals in order to heat the gaseous hydrogen which is pumped through them. The active zone of the reactor is surrounded by a beryllium reflector 150 mm thick. The thermal shielding attenuates direct radiation which is directed toward the high-pressure chamber walls, the turbine pump unit, and also the working medium, the tank, and the payload,

which are located in front of the nuclear apparatus.

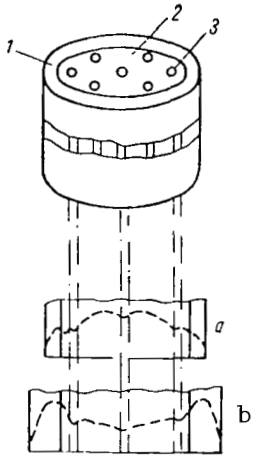

Figure 9.4

Radial Distribution of a Neutron Stream in the Heterogeneous Active Zone with a Thin (a) and Thick (b) Reflector:

1- Reflector; 2- Moderator; 3- Fuel Element.

In a heterogeneous reactor (Figure 9.5, b), uranium is contained in tungsten fuel elements which are located in the active zone with a moderator made of BeO, which has additional canals to cool it. All of the other construction elements, including the beryllium reflector, are similar for both types of reactors.

The working medium - liquid hydrogen - is supplied to the reactor with a turbine pump unit at a given input pressure, after it first cools the nozzle, reflector, and thermal shielding. In a reactor with tungsten fuel elements, the system for circulating hydrogen is somewhat more complex: the coolant current around the fuel elements first cools the moderator, and then - after passing through the fuel elements in the opposite direction - cools them. After being heated to a high temperature in the active zone of the reactor, hydrogen is ejected through the nozzle in order to create the jet thrust. /269

Thus, the reactor device includes an active zone, reflector, shielding, turbine pump unit, high pressure chamber, and nozzle. Figure 9.6 shows the arrangement for placing the reactor apparatus on a rocket. The basic components of such a nuclear rocket are: payload, control and guidance system, tank and frame, working medium and reactor apparatus. In order to illustrate the interconnection

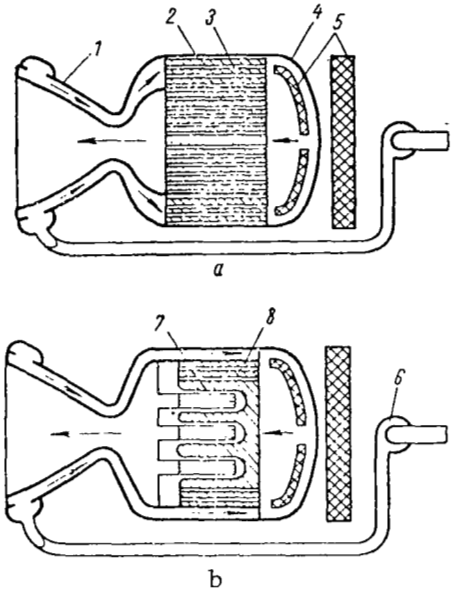

/268

Figure 9.5

Arrangement for a Reactor Energy Device for Homogeneous (a) and Heterogeneous (b) Reactors:

1- Nozzle; 2- Active Zone of the Reactor; 3- Reflector; 4- High-pressure chamber; 5- Shielding; 6- Pump; 7- Fuel Element; 8- Moderator.

between the reactor parameters and the performance of a nuclear rocket, we can cite the results derived from computational studies on determining the performance of single-stage nuclear rockets with hydrogen as the working medium, which employ the thermal-exchange type of reactors (Ref. 10). The two types of reactors given above (see Figure 9.5), having different dimensions and under different operational conditions, were examined in the study. A determination was made of the characteristic dependences of the payload on the flight weight of nuclear rockets designed to carry payloads to orbits of artificial earth satellites having an altitude of 480 km. The reactors, the limits of the research conditions, and the method of analysis will be examined at a later point.

/269

Graphite Homogeneous Reactors

Reactor and its Operational Parameters. It is assumed that in a graphite reactor the nuclear fuel (uranium) is uniformly

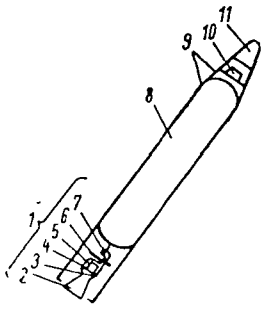

Figure 9.6

Arrangement of Nuclear Rocket:

1- Reactor Energy Device; 2- Nozzle; 3- High-Pressure Chamber; 4- Reflector; 5- Active Zone; 6- Shielding; 7- Turbine Pump Unit; 8- Working Medium; 9- Tank and Frame; 10- Control and Guidance System; 11- Payload.

distributed in the graphite moderator of the active zone. The graphite active zone can consist of plates, tubes, or simply solid cylinders with canals which intersect it. The active zone is examined below, in the form of a stack of parallel, flat plates which are divided by canals, in order to heat the gaseous hydrogen. In order to prevent erosion due to interaction with strongly- heated hydrogen, the blocks of graphite must have appropriate covering. The geometry of the reactor's active zone is determined by the requirements for heat transfer for the given active zone height and by the selected coolant volume. Such factors as the thermal stress which is formed in the fuel plates and the stability of the active zone design for the reactor must be taken into account in building a reactor.

The dimensions for the active zone of a graphite reactor were /270
calculated, based on the utilization of a beryllium reflector 150 mm thick. Special study showed that this thickness approaches the optimum thickness with respect to the minimum reactor weight per unit of stream cross-section in the active zone. In addition, it was assumed in the calculations that the ratio of atomic concentrations for graphite and uranium equals 500. This value was selected, because it was desired to have the maximum uranium concentration in graphite without serious damage to the stable properties of the latter. The

effect of the material for the graphite covering was not taken into account in the reactor calculations.

The critical diameters of the active zone were determined on the basis of the given assumptions, using a calculational procedure based on examining a tri-phase reactor with six groups of neutrons, which has been described in detail in other works (Ref. 13, Ref. 14). Table 9.2 presents the necessary data on graphite reactors which were selected for the study. For a given height of the reactor active zone, its diameter, and coolant volume, the operational parameters are also given in this Table, which must be given in order to determine the performance of the reactor heat transfer. It is assumed that hydrogen enters the reactor in a gaseous state at a temperature of 56°K. In order to determine the effect of the operational parameters on the performance of the nuclear rocket, the following limits were assumed for their change: hydrogen pressure at the input p_1 = 63 - 105 abs. atm., the effective wall temperature of the reactors $T_{w,eff}$ = 1890-2780°K. The hydrogen temperature at the output of the reactor T_2 was assumed to correspond to the thermal exchange efficiency $\varepsilon^* = 0.85$[1]. /271

TABLE 9.2
DATA FOR THREE GRAPHITE REACTORS AND THEIR OPERATIONAL PARAMETERS /270

Reactor Data	I	II	III
Atomic graphite-uranium ratio, R_a	500	500	500
Thickness and material of reflector, mm	150	150	150 (Be)
Active zone diameter $D_{a.z}$, m	0.94	1.07	1.23
Active Zone height $H_{a.z}$, m	0.7	0.85	0.99
Coolant volume, α	0.2	0.3	0.4
Load weight of uranium G_U, kg	27.7	35	46.4
Operational Parameters			
Effective wall temperature of reactor $T_{w, eff}$, °K	1890-2780		
Temperature at reactor output T_2, °K.....	1610-2370		
Temperature at reactor input T_1, °K	56		
Number M_1 at reactor input	0.05		
Pressure at reactor input p_1, abs. atm.	63-105		

A value was calculated for the Mach number M_1 which would approximate the critical regime at the reactor output; in every case, it was

[1] $\varepsilon^* = \frac{(T_2 - T_1)}{(T_{w, eff} - T_1)}$ - thermal exchange efficiency in the reactor.

found equal to 0.05.

Analysis Method. The characteristics of heat transfer and pressure drop in the reactor were calculated along the reactor axis for the assumed values of the operational parameters. It was necessary to use this calculational method due to the great changes in the gas temperature and, consequently, its physical properties within the reactor limits. Thus, for example, if the mean properties of the coolant are used for calculating the characteristics of heat transfer, the obtained results exceed the accurate ones by 30%.

The final results of these calculations for the given reactor are: hydrogen pressure at the reactor output p_2, the number M_2, the required hydraulic canal diameter for the given T_2, and the assumed values of $T_1, p_1 T_{w,eff}$. Then the corresponding performance of a nuclear rocket utilizing the given reactor is determined. The flight weight of the rocket is mainly a function of the mass ratio (ratio of fuel weight to flight weight), weight of the tank and frame, weight of the power device, and the payload. The mass ratio is a function of the velocity at the end of the active phase and the specific impulse, if the effect of gravity and aerodynamic resistance is disregarded. The following were determined: the active zone of the reactor, the nuetron reflector, the high-pressure chamber, nozzle, thermal shielding, and turbine pump unit. Apart from other parameters, the flight weight was calculated on the basis of the ratio of the thrust to the flight weight $\frac{F}{G_d} = 2$. The mass ratio as a function of the specific impulse, the ratio of the thrust to the flight weight, and the requirements for velocity increase were determined on the basis of a formula, which was formulated under the assumption of a vertical flight in a uniform gravitational field, without taking into account aerodynamic resistance. It was assumed that Δv equals 7.93 km/sec. However, very good agreement was found when the values, which were thus obtained for the mass ratio, were compared with the results derived from calculations for the actual flight trajectory.

On the basis of the resulting requirements for the ratio of fuel rate, tank and frame, reactor device, and flight weight, the permissible payload was obtained for a flight into an artificial satellite orbit.

Figure 9.7 shows the characteristics for three graphite reactors with a coolant volume of $\alpha = 0.2$; 0.3 and 0.4. In each case, the effective wall temperature of the reactor canals $T_{w,\,eff}$ fluctuated within 1890-2780°K for the corresponding change in hydrogen temperature at the reactor output T_2 within the limits of 1610-2360°K. The hydrogen pressure at the reactor input changed within the limits of $p_1 = 63 - 105$ abs. atm.. The hydrogen temperature at the reactor /273

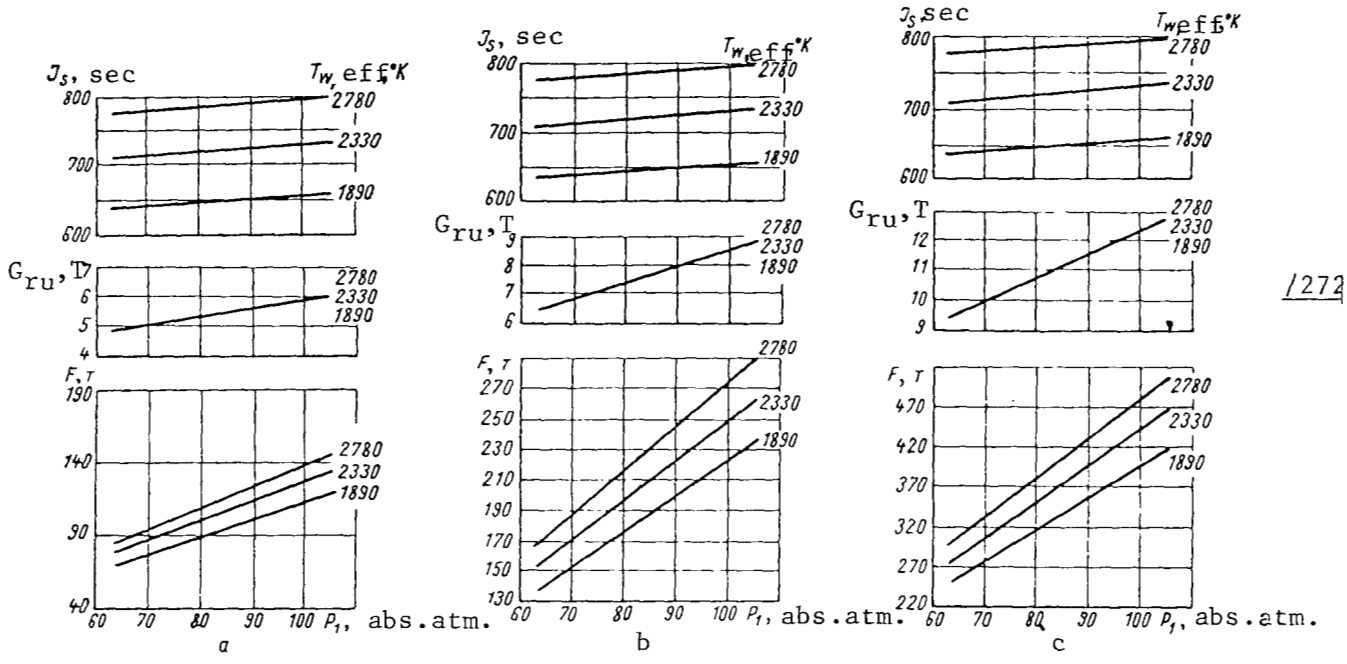

/272

Figure 9.7

Characteristics of Graphite Reactors:

a- Coolant Volume α = 0.20; Active Zone Diameter 0.94 m; Heighth of Active Zone, 0.75 m, and Weight of Uranium Load 27.7 kg;
b- Coolant Volume α = 0.30; Active Zone Diameter, 1.07 m; Active Zone Heighth, 0.85 m, and Weight of Uranium Load 35 kg;
c- Coolant Volume α = 0.40; Active Zone Diameter, 1.23 m; Active Zone Heighth, 0.99 m, and Weight of Uranium Load 46.4 kg.

input equaled T_1 = 56°K, and the M_1 number was assumed to equal 0.05. A typical value for the ratio of the total pressures at the reactor input and output equaled 0.66 for the number M_2 = 0.70. /273

The engine thrust F, the weight of the nuclear device $G_{r.u.}$, and the specific impulse J_s are shown in Figure 9.7 as a function of the pressure at the reactor input p_1 and the effective wall temperature for the reactor $T_{w,eff}$.

The increase in the thrust, which can be observed in Figure 9.7, a, as p_1 increases, at a constant temperature $T_{w,eff}$, is caused by an increase in the hydrogen density and an increase in

its consumption. The increase in the weight of the nuclear device G_{ru} (including the entire active zone of the reactor, nozzle, shielding, and turbine pump unit) as p_1 increases is caused by an increase in the weight of the high-pressure chamber, the nozzle, and the turbine pump unit. The small increase in the specific impulse with an increase in p_1 is caused by an increase of the expansion ratio in the nozzle.

The increase in thrust with temperature $T_{w,eff}$ at constant pressure p_1 is caused entirely by an increase in the specific impulse for a corresponding increase in the gas temperature at the output. In view of the fact that a change in the nuclear device weight is negligible with an increase in the temperature $T_{w,eff}$, only one curve is shown for all the temperatures.

An analogous picture can be observed in Figure 9.7, b and c for two other reactors. It should be noted that with an increase in the coolant volume α for the same values of p_1 and $T_{w,eff}$, the thrust F increases, which is caused by an increase in the coolant stream cross-section, and consequently an increase in the consumption. The weight of the nuclear device increases when the reactor dimensions increase, while the specific impulse remains constant.

Rocket Performance. The corresponding effect of p_1 and $T_{w,eff}$ on the performance of nuclear rockets utilizing these reactors is shown in Figure 9.8. As was pointed out above, the ratio F/G_d was assumed to equal 2, and the mass ratio (i.e., the ratio of the fuel weight to the initial flight weight) was selected, based on the requirements for an artificial earth satellite on an orbit at an altitude of 480 km. The flight weight of the nuclear rocket G_d, the mass ratio m_0, and the permissible payload G_p - which corresponds to the given flight weight - are given as functions of p_1 and $T_{w,eff}$. An increase in the flight weight for an increase in p_1 or $T_{w,eff}$ (see Figure 9.8, a) reflects an increase in thrust, which is shown in Figure 9.7. A decrease in the required mass ratio m_0 with an increase in temperature $T_{w,eff}$ is the result of an increase in the specific impulse for an increase in $T_{w,eff}$ and, consequently, the temperature at the output. The resulting payload G_p increases with an increase in p_1 and $T_{w,eff}$, which is related to an increase /275
in the flight weight and a decrease in the mass ratio, respectively. A similar interdependence is observed in Figure 9.8, b and c for the two other reactors. In addition, it should be noted that with an increase in the coolant volume α and the constants p_1 and $T_{w,eff}$, the flight weight increases. This is related to an increase in the stream cross-section and the thrust. As a result, a corresponding increase in the permissible payload is observed. The mass ratio remains constant.

Effect of Operational Parameters. Figures 9.9 - 9.11 show the effect which operational parameters - such as the hydrogen pressure

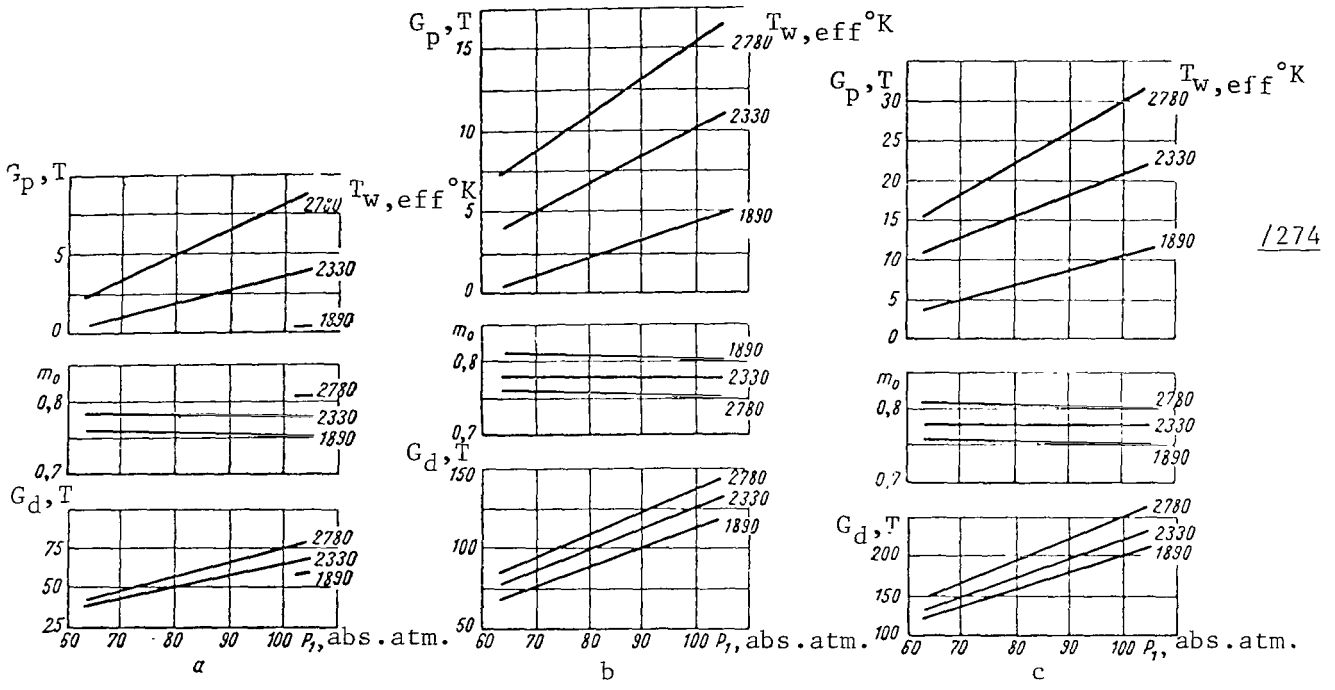

/274

Figure 9.8

Characteristics of Rockets with Graphite Reactors:

a- Coolant Volume α = 0.30; Reactor Active Zone Diameter 0.94m; Active Zone Heighth, 0.7 m and Weight of Uranium Load 27.7 kg;
b- Coolant Volume α = 0.30; Active Zone Diameter, 1.07 m; Active Zone Heighth 0.95 m and Weight of Uranium Load 35 kg;
c- Coolant Volume α = 0.40; Active Zone Diameter, 1.23 m; Active Zone Heighth, 0.96 m, and Weight of Uranium Load 46.3 kg.

at the input, the effective wall temperature of the reactor canals, and the ratio of thrust to flight weight - upon the reactor performance. /275

Figure 9.9 shows the effect of hydrogen pressure at the input for a graphite reactor. The flight weight of the rocket and the effective wall temperature of the reactor canals remain constant and equal G_d = 91 m and $T_{w,eff}$ = 2780°K respectively. The payload, the coolant volume, and the diameter of the reactor active zone are shown as a function of the pressure at the reactor input.

Since the ratio F/G_d = 2 remains constant, the fact that the

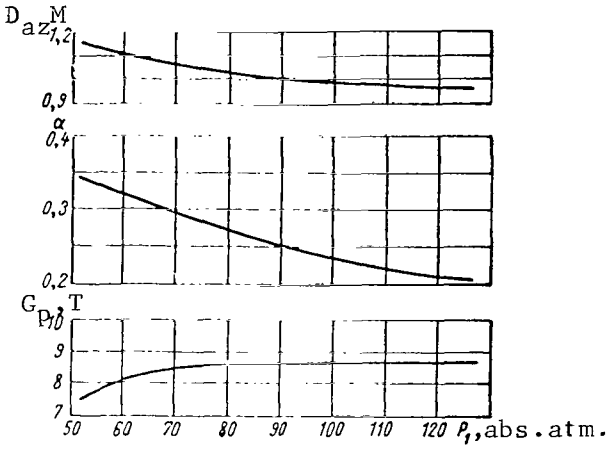

Figure 9.9

Effect of Pressure at the Reactor Input on the Performance of Graphite Reactors.

flight weight does not change points to significant uniformity in the stream rate with an insignificant decrease in the specific impulse. The stream rate remains constant due to simultaneous pressure increase at the input p_1, and a decrease in the coolant volume α and, consequently, the critical diameter of the active zone D_{az} - as can be seen from the graph. A decrease in the reactor active zone diameter leads to a decrease in the weight of several components of the nuclear device (active zone, reflector, high-pressure chamber, nozzle, and turbine pump unit). The total results are shown in the form of a payload curve. An increase in the payload G_p, with an increase in the pressure at the input of greater than 84 abs. atm., does not justify the difficulties which are entailed with a high operational pressure. Therefore, p_1 = 84 abs. atm. will be used as the basis for further comparisons.

Figure 9.10 shows the effect of the effective wall temperature /276 of the reactor. The flight weight of the rocket and the hydrogen pressure at the input are assumed to be constant and to equal G_d = 91 m and p_1 = 84 abs. atm.. The payload, the coolant volume, the diameter of the reactor active zone, and the mass ratio are shown as a function of the effective wall temperature of the reactor.

As was noted previously, if G_d and $\frac{F}{G_d}$ are constant, this means

that the thrust is also constant. With an increase in $T_{w,eff}$, the temperature at the reactor output and, consequently, the specific impulse also increase; as a result - as can be seen from Figure 9.10 - the mass ratio m_0 decreases. In order that the thrust remain constant with an increase in the specific impulse, a corresponding decrease in the coolant volume α and, consequently, the critical diameter of the active zone D_{az} is necessary. The resulting effect produced by decreasing the mass ratio and weight of the nuclear device is expressed in a corresponding increase in the payload with an increase in $T_{w,eff}$.

With an increase in $T_{w,eff}$ by 55°K, the payload increases by 340 kg. It is assumed that the operational temperature must be the largest possible one, taking into account the limitations imposed by the reactor materials. In order to realize ideal conditions with respect to a uniform wall temperature, a non-uniform distribution of uranium and of the coolant volume - both with respect to radius and with respect to the axis - is necessary. For purposes of later comparisons, the effective wall temperature of the reactor was selected as $T_{w,eff}$ = 2780° K.

Figure 9.11 shows the effect produced by the ratio of thrust to flight weight. The effective wall temperature of the reactor canals and hydrogen pressure at the input were assumed to be constant and to equal 2780° K and 84 abs. atm., respectively. The payload and the flight weight are shown as a function of the coolant volume for several values of the ratio of thrust to flight weight. For a given reactor or coolant volume α, the maximum payload occurs for $\frac{F}{G_d}$ = 1.6. The /277
intersection of the graph in Figure 9.11 along the line for constant flight weight shows even more clearly the increase of the payload for F/G_d = 1.6, although an increase in the frame weight and the aerodynamic resistance (the latter is not taken into account in the present study) can influence this result. For this analysis, the ratio F/G_d was chosen as being equal to 2, as a possible value which was compatible with the assumed values for the tank and frame weight.

Total Characteristics. The expected characteristics of nuclear rockets employing graphite reactors are summed up in Figure 9.12. Hydrogen pressure at the input and the ratio F/G_d were assumed to be constant and to equal p_1 = 84 abs. atm. and F/G_d = 2. The flight weight of the rocket and the payload are shown as a function of the consumption of hydrogen, and curves are shown for all three values of $T_{w,eff}$.

For example, if a graphite reactor with a coolant volume α = 0.3 operates at a hydrogen pressure at the input, which equals 84 abs. atm., and an effective wall pressure of the reactor canals which equals 2780° K, then the anticipated payload will be 11.8 tons for a rocket flight weight of 113.5 tons and for the hydrogen consumption which /278
is shown. If the effective wall temperature of the reactor canals

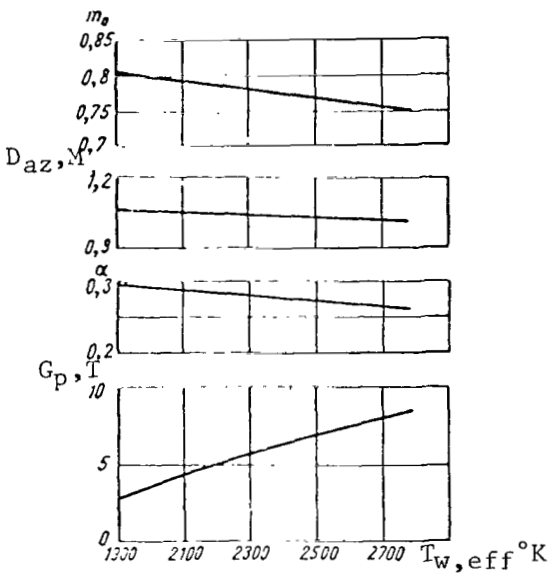

Figure 9.10

Effect of Effective Reactor Wall Temperature upon Performance of Graphite Reactors.

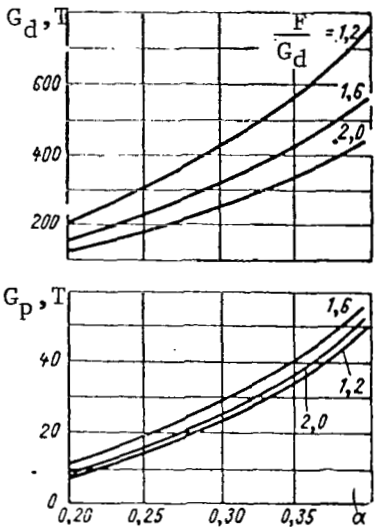

Figure 9.11

Effect of Ratio of Thrust to Flight Weight on Graphite Reactor's Performance. Effective Wall Temperature of Reactor Canals $T_{w,eff}$=2780°K, Pressure at the Reactor Input p_1 = 84 abs. atm.

is lowered to 2340° K, then the payload will equal either 7.28 tons, with a certain decrease in the flight weight for the same reactor, or G_p = 8.64 tons for the same flight weight but for a somewhat larger reactor, or for a greater hydrogen consumption.

The results derived from the study for a graphite reactor are as follows: 1) the increase in the payload, with an increase in the hydrogen pressure at the input of greater than 84 abs. atm., is apparently insufficient to compensate for the difficulties entailed with increased pressure; 2) with an increase in the effective wall temperature of the reactor canals by 50° K, the payload increases by 400 kg; 3) for an effective wall temperature of the reactor canals $T_{w,eff}$ = 2780° K, a pressure at the reactor input of p_1 = 84 abs. atm., and a flight weight of G_d = 113 tons, the payload for a rocket having a graphite reactor is G_p = 11.8 tons; 4) the payload of a nuclear rocket is 6 - 10% of the initial flight weight.

BeO-Tungsten Heterogeneous Reactors

We shall examine the premises and the analysis method employed in

calculating the performance of BeO-Tungsten reactors only with respect to the manner in which it differs from the performance for graphite reactors.

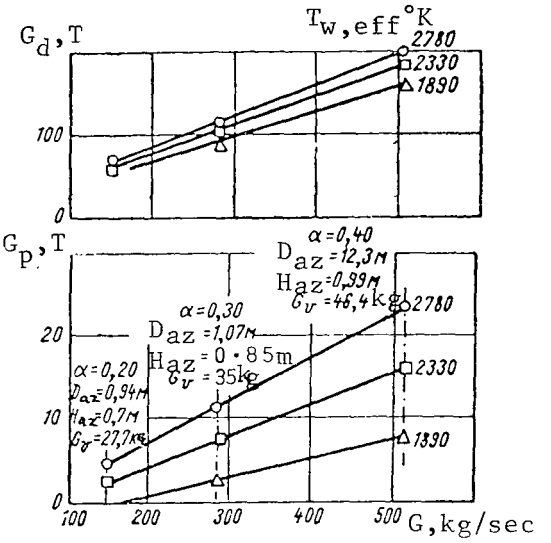

Figure 9.12

Total Characteristics of Nuclear Rocket with Graphite Reactor. The Dashed Lines Designate the Points Corresponding to Reactors Studied.

Active zones having a different geometry can be utilized for BeO-Tungsten reactors. For example, each fuel element can be made of several concentrated, thin-walled tungsten tubes which contain uranium, having radial clearances which serve as canals for heating gaseous hydrogen. Several such fuel elements can be inserted in parallel canals, which penetrate a cylinder made of BeO in an axial direction. Other designs for the active zone are also possible - for example, consisting of flat plates. During the operation of tungsten fuel elements at the temperatures under consideration, additional cooling of the moderator made of BeO is necessary. Under the assumption that 5% of the entire fission energy is given off in the moderator, it was found that the required additional stream cross-section, which was necessary for cooling the moderator, was about 20% of the cross-section for the main stream penetrating the fuel elements. Thus, in the initial passage through the active zone, the total hydrogen stream cools the moderator, and in the second passage through the active zone - passing mainly through the fuel elements - it absorbs the remaining 95% of the liberated heat. An increase by 20% in the stream cross-section was assumed for cooling the moderator, when designing all BeO-Tungsten reactors.

The dimensions of the BeO-Tungsten active zone were calculated on the assumption of a 150 millimeter beryllium reflector and a BeO-Uranium atomic ratio which equalled 250. The volumetric UO_2-tungsten ratio was /279 selected as 30.0%, which corresponds to the maximum possible content of UO_2 in tungsten, which determines the structure of the fuel elements. It was also assumed that UO_2 can be retained in tungsten within the temperature limits being studied. Based on these assumptions, the critical diameters for the active zone of a BeO-Tungsten reactor were calculated, and the computational method which was used was similar to that described in other works (Ref. 12, 13, 14). In the calculations, the heterogeneous active zone was replaced by a zone which was equivalent to it - consisting of a homogeneous mixture of materials; the resonance effects in tungsten were thus disregarded. Attention should be called to the feasible possibility of separating and utilizing the isotope W^{184}, instead of natural tungsten. This presents greater possibilities, as compared to decreasing the dimensions and weight of the reactor, due to the fact that - when W^{184} is employed - the absorption of neutrons both in the resonance and in the thermal energy regions decreases considerably. Table 9.3 presents the necessary data for heterogeneous reactors, which have been chosen for future study.

TABLE 9.3.

DATA FOR THREE BeO-TUNGSTEN REACTORS AND THEIR OPERATIONAL PARAMETERS

Reactor Data	I	II	III
BeO-Uranium Atomic Ratio	250	250	250
Thickness and Material of Reflector, mm	150	150	150(Be)
Active Zone Diameter, D_{az}, m	1.1	1.2	1.36
Active Zone Height, H_{az}, m	0.75	0.85	0.98
Coolant Volume, α	0.168	0.276	0.315
Weight of Uranium Load, G_U, kg	64.5	76	96.4
Operational Parameters			
Effective Wall Temperature of Reactor $T_{w,eff}$, °K			2330-3060
Temperature at the Reactor Output, T_2, °K			1990-2630
Temperature at Reactor Input, T_1, °K			171-211
M_1 Number at the Reactor Input			0.10
Pressure at the Reactor Input p_1, abs. atm.			63-105

The limits within which the operational parameters changed were given first, in order to determine their effect upon the performance of nuclear rockets. The numerical values for these parameters are shown in Table 9.3. In view of the fact that tungsten can undergo a much higher

temperature than graphite, the level of the effective wall temperature for the reactor's canals was somewhat increased in the given case, as compared with the temperature for a graphite reactor.[1] The hydrogen /280 temperature at the reactor output was based, just as was done previously, on the heat exchange efficiency $\varepsilon = 0.85$. In this case, the input temperature of hydrogen is somewhat higher than the corresponding temperature in a graphite reactor, due to preliminary cooling of the moderator. The M_1 number at the input was again varied, and it was found that its optimum value must equal 0.10 in every case, in order to approximate the critical regime at the output. The limits within which the pressure changed at the input were assumed to be the same as those for a graphite reactor.

Within the limits of the given assumption, the study revealed the following: 1) in order to obtain the same performance as is produced when a graphite reactor is used, a BeO-Tungsten reactor must operate at temperatures which are 10% higher than a graphite reactor; 2) the graphite reactor requires a small amount of uranium, and its construction is considerably simpler; 3) a BeO-Tungsten reactor can apparently operate at a higher temperature, although the actual performance of any system depends on the temperature limits of the materials, which has not yet been established; 4) the payload for a nuclear rocket utilizing one or the other reactor is 10% of the flight weight, for the examined conditions.

These examples present an idea of the principles underlying a theoretical approach to the problem of employing NRE on space vehicles.

Experimental Study of NRE

According to a statement made by the president of AEC, Seaborg, intense studies are being carried out in the United States on building a nuclear rocket engine (with continuous heating of the working medium in the active zone), and it is assumed that in 1965 - 1976 the first rocket will be launched with a nuclear engine (Ref. 15, Ref. 16). A nuclear rocket engine is being developed by AEC - NASA under the "Rover" project (Ref. 17, Ref. 18). Work is being carried out on the basic elements of the NRE. Tests were made on the experimental reactors "Kiwi-A" (July 1, 1959), "Kiwi-A1" (July 8, 1960), "Kiwi-A3"

[1] This assumption must be made very cautiously, due to the fact that graphite retains its mechanical strength up to 2500° C, while tungsten can lose it at lower temperatures.

(November 19, 1960), "Kiwi-B-1A", "Kiwi-B-1B" (September, 1962), and "Kiwi-B-4A" (November 30, 1962) (Ref. 18).

In the "Kiwi-A" reactor, fuel elements were used made of graphite plates, which were impregnated with uranium, and they were located in a circular zone around the central part having a diameter of 380 mm. The central part contained control shafts, cooled by circulating heavy water D_2O. A graphite cylinder, which separated the coolant streams passing through the reactor, a graphite reflector, and a /281 vessel under pressure, which was cooled by water and which was made of aluminum and had double walls, were located outside of the active zone.

The heat-releasing plates were located in a cylindrical graphite chamber. Each plate was impregnated with uranium uniformly, but the impregnation of different plates differed in accordance with calculated ratios with respect to heat transfer and fission rate distribution, and also in accordance with radial or axial location of the plates. A graphite disc, which was penetrated by cooling canals, served as the reflector of neutrons at the input side of the reactor active zone. The central part contained regulating, compensating, and safety shafts, which were set in motion by double-action, hydraulic piston drives passing through a seal at the end of the central part; these piston drives were located outside of the body.

U^{235} is the fuel. The plates are divided by ribbing; hydrogen passes between the plates and is heated. The outer forms of the first three types of reactors are identical, but the geometry of the active zone in the "Kiwi-A" and "Kiwi-A3" reactors is different. Gaseous hydrogen was used in the first experiments, and the nozzle and reactor were cooled with water. The test results were successful with respect to the construction parameters and the materials. The Los Alamos scientific laboratory at Jackass Flats, Nevada,tested the experimental reactor "Kiwi-B-1A" under a program which was developing a nuclear engine for the "Nerva" rocket. Gaseous hydrogen was used to cool the reactor. This was the last test using gaseous hydrogen. In all the subsequent reactors of the "Kiwi" series, liquid hydrogen was used as the working medium, and different designs were tested. Parallel with this, a rocket system is being developed for testing the reactor during flight (RIFT*).

Under the "Feb" program, a reactor will be developed for rapid neutrons, which will have more power than the "Kiwi-B" type of reactor. This program represents a subsequent stage in the development of nuclear rocket engines for space vehicles (Ref. 19, Ref. 20).

When the reactors "Kiwi-B" were tested at Jackass Flats, data were obtained on the operation of the reactor at high temperatures and stresses, as well as information regarding the power output, the use of liquid hydrogen, rapid launch, and shutting off and turning on the

* Note: RIFT designates Reactor In-Flight Test system.

engine repeatedly. For a thermal power equivalent to 1000 Mw, the "Nerva" NRE will provide thrust on the order of 22.7 tons. It is assumed that a NRE in a series, which is designed for piloted space vehicles, will produce a power which is 4 - 5 times greater than the "Nerva" NRE.

Possibilities for Nuclear Rocket Engines /282

A nuclear rocket engine, which is to be used on future space vehicles, has a performance which is potentially one order of magnitude greater than similar engines using chemical fuel. When such NRE are used for flights of manned space vehicles around the moon or to the moon, their performance is 2 - 3 times greater than the performance of rocket engines using chemical fuel, while for flights to planets they have the greatest advantages. For space rocket engines which are designed for flights to other planets, reactors can be used having the same power as those for the NRE, to be used for flights to the moon, but they can be combined into a bundle in order to obtaine greater power (Ref. 21, Ref. 22).

A nuclear rocket engine has significant advantages for interplanetary flights. Its performance is one order of magnitude better, and it has much greater reliability. It also makes it possible to increase the payload, thus providing better maneuverability and safety, and in addition it enlarges the possibilities for flights in cosmic space.

For flights to the moon - i.e., flights over short distances which require less velocity increase - it is more expedient at first to use engines which are designed for obtaining interplanetary information. Rockets with nuclear engines have advantages for these initial flights; these advantages consist of less weight, which equals from one-half to one-third of the rocket weight with chemical fuel, and also they have greater reliability due to less stages (Ref. 7).

The development of rocket engines using nuclear energy is particularly important, because these engines will have greater advantages when cosmic space research has reached the stage of interplanetary journeys by man.

9.3 Electric Energy Nuclear Devices

Possibilities for Utilizing Electric Energy Nuclear Devices on Space Vehicles

Nuclear energy can be used not only for producing jet thrust directly, but also for producing electric energy which supplies the equipment and apparatus on a space vehicle. Nuclear devices, which

generate electric energy, can in their turn be utilized for supplying electric jet engines with energy, about which research and experiments are being carried out at the present time (Ref.23). In its turn, the /283 development of an electric jet engine depends on the creation of electric power devices which are light in weight and which last a long time.

Power devices having a very great output are necessary for electric jet engines. The output limits and the lifetimes for different types of power devices, which are to be used on board spacecrafts, are shown in Figure 9.13 (Ref. 24, Ref. 25). Although electric jet engines have a low thrust, they will nevertheless be primarily used for interplanetary flight, since they have a good lifetime and permit a significant increase in the payload. The power device output must be computed from the power required to maintain contact with the earth, to maintain the life-support systems for the crew, and to supply the equipment, apparatus, and engine.

Special equipment can be used in addition to the main equipment, which will serve to actuate the spacecraft engine, and which will serve as additional sources of electric energy for supplying the different apparatus on the spacecraft.

The power for maintaining contact with the earth (Ref. 21, Ref. 22) depends on the required rate of information transmittal, the quality of the communication apparatus on board the spacecraft and on the earth, the dimensions and quality of the transmitting and receiving antenna, distance, etc. From 100 to 1000 w (according to different estimates) is required per man to maintain the life-support systems. In addition, the following are typical values for the power supply required for different devices in the scientific equipment: magnetometer 5 w, microphone or recorder of micrometeorites 2.5 w, cosmic radiation detectors 2 w, and mass-spectrograph 17 w. The power required for supplying the navigational equipment and guidance system is approximately of the same order (Ref. 21, Ref. 22).

Apparatus for the crew requires a power ranging between 280 w and 1 - 5 kw of auxiliary energy. A power of several kilowatts is required for television transmittal from space. A source of electric /284 energy having an output of several hundreds and thousands of kilowatts is necessary for an electric rocket device (Ref. 21, Ref. 22). Energy from the sun, chemical energy, and nuclear energy can be used as the source of electric energy.

The use of solar energy to obtain electricity on board the space vehicle makes it possible to manage without comparatively heavy shielding from radiation coming from nuclear energy sources. In this connection, solar batteries, for example, are extensively used on present-day artificial earth satellites. A stream of thermal energy

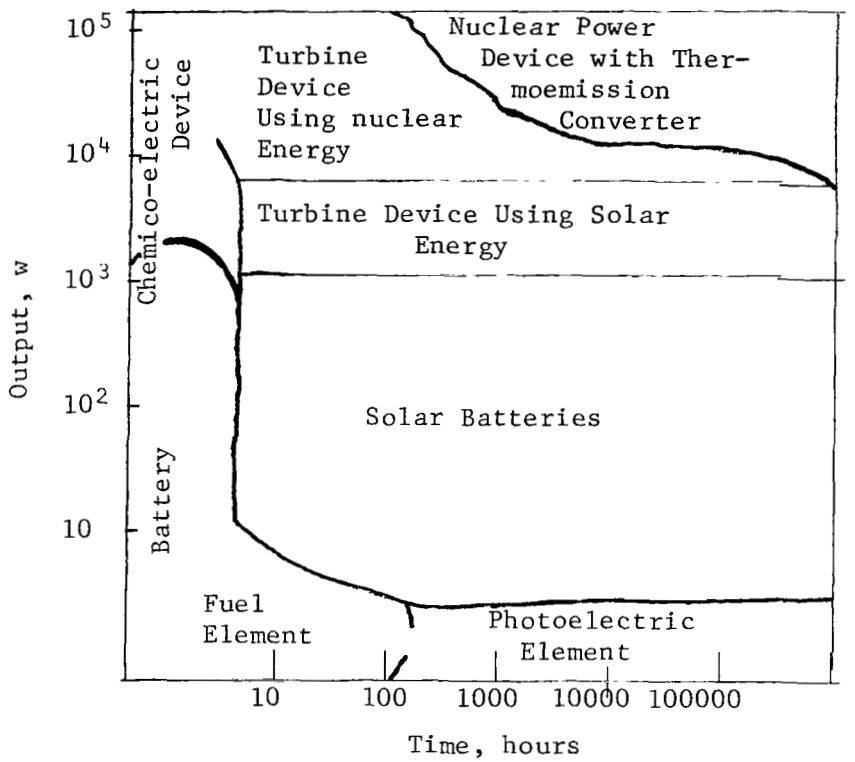

Figure 9.13

Output and Lifetime of Different Types of Electric Devices to be Used in Electric Engines.

at 1.4 kw/m^2 falls on a surface which is perpendicular to solar rays on an earth orbit. However, the utilization of solar energy for a large amount of power is difficult for the following reasons: in manoeuvering the space vehicle, it is necessary that the solar collectors be regulated in a special manner, in order that they always maintain the most favorable position with respect to the sun. The flight of the vehicle in the shade of the earth or another planet must be provided by a system of powerful accumulators of solar, thermal, or electric energy, which can cause significant weight penalties, particularly in the case of electric energy accumulators.

Thus, the specific weight of Ni - Cd accumulators, which are usually used on the order of hundreds or thousands of times for a number of discharges, amounts to approximately 500 kg/kw-hour. For a small number of discharges (several times) Zn - Ag accumulators are used with a specific weight of about 10 kg/kw-hour. Therefore, at the present time it appears that the use of solar energy on board

space vehicles will be limited by the power required for purposes other than propulsion. In order to expand the power range, a significant increase in the efficiency of the converter changing thermal energy into electric energy, as compared with present-day values (5 - 15%), is necessary.

Nuclear sources of electric energy are based on the application of radioactive isotopes and nuclear reactors. The use of radioactive isotopes will probably be limited by a power on the order of 1 kw, since,when it increases,the radioactive threat greatly increases for the launch crew. A nuclear reactor represents a lighter source for electric power on the order of several tens of kilowatts and above.

Electric Rocket Engines

Part of the electric engine system, which converts electric energy into thrust, can be called the electric rocket engines. They can be conditionally divided into three types: electrothermal rocket engine, in which a gaseous working medium is heated electrically, and then is accelerated thermodynamically in order to obtain thrust. /285
Examples of this type of engine are the electric arc device, which forms a stream of the working medium which is heated in the arc, and a device which forms a stream of working medium which is heated due to the electric resistance of the latter; an electromagnetic rocket engine, in which ionized gas (plasma) - which consists of a mixture of electrons and ions - is accelerated in an electromagnetic field; an electrostatic rocket engine, in which ions are accelerated in the electric field, and - when an ion bundle leaves the engine - electrons are injected into the bundle.

Systems for Converting Different Types of Energy into Electric Energy

The structural features of an electric energy source on a space vehicle are determined to a considerable extent by the arrangement by which the given type of energy is converted into electric energy. Figure 9.14 illustrates systems for converting different types of energy into electric energy.

In order to develop sources which can be utilized on space vehicles and which satisfy the requirements of economy, lightness, and smallness, in recent years intense studies have been undertaken to primarily determine new physical methods for converting different types of energy into electric energy; these methods are based on utilizing magnetohydrodynamic, photoelectric, ferroelectric phenomena, the phenomena of radioactive decay, and others. Along with this, interest has again been developed in the utilization of thermoelectric

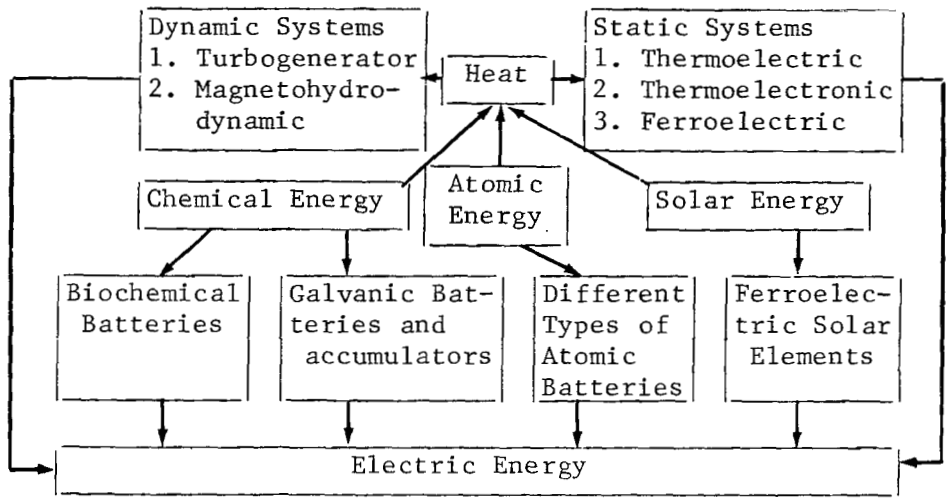

Figure 9.14

Main Methods for Converting Chemical, Atomic, and Solar Energy into Electric Energy.

phenomena for this purpose. Ideas for utilizing thermoelectronic emission for converting thermal energy into electric energy are at the stage of technical realization. Turbogenerator devices continue to receive a great deal of attention. /286

Cosmic nuclear-energy devices must satisfy the following requirements: 1) to operate at a high temperature, which facilitates the heat removal using a condenser-radiator which has a small surface, and, consequently, low weight; 2) to use a material having a high energy density as the heat source - for example, uranium carbide in reactors using rapid and intermediate neutrons; 3) the shielding which is required for the vehicle must have the least possible weight; 4) to have reliability and strength; 5) to contain as few moving parts as possible; 6) to have a minimum transfer of heat to other parts of the craft (Ref. 26). At the present time there are five well-known methods for converting thermal energy into electric energy: using thermoelectric and thermoemission converters, fuel elements, turbogenerators, and magnetohydrodynamic generators.

It is assumed that thermoelectron generator systems can satisfy the requirements given above in the best way (Ref 25). In low-power generator systems, the heat from the decay of radioisotopes will be used; in more powerful generators (from several tens of kilowatts to tens of megawatts output) the heat will be produced by small compact reactors.

Turbogenerator, Nuclear-Power Devices (NPD)

Brief Data. A turbogenerator NPD can be made with a gas turbine

or with a steam turbine arrangement. In turbogenerator systems, the thermal energy is transformed into electric energy, with intermediate transformation into mechanical energy of vapor or gas which sets the turbine in motion. Turbogenerator devices can generate an electric current both of constant and of variable high-power voltage, while both thermoelectric and thermoelectronic generators, as well as solar elements, are low-power sources of a constant current with low voltage. Turbogenerator devices have a more complex design.

At the present time, several firms in the United States, the U.S. Air Force, the Atomic Energy Commission, and the National Aeronautics and Space Administration are accelerating the program for developing nuclear-powered devices for spaceflights. The electric power sources, developed under the SNAP program, should find extensive application on satellites and other space vehicles. The program also includes the development of electric power sources which are /287 small, which can be used on underwater craft in remote regions (SNAP-4).

The turbogenerator devices which have been developed to the greatest extent at the present time are SNAP-1, SNAP-2, SNAP-4, SNAP-8, SNAP-50 (Ref. 27-29).

SNAP-1. SNAP-1 with a turbogenerator uses mercury as the working substance, and a capsule containing cerium-144 radioisotopes, which is located in a cylinder having a diameter of 100 mm and a height of 300 mm, is used as the heat source. The device provides a power of 500 w for 60 days.

SNAP-2. In this device, a nuclear reactor is used as the source of thermal energy using enriched uranium. In the first circuit, an eutectic mixture of sodium and calcium is used as the heat-transfer agent; in the second circuit, the working substance is mercury. The nuclear-power device SNAP-2 was designed for operation under conditions of high vacuum, high temperatures, large temperature drops at the moment of launch, and also under conditions of weightlessness and in the presence of cosmic radiation and bombardment by micrometeorites. It is assumed that the device will sustain strong impacts on the order of 60 g, vibrations up to 15 g, and accelerations up to 10 g (Ref. 30). The outgoing electric power of the device is 3 kw with one turbine; if two turbines are utilized with one reactor, the total power can be doubled. The thermal power of the reactor is 50 kw; the efficiency of the entire system as a whole is 6%, the voltage is 110 v, the frequency is 2000 cps. With a power of 6 kw, the device weighs (with shielding) approximately 400 kg. The weight of the mercury-vapor turbine is 135 kg. The reactor weight is 90-100kg. The reactor height is 45 cm, the diameter is 35 cm. The surface of the condenser-radiator, diffusing a power of 40 kw at a temperature of 315° C, equals 9 m^2. The heat-transfer agent temperature at the reactor input is 538° C; at the reactor output - 650° C. The rotation speed of the turbine is

40,000 rotation/min; lifetime of the apparatus is 1 year; specific power is 11 w/kg; specific energy (per 1 year's operation) is 110 kw·hour/kg.

SNAP-8. Output power is 30 kw; thermal power of the reactor, 300 kw; voltage, 43.6/75.6 v; frequency, 1,000 cps; total weight of the device 675 kg; surface of the condenser-radiator diffusing a power of 255 kw is 32.4 m^2; lifetime is 1 year. If a second turbogenerator is added, the electric power generated from one reactor can be increased up to 60 kw. The weight of this device will be 1125 kg.

SNAP-50. A turbogenerator device having an electric power of 300 kw - 1 Mw, with lithium as the heat-transfer agent and boiling potassium as the working substance (Ref. 31). For a thermal power of 8 - 10 Mw, the weight of the device (without shielding) - including the reactor, converter, and radiator - must be 4.5 kg per 1 kw thermal power. The most important criterion for the device is /288
reliable operation without attendants for 10,000 hours. It is assumed that uranium monocarbide is used as the reactor fuel, since it has a high density and thermal conductivity. Fuel elements made of uranium oxide and beryllium oxide can also be used; they have a long lifetime, and the dimension and weight of the reactor increases somewhat with them. High-melting metals will be widely used in constructing the reactor, in view of the high operational temperature (Ref. 32, Ref. 33).

Other types of power devices are planned under this program, including the following: a SNAP-50 type of device with thermoelectron converters located in the heat exchanger or the condenser-radiator; a SNAP-50 type of device with magnetohydrodynamic converters; a variation of the SNAP-50 type of boiling reactor; reactors with gas cooling; systems of boiling reactors having an electric power of 100 - 300 kw, operating at temperatures below 1100° C (Ref. 31, Ref. 32).

Thermoemission Nuclear Power Devices

General Information. The thermal emission method of converting heat into electricity is based on the phenomenon of thermoelectron emission, which was discovered in 1883 by Edison and consists of the fact that, when metallic bodies are heated in a vacuum, electrons leave their surface. However, only in the last few years has thermoelectron emission been regarded as a possibility for converting thermal energy into electric energy.

Figure 9.15 illustrates the principle underlying the action of a thermal emission converter.

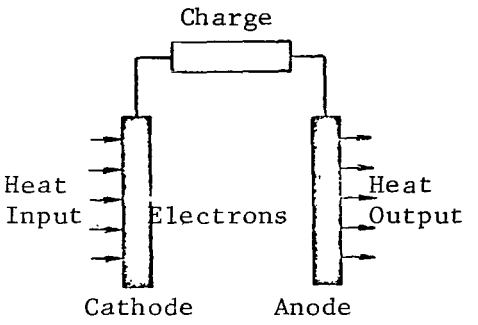

Figure 9.15

Diagram of a Thermal Emission Converter.

Under the influence of heat which is conducted to the cathode, the electron energy of the cathode material increases from the Fermi level[1] to a certain higher level. The electrons whose energy is higher than the work function of the cathode material φ_K leave the cathode and enter space close to the cathode. When there is no space charge, the electrons enter the relatively cold anode - due to the presence of a rather large kinetic energy - where their energy decreases to the work function of the anode material φ_a, which heats the anode. The residual potential energy of an electron, which equals the difference between the work function for the cathode and the anode ($\varphi_K - \varphi_a$), can be delivered to the outer electron circuit (Figure 9.16). /289

The thermal emission converter acts like a constant-current generator, whose maximum output voltage equals $\varphi_K - \varphi_a$. Thus, part of the thermal energy which compels the electrons to leave the cathode can be converted into electric energy. The output voltage of one converter usually is on the order of 1 v, and therefore it is necessary to combine a large number of converters in series, which causes additional losses. It should be noted that by modulating the stream intensity of electrons falling on the anode, it is possible to obtain an alternating current.

In order that the thermoemission converter have a high frequency, it is necessary to decrease or remove the effect of the space charge and to select the cathode and anode materials in such a way that their work functions differ significantly. The cathode must have a large

[1] The Fermi level is the maximum electron energy in a given metal at absolute zero temperature.

work function. Three types of thermoemission converters can be developed: vacuum converters with a small (on the order of several tens of microns) distance between electrodes, magnetic transistors, and gas-filled converters. A cesium element is one of the most frequently examined forms of the latter type of converter.

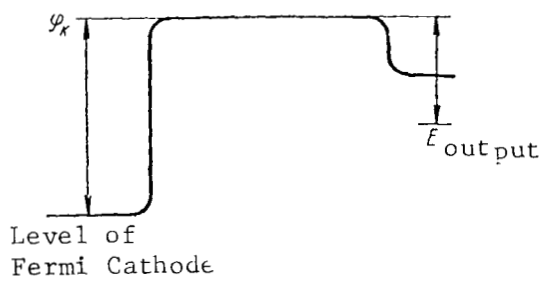

Figure 9.16

Simplified Scheme for the Distribution of Potential Energy Levels for Electrons in a Thermoemission Converter.

Combination of Thermoemission Elements with a Reactor Device. There are three basic methods for including thermoemission converters in reactor systems: the converters can be placed within the reactor, separately from it but with a mutual coolant circuit, or on the reactor surface (Ref. 34).

The thermoemission element within the reactor is combined with the fuel element, as is shown in Figure 9.17, using the example of a converter element having a cylindrical form.

There are other possible designs for thermoemission converters, for example, the flat type. The active zone of the reactor can be comprised of a set of similar units with the coolant circulating between them in order to cool the anode. Typical dimensions of the emitter /290 are: a diameter range between 6 - 25 mm; length, 25 - 250 mm; interelectronic plasma interval, 0.1 - 1 mm; and anode thickness, 0.12 - 0.75 mm (Ref. 34). The layout of the active zone in the thermoemission reactor differs from the layout of the customary reactor, with respect to the method for fastening the elements, the necessity of an electric bond between the thermal elements, and the insulation between the anodes.

The coefficient of a thermoemission converter, which equals the ratio of the output power to the input power, can be expressed by the following equation (for a vacuum regime with compensation for

the space charge):

$$\eta = \frac{(\varphi_K - \varphi_a)(I_K - I_a) - R(I_K - I_a)^2}{I_K\left(\varphi_K + \frac{2kT_K}{e}\right) - I_a\left(\varphi_a + \frac{2kT_a}{e}\right) + II_{rad} + II_{con} + E_{ion}},$$

where the numerator equals the generated electric power minus the losses at the electrodes and the leads; $I_K\left(\varphi_K + \frac{2kT_K}{e}\right)$ - the energy required for the vaporization of electrons from the cathode surface and for surmounting the barrier created by the space charge; $I_a\left(\varphi_a + \frac{2kT_a}{e}\right)$ - the energy restored to the cathode by the return current from the anode; II_{rad} - radiation losses; II_{con} - conductance losses; E_{ion} - the energy for ionization of cesium; e - electron charge; k - Boltzmann constant; T_K - cathode temperature; T_a - anode temperature; $I_{K,\ a}$ - electron current from the cathode or anode.

In any reactor, the effective output is

$$N_{el} = Vq_{max} K_v \eta ,$$

where V is the volume of the reactor active zone; q_{max} is the maximum permissible specific heat output from a unit volume of the reactor active zone; K_v - the ratio of the mean output to the maximum output generated per unit volume of active zone; η - total efficiency.

In the usual reactors, efficiency depends on the temperature of the input and output of the reactor. If the coolant flow is diaphragmed in the fuel channels, it is possible to make the efficiency independent of K_v, and the output must decrease linearly from K_v. However, in a thermoemission reactor which consists of identical thermal emission elements, the output can strongly decrease with a change in the power distribution, and the efficiency depends very greatly on K_v. It can be made independent of K_v, if the emitter temperature is constant in the entire reactor active zone - for example, by changing the ratio of the active zone surface to its volume (for a cylindrical unit - by changing its diameter). Thus K_v can approximate unity by changing the fuel concentration with respect to the individual elements or by appropriate regulation of the elements. It can be seen from these statements that if it is desirable to have uniform power distribution in the usual reactor, this requirement is almost compulsory in a thermoemission reactor. /291

One serious problem in a thermoemission reactor is contamination of the anode and the plasma by fission products which leave the emitter surface. In order to obtain a high efficiency, an anode surface with high thermal reflectivity is required, in order to decrease the thermal losses of the emitter during radiation. However,

in the presence of condensing fission products or during chemical reactions, it is difficult to maintain high surface reflectivity between the fission products and the anode. In order to increase the operational time of the thermal elements, it is desirable to remove the gases which contain fission products, either in special fuel element cavities, purifying devices, or in cosmic space - which can entail a study of several problems on biological danger.

In a thermoemission reactor, within the active zone it is necessary to use materials which trap neutrons and which dilute the active zone. These materials are necessary in order to prevent volatilization of the emitter - which is heated to a high temperature - for electric insulation of the individual elements, for the removal of large electric currents from the active zone, and for mechanical maintenance of the elements. Consequently, rapid or intermediate reactors are the most suitable types of reactors for thermal emission devices.

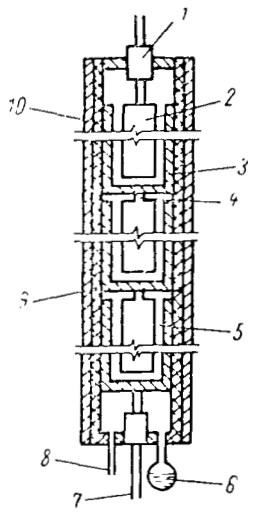

Figure 9.17

Schematic Drawing of a Section of Thermal Emission Fuel Elements with the Combination and Utilization of Cesium Vapors in Series:

1- Hot Conductor; 2- Fuel Element; Emitter; 3- Anode;
4- Cross-connector; 5- Space Filled with Plasma;
6- Reservoir with Cesium; 7- Cold Conductor; 8- Removal of Gaseous Fission Products; 9- Electric Insulator;
10- Outer Shell of Cesium Washed with Coolant.

An interreactor thermoemission device has the greatest possibilities for systems with high energy power (greater than 100 kw), since

it has a minimum temperature drop between the temperature at the emitter surface and the highest permissible fuel temperature. It is possible to obtain a large emitter surface per unit of reactor volume, which produces a high power density. It is possible to avoid a high-temperature circuit and units operating at high temperatures.

Since radiation is the only method of heat transfer in cosmic space, high-temperature heat transfer, which is necessary for a device with converter elements within the reactor, makes the /292
utilization of this nuclear device very promising under space conditions. The dimensions of the condenser-radiator, which is the heaviest part of the nuclear-powered device, can be reduced significantly. In addition, the elimination of all moving parts from the device greatly improves its reliability. Let us examine the characteristics of the reactor-generator using uranium carbide (Ref. 34).

Electric Output	300 kw
Reactor Type	Reactor using Rapid Neutrons
Coolant	Lithium
Reflector	Beryllium (5 cm)
Active Zone Heighth	28 cm
Active Zone Diameter	34 cm
Number of Fuel Elements	546
Uranium-235 Load	131 kg
Total Efficiency of Thermal Element	20%
Electric Losses in Thermal Element	0.28 kw
Net Efficiency of Thermal Element	14%
Ratio of Maximum Power to Mean Power	1.1
Mean Anode Temperature	830° C
Mean Emitter Temperature	2000° C
Input Coolant Temperature	760° C
Output Coolant Temperature	870° C
Coolant Consumption	750 l/min

It should be noted that these data are not optimum with respect to the heighth and diameter of the reactor. The reactor diameter should be reduced in order to decrease the weight of the shadow shielding. Thus, a reactor diameter reduction of 75 mm reduces the shadow shielding weight by 225 kg, for a reactor power of 1000 kw and a distance from the cabin of 30 m (Ref. 35). Therefore, the optimum relationship between the heighth and diameter of the reactor in a thermoemission reactor-generator is the subject of special studies.

When the converters are located on the periphery, they are separated from the active zone and are heated by the heat-transfer

agent which passes through the reactor. The construction is basically similar to the construction with the built-in converter, except that the fuel element is replaced by a tube containing hot liquid. For an electrical conducting heat-transfer agent, additional insulation is necessary between the heat transfer agent and the tubing. In order to obtain the desired current and voltage, a circulating system is required for the heat-transfer agent, operating at a temperature from 1400 to 2000° C.

When the thermoemission converters are located on the reactor surface (Figure 9.18), the heat-transfer agent within the reactor is not used.

The heat can be withdrawn from the anodes by radiation, thermal conductivity, or convection. This method of installing the thermal emission converters is suitable for low power levels of 10 - 50 kw. /293

The ratio of weight to power is $\frac{G}{N_m} \sim D$. The power limitations arise due to the maximum permissible temperature at the center of of the active zone and due to the limitation on the transfer of heat through the surface.

Comparison of Cosmic Nuclear Power Devices with a Turbogenerator and Thermoemission Reactor - Generator. In order to evaluate nuclear power devices, a detailed study must be made of the efficiency, the energy density, the dimensions and weight of the reactor, dimensions and weight of the shadow shielding, and the lifetime and reliability of the device. A comparison is usually made on the basis of the G/N kg/kw ratio. For devices with a turbine converter and a power of 300 - 2000 kw, the specific weight ranges between 5.7 kg/kw and 3.8 kg/kw. A theoretical analysis shows that the thermal emission principle is comparable to the turbine principle, and has an advantage in the density of the cathode current, which is about 10 amp/cm^2.

The geometric dimensions of the active zone and the composition of the active material are selected so as to obtain sufficient energy density and so as to fulfill the requirements of criticality. Figure 9.19 shows a typical relationship between the fuel portion (uranium carbide) and the volume of the active zone for a reactor with a thermal emission converter.

Figure 9.20 shows the weight of a uranium-235 load for a rapid reactor in different conversion arrangements. It is assumed that for a turbine arrangement, the volumetric portion of fuel in the active zone is two times greater than for a thermoemission reactor-generator. A comparison of the specific weights of thermal emission and turbine systems is shown in Figures 9.21 and 9.22.

The weight of the shadow shielding is calculated from the

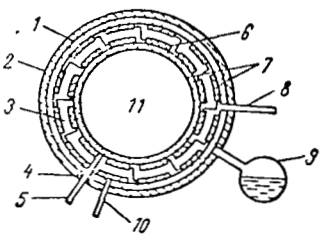

Figure 9.18

Diagram Showing Location of Thermal Ion Elements on the Reactor Surface:

1- Anode; 2- Container; 3- Plasma Space; 4- Insulator; 5- Hot Electrode; 6- Cathode; 7- Insulation; 8- Evacuation of Gaseous Fission Products; 9- Cylinder with Cesium; 10- Cold Electrode; 11- Reactor.

condition of tenfold stream attenuation due to material screens and fiftyfold attenuation due to distance. It is assumed that the condenser-radiator establishes a shielding from punctures by meteorites. All the radiators are optimized with respect to specific weight, taking the efficiency of the system into account (Ref. 36).

With an increase in the overall power, a device with direct conversion is more advantageous. A comparison of the turbine-thermoemission, and thermoelectric devices for a differing level of electric power (Ref. 18) is shown in Figure 9.23.

Electric jet engines to be used in space for interplanetary flights provide a significant increase in the payload up to 40 - 50% of the initial flight weight in orbit (Ref. 1). /295

9.4. Rocket Engines Utilizing Energy from Nuclear Explosions

The "Martin" Company has introduced a project to develop an engine for space rockets, whose operation is based on the use of small atomic bombs, exploding in a special chamber and heating the working substance up to a high temperature. Three types of a nuclear emulsion rocket have been proposed by Coyle (Ref. 37). Under very modest assumptions, the simplest model I can transport twice as much payload as a chemical rocket having the same weight. On

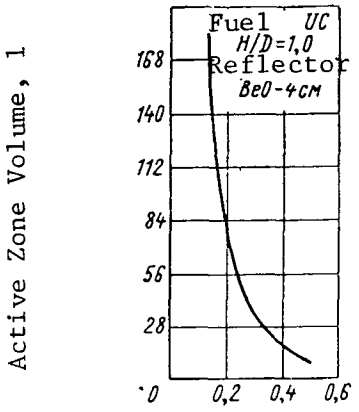

Fuel Portion UC in Active Zone Volume

Figure 9.19

Effect of Fuel Concentration on Active Zone Dimensions.

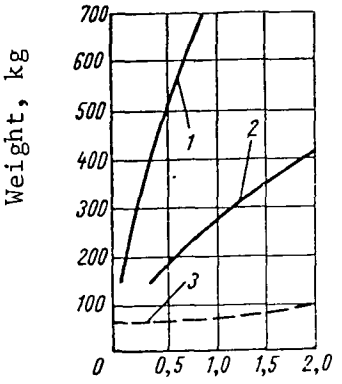

Reactor Power, Mw

Figure 9.20

Weight of U^{-35} Fuel Load in Different Conversion Arrangements:

1- Thermoelectron j_c = 3 amp/cm^2
2- Thermoelectron j_c = 10 amp/cm^2;
3- Turbine Conversion.

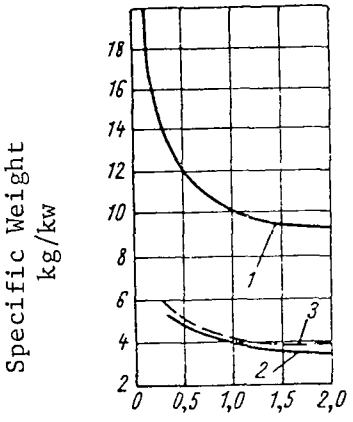

Reactor Power, Mw

Figure 9.21

Comparison of Specific Weights for Turbogenerator Device and Thermoelectron Reactor-Generator:

1- For j_c = 3 amp/cm^2; 2- For j_c = 10 amp/cm^2; 3- Turbine Conversion for η = 15%.

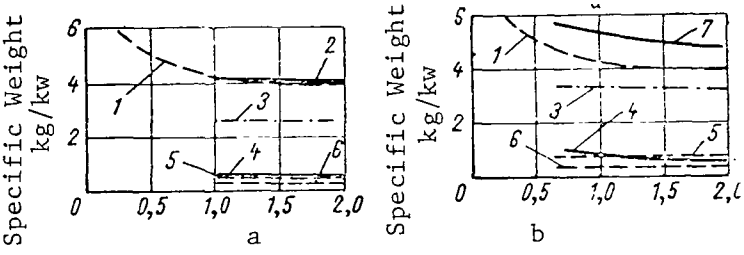

Reactor Power, Mw

Figure 9.22

Specific Weight of Devices with Thermoelectron Converters and UC + ZrC Fuel for a Specific Power of 30 w/cm^2 (a) and 20 w/cm^2 (b):

1- Specific Weight of Turbine Device η = 1.5%; 2- Total Weight of Thermoelectron Device (T_c = 2100° C, η = 11.7%, ε_c = 0.8); 3- Total Weight of Condenser-Radiator; 4- Shielding Weight; 5- Reactor Weight; 6- Auxiliary Equipment Weight; 7- Total Weight of Thermoelectron Device (T_c = 2100°C, η=9%, ε_c = 0.8).

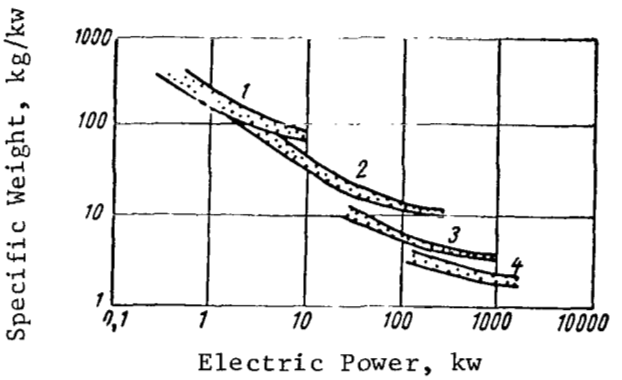

Figure 9.23

Specific Weight as a Function of Output for Nuclear Powered Devices:

1- Thermoelectric Converters; 2- Turbogenerator (Indirect Mercury Cycle); 3- Turbogenerator (Direct Rubidium Cycle); 4- Thermoelectron Converter in Active Zone; Lower Curves, for Devices Without Shielding; Upper Curves, With Shielding of Payload (Transistors).

the basis of its characteristics, the rocket proposed by Coyle is similar to a nuclear rocket of the thermal-exchange type with a reactor engine. According to calculations, it provides a specific impulse of 930 sec, which can potentially reach 3000 sec. In order to be economically advantageous, a nuclear impulse rocket must have a weight of 1000 tons, i.e., of approximately the same dimensions as a system with a gas reactor and as other long-range nuclear rockets systems which have been advanced previously. As compared with other nuclear systems, the advantages of the impulse rocket lie in the fact that a much higher mean temperature can be reached in its operational chamber and that magnetic confinement is not required in the operational chamber.

Primary attention has been directed toward possible construction and simplicity in the production of the first of the three rockets. The engine is designed to operate in interplanetary space, in order /296 to avoid the problem of radioactive contamination of the atmosphere during lift-off from the earth, although Coyle is confident that this problem will be solved with the development of "pure" nuclear bombs. Model I of the nuclear impulse rocket (Figure 9.24) with a height of 90 m has a spherical operational chamber, with a diameter of 39 m and a weight of 454 tons. The steel chamber walls are 1.27 cm thick. The total rocket weight is 1600 tons (934 tons of water and 159 tons of payload). When launched from the orbit, such a rocket can fly to

the moon and back with a landing on the moon.

Small (with a power of 0.01 kilotons) atomic bombs serve as the energy source in the rocket, in the form of small capsules. A stockpile of the working substance is located in the rocket section over the operational chamber; a pneumatic gun is also located here, which shoots the capsules with the bombs into the operational chamber. When there is a detonational frequency of one explosion per 1 sec, the mean thrust is 3600 tons. The thrust can be increased by increasing the explosion frequency.

The working substance in this construction is assumed to be water, which can be used simultaneously as a coolant for the walls of the operational chamber. 390 kg of water will be ejected for each impulse. Coyle has calculated that with the power of 2400 atomic bombs, with 0.01 kilotons and 934 tons of water, Model I can transport a payload with the weight of 159 tons at a velocity of 7.93 km/sec. It is thus assumed that 40% of the liberated energy is converted into kinetic energy of the ejected gases.

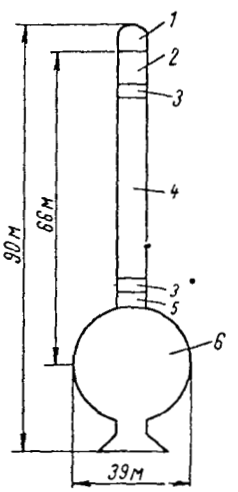

Figure 9.24

Model of Nuclear Impulse Rocket·
1- Cabin; 2- Payload; 3- Shock Absorber;
4- Capsules and Working Substance;
5- Pneumatic Gun; 6- Operational Chamber.

The principal problem (and the feasibility of this project depends on the solution of this problem) lies in constructing an operational chamber which is stable enough to sustain atomic explosions and, at the same time, light enough to be part of the aircraft. Coyle has calculated that a steel chamber of 450 tons

satisfies these requirements. The problem of insulating the forward part of the rocket from shock during the explosions in the operational chamber can be solved by building the operational chamber out of two concentric shells. The space between these shells can be filled with a gas which extinguishes the shock. The problem can also be solved by placing a shock absorbent system over the operational chamber.

In Model II of the nuclear impulse rocket, the safety factor is decreased from 20 to 4 in calculating the weight of the operational chamber. The spherical steel operational chamber, with a diameter of 30 m, in this case weighs 91 tons, instead of 454 tons. It is assumed that /297 the rocket parameters are the following: escape velocity, 11.35 km/sec (specific impulse 1150 sec); payload 1325 tons; total rocket weight 3050 tons; amount of explosions, 5800; weight of working medium ejected in one explosion, 253 kg.

Model II-A is even more economical (an enlarged variation of Model II); it employs bombs with a power of 0.1 kilotons. The operational chamber diameter in this variation is 86 m, and a weight of 907 tons. The total rocket weight is 30,480 tons, and the payload weight is 13,245 tons.

In contrast to the preceding models, Model III does not have a rocket and air-jet engine. Its purpose is to fly with a load from the surface of the earth into orbit.

In addition to this firm, "General Atomics" is carrying out work on a similar project, "Orion". Figure 9.25 shows the principal arrangement for a pulsed nuclear rocket engine, developed under the "Orion" project. The principle underlying the operation of the nuclear rocket engine, of the "Orion" type, is very simple: periodically, (every 0.1-1 sec) small atomic bombs (0.01 kilotons) are dropped from the space vehicle, which explode at a distance of 30 - 300 m from the vehicle. Besides the nuclear charge, the bomb includes a working substance (substance with low molecular weight). During the explosion of the bomb, the explosion energy of the nuclear charge changes into kinetic energy of the working substance, which is transformed into energy of motion for the space vehicle with the aid of a pushrod. The pushrod is made of a welded material and is attached to the space vehicle by means of springs or buffer devices with cooling. The maximum overloads during the flight of a space vehicle with this engine is 2 - 3 g.

This type of rocket engine can bring a space vehicle to the second space velocity several minutes after launch. The nuclear devices, described above for use on space vehicles, and their performance provide a general idea of the sources of "inner" radioactive radiation in a space vehicle. They also make it possible to clarify the specific properties of problems involved in shielding

A- Electromagnetic Shock Front
B- Cloud of Evaporated Particles

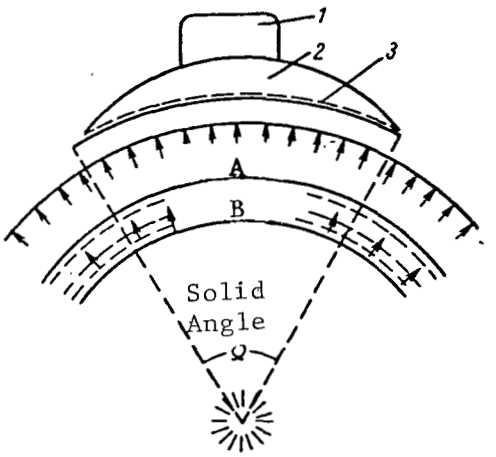

Figure 9.25

Principal Arrangement of Pulsed NRE

1- Payload; 2- Flight Apparatus;
3- Shock Absorbent Layer.

for each explicit type of nuclear device.

REFERENCES

1. Mëkel'. Voprosy Raketnoy Tekhniki, No. 3, 3, 1959.

2. Sinyarev, G. B., Dobrovol'skiy, M. V. Liquid Rocket Engines (Zhidkostnyye raketnyye dvigateli). Oborongiz, Moscow, 1955.

3. Corliss, W. R. Rocket Engines for Space Flights (Raketnyye dvigateli dlya kosmicheskikh poletov). Izd-vo Inostr. Lit., Moscow, 1962.

4. Bussard, R. W., DeLauer, R. D. Rocket with Atomic Engine (Raketa s atomnym dvigatelem). Izd-vo Inostr. Lit., Moscow, 1960.

5. Kovachik and Ross. Voprosy Raketnoy Tekhniki, No. 4, 49, 1961.

6. Sutton, G. P. Atomic Scientists, V-Vi, 194, 1961.

7. Langmuir, D. B. Astronautics, 7, 6, 20-25, 1962.

8. Bonestell, C., Ley, W. The Conquest of Space. Ch. 2, New York, Viking Press, 1949.

9. Murray, R.L. Introduction to Nuclear Engineering (Vvedeniye v yadernuyu tekhniku). Izd-vo Inostr. Lit, Moscow, 1955.

10. Sems, Ye. Voprosy Raketnoy Tekhniki, No. 4, 26, 1961.

11. Schmidt, Howard R. and Decker, R. S. Mod. Power and Engng., 54, 5, 180, 191, 1960.

12. Weinberg, A. V., Wigner, E. P. Physical Theory of Nuclear Reactors (Fizicheskaya teoriya yadernykh reaktorov). Izd-vo Inostr. Lit., Moscow, 1961.

13. Marchuk, G. I. Methods for Designing Nuclear Reactors (Metody rascheta yadernykh reaktorov). Gosatomizdat, Moscow, 1961.

14. Marchuk, G. I. Atomnaya Energiya, 11, No. 4, 356, 1961.

15. Nerva Prime Contest, Miss. and Rockets, 8, 15, 10, 1961.

16. Johnson, K. Aviat. Week. and Space Technology, 74, 17, 37, 1961.

17. Mayes, R. E. Flugwelt, 15, 4, 310, 1963.

18. Bussard, R. W. Aerospace Engng., 22, 32, 1963.

19. Advanced Nuclear Reactors Planned Aviat. Week., 75, 17, 22, 1961.

20. Kiwi B. Aviat. Week. and Space Technology, 75, 17, 26, 1961.

21. Ed. A. Zipkin and R. N. Edwards, Power Systems for Space Flight. Progress in Astronautics and Aeronautics. 11, 1963.

22. Levoy, M. The Dual Plasma-Nuclear Rocket (Electric Propulsion Conference), ARS No. 2439-62.

23. Knekht. Voprosy Raketnoy Tekhniki, 11 (95), 43, 1962.

24. Mikkel'son, V. Voprosy Raketnoy Tekhniki, No. 8, 32, 1961.

25. Lindley, B. C. Engineering, 194, 457, 1962.

26. Beller, W. Miss. Rock., 7, 14, 30, 1960.

27. SNAP-I-A Targeted for 1961 Operation. Aviat. Week, 74, 5, 71, 1961.

28. Howard, R. C. Trans. Amer. Nucl. Soc., 3, 2, 1960.

29. Zelenskiy, G. K. Atomnaya Tekhnika za Rubezhom, 7, 10, 1963.

30. Wetch, J. R., Diekamp, H. M. and Cockeram, D. J. Astronautics, 5, 12, 24, 38, 1960.

31. Nucleonics in Space Tech. Reports on SNAP-50. ORNL Space Role SNAP-50 Nucleonics, 20, 7, 28, 1962.

32. SNAP-50 Mainly In-House Project. Details of Nuclear Reactor Program Released-Power Operation Scheduled to Begin in Spring of 1965. Miss. Rock., 10, 24, 17, 1962.

33. Gets, Major P. and W. Nuclear Space Assignment: SNAP-50 Reactor Systems. Nucleonics Week., 3, 13, 1, 1962.

34. Edited by Nathan W. Snyder Progress in Astronautics and Rockets. Energy Conversion for Space Power, v. 3, Space Power Systems, v. 4; Academic Press, New York-London, 1961.

35. Miller, B. Aviat. Week., 75, 2, 61, 63, 65, 1961.

36. Johnson, K. Dynamics Versus Direct Conversion. ARS-Preprint, No. 1321, 1960.

37. Adamson, R. E. L. Nucleonics, 19, 4, 54, 1961; Finger, H. B. Nucleonics, 19, 4, p. 58, 1961; Branch, I. L. and Connor, J. A. Nucleonics, 1961; Diecamp, H. M., Balent, R. and Wetch, J. R. Nucleonics, 19, 4, 73, 1961; Schreiber, R. E. Nucleonics, 19, 4, 77, 1961; Mohler, R. R. and Perry, J. E. Nucleonics, 19, /299 4, 80, 1961; MacMillan, D. P. Nucleonics, 19, 4, 85, 1961; Meghreblian, R. V. Nucleonics, 19, 4, 95, 1961.

38. Zenger, Ye. Atomnaya Tekhnika za Rubezhom, 4, 17, 1961.

39. Snyder, N. W. Astronautics, 7, 110, 1962.

40. Silverstein, A. Aeroplane, 2605, 397, 1961.

41. Howard, R. C. Nucl. Sci. Engng., 10, 173, 1961.

42. Beckurts, K. H. and Schretzmann, K. Atomwirtschaft, VII, 69, 1962.

43. Kerr, D. L., Gessner, R. L. Some Considerations of the Problems of Minimizing the Weight of Thermopile Generators in Space Applications. Thermoelectricity. Weley John. Sons, New York, 1960.

44. Eerkens, J. W. Nucleonics, 19, 4, 100, 1961.

45. Dobretsov, L. N. Zh.Tekhn. Fiz., No. 5, 343, 1960.

46. Morgulis, N. D., Naumovets, A. T. Fizika Tverdogo Tela, No. 2, 501, 1960.

47. Wyatt, O. H. Nucl. Power, 4, 43, 100, 1959.

48. Johnson, P. G. Astronautics, 7, 12, 22, 1962; Trapp, R. F. Astronautics, 7, 12, 31, 1962; Bussard, R. W. Astronautics, 7, 12, 32, 1962; by Col. W. Scott F. Astronautics, 7, 12, 38, 1962.

CHAPTER 10

NUCLEAR REACTOR SHIELDING ON BOARD SPACE VEHICLES

10.1 Reactor as Radiation Source

/300

A nuclear reactor is the source of intense nuetron and γ-radiation. Neutrons, emanating from the reactor active zone, are formed during the fission reaction, and more than 99% of the neutrons are emitted instantaneously in less than 10^{-8} seconds. 0.73% of the neutrons (for uranium - 235) are emitted during the β-disintegration of fission fragments. Prompt fission neutrons have an energy distribution ranging from 0.075 Mev to approximately 17 Mev. The energy distribution of these neutrons is described fairly accurately by the formula of Watt:

$$N(E)\,dE = 0{,}484\,\mathrm{sh}\sqrt{2E}\,e^{-E}dE, \quad * \tag{10.1}$$

where N(E)dE is the relative number of neutrons with energies from E to E + dE; E is the neutron energy, Mev. In the energy region from 4 to 12 Mev, this distribution is described by the approximate expression

$$N(E)\,dE = 1{,}8e^{-0{,}75E}dE \tag{10.2}$$

with an error not greater than 15%. The measured energy spectrum of fission neutrons for plutonium-239 closely coincides with expression (10.1), although in the high-energy region for neutrons there are certain deviations from this formula.

If the function of the spatial distribution of specific power is known in the active zone W(r) w/cm^3, then the radiation intensity of prompt neutrons with a unit volume can be determined in the following way (taking the fact into account that per 1 w of power release, on the average, $3.1\cdot10^{10}$ fission/sec occurs):

$$q_n(r) = 3.1\cdot10^{10}\nu W(r)\ \text{neutron/cm}^3\cdot\text{sec}, \tag{10.3}$$

where ν is the number of prompt neutrons emitted per one fission (ν = 2.47 in the thermal region for uranium-235, and ν = 2.91 for plutonium-239 [Ref. 1]).

Gamma-radiation, emanating from the reactor, is formed during the fission of uranium (prompt γ-radiation), and also during the capture or inelastic scattering of fission neutrons in the reactor active zone. In addition, γ-quanta are emitted due to radioactive disintegration of fission products and to residual activity of the activated materials. The mean energy of γ-radiation, which is emitted during the fission reaction, is about 7.46 Mev per fission

/301

Translator's Note: sh(x) = sinh(x).

(Ref. 1). On the average, 7.51 quanta are emitted per 1 fission. The energy distribution of fission quanta in the energy interval of 0.2 to 7 Mev is described with an accuracy of up to ±30% by the following formula:

$$I_\gamma(E) = 7{,}5\, e^{-E}, \tag{10.4}$$

where $I_\gamma(E)$ is the number of quanta having the energy E which are emitted in the energy interval of 1 Mev; E is the quantum energy, Mev. We should note that the mean energy of γ-quanta is E = 0.9 Mev. Therefore, on the average, approximately 8 quanta are emitted per 1 fission, but the energy of the main energy group of γ-quanta can be assumed to equal 2.3 Mev (0.85 quanta/fission) (Ref. 2). The mean intensity of prompt γ-radiation per unit of volume is

$$q_{\gamma,\ \text{prompt}}(r) = 2.48 \cdot 10^{11} W(r)\ \gamma\text{-quanta/cm}^3 \cdot \text{sec}. \tag{10.5}$$

The energy of γ-radiation and the corresponding half-life period of the fission products change within very wide limits. Figure 10.1 presents certain data (Ref. 1) on γ-energy release of uranium-235 fission products, divided into seven energy groups. The energy release of the $\underline{i\text{th}}$ group of $\Gamma_i(\infty, T_d)$ is given for an infinite operational time of the reactor for T_d days after it has stopped. For any other time interval T_0 of the reactor operation, the energy release is (Ref. 2):

$$\Gamma_i(T_0, T_d) = \Gamma_i(\infty, T_d) - \Gamma_i(\infty, T_0 + T_d). \tag{10.6}$$

For a mean energy E_γ = 0.7 Mev, 6 Mev energy of γ-rays of disintegration products is emitted per 1 fission. The rate at which energy is released decreases with time in accordance with the expression

$$\Gamma = 1.3t^{-1.2}\ \text{Mev/sec} \cdot \text{fission for}\quad t > 10\ \text{sec}, \tag{10.7}$$

where t is the time which passes after the fission, sec.

The intensity of γ-radiation from fission products, after the reactor has stopped for the time t > 10 sec, can be determined according to the formula

$$P_\gamma = 0{,}032W\ [t^{-0{,}2} - (t + t_0)^{-0{,}2}], \tag{10.8}$$

where t_0 is the reactor operational time per constant power W, sec. If the power W is expressed in watts, and P_γ in Mev/sec, formula (10.8) can be rewritten as follows:

$$P_\gamma = 2 \cdot 10^{11} W\ [t^{-0{,}2} - (t + t_0)^{-0{,}2}]. \tag{10.9}$$

The energy release rate during the first 10 seconds is somewhat higher than for $t \gg 10$ sec. The spectrum for γ-quanta, which are emitted directly after the reactor has stopped, has a peak for $E_\gamma = 0.8$ Mev and extends approximately up to 3 Mev. /302

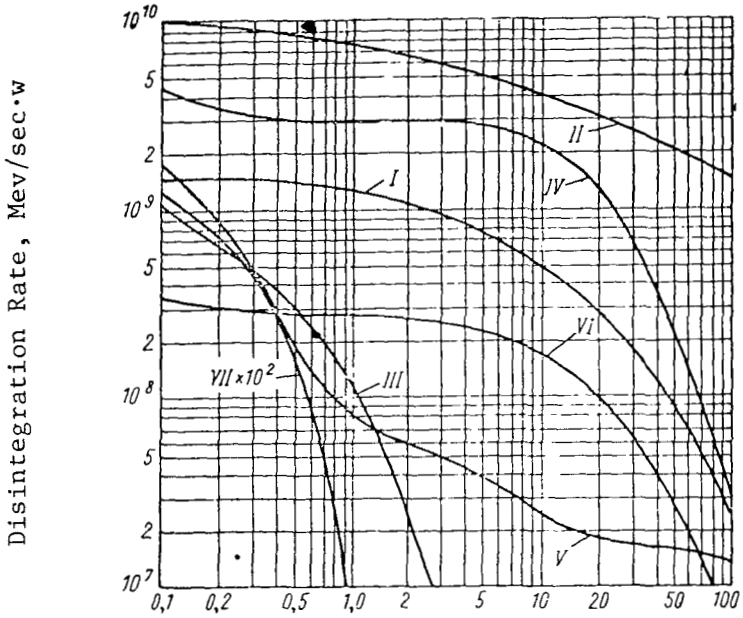

Figure 10.1

Disintegration of Fission Products after Long Reactor Operation.

I - Effective Energy, Equalling 0.4 Mev; II- 0.8 Mev; III- 19 Mev; IV-1.7 Mev; V- 2.2 Mev; VI- 2.5 Mev; VII- 2.8 Mev.

γ-quanta which are formed when neutrons are captured in the active zone make a large contribution to γ-radiation from the reactor. The space-energy distribution of the sources for the captured γ-quanta in the active zone is

$$q_{\gamma,\ \text{capt.}}(E,r) = \alpha(E)\int_0^\infty \Sigma(E')\,\Phi(E',r)\,dE, \qquad (10.10)$$

where $\alpha(E)$ is the number of γ-quanta having the energy E, which are emitted during the absorption of one neutron; E - neutron energy; $\Phi(E', r)$ - space-energy distribution of neutron stream; $\Sigma(E')$ - macroscopic cross-section of neutron capture.

Thus, the volumetric density of sources in the active zone will

equal

$$q_{v,\gamma} = q_{\gamma,\ \text{prompt}} + q_{\gamma,\ \text{capt.}} \qquad (10.11)$$

In addition to this, consideration must be given to γ-radiation which accompanies inelastic scattering of rapid neutrons, and γ-radiation of activated materials in the active zone. /303

If the intensity of the delayed and prompt γ-quanta are compared when determining the shielding, it is found that γ-radiation which is formed during fission predominates. However, the radiation accompanying the neutron capture in the active zone can be a very dangerous form of γ-radiation, in view of its great penetrating ability (energy of captured γ-quanta approximately equals the neutron binding energy in the nucleus $E_{bind.} = 8$ Mev). If it is assumed that 1.5 neutrons are consumed in loss and radiation capture out of 2.5 neutrons, which are formed during uranium-235 fission, then the largest number of captures equals $4.5 \cdot 10^{13}$ capture/kw. Since self-absorption radiation occurs in the active zone, only exterior regions of the active zone will radiate effectively.

For a distribution of the sources for γ-quanta or neutrons, which is uniform with respect to the active zone area, the escape of radiation from the surface of this area (Ref. 1) is

$$i(\theta) = \frac{q\lambda_c}{4\pi}\cos\theta, \qquad (10.12)$$

where $i(\theta)$ is the escape velocity (γ-quanta or neutrons) from a surface unit of the volumetric source per unit of a solid angle, in the direction which is formed by the angle θ with the normal to the surface, particle/cm^2·sec; θ - is the angle between the flight direction of the quantum (or neutron) and the normal to the surface of the radiating volumetric source; q_v is the specific power of the source, particle/cm^3·sec; λ_c - is the radiation relaxation length in the radiative medium; for rapid neutrons $\lambda_c = \frac{1}{\Sigma_{rem}}$, where Σ_{rem} is the macroscopic removal cross-section (rapid neutrons) for the active zone; for γ-quanta $\lambda_c = \frac{1}{\mu}$, where μ is the total linear absorption coefficient for the active zone. When formula (10.12) is used, it is assumed that the quantity λ_c is small as compared with the dimensions of the source and with the local radius of curvature for the source - shielding interface. The total escape from a surface unit of the source will equal

$$I = \int_0^{\pi/2} i(\theta)\, d\Omega = \frac{q_v\lambda_c}{4}. \qquad (10.13)$$

This expression can be used to calculate the heat release from

γ-quanta, and also to calculate the sources of captured γ-quanta in the internal shielding regions.

For thick shieldings, the most penetrating radiation, which leaves the source surface in a direction close to the normal, is a controlling factor. Based on this, the equivalent surface source ($\theta = 0$) is selected /304

$$S_{equiv.} \approx q_v \lambda_c, \qquad (10.14)$$

where $S_{equiv.}$ represents the isotropic surface source which - when placed on the interface between the volume source and the shielding - gives the same dose on the outer side of the shielding as is obtained from the volume source, particle/cm^2·sec. It is assumed that this source gives the same radiation per unit of solid angle in the normal direction.

When the region in which the sources are distributed is not greater than λ_c, the preceding result must be refined to a certain extent by integration with respect to the volume occupied by the sources. For very small sources, we have

$$S_{equiv.} = q_v h, \qquad (10.15)$$

where h is the thickness of the region occupied by the sources, which is small as compared with λ_c, cm.

When shieldings are designed for reactors, attention must be given to a great number of sources which are distributed with respect to the volume of the absorbing material, i.e., to a spatially-distributed source. In order to determine the radiation intensity function of such a source at a point under consideration, it must be integrated with respect to the volume occupied by individual point sources (Ref. 1 - 3). Conversions from one geometric form of the radiation source to another (from a point, line, and disc to a cylinder) can also be utilized. Based on the calculational or experimental data for the dose rate created by a radiation source of one form, these conversions make it possible to determine the dose rate from a source having another form (Ref. 4).

10.2 Attenuation of Rapid Neutrons

Effective cross-sections for the interaction of neutrons with matter decrease quite strongly with an increase in the neutron energy; for this reason, the most penetrating ones are rapid neutrons, although there are relatively few of them in the total radiation from the reactor. Consequently, the shielding thickness must be calculated on the basis of the required attenuation of rapid neutrons. A great deal of study (for example, [Ref. 5 - 8], and others) has been devoted to the penetration of neutrons through matter, which is described

by the transport theory. However, the difficulty entailed in and the cumbersome nature of solutions for these problems - together with the present existence of rather comprehensive information on elementary processes during the interaction of neutrons with matter (apart from certain data on neutron cross-sections in the high-energy region) - make it necessary to utilize semiempirical methods, which are less exact but more fruitful. One of the most widely used methods is the method of removal cross-section, first advanced by Albert and Welton (Ref. 9). /305

The physical bases for the method utilizing the removal cross-section have been fairly well developed at present, and are described in detail in several works (Ref. 2, 3, 7). The mathematical basis of the method consists of the fact that the attenuation of rapid neutrons having the energy E is described by an exponential law, based on the shielding thickness.

A stream of rapid neutrons can be expressed as:

$$\varphi(E) \sim e^{-\Sigma_{\text{equiv.}}^{(E)} t}, \qquad (10.16)$$

where $\Sigma_{equiv}(E)$ is the macroscopic removal cross-section; t is the shielding thickness, cm. This law can be used both for homogeneous and for heterogeneous media which contain not less than 20% hydrogen (by volume). The removal cross-sections can be measured experimentally or calculated approximately according to the following formula (Ref. 3):

$$\Sigma_{\text{equiv.}}(E) = \Sigma_{tot}(E) - \Sigma_s(E)\overline{\cos\theta}, \qquad (10.17)$$

where $\Sigma_{tot}(E)$ is the total cross-section; $\Sigma_s(E)$ is the scattering cross-section ; $\cos\vartheta$ is the mean cosine of the scattering angle. Formula (10.17) cannot be applied to a homogeneous medium which contains hydrogen. The following expression must be used in this case

$$\Sigma_{\text{equiv.}}(E) = \sum_i [\Sigma_{itot}(E)] - \sum_i [\Sigma_{is}(E)\overline{\cos\theta_i}(E)], \qquad (10.18)$$

where all the elements which are included in the shielding composition are summed up (in the second sum, hydrogen is excluded). The results derived from the calculation using formula (10.18) closely coincide with the experiments, a large portion of which were conducted for the the fission spectrum, but experiments were also carried out for monoenergetic neutron sources. It was found that the removal cross-section equals approximately 0.6 - 0.7 of the total cross-section for an energy of 8 Mev. Per unit of mass, the removal cross-section increases quite smoothly with a decrease in the atomic weight (Ref. 3) (Figure 10.2). The energy dependence of the removal cross-section for certain elements, which has been

examined in other works (Ref. 10-17), is shown in Figures 10.3 - 10.6 (see also [Ref. 18]) and in Table 10.1. The following formula can be used for the total hydrogen cross-section in the interval from 2 to 12 Mev (Ref. 7):

$$\sigma_H = \frac{5{,}13}{E^{0{,}725}}, \qquad (10.19)$$

where the cross-section σ_H is in barn, and the neutron energy E - Mev. Appendix 1 gives the removal cross-section magnitudes for different elements and materials for the neutrons of the fission spectrum (Ref. 10, Ref. 11).

The exponential law given above for attenuation of rapid neutrons is approximate, and hydrogen-containing media do not fulfill it as well as other media. As was indicated above, the total cross-section /306 decreases with an energy increase, and, consequently, the hardness of the spectrum will increase as the neutrons penetrate the shielding. As a result of this, the relaxation length of rapid neutrons will increase with an increase in the material thickness, which is particularly noticeable for media in which the main moderator is hydrogen, due to a great decrease in its cross-section in the region of several megaelectronvolts.

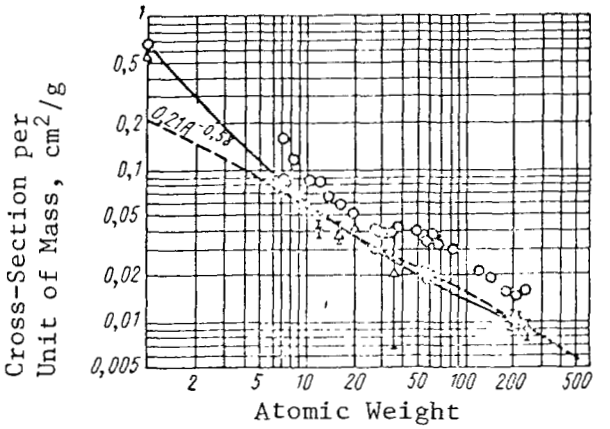

Figure 10.2

Removal Cross-Section for Fission Neutrons per Unit of Mass as a Function of Atomic Weight:

o - Total Cross-Section for 8 Mev; Δ-Removal Cross-Sections Obtained in Measurements for Mixtures; •-Cross-Sections Obtained in Measurements for Elements.

TABLE 10.1.

DEPENDENCE OF MACROSCOPIC REMOVAL CROSS-SECTION ON NEUTRON ENERGY.

Substance	Density, g/cm^3	Macroscopic Removal Cross-Section, barn, for Neutron Energies, Mev			
		2.9(Ref.26)	4.0(Ref.29)	6.7(Ref.25)	14.9(Ref.29)
H_2O	1	-	0.165±0.08	0.112	0.084±0.004
B_4C	1.67	0.129	0.083±0.003	-	0.058±0.002
C	1.67	0.132±0.0027	-	0.069±0.002	-
Fe	7.83	0.166±0.0033	0.169±0.007	0.193±0.0076	0.137±0.005
Pb	11.3	0.122±0.005	0.113±0.005	0.124±0.005	0.097±0.005

Thus, in shielding thickness calculations, the attenuation functions of rapid neutrons must be written separately for heavy and hydrogen-containing materials, and the dose of rapid neutrons D(r), at a distance r from the source, will be expressed in the following way for heterogeneous shielding: /309

$$D(r) = D_0 D(t_{H_2}) e^{-\sum_i (\Sigma_i \text{ equiv.}\, t_i)}, \quad (10.20)$$

where D_0 is the dose rate of rapid neutrons falling on the shielding; t_{H_2} - thickness of hydrogen-containing material; t_i - thickness of i^{th} heavy material; Σ_{equiv} - macroscopic cross section of the i^{th} heavy material; $D(t_{H_2})$ - dosage attenuation for the thickness of a hydrogen-containing material.

For a homogeneous shielding, formula (10.20) assumes the following form:

$$D(r) = D_0 D\left(\frac{A_{H_2}\rho t}{\rho_{H_2}}\right) e^{-\sum_i \left(\Sigma_i \text{equiv.} A_i \frac{\rho t}{\rho_i}\right)}, \quad (10.21)$$

where A_i is the weight portion of the hydrogen-containing material; A_{H_2} - weight fraction of hydrogen - containing material; ρ_i = the eigen density of the i^{th} heavy material; ρ_{H_2} - eigen density of the hydrogen-containing material; ρ - actual density of the shielding; t - total shielding thickness. Experimental curves for attenuation or removal cross-sections for these materials can be used to determine the dosage attenuation in hydrogen-containing material. Figures 10.7 and 10.8 present the results derived from experiments on the penetration of rapid neutrons in water, hydrogen (Ref. 1), and lithium hydride (Ref. 21). Appendix 1 presents the removal

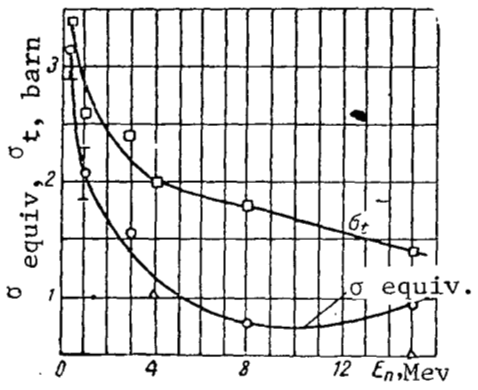

Figure 10.3

Dependence of Removal Cross-Section on Energy for Carbon:

o - Measurement Results from (Ref. 13, 14); Δ - Results from Measurements of Inverse Relaxation Lengths (Ref. 17); □ - Total Cross-Sections; Removal Cross-Section for 8 Mev taken from (Ref. 10) for the Fission Spectrum.

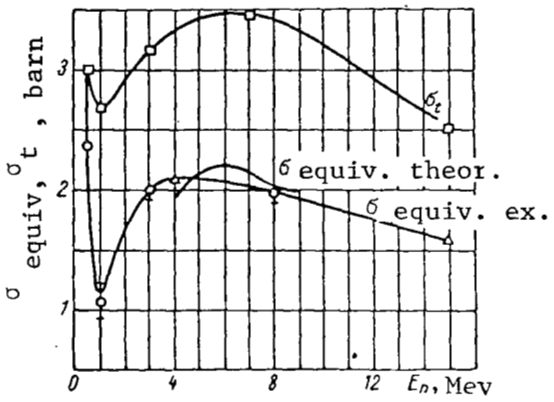

Figure 10.4

Dependence of Removal Cross-Section on Energy for Iron:

o - Measurement Results from (Ref. 13, Ref. 14); Δ - Results from Measurements in a Heterogeneous Mixture of Iron and B_4C (Ref. 15); □ - Total Cross-Sections; Removal Cross-Section for 8 Mev taken from (Ref. 10) for the Fission Spectrum; Theoretical Calculations taken from (Ref. 11).

cross-section for certain hydrogen-containing materials (Ref. 1). The dosage attenuation of rapid neutrons in hydrogen can also be determined analytically (Ref. 16)

$$D_{\text{H}}(r) = D_0 B(r)\, e^{-\Sigma_{\text{H}} r}, \qquad (10.22)$$

where Σ_{H} is the total cross-section of hydrogen for a given energy; r - distance from the source to the point under consideration; D_0 - dose for r = 0; $B(r) = 1 - \Sigma_{\text{H}} r$. The results obtained with this formula closely coincide with accurate data obtained by the moment method.

If a non-monoenergetic stream of neutrons falls on the shielding - whose spectrum differs from the fission spectrum - then the spectrum of $D_0(E)$ for incident neutrons must be taken into account, and the energy dependence of the removal cross-section must be used. In this case, formula (10.20) will be complicated:

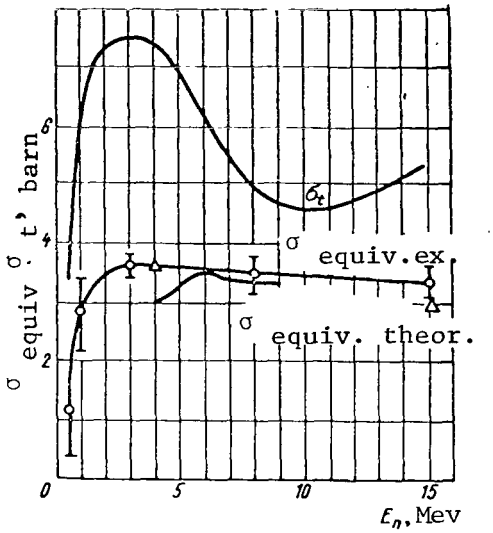

Figure 10.5

Dependence of Removal Cross-Section on Energy for Lead:

o - Measurement Results from (Ref. 13, 14); Δ - Results from Measurements in Heterogeneous Mixture of Lead and B_4C (Ref. 15). Removal Cross-Section for Energy of 8 Mev taken from (Ref. 10) for the Fission Spectrum.

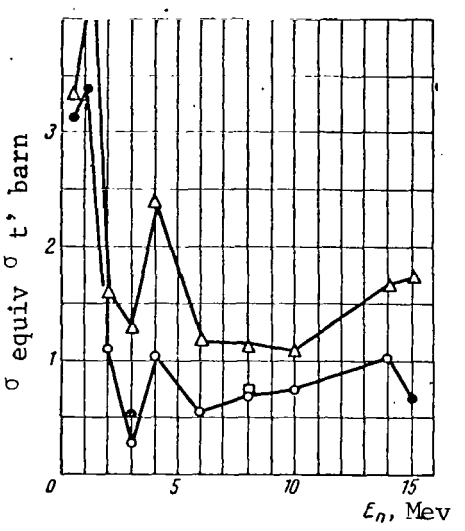

Figure 10.6

Dependence of Removal Cross-Section on Energy for Oxygen: /307-8

o - Calculation Using Moment Method (Ref. 16); • - Experimental Data from (Ref. 19, Ref. 20); □ - Measurement Results for Fission Spectrum (Ref. 10); Δ - Total Cross-Sections σ_t.

/309

$$D(r) = \int_E D_0(E)\, D(E, t_{H_2})\, e^{-\sum_i [\Sigma_i \text{ equiv.}^{(E)} t_i]}\, dE. \quad (10.23)$$

Since the cross-sections for intermediate and heavy nuclei change very little in the energy interval from 3 to 15 Mev (in contrast to heavy nuclei- such as for Be, C, and B) (Ref. 18), when the spectrum of neutrons falling on the shielding does not differ greatly from the fission spectrum in the energy region 2 - 3 Mev, the removal cross-sections can be used for these nuclei which are determined for the fission spectrum. In the opposite case, corrections must be introduced, which can be particularly significant for light nuclei. In addition, it was found that, for a neutron energy higher than 3 Mev, the removal cross-sections coincide with the cross-sections obtained from the inverse relaxation lengths, and can be used for calculating media which do not contain hydrogen. /310

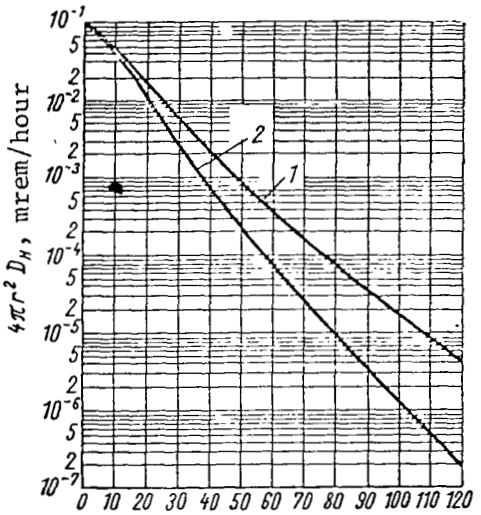

/308

water thickness, cm

Figure 10.7

Dosage Attenuation of Rapid Neutrons in Water and Hydrogen as a Function of Distance of the Point Isotropic Source of Fission:

1- In Hydrogen with Density of 0.111 g/cm^3;
2- In Water with a Density of 1 g/cm^3.

We should note that the shielding thickness, determined only /310
for rapid neutrons, can be inadequate, if the contribution from thermal or intermediate neutrons to the dose is taken into consideration - in spite of their relatively lower biological effectiveness. In this case, corresponding corrections must be introduced in the shielding thickness calculation, which can be made by using the multigroup method or any other method. When shieldings, which are made of different materials, are designed for protection from neutrons from the fission spectrum, the decisive effect in the different media as neutrons from different energy groups must be /311
taken into account (Ref. 22). By way of an example, the spectral-dosage characteristics of fission neutrons in water, carbon, and concrete media were studied for the case of infinite geometry. The curves for the change in stream and dose for neutrons from different energy groups were calculated with respect to spectral distributions. An analysis of these data shows that for an aqueous shielding the dose from neutron fission streams is mainly caused by rapid neutrons. The thermal neutrons make a contribution which is commensurate with the group of intermediate neutrons; the contribution of slow neutrons to the dose is 100 times less - and for intermediate neutrons, 10 times

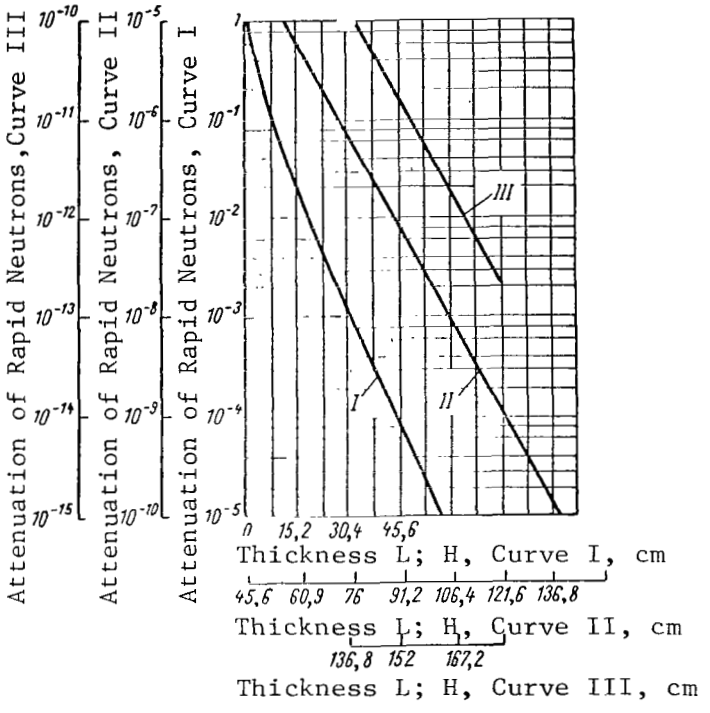

Figure 10.8

Dosage Attenuation of Rapid Neutrons in Lithium Hydride; Measurements Carried out Along the Axis of the Disc Source with a Diameter of 71 cm.

less - than the contribution from rapid neutrons. For a carbon shielding, beginning with a thickness of 50 - 60 g/cm^2, the total dose is practically determined by thermal neutrons; at smaller distances, the contribution of rapid neutrons to the dose is significant. Concrete is more similar to water than to carbon; therefore, the dose of intermediate and slow neutrons differs to a lesser extent from a dose of rapid neutrons - i.e., neutrons with every energy must be taken into account.

10.3. Attenuation of γ-Radiation

The interaction of γ-quanta with matter has been quite well studied at the present, and detailed data on this problem are given in several works (Ref. 2, 3, 7, 23). γ-radiation is attenuated due to three processes: the photoelectric effect, Compton scattering,

the formation of vapor. The sum of the cross-sections of each of these elementary processes $\sigma = \sigma_f + \sigma_{C.} + \sigma_{vap.}$ quantitatively characterizes the interaction of γ-quanta with matter. The probability for the interaction of γ-quanta per unit of trajectory length is determined by the linear absorption coefficient

$$\mu = \sigma N \; 1/см,$$

where N is the number of atoms per 1 cm^3; for a homogeneous mixture of elements, we have

$$\bar{\mu} = \sum_i (\mu_i \varepsilon_i),$$

where ε_i is the volumetric portion of the i^{th} component. The mass absorption coefficient μ/ρ, cm^2/g is frequently used, where ρ is matter density. An approximate indication of the energy intervals can be given, in which one of the above types of interaction predominates (Table 10.2).

The energy of the most penetrating portion of γ-radiation of a nuclear reactor ranges from 2 - 8 Mev, and for this reason the Compton scattering is the basic process by which the γ-quanta are attenuated in the shielding. With a decrease in energy (especially for heavy elements), the total cross-section increases due to the photo effect, and increases due to the formation of vapors at large energies. Thus, the curve for the dependence of the total cross-section on energy /312 has a minimum; Figure 10.9 shows this dependence for lead. For

TABLE 10.2

ENERGY FOR DIFFERENT TYPES OF INTERACTION BETWEEN γ-QUANTA AND MATTER

Substance	Energy, Mev		
	Photo-effect	C. Scat-tering	Formation of Vapors
Air	0.02	0.02 < E < 23	23
Aluminum	0.05	0.05 < E < 15	15
Iron	0.12	0.12 < E < 9.5	9.5
Lead	0.5	0.5 < E < 4.7	4.7

very heavy elements (for example, U, W), the energy at which the cross-section is at a minimum (E_{min}) equals 3.5 Mev. For mean nuclei (for example, Fe), it approximately equals 8 Mev, and for light nuclei it is greater than 10 Mev. These data are shown in Table 10.3 for different elements (Ref. 7). It can be shown that

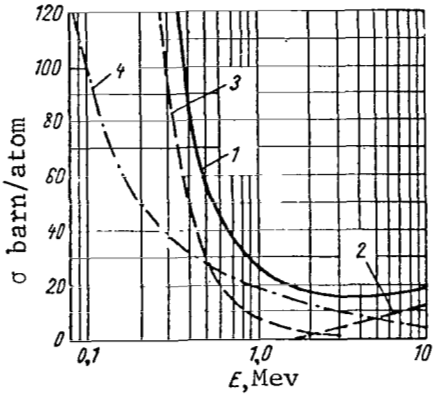

Figure 10.9

Dependence of Total Cross-Section for Interaction of γ-Quanta on Energy for Lead:

1- Total Cross-Section; 2- Formation of Vapors; 3- Photoeffect; 4- Compton Scattering.

in the given energy interval, for which the Compton effect is characteristic, the mass absorption coefficients μ/ρ do not depend on the nucleus charge Z for light nuclei and compounds of light elements. Therefore, the linear absorption coefficients of γ-radiation will be proportional to the density of matter.

An examination of the law for attenuation of γ-radiation shows that for intense absorption (photoeffect and formation of vapors) the radiation intensity with respect to the shielding thickness changes by an exponential law. However, the presence of Compton scattering disturbs the exponential attenuation law. This is particularly true for wide bundles of incident radiation and for thick shieldings, due to the fact that the scattered, high-energy radiation moves primarily in a forward direction. A study of this secondary radiation is a basic problem in the theory for penetration of γ-quanta in matter. The problem of the distribution of γ-quanta with respect to energy and direction as they penetrate matter has been studied in detail by several authors (Ref. 7, 8, Ref. 23-25), and it will not be discussed /313 here.

In practice, secondary scattering radiation is taken into account in shielding designs by the introduction of a multiplier, called the accumulation factor, which is determined as the ratio of radiation

intensity (or energy stream, energy absorption, dose) - taking into account scattered γ-quanta - to the intensity of primary radiation. In the simplest case of a monoenergetic, point (or flat monodirectional) source, the dosage attenuation is described in the following way:

$$D(r) = D_0 B(r) e^{-\mu_0 t}, \quad (10.24)$$

where D_0 is the dose rate of γ-radiation when there is no shielding at the point r; D(r) is the dose rate of γ-radiation behind the shielding at the point r; B(r) is the dosage accumulation factor for a point (or flat) source; μ_0-linear attenuation coefficient of γ-radiation with the initial energy E_0; t - shielding thickness.

TABLE 10.3

ENERGY E_{min} CORRESPONDING TO THE MINIMUM ABSORPTION CROSS-SECTION FOR DIFFERENT ELEMENTS

z	Element	E_{min} Mev	z	Element	E_{min} Mev
1	H	100	18	Ar	15
3	Be	94	20	Ca	13
6	C	56	26	Fe	9,0
7	N	46	29	Cu	7,5
8	O	39	42	Mo	5,0
11	Na	28	50	Sn	4,0
13	Al	22	74	W	3,5
14	Si	20	82	Pb	3,4
			92	U	3,3

When a linear attenuation coefficient is selected, it should be kept in mind that for $E_0 > E_{min}$ the incination of the radiation attenuation curve at large shielding depths is determined primarily by γ-quanta having the energy $E \approx E_{min}$. Therefore, the value μ must be used for $E = E_{min}$. This pertains particularly to heavy elements, for which the coefficient μ has a particularly sharp minimum. The values of the attenuation coefficient (Ref. 26) are given in Appendix 2. The function of the dosage attenuation for a point source can be used to calculate the dosage from extended sources by integrating this function with respect to the surface (or volume) of the given sources.

It is quite difficult to calculate the build-up factors, and several studies have been devoted to this, including the most comprehensive one of Goldstein and Wilkins (Ref. 24). In this study, the build-up factors were calculated for shielding thicknesses up /314 to twenty mean free paths by the moment method for different elements and

radiation sources having different geometry. However, in practice it is possible to utilize the simplified method advanced by Taylor for calculating the build-up factors. This method represents the quantity to be determined (for a point isotropic source) in the form of the sum of the exponents

$$B(\mu_0 r) = A_1 e^{-\alpha_1 \mu_0 r} + A_2 e^{-\alpha_2 \mu_0 r}, \qquad (10.25)$$

where $A_2 = 1 - A_1$; the coefficients α_1 and α_2 depend on the energy E_0, and are selected so that the values of $B(\mu_0 r)$ - calculated according to formula (10.25) - agree with the values of $B(\mu_0 r)$ - which are calculated by the moment method for thicknesses from $\mu_0 r = 1$ to $\mu_0 r = 20$ and values of the energy E_0 between 0.5 Mev and 5 Mev. This method has the advantage that the quantities A_1, α_1 and α_2 do not depend on the shielding thickness. The build-up factors obtained in the work (Ref. 24) for different elements, and also the coefficients A_1, α_1 and α_2, which are given in other works (Ref. 3, Ref. 7) are presented in the Appendices 3 - 9. The coefficients α_1, α_2, A_1, A_2, are selected for relatively large thicknesses, while for small thicknesses (particularly for light elements) the radiation attenuation - calculated with the given coefficients - can disagree with the experimental data to a significant extent (Ref. 27). We should note that the analytical concept of the build-up factors which was presented above can be used advantageously in integrating the attenuation function from separate point sources.

The build-up factors for point sources (Ref. 43) were utilized to calculate the dosage build-up factors for isotropic radiative discs. The calculations were carried out for lead, iron, water, and concrete at initial γ-quanta energies from 0.5 to 3 Mev and for shielding thicknesses from 0.5 to 10 attenuation lengths, as a function of the angle at which the disc is seen from a given point. The dosage build-up factors from cylindrical sources were obtained using the equivalent absorption length for water, aluminum, iron, and lead at an initial radiation energy from 0.5 to 6 Mev.

The build-up factors given in Appendices 3-9 were calculated for individual elements, and in practice the shielding can consist of a homogeneous or heterogeneous mixture of elements. If the elements included in the homegeneous mixture are close to the atomic number of Z, then the build-up factor can be used for the element with an intermediate Z. If the atomic numbers for the elements differ greatly from each other, then a build-up factor is used for the material with a certain effective Z, and the method for determining this is also presented in the works (Ref. 24, Ref. 7). The dependence of the dosage build-up factor on the atomic number, which was obtained in the work (Ref. 24), for a point isotropic source with energies between 2 - 10 Mev is shown in Appendix 10.

For heterogeneous shieldings, it is rather difficult to calculate the build-up factors. In this case, one must use the results derived from calculations on the penetration of γ-radiation through multi-layered media, obtained by different authors [see the citation in the work (Ref. 7)], and also general physical considerations. For a two-layered shielding, in which the heavy element is behind the light element, the effective build-up factor is much less than the product of the build-up factors for each of the two shielding layers taken separately (Ref. 3, Ref. 7). It can be approximately assumed that it equals the build-up factor for shielding comprised of one layer of a heavy element with a thickness (in mean free paths) which equals the total thickness of the two-layered shielding. For a reverse arrangement of the layers, the total build-up factor will approximately equal the product of the build-up factors for each layer individually. /315

These recommendations are confirmed to a certain extent by the results of an experimental work (Ref. 29) in which the build-up factors were measured for a two-layered shielding consisting of different combinations of lead, iron, and aluminum (E_0 = 1.25 Mev). A formula is given in this study which makes it possible to calculate the build-up factors for arbitrary initial energies of γ-quanta and materials, if the spectrum for radiation scattered after penetration of the first layer is known.

The build-up factors given in Appendix 10 were calculated by the moment method for infinite media, and therefore they will be somewhat less for real shieldings having limited dimensions. The appropriate corrections for the build-up factor in an infinite medium were calculated by Berger (Ref. 30) for the energies and materials which are most important in practice. However, these corrections are important for a shielding only for light materials and low-energy sources, and in other cases they can be disregarded.

The data presented above on calculations of γ-radiation attentuation pertain to monoenergetic γ-quanta. However, the real thickness of a designed shielding must be selected on the basis of the complex spectral composition of γ-radiation from nuclear reactors. This can be done, for example, using the method of competing lines, which was discussed in detail in another work (Ref. 31) [see also the use of this method for shielding design in the work (Ref. 43)]. In several practical cases for designing shielding from γ-radiation, general tables can be used (Ref. 31 - 34, and others).

10.4. Outflow of Captured γ-Radiation

The absorption of neutrons when they penetrate a shielding is accompanied by the emission of captured γ-quanta, whose energy approximately equals the neutron binding energy in the nucleus.

The spectra of captured γ-quanta (see Appendix 11) depend on the distance between the energy levels of the nuclei, and can be divided into three groups: all of the energy of the γ-radiation for elements of this group belongs to one photon. The spectrum has a line structure - i.e., emission of several γ-quanta having different energies is possible. γ-quanta having different energies are possible; however, for energies below 5 Mev the radiation spectrum is continuous. As a rule, this is softer radiation than in the preceding group. /316

Since the neutron absorption cross-section decreases with an increase in energy, the thermal neutrons are captured to the greatest extent. The shielding - thickness distribution of a stream of thermal and epithermal neutrons, which are formed when rapid neutrons are moderated, is determined by the spatial distribution of rapid neutrons. The attenuation of a stream of thermal neutrons, emanating from the reactor active zone and falling on the inner shielding surface, is described by a simple exponential law with an index equalling the diffusion length.

The neutron spectrum at a given point on the shielding depends not only on the moderating and absorbing properties of the shielding material, but also on the spectrum for neutrons emanating from the reactor active zone, and on the location of this point. An equilibrium spectrum is established for large distances from the source in the shielding; this spectrum does not depend on distance. In this case, the following relationship between the streams of rapid and thermal neutrons can be written (Ref. 3):

$$\frac{\varphi_{\text{therm}}}{\varphi} \approx \left[\lambda_0 \Sigma_c \left(1 - \frac{L^2}{\lambda_0^2}\right)\right] e^{\frac{L_s^2}{\lambda_0}}, \qquad (10.26)$$

where φ_{therm} is the stream of thermal neutrons; φ is the stream of rapid neutrons; λ_0 - the relaxation length of rapid neutrons; Σ_c - macroscopic absorption cross-section of thermal neutrons; L_s - moderation length; L - diffusion length.

It is necessary to know the neutron spectrum in order to determine the spatial distribution of sources of captured γ-quanta at each point in the shielding and, consequently, in order to solve the problem of the outflow of captured γ-radiation beyond the shielding. Thus, the solution for the problem of captured γ-radiation can be reduced to determining the spatial-energy distribution of neutrons in the shielding media.

The propagation of neutrons in matter can be described by the well-known integro-differential equation of Boltzmann, the solution

of which represents a very complex problem. Therefore, an approximate solution is usually presented. One of the basic methods which can be used to solve the kinetic equation is the method of spherical harmonics. The diffusion approximation (or P_1-approximation) and the age-diffusion P_2 and P_3-approximations, obtained by this method, are usually used. When one or the other approximation is selected, it should be kept /317 in mind that the age-diffusion approximation does not take into account inelastic neutron scattering, and also it is not applicable in the presence of hydrogen (or other light nuclei) or strong absorbers. However, this method can be used in many cases (Ref. 35), which is confirmed by the close agreement between calculational results and experimental data. The P_2-approximation is most effective for designing a shielding from neutron radiation, and particularly for calculating the captured γ-radiation, since it makes it possible to accurately describe (as compared with the diffusion approximation) a neutron stream at large distances from the active zone. If the method of spherical harmonics is utilized, the P_2-approximation of the basic kinetic equation of Boltzmann (Ref. 5) can be obtained in spherical geometry.

Let us examine the kinetic equation of moderation in phase space (r, v, Ω) in the absence of external nuetron sources

$$\Omega\nabla\varphi + \Sigma\,\varphi = \int d\Omega' \int dv'\varphi(\mathbf{r}, v', \Omega')\,W(\mu_0, v' \to v), \tag{10.27}$$

where φ(r, v, Ω) is a stream of neutrons; Ω is the unit vector of neutron direction of motion; r is the radius vector; v is the neutron velocity; $\Sigma = \Sigma_c + \Sigma_s$ is the total macroscopic cross-section (capture plus scattering) of neutrons; $W(\mu_0, v' \to v)$ - function of neutron scattering as a result of elastic and inelastic collisions with a nucleus; μ_0 - cosine of the angle between directions of motion before and after neutron collision with a nucleus.

The boundary conditions are given as follows:

1. φ(r, v, Ω) = 0 on the surface of the medium S for Ω n < 0, where n is the external normal to the surface.

2. The functions φ(r, v, Ω) must be continuous during the change from a region with certain physical properties to a region with other physical properties. With a change to spherical geometry (the system r, v, θ, ψ), equation (10.27) assumes the form:

$$\mu\frac{\partial\varphi}{\partial r} + \frac{1-\mu^2}{r}\frac{\partial\varphi}{\partial\mu} + \Sigma\,\varphi = \int_0^{2\pi} d\psi' \int d\mu' \int dv'\varphi W(\mu_0, v' \to v), \tag{10.28}$$

where φ(r, v, μ) does not depend on the azimuth ψ; $\mu = \cos\theta$. Let us

assume that at the outer surface $\varphi(r, v, \mu) = 0(-1 < \mu < 0)$. Let us represent the function $W(\mu_0, v' \to v)$ in the form of a series of Legendre polynomials

$$W(\mu_0, v' \to v) = \frac{1}{4\pi} \sum_{l=0}^{\infty} (2l + 1) W_l(v' \to v) P_l(\mu_0), \qquad (10.29)$$

where /318

$$W_l(v' \to v) = \int_0^{2\pi} d\psi \int_{-1}^{+1} d\mu_0 W(\mu_0, v' \to v) P_l(\mu_0).$$

The solution of equation (10.28) will have the following form:

$$\varphi(r, v, \mu) = \frac{1}{4\pi} \sum_{n=0}^{\infty} (2n + 1) \varphi_n(r, v) P_n(\mu), \qquad (10.30)$$

where

$$\varphi_n(r, v) = \int_0^{2\pi} d\psi \int_{-1}^{1} d\mu \varphi(r, v, \mu) P_n(\mu).$$

Let us multiply equation (10.28) term by term by $P_m(\mu)$, and let us integrate the result with respect to ψ and μ. Let us substitute the expansions (10.29) and (10.30) in the obtained expression, and, utilizing the well-known relationships for Legendre polynomials

$$\left.\begin{aligned} &\int_{-1}^{+1} P_n(\mu) P_m(\mu) d\mu = \begin{cases} 0, \ \ldots\ m \neq 0, \\ \dfrac{2}{2n+1}, \ \ldots\ m = n; \end{cases} \\ &\mu P_n(\mu) = \frac{n+1}{2n+1} P_{n+1}(\mu) + \frac{n}{2n+1} P_{n-1}(\mu); \\ &(1 - \mu^2) \frac{dP_n}{d\mu} = (n+1)[\mu P_n(\mu) - P_{n+1}(\mu)], \end{aligned}\right\} \qquad (10.31)$$

we obtain the following system of integro-differential equations:

$$\frac{m}{2m+1} r^{m-1} \frac{\partial}{\partial r} \frac{\varphi_{m-1}}{r^{m-1}} + \frac{m+1}{2m+1} \frac{1}{r^{m+2}} \cdot \frac{\partial}{\partial r} r^{m+2} \varphi_{m+1} + \sum \varphi_m =$$

$$= \int d v' \varphi_m W(v' \to v), \qquad (10.32)$$

to which the boundary conditions at the center of the sphere must be added $\frac{\partial \varphi_0}{\partial r} = 0$; $\varphi_m = 0$ (m = 2, 4, 6); at the outer boundary, $\sum_{m=0} \alpha_{im} \varphi_m = 0$(i, m = 0, 1, 2), where the coefficients α_{im} are determined by the relationship

$$\alpha_{im} = (2m + 1) \int_{-1}^{0} \mu^{2i+1} P_m(\mu) d\mu.$$

In order to determine the approximate solution of the problem, it is necessary to confine oneself to the given number of terms in

the series (10.30). Confining ourselves to three terms, we obtain the P_2-approximation for the main kinetic equation of moderation. The system of integro-differential equations will have the following form: /319

$$\left.\begin{aligned} \frac{1}{r^2}\frac{\partial}{\partial r}r^2\varphi_1+\sum\varphi_0&=\int dv'\varphi_0 W_0(v'\to v);\\ \frac{1}{3}\frac{\partial\varphi_0}{\partial r}+\frac{2}{3}\frac{1}{r^3}\frac{\partial}{\partial r}r^3\varphi_2+\sum\varphi_1&=\int dv'\varphi_1 W_1(v'\to v);\\ \frac{2}{5}r\frac{\partial}{\partial r}\frac{\varphi_1}{r}+\sum\varphi_2&=\int dv'\varphi_2 W_2(v'\to v). \end{aligned}\right\} \qquad (10.33)$$

In this case, the following boundary conditions must be assumed: at the center of the sphere $\frac{\partial\varphi_0}{\partial r}=0$, $\frac{\partial\varphi_2}{\partial}=0$ for $r=0$; at the outer surface: $4\varphi_0-8\varphi_1+5\varphi_2=0$; $10\varphi_0-24\varphi_1+25\varphi_2=0$.

The most effective method for solving different approximations of the kinetic equation is the group method (Ref. 5). The essence of this method consists of the fact that the entire neutron velocity interval is divided into several partial intervals - groups, within which it is assumed that the cross-sections of nuclear processes are independent of the neutron velocities. Within the limits of each energy group, the main equation is integrated, and the integral neutron streams are selected by groups as the unknowns. As a result, a system of multigroup constants is obtained, whose calculation requires the neutron spectrum in the medium under consideration. The method for averaging the constants depends on the explicit conditions of the given problem. When a large number of groups is utilized, in which the group intervals are so small that the neutron stream changes very slightly within the limits of each group, the method by which the physical constants are averaged is not important. In this case, it is possible to determine a universal system of group constants, which is not dependent on the neutron spectrum in the medium under consideration (Ref. 36). One of the methods for obtaining a system of group constants for designing a biological shielding, which consists of hydrogen-containing and heavy materials, is examined in another work (Ref. 35). Reference books can be utilized to formulate systems of group constants (Ref. 1, 26, 37, 38).

A multigroup system of equations can be written in finite-difference form, and can be solved numerically by the method of different factorization (Ref. 5). In the given approximations, this problem can be effectively solved on computers (Ref. 36).

The spatial - energy neutron distribution, which is obtained as a result of solving a multigroup system of equations, can be utilized to determine the spatial distribution of sources of captured γ-quanta in the following way:

$$q_v(r) = \int_0^\infty \varphi(r, E)\,\Sigma_c(E)\,dE, \qquad (10.34)$$

where $q_v(r)$ represents the amount of γ-quanta formed per 1 cm^3/sec at /320 the point r; $\varphi(r, E)$ - a neutron stream at the point r having the energy E in the interval dE; $\Sigma_c(E)$ - macroscopic cross-section for the capture of neutrons having the energy E. If neutrons are mainly captured in the thermal region - which is impossible to tell with nuclear reactors for rapid and intermediate neutrons with a hard spectrum of outgoing radiation - in many cases a stream of thermal neutrons φ_{therm}, determined by formula (10.26) for a certain spatial distribution of rapid neutrons, can be used to determine the function $q_v(r)$.

The function of spatial - energy distribution of sources of captured γ-quanta is determined as

$$Q_v = (r, E) = \alpha(E)\,q_v(r), \qquad (10.35)$$

where $Q_v(r, E)$ is the number of γ-quanta at the point r having the energy E in the energy interval ΔE; $\alpha(E)$ - the portion of γ-quanta having the energy E in the energy interval ΔE which are formed during the absorption of one neutron.

The function which is obtained for the spatial distribution of sources of captured γ-quanta can be represented in the following form, which is most advantageous for calculating the outflow of quanta from the outer surface of the layer under consideration (for flat geometry):

$$q_v(r) = q(r_0)\exp\left[-\left(\sum_{i=1}^{n}\frac{t_i}{\lambda_i} + \frac{r - r_0 - \sum_{i=1}^{n} t_i}{\lambda}\right)\right], \qquad (10.36)$$

where r_0 is the coordinate for the inner surface of the shielding layer under consideration; t_i is the thickness of the ith section of the layer under consideration, for which the relaxation length λ_i of the function $q_v(r)$ is characteristic; n is the number of sections (with different relaxation lengths) which precede the section in which the point r under consideration is located and to which the relaxation length λ corresponds.

If the shielding layer of any material is investigated, for individual sections of which the quantity λ is characteristic, then the intensity of the outflow of captured γ-quanta from the outer surface of the entire layer can be conveniently regarded as the sum of the intensities for the outflow of these quanta from each section separately, taking into account the radiation attenuation in all subsequent sections. The buildup of scattered quanta and geometric attenuation must also be taken into account. In order to obtain the outflow of captured γ-quanta from the surface of the shielding section

under consideration, it is necessary to integrate the stream of quanta with respect to the entire thickness of this section. Assuming that the function of spatial distribution for the sources of captured γ-quanta can be described as an exponential function, after this integration we obtain the following formula for the outflow of quanta from the surface of a flat layer having the thickness t with the constant quantity λ (scattered quanta are not taken into account): /321

$$I_\gamma = \frac{q(r_0)}{2} \cdot \frac{e^{-t/\lambda} - e^{-\mu t}}{\mu - \frac{1}{\lambda}}, \qquad (10.37)$$

where μ is the linear absorption coefficient of captured γ-quanta. It is assumed that only half of the quanta formed at each point are propagated forward. A similar formula can be readily obtained for the increasing [in contrast to formula (10.36)] function of the spatial distribution of sources of captured γ-quanta. If the energy distribution of γ-quanta, formed during the capture of neutrons, is unknown for any individual element, when the outflow of these quanta is calculated it can be assumed that the total binding energy of the neutron in the nucleus of this element is set free in the form of γ-quanta having the energy $E = E_{min}$, for which the shielding is most transparent. This must be taken into account in selecting the coefficient μ.

In conclusion, we should note that the spectral distribution of captured γ-radiation is not only described by the three groups indicated above, but very soft γ-quanta can appear as the result of neutron reactions with the emission of charged particles (for example, captured γ-quanta having an energy of 0.5 Mev are formed during the absorption of neutrons by the isotope of boron-10). Table 10.4 presents some of these reactions.

TABLE 10.4

REACTIONS WITH EMISSION OF CHARGED PARTICLES

Reactions for Slow Neutrons	Reaction Energy, Mev	Isotope Content, %	Isotope Cross-Section, barn	Natural Mixture Cross-Section, barn
$He^3(n, p) H^3$	0.7637	$(1-10)\cdot10^{-5}$	5400±300	-
$Li^6(n, \alpha) H^3$	4.784	7.52	945±100	71±1
$B^{10}(n, \alpha) Li^7$	2.792	18.8	266	50
$B^{10}(n, \alpha)Li^7$ + 0.48 Mev γ	2.792	18.8	3720	700
$N^{14}(n, p) C^{14}$	0.624	99.63	1.68	1.68
$Cl^{35}(n, p) S^{35}$	0.62	75.4	0.3 ± 0.1	0.23±0.08

Thus, when a shielding is designed which is compact and economical in terms of weight, it must be kept in mind that the intensity of the outflow of captured γ-radiation - and, consequently, the shielding weight - can be reduced by introducing boron into the shielding material. Boron can be added both homogeneously, and in the form of layers. In practical terms, when shieldings are constructed, boron can be added not in a pure form, but combined with different elements. Certain computational data on the decrease of the biological dose from captured γ-radiation when boron is added to water are given in the work (Ref. 3) . In another work (Ref. 39), the effect of a /322
boron carbide layer, which is placed between steel and plexiglass, on the outflow of γ-quanta from steel is studied.

10.5. General Principles for Designing Compact Shielding

One basic factor which determines the composition and construction of the radiation shielding for any atomic device is the purpose of this device. When shielding is designed for radiation from a nuclear reactor, which is located on a space vehicle, it must be taken into account that minimum weight (and sometimes overall size) is a primary requirement imposed on radiation shielding. Otherwise, the atomic device cannot fulfill its primary purpose, at least for the present level of development of science and technology. The ratio for the weight of the device to its output can serve as a measure for a successful shielding design on a given device. It is necessary that this ratio be kept to a minimum. The ratio of the engine thrust to its weight (including the shielding weight) can also be regarded as a criterion for successful shielding design. It is interesting to note that the maximum value of this criterion must not necessarily correspond to the minimum shielding weight, since the thrust can depend on the shielding construction, and also on the reactor dimensions - which, in their turn, influence the shielding weight (Ref. 40).

The requirement for minimum weight leads to the necessity of utilizing one of the following three principles for the shielding arrangement when the shielding is designed: the location of the shielding material around the object to be shielded (payload); location of the shielding around the reactor; separation of the shielding into two parts - around the reactor and around the object to be shielded. Shielding which is located around the reactor must be only the shadow type - i.e., the object to be shielded must be located in the "shade" formed by this shielding. Otherwise, the shielding weight will be far from minimum.

Neutrons and γ-rays represent penetrating forms of radiation from a nuclear reactor. The purpose of radiation shielding is to lower the radiation where the device is located down to a specific

level, which represents the maximum permissible level. The following principles must underly a compact shielding design:

1. Rapid neutrons having energies up to 14-18 Mev represent the most penetrating radiation from a nuclear reactor. Since the cross-sections decrease with an energy increase, the absorption of such neutrons is small. Neutrons with an energy of 8 Mev, which comprise only 0.01% of the total number of neutrons in the reactor, can play a basic role behind a shielding (Ref. 19). It must be taken into account that the RBE of neutrons increases with an increase in energy (at least, up to 3 Mev). Consequently, the thickness of /323
the entire shielding will be determined by rapid neutrons. The combination of heavy elements with hydrogen or with another moderator makes it possible to slow down neutrons of even very high energies. Heavy elements are introduced for the reason that the scattering cross-section of hydrogen is small for neutrons having high energies, and inelastic scattering for heavy nuclei makes it possible to decrease the neutron energy to the level (0.5 Mev) when the cross-section of hydrogen elastic scattering becomes significant. For high energies, the total cross-section is

$$\sigma_t \sim 2\pi R^2,$$

where R is the nucleus radius. Since $R \sim A^{1/3}$, where A represents the mass number, then we have $\sigma_t \sim A^{2/3}$. The number of atoms (or nuclei) per unit of mass of any substance is inversely proportional to the atomic weight. Consequently, the effectiveness of the given material mass is inversely proportional to $A^{1/3}$ - i.e., the weight of the shielding material, which is required to slow down rapid neutrons to a specific energy, will be less for elements having a low mass number. Thus, less iron is required than lead or tungsten for identical effectiveness in attenuating rapid neutrons. The absorption of decelerated neutrons is relatively easy, since the majority of construction materials have an adequate absorption cross-section for thermal neutrons.

2. When γ-radiation penetrates the shielding, multiple Compton scattering occurs, which is taken into consideration by introducing a buildup factor when designing the shielding thickness. This factor depends on the atomic number of the shielding material, on the energy of γ-quanta, and also on the geometry of the source or the shielding. If it is approximately assumed that the attenuation of γ-rays conforms to an exponential law, and the buildup factor changes linearly with the thickness or is equal to unity, then the necessary thickness will be proportional to the linear absorption coefficient (μ). It is apparent that the larger the material density, the smaller the shielding thickness. The relative shielding mass for a given attenuation degree, which equals the shielding thickness multiplied by the density, will be inversely proportional to the mass absorption coefficient μ/ρ(ρ - density of the material). The values for this coefficient are approximately

constant for different materials (0.032 cm^2/g); therefore, for flat geometry it can be approximately assumed that the weight of the shielding from γ-radiation does not depend on the material. However, the weight of certain types of shadow shielding (for example, in the form of a cone, lens, and others) will be smaller for material with a large specific weight. The heavy shielding component, which is intended for effective absorption of γ-rays, will also serve for inelastic scattering of rapid neutrons.

3. As is known, when neutrons are absorbed, captured γ-radiation is formed in the shielding material; this radiation can greatly exceed the primary γ-radiation emanating from the active zone. The /324 amount of the heavy material, or part of the heavy material relative to the outer shielding surface, can be increased in order to suppress this radiation. In this case, the shielding weight will be considerably increased. The shielding weight (particularly, the shadow type of shielding) can be reduced to a minimum only by dividing the heavy shielding component into several layers, between which a light, hydrogen-containing material must be located, and by selecting the optimum ratio between the heavy and light layers (Ref. 3). The outflow of captured γ-radiation can be decreased by introducing boron-10 into the heavy shielding component, since the absorption of neutrons by this boron isotope takes place due to the reaction (n, α) with the emission of soft γ-radiation. Thus, the weight of shadow shielding is determined to a significant degree by captured γ-radiation.

In addition, it must be added that nuetrons are accumulated in the energy region less than 1 Mev for large thicknesses of the heavy materials. This is due to the fact that the attenuation of neutrons due to inelastic collisions occurs only above the threshold of this process in heavy materials: below this energy, only elastic scattering takes place, but it is ineffective (Ref. 20). The loss of neutrons having intermediate energies can also be increased by the presence of strong antiresonances at these energies. For example, iron has a strong antiresonance in the region of 25 kev, so that - if rapid neutrons having energies above 1 Mev are attenuated with a relaxation length of 6 - 7 cm - the reaction length of epithermal and resonance neutrons will be greater than 30 cm (Ref. 41, 42). This is an additional reason that it is advantageous to divide the larger thicknesses of heavy materials into individual layers, and to place a light material between them.

4. The shadow type of shielding leads to the necessity of a strict calculation of the radiation which is scattered when passing around such a shielding, and also radiation which is scattered from the air and from construction elements which are located outside the "shadow", which is created by the shielding. The problem of scattered radiation is one of the most complex and important problems

since it is very difficult to calculate scattered radiation, and shielding from scattered radiation comprises a significant portion of the total shielding weight.

5. The design of a reliable and economical shielding must necessarily include an examination of the real geometry of radiation forces. The radiation of extended sources is attenuated in the shielding to a greater extent than is radiation from a point source. Therefore, it is of great importance to calculate the real dimensions and forms of an extended source when designing a shielding of minimum weight - especially, if attention is paid to the fact that multiple attenuations, which amount to several orders of magnitude, are frequently required in practice for shielding from radiation from such sources (Ref. 43).

6. In certain cases, the weight of the shadow shielding can be reduced by shaping the shielding surface. The shielding shape is selected on the basis of obtaining a given dosage field, with a minimum weight of the shielding screen for a source having a specific form (Ref. 44 - 46). /325

7. During spaceflights at high altitudes, where there is absolutely no scattering medium, the weight of the radiation shielding can be decreased by utilizing shadow shielding of special geometric forms. The purpose of this is not only to attenuate the radiation in the "shadow", which is created by this shielding, but also to scatter the radiation in surrounding space. One characteristic of a scattering shielding is its division into separate layers. This division is only effective when the accumulation of scattered radiation is large in the shielding itself, and the geometric characteristics do not play a significant role (Ref. 47).

8. The shielding design must completely conform to the arrangement of the entire device as a whole. To a significant extent, the shielding weight depends on the extent to which the physical and engineering problems are successfully solved. The following pounts should be noted in this connection:

a) an efficient arrangement of the thermal exchange equipment is necessary (heat exchanger, condenser-radiator, tubing, etc.), as well as the electromechanical equipment, tanks with the working substance, engines, instruments, etc., so that - when possible - all the equipment is utilized to the maximum extent as additional shielding and does not serve as a source of scattered radiation at the same time;

b) the arrangement of canals, cavities, and discontinuities in the shielding, which inevitably occur in the design, must be such as to reduce the leaking radiation to a minimum. In its turn,

a special shielding must be designed for this radiation;

c) in several cases, it is necessary to design a counter-activation shielding, so as to lower to a permissible level the activity of the equipment and instruments which must be accessible after the reactor has stopped, as well as the activity of the coolant of the second circuit;

d) not only the nuclear - physical characteristics, but also the mechanical, chemical, and heat-engineering properties must be taken into account when selecting shielding material. Heavy metals (tungsten, lead, nickel, molybdenum, uranium, and stainless steel), heavy high-melting alloys, and also light and hydrogen-containing substances (boron carbide, graphite, paraffin, polyethylene, boral, and others) can be recommended in designs for compact shieldings which are optimum in terms of weight. Apart from this, the hydrides of different metals can be used; the most suitable one of these is lithium hydride;

e) provision must be made for a cooling system for those shielding screen units whose temperature exceeds the permissible temperature, due to radiation heating. /326

In conclusion, we should note that the experience which has been acquired by different Soviet and foreign authors in designing shieldings (Ref. 2, 3, 48) shows that it is very difficult to design a nuclear reactor shielding accurately. This is due to the rather large number of complex processes which take place when radiation penetrates matter (for example, multiple scattering in the shielding, self-absorption at the source, a change in the radiation spectrum when the shielding is penetrated, the influence of the source geometry on the magnitude of attenuation, etc.), and also due to insufficient data on the elementary processes during the interaction of radiation with matter. For this reason, in the last stage of the design the shielding model must be checked experimentally in full size, and the corresponding corrections must be introduced in the final plan.

10.6. Optimization of Shielding Weight

As was already indicated above (see Section 10.5), one of the conditions under which the weight of shadow shielding can be reduced to a minimum is the utilization of a heterogeneous shielding, with an optimum ratio between heavy and light layers. This ratio depends on the type and spectrum of the radiation falling on the shielding, the nuclear-physical properties of the shielding materials, and also on the geometry of the sources in the shielding. The method of undetermined multipliers of Lagrange can be utilized to solve this problem. If we express the shielding weight G and the dose rate on the outer

shielding surface D as a function of the thickness of individual layers t_i, then the following relationship represents the condition for minimization of the weight function:

$$\frac{\partial G(t_1, t_2, \ldots, t_n)}{\partial t_i} = \Lambda \frac{\partial D}{\partial t_i}, \tag{10.38}$$

and

$$D = D(t_1, t_2, \ldots, t_n) = [D] = \text{const}; \tag{10.39}$$

Λ is the constant coefficient.

The additional equation (10.39), which is called a continuity equation, usually expresses the requirement for the dose rate decrease (or dose) on the outer shielding surface to a permissible quantity. This equation can be formulated for neutron and γ-radiation emanating from the reactor active zone, or for secondary γ-radiation which is formed in the shielding itself - and also for both radiations together, as a function of the specific conditions of the problem under consideration. Thus, for example, the total thickness of the heavy and light components can be determined on the basis of the required attenuation of radiation emanating from the active zone, and equation (10.39) can be formulated only for secondary γ-radiation. If the secondary radiation which is produced in the shielding can be disregarded, this equation is formulated only for primary radiation emanating from the active zone. /327

In order to illustrate the use of the system of equations (10.38) and (10.39), let us examine the case of a double layer, spherical shielding from a source of γ-radiation (Ref. 49). The function for the weight of the spherical, double layer shielding can be described as follows:

$$G = \frac{4\pi}{3}\left[\varrho_2 (R_2^3 - R_1^3) + \varrho_1 (R_1^3 - R_0^3)\right], \tag{10.40}$$

where R_0 is the outer radius of the source; R_1 - the outer radius of the inner layer of heavy shielding material; R_2 - the outer radius of the outer layer of light shielding material; ρ_1 and ρ_2 the densities of the inner and outer layers, respectively.

If the radiation is attenuated according to the law e^N, then the continuity equation has the following form:

$$N = \mu_2 (R_2 - R_1) + \mu_1 (R_1 - R_0), \tag{10.41}$$

where μ_1 and μ_2 represent the linear coefficients for radiation attenuation in the inner and outer layers, respectively. The index N is determined by the given dose attenuation. In addition, we can write the condition for reducing the weight function to a

minimum

$$\frac{\partial G}{\partial R_1} = \Lambda \frac{\partial N}{\partial R_1} \;\&\; \frac{\partial G}{\partial R_2} = \Lambda \frac{\partial N}{\partial R_2}, \qquad (10.42)$$

or, substituting equations (10.40) and (10.41) in the system (10.42), we obtain

$$\left.\begin{aligned} 4\pi(\varrho_1 - \varrho_2) R_1^2 - \Lambda(\mu_1 - \mu_2) = 0; \\ 4\pi\varrho_2 R_2^2 + \Lambda\mu_2 = 0. \end{aligned}\right\} \qquad (10.43)$$

Solving equations (10.41) and (10.43 together, we finally obtain the desired dimensions of a double layer, spherical shielding having minimum weight

where

$$\left.\begin{aligned} R_2 &= \pm m R_1, \\ m &= \sqrt{\frac{\mu_2(\varrho_1 - \varrho_2)}{(\mu_1 - \mu_2)\varrho_2}}; \\ R_1 &= R_0\left[\frac{\mu_1 + \frac{N}{R_0}}{\pm\mu_2 m + (\mu_1 - \mu_2)}\right]. \end{aligned}\right\} \qquad (10.44)$$

The plus sign corresponds to the minimum radius and, consequently, to the minimum weight. Substituting the determined radii R_1 and R_2 in formula (10.40), we obtain the minimum weight of the shielding under consideration.

In order to provide one example of a design for shielding having minimum weight, we can cite the case of a double layer, shadow shielding of a reactor-generator (Ref. 21). The shielding is made of lead and lithium hydride in the form of a spherical section. The reference data are as follows: thermal output of the reactor 2 Mw; length of the active zone - 28 cm, radius - 13.3 cm, thickness of the beryllium reflector - 7.6 cm; without a shielding, at a distance of about 9 m from the center of the active zone in an axial direction, the dose rates are as follows: from neutrons $I_2 = 1 \cdot 10^6$ rem/hour, from γ-rays - $I_1 = 2.4 \cdot 10^4$ rem/hour; the diameter of the shielded cabin is 4.5 m. /328

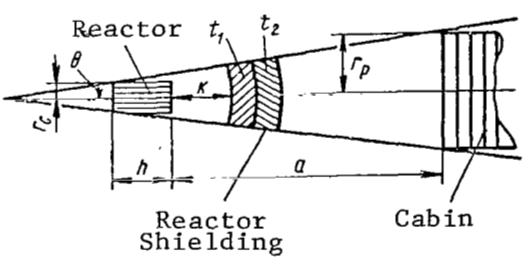

Figure 10.10

Geometry of Shade Shielding of a Nuclear Reactor on a Spacecraft.

The weight of a spherical, double layer section can be described as follows:

$$G = \frac{2\pi\beta}{3}\{t_1\varrho_1[3c^2 + 3ct_1 + t_1^2] + t_2\varrho_2[3(c + t_1)^2 + 3t_2(c + t_1) + t_2^2]\}. \quad (10.45)$$

The following notation is utilized here (Figure 10.10):

$$c = \frac{r_c(a + h)}{(r_p - r_c)} + h + k;$$

$$\beta = 1 - \left[1 + \frac{(r_p - r_c)^2}{(a + h)^2}\right]^{-1/2};$$

r_c - radius of the reactor active zone; r_p - radius of the cabin for the crew; a - distance between the reactor and cabin; h - reactor length; k - distance between the reactor and shielding; t_1 - thickness of the inner shielding layer; t_2 - thickness of the outer shielding layers; ρ_1 - density of heavy shielding from γ-radiation; ρ_2 - density of light neutron shielding.

In order to construct the conditions for minimization of the function G, we obtained the following expressions in advance:

$$\left.\begin{aligned}\frac{\partial G}{\partial t_1} &= 2\pi\beta[\varrho_1(c + t_1)^2 + \varrho_2 t_2(2c + 2t_1 + t_2)];\\ \frac{\partial G}{\partial t_2} &= 2\pi\beta\varrho_2(c + t_1 + t_2)^2.\end{aligned}\right\} \quad (10.46)$$

We can write the continuity equation based on the conditions for the required attenuation of γ-quanta and neutrons emanating from the active zone (we shall disregard captured and scattered γ-radiation)

$$D = I_1 e^{-(\mu_1 t_1 + \mu_2 t_2)} + I_2 e^{-(\Sigma_1 t_1 + \Sigma_2 t_2)} = [D], \quad (10.47)$$

where Σ_1 and Σ_2 represent the macroscopic removal cross-sections of rapid neutrons for the first and second shielding layers, respectively; /329
μ_1 and μ_2 - linear absorption coefficients of γ-quanta, respectively, for the first and second shielding layers. The magnitude of the permissible dose rate [D] changes within the limits of 10^{-1} to 10^{-5} rem/hour.

For a double layer shielding, the system of equations (10.38) can be written as follows:

$$\frac{\partial D}{\partial t_1} \Big/ \frac{\partial G}{\partial t_1} = \frac{\partial D}{\partial t_2} \Big/ \frac{\partial G}{\partial t_2}. \quad (10.48)$$

Differentiating equation (10.47) with respect to t_1 and t_2, and substituting the result obtained - together with expression (10.46) - in equation (10.48), we finally obtain

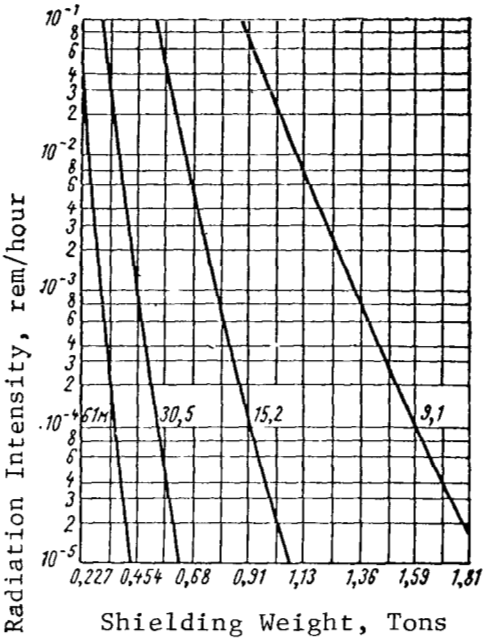

Figure 10.11

Optimum Shielding Weights as a Function of the Dose Rate for Different Distances from the Reactor to the Cabin.

$$\left.\begin{aligned}&\left[\mu_1 I_1 e^{-(\mu_1 t_1+\mu_2 t_2)} + \sum_1 I_2 e^{-(\Sigma_1 t_1+\Sigma_2 t_2)}\right] \times \\ &\times [\varrho_2 (c + t_1 + t_2)^2] = [\mu_2 I_1 e^{-(\mu_1 t_1+\mu_2 t_2)} + \\ &+ \sum_2 I_2 e^{-(\Sigma_1 t_1-\Sigma_2 t_2)}] [\varrho_1 (c + t_1)^2 + \varrho_2 t_2 (2c + 2t_1 + t_2)].\end{aligned}\right\} \quad (10.49)$$

Equation (10.49) and expression (10.47) can be solved graphically. Figure 10.11 presents the results derived from calculating the optimum shielding weight for different permissible dose rates and for different distances from the reactor to the point under consideration.

10.7. Scattering Shielding

At the present time, the elementary processes occurring during the interaction of both γ-radiation and neutrons with the shielding material are well-known. The macroscopic effects, to which repetition of these processes leads, are satisfactorily described by such concepts as the relaxation length, removal cross-section, and the dosage, energy, and numerical buildup factors. The numerical /330

values for the buildup factors were examined above.

What is the basic role of a shielding, what basic requirement determines the selection of the material and the construction of the shielding? Up until recently, a shielding was chosen so that the radiation which penetrated it lost as much energy as possible in interactions with the shielding material. It is thus assumed that a small dose per man or per unit of equipment located behind the shielding corresponds to a small stream of energy, for example, of γ-radiation. For shielding from γ-radiation, all elements are equally justified with respect to Compton scattering, if the shielding is flat (one-dimensional geometry), which is related to the almost constant density of electrons per 1 g of any material, which equals approximately $3 \cdot 10^{23}$ electron/g. In a spherical or cylindrical shielding, a heavy material provides the necessary thickness per 1 g/cm^2 with a lower, overall weight than is the case for a light material.

However, in a shielding having any form it is more desirable to use materials having a large atomic number, since photoabsorption of γ-quanta occurs in them for a larger energy than in materials with a small atomic number.

In a determination of the maximum radiation energy loss in matter, preference is given to hydrogen-containing materials in the construction of a neutron shielding. Actually, during elastic scattering in hydrogen nuclei, a neutron loses a greater portion of its energy than during scattering in heavier nuclei. For a neutron energy which is higher than the threshold of inelastic scattering, a shielding is quite effective which is made of lead and iron, which is utilized primarily for γ-radiation. The utilization of the effect of a large energy loss during inelastic scattering also confirms the principles mentioned previously.

It can thus be stated that only one side of the processes of elastic and inelastic scattering is actively used - namely, a change in the radiation energy. A change in the direction of radiation propagation after scattering can only be used passively. Thus, for example, the removal cross-section of neutrons depends on the mean cosine of the scattering angle. In other words, there is no way to utilize the effect of scattering to a greater or lesser extent when constructing shieldings of stationary reactors.

Therefore, it is not accidental that the most up-to-date mathematical procedure for calculating the penetration of radiation in matter - for example, the solution of a transport equation by the method of moments - is primarily directed toward determining the spatial - energy distributions of γ-radiation or neutrons in the shielding. It should thus be added that this method is limited to

an infinite shielding. Angular distributions are obtained from a solution of the transport equation of γ-quanta only in the approximation of scattering at small angles. For neutrons, the solution /331
of the transport equation yields only a mean cosine of the scattering angle. Accurate values for the angular dependence of an energy stream of γ-radiation can be calculated by the Monte-Carlo method. It is difficult to use this method for large shielding thicknesses ($\mu\delta = 10$), due to the cumbersome nature of the calculations. But, on the other hand, it makes it possible to calculate the penetration of radiation in limited and even heterogeneous media.

Up to the present time, there have been several experimental studies on determining the spectral - angular distributions of scattered γ-radiation from sources having a different form and energy. They have been primarily directed toward correcting existing methods for calculating the energy spectra of radiation beyond a shielding having a different thickness and toward determining the energy buildup factors; they closely coincide with the calculated data. However, the form of angular distributions obtained from the experiments has not been used directly in shielding designs up to the present.

The concept of the energy buildup factor (or dose) of γ-radiation, which is widely employed in shielding designs, is a generalized concept. It does not express the angular or energy characteristics of radiation emanating from the shielding, although its magnitude is determined by them.

However, a detailed knowledge of the penetration of radiation through matter is not necessary in determining a dose behind a shielding which has axial, spherical, or flat geometry. The radiation spectrum at any point beyond such a shielding is identical, and the angular radiation distributions are identical at all points beyond a flat shielding. Such a generalized concept as the removal cross-section of neutrons can also only be applied to a shielding which is unlimited in a transverse direction.

In the case of a shade shielding, when the transverse shielding dimensions are limited, the detector and the source are located at a certain distance from the shielding, and the buildup factor is inapplicable for a semi-infinite or barrier shielding. It must decrease as the detector and the source are removed from the shielding, and - if the scattering in the surrounding medium is disregarded - it tends toward unity. It must be noted that the concept of the build-up factor is generally not applicable for a shade shielding.

The problem of a shielding for a nuclear power device in space is characterized primarily by the absence of a surrounding scattering medium, with the exception of the construction of the craft itself. The mutual distance of the reactor and the cabin for the crew which

is shielded is also a specific problem.

The dimensions of the reactor active zone in the spacecraft depend essentially on the purpose of the reactor. It can have a diameter of 0.35 - 0.7 m, and the diameter of a nuclear jet engine amounts to 1.5 m in existing plans. The dimensions of the cabin for the crew depends on the type of spacecraft, and are small in general. A plan has been discussed for a craft having a length of /332
50 m and a diameter of 5 m, on which a reactor with an output of 182 Mw is located; the purpose of this reactor is to heat up the working substance - hydrogen (Ref. 50). The reactor has a diameter of about 1.5 m. A cabin with the same diameter is located 30 m from the reactor. "NASA" (Ref. 51) has announced a competition for designing the spacecraft "Apollo" with the following characteristics: length of the inhabited compartment 3.66 m; diameter 4 - 4.6 m; total length of the craft 16.8 - 18.3 m. Thus, the angular dimensions of the reactor with respect to the center of the cabin comprise 1 - 10°.

For small angles, there is no apparent change in the ratio of total intensity to intensity of primary radiation as only the detector is moved away. It depends on the angular distribution of primary and scattered radiation on the shielding surface, which - in its turn - is related to the spectral - angular characteristics of the source, and to the thickness and form of the shielding. The existing experimental and computational data are inadequate for determining such a change. However, if the conclusions presented in a study by V. A. Vorob'yev (Ref. 52) are taken into account regarding the cosinusoidal distribution of a stream of energy from the point γ-source per unit of solid angle - which is integrated over the entire shielding surface - and if the cosinusoidal radiation distribution from a volume source is examined, then an increase in the buildup factor can be expected as the limited dimensions are moved away from the shielding.

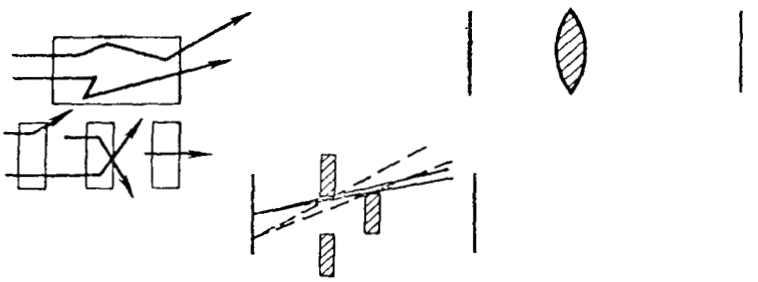

Figure 10.12

Possible Forms for a Scattering Type of Shielding

With the exception of a work by J. Moteff (Ref. 53), there are no data on the angular and energy distributions of neutrons behind a shielding. His results also indicate that the buildup factors, which are determined for an infinite medium, are not applicable for a shade shielding for a space reactor.

It is thus apparent that it is very important to know the real values for the buildup factors at different distances from the shade shielding. There are no data in the literature on the spectral-angular distributions of scattered neutrons behind a shielding. However, if the smaller anisotropic distribution of neutrons is taken into account for elementary interactions with nuclei of the shielding material, it can be assumed that the portion of scattered neutrons /333
far from the shade shielding is less than in the case of γ-radiation.

It was first shown in work (Ref. 54) that it is possible to decrease the portion of scattered radiation falling on the shielded region by the form of the shade shielding for a nuclear reactor on board a spacecraft, when there is no surrounding medium - as compared with a disc shielding. Several examples are given in this study (Figure 10.12) showing the influence of the shielding form on the intensity of the scattered radiation in the shielded region. Thus, in a disc shielding the direct and scattered radiations are "intercepted", and as a result of the scattering can be directed into the shielded region. If the disc shielding is stratified into several thinner discs, then the scattered radiation will be directed toward the side of the shielded region. If the shielding is made in the form of a ring with the central part extended toward the shielded region, then the scattering of primary radiation past the shielded region will be prevented. The author also proposes a lens-like shielding, in which the effective thickness will be more uniform along the various directions in which we are interested.

The savings in weight amounts to 0.3 on the average for a shielding in the form of several discs, having a diameter equalling the diameter of the source and the cabin (Ref. 54). A table is also given in this work showing the savings in weight for an energy of γ-radiation of 2.3 and 6 Mev, for water thicknesses of 1, 2, 4, 7, 10 , and 15 attenuation lengths. The savings in weight is calculated under the assumption that the buildup factor can be reduced to unity, and can be written in the form

$$W = \frac{\ln B(\mu_0 x, E)}{\mu_0 x},$$

where B is the buildup factor; $\mu_0 X$ - the number of attenuation lengths; E - the energy of γ-radiation.

The values thus obtained for W are given in Table 10.5.

TABLE 10.5

SAVINGS IN WEIGHT

$\mu_0 x$	E, Mev		
	2	3	6
1	0,550	0,458	0,308
2	0,433	0,358	0,263
4	0,335	0,290	0,212
7	0,260	0,225	0,169
10	0,217	0,186	0,143
15	0,170	0,148	0,116

The type of shieldings discussed above (Ref. 54) are called scattering shieldings, in contrast to present-day shieldings which are called absorbing shieldings. It is characteristic that a scattering shielding does not represent a monolith which is adjacent to the source, but is distributed by sections in the space between the source and the shielded region. The progressiveness of the scattering shielding is illustrated quite clearly in this work (Ref. 54), but specific examples deserve mention. First of all, for a single layer and ring-like shielding a considerable increase in weight is required, if the shielded region is increased. In practice, the diameter of the cabin must exceed the reactor dimensions by several factors. The savings in weight can then be more correctly determined as /334

$$\overset{*}{W} = \frac{\ln B(\mu_0 x)}{\mu_0 x + \ln B(\mu_0 x)},$$

which gives, for example, a savings of only 0.23, instead of 0.3.

In spite of these defects, the basic principles underlying the scattering shielding are valid (Ref. 54): 1) the scattering shielding must have a form, such that the outflow of direct radiation into the surrounding space can occur without a decrease in the effective thickness in the direction of the shielded region; 2) the shielding form must provide a maximum loss of scattered radiation into surrounding space; 3) the shielding material must lead to as much isotropic radiation scattering as possible during each interaction. A shielding made of stratified discs was also discussed in another work (Ref. 55), which indicates the interest which prevails at the present time in a scattering type of shielding.

The requirements imposed on a scattering shielding inevitably direct attention to a shielding which has a different form than that divided into individual layers. Let us examine the effect of a flat shielding, placed obliquely between a flat source and a

flat detector of comparable dimensions, as is shown in Figure 10.13.

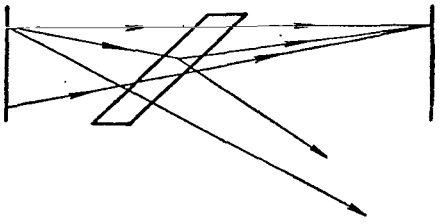

Figure 10.13

Scattering Properties of an Oblique Barrier

The anisotropic nature of the shielding properties presented by an oblique barrier is fully apparent. This must lead to field nonuniformity both of primary and of scattered radiation in the detection region, while the radiation intensity is smallest at the point which is closest to the shielding. At the present time, it /335
is difficult to calculate the effect under consideration. In the literature, there are data on an increase in the total intensity of scattered γ-radiation behind the barrier for large angles of inclination (Ref. 56 - 58), and on the simultaneous softening of the spectrum. The same picture is observed for oblique incidence of neutrons on the barrier shielding (Ref. 59).

However, the spectral - angular characteristics of scattered radiation are unknown behind an oblique barrier, which are necessary in order to calculate the radiation fields in the region of limited dimensions.

All of the information presented above regarding the penetration of radiation through an oblique shielding points to the expediency of extending similar geometry to a shielding for a cosmic nuclear-power device. Under conditions of axial symmetry, a conical layer which is turned with the apex toward the shielded region represents the analog of an oblique shielding. It is very apparent that if the sides of the conical layer have a constant thickness and if the generatrix is a straight line, then the intensity of direct radiation must increase as one moves away from the axis in the shielded region. However, in order to calculate the intensity correctly of only direct radiation, it is necessary to take into account the real form of the source, the dimensions of the source and of the shielded region, and their mutual location.

Thus, a study of the shielding properties presented by an axial analog of an oblique barrier - of a conical layer turned with

the apex toward the shielded region, represents one variation of the attempts to utilize the scattering properties of a shade shielding in space.

It can be stated that the problem of optimizing the form of a scattering shielding is inseparably connected to the problem of optimizing it only with respect to direct radiation (Ref. 46). In this work, the author discovered a form for the outer shielding surface adjacent to the linear source, so as to produce a minimum weight for a given dose at the shielded point. The illustration given by the author for applying this variational method to shielding problems does not correspond to any practical problem. In another work (Ref. 60), a solution was presented for solving the problem of an optimum ratio between the thickness of a neutron and γ-shielding and a point source, for a shielding form which had been selected previously (see Figure 10.10). If a variational method is applied in the first work, a conditional extremum for the function of two variables is presented in the second work.

The problem of determining an optimum thickness, with respect to different simultaneous directions, for a reactor shielding and for a shade shielding, which protects the cabin from direct reactor radiation and from radiation scattered in air, has been solved in other works (Ref. 61, 62). In similar problems, the equation resulting from the variational method for determining the conditional extremum has not been solved with respect to the desired function, as was done by the author of the work (Ref. 46), due to the incorrectness of the area element. Therefore, the shielding was selected in a multistage form. However, the solution /336
of a system of linear equations, which arise during the search for the conditional extremum of the function of several variables, is difficult due to the large number of these equations which equals the number of stages into which the shielding is divided. Calculations (Ref. 61) have been performed on an electronic computer using the method of quickest descent (the gradient method).

It is apparent that the optimum shielding of a point from an extended source must adjoin this point, and the shielding of the cabin from a point source must adjoin the source. In actuality, the source and the shielded region have finite dimensions; therefore, one must search for an optimum form, assuming any arrangement of its surfaces. If it is possible to calculate the intensity of direct radiation behind a shielding having any form, for any point in the shielded region, this is difficult to do for scattered radiation. However, the nonuniformity of the dosage field in the shielded region is fully apparent in a real case.

When the shielding form is optimized with respect to direct and scattered radiation, nonuniformity of the dosage field in the

shielded region must be assumed. The mean dose with respect to the shielded region or any cross-section of it must be used as a criterion, and it is possible to take the average of the probability for man to stay at different points in this region. An additional condition which limits the maximum value of the radiation level is also necessary.

The determination of an optimum form for a shade shielding encompasses two factors. First, it is necessary to calculate the dose at different points in a shielded region behind the shade shielding having any axial form, taking into account both primary and scattered neutrons and γ-radiation, as well as captured γ-quanta. Secondly, the chosen mathematical method must make it possible to determine the optimum form as rapidly and as accurately as possible. Depending on the methods for solving the first problem, different methods are employed to perform the second stage. As a whole, the problem can be solved only by expanding the existing experimental data and computational methods for the penetration of radiation through a shielding having finite dimensions.

10.8. Arrangement of a Radiation Shielding for Space Vehicles

The general physical and technical principles for the design of a compact shielding must underlie the arrangement of a radiation shielding on space vehicles. The arrangement selection depends to a significant extent on the type and purpose of the space vehicle, and is closely related to the arrangement of the entire device as a whole - i.e., it is part of the overall design problem. The general weight characteristics depend on the successful solution of this problem, since the weight of the radiation shielding comprises a significant portion of the total vehicle weight. We must point out that there is a significant difference in the shielding problem between space vehicles having small and large thrust (Ref. 63). For this reason, the diagrams for the radiation shielding arrangement can be divided into two basic types, depending on the purpose of the nuclear reactor: the nuclear reactor serves to heat the working substance which emanates outside through a nozzle (system with large thrust), and a nuclear reactor which represents part of the nuclear-power device. The purpose of this device is to produce electric energy, which can be used for operating the ion or plasma engine (system with small thrust), or as an additional fuel source. Let us examine each of the two types of radiation shielding arrangement in their general outline.

The following are the most characteristic features of an arrangement of the first type (Ref. 64). The shielding design takes the fact into consideration that the crew undergoes brief irradiation of high intensity. A tank (or several tanks) with the working substance - for which hydrogen or ammonia are usually

used - is placed between the reactor and the shielded cabin. As a rule, the reactor operates on thermal neutrons, and has relatively large dimensions. The shielding is divided up - i.e., part of the shielding is located between the reactor and the tank containing the working substance, and the other part of the shielding is located around the inhabited portion of the cabin which is used as a radiation shelter (Figure 10.14) (Ref. 64). The crew stays in this shelter when the reactor is in operation, when the radiation zones of the earth are crossed, or during intense solar flares. The shade shielding around the reactor, which absorbs only part of the primary radiation from the reactor, prevents the tank with the working substance from overheating due to radiation (otherwise, significant evaporation of the working substance can occur). At the same time, this shielding - if it includes a boron-containing component which absorbs thermal neutrons - eliminates /338
the possibility of the reaction (n, γ) in the nitrogen of air. When this shielding is being designed, it is necessary to determine the optimum ratio between its weight and the weight of the evaporated fuel, in order to reduce the total weight to a minimum. The shielding for the radiation shelter lowers to a permissible level the reactor radiation which falls on the inhabited section as a result of scattering in the earth's atmosphere (or other planets) during corresponding portions of the flight, radiation which is scattered from the nozzle rocket, and also that portion of direct

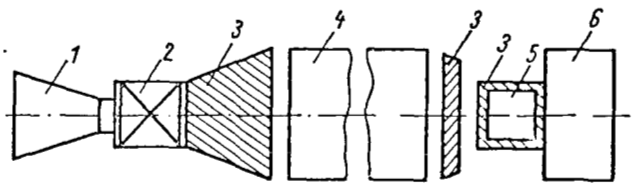

Figure 10.14

Diagram of a Nuclear Rocket with Direct Ejection of the Working Substance.

1- Nozzle; 2- Reactor; 3- Shielding; 4- Tank with Working Substance; 5- Radiation Shelter; 6- Cabin for Crew.

reactor radiation which penetrates the shade shielding and the tank containing the working substance. The side of the shielding which is adjacent to the tank containing the working substance must also contain a hydrogen-containing component, in order to capture the thermal neutrons emanating from the tank with the working substance,

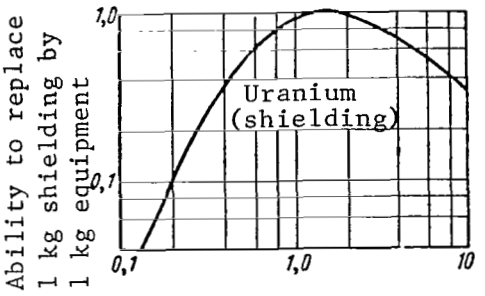

Figure 10.15

Ability to Replace Shielding Material by Equipment

in which rapid neutrons are slowed down to thermal energies. The tank with the working substance absorbs a considerable portion of primary radiation from the reactor, and the requirements for the shielding protecting the cabin from direct radiation must take into account the fuel consumption during the flight. Attention must be given to the fact that the period of time when a shielding is necessary from direct radiation does not coincide with the period when shielding from scattered radiation is necessary. For this reason, it is sometimes advantageous to use liquids (for example, mercury) for shielding from scattered radiation; when necessary, these liquids can be transferred over to the location of the shielding from direct radiation. If this is not feasible, the heaviest materials - for example, uranium-238 - can be used instead of a liquid shielding. The replacement of mercury by uranium decreases the shielding weight by approximately 30% (Ref.65). Shielding from scattered radiation can also be used for shielding from protons from solar flares and radiation from the radiation zones of the earth.

The weight of the cabin shielding can be reduced by utilizing supplies and equipment for the inhabited section as a shielding (Figure 10.15) (Ref. 64). Several works (Ref. 64 - 68) have discussed specific plans for spacecrafts of this type and have presented data on the results derived from designing the shielding and its arrangement. Thus, for example, in work (Ref. 66) the flight for a spacecraft to Mars is designed, and a plan is presented for the inhabited cabin to contain a crew of seven men. The work also presents the results derived from designing a shielding

thickness as a function of the reactor output for different permissible radiation doses and for different distances between the reactor and the inhabited cabin (Figure 10.16).

Another work (Ref. 67) also presents the design for a spacecraft /339
flying to Mars, and also gives the volumetric composition of the shade shielding (uranium 30%, lithium hydride 55%, steel 8%, free volume 7%) which is located around a reactor having a thermal output of 2000 Mw (distance between reactor and cabin is 60 m). In the design for a flight to the moon (Ref. 64), the primary shielding is located between the tank containing the working substance (NH_3) and the cabin, and consists of layers of lead (20 cm), polyethylene (30 cm) and boral (2.5 cm). The reactor output is 3310 Mw, the distance between the active zone and the shielding is 19 m, the length and diameter of the tank are 16.5 and 2.4 m, respectively.

The problems entailed in designing a radiation shielding on a spacecraft which is to go to Mars are discussed in another work (Ref. 65). This work presents the results derived from calculating the intensity of direct and scattered radiation, and also the weight of a shielding made of mercury around a cabin for these types of radiation, for different reactor output levels, and for different distances between the reactor and the cabin. The shade shielding around the reactor is selected on the basis of the optimum ratio between the weight of this shielding (uranium-238) and the weight of the working substance (hydrogen), in order to protect the working substance from evaporation. Figures 10.17 - 10.21 present these data, which were obtained for a cabin having a dimension of 0.915x1.83x2.13 m, and the diagram of the cabin is shown in Figure 10.22. In these calculations, it was assumed that the atmosphere on Mars is equivalent the earth's atmosphere, which somewhat exaggerates the dose of radiation scattered in the atmosphere of Mars. The graphic dependences of the weight for the radiation shelter shielding are given individually for direct and scattered radiation, for different distances between the cabin and the reactor whose output is $2.1 \cdot 10^4$ Mw (Figure 10.23). These data were compiled for a specific operational time of the reactor, corresponding to the flight to Mars and back (with landing and without landing). It was assumed that, as required, the shielding from scattered radiation can be utilized for attenuating primary radiation, and that the total lift-off weight of the shielding equals the weight of the shielding from scattered radiation plus the optimum total weight of the shade shielding (around the reactor) and the liquid hydrogen. These dependences clearly show the shielding designer the manner in /340
which the selection of the permissible doses influences the shielding weight, and vice versa, for a specific flight problem. Table 10.6 presents several such examples, and an investigation is made of the case in which - after the earth's atmosphere is crossed - part of the shielding from scattered radiation is jettisoned, and the other part is utilized for shielding from direct radiation.

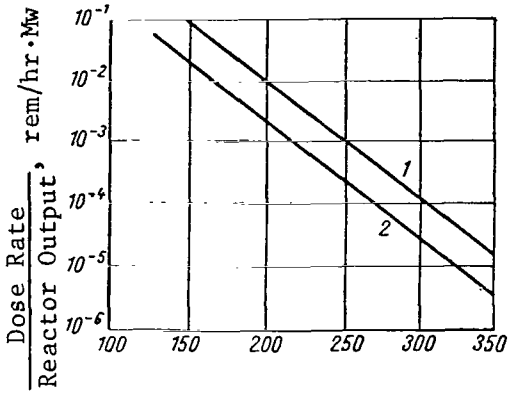

/339

Shielding Thickness, g/cm^2

Figure 10.16

Shielding from Nuclear Engine Radiation (Length of Tank with Working Substance 30.5 m) at a Distance of 30.5 m from the Reactor (1); 61 m (2).

The characteristics of space vehicles with a nuclear power device on board, which must be taken into account when the radiation shielding is arranged, are as follows: 1) the presence of a condenser-radiator and a heat exchanger (in a two-circuit arrangement) in the thermal exchange circuit of the reactor: 2) the possibility of scattering reactor radiation only from construction elements and close to the outer surface of the shade shielding, and not in air, since the reactor begins to operate only outside the earth's atmosphere after the vehicle is placed in the required orbit. In this connection, shielding from reactor radiation must be of only the shade type and must be located primarily close to the reactor; a shielding from cosmic radiation must be primarily arranged around the cabin; 3) the presence of a counter-activation shielding for protecting the second circuit from excessive activation. Part of the shade shielding from direct radiation can be used as counter-activation shielding; 4) utilization of the reactor for rapid or intermediate neutrons with maximum power density; 5) subjection of the crew to long chronic irradiation.

/340

/346

The characteristics cited above lead to the conclusion that the radial type of arrangement is most efficient in this case - i.e., when the shielded cabin, the condenser-radiator, the heat exchanger, the tank with the working substance, the tubing, and also all possible auxiliary thermal-exchange and electro-mechanical equipment, etc. are located in the "shade" created by the shielding (Ref. 69). The results derived from calculating the thickness of

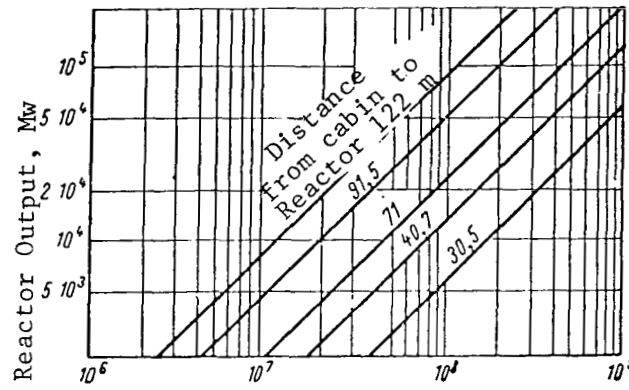

/240

Dose Rate, rem/hour

Figure 10.17

Dose Rate from Direct Radiation in an Unshielded Cabin in a Spacecraft during Reactor Operation

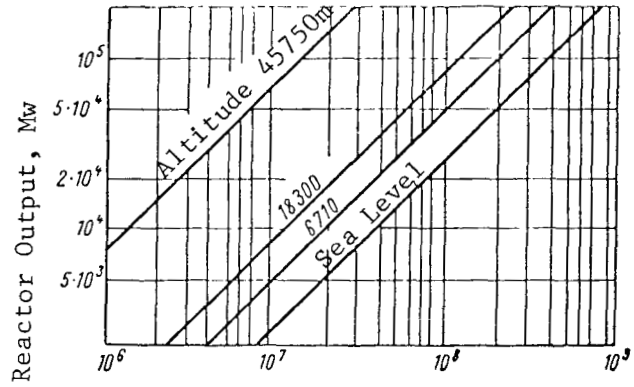

Dose Rate, rem/hour

Figure 10.18

Dose Rate from Scattered Radiation in Unshielded Cabin Located 30.5 m from the Reactor

a shielding made of lithium hydride and uranium-238, as a function of the reactor thermal output and the permissible dose rate for a given distance between the reactor and the shielded object, can be utilized in designing this type of arrangement. These data are given in Figure 10.24 .

/246

By way of an example for the second type of arrangement, we shall present various variations of the radiation shielding for reactors of the SNAP type (Ref. 70). The following reference data

TABLE 10.6

EXAMPLES OF FLIGHT FROM EARTH TO MARS AND BACK

Purpose of Expedition	Distance from reactor to cabin, m	Reactor operation in atmosphere		Flight from Earth to Mars				Flight from Mars to Earth				Total Dose during Flight, rem
				Scattered Radiation		Direct Radiation		Scattered Radiation		Direct Radiation		
		Earth	Mars	Dose rem	Weight of Shielding made of Hg, kg	Dose rem	Weight of Shielding made of Hg, kg	Dose rem	Weight of Shielding made of Hg, kg	Dose rem	Weight of Shielding made of Hg, kg	
Earth - Orbit Mars - Earth	30.5	Yes	No	5.2	11,300	small	0	0	0	1.3	4536	6.5
	30.5	Yes	No	71	6,800	small	0	0	0	1.3	4536	72
	91.5	Yes	No	1.8	11,300	small	0	0	0	0.15	4536	2.0
	91.5	Yes	No	110	4,536	small	0	0	0	0.15	4536	110
Earth - Land on Mars - Earth	30.5	Yes	Yes	5.2	11,300	small	0	5.2	11,300	1.3	4536	12
	30.5	Yes	Yes	5.2	11,300	small	0	71	6,800	small	6800	76
	91.5	Yes	Yes	1.8	11,300	small	0	24	6,800	small	6800	26
	91.5	Yes	Yes	6.2	9,072	small	0	110	4,536	0.15	4536	117

Reactor Output - 21,000 Mw; Specific Impulse - 865 seconds, Fuel - H_2

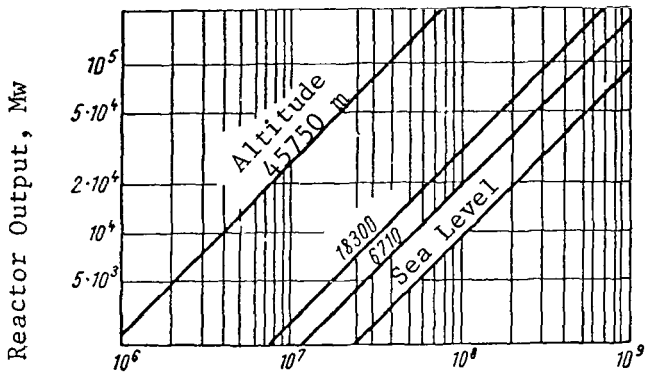

Figure 10.19

Dose Rate from Scattered Radiation in Unshielded Cabin Located 61 m from the Reactor

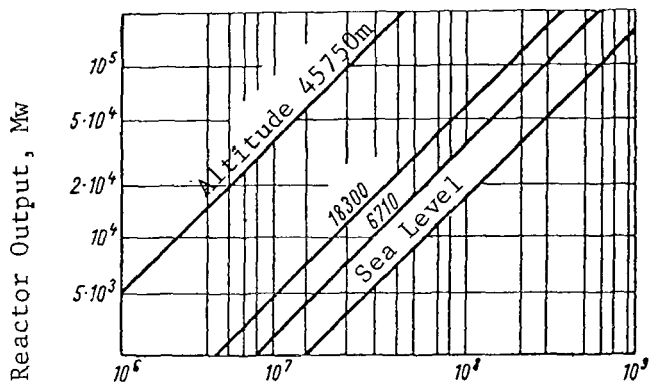

Figure 10.20

Dose Rate from Scattered Radiation in Unshielded Cabin Located 91.5 m from Reactor.

were chosen for calculating the thickness and weight of the shielding:/346 reactor thermal output 250 kw; reactor operational time 1 year; dimensions of reactor having cylindrical form: H = 15.5 m and diameter D = 15.5 m; payload consists of instruments using transistors for which the integral dose of 10^{12} rapid neutrons per 1 cm^2 and 10^7 roentgen/cm^2 was assumed to be permissible - which corresponds (during an operational time of 1 year) to streams of $3 \cdot 10^4$ rapid neutrons per 1 $cm^2 \cdot sec$ and 10^3 roentgen/$cm^2 \cdot hour$, for γ-radiation -; the shielding is made of lithium hydride with a density of

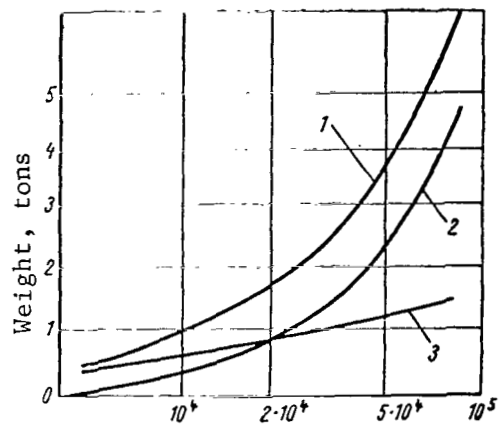

Figure 10.21

Optimum Weight of Shade Shielding:
1- Total Weight; 2- Shade Shielding made of Uranium-238;
3- Working Substance (Hydrogen).

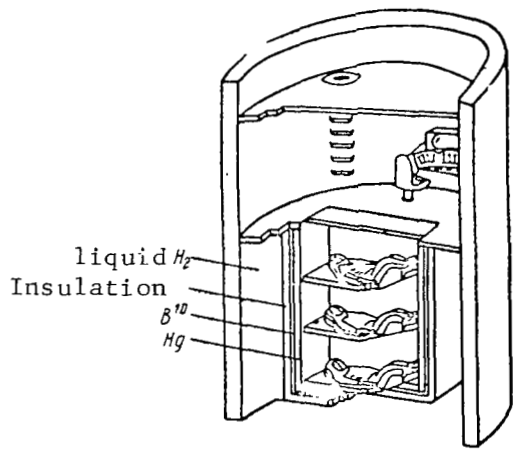

Figure 10.22

Diagram of Cabin in Spacecraft.

γ = 0.9 g/cm^3; in calculations of the scattered radiation, it is assumed that an aluminum radiator has an effective thickness of 0.7 - 1 mm; it is assumed that the doses from direct and scattered radiation are equal, and that the radiator surface equals approximately 37 m^2; scattering from air is not taken into account, since the density of air at high altitudes is small. /347

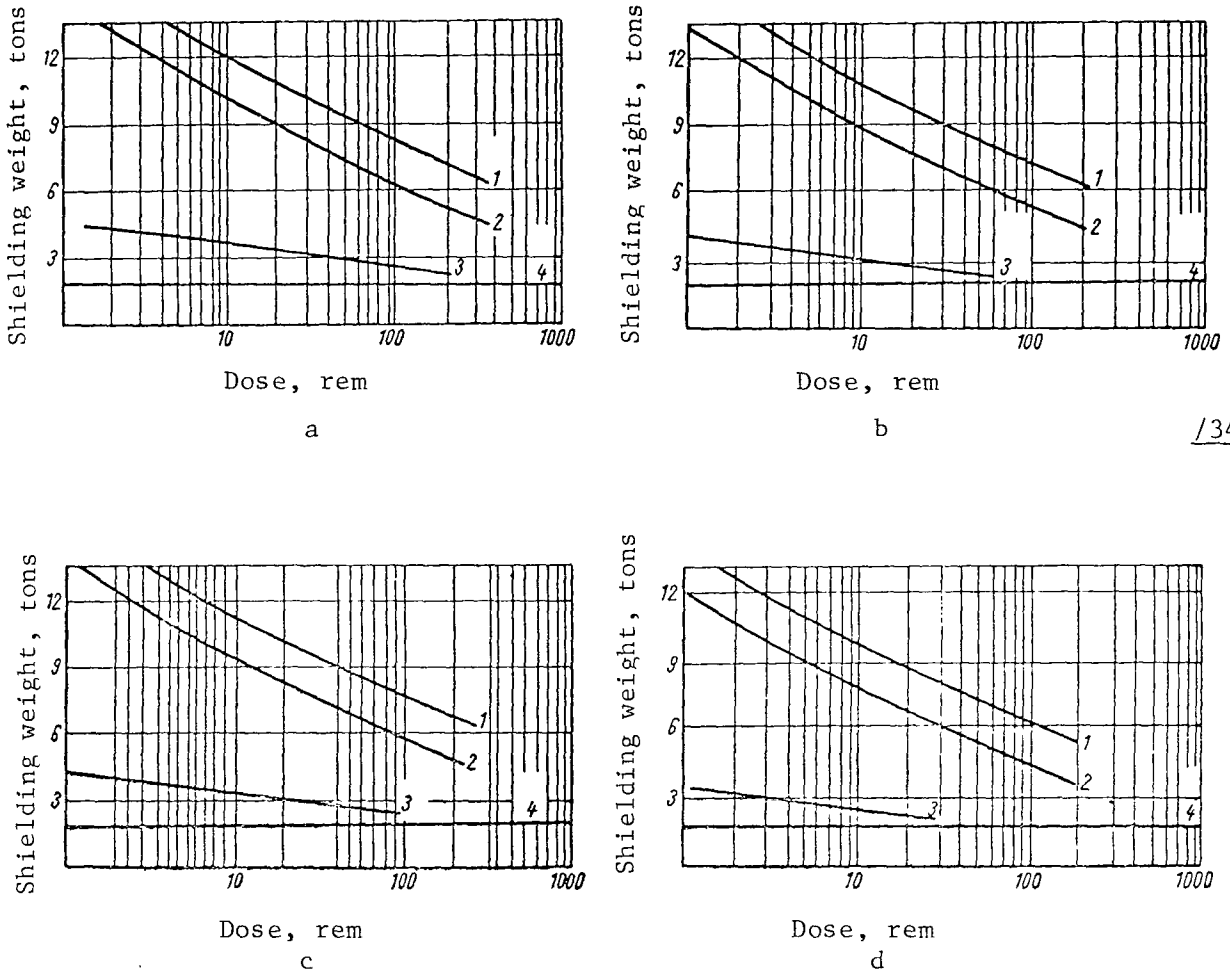

/344-5

Figure 10.23
Integral Doses from Scattered and Direct Radiation for Different Shielding Weights:

a- Distance between Reactors and Cabins 30.5 m, Reactor Output 21,000 Mw; b- Distance between Reactor and Cabin 41.5 m; c- Distance between Cabin and Reactor 60.1 m; d- Distance between Cabin and Reactor 91.m; 1- Total Optimum Weight of Shielding made of U^{238} + Hg and Fuel of H_2; 2- Shielding for a Cabin from Scattered Radiation (Hg); 3- Cabin Shielding from Direct Radiation Hg; 4- Optimum Weight of Shade Shielding made of U^{238} and Fuel of H_2.

Nine variations of an arrangement for a radiation shielding for /347
the reactor discussed above are briefly presented below, and in all cases the integral dose of γ-radiation behind the shielding is less than 10^7 roentgens, so that the entire shielding thickness is determined by rapid neutrons.

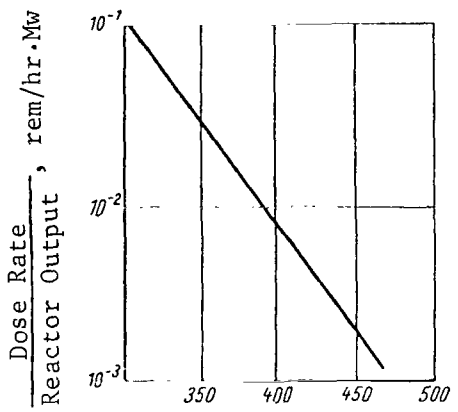

/346

Figure 10.24

Dose Rate as a Function of Shielding Thickness; Distance from Reactor to Point under Consideration 1.5 m; Shielding Material LiH + U^{238}.

/347

Variation I (Figure 10.25, a). The reactor is located between the payload and the accelerator of the last stage, and the entire shielding is located in front of the payload. The shielding weight equals approximately 5000 kg.

Variation II (see Figure 10.25, b). The reactor is located between the payload, which is placed in the nose of the rocket, and the accelerator of the last stage. The shielding weight is 1680 kg. It is characteristic that shielding from scattered radiation weighs more (1290 kg) than does shielding from direct radiation (390 kg).

Variation III (see Figure 10.25, c) is similar to variation II, with the exception that the radiator is located under the reactor. The weight of shielding from direct radiation does not change in this case, while the weight of shielding from scattered radiation is reduced to 660 kg. One disadvantage of this arrangement is the necessity of ejecting the outer casing between the payload and the radiator, when the system is placed in orbit, in order to prevent scattering of neutrons. In addition, the frame which supports the payload must be located in the shade of the shielding from direct radiation,which creates additional construction difficulties.

Variation IV (see Figure 10.25, d). The radiator is stored, which decreases the shielding weight, but leads to additional construction difficulties.

Variation V (see Figure 10.25, e). After the system is placed in orbit, the reactor and the radiator are transferred 30 m behind, and due to this the shielding weight decreases to 288 kg (without taking into account the weight of related mechanisms). The reliability of the system decreases in this case.

Variation VI (see Figure 10.25, f). After the system is placed in orbit, the reactor and the shielding are shifted by 2.7 m. The weight of the shielding from direct radiation decreases to 210 kg. However, the weight of the shielding from radiation scattered from the cylindrical radiator increases to 265 kg. If the radiator is located along the dotted line, it is then possible to decrease the total shielding weight to the weight of shielding from direct radiation.

Variation VII (Figure 10.26). A single-ribbed radiator is used; shielding weight is 251 kg.

Variation VIII (Figure 10.27). This is similar to Variation VII, but the radiator is three-ribbed.

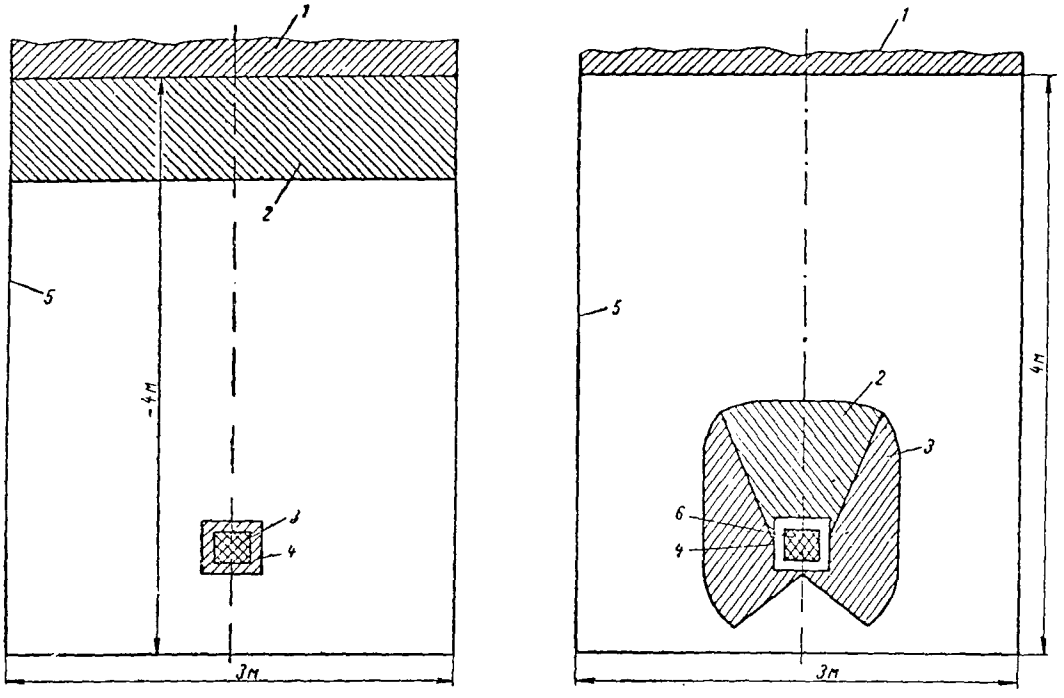

a Figure 10.25 b

(continued on next page)

Diagrams of Shielding Arrangement for a Reactor with Cylindrical Radiator:

a- Total Shielding Weight 5 Tons: 1- Payload; 2- Shielding; 3- Reactor; 4- Reflector; 5- Cylindrical Radiator; b- Total Shielding Weight about 1.7 tons: 1- Payload; 2- Shielding from Direct Radiation about 1.3 Tons; 5- Radiator; 6- Reactor;

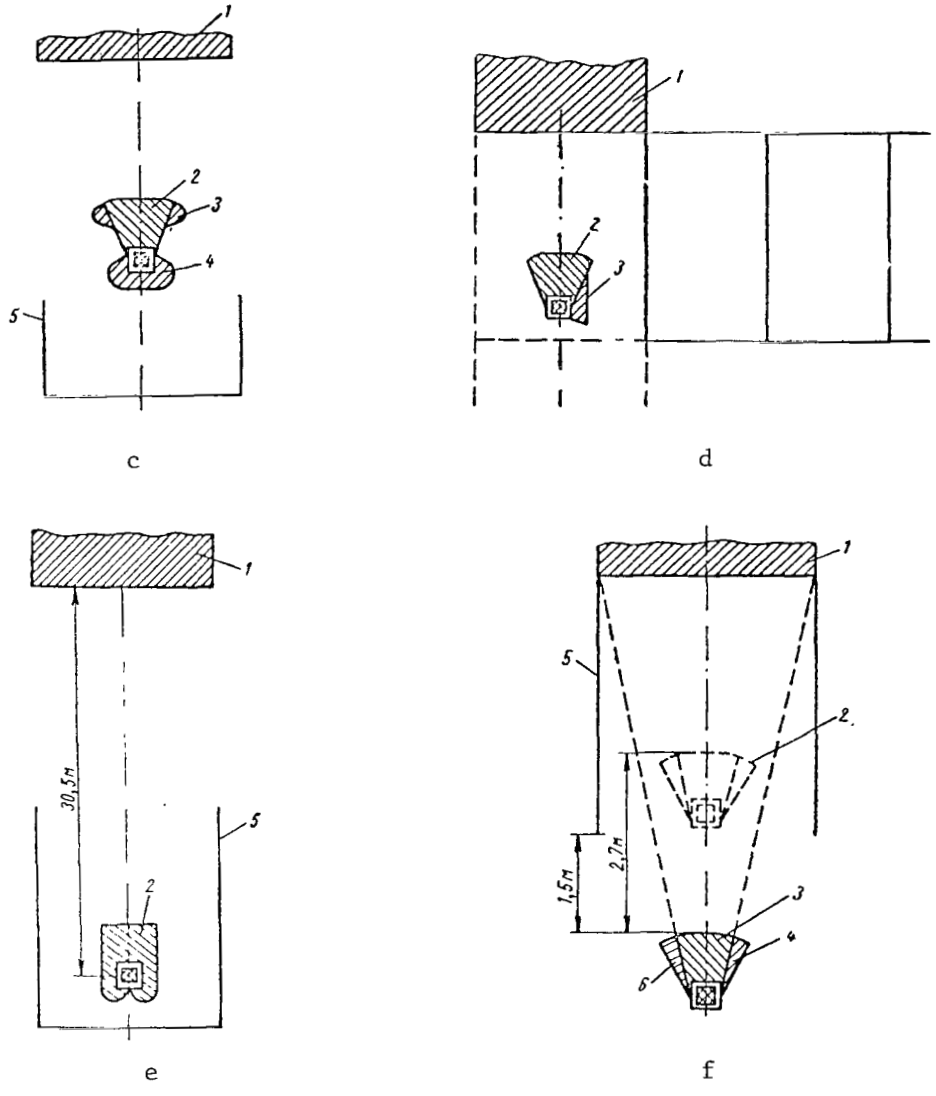

Figure 10.25
(Continuation)

c- Total Shielding Weight 1.062 Tons: 1- Payload; 2- Shielding from Direct Radiation 0.4 Tons; 3- Shielding from Scattered Radiation 0.422 Tons; 4- Shielding from Scattered Radiation 0.24 Tons; 5- Radiator; d- Total Shielding Weight 0.474 Tons: 1- Payload; 2- Shielding from Direct Radiation; 3- Shielding from Scattered Radiation 0.074 Tons; e- Total Shielding Weight 0.288 Tons: 1- Payload; 2- Shielding; 5- Radiator; f- Total Shielding Weight 0.475 Tons: 1- Payload; 2- Initial Location of Reactor and Shielding; 3- Shielding from Direct Radiation 0.21 Tons; 4- Shielding from Scattered Radiation 0.265 Tons; 5- Radiator; 6- Position of Reactor and Shielding in Orbit.

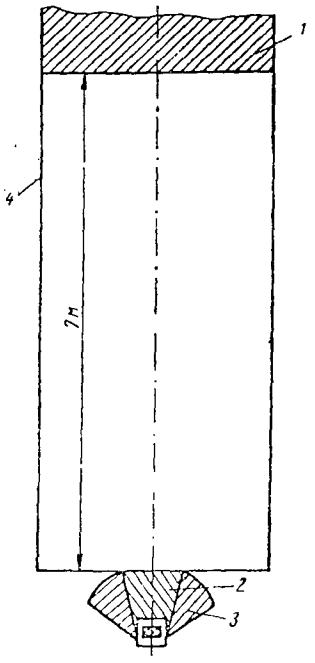

Figure 10.26

Diagram of Shielding Arrangement for Reactor with Single-Ribbed Radiator:

1- Payload; 2- Shielding from Direct Radiation 0.178 Tons; 3- Shielding from Scattered Radiation 0.073 Tons; 4- Single-Ribbed Radiator.

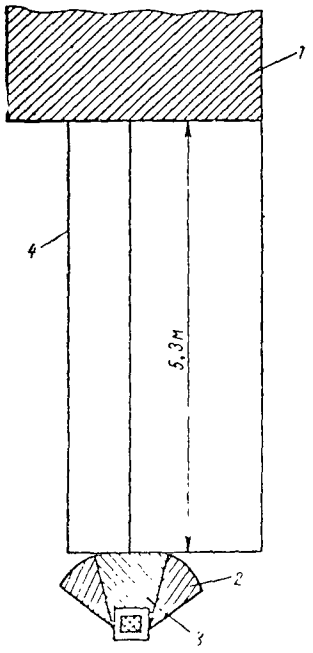

/350

Figure 10.27

Diagram of Shielding Arrangement for Reactor with Three-Ribbed Radiator; Total Shielding Weight 0.41 Tons:

1- Payload; 2- Shielding from Scattered Radiation 0.133 Tons; 3- Shielding from Direct Radiation 0.227 Tons; 4- Three-Ribbed Radiator.

Variation IX (Figure 10.28). The reactor is located in the nose cone, and the shielding is underneath it. A shielding from scattered radiation is not necessary; total shielding weight is 204 kg. The radiator has the form of a frustum of a cone, which has a small scattering surface and which leads to great savings in weight. /351

The weight of the radiation shielding for the given variations is approximate, and can be utilized to compare the diagrams of these arrangements. We would like to point out two factors which must necessarily be taken into account when choosing the radiation shielding arrangement independently of the purpose of the entire device as

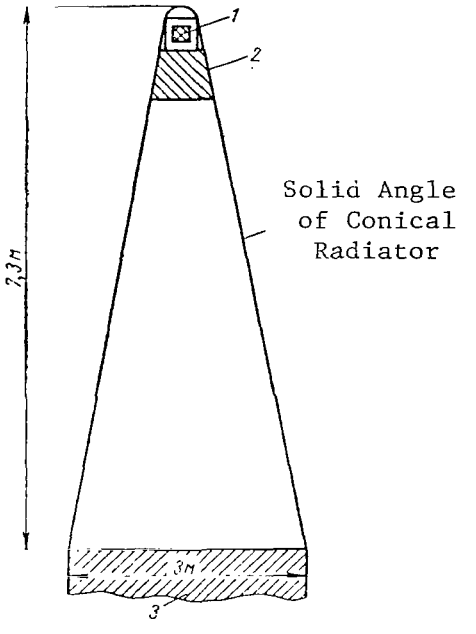

/350

Figure 10.28

Diagram of Shielding Arrangement for Reactor with Conical Radiator:

1- Reactor; 2- Shielding from Direct Radiation 0.2 Tons; 3- Payload.

a whole. First, the electromechanical equipment which is located on the outer side of the reactor, and also all of the scientific instruments, radio engineering, and telemetry devices, etc. will undergo radiation damage, which must be taken into consideration when selecting the shielding arrangement. Each type of equipment and instrument tolerates a specific integral, threshold dose of radiation without changing the mechanical and thermo-physical properties, regimes, and operational performance. Another work (Ref. 2) presents some data on this problem. Consequently, the arrangement of the instruments and equipment must strictly correspond to the spatial distribution of radiation intensity beyond the reactor limits, taking into account the irradiation time. A great many studies have been devoted to the problem of the influence of irradiation on the material and instruments; a general picture of the behavior of certain materials and equipment in radiation fields is presented in the work (Ref. 71). Secondly, it should be noted that the slits, canals, cavities, and nonuniformities in the

shielding must be arranged in such a way that the leaking radiation through them is reduced to a minimum, while not increasing the amount of shielding material to a significant extent. Recommendations on the design for radiation penetration through different nonuniformities in a shielding are given in the works (Ref. 2, 3, 72-75).

10.9. Radiation Safety During Servicing and Repair of Nuclear Devices

The servicing and repair of nuclear devices is a very difficult problem under spaceflight conditions. The requirement for minimum weight leads to the necessity of a shielding from reactor radiation for very limited sections and volumes of the space vehicle, if only to keep the equipment and instruments from undergoing radiation damage and to permit the normal activity of the crew. For this reason, during the active sections of the flight when the nuclear reactor is in operation, which in this case is partly an engine and not an additional source of power, even any brief repair work on inadequately-shielded sections is permitted in unusual cases, and in some poorly-shielded locations it is simply impossible /352
for man to remain for even a very short time. This problem can be frequently solved by the use of various manipulators, which make it possible to perform certain operations at a distance. Consequently, prophylactic and repair work of a different type must be carried out during the passive portions of the flight, when the reactor is shut off. But even in this case access to the reactor and to individual units is restricted due to the residual γ-activity of fission products and of γ-radiation from activated materials which are effected by a neutron stream. Individual construction elements which have a high residual activity, a coolant which passes through the active zone of the reactor, etc., belong here. Section 10.1 listed the intensity of residual γ-activity of fission products as a function of the reactor operational time and the time lag after the reactor is shut off. If these data are utilized, it is possible to calculate the time which a man may remain around the reactor for a specific permissible irradiation dose.

Utilizing the law of radioactive decay, one can readily calculate (Ref. 2, 3) the residual activity of construction materials and coolants. In order to calculate the activity, it is necessary to know the stream of neutrons, the chemical composition of the material, the activation cross-sections, and the type of decay for the different elements (Ref. 3, 76). When calculating the activity, one should keep the fact in mind that one can frequently determine the activity, not of the material itself, but of the admixtures contained in it. Thus, for example, immediately after irradiation the activity of stainless steel (Ref. 3) was determined by the

manganese which made up 1% of its composition. In spite of the fact that the activation cross-sections increase with a decrease in the neutron energy, when the activation is calculated it is impossible to disregard the very rapid neutrons, which can produce reactions with the emission of charged particles, forming long-lived radioactive isotopes(Ref. 3). Thus, when irradiated by rapid neutrons, as a result of the (n, α)-reaction,aluminum is changed into a long-lived radioactive isotope sodium-24.

For practical calculations, it is advantageous to utilize a rapid method of estimating induced activity for 100 nuclei (Ref. 77), nomograms of radioactivity caused by irradiation (Ref. 78, 79), and also an examination of radiation of plates and cylinders activated by neutrons (Ref. 80).

The possibility of performing repair-prophylactic work is frequently determined by the induced activity, not of construction elements, but by the activity of the coolant surrounding the reactor. The magnitude of this residual activity can make the access to the thermal exchange equipment difficult to a considerable extent. Apart from the intensity of irradiation by neutrons, the activity of the coolant can be caused by solution and erosion of the active material which is adjacent to the coolant, by fission products falling into the coolant, and by several other factors. The nature /353
of the coolant determines which factor makes the greatest contribution. The work (Ref. 3) presents data which are necessary to calculate the induced activity of certain pure coolants. In another work (Ref. 81), an examination is made of the connection between the specific activity of the liquid and the dose rate on the surface of cylindrical tanks or tubes. If there is a second circuit in the thermal exchange circuit, its activation can be reduced to a permissible magnitude by placing a counter-activation shielding between the reactor and the heat exchanger (Ref. 82). Apart from the heat exchanger, a counter-activation shielding can be provided for other individual units and sections which require prophylactic inspection or repair during the flight.

APPENDIX 1

/354

REMOVAL CROSS-SECTIONS FOR NEUTRONS OF A FISSION SPECTRUM

Substance	Density, g/cm^3	σ barn	Σ, cm^{-1}	Substance	Density g/cm^3	σ barn	Σ, cm^{-1}
Hydrogen	$8{,}987 \cdot 10^{-5}$	1,0	—	Paraffin $C_{30}H_{62}$	0,89	80,5	0,102
Lithium	0,53	1,01	0,046	Steel	7,8	1,98	0,167
Beryllium	1,8	1,07	1,128	Steel in Water	7.8	1,99	0,172
Boron	2,5	0,97	0,135	Monel Metal	8,51	—	0,176
Graphite	2,25	0,72	0,092	Boron Stainless Steel	7,0	-	0,154
Oxygen	$1{,}429 \cdot 10^{-3}$	0,92	—	Pb + 6.5% Sb	10,8	--	0,105
Fluorine	—	1,29	—	Pb + 2% Sb	11,4	--	0,115
Aluminum	2,702	1,31	0,079	Polyethylene	0,92	3,28	0,130
Chlorine	$3{,}24 \cdot 10^{-3}$	1,2	—	Polyethylene with Boron	1,01	3,0	0,130
Iron	7,86	1,98	0,168	Oil	0,82	3,25	0,114
Nickel	8,9	1,89	0,173	Sodium	0,97	1,77	0.045
Copper	8,92	2,04	1,173	Ammonia	0,771	4,07	0,111
Tungsten	19,3	2,51	0,158	Lithium borhydride	0,686	5,9	0,113
Lead	11,34	3,53	0,116	Lithium Hydride	0,82	2,01	0,125
Bismuth	9,8	3,49	0,098	Water	1,0	2,95	0,100
Uranium	18,9	3,6	0,17	Gasoline C_8H_{18}	0,71—0,73	24,5	0,093
Boron Oxide B_2O_3	1,85	4,3	0,066	Rubber $(C_5H_8)_n$	0,92	12,1	0,098
Boron Carbide	2,5	5,1	0,141	Heavy Water	1,1076	2,76	0.0916
Oil CH_2	0,9	2,84	0,111	Steel + 1.57% B	7,75	1,98	0,166

APPENDIX 2

MASS ATTENUATION COEFFICIENTS OF γ-RAYS
μ/ρ, cm^2/g

/355

Substance	Energy of γ-radiation, Mev										
	0.1	0.5	1	1.5	2	3	4	5	6	8	10.0
H	0.295	0.173	0.126	0.103	0.0876	0.0691	0.0579	0.0502	0.0446	0.0371	0.0321
Be	0.132	0.0773	0.0565	0.0459	0.0394	0.0313	0.0266	0.0234	0.0211	0.0180	0.0161
C	0.149	0.087	0.0636	0.0518	0.0444	0.0356	0.0304	0.0270	0.0245	0.0213	0.0194
N	0.150	0.0869	0.0636	0.0517	0.0445	0.0357	0.0306	0.0273	0.0249	0.0218	0.0200
O	0.151	0.087	0.0636	0.0518	0.0445	0.0359	0.0309	0.0276	0.0254	0.0224	0.0206
Na	0.151	0.0833	0.0608	0.0496	0.0427	0.0348	0.0303	0.0274	0.0254	0.0229	0.0215
Mg	0.160	0.086	0.0627	0.0512	0.0442	0.0360	0.0315	0.0286	0.0266	0.0242	0.0228
Al	0.161	0.084	0.0614	0.0500	0.0432	0.0353	0.0310	0.0282	0.0264	0.0241	0.0229
Si	0.172	0.0869	0.0635	0.0517	0.0447	0.0367	0.0323	0.0296	0.0277	0.0254	0.0243
P	0.174	0.0846	0.0617	0.0502	0.0436	0.0358	0.0316	0.0290	0.0273	0.0252	0.0242
S	0.188	0.0874	0.0635	0.0519	0.0448	0.0371	0.0328	0.0302	0.0284	0.0266	0.0255
Ar	0.188	0.0790	0.0573	0.0468	0.0107	0.0338	0.0301	0.0279	0.0266	0.0248	0.0241
K	0.215	0.0852	0.0618	0.0505	0.0438	0.0365	0.0327	0.0305	0.0289	0.0274	0.0267
Ca	0.238	0.0876	0.0634	0.0518	0.0451	0.0376	0.0338	0.0316	0.0302	0.0285	0.0280
Fe	0.344	0.0828	0.0595	0.0425	0.0424	0.0361	0.0330	0.0313	0.0304	0.0295	0.0294
Cu	0.427	0.0820	0.0585	0.0476	0.0418	0.0357	0.0330	0.0316	0.0309	0.0303	0.0305
Mo	1.03	0.0851	0.0575	0 0467	0.0414	0.0365	0.0349	0.0344	0.0344	0.0349	0.0359
Sn	1.59	0.0886	0.0563	0.0459	0.0408	0.0367	0.0355	0.0355	0.0358	0.0368	0.0383
I	1.83	0.0913	0.0571	0.0460	0.0409	0.0370	0.0360	0.0361	0.0365	0.0377	0.0394
W	4.21	0.125	0.0640	0.0492	0.0437	0.0405	0.0402	0.0409	0.0418	0.0438	0.0465
Pt	4.75	0.135	0.0659	0.0501	0.0449	0.0414	0.0411	0.0418	0.0427	0.0448	0.0477
Tl	5.16	0.143	0.0675	0.0508	0.0452	0.0420	0.0416	0.0423	0.0433	0.0454	0.0484
Pb	5.29	0.145	0.0684	0.0512	0.0457	0.0421	0.0420	0.0426	0.0436	0.0459	0.0489
U	1.06	0.176	0.0757	0.0548	0.0484	0.0445	0.0440	0.0446	0.0455	0.0479	0.0511
Air	0.151	0.0868	0.0655	0.0517	0.0445	0.0357	0.0307	0.0274	0.0250	0.0220	0.0202
H_2O	0.167	0.0966	0.0706	0.0575	0.0493	0.0396	0.0339	0.0301	0.0275	0.0240	0.0219
Live Tissue	0.163	0.0936	0.0683	0.0556	0.0478	0.0384	0.0329	0.0292	0.0267	0.0233	0.0212

APPENDIX 3

DOSAGE BUILDUP FACTOR FOR AN ISOTROPIC POINT SOURCE

Substance	E_0, Mev	$\mu_0 r$						
		1	2	4	7	10	15	20
Water	0.5	2.52	5.14	14.3	38.8	77.6	178	334
	1.0	2.13	3.71	7.68	16.2	27.1	50.4	82.2
	2.0	1.83	2.77	4.88	8.46	12.4	19.5	27.7
	3.0	1.69	2.42	3.91	6.23	8.63	12.8	17.0
	4.0	1.58	2.17	3.34	5.13	6.94	9.97	12.9
	6.0	1.46	1.91	2.76	3.99	5.18	7.09	8.85
	8.0	1.38	1.74	2.40	3.34	4.25	5.65	6.95
	10.0	1.33	1.63	2.19	2.97	3.72	4.90	5.98

Appendix 3 (continuation)

Substance	E_0 Mev	$\mu_0 r$						
		1	2	4	7	10	15	20
Aluminum	0.5	2.37	4.24	9.47	21.5	38.9	80.8	141
	1.0	2.02	3.31	6.57	13.1	21.2	37.9	58.5
	2.0	1.75	2.61	4.62	8.05	11.9	18.7	26.3
	3.0	1.64	2.32	3.78	6.14	8.65	13.0	17.7
	4.0	1.53	2.08	3.22	5.01	6.88	10.1	13.4
	6.0	1.42	1.85	2.70	4.06	5.49	7.97	10.4
	8.0	1.34	1.68	2.37	3.45	4.58	6.56	8.52
	10.0	1.28	1.55	2.12	3.01	3.96	5.63	7.32
Iron	0.5	1.98	3.09	5.98	11.7	19.2	35.4	55.6
	1.0	1.87	2.89	5.39	10.2	16.2	28.3	42.7
	2.0	1.76	2.43	4.13	7.25	10.9	17.6	25.1
	3.0	1.55	2.15	3.51	5.85	8.51	13.5	19.1
	4.0	1.45	1.94	3.03	4.91	7.11	11.2	15.0
	6.0	1.34	1.72	2.58	4.14	6.02	9.89	14.7
	8.0	1.27	1.56	2.23	3.49	5.07	8.50	13.0
	10.0	1.20	1.42	1.95	2.99	4.35	7.51	12.4
Tungsten	0.5	1.28	1.50	1.84	2.24	2.61	3.12	—
	1.0	1.44	1.83	2.57	3.62	4.64	6.25	(7.35)
	2.0	1.42	1.85	2.72	4.09	5.27	8.07	(10.6)
	3.0	1.36	1.74	2.59	4.00	5.92	9.65	14.1
	4.0	1.29	1.62	2.41	4.03	6.27	12.0	20.9
	6.0	1.20	1.43	2.07	3.60	6.29	15.7	36.3
	8.0	1.14	1.32	1.81	3.05	5.40	15.2	41.9
	10.0	1.11	1.25	1.64	2.62	4.65	14.0	39.3
Lead	0.5	1.24	1.42	1.69	2.00	2.27	2.65	(2.73)
	1.0	1.37	1.69	2.25	3.02	3.74	4.81	5.85
	2.0	1.39	1.76	2.51	3.66	4.84	6.87	9.00
	3.0	1.34	1.68	2.43	3.75	5.30	8.44	12.3
	4.0	1.27	1.56	2.25	3.61	5.41	9.80	16.3
	6.0	1.18	1.40	1.97	3.34	5.69	13.8	32.7
	8.0	1.14	1.30	1.74	2.89	5.07	14.1	44.6
	10.0	1.11	1.23	1.58	2.52	4.34	12.5	39.2
Uranium	0.5	1.17	1.30	1.48	1.67	1.85	2.08	—
	1.0	1.31	1.56	1.98	2.50	2.97	3.67	—
	2.0	1.33	1.64	2.23	3.09	3.95	5.35	(6.48)
	3.0	1.29	1.58	2.21	3.27	4.51	6.97	9.31
	4.0	1.24	1.50	2.09	3.21	4.66	8.01	12.7
	6.0	1.16	1.36	1.85	2.96	4.80	10.8	23.0
	8.0	1.12	1.27	1.66	2.61	4.36	11.2	28.9
	10.0	1.09	1.20	1.51	2.2	3.78	10.5	28.5

APPENDIX 4

DOSAGE BUILDUP FACTOR FOR A FLAT MONODIRECTIONAL SOURCE

Substance	E_0, Mev	$\mu_0 x$ = 1	2	4	7	10	15
Water	0,5	2,63	4,29	9,05	20,0	35,9	74,9
	1,0	2,26	3,39	6,27	11,5	18,0	30,8
	2,0	1,84	2,63	4,28	6,96	9,87	14,4
	3,0	1,69	2,31	3,57	5,51	7,48	10,8
	4,0	1,58	2,10	3,12	4,63	6,19	8,54
	6,0	1,45	1,86	2,63	3,76	4,86	6,78
	8,0	1,36	1,69	2,30	3,16	4,00	5,47
Iron	0,5	2,07	2,94	4,87	8,31	12,4	20,6
	1,0	1,92	2,74	4,57	7,81	11,6	18,9
	2,0	1,69	2,35	3,76	6,11	8,78	13,7
	3,0	1,58	2,13	3,32	5,26	7,41	11,4
	4,0	1,48	1,90	2,95	4,61	6,46	9,92
	6,0	1,35	1,71	2,48	3,81	5,35	8,39
	8,0	1,27	1,55	2,17	3,27	4,58	7,33
	10,0	1,22	1,44	1,95	2,89	4,07	6,70
Lead	0,5	1,24	1,39	1,63	1,87	2,08	—
	1,0	1,38	1,68	2,18	2,80	3,40	4,20
	2,0	1,40	1,76	2,41	3,36	4,35	5,94
	3,0	1,36	1,71	2,42	3,55	4,82	7,18
	4,0	1,28	1,56	2,18	3,29	4,69	7,70
	6,0	1,19	1,40	1,87	2,97	4,69	9,53
	8,0	1,24	1,30	1,69	2,61	4,18	9,08
	10,0	1,11	1,24	1,54	2,27	3,54	7,70
Uranium	0,5	1,17	1,28	1,45	1,60	1,73	—
	1,0	1,30	1,53	1,90	2,32	2,70	3,60
	2,0	1,33	1,62	2,15	2,87	3,56	4,89
	3,0	1,29	1,57	2,13	3,02	3,99	5,94
	4,0	1,25	1,49	2,02	2,94	4,06	6,47
	6,0	1,18	1,37	1,82	2,74	4,12	7,79
	8,0	1,13	1,27	1,62	2,39	3,65	7,36
	10,0	1,10	1,21	1,48	2,12	3,21	6,58

APPENDIX 5

BUILDUP FACTOR OF ABSORBED ENERGY FOR AN ISOTROPIC POINT SOURCE

Substance	E_0, Mev	$\mu_0 r$ = 1	2	4	7	10	15	20
Water	0,5	2,46	4,93	13,4	36,1	71,5	163	305
	1,0	2,13	3,71	7,85	16,8	28,2	51,9	83,8
	2,0	1,85	2,82	4,99	8,67	12,9	20,0	28,6
	3,0	1,74	2,52	4,10	6,57	9,12	13,4	17,9
	4,0	1,59	2,18	3,37	5,18	7,01	10,1	13,0
	6,0	1,46	1,89	2,76	3,98	5,18	7,07	8,83
	8,0	1,38	1,74	2,42	3,36	4,28	5,70	7,00
	10,0	1,31	1,60	2,13	2,88	3,60	4,73	5,76

Appendix 5 (continuation)

Substance	E_0, Mev	$\mu_0 r$						
		1	2	4	7	10	15	20
Aluminum	0,5	2,61	4,92	11,4	26,9	49,2	104	185
	1,0	2,15	3,64	7,4	15,0	23,2	44,1	69,1
	2,0	1,80	2,74	4,93	8,63	12,8	20,2	28,3
	3,0	1,66	2,37	3,88	6,25	8,94	13,4	18,2
	4,0	1,54	2,09	3,24	5,05	6,93	10,2	13,5
	6,0	1,40	1,81	2,63	3,92	5,27	7,62	9,92
	8,0	1,31	1,62	2,26	3,25	4,28	6,10	7,88
	10,0	1,25	1,51	2,02	2,83	3,70	5,22	6,74
Iron	0,5	2,80	4,84	9,97	20,4	34,2	64,3	101
	1,0	2,19	3,58	7,00	13,6	21,9	38,8	58,5
	2,0	1,78	2,64	4,53	7,90	11,9	19,3	27,4
	3,0	1,58	2,21	3,61	6,05	8,82	14,0	19,8
	4,0	1,45	1,95	3,03	4,90	7,10	11,1	16,7
	6,0	1,30	1,63	2,38	3,73	5,35	8,67	12,7
	8,0	1,21	1,45	1,99	2,99	4,23	6,89	10,4
	10,0	1,16	1,35	1,78	2,61	3,69	6,17	9,89
Lead	0,5	1,51	1,80	2,19	2,61	3,01	3,52	—
	1,0	1,76	2,37	3,39	4,74	6,01	7,78	9,70
	2,0	1,58	2,10	3,14	4,70	6,32	9,05	12,0
	3,0	1,37	1,73	2,50	3,85	5,43	8,65	12,6
	4,0	1,24	1,49	2,09	3,25	4,79	8,46	13,9
	6,0	1,14	1,29	1,70	2,63	4,20	9,46	21,5
	8,0	1,10	1,21	1,50	2,21	3,50	8,60	23,0
	10,0	1,08	1,16	1,38	1,92	2,92	7,15	20,4

APPENDIX 6

ENERGY BUILDUP FACTOR FOR AN ISOTROPIC POINT SOURCE

Substance	E_0, Mev	$\mu_0 r$						
		1	2	4	7	10	15	20
Water	0,5	2,56	5,10	13,5	35,0	68,1	153	283
	1,0	2,10	3,58	7,42	15,2	25,1	45,7	73,2
	2,0	1,73	2,55	4,40	7,51	10,9	17,1	24,2
	3,0	1,58	2,18	3,42	5,35	7,35	10,7	14,3
	4,0	1,47	1,95	2,91	4,37	5,85	8,34	10,7
	6,0	1,36	1,72	2,40	3,39	4,36	6,28	7,35
	8,0	1,30	1,59	2,05	2,91	3,67	4,85	5,94
	10,0	1,26	1,51	1,97	2,63	3,26	4,26	5,19
Aluminum	0,5	2,45	4,43	10,0	22,94	41,7	87,0	152
	1,0	2,01	3,29	6,52	12,95	21,0	37,6	58,1
	2,0	1,67	2,43	4,21	7,21	10,6	16,6	23,2
	3,0	1,53	2,11	3,33	5,31	7,41	11,1	14,9
	4,0	1,44	1,88	2,82	4,28	5,81	8,42	11,2
	6,0	1,33	1,68	2,37	3,47	4,61	6,61	8,60
	8,0	1,27	1,54	2,09	2,95	3,86	5,45	7,04
	10,0	1,22	1,45	1,91	2,64	3,42	4,78	6,18

Appendix 6 (continuation)

Substance	E_0, Mev	$\mu_0 r$						
		1	2	4	7	10	15	20
Iron	0,5	2,02	3,20	6,16	12,1	19,9	36,8	57,7
	1,0	1,84	2,84	5,17	9,95	15,8	27,5	41,5
	2,0	1,60	2,28	3,82	6,54	9,78	15,6	22,2
	3,0	1,48	1,98	3,18	5,17	7,44	11,7	16,5
	4,0	1,38	1,80	2,71	4,30	6,14	9,59	13,6
	6,0	1,28	1,58	2,27	3,51	4,99	8,03	11,8
	8,0	1,21	1,45	1,99	2,99	4,23	6,89	10,3
	10,0	1,17	1,36	1,81	2,66	3,78	6,36	9,14
Tungsten	0,5	1,27	1,49	1,83	2,23	2,58	3,09	—
	1,0	1,42	1,80	2,51	3,51	4,49	6,05	(7,10)
	2,0	1,39	1,76	2,55	3,79	5,10	7,39	(9,66)
	3,0	1,31	1,64	2,38	3,69	5,26	8,47	12,4
	4,0	1,24	1,52	2,19	3,53	5,40	10,1	17,4
	6,0	1,16	1,35	1,87	3,07	5,15	12,3	27,8
	8,0	1,11	1,26	1,65	2,58	4,34	11,3	29,8
	10,0	1,09	1,20	1,51	2,25	3,71	10,2	27,3
Lead	0,5	1,24	1,41	1,68	1,99	2,26	2,27	(2,71)
	1,0	1,35	1,66	2,21	2,95	3,65	4,34	5,25
	2,0	1,35	1,68	2,37	3,41	4,49	6,33	8,27
	3,0	1,29	1,59	2,25	3,39	4,74	7,46	10,7
	4,0	1,23	1,49	2,06	3,20	4,72	8,33	13,7
	6,0	1,15	1,33	1,79	2,87	4,70	10,91	25,2
	8,0	1,11	1,24	1,59	2,48	4,11	10,68	29,5
	10,0	1,09	1,19	1,46	2,16	3,49	9,25	27,6
Uranium	0,5	1,17	1,29	1,48	1,67	1,84	2,05	—
	1,0	1,30	1,54	1,94	2,45	2,91	3,59	—
	2,0	1,30	1,59	2,13	2,92	3,71	5,01	(6,08)
	3,0	1,25	1,51	2,07	3,01	4,10	6,26	8,77
	4,0	1,21	1,43	1,93	2,88	4,11	6,92	10,9
	6,0	1,14	1,30	1,70	2,61	4,08	8,75	18,3
	8,0	1,10	1,22	1,53	2,27	3,61	8,69	20,9
	10,0	1,08	1,17	1,42	2,02	3,16	8,04	20,8

APPENDIX 7

ENERGY BUILDUP FACTORS FOR A FLAT MONO-DIRECTIONAL SOURCE

Substance	E_0, Mev	$\mu_0 x$					
		1	2	4	7	10	15
Water	0,5	2,75	4,49	9,11	20,2	34,5	70,6
	1,0	2,21	3,28	5,89	10,7	16,6	28,3
	2,0	1,73	2,42	3,87	6,08	8,74	12,8
	3,0	1,58	2,09	3,16	4,79	6,44	9,23
	4,0	1,47	1,91	2,74	4,00	5,28	7,24
	6,0	1,36	1,69	2,33	3,26	4,17	5,74
	8,0	1,29	1,56	2,07	2,78	3,49	4,71

Appendix 7 (continuation)

Substance	E_0, Mev	$\mu_0 x$					
		1	2	4	7	10	15
Iron	0,5	2,09	2,96	4,91	8,39	12,5	20,9
	1,0	1,89	2,68	4,45	7,57	11,2	18,2
	2,0	1,61	2,20	3,44	5,51	7,85	12,2
	3,0	1,49	1,93	2,95	4,59	6,38	9,67
	4,0	1,39	1,78	2,60	3,96	5,47	8,27
	6,0	1,28	1,57	2,19	3,25	4,47	6,87
	8,0	1,22	1,45	1,93	2,80	3,82	5,94
	10,0	1,17	1,36	1,77	2,51	3,44	5,48
Lead	0,5	1,24	1,39	1,61	1,84	2,04	—
	1,0	1,37	1,65	2,12	2,71	3,28	4,17
	2,0	1,36	1,68	2,28	3,14	4,03	5,48
	3,0	1,31	1,61	2,23	3,21	4,31	6,33
	4,0	1,24	1,45	1,99	2,95	4,09	6,70
	6,0	1,15	1,32	1,73	2,60	3,98	7,78
	8,0	1,12	1,22	1,53	2,23	3,39	6,88
	10,0	1,09	1,17	1,40	1,93	2,81	5,60
Uranium	0,5	1,17	1,28	1,44	1,60	1,73	—
	1,0	1,29	1,51	1,87	2,28	2,65	3,52
	2,0	1,30	1,57	2,06	2,73	3,38	4,60
	3,0	1,26	1,50	2,01	2,80	3,67	5,38
	4,0	1,21	1,43	1,87	2,67	3,62	5,66
	6,0	1,14	1,30	0,67	2,41	3,51	6,41
	8,0	1,11	1,22	1,50	2,12	3,10	5,92
	10,0	1,08	1,18	1,40	1,90	2,74	5,26

APPENDIX 8

CONSTANTS FOR CALCULATING DOSAGE BUILDUP FACTOR FOR AN ISOTROPIC POINT SOURCE

Substance	E_0, Mev	A_1	α_1	α_2
Water	0,5	24	0,138	0,0
	1,0	11,0	0,104	0,030
	2,0	6,4	0,076	0,092
	3,0	5,2	0,062	0,108
	4,0	4,5	0,056	0,117
	6,0	3,6	0,050	0,124
	8,0	3,0	0,045	0,128
	10,0	2,7	0,042	0,130
Aluminum	1,0	8,0	0,11	0,044
	2,0	5,5	0,082	0,093
	3,0	4,5	0,074	0,116
	4,0	3,8	0,066	0,130
	6,0	3,1	0,064	0,152
	8,0	2,3	0,062	0,150
	10,0	2,25	0,060	0,128

Appendix 8 (continuation)

/361

Substance	E_0, Mev	A_1	α_1	α_2
Iron	0,5	10	0,0948	0,0212
	1,0	8,0	0,0895	0,04
	2,0	5,5	0,0788	0,07
	3,0	5,0	0,074	0,075
	4,0	3,75	0,075	0,082
	6,0	2,9	0,0825	0,075
	8,0	2,35	0,0333	0,0546
	10,0	2,0	0,095	0,0116
Tungsten	1,0	3,0	0,043	0,148
	2,0	2,9	0,069	0,188
	3,0	2,7	0,086	0,134
	4,0	2,05	0,118	0,070
	6,0	1,2	0,171	0,00
	8,0	0,7	0,205	0,052
	10,0	0,6	0,212	0,144
Lead	0,5	1,65	0,032	0,296
	1,0	2,45	0,045	0,178
	2,0	2,60	0,071	0,103
	3,0	2,15	0,097	0,077
	4,0	1,65	0,123	0,064
	6,0	0,96	0,175	0,059
	8,0	0,67	0,204	0,067
	10,0	0,50	0,214	0,08

APPENDIX 9

CONSTANTS FOR CALCULATING ENERGY BUILDUP FACTOR FOR AN ISOTROPIC POINT SOURCE

Substance	E_0, Mev	A_1	α_1	α_2
Water	0,7	20	0,115	—0,039
	1,0	12	0,095	0,016
	2,0	6,4	0,067	0,086
	3,0	4,9	0,069	0,1083
	4,0	4	0,050	0,1195
Iron	0,5	11,0	0,0884	0,0185
	1,0	9,0	0,082	0,0257
	2,0	6,0	0,0735	0,040
	3,0	4,6	0,0725	0,059
	4,0	3,5	0,073	0,065
	6,0	2,6	0,0785	0,0718
	8,0	2,0	0,0851	0,0588
	10,0	1,6	0,093	0,0363
Lead	0,5	2,20	0,013	0,140
	1,0	2,65	0,038	0,141
	2,0	2,69	0,568	0,1385
	3,0	2,18	0,080	0,133
	4,0	1,68	0,105	0,125
	5,11	1,19	0,135	0,1135
	6,0	0,87	0,1675	0,0995
	8,0	0,45	0,206	0,0156
	10,0	0,30	0,221	0

APPENDIX 10

DOSAGE BUILDUP FACTOR OF γ-RADIATION OF AN ISOTROPIC POINT SOURCE AS A FUNCTION OF THE ATOMIC NUMBER OF SHIELDING MATERIAL

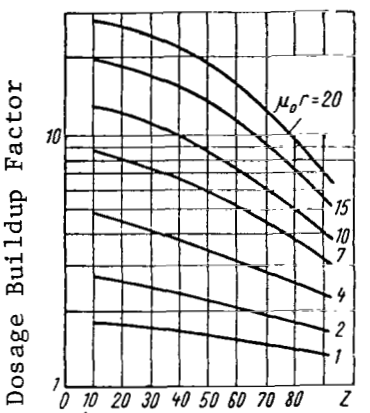

a

a- Initial Energy 2 Mev

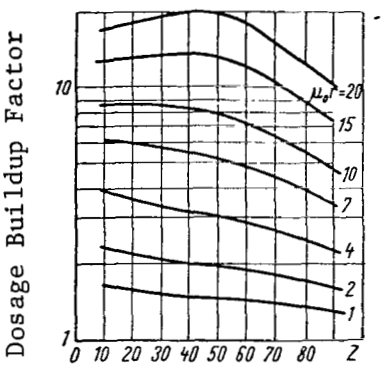

b

b- Initial Energy 3 Mev

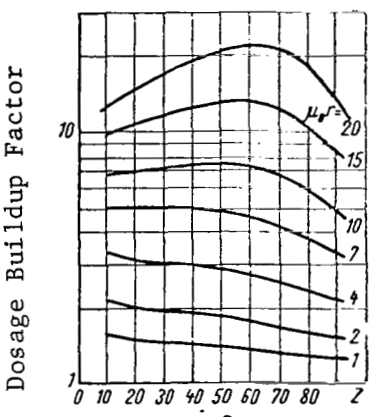

c

c- Initial Energy 4 Mev

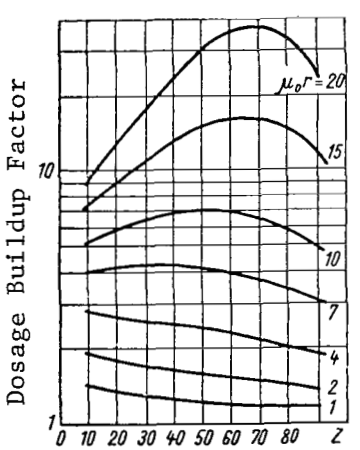

d

d- Initial Energy 6 Mev

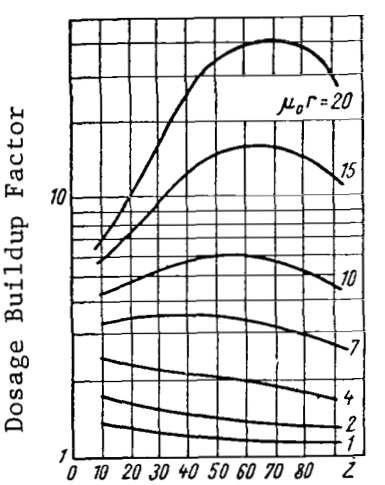

e

e- Initial Energy 8 Mev

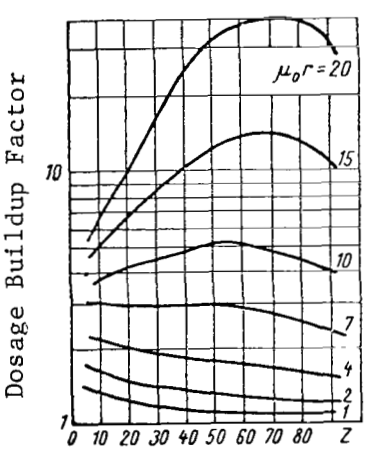

f

f- Initial Energy 10 Me

APPENDIX 11

GAMMA-RADIATION FORMED DURING CAPTURE OF THERMAL NEUTRONS

/364

Element	Spectrum Type	Number of γ-quanta emitted in a given energy interval (Mev) per each 100 captures					mean no. of photons per capture	Maximum energy of γ-quantum Mev	Radioactive decay with emission of γ-radiation [a]
		0—1	1—3	3—5	5—7	>7			
Al	1	?	>13	77	21	35	~2	7,724	2,3min Al^{28}: 100 (1,8)
Sb	3 [b]	?	~80	36	12			6,80	
As	3 [b]	?	~80	47	22	1	2,7	7,30	
Ba	3 [b]	?	~80	75	14	1		9,23	
Be [c]	1	0	0	50	75	0		6,814	
Bi [c]	1	0	0	100	0	0		4,17	
B^{10} [d]	4	0	0	0	0	0		0,478	
Cd	3 [b]	>120	20	73	17	1	4,1	9,046	
Cd^{113}		123	>44						
Ca	2	?	50	60	101	2,4		7,83	
C	1	?	<30	100	0	0	1,3	4,95	
Cl	2	?	20	13	18	21	3,1	8,56	
Cr	1 [b]	>37	16	12	18	69	>2	9,716	
Co	2 [b]	?	?	36	49	8		7,486	5,3 years Co^{60}: 100 (1,17) 100 (1,33)
Cu	1 [b]	?	?	>23	22	42	2,6	7,914	
F	1	?	?	?	35	0		6,63	12sec F^{20}: :100 (1,63)
Cd	3 [b]	?	80	23	4	2	3,9	7,78	
Au	3 [b]	?	?	66	38	0	3,5	6,494	
H [c]	1	0	100	0	0	0		2,230	
In	3 [b]	?	?	36	4	0	3,3	5,86	54,3 min In^{116}: 18 (2,1) 15 (1,49) 54 (1,27) 39 (1,09)
I	3	—	?	?	?	?		7,0—0,4	
Fe	1 [b]	?	<10	24	22	50	1,7	10,16	
Pb [c]	1	0	0	0	7	93		7,38	
Li^6	4	0	0	0	0	0		0	
Mg	2	?	>59	110	25	11		9,216	9,58 min Mg^{27}: 10 (0,84) 2 (1,01)
Mn	2 [b]	?	?	>27	30	27	2,6	7,261	2.59hr. Mn^{56}: 100 (0,845), 25 (1,81) 15 (2,13)
Hg	3 [b]	?	?	86	41	0	3,3	6,446	
Mo	3 [b]	?	?	84	26	3		9,15	
Ni	1	?	?	>14	30	72		8,997	

Appendix 11 (continuation)

Element	Spectrum Type	Number of γ-quanta emitted in a given energy interval (Mev) per each 100 captures					mean no. of photons per capture	Maximum energy of γ-quantum Mev	Radioactive decay with emission of γ-radiation [a]
		0—1	1—3	3—5	5—7	>7			
Nb	3[b]	?	?	54	14	0	2,6	7,19	
N	2,4	?	<5	>35	90	39		10,8	
P	2	?	?	115	43	11		7,94	
Pt	3[b]	?	~120	45	15	1		7,92	
K	2	?	36	36	32	12		9,28	
Pr	3[b]	?	~80	34	8	0		5,83	19 hrs Pr^{142} : 4(1,58)
Rh	3[b]	?	~70	38	10	0		6,79	
Sm	3[b]	?	~150	45	5	1	5,6	7,89	
Sc	3[b]	?	?	63	29	14		8,85	85 days Sc^{46} 100 (1,12) 100 (0,89)
Se	3[b]	?	?	65	27	11		10,483	
Si	2	?	>100	229	41	16		10,55	
Ag	3[b]	?	~90	70	17	0,5	2,9	7,27	
Na	2	≈100	>50	61	29	0	<2	6,41	14,9hrs Na^{24} 100 (2,76) 100 (1,38)
Sr	(2—3)[b]	?	~140	62	49	13		9,22	
S	2	?	>19	80	91	8		8,64	
Ta	3[b]	—	~50	26	2	0		6,07	
Te	3[b]	?	~100	76	62	0		6,54	
Sn	3[b]	?	?	139	33	4		9,35	
Ti	2[b]	>50	100	33	99	10		9,39	
W	3[b]	?	?	53	14,5	0,5		7,42	
V	3[b]	?	?	24	54	18	2,5	7,305	3,74 min V^{52}:100 (1,46)
Zn	(2—3)[b]	?	?	48	29	17		9,51	250 days Zn^{65} : 2,5 (1,12)
Zr^{e}	3[b]	?	?	113	35	4		8,66	65 days Zr^{95} : 98(0,75) 35 days Nb^{100} (0,76)

a. The period of half-decay is given first. In addition, the number of γ-quanta having energies of 750 kev which are formed per each 100 neutron captures are given. The energy of a γ-quantum is given in the parentheses

b. Unauthorized numbers of quanta are given for these elements; for all others, the intensities of only authorized lines are given.

c. For these elements, the maximum energy of γ-quanta belongs only to photons of a very high energy interval. For example, for lead seven γ-quanta have an energy between 5 - 7 Mev; more accurately,

all of these quanta have an energy of 6.73 Mev.

d. When a neutron is absorbed by boron-10, α- and γ-particles are emitted, and an excited nucleus of lithium-7 is formed, which emits soft (0.47 Mev) γ-radiation (94 quanta per 100 captures).

e. Intensity of captured γ-radiation is determined within an accuracy of 50%.

REFERENCES

1. Nuclear Engineering Handbook. McGraw-Hill Book Company, Inc., 1958. /366

2. Rockwell, T. Shielding of Nuclear Reactors (Zashchita yadernykh reaktorov). Izd-vo Inostr. Lit., Moscow, 1958.

3. Price, B.J., et al. Shielding from Nuclear Radiation (Zashchita ot yadernykh izlucheniy). Izd-vo Inostr. Lit., Moscow, 1959.

4. Popov, V. I. Conversion from a Point and other Simple Forms of a Source to a Cylinder. In the Collection: "Instruments and Methods for Analyzing Radiation (Preobrazovaniye ot tochki i drugikh prosteyshikh form istochnika k tsilindru. V sb. "Pribory i metody analiza izlucheniy"). Gosatomizdat, Moscow, 1962.

5. Marchuk, G. I. Methods of Designing Nuclear Reactors (Metody rascheta yadernykh reaktorov). Gosatomizdat, Moscow, 1961.

6. Devison, B. Theory of Neutron Transfer (Teoriya perenosa neytronov). Atomizdat, Moscow, 1960.

7. Gol'dshteyn, G. Bases of Reactor Shieldings (Osnovy zashchity reaktorov) Gosatomizdat, Moscow, 1961.

8. Nelipa, N. F. Introduction to the Theory of Multiple Particle Scattering (Vvedeniye v teoriyu mnogokratnogo rasseyaniya chastits). Atomizdat, Moscow, 1960.

9. Albert, R. D. and Wellton, A. Simplified Theory of Neutron Attenuation and Application to Reactor Shield Design, WAPD-15 (decl. December, 1955).

10. Chapman, G. T. and Storrs, C. U. Effective Neutron Removal Cross-Sections for Shielding, AECD-3978 (ORNL-1843), September 19, 1955.

11. Sourgeois, J. et al. Report No. 1190 (France) Presented at the Second International Conference on the Peaceful Utilization of Atomic Energy (Doklad No. 1190 [Frantsiya], predstavlennyy na Vtoryyu mezhdunarodnuyu konferentsiyu po mirnomu ispol'zovaniyu atomnoy energii). Geneva, 1958.

12. Kukhtevich, V. I. et al. Atonmaya Energiya, 5, 5, 565, 1958.

13. Degtyarev, S. F. et al. Neutron Physics. A Collection of Articles (Neytronnaya fizika. Sb. statey). Edited by P. A. Krupitskiy. Gosatomizdat, Moscow, 1961.

14. Kukhtevich, V. I., Sinitsyn, B. I. Atomnaya Energiya, 10, 5, 511, 1961.

15. Broder, D. A. et al. Atomnaya Energiya, 6, 5, 578, 1959.

16. Aronson, R. et al. Penetration of Neutrons from a Point Isotropic Monoenergetic Sources in Water, Report No. 40-6269, 1954.

17. Broder, D. A., Kutuzov, A. A. et al. Atomnaya Energiya, 7, 10, 313, 1959.

18. Sinitsyn, B. I., Tsypin, S. G. Atomnaya Energiya, 12, 4, 306, 1962.

19. Glasstone, S. Principles of Nuclear Reactor Engineering, Sec. 10, 78-10, 79, Van Nostrand, Princeton, New Jersey, p. 600, 1956.

20. Material from the Atomic Energy Commission, USA, Vol. 1. Physics of Nuclear Reactors (Materialy komissii po atomnoy energii SShA, t. 1. Fizika yadernykh reaktorov). 1958.

21. Reitz, D. Allowable Nuclear Reactor Radiations for a Manned Space Station in Cosmic Ray Environment, IAS Paper, No. 60-62, 1960.

22. Kramer-Ageyev, Ye. A., Mashkovich, V. P. Dosage Distribution of Fission Neutrons in Certain Shielding Media. In the Collection "Problems of Dosimetry and Shielding from Radiation" (Dozovoye raspredeleniye neytronov deleniya v nekototykh zashchity sredakh. V sb. "Voprosy dozimetrii i zashchity ot izlucheniy"). Edited by V. I. Ivanov. No. 1. Gosatomizdat, Moscow, 1962.

23. Leypunskiy, O. I. et al. Propagation of Gamma-Quanta in Matter (Rasprostraneniye gamma-kvantov v veshchestve). Fizmatgiz, Moscow, 1960.

24. Goldstein, H., Wilkins, J. Calculations of the Penetration of Gamma-Rays, Final Report, No. 40-3075, 1954.

25. Galishev, V. S. et al. Uspekhi Fiz. Nauk, 61, 161, 1957.

26. Reactor Physics Constant, ANL-58, 1958. /367

27. Bibergal', A. B., Leshchinskiy, N. I. Atomnaya Energiya, 8, 4, 372, 1960.

28. Gorshkov, V. V. Gamma-Radiation of Radioactive Materials and Design Elements for Shielding from Radiation (Gamma-Izlucheniye radioaktivnykh tel i elementov raschetov zashchity ot izlucheniy). Izd-vo AN SSSR, Moscow, 1959.

29. Kimel', L. R. Atomnaya Energiya, 10, 2, 173, 1961.

30. Berger, M. J. J. Res. Nat. Bur. Standards, 56, 111, 1956.

31. Gusev, N. G. Handbook on Radioactive Radiation and Shielding (Spravochnik po radioaktivnym izlucheniyam i zashchite). Medgiz, Moscow, 1956.

32. Mikhaylov, L. M., Aref'yeva, Z. S. Atomnaya Energiya, 11, 2, 187, 1961.

33. Green, M. Nucleonics, 17, 10, 77, 1959.

34. Gusev, N. G., Kovalev, Ye. Ye. Nomogram for Designing Shielding from Gamma-Rays (Nomogrammy dlya rascheta zashchity ot gamma-luchey). Atomizdat, Moscow, 1959.

35. Broder, D. L. et al. Atomnaya Energiya, 12, No. 2, 129, 1962.

36. Marchuk, G. I. Atomnaya Energiya, 11, No. 4, 356, 1961.

37. Gordeyev, I. V. et al. Handbook on Nuclear-Physical Constants for Designing Reactors (Spravochnik po yaderno-fizicheskim konstantam dlya rascheta reaktorov). Atomizdat, Moscow, 1960.

38. Hughes, D. J. Atlas of Effective Neutron Cross Sections (Atlas effektivnykh neytronnykh secheniy). Izd-vo Inostr. Lit., Moscow, 1959.

39. Broder, D. L. et al. Atomnaya Energiya, 8, No. 1, 49, 1960.

40. Glauco, P. Biological Shielding of Nuclear Rockets, XI Internat. Astronaut. Congr., Stockholm, 1960.

41. Wood, D. E. Nucl. Sci. Engng., 5, 1, 45, 1959.

42. Broder, D. L. et al. Atomnaya Energiya, 3, No. 7, 55, 1957.

43. Gusev, N. G., Kovalev, Ye. Ye. et al. Shielding from Radiation of Extended Sources (Zashchita ot izlucheniy protyazhennykh istochnikov). Gosatomizdat, Moscow, 1961.

44. Kimel', L. R. Atomnaya Energiya, 7, No. 3, 265, 1959.

45. Beynam, E. Atomkernenergie, 11, 11, 1961.

46. Kimel', L. R. Methods of Non-linear Gradient Programming for Designing a Minimum Weight Shielding (Metody nelineynogo gradientnogo programmirovaniya dlya rascheta zashchity minimal'nogo vesa). In the Collection: Instruments and Methods of Analyzing Radiation (Pribory i metody analiza izlucheniy). Gosatomizdat. Moscow, 1962.

47. Klahr, C. N. Nucleonic, 19, 110, 112, 1961.

48. Kukhtevich, V. I., Tsypin, S. G. Atomnaya Energiya, 5, 4, 1958.

49. Bouguet, F. L. IRE Transactions, 9, 2, April, 1962.

50. Myron, M., Newgard, J. I. Nucleonics, 16, 7, 66, 1958.

51. Miss. and Rockets, 9, 6, 13, 1961.

52. Borob'yev, V. A. Atomnaya Energiya, 15, No. 1, 1963.

53. Moteff, J. Neutron Dosimetry, Vienna, 1963.

54. Klahr, C., Held, K. TID 6302.

55. Berga, J. Air Force Inst. Techn., March, 1962.

56. Kirn, F. S., Kennedy Radiology, 63, 1, 1954.

57. Peebls, G. H. Rep. R-240. The Rand Corporation, Santa Monica, California.

58. Raso, D. J. Health Physik, 5, 3/4, 126, 1961.

59. Reactor Handbook Second Edition, VIII, p. B.

60. Reitz, D. Aerospace Engng., 20, 4, 1961.

61. Sheffild, R. D. Convair, Fort Worth Report MR-N-186 (NARF-57-62T), 1957.

62. Granford, W., Miller, R. A. TID-6302.

63. Hunter, M. W., and Techirgi, J. M. The Advantages of High Thrust Space Vehicles, ARS Preprint, 991-59.

64. Konecci, E. B. et al. Aerospace Engng., 19, 33, 1960.

65. Konecci, E. B., Trapp, R. F., Aerospace Med., 30, 7, 487, 1959.

66. Himmel, S. C., Dugan, J. F. Aerospace Engng., 20, 7, 18, 1961.

67. Flagy, A. H. et al. Techn. Session Preprints Amer. Astronaut. Soc., 8, 1960.

68. Miller, G. H. Feasibility Study of Atomic Powered Rockets. Report Presented at the 14th Yearly Meeting of the American Rocket Society (Doklad predstavlennyy na 14-e yezhegodnoye sobraniye Amerikanskogo raketnogo obshchestva). Washington, November 16-20, 1959.

69. Trapp, R. F. et al. Aerospace Engng., 19, 2, 49, 1960.

70. Keshishian, V. Shield for SNAP Reactors, ARS, Preprint, 1334-60

71. Bussard, R.W., DeLauer, R.D. Rockets with Atomic Engines /368
(Raketa s atomnym dvigatelem). Izd-vo Inostr. Lit., Moscow, 1960.

72. Mironov, B. N. Atomnaya Energiya, 12, No. 3, 211, 1962.

73. Bergel'son, B. R. Atomnaya Energiya, 10, No. 4, 388, 1961.

74. Fischer, E. Nucl. Sci. Engng., 1, 222, 1956.

75. Beiman, E. Atomkernenergie, 6, 6, 233, 1961.

76. Hughes, D. J. Neutron Studies on Nuclear Reactors (Neytronnyye issledovaniya na yadernykh kotlakh). Izd-vo Inostr. Lit., Moscow, 1954.

77. Mesler, R. Nucleonics, 18, 1, 73, 1960.

78. Mesler, R. Nucleonics, 14, 8, 65, 1956.

79. Eastwood, T. A. Nucleonics, 19, 1, 1961.

80. Lewis, W. B. Nucleonics, 19, 4, 1961.

81. Kattwinkel, W. Atomkernenergie, 4, 11, 442, 1959.

82. Mecger, F. W. Nucl. Sci. Engng., 4, 1, 96, 1958.

83. Sanitary Rules for Working with Radioactive Substances and Sources of Ionizing Radiation (Sanitarnyye pravila raboty s radioaktivnymi veshchestvami i istochnikami ioniziruyushchikh izlucheniy). Gosatomizdat, Moscow, 1960.

84. Gusev, N. G. Principles for Designing Maximum Permissible Levels of Outer Streams of Ionizing Radiation. In the Collection: "Studies in the Field of Dosimetry and Ionizing Radiation" (Printsipy rascheta predel'no dopustimykh urovney vneshnikh potokov ioniziruyushchikh izlucheniy. V. sb. "Issledovaniya v oblasti dozimetrii ioniziruyushchikh izlucheniy). Izd-vo AN SSSR, Moscow, 1957.

Scientific Translation Service
1144 Descanso Dr.
La Canada, California

NASA-Langley, 1966

"The aeronautical and space activities of the United States shall be conducted so as to contribute . . . to the expansion of human knowledge of phenomena in the atmosphere and space. The Administration shall provide for the widest practicable and appropriate dissemination of information concerning its activities and the results thereof."

—NATIONAL AERONAUTICS AND SPACE ACT OF 1958

NASA SCIENTIFIC AND TECHNICAL PUBLICATIONS

TECHNICAL REPORTS: Scientific and technical information considered important, complete, and a lasting contribution to existing knowledge.

TECHNICAL NOTES: Information less broad in scope but nevertheless of importance as a contribution to existing knowledge.

TECHNICAL MEMORANDUMS: Information receiving limited distribution because of preliminary data, security classification, or other reasons.

CONTRACTOR REPORTS: Technical information generated in connection with a NASA contract or grant and released under NASA auspices.

TECHNICAL TRANSLATIONS: Information published in a foreign language considered to merit NASA distribution in English.

SPECIAL PUBLICATIONS: Information derived from or of value to NASA activities. Publications include conference proceedings, monographs, data compilations, handbooks, sourcebooks, and special bibliographies.

TECHNOLOGY UTILIZATION PUBLICATIONS: Information on technology used by NASA that may be of particular interest in commercial and other nonaerospace applications. Publications include Tech Briefs; Technology Utilization Reports and Notes; and Technology Surveys.

Details on the availability of these publications may be obtained from:

SCIENTIFIC AND TECHNICAL INFORMATION DIVISION

NATIONAL AERONAUTICS AND SPACE ADMINISTRATION

Washington, D.C. 20546